Development and Operation of High-Precision Laser Systems for the Search for Ultra-Light Dark Matter and Spectroscopy of Molecular Hydrogen Ions

Inaugural-Dissertation

zur Erlangung des Doktorgrades
der Mathematisch-Naturwissenschaftlichen Fakultät
der Heinrich-Heine-Universität Düsseldorf

vorgelegt von

Victor Alexander Vogt
aus Düsseldorf

Düsseldorf, Dezember 2025

Aus dem Institut für Experimentalphysik
der Heinrich-Heine-Universität Düsseldorf

Gedruckt mit der Genehmigung der
Mathematisch-Naturwissenschaftlichen Fakultät der
Heinrich-Heine-Universität Düsseldorf

Berichterstatter:

1. Professor Stephan Schiller, Ph.D.

2. Professor Dr. Stefan Ulmer

Tag der mündlichen Prüfung: 25.11.2025

Abstract

Two measurement campaigns aimed at searching for ultra-light dark matter via vibrational spectroscopy in iodine and acetylene required the development of ultra-stable laser systems. These systems were designed to achieve a spectral frequency noise density at the level of $10^{-13} - 10^{-12}\mathrm{Hz}^{-1/2}$ across Fourier frequencies ranging from 10 Hz to 100 kHz. Long-term frequency stability was also targeted to ensure minimal drift relative to transition linewidths over several days, enabling the potential detection of oscillatory variations in fundamental constants induced by a scalar dark matter field at the given resolution. The lasers were built and employed in the respective dark matter detectors, which yielded upper limits for the coupling strength for dark matter of masses in the range of 4×10^{-14} eV to 4×10^{-10} eV with respect to specific fundamental constants.

In addition, ultra-stable laser systems were developed for high-resolution optical spectroscopy of rovibrational transitions in the molecular hydrogen ions HD^+ and H_2^+, in both a Paul trap and a Penning trap, the latter in collaboration with HHU Düsseldorf and the MPIK Heidelberg. A transportable metrology system with hydrogen maser, frequency comb, reference laser, and phase-stabilized transfer laser was set up, largely fiber-coupled, and equipped with two fiber noise cancellations for the paths to the Penning trap ALPHATRAP. The system offers optical line widths of less than 10 Hz, at carrier frequencies of 260 THz, frequency stabilities in the range of less than 10^{-14} and, thanks to comparison via satellite with the international standard at the PTB Braunschweig, a frequency uncertainty in the range of less than 10^{-14}. It also enabled the generation of radiation in the mid-infrared range via difference frequency generation as well as remote control and automatic re-lock processes. The system was successfully transported over 300 km from Düsseldorf to Heidelberg. This thesis presents the first on/off signal measurement on a rovibrational transition in a single molecular ion, HD^+, indicative of an optical molecular transition.

Additionally research on resonators was conducted. The first fiber ring resonator incorporating a design with a zero coefficient of thermal expansion at temperatures achievable using conventional thermoelectric coolers ($T_{ZCTE} \approx -30\,^{\circ}\mathrm{C}$) was developed and characterized. Research was also conducted on optical resonators serving as mode cleaners optimized for low Fourier frequencies, with potential application in dark matter detection reaching below $10^{-15}\,\mathrm{Hz}^{-1/2}$ in frequency noise. In parallel, strategies for suppressing residual amplitude modulation were investigated, reaching contributions below the level of 10^{-17} in fractional frequency instability. Finally, the lowest ever recorded aging drift of a room-temperature graded resonator was observed in a NEXCERA-based optical reference at the level of $2 \times 10^{-18}\,\mathrm{s}^{-1}$.

Zusammenfassung

Zwei Messkampagnen zur Suche nach ultraleichter Dunkler Materie mittels optischer Spektroskopie in Jod und Acetylen erforderten die Entwicklung ultrastabiler Lasersysteme. Diese wurden so konzipiert, dass sie eine spektrale Frequenzrauschdichte von $10^{-13}\,\mathrm{Hz}^{-1/2}$ bis $10^{-12}\,\mathrm{Hz}^{-1/2}$ im Bereich von 10 Hz bis 100 kHz sowie langfristige Frequenzstabilität bieten, um Drift relativ zu den Übergangslinienbreiten über mehrere Tage zu minimieren. So konnten potenzielle oszillatorische Schwankungen von Fundamentalkonstanten durch ein skalares Dunkle-Materie-Feld untersucht werden. Die Laser kamen in zwei Detektoren zum Einsatz, die Obergrenzen für die Kopplungsstärke von Dunkler Materie mit Massen zwischen $4\times10^{-14}\,\mathrm{eV}$ bis $4\times10^{-10}\,\mathrm{eV}$ lieferte.

Zudem wurden Lasersysteme für die hochauflösende Spektroskopie von Rovibrationsübergängen in HD^+ und H_2^+ entwickelt, in Paul- und Penning-Fallen, Letztere in Kooperation mit der HHU Düsseldorf und dem MPIK Heidelberg. Ein transportables Metrologiesystem mit Wasserstoffmaser, Frequenzkamm, Referenzlaser und phasenstabilisierten Transferlaser wurde aufgebaut, weitgehend fasergekoppelt und mit zwei Faserrauschunterdrückungen für die Wege zur Penningfalle ALPHATRAP ausgestattet. Das System bietet optische Linienbreiten im Bereich von unter 10 Hz, bei Trägerfrequenzen von 260 THz, Frequenzstabilitäten im Bereich unter 10^{-14} und, dank des Vergleichs über Satellit mit dem internationalen Standard an der PTB Braunschweig, eine Frequenzunsicherheit im Bereich unter 10^{-14}. Es ermöglichte zudem die Erzeugung von Strahlung im mittleren Infrarotbereich per Differenzfrequenzgenerierung und bot Fernsteuerung und automatische Re-Lock-Prozesse. Das System wurde erfolgreich über 300 km nach Heidelberg transportiert. Erstmals wurde ein On/Off-Signal an einem Rovibrationsübergang in einem einzelnen Mölekülion, HD^+, gemessen, das auf einen optischen Übergang hinweist.

Zusätzlich wurden Untersuchungen zu Resonatoren durchgeführt. Der erste Faserringresonator wurde entwickelt und charakterisiert, der bei Temperaturen, die mit herkömmlichen thermoelektrischen Kühlern ($T_{ZCTE} \approx -30\,^\circ\mathrm{C}$) erreicht werden können, einen thermischen Ausdehnungskoeffizienten von Null aufweist. Außerdem wurden optische Resonatoren untersucht, die als Modenreiniger optimiert sind für niedrige Fourier-Frequenzen und potenziell in der Dunkle-Materie-Detektion mit Frequenzrauschen unter $10^{-15}\,\mathrm{Hz}^{-1/2}$ eingesetzt werden können. Parallel dazu wurden Strategien zur Unterdrückung der Restamplitudenmodulation untersucht, die zu Beiträgen unter 10^{-17} der relativen Frequenzinstabilität führten. Schließlich wurde in einer NEXCERA-basierten optischen Referenz die niedrigste jemals gemessene Alterungsdrift eines Raumtemperaturresonators auf einem Niveau von $2\times10^{-18}\,\mathrm{s}^{-1}$ beobachtet.

Acknowledgement

I would like to express my deepest gratitude to Prof. Stephan Schiller for providing me with the opportunity, guidance, and tools that made the work presented in this thesis possible. His support has been instrumental throughout this journey.

I would also like to thank Prof. Sven Sturm and Prof. Klaus Blaum from MPIK Heidelberg for giving me the opportunity to contribute to the collaborative project on laser spectroscopy of molecular hydrogen ions in a Penning trap funded by the Deutsche Forschungsgemeinschaft under grant: INST 208/809-1 FUGG, project number: 460457764.

I am grateful to my mentor, Prof. Axel Görlitz, for his guidance and support. I would like to thank Prof. Stefan Ulmer for kindly agreeing to act as my second examiner.

Special thanks go to U. Rosowski for his invaluable technical assistance and for organizing the transport of the metrology system from Düsseldorf to Heidelberg.

I am also grateful to I. V. Kortunov for his collaboration at MPIK Heidelberg and his continued support with the laser system from afar. I would also like to thank C. König and J. Morgner for their valuable assistance in setting up the system at MPIK.

I warmly thank I. V. Kortunov, C. J. Kwong, S. Alighanbari, R. Oswald, and my dear and cherished friend M. R. Schenkel for the many coffee breaks — both work-related and otherwise — and for their scientific insight, collaboration, and camaraderie throughout the years.

I would also like to thank D. Iwaschko and R. Gusek for their continuous technical support, and W. Bian for his assistance during the early stages of the dual cavity setup.

I am furthermore grateful to P. Schulte, Z. Hou, and M. Castelein for their valuable support and collaboration on the NEXCERA, dual cavities, and fiber ring resonator projects.

I wish to express my appreciation to all colleagues at MPIK Heidelberg, PTB Braunschweig, and HHU Düsseldorf with whom I had the pleasure to work with over the past five years.

I am also grateful to Prof. Stephan Schiller for reading the thesis and providing invaluable feedback, as well as to S. Alighanbari, M. Bohman, F. Heiße, C. J. Kwong, C. Wellers and R. Oswald for reviewing portions of the text or for helpful discussions related to it.

I sincerely thank my parents, Heike and Wolfgang, and my sister Julia for their constant support throughout this journey. I also thank my friends for their unwavering encouragement and companionship.

Finally, I want to thank my partner Valeria, who has been my pillar of strength since day one.

Decleration of Authorship

Ich versichere an Eides Statt, dass die Dissertation von mir selbständig und ohne unzulässige fremde Hilfe unter Beachtung der „Grundsätze zur Sicherung guter wissenschaftlicher Praxis an der Heinrich-Heine-Universität Düsseldorf“ erstellt worden ist.

. . . . . .

Tools and Assistance Statement

I used AI-based tools, including DeepL Pro and ChatGPT 4.0, to assist with grammar, wording, and clarity **after** writing the main text of this thesis, including the translation of the abstract into German. Additionally, I used ChatGPT 4.0 as an extended literature research tool only to help identify DOIs and references. All sources were subsequently verified through their respective official journal websites.

No scientific text, data analysis, figures, or other substantive content in this thesis was generated using AI. All scientific content (unless otherwise referenced), original text, and interpretations are entirely my own.

Every plot, graphic, and schematic of the main body of this thesis (Chapters 1 to 9) and Appendix A was created solely by me. Plots were generated using Mathematica 12, and schematics were produced in Keynote. The thesis was written using Lyx.

All images presented in the main body of this thesis, except one, were taken by me. The photo shown in the bottom panel of Figure 5.5 was kindly provided by M. Castelein.

Contents

Abstract i

Zusammenfassung iii

Acknowledgement v

Decleration of Authorship vii

Tools and Assistance Statement ix

List of Figures xv

List of Tables xix

Nomenclature xxv

1 Introduction: The Pursuit of Pure Monochromatic Light 1

2 Theoretical Background 9
2.1 Foundations of Optical Resonators . . . 10
2.1.1 Light Trapped in Time: Standing Wave Resonators . . . 10
2.1.2 Imperfect Realities: Understanding Optical Losses . . . 14
2.1.3 Directing Light: Fiber Types, Splitters, and Circulators . . . 16
2.1.4 Light in a Loop: Principles of Fiber Ring Resonators . . . 19
2.2 Resonators for Frequency Stabilization . . . 26
2.2.1 Anchoring Light: Resonators as Optical References . . . 26
2.2.2 Beating Drift: Thermal Expansion and Shielding . . . 30
2.2.3 Fundamental Limits: Thermal Noise in Resonators . . . 32
2.2.4 Fundamental Limits: Thermal Noise in Optical Fibers . . . 35
2.3 Stabilizing Light: The Pound-Drever-Hall Technique . . . 37
2.3.1 The Core Principle: Phase Modulation and Error Signals . . . 38
2.3.2 Offset Locking: Tuning the Frequency Gap . . . 42
2.3.3 Residual Amplitude Modulation: Limitations and Corrections . . . 44
2.4 Frequency Metrology: Measuring Light with Precision . . . 52
2.4.1 Noise Cancellation: Stabilizing Light Through Fibers . . . 53
2.4.2 Long-Term References: Hydrogen Masers and GNSS . . . 56

2.4.3 Putting It All Together: Frequency Analysis and Measurement 58

3 Ultra-Stable Laser Systems for Metrology 67
3.1 ULE-Based Dual Resonator System 68
3.1.1 Geometry and the Thermal Noise Floor 69
3.1.2 Experimental Apparatus 70
3.1.3 Resonator Properties 76
3.1.4 Real-Time Monitoring and Laser Stability 78
3.2 NEXCERA-Based Resonator 90
3.2.1 Geometry and the Thermal Noise Floor 91
3.2.2 Experimental Apparatus 92
3.2.3 Resonator Properties and Laser Frequency Stability 95
3.3 Frequency Metrology System 96
3.3.1 Setup and Architecture 98
3.3.2 System Characterization 105

4 Developments in Ultra-Stable Lasers 119
4.1 Mitigation of RAM below Thermal Noise 119
4.2 Transmission Filtering: Resonators as Mode Cleaners 126
4.3 An Ultra-Stable Optical Parametric Oscillator 133
4.4 Guidelines for Ultra-Stable Lasers at the 10^{-17} Level 134

5 Non-Cryogenic Fiber Ring Resonator 137
5.1 Concept and Design 138
5.2 Thermal Properties and Resonator Design 142
5.3 Experimental Apparatus 145
5.4 Resonator Characterization 148
5.5 Laser Frequency Stability and Thermal Sensitivity 151

6 Ultra-Low Drift of a Room-Temperature Reference 155

7 Search for Dark Matter in the Fourier Domain 169
7.1 Search for Dark Matter in Iodine 172
7.2 Search for Dark Matter in Acetylene 174

8 Precision Spectroscopy of Molecular Hydrogen Ions 177
8.1 Ion Trapping and Cooling 180
8.2 Spectroscopy of HD^+ in a Linear Paul Trap 1 193
8.3 Spectroscopy of HD^+ in a Linear Paul Trap 2 198
8.4 Spectroscopy of HD^+ in ALPHATRAP 200

9 Summary and Outlook 209

A From Wave to Metrology: A Tutorial **213**
A.1 Foundations of Light: Waves and Interfaces . . . 215
A.1.1 Light as a Wave: Electromagnetism and Polarization . . . 215
A.1.2 Boundaries of Light: Matching Fields at Interfaces . . . 217
A.1.3 Reflection and Transmission: The Fresnel View . . . 220
A.1.4 Layered Insight: The Transfer Matrix Method . . . 224
A.1.5 Mirrors of Light: The Physics of Dielectric Coatings . . . 226
A.1.6 Light Trapped in Time: Standing Wave Resonators . . . 232
A.1.7 Imperfect Realities: Understanding Optical Losses . . . 232
A.2 Gaussian Optics: Beams, Fibers, and Cavities . . . 232
A.2.1 Intensity in Focus: Transverse Profiles and the Helmholtz Equation . . . 232
A.2.2 The Ray Matrix Method: Understanding the $q-$Parameter . . . 243
A.2.3 Guiding Light: The Basics of Optical Fibers . . . 249
A.2.4 Keeping Light In: Conditions for Cavity Stability . . . 258
A.2.5 Mode Matching: Efficient Coupling Between Beams and Cavities . . . 261
A.2.6 A Quick Note on Cavity Modes . . . 264
A.3 Optical Components: Routing, and Modulating Light . . . 264
A.3.1 Directing Polarized Light: Wave Plates, Isolators, and Beam Splitters . . . 265
A.3.2 Steering with Sound: The Acousto-Optic Modulator . . . 269
A.3.3 Modulating Light with Voltage: The Electro-Optic Effect . . . 271
A.3.4 Directing Light: Fiber Types, Splitters, and Circulators . . . 274
A.3.5 Light in a Loop: Principles of Fiber Ring Resonators . . . 274
A.4 Essential Electronics: Lasers, RF, and Feedback Systems . . . 274
A.4.1 Coherent Light: How Lasers Work . . . 275
A.4.2 RF Electronics: Signals at High Frequencies . . . 278
A.4.3 Feedback Control: The PID Framework . . . 281
A.5 Optical Stability and Noise – From Linewidth to Limits . . . 283
A.5.1 Linewidth and Phase: Laser Stability Fundamentals . . . 283
A.5.2 Tracking Jitter: Measuring Phase and Frequency Noise . . . 286
A.5.3 Long-Term Fluctuations: Allan Deviation Analysis . . . 292
A.5.4 Understanding the Spectrum: Types of Noise . . . 295
A.5.5 Anchoring Light: Resonators as Optical References . . . 298
A.5.6 Beating Drift: Thermal Expansion and Shielding . . . 298
A.5.7 Fundamental Limits: Thermal Noise in Resonators . . . 298
A.5.8 Fundamental Limits: Thermal Noise in Optical Fibers . . . 298
A.6 Stabilizing Light: The Pound-Drever-Hall Technique . . . 298
A.6.1 The Core Principle: Phase Modulation and Error Signals . . . 299
A.6.2 Offset Locking: Tuning the Frequency Gap . . . 299
A.6.3 Residual Amplitude Modulation: Limitations and Corrections . . . 299
A.7 Frequency Metrology: Measuring Light with Precision . . . 299
A.7.1 Mode-Locked Lasers: The Foundation of Frequency Combs . . . 299
A.7.2 Noise Cancellation: Stabilizing Light Through Fibers . . . 307
A.7.3 Wavelength Meters: Measuring Optical Frequencies . . . 307
A.7.4 Long-Term References: Hydrogen Masers and GNSS . . . 310
A.7.5 Putting It All Together: Frequency Analysis and Measurement . . . 310

B Publications and Contribution **311**
B.1 Ultra-Light Dark Matter 313
B.1.1 Search for Dark Matter Using Iodine Spectroscopy 315
B.1.2 Search for Dark Matter Using Acetylene Spectroscopy 335
B.2 Spectroscopy of Molecular Hydrogen Ions 353
B.2.1 Rovibrational Spectroscopy of HD^+ 355
B.2.2 Rovibrational Spectroscopy of H_2^+ 363
B.3 Optical References and Frequency Metrology 371
B.3.1 Ultra-Stable Optical Parametric Oscillator 373
B.3.2 Design Guidelines for Ultra-Stable Lasers 393

Bibliography **413**

List of Figures

2.1 Illustration of a Standing Wave Resonator . . . 12
2.2 Schematic of Fiber TC and Circulator . . . 17
2.3 Schematic of SM and PM Fibers . . . 19
2.4 Schematic of a SFRR . . . 22
2.5 Schematic of a DFRR . . . 23
2.6 Simulation of a DFRR . . . 25
2.7 Cavity Shielding Setup . . . 28
2.8 Thermal Noise Floor of an otpical Fiber . . . 37
2.9 Classic PDH Error Signal . . . 40
2.10 Concept of the PDH Technique . . . 41
2.11 Offset Lock PDH Error Signal . . . 43
2.12 RAM Loss Coefficients . . . 49
2.13 RAM Induced Error Signal . . . 51
2.14 Motivation for Optical Fiber Links . . . 53
2.15 Concept of a FNC . . . 54
2.16 Frequency Metrology Setup . . . 58

3.1 Dual High-Finesse ULE Resonator Setup . . . 72
3.2 ULE Resonators and In-coupling Boxes . . . 74
3.3 Complete Dual Cavity ULE System in Lab 1 . . . 74
3.4 Free-Space FNC at 1064 nm . . . 75
3.5 Complete Dual Cavity ULE System in Lab 2 . . . 75
3.6 ULE System Laser Breadboard . . . 76
3.7 Transmission scan C2 . . . 77
3.8 ULE System Frequency Monitor Output 1 . . . 81
3.9 ULE System Frequency Monitor Output 2 . . . 82
3.10 ULE Cavities: Tilt Correlation with Beat Frequency . . . 83
3.11 ULE System Long Term Performance . . . 84
3.12 ULE System Allan Deviation Between Laboratories . . . 85
3.13 ULE Beat Allan Deviations in Tower Setup . . . 86
3.14 ULE Cavities Spectral Phase and Frequency Noise Density . . . 88
3.15 NEXCERA Cavity and Lock Schematic . . . 92
3.16 Nexcera Resonator Setup on a Trolley . . . 93
3.17 Transportable Nexcera System in Rack . . . 94
3.18 NEXCERA Finesse Measurement . . . 96

3.19 Schematic of the Metrology System . . . 100
3.20 Photograph and Schematic of the Fully Fiberized FNC . . . 101
3.21 Frequency Metrology System at HHU and MPIK . . . 103
3.22 Move from HHU Düsseldorf to MPIK Heidelberg . . . 104
3.23 Metrology System Allan Deviations - No Drift Mitigation . . . 106
3.24 Metrology System Allan Deviations - With Drift Mitigation . . . 108
3.25 Drift Mitigation and Wideband Frequency Selection . . . 110
3.26 Automated Relock of the OFC and Reference Light . . . 111
3.27 Linewidths of the Metrology System . . . 114
3.28 Metrology System Spectral Frequency Noise Density . . . 115
3.29 Metrology System FNC . . . 116
3.30 EDFA Spectral Frequency Noise Density . . . 117

4.1 ULE Resonator RAM Error Signal . . . 122
4.2 ULE Resonators RAM Landscapes . . . 124
4.3 ULE Resonators RAM Depth and Frequency Instability . . . 125
4.4 ULE Transmission Beat Phase Noise and Transfer Function . . . 128
4.5 ULE Transmission Beat Frequency Noise . . . 129
4.6 Incident and Transmission Beats of NEXCERA . . . 130
4.7 NEXCERA as Mode Cleaner . . . 132
4.8 NEXCERA Best Allan Deviation . . . 134

5.1 DFRR Ring Length Simulations . . . 141
5.2 DFRR Simulation . . . 144
5.3 Schematic of the Fiber Ring Resonator . . . 146
5.4 Photos of the DFRR and Temperature Stabilization . . . 147
5.5 Photographs of the DFRR Electronics . . . 148
5.6 DFRR Finesse and Linewidth Measurement . . . 150
5.7 DFRR ZCTE Measurement . . . 151
5.8 DFRR Linewidth Measurement . . . 152
5.9 DFRR Allan Deviation and CTE . . . 153

6.1 History of Material Aging Drifts . . . 156
6.2 Setup for the Long-Term Drift Measurement . . . 159
6.3 Maser Corrected Laser Frequency . . . 161
6.4 ZCTE of NEXCERA N118C . . . 162
6.5 Long-Term Drift of NEXCERA N118C . . . 164
6.6 Temperature-to-Frequency Correlation . . . 165

7.1 Search for UDM in Molecular Spectroscopy . . . 170
7.2 Spectral Frequency Noise Density for Iodine . . . 173
7.3 Spectral Frequency Noise Density for Acetylene . . . 175

8.1 Collage of HD^+ Structure and Energy Levels . . . 178
8.2 Schematic of a Linear RF Trap . . . 183
8.3 Schematic of a Penning Trap . . . 188

8.4 Schematic of the AT and PT in ALPHATRAP . . . 191
8.5 Schematic of a TCH for Beat Frequencies . . . 194
8.6 Linewidths of Beats in a TCH Measurement . . . 195
8.7 Allan Deviations from a TCH Analysis . . . 196
8.8 Frequency Noise in a TCH Measurement . . . 197
8.9 ULE Beat Linewdith in Lab 2 . . . 199
8.10 ULE Beat Allan Deviations in Lab2 . . . 199
8.11 On / Off Measurement Scheme in HD^+ . . . 205
8.12 Optical Rovibrational Transition in a Single Molecule . . . 206

A.1 Electromagnetic Wave Representation . . . 216
A.2 Visualization of Faraday's Law . . . 219
A.3 Reflection and Refraction at an Interface . . . 221
A.4 Visualization of Fresnel Equations . . . 223
A.5 Layered Design of a Dielectric Mirror . . . 227
A.6 GB Geometry . . . 238
A.7 Wavefront Structure of a Gaussian Beam . . . 239
A.8 Phase Evolution & Electric Field of Selected TEM Modes . . . 241
A.9 Spatial Profiles of Selected TEM Modes . . . 244
A.10 Shaping of Gaussian Beams via Selected Optical Elements . . . 246
A.11 GB Propagation Through a Thin Lens . . . 249
A.12 Structure of a Step Index Optical Fiber . . . 251
A.13 Spatial Profiles of Selected LP Modes . . . 256
A.14 Mode Overlap: TEM_{00} and LP_{01} . . . 257
A.15 Optical Resonator Supporting Gaussian Modes . . . 260
A.16 Simulation of Mode Matching . . . 263
A.17 Linear and Circular Polarization of EM Waves . . . 266
A.18 Waveplate and Polarizing Beam Splitter . . . 268
A.19 Isolator Using the Faraday Effect . . . 269
A.20 Principle of an AOM . . . 271
A.21 Concept of an EOM . . . 273
A.22 Diagram of a Solid-State Laser . . . 277
A.23 Schematic of Diode and Fiber Lasers . . . 278
A.24 Feedback Control with PID . . . 282
A.25 Power Spectrum and Phase Noise . . . 287
A.26 Spectral Frequency Noise Density . . . 289
A.27 Fourier Spectrum of Time Domain Data . . . 290
A.28 Frequency Noise Density Comparison . . . 290
A.29 Modified Allan Deviation . . . 294
A.30 Frequency Noise Type Plots . . . 297
A.31 Temporal Profile of Pulse Train . . . 302
A.32 Pulse Sharpness and Mode-Locking . . . 303
A.33 Temporal Profile of Gaussian Pulse . . . 304
A.34 Spectral Lines of an Optical Frequency Comb . . . 306
A.35 Michelson Wavelength Meter . . . 307

A.36 Fizeau Wavelength Meter 309

List of Tables

2.1 Parameters of an SMF-28 Optical Fiber 36

3.1 Thermal Noise Floor of one ULE Cavity 70
3.2 FSRs of the Dual ULE Cavities 78
3.3 ULE Beat Frequency Sensitivities 79
3.4 Thermal Noise Floor of the NEXCERA Cavity 91
3.5 Rovibrational Transitions in ALPHATRAP 97
3.6 OFC Parameter Table 108

5.1 DFRR Splitter Parameter Table 140
5.2 DFRR Experimental Resonator Characteristics 149
5.3 DFRR CTE Table 154

6.1 Thermal Properties in Different Resonators 166

7.1 Sensitivity factors of the UDM detectors 172

8.1 Fine Splitting of HD^+in $1S\sigma$, $(v, N = 0/1)$ 180
8.2 Multipole Transitions in HD^+ 202
8.3 All 12 Spin Conserving Transitions. 203

A.1 Noise Type Table 298

B.1 List of Publications 311

Nomenclature

AC	Alternating Current
ACES	Atomic Clock Ensemble in Space
ADEV	Standard Allan Deviation
AM	Amplitude Modulation
AOM	Acousto-Optic Modulator
APC	Angled Physical Contact Fiber Connector
AT	Analysis Trap, Penning Trap Segment
AVI	Active Vibration Isolation Unit
BBR	Blackbody Radiation
BS	Beam Splitter
BSM	Physics Beyond the Standard Model
CCD	Charge-Coupled Device
CEO	Carrier-Envelope Offset
CERN	Conseil Européen pour la Recherche Nucléaire
CPT	Charge, Parity, and Time Reversal Symmetry
CTE	Coefficient of Thermal Expansion
DAC	Digital-to-Analog Converter
DAQ	Data Acquisition
DC	Direct Current
DDS	Direct Digital Synthesizer
DFG	Difference Frequency Generation Process

DFG	Difference Frequency Generation
DFRR	Dual-Splitter Fiber Ring Resonator
DFT	Discrete Fourier Transform
DSB	Double Sideband
DUT	Device Under Test
EBIT	Electron Beam Ion Trap
EDFA	Erbium-Doped Fiber Amplifier
EM	Electromagnetic Wave
EOM	Electro-Optic Modulator
ESR	Electron Spin Resonance Transition
FC	Ferrule Connector for Optical Fibers
FCT	Fundamental Constants in Physics
FEM	Finite Element Method
FFT	Fast Fourier Transform
FM	Frequency Modulation
FNC	Fiber Noise Cancellation
FP	Fabry-Pérot Resonator
FRR	Fiber Ring Resonator
FS	Fused Silica
FSR	Free Spectral Range
FWHM	Full Width at Half Maximum
GB	Gaussian Beam
GNSS	Global Navigation Satellite System
GPS	Global Positioning System
GR	General Relativity Theory
HCF	Hollow-Core Fiber
HHU	Heinrich-Heine-Universität Düsseldorf

HO	Harmonic Oscillator
ISS	International Space Station
KAGRA	Kamioka Gravitational Wave Detector
LIGO	Laser Interferometer Gravitational-Wave Observatory
LISA	Laser Interferometer Space Antenna
LO	Local Oscillator
LP	Linearly Polarized Mode
MACHO	Massive Astrophysical Compact Halo Object
MC	Optical Resonator as Mode Cleaner
MDEV	Modified Allan Deviation
MHI	Molecular Hydrogen Ions
MIR	Mid-Infrared Region of the Electromagnetic Spectrum
MJD	Modified Julian Date
MPIK	Max-Planck-Institut für Kernphysik Heidelberg
MS	Mating Sleeve / Fiber Connector Alignment Sleeve
MW	Microwave
NA	Numerical Aperture
NIR	Near-Infrared Region of the Electromagnetic Spectrum
NIST	National Institute of Standards and Technology
ODEV	Overlapped Allan Deviation
OFC	Optical Frequency Comb
OL	Optical Path Length
OPO	Optical Parametric Oscillator
PBS	Polarizing Beam Splitter Cube
PC	Physical Contact Fiber Connector
PD	Photo Detector
PDH	Pound-Drever-Hall Laser Frequency Stabilization Technique

PHM	Phase Modulation
PID	Proportional-Integral-Derivative Controller
PLL	Phase-Locked Loop
PM	Polarization Maintaining Fiber
PT	Precision Trap, Penning Trap Segment
PTB	Physikalisch-Technische Bundesanstalt Braunschweig
QED	Quantum Electrodynamics
RAM	Residual Amplitude Modulation
RBW	Resolution Bandwidth
RF	Radio Frequency
RMS	Root Mean Square
S/N	Signal-to-Noise Ratio
SA	Spectrum Analyzer
SAP	Stress Applying Parts
SFRR	Single-Splitter Fiber Ring Resonator
SHG	Second-Harmonic Generation
SI	International System of Units
SM	Single Mode Fiber
SME	Standard-Model Extension
SMP	Standard Model of Particle Physics
SSB	Single Sideband
SYRTE	Systèmes de Référence Temps-Espace
TC	Tap Coupler / Fiber Splitter
TCH	Three-Cornered Hat Analysis
TE	Transverse Electric Mode
TEC	Thermoelectric Cooler
TEM	Transverse Electromagnetic Mode

TM	Transverse Magnetic Mode
UDM	Ultra-Light Dark Matter
ULE	Ultra-Low Expansion Glass
VCA	Voltage-Controlled Attenuator / Voltage-Variable Attenuator
VCO	Voltage-Controlled Oscillator
VIRGO	Virgo Interferometer
WIMP	Weakly Interacting Massive Particle
ZCTE	Zero Coefficient of Thermal Expansion

Chapter 1

Introduction: The Pursuit of Pure Monochromatic Light

Since the first concept of an optical maser by Schawlow and Townes in 1958 [1] and its experimental implementation by Maiman in 1960 [2], precision physics has changed. The preparation of many coherent photons with the same energy and phase traveling in the same direction led to the invention of the light amplification by stimulated emission of radiation, also known as a laser. This light has several key advantages: it is monochromatic, directional, and exhibits high intensity. Many experiments have benefited from the light's high frequency stability, e.g., in the work of [3], which employed He-Ne "infrared masers," now called lasers, to test the isotropy of light to the 10^{-11} level. This was three times better than previous lamp-based Michelson-Morley-type experiments.

While this improvement may not sound groundbreaking, the second important invention made ultra-stable light revolutionary. Zooming in, lasers are not monochromatic; rather, they exhibit a mean optical carrier frequency ν_0, which varies in time and has a certain width because not all photons have the same energy. The line width and power spectrum of the light resemble a delta function compared to that of a light bulb but can be large and noisy with respect to atomic transitions.

To overcome this problem, Fox and Li [4] introduced the optical Fabry–Pérot (FP) resonator as a tool to select resonance modes and Drever et al. [5] used it to stabilize lasers to them. A FP resonator consists of two mirrors at a fixed distance L, which allows for the selection of distinct modes defined by the wavelengths of light that can form standing waves inside the resonator. The resonance wavelengths λ_{res} and frequencies ν_{res} are given by

$$\lambda_{res} = \frac{2L}{m} \text{ and } \nu_{res} = m\frac{c_n}{2L},$$

where m is an integer describing the mode number and c_n is the speed of light in the medium between the mirrors.

The benefit: The light locked to the resonance mode of the cavity $\Delta\nu$ follows the length variation ΔL of the resonator. In particular

$$\frac{\Delta\nu}{\nu_0} \approx \frac{\Delta L}{L}.$$

Thus, the greater the length stability and the narrower the mode linewidth of the resonator, the greater the stability of the locked light, the narrower its linewidth, and the purer its power spectrum. In the context of the Michelson-Morley type experiment, the isotropy of light was tested to a level below 10^{-17}, an improvement of six orders of magnitude [6], by employing light stabilized to optical resonators.

Today, lasers play a pivotal role in industrial and daily life applications, including information transfer, micromachining, and medical applications. Among the various research facilities, universities, and institutions, laser light has become the highest grade measurement tool. The Laser Interferometer Gravitational-Wave Observatory (LIGO) [7, 8, 9], employs detectors in a Michelson interferometer configuration, with stabilized lasers propagating along arm lengths of several kilometers, to detect gravitational waves. It was already able to detect gravitational waves from a binary black hole merging [10] and a binary neutron star inspiral [11].

The detector network is being, and has been, augmented with the addition of analogous detectors, including VIRGO / Advanced VIRGO [12, 13] and KAGRA [14]. The research initiative on a Laser Interferometer Space Antenna (LISA) is pursuing the utilization of active laser links in free space, extending over distances of 2.5×10^6 km, with the objective of enhancing the sensitivity to gravitational waves [15].

In order to test Einstein's theory, ultra-stable lasers driving optical clocks are utilized to probe general relativity (GR). An example of this was a measurement conducted on the Tokyo Skytree tower [16]. This can be further explored to perform geodesy using optical clocks in space [17, 18, 19, 20]. Optical clocks have a variety of applications, including quantum logic spectroscopy on controlled quantum states of trapped particles, all requiring state-of-the–art and beyond frequency stability of optical light.

The standard of modern time, the second, as defined by the International System of Units (SI), is based on a hyperfine transition in Cesium−133, interrogated by microwaves (MW) within an atomic clock. Clocks based on optical transitions [21, 22, 23, 24, 25], such as those utilizing Strontium, or Ytterbium, have demonstrated the capacity to exceed the current standard's uncertainty (NIST [26], PTB [27], SYRTE [28]) by orders of magnitude, thereby challenging the prevailing definition of the second.

In Summary, ultra-stable lasers play a vital role in navigation, geodesy, quantum technology, and fundamental physics research, underscoring the need for ongoing research to enhance frequency stability and reduce uncertainties.

The fundamental scientific applications that motivate the development of ultra-stable lasers, the subject of this thesis, can be categorized into four distinct sections that are key areas of research at the Institut für Experimentalphysik at Heinrich-Heine-Universität (HHU) Düsseldorf:

- Tests of Lorentz invariance [29, 6, 30]
- Rovibrational transitions in molecular hydrogen ions [31, 32, 33, 34, 35]
- Search for ultra-light dark matter [36, 37]
- Optical clocks [38, 39, 40]

All of these applications have one thing in common: the potential to test physics beyond the standard model (BSM). In short, the Standard Model (SMP) of particle physics describes three fundamental forces: weak nuclear, strong nuclear, and electromagnetic. It includes twelve elementary matter particles (fermions), including the quarks that form the nuclei as well as the leptons, such as the electron, muon, tau, and their respective neutrinos. The SMP also entails force carriers (bosons), including the gluon, photon, Z boson, and W boson. Finally, it includes the Higgs boson, which is responsible for mass. Together with GR, which describes gravity, the SMP forms the basis of modern physics. However, the SMP is a quantum theory, while GR is classical, resulting in conflicts at small scales and high energies. Thus, they are not unified.

Lorentz Invariance

Within the SMP, a strong theorem exists. It states that in any theory that is Lorentz invariant, local, and unitary, the charge, parity, and time reversal symmetry (CPT) is conserved. This means that, in any process, if a particle is swapped with its antiparticle (C), flipped like a mirror image (P), and reversed in time (T), it will behave identically to the initial particle. For example, a decaying particle moving from left to right behaves like its forming antiparticle moving from right to left in reverse time. However, if Lorentz invariance is violated by an anisotropy of speed in space, CPT symmetry could break, pointing towards BSM physics.

This can be tested by measuring the directional behavior of light using ultra-stable lasers, for example, by observing their rotation. Such a measurement requires two perpendicular optical references with high frequency stability, σ_ν, at the scale of the rotation period. Using the simple relation $c_n = \lambda_n \nu_0$, where λ_n is the wavelength inside the propagation medium, the difference frequency, or beat, between the light of the two lasers can be examined with respect to time variations correlated to the rotation. These oscillations would indicate a preferred propagation direction of c_n, thus testing Lorentz invariance and BSM physics.

Objective A: For a next-generation Michelson-Morley type experiment, a dual-cavity setup must be set up at a wavelength of 1064 nm. The goal is to achieve a frequency instability level of $\sigma_\nu \nu_0^{-1} = 10^{-15}$ with respect to the optical carrier frequency of the light, ν_0, at time scales between 1 s and 100 s. This setup is further explored in Section 3.1.

Precision Spectroscopy

Quantum mechanics teaches that bound systems, such as atoms or molecules, exhibit distinct vibrational and rotational energies. In the context of the work at the institute, there is a strong emphasis on molecular hydrogen ions (MHI), particularly HD^+ and H_2^+.

These ions form the simplest three-body systems and are advantageous because they are more sensitive to the electron-to-nuclei mass ratio in energy levels than hydrogen. While single particles can be studied in Penning traps (see Section 8.4) with respect to their $g-$factor, or mass to atomic mass ratio, two-body systems such as the hydrogen atom, can be used to determine the Rydberg constant R_∞ and fine structure constant α, as well as the electron-to-proton mass ratio m_e/m_p through the sensitivities of the vibrational energy states. Furthermore, the experimentally determined transition frequency, thus energy E_{exp}, can be compared to the theoretical one. This can be utilized to study QED theory as well as relativistic correction terms E_{qed} and E_{rel}, which add to the classical energy

$$E_{exp} \stackrel{?}{=} E_{classical} + E_{qed} + E_{rel},$$

within the estimated uncertainties. MHIs are the simplest form of molecules, where the addition of the second nucleus adds the study of rotational energy levels. Next to being sensitive to α and R_∞, this increases the sensitivity to electron-to-nuclear mass ratio, which can enhance the precision of m_e/m_p, m_e/m_d or m_e/m_t measurements (d: deuteron, t: triton). Further the additional nucleus opens the study of the interaction of the nuclei, and elevates the study of QED and relativistic correction terms to the molecular scale. Deviations, or variations, depending on location or time of performing the experiment, may hint at BSM physics, such as fifth forces or dark matter. If theory and experiment match, they can be used to improve the constraints and precision of the fundamental constants (FCTs).

Moreover, it is technically more straightforward to constrain and cool single ions than it is to do so with a neutral atom. However, the most elementary ion would be H^+, which is characterized by the absence of an electron. Therefore, the study of molecular ions is necessary to gain sensitivity to m_e/m_p. Simple hydrogen-like ions such as He^+ are less sensitive to the respective electron-to-nuclear mass ratio. MHI, specifically H_2^+, are of particular interest due to their unique rovibrational energy structure. A total of six isotopologues exist: H_2^+, D_2^+, T_2^+, HD^+, HT^+, and DT^+. The historical experimental focus has been on HD^+ because all triton isotopes are radioactive and H_2^+ and D_2^+ do not exhibit a dipole moment due to their center-of-mass to center-of-charge symmetry. The observation of optical quadrupole transitions necessitates laser intensities of a greater magnitude. Only recently, however, has high-precision spectroscopy of H_2^+ been achieved [41].

In the future, comparing the constraints on FCTs coming from spectroscopy of the particle to the respective values determined on its anti-matter counterpart can be used to test CPT symmetry. This can for example be achieved by precisely determining and comparing the electron-to-proton mass ratio to the respective anti-matter mass ratio through a spectroscopy campaign on H_2^+ and anti-H_2^+ [42, 43].

The spectroscopy of the transition energy between rovibrational states can be performed by MWs and lasers. The primary benefit of the latter is that it exhibits orders of magnitude better fractional frequency stability and linewidth, as well as a small wavelength scale that ranges from nanometers to micrometers. These properties offer significant advantages in terms of spatial and frequency resolution, which are of paramount importance in high-precision rovibrational spectroscopy.

In particular, the linewidth of transitions can reach levels as narrow and narrower than 10^{-14} fractional frequency level. The energy difference E_{exp} between different rovibrational states in MHI can be probed with photons of this energy; therefore, the frequency of the light is given by $\nu_{rovib} = E_{exp}/h$. This identity illustrates the requirements that must be met by the laser in order to ensure a high resolution of ν_{rovib}. A more in-depth introduction to MHIs, and their placement within current fundamental physics can be found in [44].

A comprehensive review of the theoretical determination of QED and relativistic correction terms, as well as high-precision spectroscopy of molecules, has been meticulously outlined in [45, 46, 47, 48]. Eventually, high-precision optical spectroscopy on HD^+ and H_2^+ [49, 33, 34, 35, 41] has reached experimental uncertainties that compare to and match theory at and below the 10^{-11} level of uncertainties. The experimental uncertainty is due to systematic effects in the experiment, where transition linewidths at the order of and below 10 Hz were observed. The ultra-stable reference light for the majority of the experimentation on HD^+ in [34] is also subject of this thesis. However, a common factor of all measurements is that they are exclusively performed in Paul traps on clusters of ions.

The removal of ensemble-related systematics and ion-ion interactions by single particles would increase the lifetime of the particles in the trap and improve the control over them. This would also result in higher precision, making it a highly desired spectroscopy target. However, this method also presents the additional challenge of preparing and isolating the individual particle. A collaborative endeavor between the institute at HHU and the Max-Planck-Institut für Kernphysik (MPIK) in Heidelberg sought, and still seeks, to address this unmet need by undertaking the inaugural optical rovibrational spectroscopy on a single molecular ion. While rotational spectroscopy using stimulated Raman transitions has been demonstrated on a single molecular $^{40}CaH^+$ ion in a linear Paul trap [50] at NIST, (optical) rovibrational spectroscopy has not yet been performed. A central objective of this research is to achieve high-precision laser spectroscopy on both HD^+ and H_2^+ in the Penning trap apparatus ALPHATRAP. This collaborative project, specifically the development of the metrology system, constitutes a pivotal subject of this thesis, as elaborated in Section 8.

This high-precision spectroscopy requires not only ultra-stable lasers but also a full frequency metrology suite. This necessity arises from the inherent uncertainty associated with the absolute laser frequency. Usually, the laser frequency is compared to local clocks in laboratories; however, even state-of-the-art laboratory clocks such as a Hydrogen-based maser may exhibit deviations at the 1–10 kHz level, at optical frequencies at the 100 THz level, with respect to SI defined by Cs atomic clocks. The comparison of the laser frequency to SI can be achieved by comparing the laboratory clock to a Cs-steered clock in PTB using the Global Navigation Satellite System (GNSS).

Objective B: For a measurement campaign on rovibrational transitions in HD^+ and H_2^+, a frequency metrology system with state-of-the-art performance levels had to be set up for the spectroscopy light, including linewidths of 10 Hz, frequency instabilities below the 10^{-14} level, and a frequency uncertainty at the same level with respect to international SI standard. The comparison to international standard at PTB has to be continuously performed via common view using GNSS. The

reference laser must be at 1.5 µm, and the spectroscopy laser must be at 1.1 – 1.2 µm to generate light at mid-infrared (MIR) wavelengths of 4 – 5 µm by utilizing difference frequency generation (DFG). This setup had to be built and characterized at HHU Düsseldorf and then transported to MPIK in Heidelberg for this joint collaboration, in which it had to be capable of remote operation. This system is discussed in Section 3.3. Further, an ultra-stable reference lasers for a measurement campaign on HD^+ clusters in a Paul trap had to be set up and maintained at HHU.

The Search for Dark Matter

In 1933, Fritz Zwicky published an article on the anomalous behavior of galactic Coma Clusters [51]. He calculated the gravitational force between them and deduced that the visible mass alone was insufficient to bind them. He posited that the remaining mass must originate from an invisible dark matter. Four decades later, Vera Rubin and Kent Ford observed that the speed of stars located farther from the center of a galaxy was higher than could be explained by the visible mass. This further indicated the existence of dark matter [52]. In contemporary research, a multitude of models regarding dark matter exist, ranging from massive astrophysical compact halo objects (MACHO, [53]) to weakly interacting massive particles (WIMP, [54]) and even ultralight dark matter (UDM, [55]), the latter of which includes the axion [56]. The work presented in this thesis focuses on UDM, which is a subject that can be investigated through tabletop experiments that utilize ultra-stable lasers.

The existence of dark matter particles is BSM physics by definition. One interesting model of UDM as an oscillating scalar field hypothesizes that UDM couples with the electromagnetic field and the mass of matter, leading to oscillations of FCTs, such as the fine structure constant α or nuclear and electron masses [57]. This can be tested by observing the absorption signal in vibrational molecular spectroscopy and searching for frequency peaks in the Fourier domain, which would indicate potential candidates of UDM. Here, the different sensitivities of the cavity length, stabilizing the laser, and the energy states of the molecule are compared to each other, yielding a non-zero sensitivity to oscillating FCTs due to UDM.

In the realm of historical research, there have been gaps in probing for the coupling strength for potential masses of UDM, for example within the range below 10^{-14} eV and 10^{-6} eV. Exclusion plots that provide a comprehensive overview of the extant research in this domain are presented in the final figures of the work [36], which can be found in Appendix B.1.1. A collaborative effort was initiated by HHU Düsseldorf, the Johannes Gutenberg-Universität in Mainz, the Helmholtz-Institut GSI Helmholtzzentrum für Schwerionenforschung in Mainz and the Department of Particle Physics for Astrophysics at the Weizmann institute of Science in Rehovot, Israel, with the objective of targeting this energy range. Two UDM detectors were to be built to search for oscillations in FCTs due to dark matter at different energy ranges. The detector at HHU was searching for dark matter by the described method employing cavity stabilized lasers on vibrational spectroscopy in Iodine. Within the window of 10 Hz and 100 kHz, where the laser light tightly follows the cavity length, which allowed testing for masses between 4×10^{-14} eV to 4×10^{-10} eV, derived from the Compton frequency of the scalar field. This collaboration and specifically the laser light for the detector at HHU [36] as well as the light for a next generation UDM detector on

Acetylene [37] were the subject of development and operation within this thesis. Further details are provided in Section 7. The interrogating light must have excellent long-term stability and high spectral purity within the observed frequency ranges to not limit the resolution of the detector.

Objective C: For two experiments searching for UDM in spectroscopy on Iodine and Acetylene, ultra-stable lasers with a spectral purity of $\left(10^{-13} - 10^{-12}\right)\,\mathrm{Hz}^{-1/2}$ level for frequencies between 10 Hz and 10^5 Hz in the Fourier domain were needed. Coincidentally, lasers at wavelengths of 1064 nm and 1.5 µm were required. Thus, the systems for the above projects could be employed if they fulfill the stability requirement.

Optical Clocks and Novel Resonators

Additionally, optical clocks are among the most advanced tools for probing BSM physics. They are fundamentally connected to extremely narrow atomic transitions. Two clocks in different locations can be compared to test for variations in FCT, as well as the principles of GR, by comparing them at different heights in a gravitational potential. The most advanced developments in ultra-stable lasers have been in connection with optical clocks [58, 59, 60, 61]. The institute at HHU Düsseldorf is involved in the development of optical clocks as referenced above. A project is underway to compare a stationary optical clock with one on the International Space Station (ISS) as part of the Atomic Clock Ensemble in Space (ACES) initiative. The ground optical clock, which is currently characterized in the Physikalisch-Technische Bundesanstalt (PTB) Braunschweig, will be provided by HHU. This thesis contributes to the project by developing an automatic re-stabilization system for the employed clock laser.

The last decade has shown that the next advancement in ultra-stable lasers lies in cryogenic cavities, which reduce the fundamental thermal noise floor that limits the stability of locked light. Cryogenic silicon cavities have also been the subject of research at the institute at HHU [62, 63, 64, 65, 66]. Within this scope, a new project has opened the possibility of working on an alternative to FP-type optical resonators in the form of fiber resonators. Their advantage lies in the very long path lengths of light inside the resonator, which could potentially benefit the linewidth of the resonator. As an initial test, the concept of a fiber resonator in ring configuration is to be examined.

Objective D: Set up and test an optical fiber ring resonator at room temperature and evaluate its potential as an optical reference for future projects compared to classical FP cavities.

Roadmap of Experimental Work

In order to address all objectives, a total of three high-performance, state-of-the-art optical resonators must be set up, as well as a metrology system that includes a comb and a spectroscopy laser. Three systems suffice due to the overlap of requirements, especially in regard to the employed wavelengths. The metrology system must be transportable, automated, and remotely controllable while employed at MPIK Heidelberg. Additionally, a fourth proof-of-concept resonator based on optical fibers must be set up.

While working on these tasks, additional research was performed. This includes the transmission filtering of cavities for spectrally pure light at low frequencies (Section 4.2); the reduction of residual amplitude modulation (RAM) beyond the thermal noise floor using a straightforward approach (Section 4.1); the contribution to a collaborative guideline work on next generation ultra-stable lasers (Section 4.4, [67]); the discovery of the lowest aging drift ever observed in a room-temperature graded optical cavity (Section 6); the characterization of a spectroscopy grade optical parametric oscillator (OPO) (Section 4.3, [68]); and the set up of the first fiber-based ring resonator with a zero coefficient of thermal expansion (ZCTE) at a temperature level achievable by thermoelectric coolers (TECs) (Section 5).

The Structure of this Thesis

This thesis integrates the conceptualization of ultra-stable light with concrete applications in reality, beginning from the foundational level. Chapter 2 (Appendix A) discusses the theoretical framework and underlying principles of ultra-stable lasers, frequency combs, and metrology. This discussion is highly tailored to the practical work of this thesis.

Chapter 3 builds upon these concepts through an in-depth examination of the experimental setups of laser systems constructed during this research. This includes novel achievements in the field of ultra-stable lasers and how they compare to existing literature.

Research on ultra-stable lasers is detailed in Chapter 4. Each section in this chapter addresses an independent topic; however, as they are relatively brief, and to avoid overloading the thesis with separate chapters, they are presented together here.

Chapters 5 and 6 cover two additional major research efforts conducted on resonators as part of this thesis: the development of a non-cryogenic fiber ring resonator, and the observation of the lowest aging drift in a room-temperature optical reference.

Chapter 7 is explaining how the lasers are employed for measurements searching for UDM. Chapter 8 demonstrates how the systems contribute to spectroscopy campaigns on MHI.

The final Chapter, 9, provides a comprehensive summary and future outlook.

Chapter 2

Theoretical Background

This work's primary focus lies in the construction, characterization, and implementation of setups, which are utilized to create ultra-stable light for the purpose of scientific research. The original version of this chapter is devoted to the understanding of light and the methodologies employed for its manipulation to achieve this objective. There is an emphasis on a theoretical foundation; however, it should be noted that this theoretical basis is not derived directly from textbooks. In particular, every single formula and equation that is not basic knowledge has been explicitly calculated or derived during this work, unless otherwise stated.

Therefore, it is possible that certain derivations of formalisms may be more or less proximate to the typical textbook style. Nonetheless, almost all the knowledge presented herein is not original; rather, it has been acquired through a conventional academic program in physics or advanced literature. This will be made evident and referenced accordingly in the subsequent sub-chapters. However, it should be noted that certain concepts and calculations are incorporated into the text that are not commonly found in standard textbooks.

For the purpose of this thesis, the original theory chapter—spanning approximately 150 pages—has been moved to the appendix under the title "From wave to Metrology: A Tutorial" (see Appendix A). The objective of this chapter is to establish a miniature literature for the specific task of developing a frequency metrology system that can stabilize light of a particular frequency to the 10^{-15} level and beyond. This system is designed to transfer this stability to other carrier frequencies and to measure the absolute frequency with uncertainties below the 10^{-14} level with respect to the international standard. The explanation commences with the wave formalism of light, elaborating on the fundamental concept of dielectric mirrors and resonators.

It then progresses to the concept of typical continuous-wave lasers. There, the text will introduce critical electric and optical components and provide a comprehensive explanation of more advanced devices, including the wavemeter and frequency comb. The explanations provided herein have been customized to align with the specific systems that have been established within the scope of this thesis. Notwithstanding, this chapter may still offer a valuable source of information for anyone seeking to acquire fundamental understanding of laser light stabilization. Furthermore, an in-depth examination of characteristic analysis methods of light, including line-width, frequency noise, phase noise, and Allan deviation, is conducted.

In combination with the literature research of the state-of-the-art systems in chapters 3 and 4, it is written in a style that may potentially be modified to become a tutorial paper, in example for Advances in Optics and Photonics. Sections directly related to the core contributions of this thesis have been moved to the main body of the text. Specifically, this includes material on the optical standing-wave resonator and the fiber ring resonator—covering their setup, fundamental stability limitations, and stabilization techniques. It also includes the concept of frequency metrology, including the comparison of frequencies with respect to SI. The original locations of these sections within the full theory chapter in the appendix are clearly indicated, allowing the reader to refer back to the broader context and detailed derivations as needed.

2.1 Foundations of Optical Resonators

This section will provide an overview of the theoretical model of optical standing wave resonators as well as fiber based ring resonators. The theory of electromagnetic waves interacting with surfaces, dielectric mirrors, and the transfer matrix method; the model of GBs in free space and their counterparts in fiber optics; as well as components such as EOMs, AOMs, waveplates, and beam splitters that manipulate certain characteristics of light, are presented in the respective appendix chapters preceding the sections discussed here. In particular, the derivation of the transfer matrix for dielectric mirrors precedes the first subsection presented herein.

2.1.1 Light Trapped in Time: Standing Wave Resonators

Originally located in Appendix A.1.6. As established, a fundamental component of this work is the set-up and application of standing wave resonators, otherwise referred to as FP cavities. These resonators are composed of two dielectric mirrors, which are positioned at a distance L within a medium, in this context, typically a vacuum. In the context of an incident wave with the electric field E_0, directed towards the resonator, the final transfer matrix $\boldsymbol{M}_{res}$ is derived through the multiplication of the individual matrices of both mirrors. The front mirror serves as the reference phase, while the second mirror is defined by the phase shift of $\phi = k_m L$, which is attributed to the optical travel distance between the two mirrors. The mirrors are arranged in a configuration such that the coatings face each other, thereby constituting the inner part of the resonator. Consequently, the total matrix is

$$\begin{aligned}\boldsymbol{M}_{res}(\phi) = \boldsymbol{M}_{M_2}(\phi)\,\boldsymbol{M}_{M_1}(0) &= \frac{n_0}{n_0}\frac{1}{t}\begin{pmatrix} 1 & -re^{-2i\phi} \\ -re^{2i\phi} & 1 \end{pmatrix}\cdot\frac{1}{t}\begin{pmatrix} 1 & r \\ r & 1 \end{pmatrix} \\ &= \frac{1-r^2e^{2i\phi}}{t^2}\begin{pmatrix} \frac{1-r^2e^{-2i\phi}}{1-r^2e^{2i\phi}} & \frac{r\left(1-e^{-2i\phi}\right)}{1-r^2e^{2i\phi}} \\ \frac{r\left(1-e^{2i\phi}\right)}{1-r^2e^{2i\phi}} & 1 \end{pmatrix},\end{aligned}$$

with the determinant

$$\det(\boldsymbol{M}_{res}) = \left(\frac{1-r^2e^{2i\phi}}{t^2}\right)^2\left(\frac{1-r^2e^{-2i\phi}}{1-r^2e^{2i\phi}} - \frac{r\left(e^{-2i\phi}-1\right)}{1-r^2e^{2i\phi}}\frac{r\left(e^{2i\phi}-1\right)}{1-r^2e^{2i\phi}}\right) = \ldots = 1$$

In this case, the coefficients are not readily calculable by examining the matrix directly because they are complex. Therefore, Equation (A.29) is employed to derive these coefficients. In addition, the indices for reflection, r, and transmission, t, coefficients are omitted to facilitate comprehension and it is hypothesized that both mirrors are identical, i.e. $r_1 = r_2 := r$. The latter is a soft approximation, as the formalism that will be derived includes factors $r^2 = r_1 r_2$ and $r = \sqrt{r_1 r_2}$, such that the individual mirror is replaced by the system. The reflected field E_r in front of the first mirror is determined by the normalized reflection coefficient $F(\phi)$, which is expressed as

$$\frac{E_r}{E_0} := F(\phi) = -\frac{M_{21}}{M_{22}} = \frac{r\left(e^{2i\phi} - 1\right)}{1 - r^2 e^{2i\phi}}. \tag{2.1}$$

The field E_t transmitted through the second mirror is modeled by the normalized transmission coefficient $S(\phi)$ by

$$\frac{E_t}{E_0} := S(\phi) = \frac{\det(\boldsymbol{M}_{res})}{M_{22}} = \frac{t^2}{1 - r^2 e^{2i\phi}} = \frac{1 - r^2}{1 - r^2 e^{2i\phi}}.$$

Furthermore, a circulating field, E_c, is present within the resonator. This field can be expressed as a function of the transmitted field, which is not transmitted through the second mirror. This is given by the normalized circulation coefficient $C(\phi)$ by the means of

$$\frac{E_c}{E_0} := C(\phi) = \frac{S(\phi)}{t} = \frac{t}{1 - r^2 e^{2i\phi}} = \frac{\sqrt{1 - r^2}}{1 - r^2 e^{2i\phi}}.$$

Derivation of these formulas can also be achieved through the geometric series. Indeed, adding Equation (A.36) to (A.37) and setting the reflectivities equal, in particular $r_{10} = r_{12} = r$, will yield the same formula as in Equation (2.1). Ultimately, the primary interest lies in the intensity of the light; thus, the three formalisms become

$$\hat{I}_r = \frac{I_r}{I_0} = F(\phi) F^*(\phi) = \frac{2r^2(1 - \cos(2\phi))}{1 - 2r^2\cos(2\phi) + r^4}, \tag{2.2}$$

$$\hat{I}_t = \frac{I_t}{I_0} = S(\phi) S^*(\phi) = \frac{\left(1 - r^2\right)^2}{1 - 2r^2\cos(2\phi) + r^4}, \tag{2.3}$$

and

$$\hat{I}_c = \frac{I_c}{I_0} = C(\phi) C^*(\phi) = \frac{1 - r^2}{1 - 2r^2\cos(2\phi) + r^4}. \tag{2.4}$$

All intensities exhibit Lorentzian-like shapes. Given the intensity of the incident light, I_0, these formalisms exhibit a resonance behavior at $2\phi_{res} = 2\pi b$, with $b \in \mathbb{Z}$. This can be expressed by a resonance wavelength λ_{res} or frequency ν_{res} of the light as

$$\begin{aligned} 2\phi_{res} = 2\pi b \overset{!}{=} 2k_{res}L = \frac{4\pi}{\lambda_{res}}L = \frac{4\pi}{c_0}L\nu_{res} \\ \iff \lambda_{res}(b) = \frac{2L}{b} \iff \nu_{res}(b) = \frac{c_0}{2L}b. \end{aligned} \tag{2.5}$$

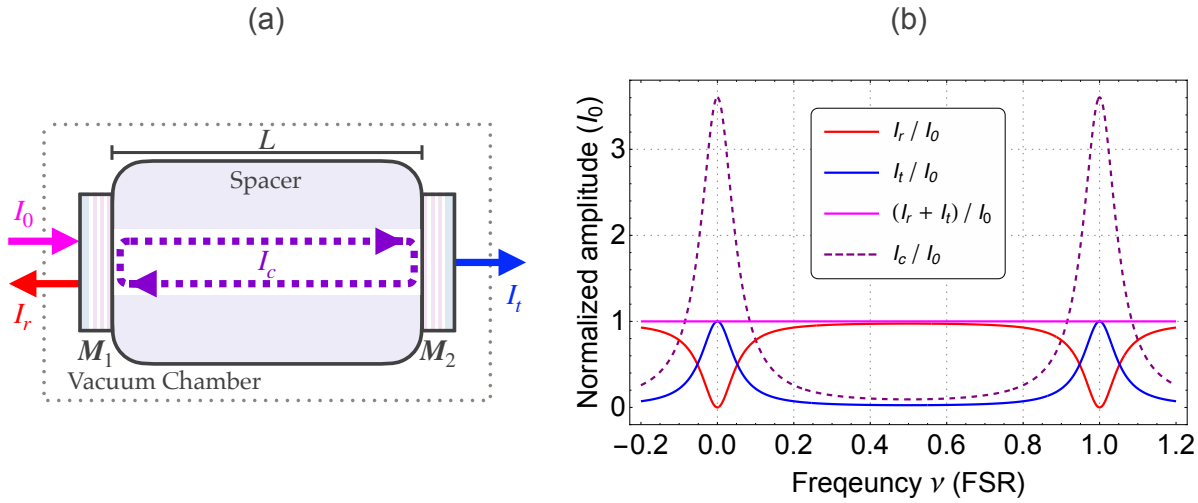


Figure 2.1: (a): Schematic representation of a FP-type resonator. It is composed of two dielectric mirrors, which are connected to a spacer of length L within a vacuum chamber. (b): The plots illustrate the resonator intensities, as given by Equations (2.2), (2.3) and (2.4), depending on the frequency in units of the FSR $\Delta\nu$.

It was used that the light is propagating inside a vacuum, thus $n = 1$ to to minimize the requisite number of indices. The resonance criteria are met if any multiple of half the wavelength of the light fits within the resonator length L. This is equivalent to the criteria for a standing wave within a resonator, as the light's nodes are positioned at the locations of the mirrors. In the context of resonance, the intensity reflection coefficient $|F(\phi)|^2$ at the front mirror approaches zero, while the intensity transmission coefficient transitions to $|S(\phi)|^2 = 1$. Additionally, the circulating field is subject to significant amplification due to constructive interference within the resonator. This formalism is more commonly expressed in terms of the light frequency. The periodicity of the cavity modes is expressed by 2π in phase. This can be converted to a value in frequency, which is designated as the free spectral range (FSR). The FSR $\Delta\nu$ is the difference between two neighboring modes, and is expressed as

$$\Delta\nu = \nu_{res}(b+1) - \nu_{res}(b) = \frac{c_0}{2L}.$$

Inserting $\Delta\nu$ into Equation (2.5), however in a general form for $\phi(\nu)$—not just in resonance—will yield the dependence

$$2\phi = 2\pi\frac{f}{\Delta\nu} = \frac{\omega}{\Delta\nu}.$$

The variable f is used to denote the variation of the frequency ν, in the scenario that $\nu = \nu_0 + f$, and the frequency, ν_0 is also a resonance frequency. Furthermore, the modes are characterized by a specific width, denoted by ϕ_c, or alternatively in terms of frequencies, denoted by f_c. This width is typically defined as the full-width half-maximum (FWHM) value, also called linewidth. As the name suggests, it represents the width of the mode when its amplitude has decreased to half of its

maximum value. It can be derived from

$$\frac{1}{2}\hat{I}_t(0) \stackrel{!}{=} \hat{I}_t\left(\frac{2\phi_c}{2}\right) = \hat{I}_t\left(\pi\frac{f_c}{\Delta\nu}\right)$$

using $\hat{I}_t(0) = 1 - \hat{I}_r(0)$ such that it is

$$f_c = \frac{\Delta\nu}{\pi}\arccos\left(1 - \frac{\left(1-r^2\right)^2}{2r^2}\right). \tag{2.6}$$

Typically, it is $r \lessapprox 1$, thereby ensuring that the argument in the trigonometric function approaches one. The Taylor series of $\cos(y)$ is expressed as follows:

$$\cos(y) = \sum_{m=0}^{\infty}(-1)^m\frac{y^{2m}}{(2m)!} = 1 - \frac{y^2}{2} + \frac{y^4}{24} - \ldots,$$

Here, the first two terms may be used to approximate the value of $\cos(y)$ when y approaches one. Therefore, the arccosine can be expressed as a function of x, with $x \approx 1$, by employing the inverse function of the approximated cosine, which is

$$x = 1 - \frac{y^2}{2} \Longleftrightarrow y = \sqrt{2(1-x)} \approx \arccos(x). \tag{2.7}$$

In conclusion, upon inserting Equation (2.6) into (2.7), the FWHM for high reflectivities is derived, given by

$$f_c \approx \frac{1-r^2}{\pi r}\Delta\nu. \tag{2.8}$$

This set of formalisms describes the FP resonator or cavity, and will be of pivotal significance to this thesis. It will become important to comprehend the concept of frequency stabilization, for which a detailed explanation will be provided in the forthcoming Section 2.3. Finally, the finesse, denoted by the symbol $\mathcal{F}$, of a cavity is defined by the ratio of its FSR to its cavity linewidth. This relationship establishes a correlation between the sharpness of the modes and their respective spacing. The fundamental equation is expressed as

$$\mathcal{F} = \frac{\Delta\nu}{f_c} \approx \frac{\pi r}{1-r^2}, \tag{2.9}$$

where the finesse ideally solely depends on the reflectivity of the resonator's mirrors. A low finesse indicates an egg-carton-like profile in the intensity time domain, whereas a high finesse corresponds to thin, spread lines, reminiscent of a comb. The terms "high finesse" and, on occasion, "ultra-high finesse" are frequently employed to denote values of greater than $\mathcal{F} \geq 10^4$, where the optical standing wave resonators examined in this thesis exhibit finesse values of at least $\mathcal{F} \geq 2\times10^5$.

In order to calculate the finesse, one needs to know r. The reflectivity of a resonator can be determined through the estimation of the lifetime of a photon within the resonator. Imagining

a single photon, at time $t = 0$, entering the resonator. The probability that the light particle will remain within the confines of the resonator is determined by the probability $p_c(t)$ which is given by

$$p_c(t) = r^{\frac{4t}{\tau_r}} := e^{-\frac{t}{\tau_c}}.$$

Here, the round-trip time τ_r in the resonator is equivalent to the inverse of the FSR, expressed as $\tau_r = \Delta\nu^{-1}$. Following each half-round trip, the photon will interact with one of the mirrors. In such an instance, there is a probability of r^2 that the photon will be reflected and remain within the resonator. The decay process can be expressed in exponential form by incorporating the characteristic time constant, denoted by τ_c, with

$$r^{\frac{4t}{\tau_r}} = e^{\frac{2t}{\tau_r}\ln(r^2)} := e^{-\frac{t}{\tau_c}} \Longleftrightarrow r^2 = e^{-\frac{\tau_r}{2\tau_c}}. \tag{2.10}$$

The evaluation of the exponential for small arguments, followed by the insertion of the round-trip time, yields

$$r^2 \approx 1 - \frac{L}{\tau_c c_0}. \tag{2.11}$$

Therefore, by monitoring the decay of photons within the resonator, it is possible to calculate the time constant, τ_c, and subsequently compare it with the round-trip time, which is determined by the cavity length and the propagation medium. This method provides insight into the reflectivity and finesse of the system. Assuming a steady state, in which a constant stream of photons enters and leaves the resonator, the transmission through the resonator will decay once the input light is instantaneously shut off. This decay is expressed by the equation

$$I_t(t) = I_0 e^{-\frac{t}{\tau_c}}, \tag{2.12}$$

which is the principle of ring down measurements, which are utilized to determine the finesse of a resonator.

2.1.2 Imperfect Realities: Understanding Optical Losses

Originally located in Appendix A.1.7. The system has thus far been regarded as lossless. However, given the imperfect smoothness of the surface, certain components of the EM wave are reflected or transmitted at an oblique angle. These components are considered to be irretrievable for the application, as they will no longer be part of the main beam. This can be expressed through the use of coefficients, denoted by δ, which quantify the extent to which light is conserved. The process is said to be lossless if the parameter is equal to one. Conversely, if δ is zero, the process is designated as being fully lossy. The losses can be incorporated into the model by the effective reflection and transmission coefficients, r_{eff} and t_{eff}, such that the formula (A.28) becomes

$$r_{eff}^2 + \frac{n_j}{n_m} t_{eff}^2 = \delta_{mj}^2.$$

In order to ensure a thorough and precise treatment, it would be necessary to assign a distinct loss coefficient to each surface, considering the unique characteristics of each process. However, this approach would significantly increase the complexity of the model. However, for the purpose

of further analysis, it is reasonable to denote a loss of a particular system, rather than for each individual reflection or transmission. Assuming δ_{mj}^2 with the property $\delta_{mj} = \delta_{jm}$ to be the fraction of light that is not lost in terms of conservation of energy, this approximation would result in $r_{eff} = \delta_{mj} r_{mj}$ and $t_{eff} = \delta_{mj} t_{mj}$. The same steps previously outlined for the formulation of the electric field components

$$\begin{aligned} E_{j\rightarrow} &= \delta_{mj} t_{mj} E_{m\rightarrow} + \delta_{jm} r_{jm} E_{j\leftarrow} \\ E_{m\leftarrow} &= \delta_{jm} t_{jm} E_{j\leftarrow} + \delta_{mj} r_{mj} E_{m\rightarrow}, \end{aligned}$$

must be repeated to create the final, loss-dependent transfer matrix $\boldsymbol{M}_{\delta,mj}(\phi)$ for a surface that incorporates the phase shift due to propagation through the initial medium. This results in the expression

$$\boldsymbol{M}_{\delta,mj}(\phi) = \frac{n_m}{n_j} \frac{1}{\delta_{mj} t_{mj}} \begin{pmatrix} \delta_{mj}^2 & -r_{mj}\delta_{mj} e^{-i2\phi} \\ -r_{mj}\delta_{mj} e^{i2\phi} & 1 \end{pmatrix}.$$

The system's determinant remains equal to one. This outcome may be regarded as somewhat unanticipated; however, upon closer examination, it is evident that this result is consistent with the established definition of losses, which are externally multiplied to the coefficients r_{mj} and t_{mj}:

$$\det\left(M_{\delta,mj}\right) = \frac{1}{t_{mj}^2}\left(1 - r_{mj}^2\right) = 1$$

An additional factor must be considered when analyzing the absorption loss inside the propagation medium along the optical path described by ϕ. However, given that this is typically a vacuum, the primary loss is attributable to the mirrors. Consequently, the absorption and/or scattering inside the medium is not addressed in this context (or can be partially attributed to the mirror loss). To get the total transfer matrix of the resonator, $\boldsymbol{M}_{res}(\phi)$, the process entails the utilization of the same steps as previously outlined in the lossless model. The expression becomes

$$\begin{aligned} \boldsymbol{M}_{\delta,res}(\phi) = \boldsymbol{M}_{\delta,M}(\phi)\,\boldsymbol{M}_{\delta,M}(0) &= \frac{1}{\delta t}\begin{pmatrix} \delta^2 & -\delta r e^{-2i\phi} \\ -\delta r e^{2i\phi} & 1 \end{pmatrix} \frac{1}{\delta t}\begin{pmatrix} \delta^2 & \delta r \\ \delta r & 1 \end{pmatrix} \\ &= \frac{1-\delta^2 r^2 e^{2i\phi}}{\delta^2 t^2}\begin{pmatrix} \delta^2 \frac{\delta^2 - r^2 e^{-2i\phi}}{1-\delta^2 r^2 e^{2i\phi}} & \frac{\delta^3 r - \delta r e^{-2i\phi}}{1-\delta^2 r^2 e^{2i\phi}} \\ \frac{\delta r - \delta^3 r e^{2i\phi}}{1-\delta^2 r^2 e^{2i\phi}} & 1 \end{pmatrix}, \end{aligned}$$

with the determinant $\det\left(\boldsymbol{M}_{\delta,res}\right) = 1$, and the loss imbued reflection $F_\delta(\phi)$ and transmission $S_\delta(\phi)$ coefficients

$$F_\delta(\phi) = \frac{\delta^3 r e^{2i\phi} - \delta r}{1 - \delta^2 r^2 e^{2i\phi}} \text{ and } S_\delta(\phi) = \frac{\delta^2 - \delta^2 r^2}{1 - \delta^2 r^2 e^{2i\phi}}. \tag{2.13}$$

In resonance, the normalized reflected intensity is given by

$$\frac{I_{\delta,r}(0)}{I_0} = |F_\delta(0)|^2 = \frac{\left(1-\delta^2\right)^2}{\delta^{-2} r^{-2}\left(1-\delta^2 r^2\right)^2} := U(\delta)^2, \tag{2.14}$$

where $U(\delta)$ is a characteristic function that will be examined extensively later in Section 2.3.3. Furthermore, the FWHM, $f_{\delta,c}$, of the resonator is calculated using the same methodology as for the

no-loss system:

$$f_{\delta,c} = \frac{\Delta\nu}{\pi} \arccos\left(1 - \frac{\left(1-\delta^2 r^2\right)^2}{2\delta^2 r^2}\right) \approx \frac{1-\delta^2 r^2}{\pi\delta r}\Delta\nu. \tag{2.15}$$

It is noteworthy that in the case of losses within the system, the sum of the reflected and transmitted intensities no longer remains one, or even constant in ϕ. Especially it is

$$\delta_{tot}(\phi) = F_\delta(\phi) F_\delta^*(\phi) + S_\delta(\phi) S_\delta^*(\phi) = \frac{\delta^2 r^2\left(1 - 2\delta^2\cos(2\phi) + \delta^4\right) + \delta^4\left(1-r^2\right)^2}{1 - 2\delta^2 r^2\cos(2\phi) + \delta^4 r^4},$$

where $\delta_{tot} = I_{\delta,tot} / I_0$ denotes the total loss parameter in the system. This parameter is defined as the remaining total intensity $I_{\delta,tot}$ (or power) in the system with respect to the incident one. The loss is maximized in resonance; therefore, the value of δ_{tot} is minimized and it follows:

$$\delta_{tot}(0) = F_\delta(0) F_\delta^*(0) + S_\delta(0) S_\delta^*(0) = \frac{\delta^2 r^2\left(1-\delta^2\right)^2 + \delta^4\left(1-r^2\right)^2}{\left(1-\delta^2 r^2\right)^2}$$

Finally, the finesse $\mathcal{F}_\delta$ is also influenced by losses, indicating that its performance is not solely contingent upon the reflectivity of mirrors anymore. For high reflectivities it is

$$\mathcal{F}_\delta = \frac{\Delta\nu}{f_{c,\delta}} \approx \frac{\pi\delta r}{1-\delta^2 r^2}.$$

Furthermore, the presence of losses within the cavity medium has the capacity to affect the finesse of the resonator. However, as previously approximated, for an evacuated resonator, this effect is negligible in comparison to the loss effects that manifest internally and at the surface of the mirrors. This statement will no longer be true when fiber resonators are discussed.

2.1.3 Directing Light: Fiber Types, Splitters, and Circulators

Originally located in Appendix A.3.4. The final significant optical components to be examined are fiber optics, with a particular focus on fiber splitters and circulators in the context of this work. A fiber splitter (also: tap coupler or fiber coupler) (TC), akin to a beam splitter, can be conceptualized as a black box with two inputs and two outputs. Each output is wired in a predetermined manner to both inputs, with one path designated as the signal and the other as the tap. In actuality, TCs are not wired devices. Rather, two fibers approach each other in such a manner that the electric fields of the respective paths can couple into each other. The overall process is more complex and beyond the scope of this work. The following formalism describes the splitter by defining the input electric fields E_1, E_2, the output electric fields E_3, E_4, the total intensity insertion loss of the splitter γ_0, and the intensity coupling coefficients κ_0 and t_0 for the signal and tap path, respectively:

$$\underbrace{\begin{pmatrix} \boldsymbol{E}_3 \\ \boldsymbol{E}_4 \end{pmatrix}}_{\text{output}} = \sqrt{1-\gamma_0} \underbrace{\begin{pmatrix} \sqrt{t_0} & i\sqrt{\kappa_0} \\ i\sqrt{\kappa_0} & \sqrt{t_0} \end{pmatrix}}_{\boldsymbol{U}} \underbrace{\begin{pmatrix} \boldsymbol{E}_1 \\ \boldsymbol{E}_2 \end{pmatrix}}_{\text{input}} \tag{2.16}$$

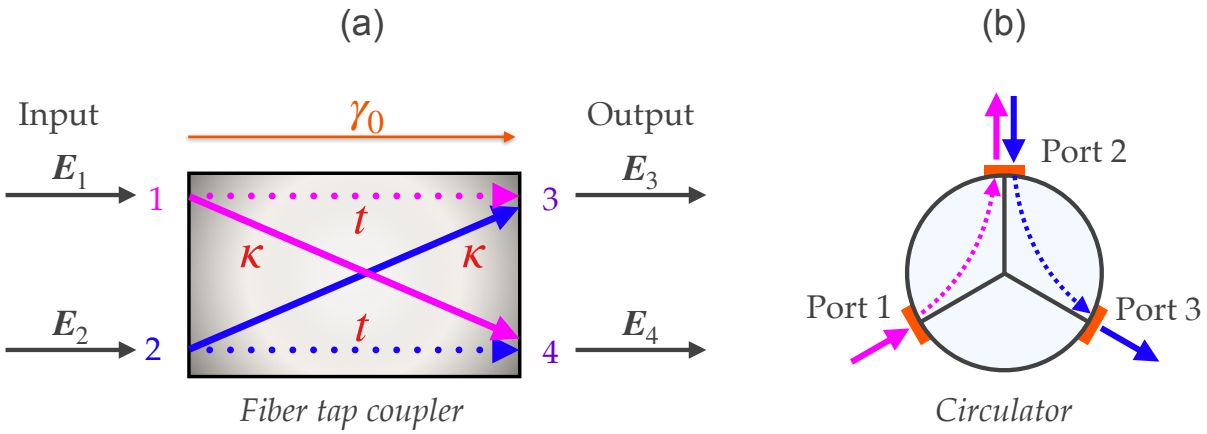


Figure 2.2: The following concept sketches depict two distinct components: (a): The fiber TC with the dotted lines representing the tap and the straight lines denoting the signal paths. (b): The fiber-coupled Faraday isolator, otherwise known as the circulator. The input light is indicated by the magenta color, while the blue color denotes light originating from a reflection path.

Figure 2.2 (a) illustrates the ports and paths. The transfer matrix for the reflection and transmission coefficients (Section A.1.4) of a mirror can be considered analogous to the transfer matrix under consideration here. In the context of fibers, however, the nomenclature will be used in which the parameters κ_0 and t_0 are real and not complex. Therefore, in the most elementary description of a beam splitter, the imaginary unit must be multiplied to the signal (or tap) path. It is essential to note that the coupling coefficients are defined in terms of intensity. Consequently, the square root must be applied to the gain the coefficients for the electric fields. The system's total loss, denoted by γ, establishes a relationship between the coupling coefficients, such that $\kappa_0 + t_0 = 1$. All of the aforementioned points are relevant to the fundamental fact that the coupling matrix $\boldsymbol{U}$ is a unitary matrix. Specifically, the condition

$$\boldsymbol{U}^T\boldsymbol{U} = \begin{pmatrix} \sqrt{t_0} & -i\sqrt{\kappa_0} \\ -i\sqrt{\kappa_0} & \sqrt{t_0} \end{pmatrix} \begin{pmatrix} \sqrt{t_0} & i\sqrt{\kappa_0} \\ i\sqrt{\kappa_0} & \sqrt{t_0} \end{pmatrix} = \begin{pmatrix} 1 & 0 \\ 0 & 1 \end{pmatrix},$$

results in a total conservation of energy within the system, provided that $\gamma_0 = 0$. The intensity is directly proportional to the square of the fields $I \propto |\boldsymbol{E}|^2$, as demonstrated by the following equations:

$$|\boldsymbol{E}_3|^2 = (1-\gamma_0)\left(\kappa_0 |\boldsymbol{E}_2|^2 + t_0 |\boldsymbol{E}_1|^2\right) \longrightarrow I_3 = (1-\gamma_0)(\kappa_0 I_2 + t_0 I_1) \tag{2.17}$$

$$|\boldsymbol{E}_4|^2 = (1-\gamma_0)\left(t_0 |\boldsymbol{E}_2|^2 + \kappa_0 |\boldsymbol{E}_1|^2\right) \longrightarrow I_4 = (1-\gamma_0)(\kappa_0 I_1 + t_0 I_2) \tag{2.18}$$

The summation of the intensities from Equations (2.17) and (2.18) results in the total intensity at the outputs in relation to the inputs, given by the following equation:

$$I_3 + I_4 = (1-\gamma_0)(I_1 + I_2)$$

This finding aligns with the unitary nature of $\boldsymbol{U}$, as evidenced by the conservation of total intensity in a lossless system when $\gamma_0 = 0$. The quantitative values forκ, t, and γ can be determined through

the calculation of insertion losses, as provided by the manufacturer. The units of measurement in which these quantities are typically expressed are decibels (dB) for the signal and tap paths, respectively. In the event that the signal loss is designated by δK and the tap loss is denoted by δT, the linear coefficients are thus determined to be $K = 10^{-\delta K/10}$ and $T = 10^{-\delta T/10}$. These coefficients encompass the coupling coefficients and the loss of the system. The expressions

$$\gamma_0 = 1 - (K + T)\,,\ \kappa_0 = \frac{K}{K+T} \text{ and } t_0 = \frac{T}{K+T},$$

are required to extract the them. In order to obtain a nomenclature analogous to that of the losses of a mirror, the following substitution is made:

$$\delta_0 = \sqrt{1-\gamma_0}\sqrt{\kappa_0}$$

The result of this process is a modified transfer matrix formulation for the electric field, expressed as

$$\begin{pmatrix} \boldsymbol{E}_3 \\ \boldsymbol{E}_4 \end{pmatrix} = \begin{pmatrix} \sqrt{(1-\gamma_0)-\delta_0^2} & i\delta_0 \\ i\delta_0 & \sqrt{(1-\gamma_0)-\delta_0^2} \end{pmatrix} \begin{pmatrix} \boldsymbol{E}_1 \\ \boldsymbol{E}_2 \end{pmatrix}. \tag{2.19}$$

The linear coefficients relating to the signal throughput parameter δ_0 of the electrical field are $T_0 = 1 - \gamma_0 - \delta_0^2$ and $K_0 = \delta_0^2$. Therefore, the electric field can also be expressed as

$$\begin{pmatrix} \boldsymbol{E}_3 \\ \boldsymbol{E}_4 \end{pmatrix} = \begin{pmatrix} \sqrt{T_0} & i\sqrt{K_0} \\ i\sqrt{K_0} & \sqrt{T_0} \end{pmatrix} \begin{pmatrix} \boldsymbol{E}_1 \\ \boldsymbol{E}_2 \end{pmatrix},$$

which is an effective method for accounting for the individual losses from tap and signal path, as previously discussed. In the prior treatment, it was only feasible to utilize the total intensity loss γ_0. The utilization of both presentations is predicated on their respective benefits, which are intended to be applied in different situations. TCs are devices that allow for the distribution of light signals from a single fiber to multiple destinations. These devices are constructed by fusing two parallel fibers in such a manner that the electric field that travels through one fiber, its signal path, also enters the second one, the tap path, and vice versa. Tap couplers are reciprocal in nature, thereby enabling light to propagate in both directions.

Another element is the optical circulator, which is a fiber-coupled Faraday isolator. In this configuration, light entering an input port is constrained to travel only in a specific direction to the next port. In many cases, these devices are configured with three ports. In such an arrangement, light entering port one is directed to port two, while light entering port two is routed to port three. The principle is shown in Figure 2.2 (b).

Generally, there are two types of fibers that can be utilized for the aforementioned elements. The standard SM fiber, mentioned briefly before, and the polarization maintaining (PM) fibers, which are identical to the SM version, with the exception of an additional physical guide that is incorporated into the cladding. This guide disrupts the radial symmetry of the fiber. Stress-applying parts (SAP) induce a change in the refractive index of the fiber, thereby inducing a birefringence behavior. This, in turn, results in a preferred polarization axis of light along either the fast or slow

axis within the fiber. A conventional methodology entails the utilization of two rods of disparate material to the fiber cladding, which are positioned symmetrically along the transverse axes of the fiber core, as illustrated in Figure 2.3. In the context of optical fiber communication, the polarization of light is of paramount importance. When light is properly coupled in, even in the presence of fiber bending or mechanical stress, the SAPs become the predominant factor in confining the polarization. This persists throughout the propagation process, ensuring a fixed polarization along the path.

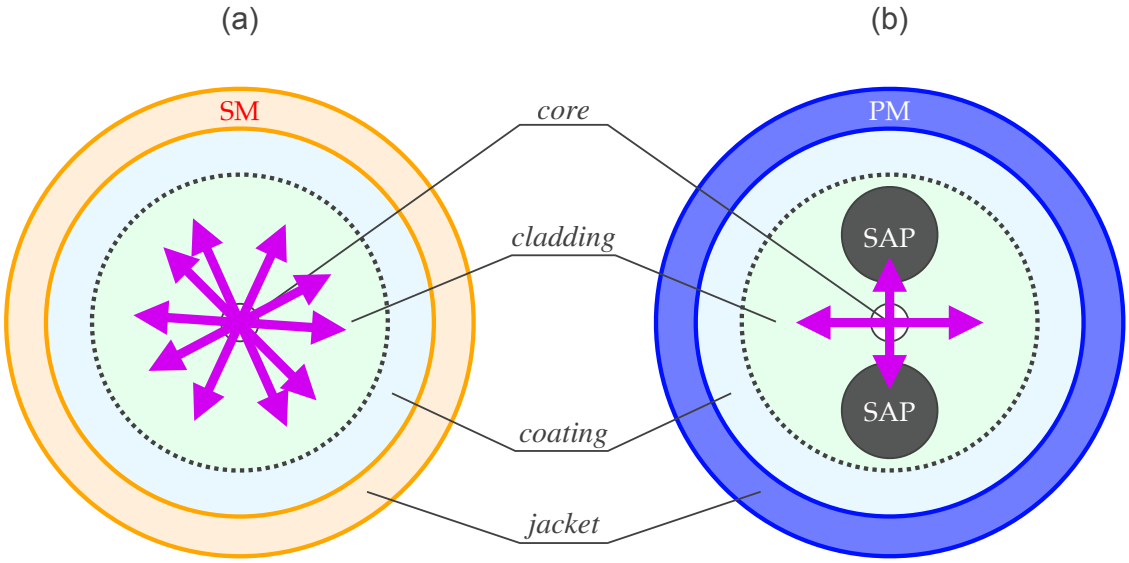


Figure 2.3: The configuration of an (a): SM and (b): PM fiber, respectively. In an SM fiber, any transverse polarization axis is possible, as indicated by the purple arrows. In a PM fiber, however, the light preferably travels when the polarization is aligned parallel or perpendicular to the SAPs, along the slow or fast axis, respectively.

2.1.4 Light in a Loop: Principles of Fiber Ring Resonators

Originally located in Appendix A.3.5. The focal point of this thesis will be the analysis of standing wave FP resonators that are based on two high-reflectivity mirrors. Nevertheless, with the objective of advancing the field, a novel type of fiber-based resonator was engineered. The experimental setup is discussed in Section 5. In this sub-section, the mathematical description of this resonator is explained. Starting from the TC as described above, by connecting the fibers of the ports of E_3 and E_2, results in the formation of a ring resonator. The length of the ring, designated as L, encompasses the lengths of the fibers in ports 3 and 2. In general, the losses due to fiber length L can be modeled $\delta_L^2 = 10^{-\left(\frac{\alpha_L L}{10}\right)}$, such that

$$I_3 = 10^{-\left(\frac{\alpha_L L}{10}\right)} I_2.$$

In this context, the parameter α_L is defined as the fiber loss parameter, which is typically expressed in units of $\frac{\mathrm{dB}}{\mathrm{km}}$. Note that δ_L is defined for the electric field, not intensity, for consistency. Another

important loss factor is due to MSs exhibiting a typical loss of $\alpha_m \lessapprox 0.5\,\mathrm{dB}$. Thereby, the intensity of the light before I_{in} and after I_{fin} the fiber connector is described by

$$I_{fin} = 10^{-\left(\frac{\alpha_m}{10}\right)} I_{in} \longrightarrow \delta_m^2 = 10^{-\left(\frac{\alpha_m}{10}\right)}.$$

The utilization of the notation of the individual δ-parameters offers the advantage of modeling the final throughput as the product of the individual δ-parameters. In other words, if one is interested in the field E_{fin} of light with an initial field E_{in} after it has traveled a certain fiber length through two MSs of a fiber splitter with δ_0, it can be expressed as

$$E_{fin} = \delta_0 \delta_m \delta_m \delta_L E_{in}.$$

The final piece of information necessary to calculate the fields both within and without the resonator is the round-trip phase shift, denoted by the symbol $\phi = \beta L$, which the light undergoes during its traversal through the fiber with a length L. The phase shift coefficient is expressed as $\beta = \frac{n\omega}{c_0}$, and consequently, the phase is defined as

$$\phi = \frac{\omega}{\Delta\nu} = 2\pi \frac{\nu}{\Delta\nu}.$$

In a manner consistent with the linear resonator, the free spectral range of the ring configuration is $\Delta\nu = \frac{nL}{c_0}$. Here, n is the refractive index of the fiber core and c_0 is the speed of light in vacuum.

A brief comment on the notation of the frequency. In this work, the symbol ν is used to represent the carrier frequency of light. This is in the order of some hundred terahertz (THz). However, in the majority of scenarios, the value that is plotted is not this value itself; rather, it is a frequency offset from this value or the variation of the carrier. The symbol used to denote these frequencies is f. Specifically, it is the relationship $\nu = \nu_0 + f$, where ν_0 specifies the constant (mean) carrier frequency of the wave. Please note that phase noise plots in this thesis will utilize $f_0 = \nu_0$ as the carrier frequency, for the sake of visual clarity. The variation of the frequency, f, is equivalent to an offset or detuning from the carrier frequency. In this particular case, the phase can be expressed as follows: $\phi(\nu) = \phi(\nu_0) + \phi(f)$, where the term $\phi(\nu_0)$ is a constant global phase (in many instances, even equal to zero) that can be neglected or canceled out with ease. In the following work, equations and plots will be defined with respect to the detuning of the carrier frequency.

For comparison purposes with the standing wave optical resonator, the intensity of the light entering the fiber ring will in the following be denoted by $I_1 \longrightarrow I_0 \propto |E_1|^2$.

In contrast to a FP resonator, the light is only traveling once through the length L before it reproduces itself. The final field, situated at the same point as the initial field, undergoes a transformation due to a single round trip by $E_{fin} = e^{-i\phi} E_{in}$. As previously indicated, E_2 is now linked to E_3, comprising an additional fiber between them and two MSs, as illustrated in Figure 2.4 (a). This is represented by the following equations for field and intensity:

$$E_2 = \delta_m^2 \delta_L E_3 e^{-i\phi}, \text{ and } I_2 = \delta_m^4 \delta_L^2 I_3 \tag{2.20}$$

By following this procedure, it is now possible to calculate two different normalized intensities. The first is the intensity that is circulating inside the resonator at E_3. The second is the intensity at the output at E_4. The first one can be calculated directly by Equation (2.19), It follows

$$E_3 = \sqrt{(1-\gamma_0)-\delta_0^2}E_1 + i\delta_0 E_2 = \sqrt{(1-\gamma_0)-\delta_0^2}E_1 + i\delta_0\delta_m^2\delta_L E_3 e^{-i\phi},$$

$$\Longleftrightarrow \frac{E_3}{E_1} = \frac{\sqrt{(1-\gamma_0)-\delta_0^2}}{\left(1-i\delta_0\delta_m^2\delta_L e^{-i\phi}\right)}. \tag{2.21}$$

The normalized intensity of the circulating field inside the resonator, denoted by $I_{n,circ,s}(f) = I_3 I_0^{-1}$, is of particular interest. The calculation of the absolute square of Equation (2.21) and the subsequent substitution of the not coupler dependent losses/throughputs as $\delta_s = \delta_m^2\delta_L$ results in the following expression:

$$I_{n,circ,s}(f) = \frac{1-\gamma_0-\delta_0^2}{1-2\delta_0\delta_s\sin\left(\frac{2\pi}{\Delta\nu}f\right)+\delta_0^2\delta_s^2}. \tag{2.22}$$

Equation (2.22) now describes the normalized circulating intensity inside of a **s**ingle-splitter **f**iber **r**ing **r**esonator (SFRR). For the output E_4 the process is analogous. Starting from the matrix given in (2.19), inserting Equation (2.20) for the circulating field, and dividing by E_1, the result is

$$\frac{E_4}{E_1} = \sqrt{(1-\gamma_0)-\delta_0^2}\delta_m^2\delta_L\frac{E_3}{E_1}e^{-i\phi} + i\delta_0\frac{E_1}{E_1}. \tag{2.23}$$

Accordingly, the normalized intensity $I_{n,ref,s}(f) = I_4 I_0^{-1}$ is derived by multiplying (2.23) this with its the complex conjugate. In addition, it is necessary to insert the term (2.21) into the equation. Performing the extensive but trivial algebra and substituting the parameter δ_s once more results in the equation

$$I_{n,ref,s}(f) = \left(1-\gamma_0-\delta_0^2\right)\left(\frac{(1-\gamma_0)\,\delta_s^2 - 2\delta_0\delta_s\sin\left(\frac{2\pi}{\Delta\nu}f\right)+\delta_0^2\delta_s^2}{1-2\delta_0\delta_s\sin\left(\frac{2\pi}{\Delta\nu}f\right)+\delta_0^2\delta_s^2}\right)+\delta_0^2, \tag{2.24}$$

which is of the form of the reflection signal of a FP resonator, but for an SFRR. This signal is frequently designated as PDH output, a reference to the technique employed to stabilize the frequency of light (see Section 2.3). It utilizes a signal of the same form. Furthermore, the expressions for the cavity linewidth $f_{D,s}$, of an SFRR can be derived by

$$\frac{1}{2}I(\nu_0) \stackrel{!}{=} I\left(\nu_0+\frac{f_{D,s}}{2}\right) \Longleftrightarrow f_{D,s} = \arccos\left(1-\frac{(1-\delta_0\delta_s)^2}{2\delta_0\delta_s}\right)\frac{\Delta\nu}{\pi}.$$

Figure 2.4 (b), presents the simulation of reflected and circulating intensities. The simulation was performed for a 50 : 50 TC with insertion losses of 3.0 dB and 3.1 dB for signal and tap paths, respectively. This results in a total loss of approximately $\gamma_0 \approx 1\,\%$, which is low but possible for well-designed TCs.

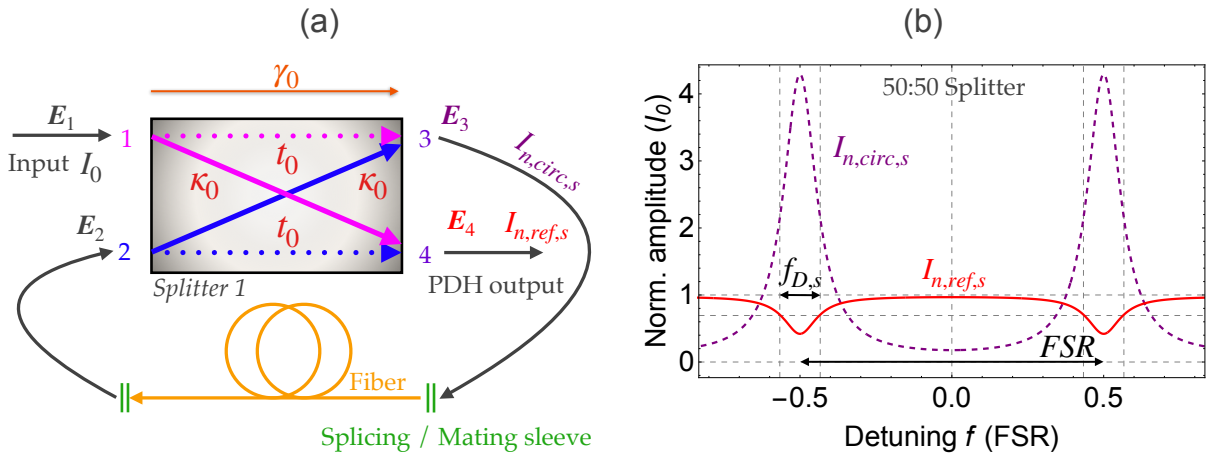


Figure 2.4: (a): The following schematic illustrates a SFRR, including an extension fiber. The green lines indicate the locations of MSs or splices in the system. (b): The simulation of a 50 : 50 splitter for light at 1.5 µm and a 1 km long fiber. The line width and FSR are indicated herein. The system has a finesse that is slightly larger than 8.

The loss in the fiber was modeled with a value of $0.18\,\mathrm{dB\,km^{-1}}$, which is a typical value for SMF-28 fibers at 1.5 µm. The MSs were estimated to result in an approximate loss of 0.2 dB per interface coupling. The total ring's fiber length is determined to be $L = 10^3$ m, which subsequently yields a free-spectral range of approximately $\Delta\nu \approx 205\,\mathrm{kHz}$, a cavity linewidth of approximately $f_{D,s} \approx 27\,\mathrm{kHz}$, and a finesse of approximately $\mathcal{F}_s \approx 7$ to 8. A noteworthy aspect of the Equation (2.24) is its tendency to exhibit peculiar behavior. In a lossless system, the fraction becomes independent of the frequency. This includes the prevention of fiber loss due to MSs or TCs. This property is not present in the reflection signal of a two mirror based standing wave resonator.

However, as will be demonstrated subsequently, the system is engineered to achieve low noise in the frequency domain. Consequently, it would be highly advantageous to utilize the output light of the resonator, which undergoes an additional filtration due to the cavity modes. In the present configuration, incorporating a single fiber splitter, it is not yet feasible to generate a signal of form of the transmitted intensity $I_{n,trans,s}$. As indicated by the PDH or reflected output, a significant portion of the signal from the input 1 is still present.

Consequently, an enhanced setup is proposed and illustrated in Figure 2.5. The system has been upgraded with the addition of a second TC. Output 3 of the first coupler is now connected to input 5 of the second. Subsequently, output 8 is linked to input 2, resulting in the additional output 7. This can be interpreted as the transmission signal of the resonator as derived in the following. The resulting system is the dual splitter fiber ring resonator (DFRR). The second coupler is characterized by the parameters δ_1 and γ_1. The field transformation expressed through the matrix formalism is

$$\begin{pmatrix} E_7 \\ E_8 \end{pmatrix} = \begin{pmatrix} \sqrt{(1-\gamma_1)-\delta_1^2} & i\delta_1 \\ i\delta_1 & \sqrt{(1-\gamma_1)-\delta_1^2} \end{pmatrix} \begin{pmatrix} E_5 \\ E_6 \end{pmatrix}. \tag{2.25}$$

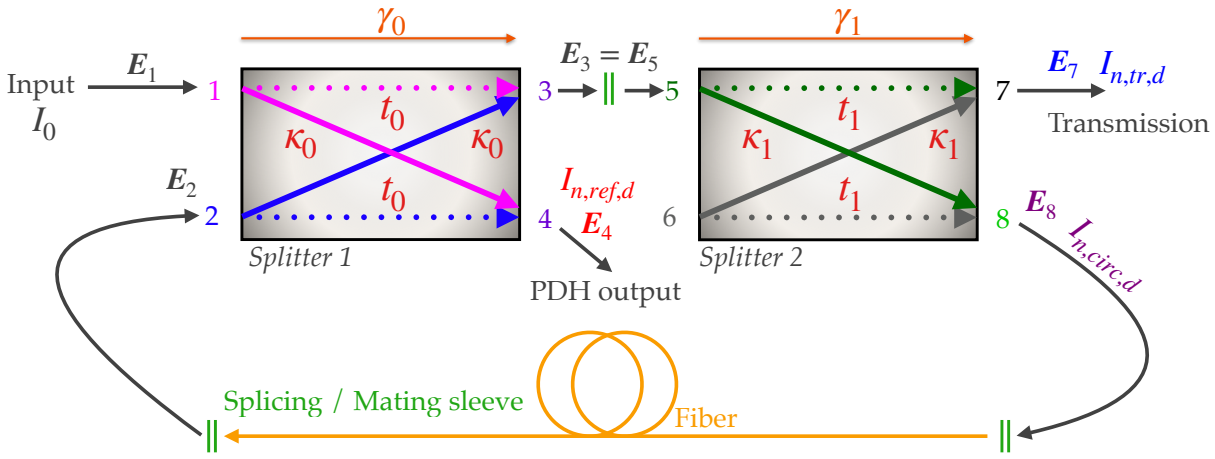


Figure 2.5: The following schematic illustrates a DFRR, including an extension fiber. The green lines denote the locations of MSs or splices within the system.

In the case of the DFRR, it is $E_6 = 0$ and $E_5 = \delta_m E_3$, on account of the fact that the splitter arms are connected by an additional mating sleeve. The relationship between E_2 and E_8 is given by $E_2 = \delta_m^2 \delta_L E_8 e^{-i\phi}$. The resulting expression for the circulating field is as follows:

$$E_8 = i\delta_1 E_5 = i\delta_1\delta_m E_3 = i\delta_1\delta_m\sqrt{(1-\gamma_0)-\delta_0^2}E_1 - \delta_1\delta_0\delta_m E_2$$

$$= i\delta_1\delta_m\sqrt{(1-\gamma_0)-\delta_0^2}E_1 - \delta_1\delta_0\delta_m^3\delta_L E_8 e^{-i\phi} \Longleftrightarrow \frac{E_8}{E_1} = \frac{i\delta_1\delta_m\sqrt{(1-\gamma_0)-\delta_0^2}}{\left(1+\delta_1\delta_0\delta_m^3\delta_L e^{-i\phi}\right)}$$

Calculating the intensity and substituting δ_s, as well as summarizing the second coupler throughput and the MS as $\delta_1' = \delta_1\delta_m$, gives an expression for the circulating intensity in the DFRR:

$$I_{n,circ,d}(f) = \frac{(1-\gamma_0)\,\delta_1'^2 - \delta_0^2\delta_1'^2}{1 + 2\delta_1'\delta_0\delta_s\cos\left(\frac{2\pi}{\Delta\nu}f\right) + \delta_1'^2\delta_0^2\delta_s^2} \tag{2.26}$$

The PDH output at 4 is, by the inclusion of the matrix in (2.25), expressed as

$$E_4 = \sqrt{(1-\gamma_0)-\delta_0^2}E_2 + i\delta_0 E_1 = \sqrt{(1-\gamma_0)-\delta_0^2}\delta_m^2\delta_L E_8 e^{-i\phi} + i\delta_0 E_1$$

$$\Longleftrightarrow \frac{E_4}{E_1} = \sqrt{(1-\gamma_0)-\delta_0^2}\delta_m^2\delta_L\frac{E_8}{E_1}e^{-i\phi} + i\delta_0.$$

In summary, the integration of all terms, in conjunction with the substitution of δ_s and δ_1', results in the normalized intensity

$$I_{n,ref,d}(f) = \left(1-\gamma_0-\delta_0^2\right)\frac{2\delta_0\delta_1'\delta_s\cos\left(\frac{2\pi}{\Delta\nu}f\right) + \delta_0^2\delta_1'^2\delta_s^2 + (1-\gamma_0)\,\delta_1'^2\delta_s^2}{1 + 2\delta_1'\delta_0\delta_m^2\delta_L\cos\left(\frac{2\pi}{\Delta\nu}f\right) + \delta_1'^2\delta_0^2\delta_s^2} + \delta_0^2.$$

This concludes the discussion of the circulating and reflected intensities in a dual splitter fiber ring resonator (DFRR). Eventually, the transmitted field is given by output 7. It can be derived in the same manner, which again requires a substantial amount of algebra. The starting point is the electric field E_7, which is expressed through the field E_5. E_5 is given by E_3, where the matrix is applied. As an alternative approach, the transmitted field can be motivated by comparing it to the circulating field at output 8. The field at output 7 is generally identical to that one, with the difference that the light did not propagate through the signal, but rather through the tap path. The concept can be expressed by the following equation:

$$I_{n,trans,d}(f) = \frac{\left(1-\gamma_1-\delta_1^2\right)}{\delta_1^2} I_{n,circ,d}$$

This equation, by incorporating Equation (2.26), yields the transmitted intensity for the DFRR as

$$I_{n,trans,d}(f) = \frac{\left(1-\gamma_0-\delta_0^2\right)\left(1-\gamma_1-\delta_1^2\right)\delta_m^2}{1+2\delta_1\delta_0\delta_m^3\delta_L\cos\left(\frac{2\pi}{\Delta\nu}f\right)+\delta_1^2\delta_0^2\delta_m^6\delta_L^2}.$$

Once more, substituting the throughputs δ_s and δ_1', results in the formalism

$$I_{n,trans,d}(f) = \frac{\left(1-\gamma_0-\delta_0^2\right)\left(1-\gamma_1-\delta_1^2\right)\delta_m^2}{1+2\delta_1'\delta_0\delta_s\cos\left(\frac{2\pi}{\Delta\nu}f\right)+\delta'^2_1\delta_0^2\delta_s^2}.$$

This signal is, in fact, of form of the transmission signal in a standing wave resonator. Thus, the system, including two TCs, can be treated as a black box, which possesses the same attributes as a classical FP cavity. An alternative method for determining the electric fields is to follow the trajectory of the light. The light at Output 4 is characterized by

$$\begin{aligned}
E_4 = {} & i\sqrt{K_0}E_1 \\
& + \sqrt{T_0}\left(\delta_m e^{-i\phi}\delta_L\delta_m i\sqrt{K_1}\delta_m\right)\sqrt{T_0}E_1 \\
& + \sqrt{T_0}\left(\delta_m e^{-i\phi}\delta_L\delta_m i\sqrt{K_1}\delta_m\right) i\sqrt{K_0}\left(\delta_m e^{-i\phi}\delta_L\delta_m i\sqrt{K_1}\delta_m\right)\sqrt{T_0}E_1 \\
& + \sqrt{T_0}\left(\delta_m e^{-i\phi}\delta_L\delta_m i\sqrt{K_1}\delta_m\right) i\sqrt{K_0}\left(\delta_m e^{-i\phi}\delta_L\delta_m i\sqrt{K_1}\delta_m\right) i\sqrt{K_0}\left(\delta_m e^{-i\phi}\delta_L\delta_m i\sqrt{K_1}\delta_m\right)\sqrt{T_0}E_1 \\
& + \ldots,
\end{aligned}$$

a relationship that can be expressed and calculated using the geometric series method:

$$\begin{aligned}
E_4 &= \frac{E_1}{i\sqrt{K_0}}\left(T_0\sum_{k=0}^{\infty}\left(-\sqrt{K_0}\delta_L\delta_m^3\sqrt{K_1}e^{-i\phi}\right)^k-(T_0+K_0)\right) \\
&= i\frac{\left(\sqrt{K_0}\delta_L\delta_m^3\sqrt{K_1}e^{-i\phi}\right)(T_0+K_0)+K_0}{\sqrt{K_0}+K_0\delta_L\delta_m^3\sqrt{K_1}e^{-i\phi}}E_1
\end{aligned}$$

The parameters $T_0 = 1 - \gamma_0 - \delta_0^2$ and $K_0 = \delta_0^2$ are introduced. Including, again, δ_s and δ_1' yields the reflection coefficient function $F_{DFRR}(f)$, given by

$$F_{DFRR}(f) = \frac{E_4}{E_1} = i\frac{\left(\delta_s\delta_1' e^{-i\phi}\right)(1-\gamma_0)+\delta_0}{1+\delta_0\delta_1'\delta_s e^{-i\phi}}.$$

This method can be used to calculate the reflected intensity function following the steps:

$$\begin{aligned} I_{n,ref,d} &= \frac{|E_4|^2}{|E_1|^2} = i\frac{\left(\delta_s\delta_1' e^{-i\phi}\right)(1-\gamma_0)+\delta_0}{1+\delta_0\delta_1'\delta_s e^{-i\phi}} \times (-i)\frac{\left(\delta_s\delta_1' e^{+i\phi}\right)(1-\gamma_0)+\delta_0}{1+\delta_0\delta_1'\delta_s e^{+i\phi}} \\ &\dots \\ &= \left(1-\gamma_0-\delta_0^2\right)\frac{(1-\gamma_0)\delta_s^2\delta_1'^2 - \delta_0^2\delta_s^2\delta_1'^2 + 2\delta_0\delta_s\delta_1'\cos(\phi)}{1+2\delta_0\delta_1'\delta_s\cos(\phi)+\delta_0^2\delta_1'^2\delta_s^2} + \delta_0^2. \end{aligned}$$

Accordingly, the linewidth of the DFRR can be expressed as by

$$f_{D,d} = \Delta\nu - \arccos\left(\frac{1-4\delta_1'\delta_0\delta_s+\delta_1'^2\delta_0^2\delta_s^2}{2\delta_1'\delta_0\delta_s}\right)\frac{\Delta\nu}{\pi}. \tag{2.27}$$

Figure 2.6 presents a simulation of a DFRR. Panel (a) depicts a system comprising two 65 : 35 splitters that are free of losses, while Panel (b) illustrates a system consisting of two 90 : 10 TCs accompanied by realistic losses. The chosen ratio has been selected to ensure the presentation's clarity and readability. The fiber path length of the resonator is 10^3 and 10^2 meters, respectively. The lossless system has a linewidth of 28 kHz and a finesse of 7. The total loss of the TCs in the second simulation is approximately 8 %. The line width of the system under consideration is approximately 18 kHz, which corresponds to a finesse of 11.

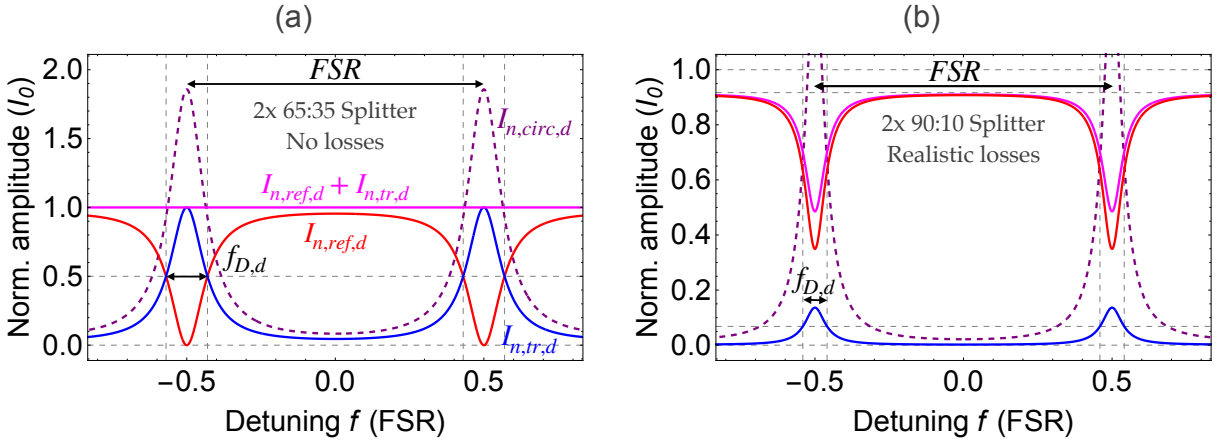


Figure 2.6: The following simulations were carried out: (a): A DFRR was simulated with two 65 : 35 TCs and no losses in the system. (b): A DFRR was simulated with two real-world 90 : 10 TCs, including MS and fiber length losses.

An ideal system, equipped with these splitters, in the absence of a MS, a fiber path length-, or fiber splitter-loss, would possess a line width of 7 kHz. This theoretical value would translate to a finesse of approximately 30. An intriguing property is evident in the plots. In a lossless system, the sum of reflected and transmitted fields is constant and equal to one. In the system incorporating losses, the magenta line falls below one. This is due to the losses within the system. However, it also undergoes a significant drop at resonance. This is presumably attributable to the fact that, during resonance, a greater number of round trips through the resonator are executed, which collectively result in a larger loss. Interestingly, the work of [69], was published at the time, that the theory was developed for this thesis. There, the finesse and linewidth of a lossless single splitter ring resonator is derived.

2.2 Resonators for Frequency Stabilization

This section covers the general concept of resonators as references for ultra-stable light and the fundamental limitations imposed by the respective thermal noise floors. Descriptions of lasers, important RF electronics, PID controllers, as well as theoretical models of linewidth, phase and frequency noise, and Allan deviations can be found in the appendix sections preceding the material presented here.

2.2.1 Anchoring Light: Resonators as Optical References

Originally located in Appendix A.5.5. Continuous-wave lasers generate streams of photons that are highly coherent and of similar energy, though not equal. In practice, state-of-the-art fiber and solid-state lasers have demonstrated the capability to achieve linewidths as narrow as 10 kHz, accompanied by frequency stabilities ranging from 100 kHz to 10 MHz in the context of the Allan deviation plot, over time frames exceeding one second. The wavelength of the laser is contingent upon the application; however, in this context, it is generally within a range that extends from ultraviolet (200 nm) to MIR (10 µm). While more 'exotic' wavelengths do exist, the dominant frequencies regime for lasers presented in this thesis is between 1064 µm and 1.561 µm. This converts to optical carrier frequencies between 192 THz and 282 THz.

These lasers have been shown to achieve fractional linewidths of 10^{-11}, with instabilities that are only slightly better than 10^{-12}. However, these instabilities can reach levels of up to 10^{-9} on time scales of up to a day, which is a significant increase. In most cases, diode lasers exhibit the most significant levels of instability, as fiber lasers are essentially upgraded versions of diode lasers. Solid-state lasers have historically dominated the performance landscape, but this dominance has been challenged by the substantial advancements made by fiber lasers in recent decades. In a multitude of applications, the performance of lasers straight out of the box is sufficient, or even optimal. The scope of this field encompasses laser cooling applications of trapped atoms or ions, as well as the spectroscopy of molecules with broad lines, photo-dissociation, and numerous other areas of study.

In the domain of high-precision physics, particularly in the context of probing narrow transitions in molecules, atoms, or ions, this performance frequently proves lacking. Transition linewidths in this

field can reach as low as 100 Hz, and in some cases, can be even magnitudes lower. Consequently, the laser must not only be as narrow as the transition line, but also maintain its stability, avoiding drift or jumps away from the transition line. This results in an increase in the requirements for laser light performance to levels in the order of 10^{-14} and lower for the linewidth and on the observation time scales that are of interest, which are typically between 1 s and 1 d. Achieving performance enhancement factors of greater than 10^3 and of the order of 10^6, in comparison to commercially available solutions, can be accomplished by utilizing a reference that is in accordance with the target performance. This reference can be the optical resonator or cavity, which has been introduced and discussed in this thesis until this point.

It has been derived that light of distinct resonance frequencies will lead to the build-up of a field inside the resonator and, eventually, in a measurable transmission behind it (see Section 2.1.1). At this particular stage, the frequency of the light is well-defined based on the criteria of resonance. Under the assumption of optimal resonator stability, signal transmission fluctuates in accordance with the frequency varying of the light that propagates towards the resonator. To observe cavity modes, it is necessary to tune the light close to the mode frequency and scan it with a periodic frequency.

In the absence of such a mechanism, the laser's inherent frequency variations are of such magnitude that a transmission is often undetectable, manifesting only as sporadic flickering observed through a camera positioned in the transmission signal. The objective is to utilize the modes as a feedback mechanism to the laser itself, thereby ensuring the continuous resonance of the light with the cavity. The conceptual part will be explained in Section (2.3), which is devoted to an exposition of the frequency locking technique. For the purpose in this section, the light is already fully stabilized to the cavity. In this particular instance, it can be demonstrated that

$$\lambda_0 = \frac{2L_0}{m}, \tag{2.28}$$

where m is an integer number, L_0 is the OL of the resonator, and λ_0 the respective resonant wavelength. If an effect induces a change in length by $\Delta L = L_1 - L_0$, the new resonance condition consequently becomes

$$\lambda_1 = \frac{2L_1}{m}, \tag{2.29}$$

where the wavelength of the light has to be altered by $\Delta\lambda = |\lambda_1 - \lambda_0|$ to stay in resonance. Inserting Equation (2.28) and (2.29) into an expression for the fractional wavelength change yields a relation of trivial appearance, yet of great power:

$$\frac{\Delta\lambda}{\lambda_0} = \frac{\lambda_1 - \lambda_0}{\lambda_0} = \frac{2}{m\lambda_0}(L_1 - L_0) = \frac{\Delta L}{L_0} \tag{2.30}$$

In regard to its optical frequency, employing the speed of light $c = \lambda_i \nu_i$ and the corresponding frequency variation $\Delta\nu = \nu_1 - \nu_0$, this formalism is expressed as

$$\frac{\Delta\lambda}{\lambda_0} = \frac{\nu_0 - \nu_1}{\nu_1} = -\frac{\Delta\nu}{\nu_1} \approx -\frac{\Delta\nu}{\nu_0}. \tag{2.31}$$

The latter part of Equation (2.31) can be considered reasonably accurate when the condition $\Delta\nu \ll \nu_0$ is met. Eventually, once it has been properly stabilized, the fractional frequency of the light stability and, consequently, its absolute, will follow the fractional stability of the optical path between the cavity mirrors. The implementation of a cavity is an effective strategy to enhance the stability of light, provided that the length variation attains a greater degree of stability compared to the free-running laser. As demonstrated in Figure 2.7, this objective is realized through multiple means. Initially, the mirrors are contacted to a spacer, which exhibits minimal sensitivity to environmental influences such as accelerations and temperature variations.

Additionally, the optical path itself propagates through a space that has been evacuated, and its pressure is maintained by an ion pump. This further improves the isolation from temperature variations as well as local changes in the refractive index n of the air along the optical path. This generally leads to configurations in which the resonator material is positioned within a vacuum chamber that incorporates one or more stages of active temperature stabilization. The design of the chamber, which holds the spacer, is optimized to minimize its acceleration sensitivity, i.e. by the use of support rods.

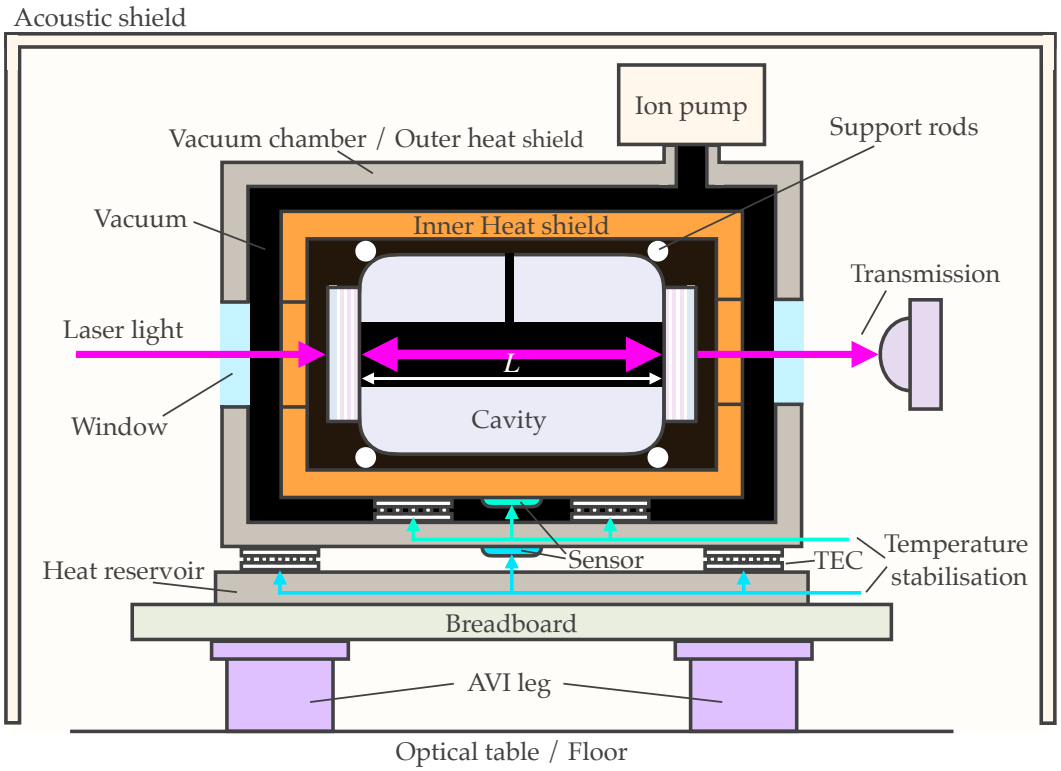


Figure 2.7: Schematic illustrating a configuration engineered to insulate the OL of a cavity from external disturbances. The cavity is situated within an evacuated vacuum chamber, wherein the pressure level is sustained by an ion pump. Two stages of active temperature stabilizations have been incorporated to mitigate external temperature variations. The utilization of an AVI serves to mitigate vibrations that reach the resonator, thereby enhancing its performance. The transmission signal can be used to stabilize the power, thus reducing variating local expansion or contraction of the mirrors. An external surrounding shield is further reducing the overall acoustic noise level.

The complete system is placed on an active vibration isolation (AVI) platform to minimize vibrations from laboratory devices or the building that reach the resonator. The addition of acoustic and thermal shielding can further enhance stability. In certain instances, the tilt of the system can also serve as a limiting factor, resulting in alterations to the effective optical path due to minor deformations. Even effects such as the heat-induced contraction and expansion of the mirrors due to fluctuations in laser power must be considered. For instance, the transmission power can be stabilized to mitigate these effects.

Appropriate systems have been shown to attain relative length instabilities at the 10^{-15} level and below. These instabilities can be translated into laser light, which frequently results in an enhancement of 10^6 or higher on the free-running specifications. This renders the system viable for specific applications such as atomic (optical) clocks and high precision spectroscopy. Some publications on the setup of ultra-stable lasers include but are not limited to [60, 70, 58, 71, 59, 72, 64, 66]. A primary objective in the implementation of ultra-stable lasers, as well as a pivotal subject of this study, is to comprehend the impact of a specific effect on the cavity length, characterize it, and develop strategies for its mitigation.

A critical component of the design of an optical resonator pertains to the selection of materials, the incorporation of mechanical support, and the configuration of the shape and geometry. While the material will be part of the discussions in later chapters, it is typically chosen to be insensitive to thermal variations at the operating temperature as well as exhibiting as low as possible acceleration sensitivities. The latter is the limiting factor in the maximum cavity length. While the fundamental limit of the fractional length stability would benefit from long resonator path lengths, the increased sensitivity to vibrations will become dominant.

This is evidenced by the fact that the longest ultra-stable resonators to date have not yet exceeded 48 cm, as exemplified by the cavity at PTB of the first reference above. The configuration of the cavity spacer and its mounting in the cavity chamber can be simulated using software that utilizes the finite element method (FEM). Through the modeling of diverse geometries and the execution of simulations that assess their response to externally applied stress, a series of optimized shapes for optical resonators have been identified. These range from vertically resting biconical cavities to cylindrical horizontal hanging geometries. It is notable that FEM simulations do not exclusively evaluate vibration sensitivities; they also assess other effects, such as temperature sensitivity and thermal noise.

FEM simulations [73, 74, 75] represent an initial step in the design process of the resonator. These simulations were also performed for the resonators that are subject to this work. However, they were previously conducted by others in advance of the work in this thesis. Consequently, they are not thoroughly explored, but rather acknowledged as a critical parameter in the design process of ultra-stable references. Furthermore, the issue of the mirrors' connection to the cavity constitutes a separate subject that must be addressed. In order to avoid introducing additional materials that could potentially compromise the length variation and composition of the cavity, the mirrors are optically contacted [76] to the spacer. Here, the two materials are connected by attractive intermolecular forces (van der Waals). To expel any air and avoid foreign particles between the surfaces, the mirrors must be extremely smooth, clean, and flat. The quality of the

optical contact can affect the performance of the resonator. This step, which may appear modest, is of great importance. The optical contacting of the resonators discussed in this study has also been performed in advance of the work of this thesis by colleagues at the institute.

2.2.2 Beating Drift: Thermal Expansion and Shielding

Originally located in Appendix A.5.6. Although the majority of extrinsic variations, including tilts, pressure, and intensity, can be readily characterized, as demonstrated in the experimental section, particularly temperature-induced OL changes necessitate a more cautious examination within the context of resonators. A common model posits that an object with an initial length of L_0 at a temperature of T_0 will undergo linear expansion or contraction when subjected to heating or cooling, respectively. This can be mathematically modeled as

$$L_{lin}(T) = \alpha_{lin}(T - T_0) + L_0,$$

where T is the final temperature, and $[\alpha_{lin}] = \mathrm{mK}^{-1}$ denotes a material dependent parameter. This model has been utilized in a variety of contexts, including the expansion of train tracks during the summer months and the use of mercury-based thermometers. A salient feature of this equation is the coefficient of thermal expansion (CTE), defined as the length change resulting from temperature fluctuations. This coefficient is expressed as follows:

$$\frac{dL_{lin}(T)}{dT} = \alpha_{lin} = const.$$

In this particular instance, the CTE is equivalent to α_{lin}, thereby acquiring the designation of the linear CTE. However, it should be noted that the linear approximation is typically only valid in a specific window of interest, namely for small temperature changes, or as long as the aggregate state does not change. Nonetheless, water is a common example of non-linear thermal expansion. Water exhibits its highest density at approximately 4 °C and undergoes expansion at higher and lower temperatures. This has also been observed in numerous optical resonators, with the influence of the spacer and mirror materials and geometries being predominantly responsible. A suitable estimation, with a high degree of accuracy, localized around a specific temperature, can be obtained by employing a quadratic function

$$L(T) = \beta_L (T - T_0)^2 + L_0, \tag{2.32}$$

where this equation requires the length L_0 to be the extremum of the function at the temperature $T = T_0$. The "curvature" parameter of the function is of units $[\beta_L] = \mathrm{mK}^{-2}$. In many cases, the fractional length change, or fractional frequency change, is of interest. By using the identity $\Delta L = L(T) - L_0$ in Equation (2.32), it becomes

$$\frac{\Delta L}{L_0} = \beta (T - T_0)^2 .$$

Therefore, in terms of frequency, it is approximately

$$\frac{\Delta\nu(T)}{\nu_0} = -\beta(T-T_0)^2\,. \tag{2.33}$$

The quantity $[\beta] = \mathrm{K}^{-2}$ is fractional constituting a more universal parameter. In particular, the fractional change with respect to temperature, or the CTE, remains temperature-dependent, shown by its first derivative

$$\frac{d}{dT}\frac{\Delta\nu}{\nu_0} = -2\beta(T-T_0)\,.$$

This function can be minimized at $T = T_0$. The value $T_0 = T_{ZCTE}$ is therefore also known as zero coefficient of thermal expansion (ZCTE) temperature. This parameter is critical to the frequency stability of resonators. The impact of external temperature variations on the cavity length is minimized when the cavity is stabilized in close proximity to T_{ZCTE}. Furthermore, protecting against temperature variations is essential. To simplify the matter, one may consider a resonator, in air, at ambient temperature T_{ZCTE},, with environmental temperatures varying by $\Delta T_{env}(t) = T_{env}(t) - T_{ZCTE}$ over time. These temperature fluctuations will induce a rapid response in the cavity medium, which follows the external temperature, resulting in appropriate expansion or contraction given by Equation (2.33) as

$$\Delta\nu(t) = -\alpha\,\nu_0\,\Delta T_{env}^2(t)\,.$$

While the CTE close to the ZCTE of such a system may be as low as $\frac{d}{dT}\frac{\Delta\nu}{\nu_0} \approx 10^{-10}\,\mathrm{K}^{-1}$ level for temperature variations in the order of 0.1 K, the resulting frequency instability would correspond to 10^{-11}. This is sufficient for many applications; however, it is a limiting factor for an ultra-stable laser and must be improved by at least three orders of magnitude. This can be achieved through two methods. The first method involves the precise determination of the ZCTE temperature and the maintenance of moderate fluctuations around it. The second method involves the reduction of effective temperature variations that can reach the cavity to a substantial degree, thereby allowing some flexibility in the precision of T_{ZCTE}.

The latter objective can be accomplished by establishing a temperature heat shield around the resonator. This shield is actively temperature stabilized to a target or set temperature, which is optimally at T_{ZCTE}. The utilization of thermoelectric coolers, in conjunction with a thermistor/sensor and a PID controller, enables the maintenance of the desired temperature. Such a system is typically defined by a time constant, denoted by the symbol τ. A temperature sensor positioned in close proximity to the resonator, measuring T_{cav}, can be utilized to estimate the time required to stabilize the temperature of the heat shield to a new set temperature, T_{set}, which is subsequently transferred to the cavity. The behavior of such a temperature change is described by a thermal low-pass filter, given by

$$T_{cav}(t) = T_{set} - \tau\frac{dT_{cav}}{dt},$$

which is solved by an exponential function

$$T_{cav}(t) = T_{set}\left(1 - e^{-\frac{t}{\tau}}\right).$$

It is estimated that the temperature T_{set} is instantaneous with respect to the time it takes the cavity to stabilize to the new temperature. The response of the cavity to the perturbation is characterized by the time constant, τ, which is influenced by the power of the TEC, the material and mass of the heat shield, and the PID parameters. It is defined as the time at which the following identity holds:

$$\frac{T_{cav}(\tau)}{T_{set}} = 1 - \frac{1}{e} \approx 63\,\%$$

In the context of resonators, the time constant is frequently of the order of many hours. This observation underscores the low-pass filter behavior of the temperature stabilization. Therefore, rapid environmental temperature fluctuations will be significantly mitigated, while slow variations in the order of the time constant being transmitted to a greater extent towards the resonator. The efficacy of the PID controller in maintaining the heat shield temperature is a crucial factor in this regard. This is also an essential instrument for the evaluation of T_{ZCTE}, as the frequency of a cavity-stabilized laser can be monitored during induced temperature changes, resulting in a plot that can be modeled using Equation (2.33). This model is demonstrated in the experimental section of this thesis (see Section 5 and 6). In certain instances, a secondary stage of temperature stabilization is employed to provide additional protection for the resonator. The introduction of a temperature gradient in the two set temperatures (in the absence of which the process would technically still be a single stage stabilization) results in the implementation of a secondary thermal low-pass filter within the system. This development leads to an increase in the effective total time constant of the cavity with respect to external changes outside the second heat shield layer, extending up to days. Utilizing this method, the temperature variations at time scales of tens of seconds can be reduced to the µK level at the resonator. This results in fractional changes in the OL below the 10^{-16} level, which is essential to reach the fundamental limit of an optical resonator.

2.2.3 Fundamental Limits: Thermal Noise in Resonators

Originally located in Appendix A.5.7. This section was written with the acquired knowledge of [77, 78, 73]. In the context of a system in which the resonator remains entirely immune to external perturbations, the stability of light locked to it nevertheless encounters a fundamental constraint. The limit in question is referred to as the "thermal noise floor." The material composition of the mirrors and spacer, their absolute temperature, and the geometry of the beam diameter on the mirror surfaces are all factors that contribute to this limit. The substrate undergoes deformation due to internal thermal dissipation when it is subjected to pressure induced by a force, such as optical light, acting on its surface. The spatial displacement, designated as $S_{x,th}(f)$, exerts a correlation with the fractional frequency noise given by

$$\frac{S_{x,th}(f)}{L^2} = \frac{S_{f,th}(f)}{\nu_0^2} \Longleftrightarrow S_{f,th}(f) = \frac{\nu_0^2}{L^2} S_{x,th}(f)\,.$$

The length L is the total resonator length, and f_0 the optical carrier frequency. The displacement depends on the frequency of the applied force $F(t) = F_0 \cos(2\pi f t)$, expressed as

$$S_{x,th}(f) = \frac{2k_B T}{(\pi f)^2} \frac{W_{diss}}{F_0^2} \text{ and } S_{f,th}(f) = \left(\frac{\nu_0}{\pi f L F_0}\right)^2 2k_B T W_{diss}. \tag{2.34}$$

Equation (2.34) is modeled by the fluctuation-dissipation theorem. In this context, W_{diss} denotes the time-averaged dissipated power resulting from external pressure oscillations at a frequency f, which is offset from the optical carrier frequency ν_0. The full derivation of the thermal noise requires complex analytical models, which are beyond the scope of this thesis. Assuming the mirrors to be cylinders within which light propagates, the material will experience stress due to the external pressure. This stress will lead to deformations of the cylinder in all dimensions. Of particular interest is the specific expansion or contraction along the propagation direction of the light. Nevertheless, thermal expansion in a single direction exerts a direct influence on all other directions as well.

It can be conceptualized as follows: A cylinder is compressed by a force perpendicular to its axis, resulting in a contraction Δz. Subsequently, the material undergoes a slight expansion along its transverse axes due to forces perpendicular to the axial direction by Δx and Δy, respectively. Therefore, it can be concluded that internal thermal dissipation, which results in radial expansion, will also result in axial contraction. The individual strains ε that the body experiences along the respective direction are given by $\varepsilon_x = \frac{\Delta x}{x_0}, \varepsilon_y = \frac{\Delta y}{y_0}$ and $\varepsilon_z = \frac{\Delta z}{z_0}$, where x_0, y_0 and z_0 are the total lengths of the body along the respective axis. he effect of a deformation in one direction directly affecting an axis that is orthogonal to it is described by the Poisson ratio, denoted by σ. In the case above, that a force is applied along z it is defined by

$$\sigma = -\frac{\varepsilon_x}{\varepsilon_z} = -\frac{\varepsilon_y}{\varepsilon_z}. \tag{2.35}$$

Equation (2.35) requires the material to be isotropic and linearly elastic. In consideration of the transverse shape of a Gaussian beam within the cylinder, the stress inside this profile yields the total strain energy U, which is given by the integration

$$U = \int_V u \, dV,$$

over the strain energy density u, which is given by the formalism

$$u = \frac{1}{2} \sum_{i=1}^{3} \sum_{j=1}^{3} \Lambda_{ij} \varepsilon_{ij} = \frac{E}{2} \sum_{i=1}^{3} \sum_{j=1}^{3} \varepsilon_{ij}^2 = \frac{1}{2E} \sum_{i=1}^{3} \sum_{j=1}^{3} \Lambda_{ij}^2. \tag{2.36}$$

The parameter $\Lambda = \frac{F}{A}$ denotes the stress, thus force F over area A, and i and j are the corresponding axes. In Equation (2.36), the relationship $E = \frac{\Lambda}{\varepsilon}$ is employed to quantify the Young's modulus E, which serves as a measure of the material's stiffness. The time-averaged dissipated power, denoted W_{diss}, is dependent on the maximum strain energy, U_{max}, at a specified time scale, and consequently

on the frequency via the following relationship:

$$W_{diss} = 2\pi f U_{max} \phi$$

The loss angle, denoted by ϕ, is a material property that characterizes the extent of strain that results in thermal dissipation. The dissipated power is the result of the combined contributions of five distinct components within the resonator. These components include two mirror substrates and coatings, in addition to the spacer itself, which results in

$$W_{diss} = 2(W_{sb} + W_{ct}) + W_{sp}. \tag{2.37}$$

The calculation of the total strain energy for the substrate is achieved through the application of the pressure distribution function $\rho(r) = \frac{2}{\pi w_0^2} e^{-2r^2/w_0^2}$. This is attributable to the fundamental Gaussian beam of radius w_0 located at the mirror surface. Subsequently, three distinct terms will be established to describe the composition of the resonator:

$$W_{sb} = 2\pi f \phi_{sb} \frac{1-\sigma^2}{2\sqrt{\pi} E_{sb} w_0} F_0^2 \tag{2.38}$$

$$W_{ct} = W_{sb} \frac{2}{\sqrt{\pi}} \frac{1-2\sigma}{1-\sigma} \frac{d}{w_0} \frac{\phi_{ct}}{\phi_{sb}} \tag{2.39}$$

$$W_{sp} = 2\pi f \phi_{sp} \frac{L}{2E_{sp}\Delta A} F_0^2 \tag{2.40}$$

The dissipated power in coating W_{ct}, of thickness d, is described by a correction factor to the substrate W_{sb}. The dissipated power in the spacer W_{sp} is determined by the actual surface area of the spacer, which is $\Delta A = \pi \left(R_{out}^2 - R_{in}^2\right)$ for a cylindrical approximation. In this description the outer radius R_{out} ,and an inner radius R_{in}, are accounting for the hollow (evacuated) space inside the resonator for light to travel through. The total thermal frequency noise is computed by inserting Equations (2.38), (2.39) and (2.40), into (2.37) and subsequently into (2.34). It follows:

$$S_{f,th}(f) = \underbrace{\left(\frac{\nu_0}{L}\right)^2}_{\text{frac.}} \underbrace{\frac{4k_B T}{\pi f}}_{\text{Flicker noise}} \left(\underbrace{\frac{1-\sigma^2}{\sqrt{\pi} E_{sb} w_0} \phi_{sb}}_{\text{substrates}} \left(1 + \underbrace{\frac{2}{\sqrt{\pi}} \frac{1-2\sigma}{1-\sigma} \frac{d}{w_0} \frac{\phi_{ct}}{\phi_{sb}}}_{\text{coatings}} \right) + \underbrace{\frac{L}{2E_{sp}\Delta A} \phi_{sp}}_{\text{spacer}} \right). \tag{2.41}$$

The general behavior will follow a flicker noise curve, representing the fundamental limit in frequency noise or the Allan deviation picture. This further depends on the effective temperature of the resonator. This fundamental limit is an approximation for the case that the beam spot size is Gaussian and the same on both mirrors as well as for cylindrical mirrors and spacers. As previously established, the beam waist on a the second mirror will be larger due to the nature of the Gaussian mode's reproducibility. However, this discrepancy is negligible, and to obtain a conservative approximation, the smallest beam waist is considered. Consequently, the Allan deviations will be

constrained to

$$\sigma_{A,th} = \sqrt{2\ln(2)}\sqrt{S_f(f)}f^{1/2}, \text{ and } \sigma_{M,th} = \frac{27\ln(3) - 32\ln(2)}{8}\sqrt{S_f(f)}f^{1/2}.$$

These are the typical values used to characterize the thermal noise floor of a resonator. This is likely attributable to the fact that they are constant values and also describe the typical regimes of interest for metrology on time scales greater than one second. The top state-of-the-art cryogenic system can exhibit thermal noise floors at the $\nu_0^{-1}\sigma_{A,th} \approx 10^{-17}$ level, while room temperature graded systems are closer to the 10^{-16} level. The utilization of optical resonators in this context is motivated by the theoretical premise that these devices permit the stabilization of light to its thermal noise floor. It is evident that this signifies complete regulation of environmental factors on the OL. As will be demonstrated in this thesis, this is feasible to a considerable extent.

2.2.4 Fundamental Limits: Thermal Noise in Optical Fibers

Originally located in Appendix A.5.8. As is the case with the noise floor of an optical resonator, fibers too will demonstrate a thermal limit for light stabilized to them. The precise analysis is not addressed in this study; therefore, the theory is herein summarized from the works of [79, 80, 81]. Given that the ring resonators (see Section 5) under discussion in this thesis will not yet be operating within the boundaries of their thermal noise floor, the analysis will not delve into that aspect. Nevertheless, as it is a prevailing element in the design and configuration of the system, it is briefly reproduced here. The frequency noise $S_f(f)$ s expressed as a function of the phase noise $S_\phi(f)$ of the system through

$$S_f(f) = \frac{c_n^2}{(2\pi L)^2}S_\phi(f) = \frac{\nu_0^2\lambda^2}{4\pi L^2 n^2}S_\phi(f), \tag{2.42}$$

where f_0 is the carrier frequency, λ the vacuum wavelength, L the length of the fiber and c_n the speed of light inside the fiber of refractive index n. The theoretical model under consideration is composed of two distinct components: a thermomechanical and a thermodynamic part. The mechanical part $S_{\phi,mech}(f)$ encompasses the structural properties of the fiber, including its cross-section, stiffness, and loss angle, given by

$$S_{\phi,mech}(f) = \frac{4\pi L}{\lambda^2}\frac{2k_B T n^2 \phi_0}{3E_0 A}\frac{1}{f}. \tag{2.43}$$

The thermodynamic component $S_{\phi,dyn}(f)$ encompasses parameters such as the thermal expansion coefficient, the temperature-dependent refractive index, and a function, $F(f)$, which incorporates the upper and lower boundary parameters of the fiber, along with its thermal diffusivity. The equations are as follows:

$$S_{\phi,dyn}(f) = \frac{4\pi L}{\lambda^2}\frac{k_B T^2}{\kappa_f}\left(\frac{dn}{dT} + n\alpha_L\right)^2 F(f) \text{ with } F(f) = \ln\left[\frac{\left(k_{max}^2 + \left(\frac{n}{c_0}f\right)^2\right)^2 + \left(\frac{f}{D}\right)^2}{\left(k_{min}^2 + \left(\frac{n}{c_0}f\right)^2\right)^2 + \left(\frac{f}{D}\right)^2}\right] \tag{2.44}$$

The total frequency noise as subsequently determined by inserting Equation (2.43) and (2.44) into (2.42) and combining them accordingly, yielding

$$\sqrt{S_f(f)} = \nu_0 \sqrt{\frac{k_B T}{L n^2}} \sqrt{\frac{T}{\kappa}\left(\frac{dn}{dT} + n\alpha_L\right)^2 F(f) + \frac{2n^2\phi_0}{3E_0 A}\frac{1}{f}}. \tag{2.45}$$

This thesis will focus on fibers with an operating wavelength of 1.5 µm in configuration as a ring resonator, with the important parameters for such a system enumerated in Table 2.1. Figure 37

Parameter	Value
Thermal conductivity	$\kappa_f = 1.37\ \frac{\mathrm{W}}{\mathrm{m\,K}}$[79]
Refractive index temp. coefficient	$\frac{dn}{dT} = 9.2\times10^{-6}\ \frac{1}{\mathrm{K}}$[79]
Refractive index	$n = 1.468$[79]
Thermal expansion coefficient	$\alpha_{fib} = 5.5\times10^{-7}\ \frac{1}{\mathrm{K}}$[79]
Loss angle	$\phi_0 = 0.01$ rad[79]
Bulk modulus of the material	$E_0 = 1.9\times10^{10}$ Pa[79]
Fiber cladding diameter	$a_f = 1.25\times10^{-6}$ m [82]
Fiber mode diameter	$2w_0 = 10.4\times10^{-6}$ m [82]
Cross sectional area of fiber	$A = \pi a_f^2$[79]
Lower fiber boundary parameter	$k_{min} = \frac{2.405}{2a_f}$[79]
Upper fiber boundary parameter	$k_{max} = \frac{2}{w_0}$[79]
Thermal diffusity	$D = 8.2\times10^{-7}\ \frac{\mathrm{m}^2}{\mathrm{s}}$[79]
Attenuation	$\alpha_L = 0.18\,\frac{\mathrm{dB}}{\mathrm{km}}$[82]

Table 2.1: The following data is crucial for the calculation of the thermal noise floor of an optical fiber of variable length L. The numerical values align with the specifications of an SMF-28 (SM) fiber, designed for telecommunications wavelengths with a central wavelength of $\lambda = 1.5\,\mu$m.

presents a simulation of the noise floor for a 100 m long fiber at temperature $T = 300$ K. The black dashed line indicates the 10^{-15} level, while the red curve represents the total frequency noise. The individual contributions of mechanical and dynamical noise are shown in blue and purple, respectively. The dynamic part scales more strongly in terms of temperature (T instead of $\sqrt{T}$), thereby becoming the dominant part at mid to large Fourier frequencies. In contrast, the mechanical part is typically more substantial at lower Fourier frequencies or in the limit above 10^7 Hz in this particular configuration. The fiber demonstrated in this simulation will be constrained by the mechanical contribution at all frequencies at temperatures below 10 K, at which point it is

$$\nu_0^{-1}\sqrt{S_f(f)} \approx \sqrt{\frac{2k_B T\phi_0}{3LAE_0}} f^{-1/2} = 7\times10^{-16} f^{-1/2}.$$

Consequently, in addition to temperature, the noise is determined exclusively by the volume, stiffness, and loss angle of the fiber, akin to the spacer material of an optical resonator. In particular, this 100 m long fiber, when measured at cryogenic temperatures, demonstrates comparable properties to a short ultra-low-expansion (ULE) glass-type resonator when measured at room temperature. Therefore, at cryogenic temperatures, it would be feasible to achieve significantly reduced thermal noise levels compared to state-of-the-art cavities by employing approximately 10 km long fibers. However, other properties, such as vibration sensitivity, may emerge as new fundamental constraints. Equation (2.45)'s formalism enables a multitude of analyses concerning varying fiber types, lengths, and geometries. When configured as a ring resonator, as outlined in Section 2.1.4, this formalism can serve as the basis for an alternative setup for laser stabilization based on optical fibers.

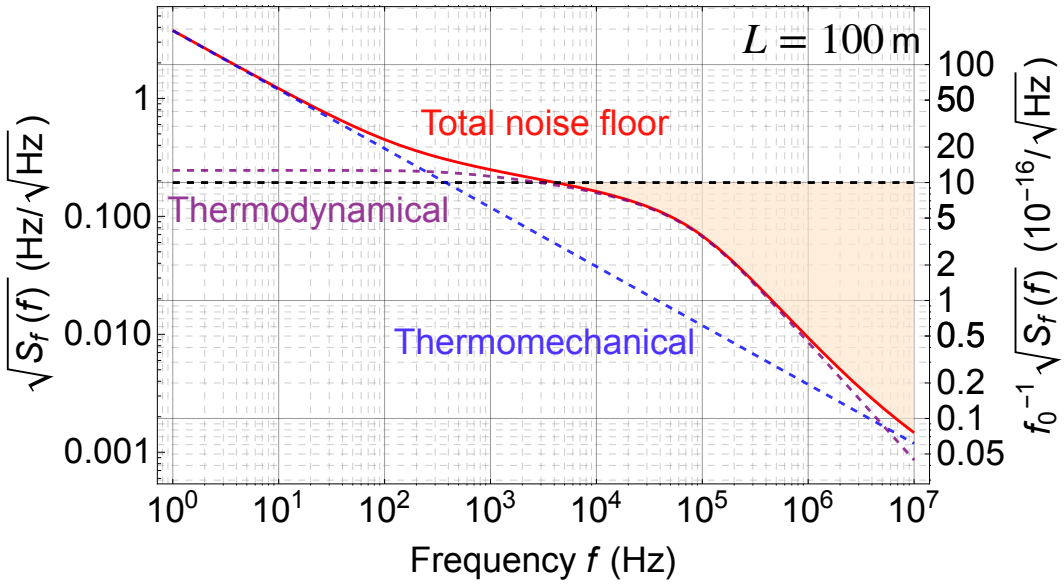


Figure 2.8: Simulation of the thermal noise floor in the frequency noise picture of a 100 m long SMF-28 optical fiber at 300 K. The parameters of Table 2.1 were inserted into Equation (2.45). The individual thermomechanical and thermodynamic components are illustrated by the blue and purple curves, respectively. The total noise is indicated in red. The black dashed line denotes the fractional stability level of 10^{-15}.

2.3 Stabilizing Light: The Pound-Drever-Hall Technique

Originally located in Appendix A.6. It has been demonstrated that resonators can be utilized as a reference for laser light. In this section, the technical implementation will be discussed. This includes the conventional implementation of the Pound-Drever-Hall (PDH) technique [5, 83], as well as a modified version for advanced manipulation of the locked light, which will become especially advantageous when paired with the full metrology suite. The implementation of both methods was executed on disparate systems, which are described in the scope of this work, and offer different advantages. Finally, a complex addition to the PDH is mathematically described in a original way.

This addition is the residual amplitude modulation (RAM). The effect of this addition is subsequently analyzed in a real-world experiment on one of the systems described in this thesis.

2.3.1 The Core Principle: Phase Modulation and Error Signals

Originally located in Appendix A.6.1. In the context of feedback loops, a common practice involves the comparison of the current value of a variable with a predetermined set point. This comparison results in the generation of an error signal, which, in turn, serves to regulate an actuator, thereby adjusting the variable's value to the set point. In this system, the set point is defined as the resonance mode of the optical resonator. The resonance mode can be measured by the power in transmission or reflected light of the resonator. The equations that describe this relationship are given in Section 2.1.1, as shown by Equations (2.2) and (2.3). A PD can be utilized to measure the voltage proportional to the normalized intensity of the reflected light $I_{r,n}$, which is split apart and directed to the PD by a PBS placed in front of the resonator. It is given by

$$I_{r,n} = F(\omega) F^*(\omega) = \frac{2r^2\left(1-\cos\left(\frac{\omega}{\Delta\nu}\right)\right)}{1-2r^2\cos\left(\frac{\omega}{\Delta\nu}\right)+r^4}.$$

To recall, the reflection coefficient of the resonator for light of frequency $\omega = 2\pi\,\nu$ is

$$F(\omega) = \frac{r\left(e^{i\frac{\omega}{\Delta\nu}}-1\right)}{1-r^2 e^{i\frac{\omega}{\Delta\nu}}},$$

with the free-spectral range $\Delta\nu$ and the mean mirror reflectivity r. Initially, the signal from the PD appears to be suitable for use as an error signal for a PID controller. This is due to the Lorentzian shape of the signal, which features a minimum in resonance. This minimum could be interpreted as a set point for the stabilization process. The crux of the issue pertains to the symmetry of $I_{r,n}$ along the ordinate surrounding the minimum. The PID controller is capable of detecting deviations in the laser's resonance frequency. This deviation is indicated by an increase in the signal reflected back from the system. However, the controller is unable to ascertain the direction of the deviation.

This will have dire consequences on the performance of the stabilization as the system must guess the direction of the frequency change. If the guess is incorrect, the stabilization will be further corrupted by pushing the frequency further away. In certain applications, the brute force approach may prove advantageous when the focus is on long-term performance. However, to optimize the system's performance, the error signal must be modified to continuously account for the direction of the frequency change. At this stage, the EOM is incorporated into the system as a phase modulator. As demonstrated in Section A.3.3, the field of the EM wave E_{inc} that is incident to the cavity mirror after passing an electro-optic modulator (EOM) modulated with a frequency of Ω is

$$E_{inc} = \underbrace{E_c e^{i\omega t}}_{\text{carrier}} + \underbrace{E_s e^{i(\omega t+\Omega t)}}_{\text{upper sb.}} - \underbrace{E_s e^{i(\omega t-\Omega t)}}_{\text{lower sb.}}.$$

The focus is exclusively on phase modulation with a limited modulation depth, in the interest of maintaining simplicity. Consequently, the focus will be on the carrier and first order sidebands.

When the wave interacts with the front mirror of the resonator, the reflection coefficient of each beam must account for their individual absolute frequency. In this case, the reflected wave E_{ref} is modeled by

$$E_{ref} = E_c F(\omega) e^{i\omega t} + E_s F(\omega+\Omega) e^{i(\omega+\Omega)t} - E_s F(\omega-\Omega) e^{i(\omega-\Omega)t}.$$

The total power P_{ref} of the reflected light subsequently comprises all nine combinations of the three beams. The terms can be arranged in a manner that incorporates three distinct types of oscillations:

- Non-oscillating components, which represent a DC part from the terms where beams interfere with themselves.
- Oscillations at the modulation frequency Ω, given by the interference of the carrier and the sidebands.
- Oscillations of order 2Ω, which form the interference of the sidebands with each other.

The power can be expressed as follows:

$$\begin{aligned} P_{ref} = {} & P_c |F(\omega)|^2 + P_s |F(\omega+\Omega)|^2 + P_s |F(\omega-\Omega)|^2 \\ & + \sqrt{P_c P_s} \left[F^*(\omega) F(\omega+\Omega) e^{i\Omega t} + F(\omega) F^*(\omega+\Omega) e^{-i\Omega t} \right] \\ & - \sqrt{P_c P_s} \left[F(\omega) F^*(\omega-\Omega) e^{i\Omega t} + F^*(\omega) F(\omega-\Omega) e^{-i\Omega t} \right] \\ & - P_s \left[F(\omega+\Omega) F^*(\omega-\Omega) e^{2i\Omega t} + F^*(\omega+\Omega) F(\omega-\Omega) e^{-2i\Omega t} \right] \end{aligned} \tag{2.46}$$

In the calculation, it was used that $E_i E_i^* = P_i$ and $E_i E_j^* = \sqrt{P_i P_j}$ because powers are real. The signal is combined with a local oscillator at $\sin(\Omega t + \phi)$ in a RF mixer. Subsequently, the signal is filtered by a low-pass filter that removes components oscillating at frequencies around Ω and higher. Therefore, components of P_{ref} that oscillate with Ω will be the only components that remain. By using the identity

$$z e^{ix} + z^* e^{-ix} = 2\Re[z]\cos(x) + 2\Im[z]\sin(x),$$

for a complex number z and a real number x, results in the following terms of interest becoming apparent:

$$\begin{aligned} \left.\frac{P_{AC}}{2\sqrt{P_c P_S}}\right|_{O(\Omega)} = {} & \Re\left[F^*(\omega) F(\omega+\Omega) - F(\omega) F^*(\omega-\Omega)\right] \cos(\Omega t) \\ & + \Im\left[F^*(\omega) F(\omega+\Omega) - F(\omega) F^*(\omega-\Omega)\right] \sin(\Omega t) \end{aligned}$$

Consequently, the output of the mixer subsequent to low-pass filtering will serve as the actual error signal ε, given by

$$\begin{aligned} \frac{\varepsilon}{2\sqrt{P_c P_S}} = {} & \Re\left[F^*(\omega) F(\omega+\Omega) - F(\omega) F^*(\omega-\Omega)\right] \sin(\phi) \\ & + \Im\left[F^*(\omega) F(\omega+\Omega) - F(\omega) F^*(\omega-\Omega)\right] \cos(\phi). \end{aligned}$$

The effective phase, ϕ, is defined as the phase that exists between the phase modulation signal and the local oscillator. Typically, a single DDS with two outputs is employed in such a scenario. One output is used to modulate the EOM with a variable amplitude, while the other output is

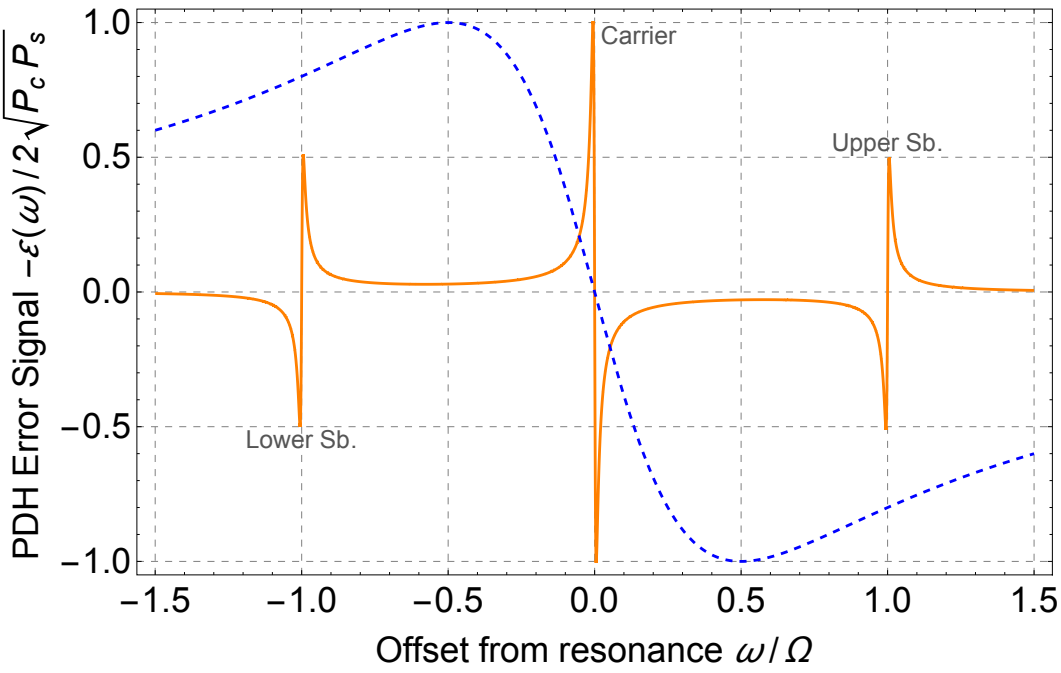


Figure 2.9: Simulation of the error signal of Equation (2.47). Orange: The error signal on the scale of the phase modulation frequency Ω. Blue: The error signal on the scale of the cavity linewidth f_c. For this one, the abcissa is in unit ω / f_c. For the simulation, a finesse of 10000 was assumed for light at 1.5 µm modulated with first order sidebands at 12.8 MHz.

directed towards the mixer. In an ideal scenario, the effective phase angle ϕ would be set to zero. However, to account for discrepancies in cable lengths, a phase regulator is incorporated into the DDS to adjust the output phase of the internal signals. Furthermore, upon closer examination, it becomes evident that the real part of the term $F^*(\omega)F(\omega+\Omega) - F(\omega)F^*(\omega-\Omega)$ is predominantly zero off resonance and is considerably smaller than the imaginary part in resonance. Therefore, the imaginary part is the component that carries the critical information of the error signal. Typically, this is presented as

$$-\frac{\varepsilon}{2\sqrt{P_c P_S}} = \Im\left[F(\omega)F^*(\omega+\Omega) - F^*(\omega)F(\omega-\Omega)\right], \tag{2.47}$$

where the relation $\Im[z] = -\Im[z^*]$ was used. A simulation of the error signal of Equation (2.47) is displayed on two scales in Figure 2.9. The orange line corresponds to the error signal at the scale of the modulation amplitude. The presence of both sidebands and the carrier is discernible. Further, the slopes of the sidebands exhibit different signs at the zero crossing compared to the carrier. This information enables the reliable locking of the carrier by adjusting the polarity of the lockbox. The blue line indicates a zoom of the orange line at the scale of the resonator linewidth, f_c, with the extreme points of the error signal at $\pm f_c/2$. The locking point is located at the zero crossing of the error signal, where a directional change in frequency can be uniquely identified. A PID controller, also referred to as a lockbox, employs the slope of the error signal as a discriminator within the feedback loop, with the objective of maintaining it at a zero, thus around the locking point. However, it should be noted that each lockbox will have its limits in terms of the extent to

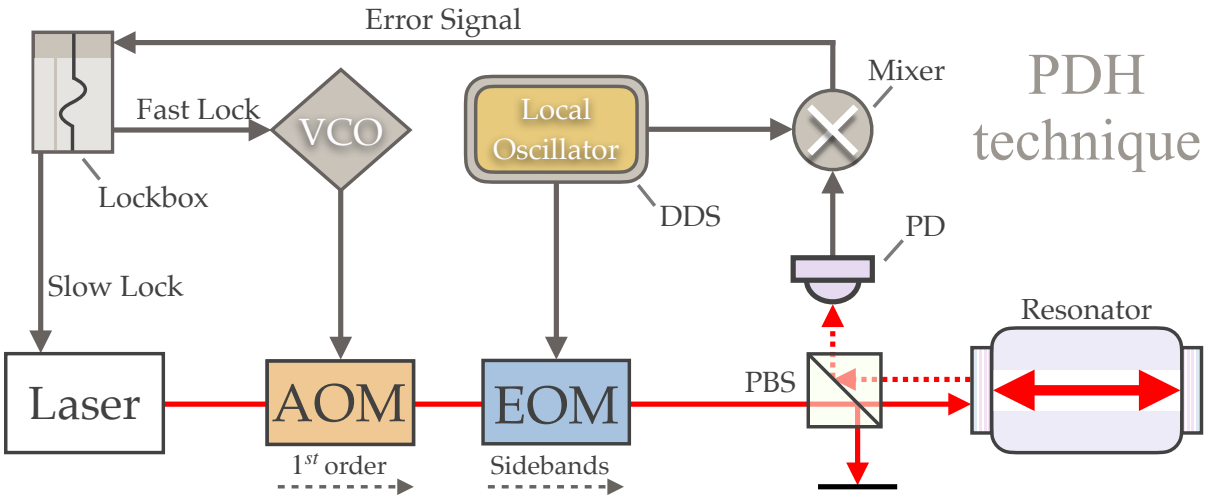


Figure 2.10: Experimental setup for the PDH technique. Laser light is modulated with sidebands through the use of an EOM. The reflected light of the resonator is mixed with the modulation frequency, thereby generating the error signal. A Lockbox acts on a VCO, which, in turn controls the AOM for fast-locking. A slow lock output of the lockbox is connected to the laser.

which it can maintain an error signal at a value of zero. In this regard, a steeper slope will yield superior results in comparison to a shallow one, as the system is capable of distinguishing it more accurately from noise. This suggests that a reduced cavity linewidth may result in improved lock, which is intuitively reasonable given that the reference becomes more precise.

The output of the lockbox is typically directed to either an AOM for rapid modulation of laser light through the diffracted beam, or it is routed directly to the current control or piezo of the laser if such rapid modulation is permitted. The bandwidth at which the combination of lockbox and actuator can operate should be sufficiently broad to span the domain in the Fourier spectrum where the majority of the laser light power is concentrated over the specified time period. Therefore, it can be deduced that the bandwidth should be substantially larger than the linewidth of the laser. Furthermore, short-term fluctuations should also be considered.

Due to the inherent property of lasers, characterized by their ability to emit light, a drift in the center frequency of the laser light is observed, manifesting as a gradual shift over time scales ranging from minutes to hours. To address this drift, a secondary output of the lockbox is connected to the laser, i.e. to the temperature of the laser crystal. This configuration serves to compensate for the drift in the laser's center frequency, thereby ensuring the stability and precision of the system. The final configuration of the setup is depicted in Figure 2.10. It is important to make a distinction between the fast-lock, which maintains the laser's stability around the error signal zero crossing, and the slow lock, which ensures the laser frequency does not deviate from the fast-lock's locking bandwidth. This concludes the general concept of laser stabilization, which is also named Pound-Drever-Hall (PDH) technique after its inventors.

2.3.2 Offset Locking: Tuning the Frequency Gap

Originally located in Appendix A.6.2. A modified version of the aforementioned concept is the offset lock. The advantages of this approach include the ability to tune the laser light while it is stabilized. In the classical PDH scheme, the incident electric field E_{inc} that exits the phase modulator is modulated by a sideband of frequency Ω with a modulation strength β. In the case of the offset lock, the sideband is subjected to further phase modulation from a modulation strength η, at a frequency Γ, which is typically smaller in magnitude than Ω. The electric field that exits the phase modulator can be expressed as

$$E_{inc} = E_0\, e^{i(\omega t + \beta \sin(\Omega t + \eta \sin(\Gamma t)))}, \tag{2.48}$$

where E_0 is the field amplitude of the light propagating towards the modulator. This expression is expanded as previously described, utilizing Bessel functions to first order in the modulation frequencies and applying the reflection coefficient $F(\omega)$ for a standing wave resonator with reflectivity r. This approach yields an expression for the reflected field E_{ref}, as detailed in Equation (2.49). The reflected light comprises contributions from seven components: the carrier wave, the two sidebands at Ω, and the four additional sidebands at $\pm\Omega \pm \Gamma$.

$$\begin{aligned} E_{ref} = {} & F(\omega) E_c e^{i\omega t} \\ & + F(\omega+\Omega) E_{s_1} e^{i(\omega+\Omega)t} + F(\omega+\Omega+\Gamma) E_{s_2} e^{i(\omega+\Omega+\Gamma)t} - F(\omega+\Omega-\Gamma) E_{s_2} e^{i(\omega+\Omega-\Gamma)t} \\ & - F(\omega-\Omega) E_{s_1} e^{i(\omega-\Omega)t} - F(\omega-\Omega-\Gamma) E_{s_2} e^{i(\omega-\Omega-\Gamma)t} + F(\omega-\Omega+\Gamma) E_{s_2} e^{i(\omega-\Omega+\Gamma)t} \end{aligned} \tag{2.49}$$

In this formalism, the Bessel functions simplify to the electric field strengths of the specific laser beams as

$$E_c = J_0(\beta)\, E_0,\ E_{s_1} = J_0(\eta) J_1(\beta)\, E_0, \text{ and } E_{s_2} = J_1(\eta) J_1(\beta)\, E_0. \tag{2.50}$$

The method for extracting the error signal remains analogous to the previous procedure; therefore, a brief overview will be provided. The calculation of the power $P_{ref} = \left|E_{ref}\right|^2$ of the reflected beam yields a total of 49 terms, which can be consolidated into oscillations at the following frequencies: Ω, 2Ω, Γ, 2Γ, $\Omega \pm \Gamma$ and $\Omega \pm 2\Gamma$. By demodulating this signal with a mixer and a DDS creating a signal of form $\sin(\Gamma t)$, accompanied by a low pass filter, only the oscillations at frequency Γ are retained. Thus, the following terms in the power are of interest

$$\left.\frac{P_{AC}}{2\sqrt{P_{s_1} P_{s_2}}}\right|_{O(\Gamma)} = \begin{array}{l} \left.\begin{array}{l} 2\Re\left[F^*(\omega+\Omega) F(\omega+\Omega+\Gamma) - F(\omega+\Omega) F^*(\omega+\Omega-\Gamma)\right]\cos(\Gamma) \\ +2\Im\left[F^*(\omega+\Omega) F(\omega+\Omega+\Gamma) - F(\omega+\Omega) F^*(\omega+\Omega-\Gamma)\right]\sin(\Gamma) \end{array}\right\} \text{upper sideband} \\ \left.\begin{array}{l} +2\Re\left[F(\omega-\Omega) F^*(\omega-\Omega-\Gamma) - F^*(\omega-\Omega) F(\omega-\Omega+\Gamma)\right]\cos(\Gamma) \\ +2\Im\left[F(\omega-\Omega) F^*(\omega-\Omega-\Gamma) - F^*(\omega-\Omega) F(\omega-\Omega+\Gamma)\right]\sin(\Gamma) \end{array}\right\} \text{lower sideband.} \end{array} \tag{2.51}$$

In order to express the error signal as desired, it is necessary to set the effective phase of the mixer to zero and to select a sufficiently far value for Γ, while ensuring that $\omega \pm \Omega$ is near resonance. The

error signal ε_{ol} can then be expressed as

$$-\frac{\varepsilon_{ol}}{2\sqrt{P_{s_1}P_{s_2}}} = \Im\left[F(\omega+\Omega)F^*(\omega+\Omega+\Gamma) - F^*(\omega+\Omega)F(\omega+\Omega-\Gamma)\right] + \Im\left[F^*(\omega-\Omega)F(\omega-\Omega-\Gamma) - F(\omega-\Omega)F^*(\omega-\Omega+\Gamma)\right]. \quad (2.52)$$

As illustrated in Figure 2.11, selecting the appropriate polarity, the locking points of the error signals are offset from the carrier wave by the modulation frequency Ω. In contrast to the original PDH scheme, the carrier wave itself does not possess a locking point. This approach, while seemingly intricate, allows for broadband frequency adjustments with a high degree of resolution. Previously, the laser frequency was constrained to fixed resonance frequencies of the cavity, $\omega_{res} = \omega$, and could only be tuned in increments of the FSR, $\Delta\nu$. Offset locking enables the carrier wave to be adjusted through the modulation frequency, resulting in $\omega_{res} = \omega \pm \Omega$. The sign of the carrier modulation frequency indicates the upper or lower sideband.

Consequently, while locked, the laser can be precisely adjusted within a range surrounding the cavity mode, which is constrained by the capabilities of the DDS. In fact, this frequency band is twice as large as the DDS range, given that both sidebands at Ω are potential locking points. Notably, the laser must be unlocked to enable the switching of the sidebands.

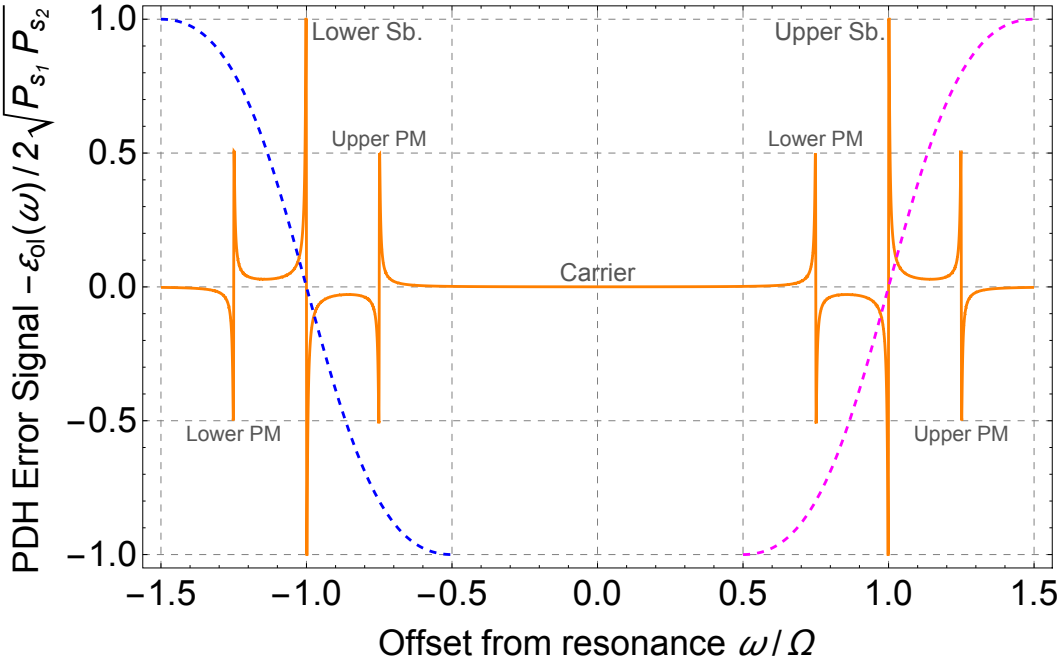


Figure 2.11: Simulation of the offset lock error signal described in Equation (2.11). Orange: The error signal is plotted on the scale of the phase modulation frequency Ω. Blue and magenta: Zooms of the error signal on the scale of the cavity line-width f_c on their respective sidebands. For those two, the abscissa is in unit ω/f_c. For the simulation, a finesse of 10^4 was assumed for light of wavelength 1.5 µm, that was modulated with sidebands at $\Omega = 4\Gamma$ and $\Gamma = 12.8$ MHz.

In addition, the phase modulation restricts the ability to adjust the sideband at frequency Ω to a range that falls within the limits of Γ. This results in a gap of size 2Γ around the cavity mode, within which the laser cannot be tuned by the sideband. Consequently, the offset lock can be utilized to set the laser to a particular frequency, with additional adjustments attainable at the target wavelength using an AOM without compromising the stabilization to the resonator. This technique has for example been implemented in [84, 85].

2.3.3 Residual Amplitude Modulation: Limitations and Corrections

Originally located in Appendix A.6.3. The error signal has thus far been described by a wave of frequency ω with an amplitude incident to the modulator, E_0, a time-varying phase given by the phase modulation (PHM) frequency, Ω, and PHM depth, β. In the following, the complete expression of the EOM (see: Section A.3.3, Equation (A.108)) will be utilized. The oscillation of the electric field amplitude at a given AM frequency, denoted by Ω', and AM depth, denoted by M', can be used to describe any AM. The AM depth is subject to variation over time, that can be modeled using a phase γ. The electric field E_{inc} after the phase modulator, but incident to the front cavity mirror is therefore

$$E_{inc} = E_0 \left(1 + \underbrace{M' e^{i\gamma} \sin(\Omega' t)}_{\text{AM}} \right) e^{i\omega t} \underbrace{e^{i\beta \sin(\Omega t)}}_{\text{PHM}} \tag{2.53}$$

In subsequent phases of the PDH scheme, the reflected signal of the front mirror is demodulated by a local oscillator at the PHM frequency. Consequently, any AM that does not correspond to this frequency is filtered out. Therefore, the initial step was to establish the equivalence of $\Omega' = \Omega$, with the objective of acquiring information regarding the residual amplitude modulation (RAM) that permeates the demodulation process. The application of Bessel formalism into Equation (2.53) and the subsequent expression of the sine function in exponential form results in the field being expressed as

$$\begin{aligned} E_{inc}(t) = & E_0 \left(1 - \frac{i}{2} M' e^{i\gamma} e^{i\Omega t} + \frac{i}{2} M' e^{i\gamma} e^{-i\Omega t} \right) \\ & \times e^{i\omega t} \left(J_0(\beta) + J_1(\beta) e^{i\Omega t} - J_1(\beta) e^{-i\Omega t} \right). \end{aligned} \tag{2.54}$$

The light that is reflected at the front mirror $E_{ref}(t)$ of the cavities is modeled by applying the reflection coefficient $F(\omega)$, given by the geometry of the resonator. This geometry is primarily described by the reflectivity r of the mirrors. The reflection coefficient in this particular system (see: Section 2.1.2, Equation (2.13) and (2.14)) is given by

$$F_\delta(\omega) = \frac{\delta^3 r e^{i\frac{\omega}{\Delta\nu}} - \delta r}{1 - \delta^2 r^2 e^{i\frac{\omega}{\Delta\nu}}}, \text{ with } |F_\delta(0)|^2 = \frac{\left(1-\delta^2\right)^2}{\delta^{-2} r^{-2} \left(1-\delta^2 r^2\right)^2} = U^2. \tag{2.55}$$

The relation in resonance ($\omega = 0$) is given in the latter equation in, where $U - 1$ is the actual coupling efficiency, which quantifies the power of the carrier that is passing through the cavity. As per usual,

the FSR is denoted by $\Delta\nu$. The expression of the electric field of the reflection, when incorporating the reflection coefficient, is

$$\begin{aligned} E_{ref}(t) = &\left(E_c + iM'e^{i\gamma}E_s\right)F_\delta(\omega)\,e^{i\omega t} \\ &+\left(E_s - \frac{i}{2}M'e^{i\gamma}E_c\right)\left[F_\delta(\omega+\Omega)\,e^{i(\omega+\Omega)t} - F_\delta(\omega-\Omega)\,e^{i(\omega-\Omega)t}\right] \\ &-\frac{i}{2}M'e^{i\gamma}E_s\left[F_\delta(\omega+2\Omega)\,e^{i(\omega+2\Omega)t} + F_\delta(\omega-2\Omega)\,e^{i(\omega-2\Omega)t}\right]. \end{aligned}$$

The calculation of the light power, $P_{ref} = E_{ref}E^*_{ref}$, and its subsequent demodulation with a local oscillator of the form $\sin(\Omega t + \phi)$ ultimately yields the error signal, ε_{ram}, as depicted below:

$$\begin{aligned} \varepsilon_{ram} = &\,2\sqrt{P_sP_c}\,\Re\left[F^*_\delta(\omega)F(\omega+\Omega) - F_\delta(\omega)F^*_\delta(\omega-\Omega)\right]\sin(\phi) && \text{(a)} \\ &+2\sqrt{P_sP_c}\,\Im\left[F^*_\delta(\omega)F_\delta(\omega+\Omega) - F_\delta(\omega)F^*_\delta(\omega-\Omega)\right]\cos(\phi) && \text{(b)} \\ &+M'(P_c+2P_s)\,\Re\left[F^*_\delta(\omega)F_\delta(\omega+\Omega) - F_\delta(\omega)F^*_\delta(\omega-\Omega)\right]\sin(\gamma)\sin(\phi) && \text{(c)} \\ &+M'(P_c+2P_s)\,\Im\left[F^*_\delta(\omega)F_\delta(\omega+\Omega) + F_\delta(\omega)F^*_\delta(\omega-\Omega)\right]\cos(\gamma)\sin(\phi) && \text{(d)} \\ &+M'(P_c+2P_s)\,\Im\left[F^*_\delta(\omega)F_\delta(\omega+\Omega) - F_\delta(\omega)F^*_\delta(\omega-\Omega)\right]\sin(\gamma)\cos(\phi) && \text{(e)} \\ &-M'(P_c+2P_s)\,\Re\left[F^*_\delta(\omega)F_\delta(\omega+\Omega) + F_\delta(\omega)F^*_\delta(\omega-\Omega)\right]\cos(\gamma)\cos(\phi) && \text{(f)} \\ &+M'P_s\,\Re\left[F^*_\delta(\omega+\Omega)F_\delta(\omega+2\Omega) - F_\delta(\omega-\Omega)F^*_\delta(\omega-2\Omega)\right]\sin(\gamma)\sin(\phi) && \text{(g)} \\ &+M'P_s\,\Im\left[F^*_\delta(\omega+\Omega)F_\delta(\omega+2\Omega) + F_\delta(\omega-\Omega)F^*_\delta(\omega-2\Omega)\right]\cos(\gamma)\sin(\phi) && \text{(h)} \\ &+M'P_s\,\Im\left[F^*_\delta(\omega+\Omega)F_\delta(\omega+2\Omega) - F_\delta(\omega-\Omega)F^*_\delta(\omega-2\Omega)\right]\sin(\gamma)\cos(\phi) && \text{(i)} \\ &-M'P_s\,\Re\left[F^*_\delta(\omega+\Omega)F_\delta(\omega+2\Omega) + F_\delta(\omega-\Omega)F^*_\delta(\omega-2\Omega)\right]\cos(\gamma)\cos(\phi) && \text{(j)} \\ &-1/2\,M'^2\sqrt{P_sP_c}\,\Re\left[F^*_\delta(\omega)F_\delta(\omega+\Omega) - F_\delta(\omega)F^*_\delta(\omega-\Omega)\right]\sin(\phi) && \text{(k)} \\ &-1/2\,M'^2\sqrt{P_sP_c}\,\Im\left[F^*_\delta(\omega)F_\delta(\omega+\Omega) - F_\delta(\omega)F^*_\delta(\omega-\Omega)\right]\cos(\phi) && \text{(l)} \\ &+1/2\,M'^2\sqrt{P_sP_c}\,\Re\left[F^*_\delta(\omega+\Omega)F(\omega+2\Omega) - F_\delta(\omega-\Omega)F^*(\omega-2\Omega)\right]\sin(\phi) && \text{(m)} \\ &+1/2\,M'^2\sqrt{P_sP_c}\,\Im\left[F^*_\delta(\omega+\Omega)F(\omega+2\Omega) - F_\delta(\omega-\Omega)F^*(\omega-2\Omega)\right]\cos(\phi) && \text{(n)} \end{aligned} \tag{2.56}$$

The error signal was sorted into 14 distinct terms, which are labeled from (a) to (n). In order to comprehend which terms are of interest, the following methodology is employed. In the context of high finesse resonators $(\mathcal{F} \gtrsim 10^4)$, the throughput and reflectivity of the resonator approach one (δ,$r \geq 0.9999$). Furthermore, the power levels in the sidebands are reduced, yet they are still large enough to neglect them. Hence, this cannot be considered a criterion for canceling a term. The modulation depth, however, is conservatively $O(M') \leq 10^{-3}$, and thus terms including M'^2 will be negligible in comparison. Therefore, it can be argued that terms (k), (l), (m) and (n) are contenders for elimination. Additionally, far away from resonances, the reflection coefficient becomes real and it follows

$$F_\delta\left(\frac{\Delta\nu}{2}\right) = \frac{\delta^3 r e^{i\pi} - \delta r}{1 - \delta^2 r^2 e^{i\pi}} = -\frac{\delta^3 r + \delta r}{1 + \delta^2 r^2} \approx -1. \tag{2.57}$$

This is a significant identity for terms that include the coefficients in a form $F^*_\delta(\omega \pm \Omega)F_\delta(\omega \pm 2\Omega)$, which will invariably be regarded as off resonance with respect to the locking point. The following

four identities are derived from this process:

$$\Re\left[F_\delta^*(\omega\pm\Omega)F(\omega\pm2\Omega)-F_\delta(\omega\pm\Omega)F^*(\omega\pm2\Omega)\right]=\Re[1-1]=0$$

$$\Im\left[F_\delta^*(\omega+\Omega)F(\omega+2\Omega)-F_\delta(\omega-\Omega)F^*(\omega-2\Omega)\right]=\Im[1-1]=0$$

$$\Re\left[F_\delta^*(\omega\pm\Omega)F(\omega\pm2\Omega)+F_\delta(\omega\pm\Omega)F^*(\omega\pm2\Omega)\right]=\Re[1+1]=2$$

$$\Im\left[F_\delta^*(\omega+\Omega)F(\omega+2\Omega)+F_\delta(\omega-\Omega)F^*(\omega-2\Omega)\right]=\Im[1+1]=0$$

Therefore, the terms (g), (h) ,(i), (m) and (n) are eliminated. From the classical PDH error signal the following identity is known:

$$\Im[F^*(\omega)F(\omega+\Omega)-F(\omega)F^*(\omega-\Omega)]\gg\Re[F^*(\omega)F(\omega+\Omega)-F(\omega)F^*(\omega-\Omega)]\approx0$$

This enables the cancellation of terms (a), (c) and (k). For reflectivities that are moderately high, resulting in finesse values of approximately 10^4, the following holds true:

$$\Re[F^*(\omega)F(\omega+\Omega)+F(\omega)F^*(\omega-\Omega)]\gg\Im[F^*(\omega)F(\omega+\Omega)+F(\omega)F^*(\omega-\Omega)]$$

This results in the cancellation of the term (d). The RAM is described by terms depending on $M'\cos(\gamma)=\Re\left[M'e^{i\gamma}\right]$, where M' is responsible for a systematic offset of the error signal and the time variation of the γ for its stability. By design, the latter fluctuates around zero, canceling the term (e). Term (l) can further be considered negligible in relation to (f). Therefore, the error signal is reduced to the following form:

$$\begin{aligned}\varepsilon_{ram}=\;&2\sqrt{P_sP_c}\,\Im[F^*(\omega)F(\omega+\Omega)-F(\omega)F^*(\omega-\Omega)]\cos(\phi) && \text{(b)}\\ &-M'(P_c+2P_s)\,\Re[F^*(\omega)F(\omega+\Omega)+F(\omega)F^*(\omega-\Omega)]\cos(\phi)\cos(\gamma) && \text{(f)}\\ &-2M'P_s\cos(\phi)\cos(\gamma). && \text{(j)}\end{aligned}\tag{2.58}$$

The effective phase, ϕ, of the demodulation is generally established to align with the phase modulation of the sidebands. This configuration, represented by the $\phi\approx0$ is implemented to optimize the magnitude of the ordinary error signal (term (b)). This assumption would have cancelled out the majority of terms that oscillate with $\sin(\phi)$, however no such terms persist in Equation (2.58) after the previous purge. The RAM-dependent part in resonance must be analyzed in steps. Initially, the following function is considered:

$$\Re[F^*(\omega)F(\omega+\Omega)+F(\omega)F^*(\omega-\Omega)]=\begin{cases}0 & \omega=\omega_{res}\\ 2 & \omega\neq\omega_{res}\text{ (far off resonance)}\end{cases}\tag{2.59}$$

The term is equivalent to 2 when the light is far off resonance and vanishes when it is in resonance, under the assumption of perfect coupling into the resonator. However, due to losses in the cavity or a mismatch in in-coupling, a residual amount of this term will persist in resonance. This is quantified by the parameter V (not the fiber V-parameter), which is given by

$$V=\frac{1}{2}\Re[F^*(\omega_{res})F(\omega_{res}+\Omega)+F(\omega_{res})F^*(\omega_{res}-\Omega)]\approx\frac{\delta^2r^2-\delta^6r^2}{1-\delta^4r^4}.\tag{2.60}$$

In this context, the approximation is made that the reflection coefficient at the modulation frequencies is far off resonance. Therefore, $e^{i\Omega/\Delta\nu} \approx e^{i\pi} = -1$. Subsequent to the aggregation of all terms in resonance, the error signal ε_{in} is thus expressed as:

$$\varepsilon_{in} = -2M'\left(VP_c + (1+2V)P_s\right)\cos(\gamma)\cos(\phi) \tag{2.61}$$

It is noteworthy that, when the light is off resonance, the reflection coefficient being one results in the error signal at the reflection detector measuring the same signal as a detector placed in front of the cavity, provided that they have the same power level. This error signal off resonance ε_{off} is then expressed as

$$\varepsilon_{off} = -2M'\left(P_c + 3P_s\right)\cos(\gamma)\cos(\phi). \tag{2.62}$$

In many cases, the measurement of RAM is conducted at this second detector, while the light is stabilized to the cavity. Therefore, the subsequent conversion factor is hereby introduced:

$$\frac{\varepsilon_{off}}{\varepsilon_{in}} = \frac{\rho+3}{(\rho+2)V+1}, \tag{2.63}$$

The relation between carrier power P_c and sideband power P_s is expressed by $\rho = \frac{P_c}{P_s}$. Close to resonance, hence for small ω, the reflection coefficient can be estimated using the first-order Taylor expansion of the exponential function $e^{ix} \approx 1 + ix$, thus

$$F_\delta(\omega)\big|_{\omega\leq 2\pi f_{\delta,c}} \approx \frac{\delta^3 r\left(1+i\frac{\omega}{\Delta\nu}\right)-\delta r}{1-\delta^2 r^2\left(1+i\frac{\omega}{\Delta\nu}\right)} = \frac{\delta^3 r+\delta^3 r i\frac{\omega}{\Delta\nu}-\delta r}{1-\delta^2 r^2-\delta^2 r^2 i\frac{\omega}{\Delta\nu}}.$$

In particular, it was utilized that the frequency is smaller than the cavity linewidth $f_{\delta,c}$ (times 2π); thus, the expression in the exponent is always smaller than the inverse of the finesse (times 2π), which, in this case, is sufficiently small. Within the context of this calculus, the frequency of $\omega = 0$ is utilized as it corresponds to the trivial resonance. The validity of the theory is not contingent upon the specific mode of cavity. In this scenario, the frequency is regarded as a detuning from the resonance mode, and it is denoted by the variable f. The following approximation for the error signal close to resonance (term (b)) is derived:

$$\begin{aligned}
\text{(b)} &= 2\sqrt{P_s P_c}\,\Im\left[F^*(\omega)F(\omega+\Omega) - F(\omega)F^*(\omega-\Omega)\right]\cos(\phi) \\
&= 2\sqrt{P_s P_c}\,\Im\left[F_\delta(\omega)\big|_{\omega\leq 2\pi f_{\delta,c}} F_\delta\left(\frac{\Delta\nu}{2}\right) - F_\delta^*(\omega)\big|_{\omega\leq 2\pi f_{\delta,c}} F_\delta\left(\frac{\Delta\nu}{2}\right)\right]\cos(\phi) \\
&= -8\sqrt{P_s P_c}\,\frac{\delta^3 r\left(1+\delta^2-\delta^4 r^2-\delta^2 r^2+\delta^4 r^4-r^4\right)}{\left(1+\delta^2 r^2\right)\left(1-\delta^2 r^2\right)}\,\frac{f}{f_{\delta,c}}\cos(\phi) \\
&:= -8\sqrt{P_s P_c}\,Q\,\frac{f}{f_{\delta,c}}\cos(\phi)
\end{aligned} \tag{2.64}$$

In this calculus, the FSR was expressed by the cavity linewidth as demonstrated in Section 2.1.2, Equation (2.15), given by the relation

$$f_{\delta,c} = \frac{\Delta\nu}{\pi}\arccos\left(1 - \frac{\left(1-\delta^2 r^2\right)^2}{2\delta^2 r^2}\right) \approx \frac{1-\delta^2 r^2}{\pi\delta r}\Delta\nu. \tag{2.65}$$

Furthermore, the dependencies on r and δ were summarized in the parameter Q, and terms of higher order $O\left(\omega^2\right)$ were neglected in the determination of Equation (2.64). Conducting the same operation for the term (f) yields the following result:

$$\begin{aligned}(\mathrm{f}) &= -M'\left(P_c + 2P_s\right)\Re\left[F^*(\omega)F(\omega+\Omega) + F(\omega)F^*(\omega-\Omega)\right]\cos(\phi)\cos(\gamma)\\ &= -2M'\left(P_c + 2P_s\right)\frac{\delta^3 r - \delta r}{1-\delta^2 r^2}\cos(\phi)\cos(\gamma)\end{aligned}$$

In the course of this calculation, no terms of order $O\left(\omega^2\right)$ were observed. Eventually, the RAM-dependent offset subsequent to linearization is obtained by adding the terms (f) and (j):

$$(\mathrm{f}) + (\mathrm{j}) = -2M'\left(VP_c + (1+2V)P_s\right)\cos(\gamma)\cos(\phi) = \varepsilon_{in}$$

This is identical to the expression of Equation (2.61). The discriminator of the total error signal around the locking point $\varepsilon_{lin}(f)$ is then approximated by adding Equation (2.64). This results in the linearized function

$$\varepsilon_{lin}(f) = -8\sqrt{P_s P_c}\,Q\frac{f}{f_{\delta,c}}\cos(\phi) - 2M'\left(VP_c + (1+2V)P_s\right)\cos(\gamma)\cos(\phi). \tag{2.66}$$

The peak-to-peak strength, $\varepsilon_{pp} = \left|\varepsilon\left(\pi f_{\delta,c}\right)\right| + \left|\varepsilon\left(-\pi f_{\delta,c}\right)\right|$, of the error signal can be derived through the application of the same algebra. When Equation (2.65) is combined with the aforementioned expression for ε_{pp}, the result is as follows:

$$\varepsilon_{pp} = \ldots = -4\sqrt{P_s P_c}\left(\frac{\delta^2 r^2 - \delta^6 r^2}{1-\delta^4 r^4}\right)\left(\frac{\delta^3 r - \delta^3 r^3}{\delta^2 r^2 - \delta^4 r^2}\right)\cos(\phi) := -4\sqrt{P_s P_c}\,C\cos(\phi)$$

Here, another parameter, C, is introduced. The current model incorporates four parameters (U, V, Q, and C) to explain the systematic effect of RAM. For high-finesse systems, the relationships between the variables is $U \approx V \approx 1 - Q \approx 1 - C$, as illustrated in Figure 2.12. Therefore, in the following, all variables will be expressed as a function of parameter V, such that the peak-to-peak error signal strength is

$$\varepsilon_{pp} = 4\sqrt{P_c P_s}\,(1-V)\cos(\phi). \tag{2.67}$$

The RAM that exerts an influence on the stability of the lock is only the RAM that appears when the light is locked, thus in resonance. In proximity to resonance, the error signal can thus be expressed as

$$\varepsilon(f) = 2\varepsilon_{pp}\frac{f}{f_{\delta,c}} + \varepsilon_{in}, \tag{2.68}$$

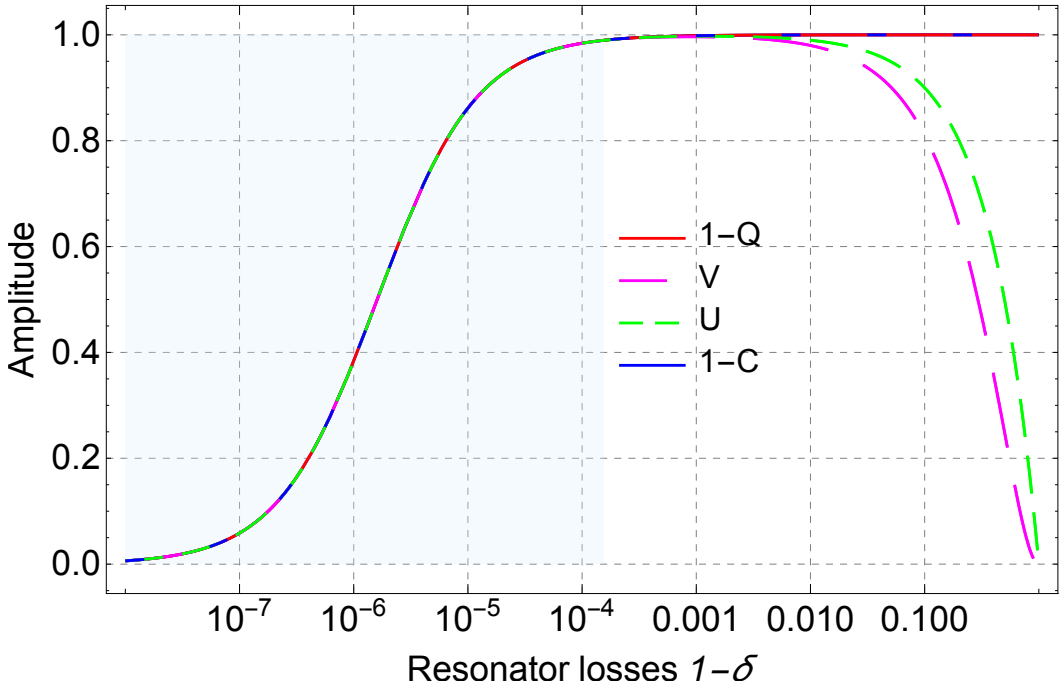


Figure 2.12: The RAM loss coefficients C,Q,U and V, determined by the resonator loss $1-\delta$, with a fixed reflectivity of $r = 0.999998$. The blue area of the graph indicates finesse values that exceed 10^4. It has been demonstrated that all coefficients are approximately equivalent within the specified region.

which agrees with Equation (2.66). When the error signal is set to zero, a frequency offset term f_{RAM} emerges, attributable to RAM, expressed as

$$f_{RAM} = -\frac{\varepsilon_{in}}{2\varepsilon_{pp}} f_{\delta,c}. \tag{2.69}$$

The fractional frequency instability, σ_f, of this signal is given by $\sigma_f = \frac{|f_{RAM}|}{\nu_0}$. This yields the equation

$$\sigma_f = \frac{f_{\delta,c}}{\nu_0}\sigma_M. \tag{2.70}$$

The RAM instability, $\sigma_M = \frac{\varepsilon_{in}}{2\varepsilon_{pp}}$, can be obtained through the utilization of a detector that quantifies the off-resonance signal. This becomes evident when the conversion factor from Equation (2.63) is inserted. It follows:

$$\begin{aligned}\sigma_M &= \frac{(\rho+2)V+1}{\rho+3}\frac{P_{PDH}}{P_{RAM}}\frac{\varepsilon_{off}}{2\varepsilon_{pp}} \\ &:= \alpha_f(V,\rho)\frac{P_{PDH}}{P_{RAM}}\frac{\varepsilon_{off}}{2\varepsilon_{pp}}\end{aligned} \tag{2.71}$$

Here, an additional factor, P_{PDH}/P_{RAM}, is included if RAM is evaluated by another PD that is not the reflection PDH detector. Furthermore, the parameter

$$\alpha_f = \frac{(\rho+2)V+1}{\rho+3}$$

encompasses the system-specific characteristics of reflectivity, sideband, carrier power, and cavity loss. In addition, σ_M can also be expressed through Equation (2.61) and (2.67):

$$\begin{aligned}\sigma_M &= -\frac{V\rho+(1+2V)}{4\sqrt{\rho}(V-1)}M'\cos(\gamma)\\ &:= \frac{1}{\alpha_\varepsilon(V,\rho)}M'\cos(\gamma)\end{aligned} \tag{2.72}$$

In this equation

$$\alpha_\varepsilon(V,\rho) = -\frac{4\sqrt{\rho}(V-1)}{V\rho+(1+2V)},$$

is another coefficient to evaluate the system's characteristic when dealing with the actual RAM depth $M'\cos(\gamma)$. A variety of theoretical approaches have been applied to the study of RAM in the existing literature [86, 87, 88, 89, 90, 91]. Nevertheless, the approach employed in this thesis is original in the method as it includes loss inside the cavity, which is described by the throughput parameter δ. In addition, the theory presented in these pages has been thoroughly and independently derived by the author of this work by implementing the conventional PDH scheme on Equation 2.54. In the case of a lossless system, also known as perfect coupling efficiency, Equation (2.70), in combination with Equation (2.72), yields

$$\sigma_f = \frac{1}{4}\sqrt{\frac{P_s}{P_c}}\frac{f_c}{\nu_0}M'\cos(\gamma). \tag{2.73}$$

A remarkable outcome of this analysis is the equation's alignment with the formalism established in [86], despite its independent derivation. This provides substantial support for the formalism, including the throughput parameters. A similar analysis has been performed in [92], which examined RAM in the context of impedance and mode matching to the resonator. The findings demonstrate a degree of similarity, thus the inclusion of losses are not entirely novel; however, a discrepancy in the approaches is evident. Combining Equation (2.71) and (2.72) yields a formalism that can be used to measure the RAM depth:

$$M'\cos(\gamma) = \alpha_\varepsilon(V,\rho)\,\alpha_f(V,\rho)\,\frac{P_{PDH}}{P_{RAM}}\frac{\varepsilon_{off}}{2\varepsilon_{pp}} \tag{2.74}$$

This presentation of RAM has been chosen as it is common practice to plot its depth, in this study defined as $M'\cos(\gamma)$. In order to estimate the RAM depth, it is necessary to consider both alpha factors (α_ε and α_f). However, the frequency instability is only dependent on α_f. Equation (2.74) will occupy a central role in the experimental determination of RAM in Section 4.1. Subsequently, the error signal strength, the reflection coefficient, and losses inside the cavity, as well as the power in the carrier and sideband, must be determined in order to ascertain RAM on a detector

signal while light is stabilized to the resonator. As illustrated in Figure (2.13), the RAM-affected error signal is depicted. Here, a relatively high RAM strength of $M' \cos(\gamma) = 0.02$ was selected with the intention of accentuating the impact of RAM. In the actual experiment, this is orders of magnitude lower, thereby rendering the approximation more accurate. However, even with this significant modulation depth, the approximated error signal, Equation (2.58), is congruent to the full formalism, Equation (2.56), by naked eye.

Additionally, the approximations for the offsets in frequency and amplitude, as well as for the peak-to-peak strength, have been determined to be accurate at this stage. The utilization of a static RAM would inevitably result in an offset in the locking point. This offset would not further impact the stability of the locked light. The "noise" becomes apparent as soon as the RAM depth undergoes temporal changes, thereby introducing a variation in the error signal offset.

This, in turn, results in a change in the zero crossing along the frequency axis. The locking electronics are incapable of distinguishing this variation from others, which results in false modulation of the light. This ultimately leads to a deterioration in the stability of the light. This can be mitigated by implementing measures to reduce the impact of amplitude modulation on the phase modulator. Among the most effective methods are temperature stabilization and shielding, the use of proper polarizers to avoid polarization mismatches leading to amplitude modulation, and the introduction of a static DC voltage, applied in addition to the RF signal.

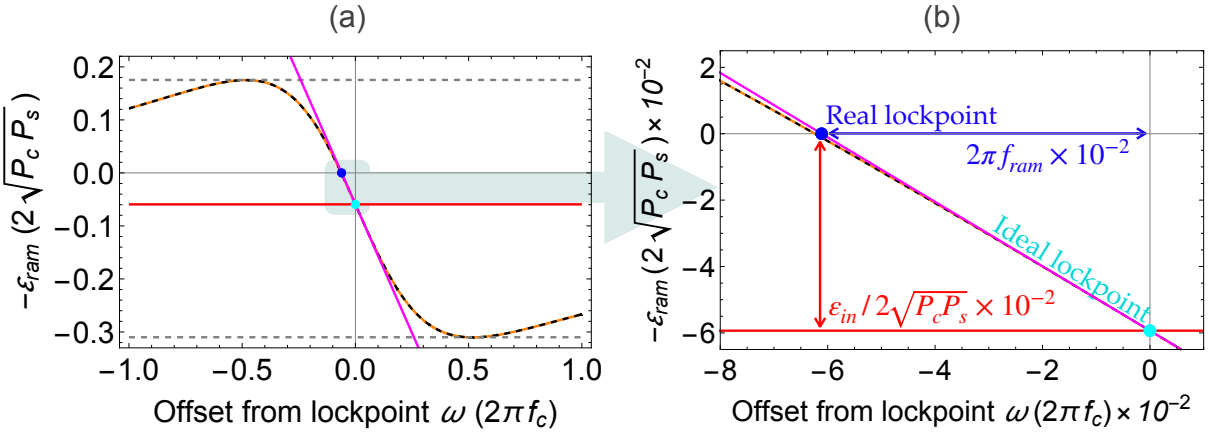


Figure 2.13: Simulation of an error signal that is affected by RAM. Orange: The error signal, as delineated in Equation (2.56). Black: The approximated error signal according to Equation (2.58). The gray dashed lines represent the peak-to-peak strength through Equation (2.67). The magenta line signifies the linearization of the error signal following Equation (2.68). The cyan dot serves as a visual indicator of the ideal lockpoint of the PDH error signal. The red line, on the other hand, demonstrates the offset induced by RAM, as depicted in Equation (2.61). The blue dot indicates the actual zero crossing of the error signal with an offset in frequency given by Equation (2.69). For the purposes of this simulation, the parameters ϕ and γ are set to zero, and $M' = 0.02$. The finesse of the resonator was set to be approximately 10^4, and the sideband modulation was found to be at $\Omega = (2\pi)\,1.58\,\mathrm{MHz}$. The right plot corresponds to a zoom of the gray box on the left plot.

An alternative approach involves a distinct implementation of sideband modulation through an EOM, as will be demonstrated in Section 4.1. Typically, RAM becomes a candidate at the mid 10^{-15} level of frequency stability. The necessity of its elimination depends on the application. Further, an intriguing observation has been documented in [93]. The study noted that measuring RAM on a detector other than the PDH detector could potentially yield inaccurate results due to polarization losses, thus the signals have to be analyzed cautiously.

2.4 Frequency Metrology: Measuring Light with Precision

Originally located in Appendix A.7. The integration of an optical resonator with a laser, locked to it, enables a range of applications in high-precision experiments. However, two fundamental issues remain unresolved. In the event that a novel experiment necessitates a distinct target wavelength, what is to do?

Resonator mirrors exhibit a wide reflectivity spectrum; consequently, they may possess a sufficiently high finesse value for wavelengths that are detuned (i.e. some 50 nm at 1.5 µm) from the central wavelength. In such a scenario, the implementation of a new laser could prove to be a viable solution, given that most free space and select fiber optics systems are capable of still functioning well when subjected to such minimal detuning. Furthermore, EOMs can be utilized as a bridge to stabilize a second laser, at the target wavelength, to the one that is locked to the the cavity, using an additional feedback loop. These phase-locked loops (PLLs) are a significant topic in this section. However, it should be noted that this solution is only applicable within the ranges of the EOM, which is typically in the order of 10 GHz, which can often times be already covered by the initial laser. Consequently, if a transition from one laser at 1.5 µm to another light at 1.1 µm is required, a complete new setup, including a new resonator or, at the very least, mirrors, is necessary. In the long term, this approach is economically inefficient and time-consuming as every new experiment would require a new resonator.

Nevertheless, this problem has a brute force solution, while the second one is more difficult: Even when an experiment generates a substantial amount of promising data and narrow linewidths in spectroscopy experiments, it is ultimately necessary to ascertain the actual absolute frequency of the light when interrogating the atoms or molecules. This is, in the end, the important data. The crux of the issue lies in the fact that, given the configuration of the cavity system as it stands at present, this absolute frequency cannot directly be measured. The data sheet and specifications of the laser allow for the refinement of the parameters to a certain extent, perhaps 10^{-4} level, but not to the extent that would correspond to the actual stability / uncertainty of the locked light. A solution exists in the form of wavemeters, which, despite their high cost, are broadband devices capable of achieving accuracies of MHz and reducing the uncertainty of the measured light to the 10^{-8} level. However, this is still a factor of 10^6 between this solution and the capacities of the systems.

At this stage, the optical frequency comb (OFC) is introduced. The solution to both issues at hand is as follows: stability of light can be transferred across a wide output range, and the absolute frequency of light can be measured down to the 10^{-14} level (against an appropriate reference),

of uncertainty. This work was ultimately recognized with the Nobel Prize in Physics for John L. Hall and Theodor W. Hänsch. Literature on the topic of wavelength meters, frequency combs, and metrology includes [94, 95, 96].

Here, a method to reduce noise in long fiber paths is presented, and subsequently, the H-maser as a highly stable RF frequency source is explained. In the concluding subsection of the chapter as a whole, the knowledge acquired throughout the entirety of the chapter is assembled within the framework of the frequency metrology system. Additionally, in the appendix's correpsonding section, the pulsed laser is introduced along with the methodology for its use as an OFC. Furthermore, two types of wavemeters are described.

2.4.1 Noise Cancellation: Stabilizing Light Through Fibers

Originally located in Appendix A.7.2. In the context of high-precision experiments that demand ultra-stable lasers, fiber links are routinely utilized between laboratories for the transmission of light. These fiber paths are vulnerable to noise in the form of acoustic, thermal, or mechanical perturbations on the fibers, which is translated to the light (see Figure 2.14). This manifests itself through the observation of broadened linewidths of the carrier and the presence of additional sidebands.

In order to minimize this effect, the light at the experimental side is sent back along the fiber to the laser laboratory. The general concept is well-established and thoroughly elaborated in [97]. As previously established, a periodic oscillation between two waves carries information regarding the difference between their respective frequencies. For instance, a periodic oscillation between the incident and reflected beam of a fiber is predominantly characterized by the frequency noise incorporated by the fiber path itself. Based on the information that has been collected thus far, the planning of a fiber noise cancellation setup can be initiated. Figure 2.15 presents a schematic representation of the proposed model. A laser light output of frequency f_l is linearly polarized and split by a PBS, where the reflected part is propagating through a quarter-waveplate towards a mirror. The frequency of the light at the mirror is measured to be

$$f_{ref} = f_l + \Delta f_1,$$

where Δf_1 contains the frequency fluctuations along the path (cyan area).

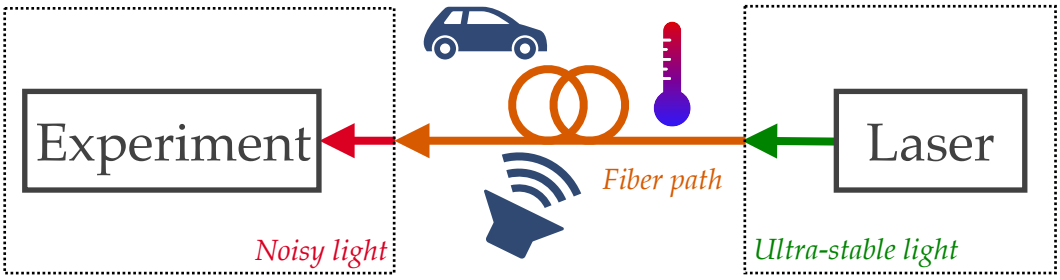


Figure 2.14: The graphical representation of the concept of external disturbances introducing noise on a fiber-optic pathway between two laboratories.

Subsequently, the light undergoes transmission once more through the PBS, and enters a PD. By doing so, it traverses through a path that induces frequency fluctuations Δf_3 (dark blue area) on the light. Therefore, the reference light at the photodetector $f_{pd,ref}$ is given by

$$f_{pd,ref} = f_l + 2\Delta f_1 + \Delta f_3. \tag{2.75}$$

The other arm, which traverses the PBS, is propagating through an AOM, shifting the frequency by f_{aom}. In this case, the first order diffracted beam propagates to a quarter-waveplate and the long fiber before it is sent to the experiment. At the point of out-coupling, the frequency of the light is given by f_{exp}, which is equal to

$$f_{exp} = f_l + f_{aom} + \Delta f_2 + \Delta f_f,$$

where Δf_2 is attributed to the optical path traversed until the fiber (pink area) and Δf_f corresponds to the intrinsic fiber noise (orange area). The light is also reflected back through the fiber. This can be accomplished by employing either a partially transmitting mirror or a fiber TC. The use of the coupler results in a small fiber path of the light entering the experiment not being completely correlated with the reflection of the light. Subsequently, the back reflection of the experimental arm propagates along the same path once more, undergoing diffraction by the AOM.

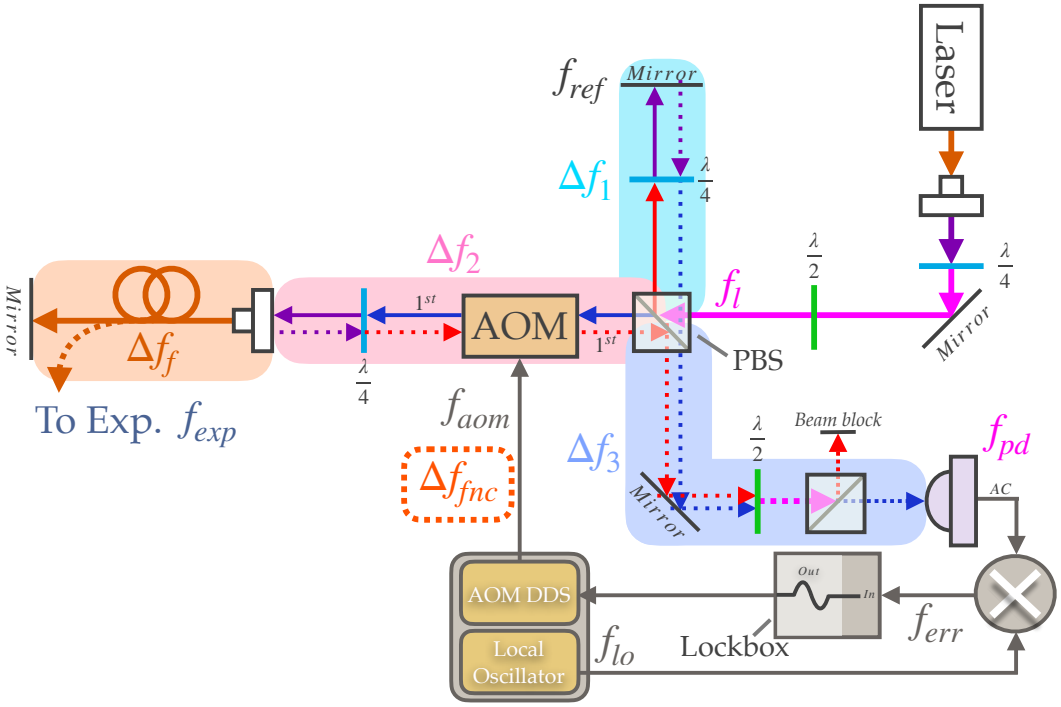


Figure 2.15: Free space fiber noise cancellation (FNC) setup. Purple: Circular polarization. Pink: Linear polarization with (p) and (s) components. Blue: $s-$polarized light. Red: $p-$polarized light. Gray: Electrical wiring. Orange: Fiber path. Note that in practice there are two beams coming out of the AOM, the zeroth and the first order beams. However, for simplicity, only the first-order beams are shown.

Thereafter, the back reflection enters the PD, where its frequency $f_{pd,exp}$ is expressed as

$$f_{pd,exp} = f_l + 2f_{aom} + 2\Delta f_2 + 2\Delta f_f + \Delta f_3. \tag{2.76}$$

In this context, the significance of quarter-waveplates becomes evident. In order for the light of both arms to overlap at the PD, the polarizations at the PBS must be matched correctly. Specifically, the light of the reference arm is first reflected and subsequently transmitted through the PBS, while the experimental arm is first transmitted and then reflected. Therefore, the polarizations of both must be orthogonal to each other and undergo a rotation of $\frac{\pi}{2}$ during their propagation along their respective arms. The rotation can be achieved by propagating twice through a quarter-waveplate, which is ideal for the system as both arms work with back reflections.

Prior to the PD, another combination of a PBS and a half-waveplate is utilized to rotate both polarizations, thereby generating a measurable beat frequency. The AOM is driven by a DDS at a frequency of f_{aom} and performs two substantial tasks. Firstly, the device can be utilized as a rapid actuator within the feedback loop. This is achieved by modulating the frequency of light in accordance with the perturbations experienced by the fiber path. Secondly, the device is utilized to generate a beat that possesses a non-zero carrier frequency. The beat frequency f_{pd} between the reference (see Equation (2.75)) and experimental arms (see Equation (2.76)) at the PD is given by

$$f_{pd} = f_{pd,exp} - f_{pd,ref} = 2f_{aom} + 2\left(\Delta f_f + \Delta f_2 - \Delta f_1\right).$$

This indicates that a SA can ascertain the spectral noise arising from the optical path and fiber around twice the DDS frequency driving the AOM. In a standard scenario, the difference in the fluctuation functions, Δf_f, is considerably larger and less predictable than Δf_1 and Δf_2. In many cases, the latter two even vanish in the measurement noise. Utilizing a mixer enables the generation of an error signal, which carries information regarding the frequency fluctuations, designated as Δf_{err}, for a lockbox through

$$\Delta f_{err} = f_{pd} \otimes f_{lo} = 2\left(\Delta f_f + \Delta f_2 - \Delta f_1\right). \tag{2.77}$$

In Equation (2.77) it was used that the local oscillator frequency is $f_{lo} = 2f_{aom}$. Consequently, this information can be translated into an output that modulates the frequency of the DDS driving the AOM by adding the term $\Delta f_{fnc} = -1/2\,\Delta f_{err}$ to it. If the FNC)is enabled, it follows:

$$\begin{aligned} f_{exp,fnc} &= f_l + \left(f_{aom} + \Delta f_{fnc}\right) + \Delta f_2 + \Delta f_f \\ &= f_l + f_{aom} + \Delta f_1. \end{aligned}$$

Therefore, the experimental light will not be disturbed by noises along its path after the PBS. However, it will receive added noise from the reference arm's path. In a well-controlled system, this added noise is negligible. In a recent study, [98], an analogous configuration was utilized to detect seismic events along a 123 km optical fiber path between Basel and Bern through the method of noise cancellation. In this thesis, a free space FNC setup was set up as well as a fully fiberized system, where the PBS was exchanged for an optical circulator. The latter is a novel approach to the topic that enables fully fiberized laser systems.

2.4.2 Long-Term References: Hydrogen Masers and GNSS

Originally located in Appendix A.7.4. The primary focus of this work has been on the stability of light, particularly laser waves, as a means for experimental research. Nevertheless, radio frequency waves are also present in many cases, as they are an essential component of the application. The production of these signals is primarily performed by the DDS, with their primary application being the modulation of beat frequencies. Additionally, they serve as reference signals for instruments such as frequency counters and SAs. In many cases, their stability is already sufficiently low, measuring in at approximately 10^{-10} with regard to fractional frequency stability over brief time frames. While this may appear to be elevated in comparison to the targeted 10^{-14}, it should be noted that their absolute frequencies are also low. In particular, a DDS operating at 100 MHz will demonstrate fluctuations at 10 mHz scales, which corresponds to 10^{-16} fractional stability for an optical wave of frequency 100 THz. In conventional applications, these components are added or subtracted from a beat signal, thereby contributing only marginally to the detected signal.

Nevertheless, two reasons justify the importance of maintaining a highly stable RF reference. This reference is used to reference all synthesizers and clocks in the laboratory, namely precision and accuracy. Two identical models of synthesizers may still exhibit an absolute frequency offset to each other when the internal oscillator is considered. As the number of devices utilized within a frequency chain increases, the potential for these offsets to impact the result becomes more significant. Therefore, it is essential to reference all devices to the same oscillator, preferably one that has a very low and known offset, in order to eliminate this error. In a similar manner, the frequency stability of the oscillator will be synchronized with the reference signal. This is of particular importance in cases where frequency conversion is performed on light that is modulated or measured with respect to the RF oscillator.

RF devices are typically equipped with inputs designated for 5 MHz, 10 MHz, and 100 MHz reference inputs. Among these, 10 MHz is the most prevalent for devices utilized in this thesis. In a multitude of modern laboratories, a Hydrogen maser (microwave amplification by stimulated emission of radiation, short: H-maser) or a Rubidium clock is utilized as global reference. Within the scope of this thesis, two H-masers were utilized to ensure the stability of all synthesizers in the laboratory settings. Consequently, the focus will be directed towards this particular type of device. A contemporary H-maser attains frequency stability that is measured to an accuracy of 10^{-13} in short-term scales and 10^{-15} over longer time scales. These devices have been observed to display frequency uncertainty that reaches an accuracy of 10^{-11} in accordance with the established international standard.

They are based on fundamental transitions in the hydrogen atom, which do not experience long-term drifts as cavities, and they make one of the best long-term standards available. The output signal of a H-maser still exhibits drift characteristics but at several orders of magnitude lower than optical references. The transition's natural frequency is 1.4 GHz, and it is converted to outputs at the previously enumerated frequencies. In many instances, a 10 MHz signal from the H-maser is transmitted to the laboratory, where it enters a low-noise distribution amplifier to generate an adequate number of reference outputs. In some cases, a 5 MHz signal is generated by the maser. This signal is then converted by a low-noise frequency doubler prior to its distribution.

It has been observed that certain RF devices are equipped with a feedthrough for the reference signal, a feature that enables their cascading configuration.

Additionally, the SI frequency standard is distributed through GNSS using H-maser and analogous devices. At the time of this work, the time and frequency standard was still defined by a ground state to hyperfine transition in Cs^{133} atoms with a frequency of $\nu_{Cs} = 9\,192\,631\,770\,\mathrm{Hz}$. The period of one second is defined as the time required for 9 192 631 770 cycles of the transition to complete. The following definition constitutes the standard for the SI. The defining transition can be measured by Cs fountain clocks with an uncertainty at the 10^{-16} level. Noteworthy developments such as state-of-the-art optical lattice clocks that are based on Ytterbium and Strontium have demonstrated the capacity to measure transitions with an accuracy of up to 10^{-18} [22, 99, 25], thereby giving rise to the notion of a redefinition of the SI second.

A H-maser can be steered with respect to the Cs clock, thereby enabling the distribution of the SI standard through GNSS. In this manner, the absolute frequency of an H-maser in the laboratory in Düsseldorf can be compared with that of a maser in the PTB in Braunschweig at the 10^{-14} level of uncertainty. This comparison is dependent upon the time scales in question, as well as the calibration of the PTB maser towards their Cs clock. The calibration of a laboratory's reference to this standard significantly enhances the comparability of results on a global scale. This calibration should be a fundamental consideration in any application focused on high-precision frequency metrology. In the absence of a standard, the stability of the measurement may be exceptional; however, the absolute accuracy of the measurement cannot be adequately evaluated. To illustrate, consider a scenario in which the linewidth of a transition is known with a precision of 10 Hz. However, the absolute frequency is only specified to the level of 100 kHz or larger. A multitude of factors can introduce significant uncertainties to the measured frequency.

In the scope of the OFC, the CEO f_{ceo} is measured through the self beat of the pulse train, typically at frequencies in the order of 10 MHz. The measurement of this frequency is conducted by a counter, and its stabilization with respect to the maser is achieved through the implementation of a PLL. This process is further elaborated upon in the subsequent section. The significance of the maser stability is attributable to the fact that all SAs and frequency counters measure the respective device under test (DUT) with respect to an internal oscillator. In typical scenarios, after the conversion of a 100 MHz optical beat to a 100 MHz electrical signal, the RF signal maintains the absolute frequency stability of the light. Therefore, for light at 100 THz with an instability level of 10^{-14} in frequency, the RF signal will maintain the 1 Hz instability. This is a fractional value of 10^{-8} with respect to the beat frequency, which is higher than that of a good RF oscillator, such that it is still possible to resolve the behavior of the light with standard counters and oscillators.

However, this is not applicable to the repetition rate of the OFC. The fractional frequency instability, as opposed to the absolute, of the light is imprinted on this signal. Therefore, in order to measure the repetition rate at 100 MHz with 10^{-14} level of resolution, it is necessary to have an adequate frequency counter and an RF signal of the similar or better performance. The H-maser is an example of such a signal. The following section will show the implementation and mathematics underlying this process.

2.4.3 Putting It All Together: Frequency Analysis and Measurement

Originally located in Appendix A.7.5. At this stage, it is possible to integrate all components and establish a system that can stabilize light, accurately measure its absolute frequency, and transfer this stability to light of various wavelengths. This system can also compare the absolute frequency with the international standard. The concept is illustrated in Figure 2.16. The global optical reference constitutes an ultra-stable optical resonator to which a laser is locked using the PDH technique (illustrated in orange). The frequency of the stabilized laser, denoted by $f_{l,1}$, is subdivided into two parts. One part is directed to a wavemeter, while the other is allocated to the OFC. The wavemeter is capable of measuring the laser frequency, denoted by $f'_{l,1}$, with a level of precision that is sufficient to resolve the repetition rate, such that the number $N_{l,1}$ of the closest mode to the laser is given by

$$N_{l,1} = \text{Round}\left(\frac{f'_{l,1}}{f_{rep}}\right).$$

The CEO frequency, denoted by f_{ceo}, is determined through the use of a self-beat of the two OFC lines (see Section A.7.1, Equation (A.143)), which is then mixed with a local oscillator—typically a DDS—that is referenced to an H-maser. The resulting error signal is then directed to a PID controller, or lockbox, which in turn connects to an actuator capable of altering the group to phase velocity difference. For instance, this may be an EOM situated within the cavity, the refractive index of which varies according to the applied field. Consequently, the CEO frequency can be locked to the local oscillator, conceptually the H-Maser, with high fidelity. The value of the CEO is determined by the absolute value of the DDS, which is set at 20 MHz in this case. The division of

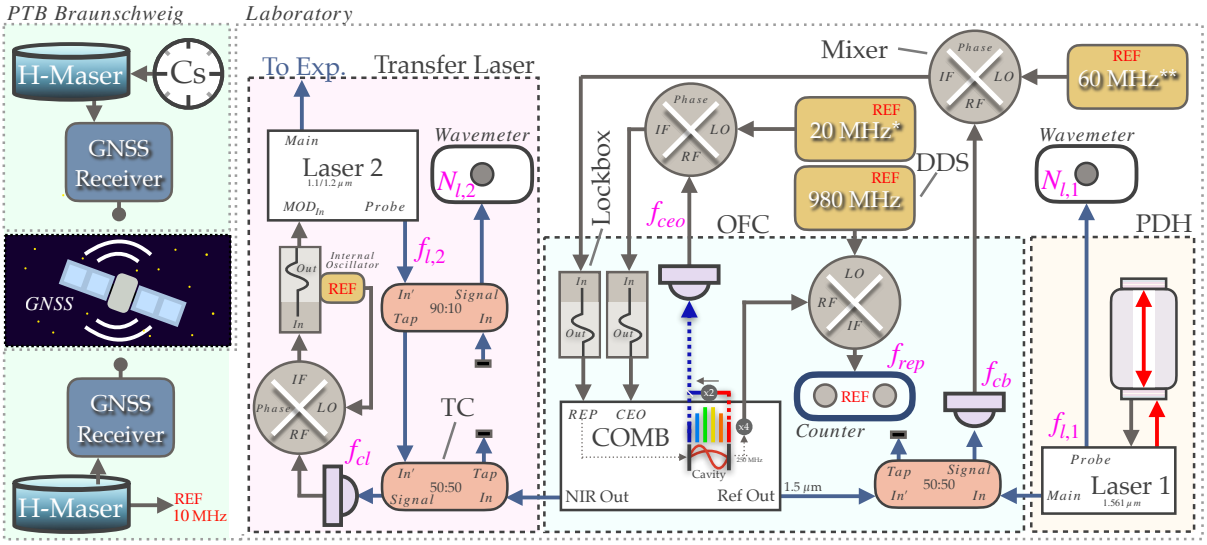


Figure 2.16: Concept of a modern frequency metrology system with some real-world numerical values. The orange box is a simplified version that includes the setup for the PDH technique. The light blue box contains the OFC, while the red box illustrates the setup necessary to stabilize the frequency of another laser to the comb and measure its absolute frequency. The green boxes serve to illustrate the comparison of the RF reference, specifically the H-Maser, to the international standard. The light travels through fibers and is routed by TCs.

the signal between the PD and the mixer facilitates the measurement of f_{ceo} through the utilization of a frequency counter. In a similar manner, a beat f_{cb} between the comb and the reference light can be determined through measurement. At this stage, the formula to measure the frequency of the reference laser is expressed as

$$f_{l,1} = f_{cb} + N_{l,1}\, f_{rep} + f_{ceo}.$$

Fluctuations in f_{cb} are attributable to variations in the comb cavity, given the active stability of all other quantities. Therefore, the signal of the beat itself can be utilized as an error signal to stabilize the repetition rate, f_{rep}, of the OFC. This process is analogous to the CEO, wherein the beat is mixed using a local oscillator at the desired lockpoint frequency, which is then fed to a lockbox that acts on the cavity. One possibility is that this is a piezo that changes the OL by moving a mirror. Alternatively, it could be an EOM that changes the OL through the effective refractive index of the light. The PID loops utilized in the context of these locks analyze the phase delay between the compared waves and adjust this to be zero, hence the designation phase-locked loop (PLL). The configuration of these devices is straightforward; however, they necessitate an already stable reference wave, $f_{l,1}$.

The stabilization of the OFC has been achieved; however, the measurement of the repetition rate remains to be obtained. In order to accomplish this objective, it is necessary to measure the signal of a PD, in which a portion of the pulse train of the OFC is divided using a frequency counter. In actuality, due to technical limitations, this may not be executed at the precise repetition rate; rather, it will be performed at a higher-order harmonic of that rate. In this configuration, the repetition rate is approximately $f_{rep} \approx 250\,\mathrm{MHz}$, while the split signal is the fourth harmonic at 1 GHz.

Additionally, the applied frequency counter may lack the bandwidth necessary to resolve signals at this particular frequency. Consequently, the signal is mixed down by a third DDS operating at 980 MHz, thereby generating a signal at 20 MHz that can be accurately measured by a high-precision counter. This counter is then referenced to the H-maser for precise calibration. The signal can be transformed back into the original 250 MHz signal, thereby concluding the measurement of the absolute frequency, given the knowledge of all parameters. In instances where the reference laser does not provide the required wavelength for the specific application, the implementation of a transfer laser becomes necessary. The frequency of this laser, $f_{l,2}$, can be measured in the same manner by

$$f_{l,2} = f_{cl} + N_{l,2}\, f_{rep} + f_{ceo}.$$

Therefore, it is necessary to establish an additional beat-line measuring f_{cl} and to measure the laser light with a wave meter to evaluate the comb tooth number $N_{l,2}$. In the event that this light has not yet been stabilized to a resonator, it can be referenced to the OFC in the same manner as the OFC is locked to the reference laser. This is achieved through the use of a PLL that acts on the transfer laser frequency. This is accomplished by comparing f_{cl} to a H-maser referenced local oscillator. This method involves the use of a comb as a bridge to map the stability of the reference laser onto the transfer laser The evaluation of the H-maser frequency is achieved by measuring the same GNSS signals in PTB and inside the laboratory of the OFC. A three-cornered hat analysis is then performed on the data, which eventually provides the absolute frequency offset between the

signal steered to the Cs-clock and the laboratory reference.

In the field of frequency metrology, it is indispensable to quantify both the absolute frequency and the time-dependent instability of an oscillator. Absolute frequency is typically measured using a wave-meter or an OFC, while time-dependent instability is assessed through beat measurements and frequency counters. The following paragraph will contain a notation for frequencies developed within the scope of this thesis. The frequency of any oscillator, $f_i(\tau)$, can be expressed as a combination of a static component, representing the accuracy $f_{i,0}$, and a time-dependent component, denoted as $\delta f_i(\tau)$, that characterizes the frequency stability of the signal. The time-varying component is directly equal to the absolute Allan deviation of the oscillator over a specified averaging time, denoted by τ. This can be expressed as

$$f_i(\tau) = \begin{pmatrix} \overbrace{f_{i,0}}^{\text{accuracy}} \\ \underbrace{\delta f_i(\tau)}_{\text{stability}} \end{pmatrix}. \tag{2.78}$$

The combination of M oscillators of frequencies $f_k(\tau)$, forming a final frequency $f_{tot}(\tau)$, as in the conceptual formalism of the frequency comb, results in the following identities:

$$f_{tot}(\tau) = \begin{pmatrix} f_{tot,0} \\ \delta f_{tot}(\tau) \end{pmatrix} \longrightarrow f_{tot,0} = \sum_{k=1}^{M} f_{k,0},\ \delta f_{tot}(\tau) = \sqrt{\sum_{k=1}^{M} \delta f_k^2(\tau)} \tag{2.79}$$

The final absolute frequency of the, $f_{tot,0}$, can be calculated through a straightforward summation. The instability, $\delta f_{tot}(\tau)$, of the combined frequencies is calculated by adding the Allan variances (not deviations). This remains valid under the condition that the oscillators are uncorrelated. Indeed, in the event that two signals, denoted by delta $\delta f_1$and $\delta f_2 = \alpha\,\delta f_1$, are found to be correlated, with the second oscillator demonstrating a tendency to follow the instability exhibited by the initial oscillator with a scaling factor α, the resulting instability of their beat $\delta f_{12}(\tau)$ can be expressed as follows:

$$\delta f_{12}^2(\tau) = \left|\delta f_1^2(\tau) - \alpha \delta f_1^2(\tau)\right|$$

In the event that $\alpha = 1$, the total correlation is thus established. Consequently, the beat signal instability $\delta f_{12}(\tau)$ will converge to zero. Illustrative examples for both scenarios will be presented shortly, as shown in Equations (2.82) and (2.85). In practice, the assumption of independent oscillators is a generally valid model of reality. In the context of oscillators synchronized to a reference, the frequency variation is dictated by the stability of the reference itself, with consideration given to the ratio of the absolute frequencies of the oscillators in question.

Furthermore, an instability, δf_{lock}, emerges as a consequence of the locking process itself. This representation is applicable to both DDS and other RF sources. In the context of a PLL, the stabilization of optical light at a frequency of $f_i(\tau)$ relative to a reference light of f_{ref} involves the introduction of an additional term, the bridge, represented by the synthesizer frequency of f_s. This term describes the local oscillator, that serves to mix down the beat signal, thereby creating the

error signal. This type of "referencing" will be denoted as $f_i(\tau)|_{ref}$ which is expressed as

$$f_i(\tau)|_{ref} = \begin{pmatrix} f_{i,0} \\ \delta f_i(\tau)|_{ref} \end{pmatrix}, \text{ with } \delta f_i|_{ref} = \sqrt{\underbrace{\left(\frac{f_{i,0}}{f_{ref,0}}\delta f_{ref}\right)^2}_{\text{Reference}} + \underbrace{\delta f_s^2}_{\text{Bridge}} + \underbrace{\delta f_{i,lock}^2}_{\text{PID}}}. \tag{2.80}$$

For the sake of clarity, the dependence on τ has been omitted in the stabilities. It is possible to characterize the absolute frequency f_l' measured by the OFC based on the information available. The prime symbol " ' " shall distinguish between the real and the measured frequency. The determination of these frequencies is based on a total of three key parameters:

- The beat frequency f_{cl} between the closest comb line and the laser.
- The repetition rate of the comb f_{rep}.
- The CEO frequency f_{ceo}.

For the purposes of the following calculations, the reference light to which the OFC is stabilized is at $f_{r,0} \approx 192\,\text{THz}$, which corresponds to a typical wavelength of approximately $1.5\,\mu\text{m}$.

The CEO Frequency The total frequency that the OFC measures is the expressed by the formalism

$$f_l'(\tau) = \begin{pmatrix} f_{cl,0} + N_l f_{rep,0} + f_{ceo,0} \\ \left(\delta f'^2_{cl} + N_l^2 \delta f'^2_{rep} + \delta f'^2_{ceo}\right)^{\frac{1}{2}} \end{pmatrix}. \tag{2.81}$$

The repetition rate, beat, and CEO are measured by frequency counters that are referenced to the H-maser. The integer number N_l of the comb line that beats with the laser is determined using a wavemeter, which has an accuracy superior to the repetition rate. This ensures that the correct line is identified. The initial CEO, operating at a frequency of 20 MHz, is divided by a factor of two and subsequently referenced to the H-maser f_m. From a mathematical perspective, this can be conceptualized as the CEO being effectively locked to twice the H-maser frequency ($2m$). The instability of the CEO that is measured by the frequency counter is

$$\begin{aligned} \delta f'_{ceo}\big|_{2m} &= \sqrt{\left|\left(\frac{f_{ceo,0}}{2\,f_{m,0}}2\delta f_m\right)^2 - \left(\frac{f_{ceo,0}}{f_{m,0}}\delta f_m\right)^2\right| + \delta f_{ceo,lock}^2} \\ &= \sqrt{\underbrace{4\delta f_m^2 + \delta f_{ceo,lock}^2}_{\text{Actual instability}} \underbrace{-4\delta f_m^2}_{\text{Frequency counter}}} \\ &= \delta f_{ceo,lock} \approx 0. \end{aligned} \tag{2.82}$$

In cases where the effects of electronic noise can be disregarded, the CEO can be considered to be following the instability of the Maser with a factor of two. The instability of the maser is at μHz level at one-second averaging time with respect to its 10 MHz signal. However, as the counter

measuring the CEO frequency is also referenced to the maser, the frequency instability obtained by the counter should only show the noise of the lock because the maser noise cancels out. It must be noted that this is in an ideal scenario, in which the reference signal and its contribution to the device under test are in phase. The primary constraint, in practical terms, arises from the resolution of the frequency counter utilized for measuring the CEO, which is within at the mHz level for signals of order 10 MHz. However, given the addition of the CEO to the total frequency instability with a factor of one, its effect on the overall frequency instability is at the level of 10^{-18}, thus negligible. This level is calculated with respect to typical telecom wavelengths at 1.5 µm.

The Repetition Rate

The comb light is stabilized to a reference laser $\delta f_{comb}|_r$, which results in the repetition rate f_{rep} following the reference instability, thus

$$f_{rep}(\tau) = \begin{pmatrix} f_{rep,0} \\ \frac{f_{rep,0}}{f_{comb,0}}\,\delta f_{comb}|_r \end{pmatrix} \approx \begin{pmatrix} f_{rep,0} \\ \frac{1}{N_R}\delta f_r \end{pmatrix}. \tag{2.83}$$

Here, $N_r = \frac{f_{r,0}}{f_{rep,0}}$ is the comb line, that is closest to the reference light. The instability of the comb is derived from a beat with the reference at $f_{cb,0} = 60\,\text{MHz}$, which is mixed down in a manner analogous to the CEO using the Maser. The approximation in Equation (2.83) arises, because the comb line and the reference light are shifted by approximately 60 MHz. However, this is a relative change of 3×10^{-7} to the optical frequency, which, within the limits of this scope, can be considered negligible. Further, the full expression of the comb instability $\delta f_{comb}|_r$ is

$$\begin{aligned} \delta f_{comb}|_r &= \sqrt{\delta f_r^2 + \left(\frac{f_{cb,0}}{6 f_{m,0}} 6\,\delta f_m\right)^2 + \delta f_{comb,lock}^2} \\ &= \sqrt{\delta f_r^2 + 36\,\delta f_m^2 + \delta f_{comb,lock}^2} \\ &\approx \delta f_r. \end{aligned} \tag{2.84}$$

The reference instability of a good system is within the range of 0.1 Hz to 1 Hz, which is five orders of magnitude larger than the typical H-maser instability. Consequently, the comb instability is fundamentally determined by the reference, as previously asserted.

In practice, the fourth harmonic of the repetition rate is emitted. A high-resolution frequency counter measures the repetition rate. However, its functionality is constrained to frequencies that do not exceed 200 MHz. Therefore, a synthesizer operating at a reference frequency of $f_{s,0} = 980\,\text{MHz}$, referenced to the H-maser, is employed to mix down the harmonic of the repetition rate to approximately $f_{mrep,0} \approx 20\,\text{MHz}$. Additionally, the frequency counter measuring f_{mrep} is referenced to the H-maser, thereby introducing a frequency correlation to the synthesizer noise.

The measured quantity f'_{mrep} can be expressed as follows:

$$f'_{mrep}(\tau) = \begin{pmatrix} \overbrace{4f_{rep,0} - f_{s,0}}^{f_{mrep,0}} \\ \left(\left(\frac{4}{N_R}\delta f_r\right)^2 + \left(\frac{f_{s,0}}{f_{m,0}}\delta f_m\right)^2 - \left(\frac{4f_{rep,0}-f_{s,0}}{2f_{m,0}}2\,\delta f_m\right)^2\right)^{\frac{1}{2}} \end{pmatrix}$$

In this equation, the negative sign of the last term in the stability arises through (perfect) correlation of the maser noise. The actual value of the repetition rate f'_{rep}, used to calculate the absolute frequency of the laser is then determined by digitally adding the synthesizer frequency and dividing by four. Thus, the chain to obtain f'_{rep} is as follows:

$$\underbrace{250\,\mathrm{MHz}}_{f_{rep}} \overset{\text{4th harm.}}{\longrightarrow} 1\,\mathrm{GHz} \overset{\text{mix with } f_s}{\longrightarrow} \underbrace{20\,\mathrm{MHz}}_{f'_{mrep}} \overset{\text{add } f_s}{\longrightarrow} 1\,\mathrm{GHz} \overset{\times 1/4}{\longrightarrow} \underbrace{250\,\mathrm{MHz}}_{f'_{rep}}$$

The mathematical description of the measured repetition rate is given by

$$f'_{rep}(\tau) = \begin{pmatrix} f_{rep,0} \\ \left(\left(\frac{1}{N_R}\delta f_r\right)^2 + \left(\frac{\left|f_{rep,0}f_{s,0} - 2f_{rep,0}^2\right|}{2f_{m,0}^2}\right)\delta f_m^2\right)^{\frac{1}{2}} \end{pmatrix}. \tag{2.85}$$

The Beat Frequency

The final piece of the puzzle is the beat frequency f_{cl}. It is measured using another frequency counter that is referenced to the H-maser and can be expressed as

$$f'_{cl}(\tau) = \begin{pmatrix} \overbrace{f_{l,0} - f_{comb,0}}^{f_{cl,0}} \\ \left(\delta f_{comb}^2 + \delta f_l^2 + \left(\frac{f_{cl,0}}{f_{m,0}}\delta f_m\right)^2\right)^{\frac{1}{2}}. \end{pmatrix}. \tag{2.86}$$

In this instance, the reference to the H-maser does not correlate with the measured quantities. Therefore, its instability is incorporated.

The OFC

Then, the total instability $\delta f'_l$ that is measured by the frequency comb is determined by combining Equation (2.82), (2.84), (2.86) and (2.85) via the formalism of (2.81)

$$\delta f'^2_l = \delta f_l^2 + \left(1 + \frac{N_l^2}{N_r^2}\right)\delta f_r^2 + \left(\frac{N_l^2 f_{rep,0}\left|f_{s,0} - 2f_{rep,0}\right| + 2f_{cl,0}^2}{2f_{m,0}^2}\right)\delta f_m^2 \tag{2.87}$$

Assuming the laser being measured is indeed the reference laser, it can be substituted that $N_l = N_r$ and $\delta f_l = -\delta f_r$, provided that the electronic noise of the PLL is negligible. The negative sign of

latter is introduced to indicate correlation, given that the beat frequency is now virtually zero and consists exclusively of locking noise. Consequently, the instability of the reference frequency f_r' can be measured as follows:

$$\begin{aligned}\delta f'^2_r &= \delta f_r^2 + \left(\frac{N_r^2 f_{rep,0}\left|f_{s,0} - 2f_{rep,0}\right| + 2f_{cb,0}^2}{2f_{m,0}^2}\right)\delta f_m^2 \\ &\approx \delta f_r^2 + \left(\frac{N_r^2 f_{rep,0}\left|f_{s,0} - 2f_{rep,0}\right|}{2f_{m,0}^2}\right)\delta f_m^2 \\ &= \delta f_r^2 + \Lambda\,\delta f_m^2\end{aligned}$$

The experimental parameters of the setup result in an amplification of the maser noise during the actual measurement. This amplification is expressed by the parameter Λ, which, in this particular instance is $\Lambda = 3.7 \times 10^{14}$. The expression of the total frequency fluctuations, δf_i in terms of the fractional fluctuations $\sigma_i = \delta f_i / f_{i,0}$ results in the following equation:

$$\begin{aligned}\sigma'^2_r &= \sigma_r^2 + 3.7 \times 10^{14}\left(\frac{f_{m,0}}{f_{r,0}}\right)^2 \sigma_m^2 \\ &\approx \sigma_r^2 + \sigma_m^2\end{aligned} \tag{2.88}$$

That the maser noise contributes with a weight factor of approximately one is due to the fact that in this particular setting it is $\left|f_{s,0} - 2f_{rep,0}\right| \approx 2f_{rep,0}$. A lower synthesizer frequency may potentially reduce the effective maser induced noise in the measurement. However, that requires said maser components to be in-phase with the reference wave which might be technically challenging. Therefore, in a realistic scenario, it can be concluded that the fractional instabilities of the laser and the maser contribute equally to the final measurement. Consequently, for averaging times, where the maser exhibits higher levels of instability, the measurement is significantly constrained by its instability (typically below 10 s).

In addition to the stability of the system, it is equally crucial to ascertain the accuracy in order to ensure the precise measurement of absolute frequencies. The precision of any frequency in relation to the international standard is predominantly determined by the global reference employed. In this configuration, the accuracy of a signal $\Delta f_{i,0}$ measured by a SA or counter is determined by the H-maser, given that all such devices are referenced to the maser. It is defined as the frequency offset with respect to SI. This relationship can be expressed as follows:

$$\breve{f}_{i,0} = f_{i,0} + \underbrace{\frac{f_{i,0}}{f_{ptb,0}}\Delta f_{m,0}}_{\Delta f_{i,0}} \text{ with } \Delta f_m = \breve{f}_{m,0} - f_{ptb,0} \Longrightarrow f_{i,0} = \frac{f'_{i,0}}{f_{ptb,0}}\breve{f}_{m,0} \tag{2.89}$$

Here, $\breve{f}_{i,0}$ denotes the true frequency with respect to SI, $f_{i,0}$ is the measured value in the laboratory, and $\Delta f_{i,0}$ is the correction due to the inaccuracy of the H-maser. The H-masers utilized in this study exhibit accuracies in the order of 2×10^{-11} with respect to the Cs clock-steered H-Maser(s) f_{ptb} at PTB, which corresponds to an offset of about 200 µHz at 10 MHz. The fractional correction is

defined by $\sigma_{si} = \frac{\Delta f_m}{f_{ptb}}$. For the beat and offset frequencies, this offset is negligible and vanishes in the resolution of the measurement. However, the repetition rate is amplified by the comb line number, N_l, resulting in the following identity:

$$\frac{N_l\, f_{rep,0}}{f_{cl,0} + f_{ceo,0}} \gtrsim O\left(N_l\right) \approx 10^5 - 10^6$$

Therefore, the accuracy of a measured laser can be evaluated by means of

$$\Delta f_{l,0} = \frac{f_{l,0}}{f_{ptb,0}} \Delta f_{m,0} = \frac{f_{cl,0} + N_l\, f_{rep,0} + f_{ceo,0}}{f_{ptb,0}} \Delta f_{m,0} \approx \frac{N_l\, f_{rep,0}}{f_{ptb,0}} \Delta f_{m,0}. \tag{2.90}$$

In terms of the down-mixed repetition rate, f_{mrep}, Equation (2.90) becomes:

$$\Delta f_{l,0} = \frac{N_l}{f_{ptb,0}} \left(\frac{f_{mrep,0} + f_{s,0}}{4} \right) \Delta f_{m,0}$$

Additionally, an offset is present in the synthesizer frequency, which is referenced to the maser. Nevertheless, the same argument applies to the CEO and repetition rate and this offset is negligible as it is not amplified. To illustrate, if the reference light is measured by the OFC with an accuracy of 10^{-11} of the H-Maser, the correction for the optical light would be equivalent to

$$\Delta f_r' \approx 3\,\mathrm{kHz}. \tag{2.91}$$

This represents a substantial offset in the realm of high precision metrology. The offset undergoes a gradual drift, attributable to the slow drift of the H-Maser over time. Consequently, the H-Maser must be continuously measured and corrected for to ensure the accuracy of the measurement. Therefore, it is continuously compared to the PTB via GNSS. Typical maser drifts are in the order of $10^{-15}\mathrm{d}^{-1}$, which translates to a drift in the frequency accuracy $\Delta f_r'$ of order of 100 Hz in a year at infrared frequencies. By correcting for the drift and offset, it is possible to measure the absolute frequency with a precision that approaches or exceeds 10^{-14} level. A concise summary of the full formalism used to describe a laser frequency $\check{f}'_l(\tau)$ that is measured by the OFC with respect to the international standard is:

$$\check{f}'_l(\tau) = \left(\frac{\left(f_{cl,0} + N_l\, f_{rep,0} + f_{ceo,0}\right)\left(1 + \sigma_{si}\right)}{\sqrt{\delta f_l^2 + \left(1 + \frac{N_l^2}{N_r^2}\right) \delta f_r^2 + \left(\frac{N_l^2 f_{rep,0} \left| f_{s,0} - 2 f_{rep,0} \right| + 2 f_{cl,0}^2}{2 f_{m,0}^2} \right) \delta f_m^2}} \right) \tag{2.92}$$

This marks the conclusion of the theoretical background, which began with an examination of the EM wave and culminated in a comprehensive description of a frequency metrology system. The following chapters will focus on the experimental implementation and characterization based on what has been learned in this chapter.

Chapter 3

Ultra-Stable Laser Systems for Metrology

Subsequent to the theoretical exposition, this chapter will address the experimental implementation of the aforementioned concepts. In this thesis, three optical resonators, one fiber resonator, and one frequency metrology system have been set up, characterized, and optimized. In this chapter, the typical characterizations in terms of Allan deviation, linewidth, and frequency noise will be accompanied by the respective experimental setups. The procedure is initiated with the configuration of two high-finesse optical resonators, which are locked by the classical PDH technique. They are meant to achieve frequency instabilities below the 10^{-15} level for high-precision applications. Hereafter, the setup of an optical reference using an, in regard to cavity spacers still fairly, novel material, NEXCERA, is presented. This apparatus is both simple and robust; it incorporates the offset lock technique, with the goal of instabilities at the 10^{-14} level. The system has been designed with portability in mind. The integration of a novel fiber-based resonator with a ZCTE, designed, at room temperature will serve as the final component of the cavity part.

A frequency metrology system was eventually established, incorporating an OFC, a H-maser, a NEXCRA-based optical reference, and a transfer laser, for a measurement campaign in collaboration with the MPIK in Heidelberg. The construction, design, and characterization of the system were completed in Düsseldorf as part of this thesis. Thereafter, the system was transported to Heidelberg via van. The system under consideration includes FNC systems for both the reference and transfer lasers. Notably, the entirety of the system, with the exception of the in-coupling to the resonator, was configured through the utilization of optical fibers. A salient feature of the system under consideration is its capacity for remote control from any global location, as well as its self-replication algorithms.

The final two sections of this chapter will address two research points on optical resonators. The first topic is the transmission profile of optical references as a tool to improve the frequency noise of the light. The second is the mitigation of the effect of RAM below the thermal noise floor limit. As a reminder, within this thesis, the symbol ν_0 denotes the carrier frequency of the light, while f_0 is used in plots for the sake of visual clarity.

3.1 ULE-Based Dual Resonator System

In order to test the anisotropy of light in the Institut für Experimentalphysik at HHU, a dual-cavity block made from ULE glass was utilized to stabilize two light paths. The beat between them was analyzed in relation to the rotation of the apparatus and compared to models that include an isotropic distribution of the speed of light, akin to the original Michelson-Morley experiment from the 19th century. As a result, it was determined that the speed of light is exhibiting isotropy at the 10^{-17} level due to the limitations of the measurement devices, specifically the stability of the light and the duration of the measurement.

The configuration and methodology of the experiment are published in [29, 100, 6, 30]. An improved dual cavity system and test on Lorentz invariance was performed in the second generation experiment at HHU detailed in [101], reaching between the mid 10^{-18} to 10^{-17} level of the coefficients within the standard model extension (SME) framework. Typical Allan deviations of the laser beat in the first generation experiment were at $(2-6)\times10^{-15}$ level [29] and for the second generation at 8×10^{-16} to 2×10^{-15} level [101] for the observed time scales between 1 s and 1 000 s. The development of a new (third) generation system was initiated with the objective of improving on the frequency stability and additionally removing one of the main disadvantages of the apparatus, the axis dependent ZCTE temperature of the cavity blocks.

The previous generations cavity blocks measured 8.4 cm in length and width and featured orthogonal optical paths. A disadvantage of the system was the disparity in temperature sensitivity among the paths, as each one was associated with a distinct T_{ZCTE} temperature value. To address this issue, a two-resonator system was designed and constructed with the additional objective of improving the stability of the system by using 30 cm long cavity spacers. The resonators were designed and configured in advance for this thesis by former members of the Institute of Experimental Physics at HHU. From the moment the second cavity was evacuated, the author of this thesis was responsible for the laser stabilization and characterization setup. However, this was during the respective Bachelor's and Master's thesis works [102, 103]. At the beginning of the work on this thesis, in October 2019, the resonators were stabilized to their respective ZCTE temperatures.

They exhibited a (drift-detrended) beat frequency Allan deviation at the 10^{-14} level for time scales between 1 s and 10^4 s. The values for finesse and cavity linewidth of both resonators have been estimated using ring-down measurements (see Section 2.1.1). At that time, the most probable contenders for the limiting factors were estimated to be intensity variations and vibrations on the system, with tilts being the next significant one.

The system was also subject of a Bachelor's thesis [104] by Z. Hou in 2023, advised by the author of this thesis, in which the laser breadboard was redesigned and set up again for a single fiber laser. Nevertheless, these topics fall outside the scope of the material presented herein. The cavities were set up in parallel, with the second generation system still operating in a tower system, configured for the means of the measurement, in a different small laboratory. Once the resonator setup was operating at a good stability, it replaced the second generation cavity setup in the tower system.

However, at that time, the dual-cavity system represented the most stable optical reference available at the institute. It was therefore used as the reference source for an OFC during a measurement campaign on HD^+, as reported in [35] (see Section 8.3, Publication in Appendix B.2.2). Due to its importance as a reference and the ongoing development of additional resonator systems, the originally planned Lorentz invariance measurement was postponed; however, the infrastructure for that experiment remains in place.

In addition, the dual-ULE system was used as the reference light source for the dark matter detector experiment published in [36] (see Section 7.1, Publication in Appendix B.1.1). It also served as reference system for the characterization of the optical parametric oscillator (OPO) laser (used for spectroscopy in [35]) which has been published in [68] (see Section 4.3, Publication in Appendix B.3.1), and for the characterization of the reference laser employed in another campaign on HD^+ reported in [34] (see Section 8.2, Publication in Appendix B.2.1). Furthermore, this resonator system formed the platform on which the RAM analysis described in this thesis was carried out (see Section 4.1), and it was one of the two systems used in the investigation of transmission filtering through optical cavities (see Section 4.2).

3.1.1 Geometry and the Thermal Noise Floor

Both resonators have been designed to be identical. Two high-finesse fused silica (FS) mirrors with a $d = 5\,\mu m$ thick dielectric coating designed for light of a wavelength of $\lambda_0 = 1064\,nm$ are optically coated to two $L = 30\,cm$ long ULE spacers. One of the mirrors is planar and the other concave, with a confocal radius of 1 m. This geometry allows for effective in-coupling into the resonator (see Section A.2.4). ULE compensation rings are attached to the mirrors, sandwiching them between ULE glass. Ultra-low expansion (ULE®) glass is single-phase, supercooled liquid produced by the company Corning.

Although ULE is designed to have a ZCTE temperature close to room temperature [105], the ZCTE temperature for FS is sub-zero. In particular, a measurement on different has evaluated ZCTEs ranging from $-97\,°C$ up to $-53\,°C$ [106]. As a result, the mirrors will shift the effective ZCTE of the resonator to lower temperatures. Compensation rings, i.e. composed of spacer material, serve to mitigate the effects of thermal expansion or contraction on the mirror substrate, thereby reducing the temperature difference between the substrate and the spacer to a value closer to that of the spacer itself [107].

The compensation rings are polished on both sides and have a diameter of 2.54 mm. They are equipped with a central bore hole that allows for the propagation of light with a diameter of 6 mm. The thermal noise floor (see Section 2.2.3) of a single cavity is calculated using Equation (2.41) and presented in table 3.1. Here, the Young modulus of the substrate is $E_{fs} = 73 \times 10^9\,GPa$, and the Young modulus of the spacer equals $E_{ule} = 67.6 \times 10^9\,GPa$ [105]. The loss angles for substrate, spacer, and coating are estimated to $\phi_{fs} = 10^{-6}$, $\phi_{ule} = 1.7 \times 10^{-5}$, and $\phi_{ct} = 4 \times 10^{-4}$ [77]. The Poisson ratios of substrate and spacer are similar with $\sigma_{ule} \approx \sigma_{fs} = 0.17$ [105, 108]. As explained in Section 2.2.1, optical contacting [76] utilizes van der Waals forces to bond the mirror to the spacer, thereby avoiding the need for an adhesive. If there is a significant disparity between the respective Poissons' ratios, there is an elevated risk of the mirror detaching during deformation.

The optimal mode-matched beam waist of a fundamental Gaussian beam at the front mirror is $w_0 = 394 \times 10^{-6}\,\mu\text{m}$, as per Equation (A.94). The ZCTE temperatures for both resonators is approximately $T = 273\,\text{K}$ ($-0.1\,^\circ\text{C}$ [103] and $-0.8\,^\circ\text{C}$ [102]). The thermal noise floor of the beat of

$\nu_0^{-1}\sqrt{S_{f,th}(f)}\left[\frac{1}{\sqrt{\text{Hz}}}\right]$	$\mathcal{L}_{db,th}\left[\frac{\text{dBc}}{\text{Hz}}\right]$	$\nu_0^{-1}\sigma_{A,th}$	$\nu_0^{-1}\sigma_{M,th}$
$7.5\times10^{-17}\,f^{-1/2}$	$-36\,\frac{\text{dBc}}{\text{Hz}} + 10\log 10\left(f^{-3}\text{Hz}^3\right)\,\frac{\text{dBc}}{\text{Hz}}$	8.9×10^{-17}	7.0×10^{-17}

Table 3.1: Thermal Noise floor of a single ULE resonator. From left to right: Fractional frequency noise spectral density. Phase noise spectral density. Fractional standard Allan deviation. Fractional modified Allan deviation.

two lasers operating at the respective cavities thermal noise floor can be estimated at the 1×10^{-16} level in terms of Allan deviations. It must be noted that this is a theoretical model; therefore, the actual noise floor may be slightly different, i.e. but not limited to differences in the actual cavity geometry. Moreover, attaining operation at the thermal noise limit is remarkably challenging.

3.1.2 Experimental Apparatus

Each cavity is enclosed by a passive copper heat shield and is held by metal strings in a tray. The tray is temperature-stabilized by a thermistor and TEC elements. It is situated within a vacuum chamber, which functions as a heat reservoir for the internal TEC elements and is stabilized by an additional pair of TECs. The vacuum chamber is situated on a heat reservoir for the outer TEC elements. The system is equipped with two active and one passive stages of temperature stabilization. Two temperature controllers are used to stabilize the two active layers with respect to a reference temperature sensor.

The reference temperature sensor is designed for a range that extends from slightly below subzero degrees Celsius to above room temperature. The inner heat shields have been stabilized to the respective ZCTE temperatures. These temperatures are designated as $T_{c1,in} = -0.8\,^\circ\text{C}$ and $T_{c2,in} = -0.1\,^\circ\text{C}$. The outer temperatures are maintained at proximities to the ambient temperature, with $T_{c1,out} = 20.0\,^\circ\text{C}$ and $T_{c2,out} = 20.5\,^\circ\text{C}$, respectively. The vacuum chamber and heat shields were constructed by the workshop at HHU. The temperature stabilizations were homebuilt by a technician of the institute.

The evacuation of both resonators was achieved through the utilization of a combination of a fore-pump and a turbo pump, resulting in pressure levels of $p_{c1} = 1.16\times10^{-7}\,\text{mBar}$ and $p_{c2} = 7.58\times10^{-7}\,\text{mBar}$, respectively. These pressure levels are maintained by $10\,\text{L}\,\text{s}^{-1}$ ion getter pumps [Gamma Vacuum, 10s TiTan]. The vacuum chamber is equipped with two windows, transparent for a wavelength of 1064 nm, enabling the transmission of light into and out of the resonator. At the planar mirror's input side, a vertically aligned in-coupling box is attached to the vacuum chamber via screws. A fiber is affixed to a collimator, in the box. The optical path and components within the box have been optimized to ensure mode-matching with the fundamental mode of the resonator for light exiting the collimator. Furthermore, a PBS and two PDs are used to

direct and measure the reflected light.

One detector is responsible for measuring the reflection of the front mirror of the resonator, which is utilized as a reference for the PDH scheme. The second detector measures a fraction of the incident light to determine RAM. The in-coupling box is encased in aluminum panels and fitted with an acrylic glass lid, also built by the workshop, which can be removed for the purpose of alignment changes. The amplifiers [Homebuilt] of the photodiodes [Hamamatsu, 1064 nm] are affixed to the exterior surface of the aluminum panels, and a short cable connects them to their respective photodiode. These boxes enable straightforward plug-and-play integration of light, permitting the locking of any laser light without the necessity of recalibrating the alignment towards the resonator.

The two resonators are aligned in a perpendicular orientation with respect to each other on a 90 cm by 90 cm optical breadboard, which is situated on an AVI [Table Stable, AVI-200] unit. A thin 60 cm by 60 cm breadboard is positioned between the resonators on top of the larger breadboard. The smaller board incorporates the lasers, optics, and actuators that are required to prepare the light for the PDH locking scheme. Initially, the system featured a single Nd:YAG laser [Innolight, Mephisto], which light was split into two paths. These paths were bridged by an AOM [ISOMET, 1206C], enabling the locking to both resonators. One of the initial objectives of this project was to redesign the laser breadboard in such a manner that it would enable the locking of two independent lasers. Further, the system was transferred between laboratories in November 2021, resulting in some variations in the experimental setup.

To define this, all work completed prior to the transition will be designated with respect to Lab 1, while all subsequent work will be assigned to Lab 2. However, it should be noted that the fundamental schematic of the setup is identical for Lab 1 and Lab 2, as illustrated in Figure 3.1. The polarization of two Nd:YAG lasers [Innolight Mephisto] with output wavelengths of 1064 nm and output power levels of 30 mW (Laser 1 or L1) and 200 mW (Laser 2 or L2) is filtered and linearized by the combination of a quarter-waveplate, half-waveplate, and a PBS. Each laser path is directed towards an AOM [Isomet], where the first order of refraction is directed to a collimator and coupled into a PM fiber. This fiber is connected to the out-coupling collimator at the cavity in-coupling box.

In this thesis, the cavities are designated CAV 1 and CAV 2, where L1 is typically locked to CAV 2 and L2 to CAV 1. The zeroth orders of the AOM are combined by a PBS onto a photodiode on the breadboard, which measures the beat of the lasers by means of a frequency counter [Hewlett Packard, 53181A] or SA [Rhode & Schwarz, FPC1000] located beneath the breadboard. Furthermore, for each laser, a path is split and coupled into a collimator, which directs the light through a short fiber to a portable FNC setup before the light travels through long fibers to the experiments.

A two-axis tilt sensor [Pinnacle, S/N 4670] was placed on the breadboard for diagnostic purposes. The light is directed towards the resonator via a telescope configuration comprising a single mode-matching lens ($f = 750$ mm). This configuration is positioned on the side of the coupling box. The distances of the collimator, lens, and cavity front mirror have been optimized to ensure optimal coupling into the fundamental mode of the cavity. A PBS positioned in front of the 45° mirror directs light towards the cavity, with a portion of the light being directed to the RAM PD.

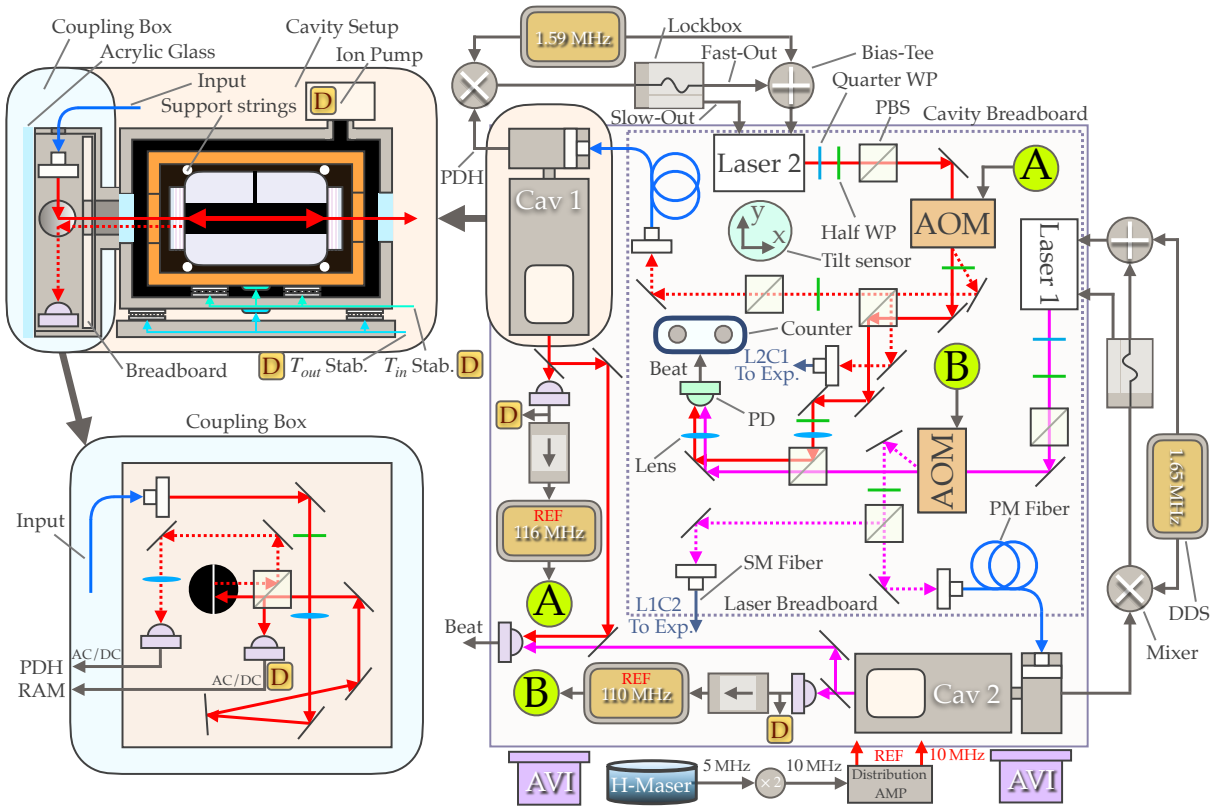


Figure 3.1: A schematic representation of the configuration of the two ultra-high finesse ULE resonators. The cavity profile is displayed in the top left corner of the figure. It corresponds to the schematic shown in Figure 2.7. The cavity is held by strings in the vacuum chamber. The schematic of the in-coupling box for mode-matching is displayed in the lower left corner. The right side of the figure illustrates a top-down view of the cavity breadboard, with the laser breadboard positioned between the resonators. The circles with labels A and B illustrate the connections for the power stabilization. The spots marked by D are measured by a DAQ Card.The frequency counter measuring the beat of the light on the breadboard is, in reality, not on but below the breadboard. WP: Waveplate. With the exception of the green detector, which is utilized for the measurement of the beat, all PDs have been custom-built and are largely similar.

The reflected light of the cavity is sent through the PBS and focused on another detector that is used for the PDH locking scheme. The typical coupling efficiency of both resonators, measured at the dip of the reflection signal, was found to be 30 %.

The detectors are constructed in-house with bandwidths of 10 MHz and de-coupled DC and AC outputs, with the AC outputs being further amplified by a factor of 10. The initial design of the coupling box was conducted in [102], but it has undergone modifications, particularly with regard to RAM monitoring, during the course of this study. The transmission signal of the resonator is transmitted to another smaller bandwidth detector, which is used to stabilize the power through the resonator. This is achieved through the use of a simple PI controller [Homebuilt] acting on the AM input of the DDS [Homebuilt], which drives the respective AOM. The power levels in transmission were stabilized at a level of 20 µW. It should be noted that the AOM is not employed for the

purpose of fast frequency modulation. The PDH signal from the detector in the coupling box is mixed down with the local oscillator signal, which was used to create the sidebands for the locking scheme. The mixed signal is then sent through a low-pass filter to the input of a lockbox, where it is used as an error signal. The fast output of the lockbox is combined with the local oscillator by a bias-tee and sent to the piezo of the respective laser.

The slow output is connected to the servo-controller of the laser, which acts on the crystal temperature. The AOM synthesizers, are referenced to the H-maser of the institute, as well as the frequency counters and SAs. The AVI carrying the setup has an active compensation range of 2 Hz to 200 Hz. As illustrated in Figure 3.1, the signals of transmission and RAM detectors, as well as the output of the temperature and pressure controllers, are monitored by a DAQ card [National Instruments, sample rate: 250 kHz]. This is indicated by the "D" in the schematic.

In Lab 1, the setup was placed on top of an optical table inside the laboratory. The system was shielded from air fluctuations by a thick plastic sheet. Figure 3.2 illustrates the configuration of the cavity in Lab 1, including the in-coupling box. In Figure 3.3, the total laboratory space for the system is displayed, including temperature, pressure, and laser controllers, as well as the diagnostics rack and portable FNC station.

A depiction of the FNC station and its schematic is provided in Figure 3.4. In the left image, the system is placed on a cascading configuration of two AVI units. However, this setup was abandoned in favor of a single AVI stage in the right image, which corresponds to the system that was used to collect data.In Lab 2, the apparatus is situated on a highly polished granite block that is supported by three adjustable feet, of which one can be elevated or lowered using hydraulic pressure.

This configuration facilitates active tilt stabilization. The core structure of the tower, granite table and hydraulic feet was A cage of metal bars and panels, situated around the cavities, serves to shield the system from further outside acoustics. A plastic sheet was placed atop and wrapped around the system to mitigate air fluctuations from the air conditioning unit, thereby stabilizing the temperature within the laboratory. The configuration of the tower is illustrated in Figure 3.5.

The photograph on the left was captured on the day the system was transferred from Lab 1 to Lab 2. On that day, the previous generation cavity setup, laser breadboard, and electronics had been removed. The dual cavity breadboard was then lifted by a crane and moved to the tower laboratory. Electronic devices and controllers were transported individually. In its operational state, the system was closed and looked as shown in the right image. The laser breadboard inside the tower system is presented in figure 3.6.

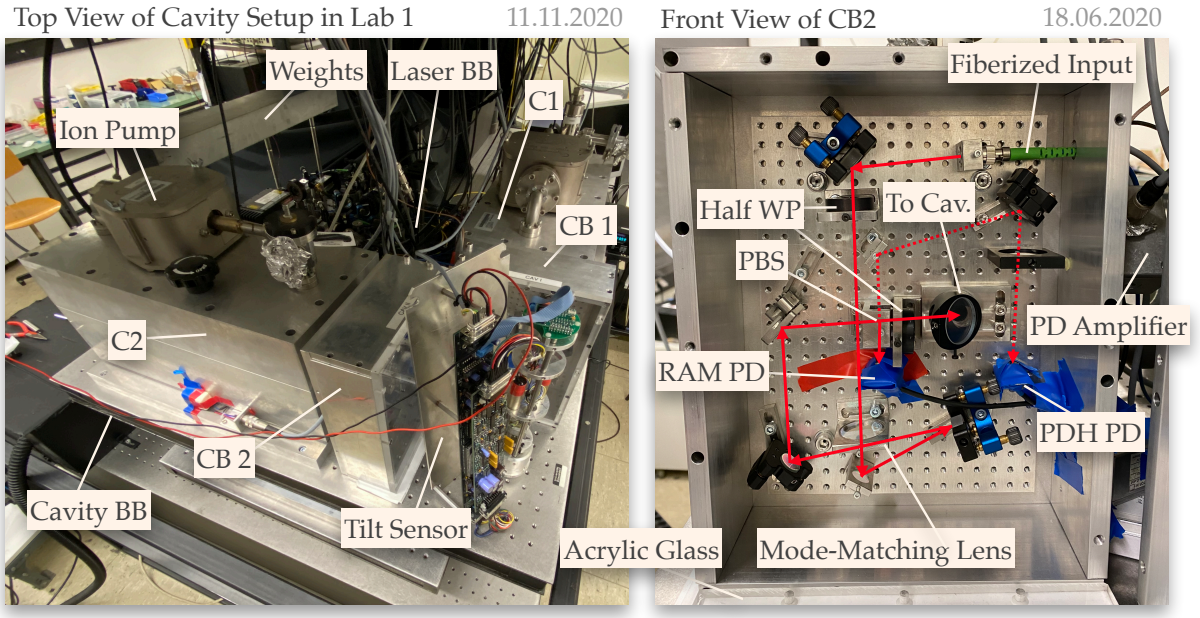


Figure 3.2: Left: Resonator setup in Lab 1. The laser breadboard is positioned between the cavities. The weights are employed to optimize the distribution of mass for the AVI to ensure proper operation. Right: In-coupling box layout. The light comes through a 0.5 m long PM fiber from the laser breadboard.

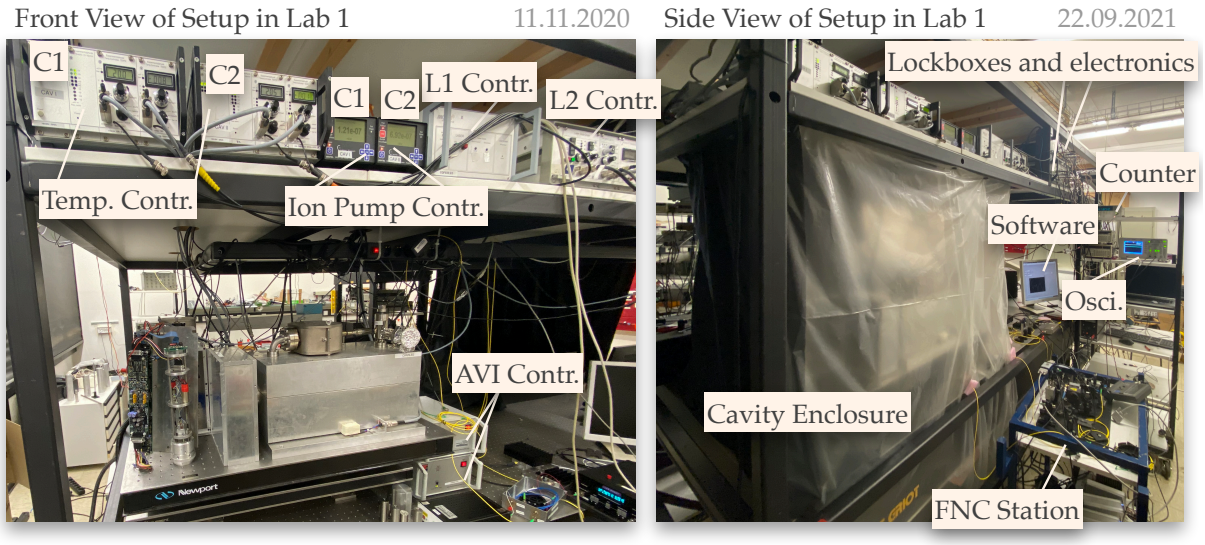


Figure 3.3: Left: Complete system setup in Lab 1, including temperature, laser, and pressure controllers.Right: System in operational status, enclosed by a plastic shield and laser protection cloth. The locked light is directed to the FNC setup before propagating to the experiment.

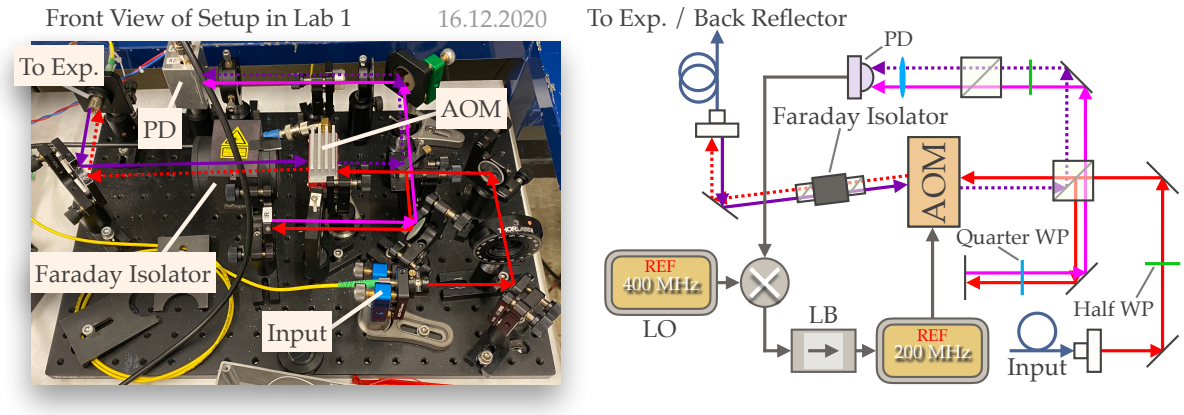


Figure 3.4: Photo and schematic of the free-space FNC for light at 1064 nm. A short SM fiber sends light from the laser breadboard to the FNC. The length of the fibers to the experiments range from some 10 m up to approximately 500 m, depending on the application.

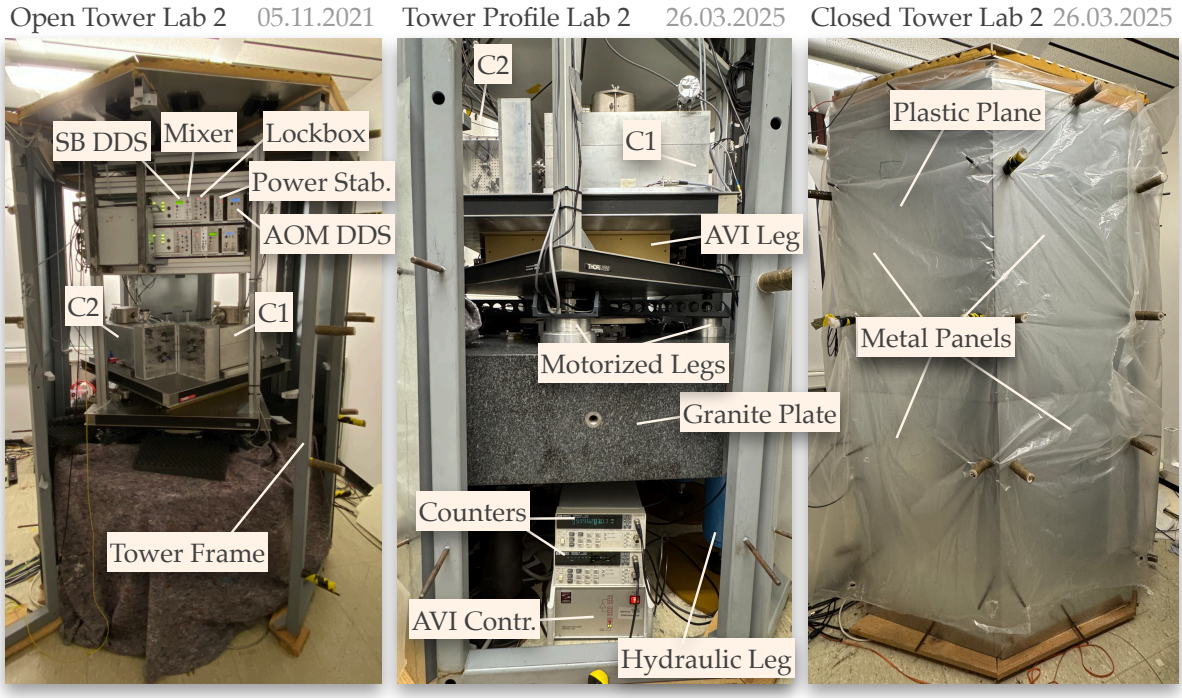


Figure 3.5: Left: The ULE-based resonator system on the day of its relocation from Lab 1. Cables were not yet connected, and a blanket was used to protect the sensitive granite table. All electronic components required for cavity locking are placed on top of the resonators. Center: Side view of the support structure. The cavities rest on a breadboard supported by two AVI legs, which themselves sit on a second breadboard mounted on motorized legs in contact with the granite table. The granite table is mounted on adjustable legs capable of inducing controlled tilt. At the bottom, two frequency counters for beat measurement and the AVI controller are visible.Right: Fully enclosed system during operation. During measurements, the portable FNC system was positioned behind the tower.

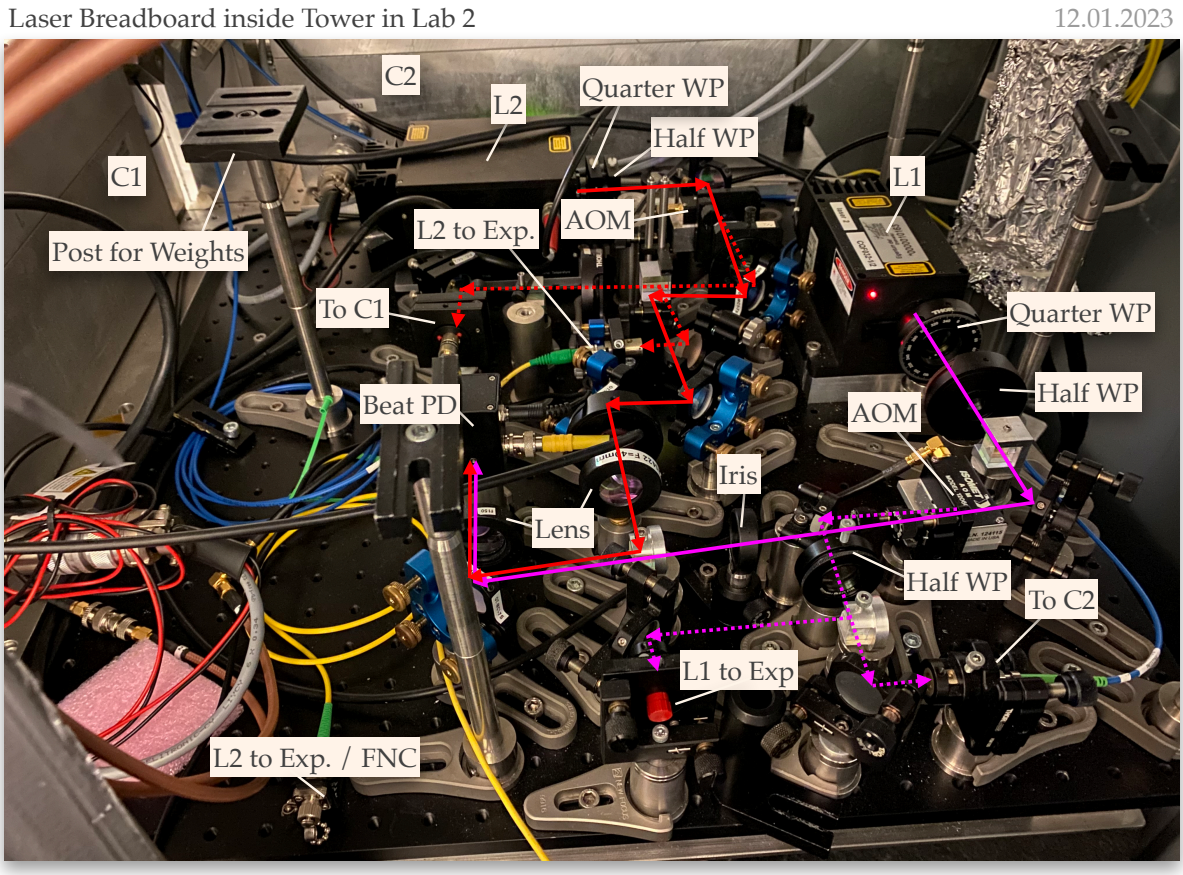


Figure 3.6: The laser breadboard responsible for the preparation and distribution of the lasers to the resonators and experiments. The beat frequency is detected by a PD on the breadboard.

3.1.3 Resonator Properties

The intrinsic characteristics, thus the ZCTE temperatures, finesse values and, the linewidth were measured in [103, 102]. The ZCTE temperatures were measured to $T_{ZCTE,c1} = -0.85(48)$ °C and $T_{ZCTE,c2} = -0.11(10)$ °C. The cavity finesses were evaluated through ring-down measurements, the methodology for which is shown in Section 3.2.3, to $\mathcal{F}_{c1} = 5.0(1)\times10^5$ and $\mathcal{F}_{c2} = 2.4(2)\times10^5$. These measurements yielded cavity line widths of approximately $f_{c1} = 960\,\text{Hz}$ and $f_{c2} = 2100\,\text{Hz}$ following Equation (2.8). The cavity linewidths and finesse values have been cross-checked within the scope of this thesis.

One method is outlined in Equation (2.9), which involves the evaluation of the reflectivity of the cavity mirrors through the measurement of the decay time of light transmitting through the resonator. This has been implemented for C1, while L2 remains locked to it. The transmission is closely monitored during steady-state conditions, and then, the lock is deactivated. The fast lock was achieved at the piezo of the laser, which exhibited response times in the order of $\leq 10\,\mu\text{s}$. The transmission signal is recorded by a DAQ card that operates at a sample rate of 250 kHz, thereby generating a data point every $4\,\mu\text{s}$. The transmission signal undergoes exponential decay. A fit is utilized to determine the time constant of $\tau_{c1} \approx 170\,\mu\text{s}$, which is larger than the piezo response time.

The result of this calculation is a finesse of $\mathcal{F}_{c1} = 5.3 \times 10^5$. The measurement as illustrated in Figure 3.7 (a). A second method is derived from the measurement of the transmission line shape of the resonator. While L2 was locked to C1, the light of L2 was partially split and directed through an AOM to bridge the frequency gap between the longitudinal modes of the two resonators. This discrepancy is approximately 106 MHz. Then, the transmission signal through the resonator, as well as the error signal output of the lockbox, are measured by the DAQ card while the frequency of the AOM is scanned in a range of 6 kHz with the resonance of C2 in the center. The frequency of the DDS that drives the AOM is shifted in steps of 100 Hz in time steps of 5 s, with a sample rate of 10 Hz.

An average of the respective voltage is then calculated and plotted over the frequency, as shown in Figure 3.7 (b). The measurement process took slightly over five minutes. The typical relative drift of the resonator modes is less than $100\,\mathrm{mHz\,s^{-1}}$, as demonstrated in a later section. This results in a minor skew of the line shape, accompanied by a negligible total correction of less than 30 Hz across the entire line. The Lorentzian fit over the transmission data yielded a cavity linewidth of 1.96(4) kHz. In consideration of the systematic effect of the drift, the mode linewidth of C2 can be conservatively approximated as $f_{c2} = 2.0(1)$ kHz, which is in agreement with the findings of prior measurements. An evaluation of the FSR and cavity length was achieved through the analysis of four beat signals between the cavity-locked lasers. While one laser is fixed at a specific mode, the other is adjusted and locked to an adjacent longitudinal mode of the respective resonator. The resulting gap in the beat is known as the free spectral range. The data is displayed in Table 3.2. Using the equation

$$f_{beat}\,(\Delta m_{c1}, \Delta m_{c2}) = \frac{c_0}{2L_{c2}}\,(m_{c2} + \Delta m_{c2}) - \frac{c_0}{2L_{c1}}\,(m_{c1} + \Delta m_{c1}),$$

in conjunction with the data presented in the table, results in a system of equations that can be solved to determine the lengths of the cavity and, consequently, an approximation for their FSRs $\Delta\nu_i$.

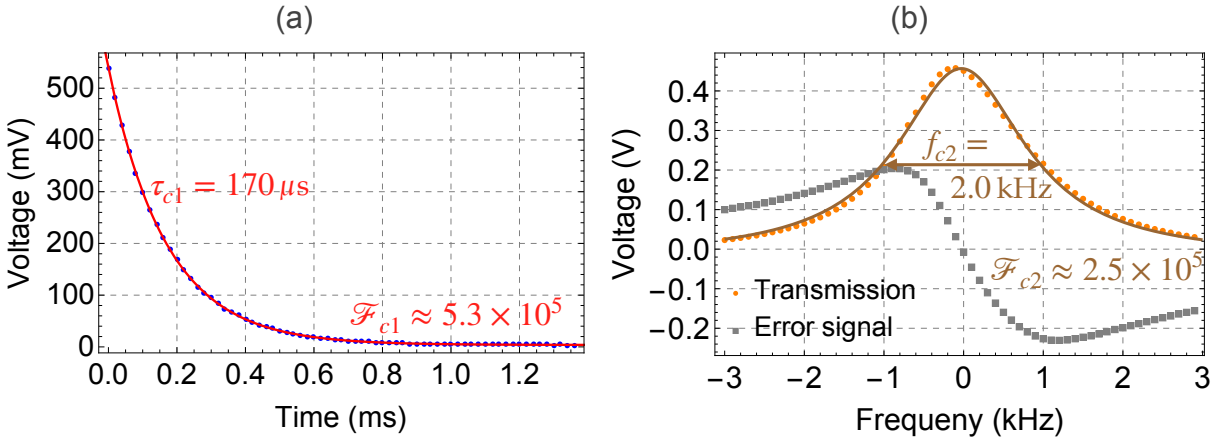


Figure 3.7: (a): Ring down measurement of the transmission signal of C1. Blue represents a five sample average of the raw data, while the red curve is the exponential fit. (b): Scan of the transmission and error single of C2 by of a laser stabilized to C1. The brown line shows a Lorentzian fit over the transmission line.

Δm_{c1}	Δm_{c2}	Beat frequency f_{beat} (Hz)
0	0	111 706 715
0	1	610 043 931
1	1	111 393 675
1	0	−386 943 491

Table 3.2: Presentation of the beat frequency of the ULE cavities for the combination of two adjacent longitudinal modes of each resonator. In the case of $\Delta m_{c1} = \Delta m_{c2}$, the modes of resonators are the closest to each other.

Eventually, it is

$$L_{c1} = 0.300\,604\text{m} \Longrightarrow \Delta\nu_{c1} = 498\,650\,\text{kHz},$$
$$L_{c2} = 0.300\,793\,\text{m} \Longrightarrow \Delta\nu_{c2} = 498\,337\,\text{kHz}.$$

The numerical values are estimated conservatively at the kHz level within the free spectral range, thereby µm in terms of length. The statistical inaccuracies are considerably smaller. However, this is merely a spotlight measurement at two longitudinal modes, and perfect vacuum was assumed for the speed of light.

Eventually, this verifies the finesse of C2 to $\mathcal{F}_{c2} \approx 2.5 \times 10^5$ and the linewdith of C1 to $f_{c1} \approx 940\,\text{Hz}$. The error signal displayed in the plot will be further addressed in the RAM section.

3.1.4 Real-Time Monitoring and Laser Stability

In the early stages of development, a monitoring software has been established to measure and evaluate the effect of certain disturbances. A DAQ card was utilized to assess various parameters, including pressure levels, inner and outer temperatures, and the DC output of the transmission detectors of each cavity. Furthermore, the AC outputs of the two RAM detectors were mixed with the output of the respective sideband generating DDS and measured by the DAQ card. This is equal to ten independent sources. Additionally, the two-axis tilt sensor is positioned on top of the breadboard, between the resonators, to measure the horizontal tilts of the cavity breadboard. This sensor also features a temperature reading of the laboratory.

Ultimately, the beat frequency between the two lasers was measured by an interleave of two frequency counters, with the objective of reducing the dead time of a single one. The synchronization of all fourteen signals to the level of one second was achieved through a comparison of the timestamps of the saved data. The measurement of all quantities was executed at a sampling rate of 1 Hz. The raw data underwent subsequent processing, and, when applicable, conversion to a frequency contribution utilizing an experimentally determined sensitivity factor. The parameters of tilt and power sensitivity were measured with precision in [102], along with the time constant of thermal response in relation to the inner heat shield of one of the resonators. The measurement of the parameter for the other resonator was previously documented in [103].

The corresponding coefficients, α_{c1} and α_{c2}, associated with the ZCTE temperatures, are estimated to be offset by one standard deviation from the ZCTE. Both works were produced by the author of this thesis. The value for pressure sensitivity is derived from [109]. The conversion factor for voltages to pressures of the ion pump controller was $1\,\mathrm{V}\hat{=}1\,\mathrm{mbar}$ while for the temperature sensors it held $1\,\mathrm{V}\hat{=}100\,^{\circ}\mathrm{C}$. The conversion factor for power was typically designated as $1\,\mathrm{V}\hat{=}1\,\mathrm{mW}$, on any given home-built PD. However, an additional amplifier was incorporated into the transmission signal, necessitating a re-evaluation of the conversion factor for the power sensitivity for each detector. The tilt sensor has been developed to express the tilts in units of radians.

Laboratory I

The sensitivity factors employed in the evaluation of the contribution to the total frequency instability are evaluated with respect to the beat frequency between the resonators and are summarized in Table 3.3. The evaluation of RAM has been adapted from the method outlined in Section 2.3.3. Specifically, the low-pass filtered output ε_{off} of a mixer is measured, that combines the AC signal of the RAM detector in front of the cavity with an output of the DDS for the sideband modulation. At this time, the calculation does not include a correction factor for the coupling efficiency and losses as well as the factor of $1/2$ for the error signal peak to peak strength. However, this would be

Year	Sensitivity	Fluctuation level	Frac. freq. contribution
Power C1	$\beta_{c1} = 290(45)\,\frac{\mathrm{mHz}}{\mu\mathrm{W}}$	$\Delta P_{c1} \leq 20\,\mathrm{nW}$	$\nu_0^{-1}\Delta f_{pow} \leq 8\times10^{-17}$
Power C2	$\beta_{c1} = -270(20)\,\frac{\mathrm{mHz}}{\mu\mathrm{W}}$	$\Delta P_{c2} \leq 80\,\mathrm{nW}$	
Tilt x (para. C1)	$\gamma_x = 540(43)\,\frac{\mathrm{mHz}}{\mu\mathrm{rad}}$	$\Delta\theta_x \leq 0.8\,\mu\mathrm{rad}$	$\nu_0^{-1}\Delta f_{tilt} < 2\times10^{-15}$
Tilt y (para C2)	$\gamma_y = 130(34)\,\frac{\mathrm{mHz}}{\mu\mathrm{rad}}$	$\Delta\theta_y \leq 1.5\,\mu\mathrm{rad}$	
Pressure C1	$\delta = 2.7\times10^{-7}\nu_0\frac{1}{\mathrm{mbar}}$	$\Delta D_{c1} \leq 0.3\,\mathrm{pbar}$	$\nu_0^{-1}\Delta f_{pres} \leq 3\times10^{-16}$
Pressure C2	$\delta = 2.7\times10^{-7}\nu_0\frac{1}{\mathrm{mbar}}$	$\Delta D_{c2} \leq 0.3\,\mathrm{pbar}$	
Temp. C1	$\alpha_{c1} = 8\times10^{-10}\nu_0\frac{1}{\mathrm{K}}, \tau_{c1} = 1\,\mathrm{d}$	$\Delta T_{c1} \leq 0.5\,\mathrm{mK}$	$\nu_0^{-1}\Delta f_{temp} \leq 2\times10^{-15}$
Temp. C2	$\alpha_{c2} = 2\times10^{-10}\nu_0\frac{1}{\mathrm{K}}, \tau_{c2} = 3\,\mathrm{d}$	$\Delta T_{c2} \leq 0.6\,\mathrm{mK}$	
RAM C1	$\eta_{c1} = (70\text{ to }145)\,\frac{\mathrm{Hz}}{\mathrm{V}}$	$\Delta\varepsilon_{off,c1} \leq 40\,\mathrm{mV}$	$\nu_0^{-1}\Delta f_{ram} \leq 2\times10^{-16}$
RAM C2	$\eta_{c2} = (80\text{ to }190)\,\frac{\mathrm{Hz}}{\mathrm{V}}$	$\Delta\varepsilon_{off,c2} \leq 40\,\mathrm{mV}$	

Table 3.3: Limitations in Lab 1: Sensitivity parameters, fluctuation levels, and the corresponding fractional frequency contribution at the optical beat between the resonators. The contribution attributable to temperatures exhibits drift-like behavior over extended periods (500 s) and can be detrended during the analysis At short time scales, below 40 s, the contribution is at the 10^{-17} level. The actual limitations on the beat instability in descending order are: Tilts – Pressure – RAM – Power – Temperature.

a total correction close to $\alpha_f/2 \approx 0.4$. Therefore, the RAM evaluation can be regarded as an upper bound. A thorough examination of RAM is presented in Section 4.1, as it is not as straightforward as the other characterizations. The ideal sensitivity factor for RAM, in terms of absolute frequency, is given by

$$\eta_i = \frac{P_{PDH,i}}{P_{RAM,i}} \frac{f_{c,i}}{\varepsilon_{pp,i}},$$

which is dependent on the respective cavity linewidth, f_c, the total laser power at the PDH detector, P_{PDH}, and the total power at the RAM detector, P_{RAM}, as well as the peak-to-peak strength of the error signal, ε_{pp}, of the respective resonator. The sensitivity factor is found to be dependent on parameters of a measurement (sideband amplitude, coupling efficiency, modulation frequency), and as such, the table provides a range of values for the measurements analyzed in this thesis.

The contributions of individual external disturbances, in terms of frequencies, to the measurement of beats are demonstrated in the following:

$$\begin{aligned}
\Delta f_{temp}(t) &= \alpha_{c1}(T_{c1})\Delta T_{c1}\left(1 - e^{-\frac{t}{\tau_{c1}}}\right) + \alpha_{c2}(T_{c2})\Delta T_{c2}\left(1 - e^{-\frac{t}{\tau_{c2}}}\right) \\
\Delta f_{pow}(t) &= \beta_{c1}\Delta P_{c1}(t) + \beta_{c2}\Delta P_{c2}(t) \\
\Delta f_{tilt}(t) &= \gamma_x \Delta\theta_x(t) + \gamma_y \Delta\theta_y(t) \\
\Delta f_{pres}(t) &= \delta(\Delta D_{c1}(t) + \Delta D_{c2}(t)) \\
\Delta f_{ram}(t) &= \eta_{c1}\Delta\varepsilon_{off,c1}(t) + \eta_{c2}\Delta\varepsilon_{off,c2}(t)
\end{aligned} \tag{3.1}$$

The parameters ΔP, $\Delta\theta$, ΔD, and $\Delta\varepsilon$ are the measured time variations of the powers, tilts, pressures and error signals. The first equation holds for temperature changes ΔT of the resonator (heat shield) that appear instantaneous with respect to the time constants τ_i. This assumption is reasonable here because the time constants are one and three days. The parameters ΔP, $\Delta\theta$, ΔD, and $\Delta\varepsilon$ represent the measured time variations of power, tilt, pressure, and error signals, respectively. The first equation applies to temperature changes ΔT of the resonator (or heat shield) that appear instantaneous relative to the time constants τ_i, which in this case are one and three days.

The quantities were systematically observed and documented through various means. These included the time trace, the Allan deviation, and the frequency contribution to the beat for each measurement. At the beginning of the work, following the installation of the laser breadboard for two independent laser locks, the performance of the beat was at a low level of 10^{-14} between 1 s and a few 100 s. However, the frequency drift eventually dominated. The initial focus of the project has been on two primary components: RAM optimization and the implementation of power stabilizations through both resonators.

Power fluctuations have been reevaluated to contribute at the 10^{-14} level to the beat instability. This was one of the earliest limitations on frequency stability, and its effect was reduced by implementing transmission power stabilization in both cavities. This change alone already resulted in an improvement of the beat instability to a level between low and mid 10^{-15} during the observed time scales. Furthermore, a cascading configuration of two AVI units was subjected to testing. Nevertheless, the system's vibration performance was neither enhanced nor degraded as a result

of these modifications. However, the manufacturer of the AVI has indicated that the cascading configuration may result in a substantial increase in sensitivity to tilts for the system.

In the end, the system was placed on a single AVI unit consisting of two legs. In lieu of presenting numerous plots that illustrate the enhancement in performance over time, a sample output of the monitoring software is displayed in Figure 3.8 and 3.9.

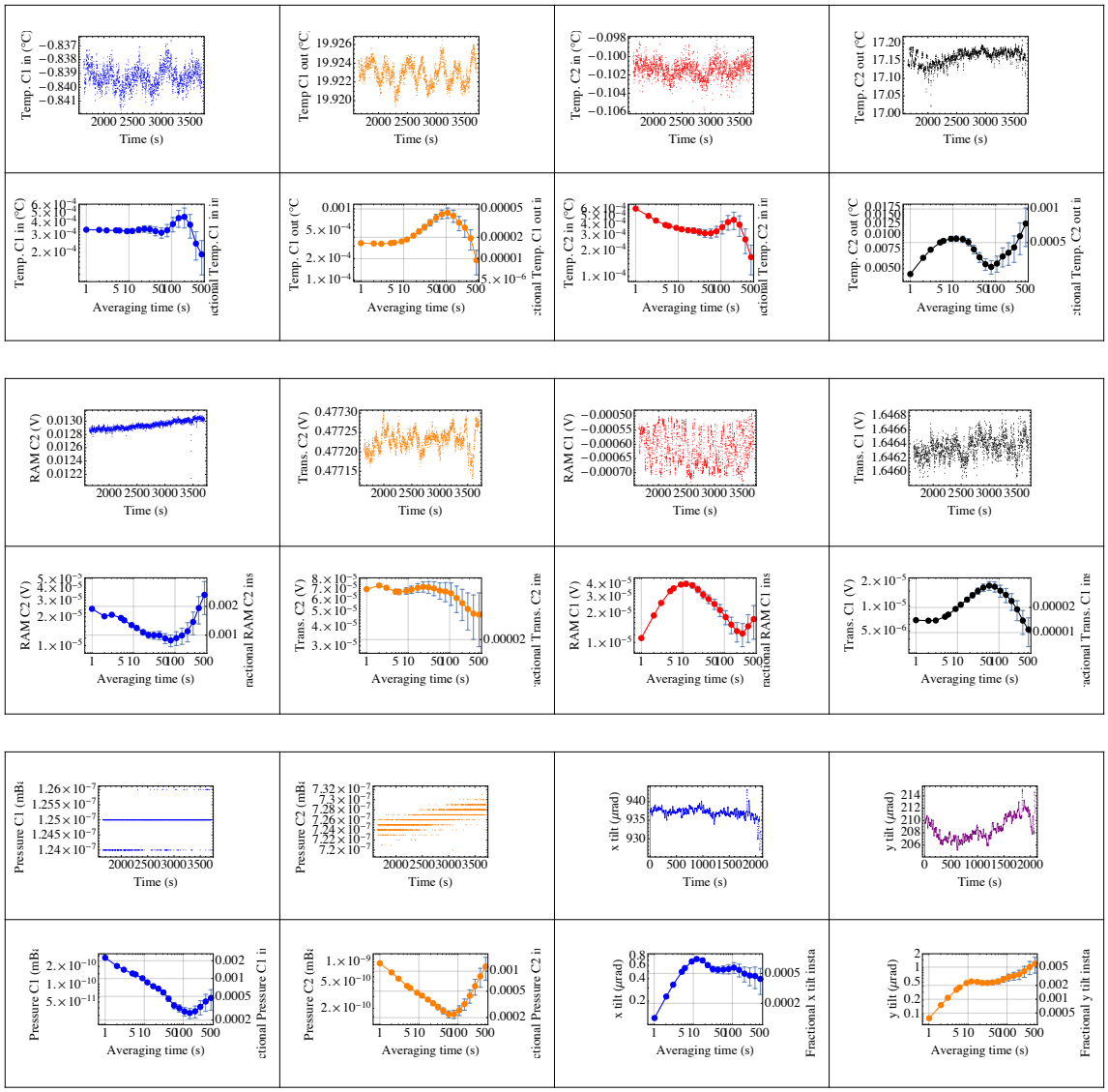


Figure 3.8: Lab1: Part 1 of an actual output of an early-day measurement after initial RAM optimization and implementation of power stabilizations at the transmission signals of both resonators. The three blocks present the data as measured and their corresponding Allan deviations for temperatures, RAM, cavity transmission, pressures and tilts.

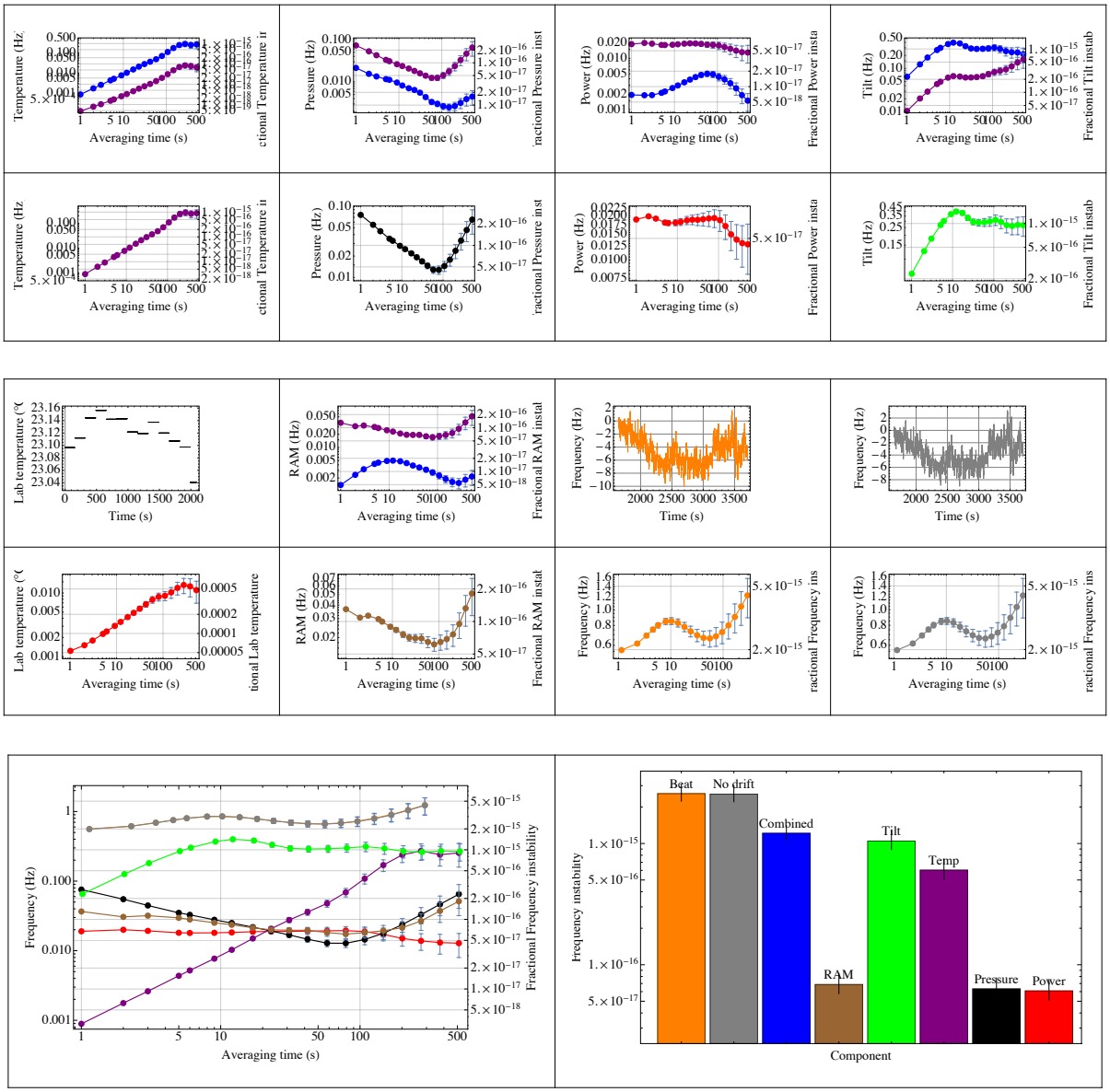


Figure 3.9: Lab 1: Part 2 of an actual output of an early-day measurement after initial RAM optimization and implementation of power stabilizations at the transmission signals of both resonators. In the top two blocks, the calculated frequency effect is illustrated for temperatures, pressures, power, tilts, and RAM. This is achieved by multiplying the measured signal with the respective sensitivity factors at that time. The explicit formalism is shown in Equation 3.1. The bottom block combines all Allan deviations and compares them to the beat frequency instability. In this particular measurement, linear drift was not observed. As a result, the detrended line (gray) overlaps with the non-detrended line (orange). The right bar chart provides a visual representation of the data by cutting through the left plot at the 100 second mark. The blue bar is the combination of all external factors.

As previously stated, the measurement of RAM was an upper bound because it was conducted without the coupling efficiency pre-factor and the factor of two in the denominator. Furthermore,

the error signal was measured by scanning the laser through adding a frequency synthesizer output to the piezo of both lasers and observing the error signal output of the lockbox. This generally results in smaller peak-to-peak amplitudes, denoted by ε_{pp}, due to the suppression of the scanning amplitude, further contributing to an upper bound. The data indicates the limitations that were present during the system's operation in Lab 1. At that time, the most probable constraints were vibrations and tilts. The argument can be made that these are physically equivalent disturbances on disparate time scales.

An examination of the shape of the Allan deviations of beat instability and tilts revealed a similar behavior at time scales ranging from 10 to 100 seconds, averaging time. The performance indicated in the figures is indicative of the optimal results that could be attained while the system has been operating in Lab 1. An in-depth measurement evaluating linewidth, Allan deviation, and frequency noise spectra while the system was in Lab 1 is shown in Section 8.2 and 7.1. This topic is not addressed in this section, as it is part of a publication [36] and is part of data that has been published [34].

However, it can be stated that the linewidths of the lasers were below 1 Hz while locked. After thorough examination, it was determined that tilt may indeed be the limiting factor in the system. In Figure 3.10, a measurement in Lab 1 relating the tilts to the beat frequency is presented. The sensitivities were recalibrated by the data above to account for the tilt and beat overlap, resulting in sensitivities that are approximately one order of magnitude larger than the previously evaluated values.

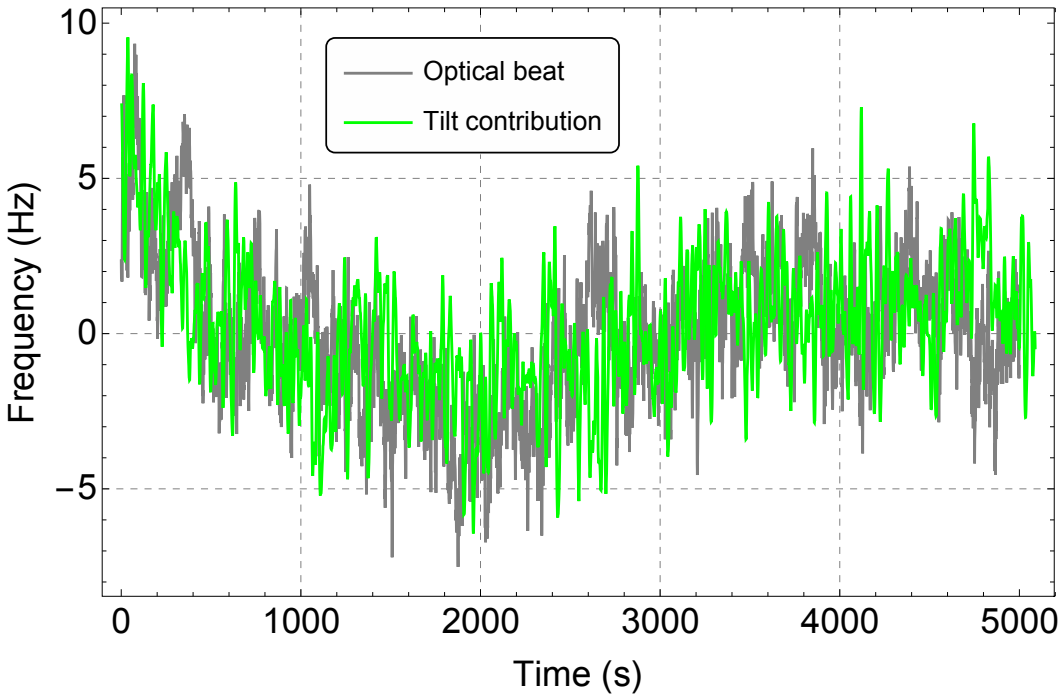


Figure 3.10: Lab 1: Correlation of a time trace of the beat frequency with tilts in the system during the same time interval. The sensitivities of tilt in this measurement are approximately an order of magnitude larger than those previously evaluated.

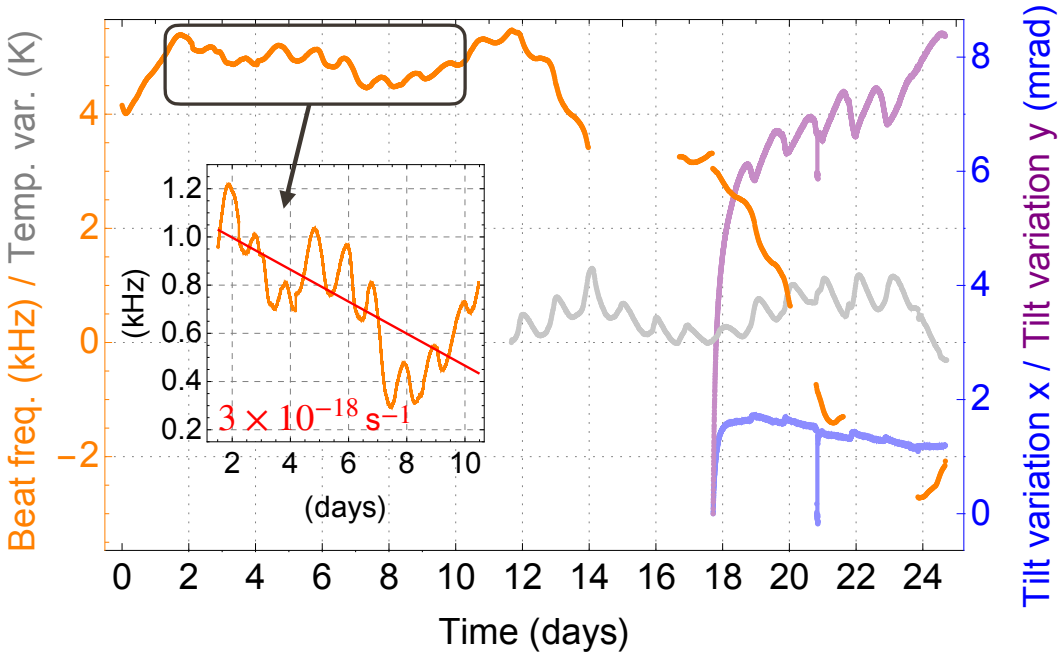


Figure 3.11: Lab 1: Long-term performance of the dual cavity system. The data corresponds to the period during which the system was utilized for data collection in [36]. The orange line in the graph represents the raw beat frequency, while the gray line indicates the ambient temperature inside the plastic cover surrounding the resonators. The respective tilts are indicated by purple and blue.

Nevertheless, a substantial correlation is evident in the overall structure of the data. A secondary interest lies in the system's long-term performance. As illustrated in Figure 3.11, the measurement of beat frequency was conducted over a period exceeding three weeks, concurrently with the monitoring of laboratory temperature and tilts on the cavity breadboard. The periodic fluctuations in the beat and tilts are presumably attributable to the 24 hour temperature cycle. In a period of approximately 10 days, during which the system was particularly stable, the beat demonstrated a drift of $3 \times 10^{-18}\,\mathrm{s}^{-1}$, which corresponds to an amplitude of less than $1\,\mathrm{mHz\,s}^{-1}$. For a ULE resonator, this represents exceptional value. However, it should be noted that this is the drift of the beat between lasers stabilized to similar cavities with frequency drifts in the same direction. The individual drifts are typically magnitude(s) larger. Nevertheless, a differential drift of this magnitude indicates the high degree of similarity between the two resonators. The plot also illustrates the system's capacity for prolonged periods (two weeks) of continuous locking, a feature that is of significant importance. This is particularly relevant in applications such as the averaging of an optical clock or the measurement of rovibrational transitions in Penning traps, where the acquisition time of data is a crucial factor.

Laboratory II

As the system was designed to operate in an entirely different laboratory that featured a rotatable breadboard and tower system, after evaluating tilts as the current limitation on the frequency stability, the system was transferred. The relocation of electronics and components to the uppermost level of the tower was subsequently undertaken. The resonators were transferred in conjunction

with their respective breadboards via the utilization of a crane. These actions were executed by the author of this thesis, with helpful assistance of members of the institute. The ion pumps were deactivated during the transport, which lasted approximately 30 minutes. However, due to the inability to maintain one of the pressures, one cavity (C2) had to be re-evacuated after the move. Both cavities' mode-matching have demonstrated resilience in the face of this migration. The laser breadboard was then moved as a single unit. Immediately upon the activation of all systems and the reestablishment of power stabilization and beat measurements, the system's performance exhibited an enhancement ranging from a factor of 2 to 5, depending on the averaging time, as depicted in Figure 3.12. The improvement is predominantly observed around an averaging time of 5 seconds, where tilts are estimated to be substantial. Eventually, the instability of a single laser in Lab 1 was found to be in the low to mid 10^{-15} level, while it improved to mid to high 10^{-16} level in Lab 2. While this enhancement may appear small on paper, it is substantial in practice, particularly given the escalating complexity of improvements as the system approaches the thermal noise limit. The system was utilized as a reference in two publications [35, 68] while operating in Lab 2.

A detailed analysis of linewidth and partially Allan deviations can be found in Section 8.3 and 4.3, respectively. However, the overall performance of the beat or single laser is within an order of magnitude of the respective thermal noise floor across all observed time scales when the linear drift effect is removed. As illustrated in Figure 3.13, the measurement of the beat frequency was conducted over the course of eight hours during the operation of the enclosed tower.

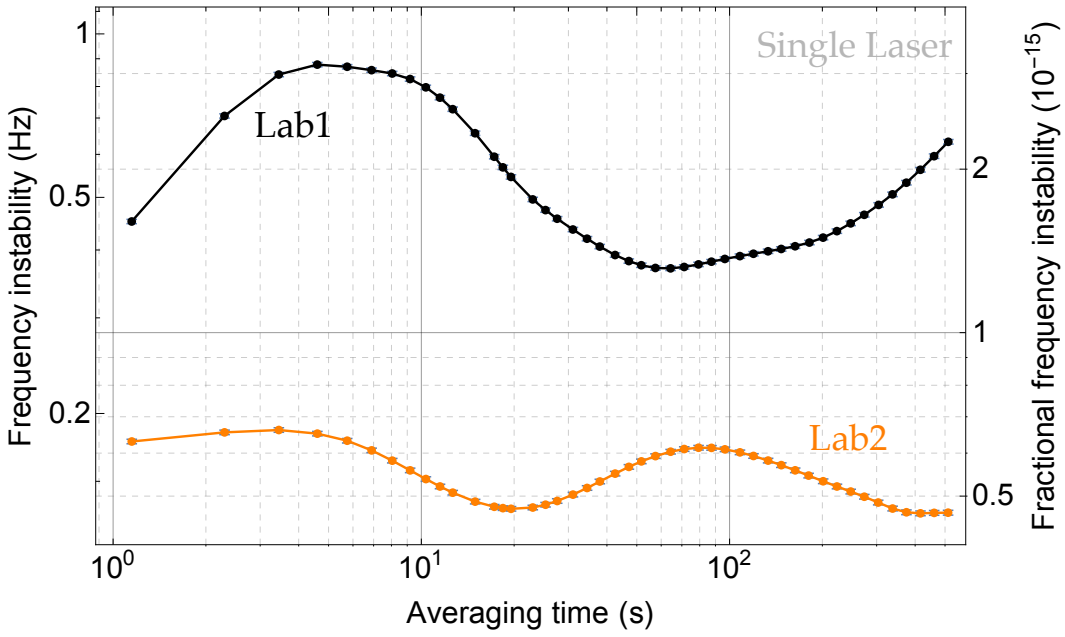


Figure 3.12: Allan deviations of a single laser just before and just after the move from Lab 1 to Lab 2. The approximation was derived by dividing the beat instability by a factor of $\sqrt{2}$. In both cases, the linear drift was detrended.

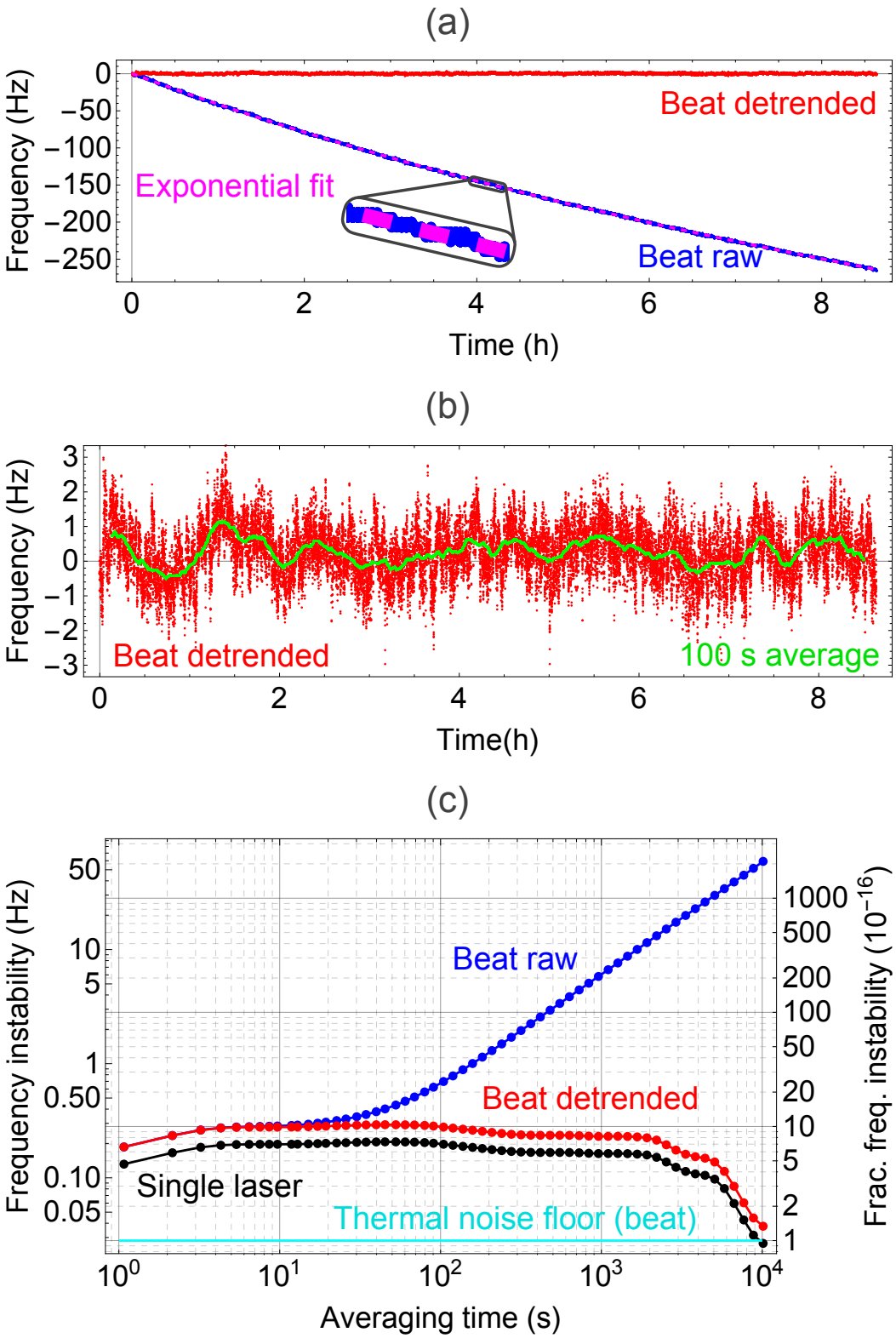


Figure 3.13: Lab 2: Performance of the two ULE-locked lasers within the enclosed tower system over a period of eight hours. (a): Beat frequency and detrended data, after an exponential fit is applied. (b): A zoom into the detrended data, including a 100 seconds moving average. (c): Allan deviations of the beat, detrended beat, and the approximated single laser, including the thermal noise floor.

An exponential fit was applied to account for the slowly varying drift of frequency, as demonstrated in Panel (a). As illustrated in Panel (b), a zoom at the detrended frequency is presented, along with a 100 second moving average overlaid on the same scale. The data exhibits fluctuations within a 6 Hz band, while the averaged data is constrained within a 2 Hz band. Panel (b) displays the respective Allan deviations, including the thermal noise floor limit. For time scales ranging from 1 s to 2000 s, the performance of a single laser is approximately $(4-7)\times10^{-16}$.

As the time scale increases, the system approaches and reaches the thermal noise limit, at approximately 10^4 s, approximately one third of the data set length. Indeed, this is a standard performance of the beat; nevertheless, it can be contended that, at large time scales, limitations in the Allan deviation formalism are encountered, resulting in the performance on these time scales being disregarded in a conservative estimate. Moreover, the focus is typically on the single laser. However, this is merely an estimate of the worst-case scenario for the better laser. It is also possible for one laser to operate at the actual thermal noise floor, while the other is predominantly limiting the measurement. The validity of this claim can be verified through a three-cornered hat measurement, a method previously outlined in Section 8.2. This procedure involves the use of a third oscillator at similar performance level.

Finally, the frequency noise spectrum of the beat was analyzed for a range spanning over nine decades in the Fourier picture, between 1×10^{-3} Hz up to 10^6 Hz. It was possible to reach even higher frequencies; however, the signal-to-noise ratio of the carrier signal would soon reach the noise floor of the SA. The measurement utilized all the knowledge acquired in Section A.5.2. The data is displayed in Figure 3.14. At lower frequencies up to 1 Hz, the beat was measured by the frequency counter, analyzed in terms of Allan deviations, and then converted to phase noise by employing Equation (A.126). For the frequency range between 1 Hz and 70 kHz, the beat was mixed down to 1 kHz and 10 kHz, for two measurements respectively, and was obtained directly via the high sample rate DAQ card. Then, the Fourier formalism elucidated in Equation (A.121) is applied and converted to phase and frequency noise.

The acquisition of the longest frequencies is accomplished through the utilization of a SA and its integrated software (SignalHound, Spike). A close examination of the methods reveals a high degree of consistency among them. The top Panel (a) displays the spectral phase noise density, while Panel (b) displays the spectral frequency noise density. The green line signifies a white noise type floor at $7\times10^{-15}\,\mathrm{Hz}^{-1/2}$. This must not be confused with the pink noise type thermal noise floor. White noise has been selected as the data appears to exhibit a stronger resemblance with white noise. The noise spectra demonstrate a high degree of purity, exhibiting only sidebands at and adjacent to the difference frequency between the modulation frequencies for the PDH lock (1.6468 MHz − 1.59 MHz = 56.8 kHz).

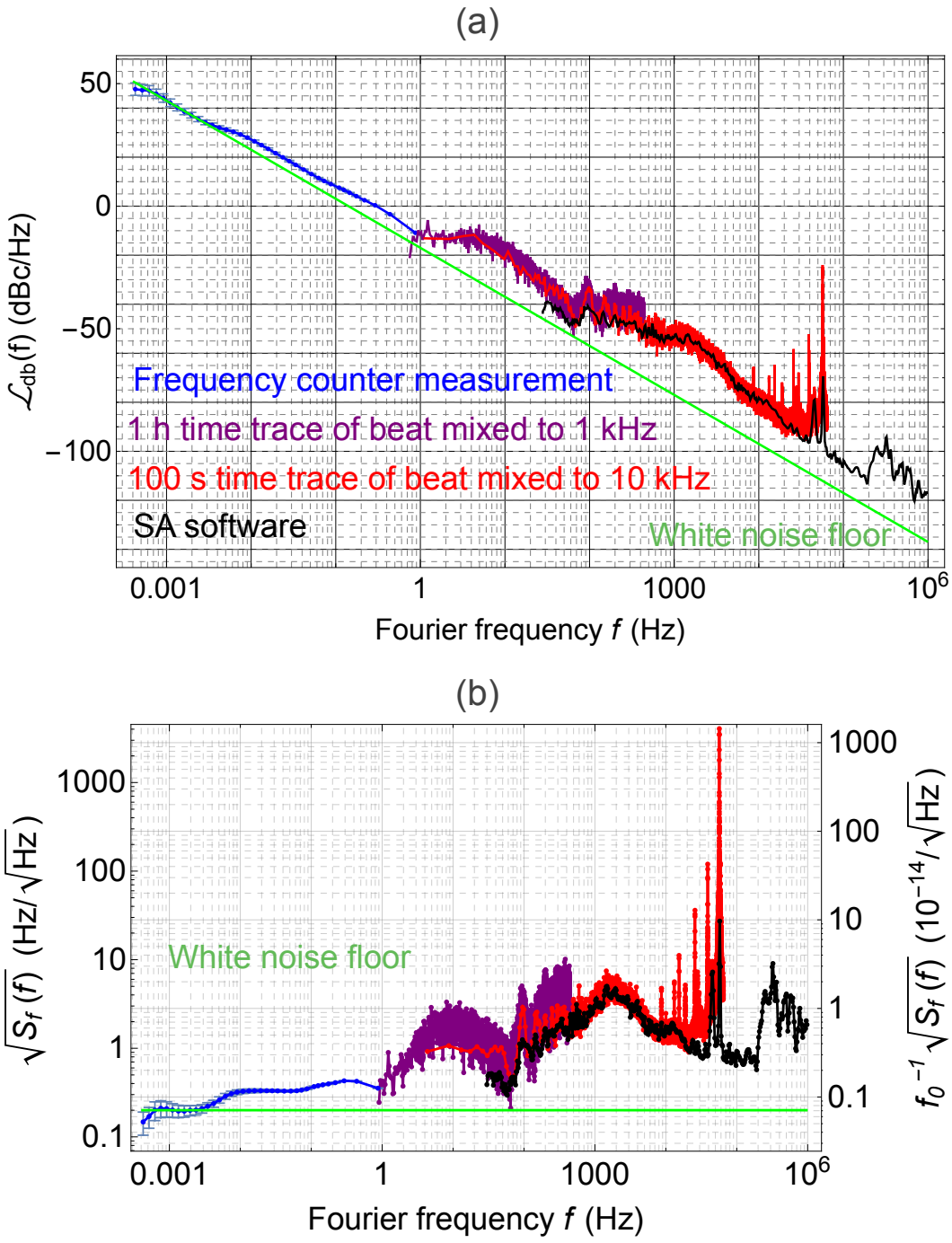


Figure 3.14: Lab 2: Spectral phase (a) and frequency (b) noise density of the ULE beat measured by the means of a frequency counter (blue), a mixed down beat and a DAQ card (purple, red) and a SA (black). The prominent sideband at 58 kHz arises from the difference between the PDH sideband frequencies of the respective locks. The green line indicates a white noise floor at $7 \times 10^{-15}\,\text{Hz}^{-1/2}$.

Comparative Analysis

For reference, the most notable room-temperature optical references of the last decade, in comparison to the resonators in this work, as of the time of writing this thesis, include:

- [60] 2015: 48 cm ULE spacer with FS dielectric mirrors. Thermal noise (Allan) 5.4×10^{-17}. Stability between 8×10^{-17} and 1×10^{-16} for averaging times between ≈ 1 s to 2000 s.
- This work in 2021: Two 30 cm ULE spacer with FS dielectric mirrors. Thermal noise (Allan) 1×10^{-16}. Stability between 4×10^{-16} and 7×10^{-16} for averaging times between 1 s to 2000 s.
- [110] 2022: 20 cm ULE spacer with crystalline coatings. Thermal noise (Allan) 7×10^{-17}. Stability at 1.6×10^{-16} at ≤ 1 s.
- [111] 2024: 30 cm ULE spacer with crystalline coatings. Thermal noise (Allan) 4.4×10^{-17}. Stability at below 2×10^{-16} for averaging times between 1 s to 50 s.
- [112] 2024: 30 cm ULE spacer with FS dielectric mirrors. Thermal noise (Allan) 1.1×10^{-16}. Stability of 1.3×10^{-16} at 1 s.

Further mention of ultra-stable lasers at the (low) 10^{-16} level can be found in the works reported in [113] and [114]. A significant proportion of the most ultra-stable lasers are utilized for optical lattice clocks. In this domain, a high degree of frequency instability (among factors such as narrow laser linewidths) is essential for achieving effective averaging during the interrogation of clock transitions.

The ULE cavities examined in this study are within an order of magnitude with the most advanced systems in terms of frequency instability. A notable advantage of these cavities is their configuration as a pair of identical systems, a feature that sets them apart from other systems and provides a unique advantage in certain applications. The best room temperature cavity to date is operated at PTB. The length of 48 centimeters contributes to the reduction of the thermal noise floor. Furthermore, crystalline coatings, are gradually replacing dielectric ones due to their superior thermal noise floor [115, 116]. However, the most advanced technology in the world, to date, is within a factor of 5 of the resonators established in this thesis.

However, the lowest recorded frequency instabilities worldwide are attributed to cryogenic systems, which have been demonstrated to enhance the thermal noise floor by addressing the "thermal" component of the noise. The utilization of silicon spacers is primarily driven by the fact that silicon exhibits ZCTE behaviors at cryogenic temperatures. The following systems have been determined to be among the best of the best to date:

- [61] 2017: 6 cm silicon spacer at 4 K with dielectric coatings. Thermal noise (Allan) 4×10^{-17}. Stability at 4×10^{-17} for averaging times between 0.8 s to a few 10 s.
- [117] 2019: Two 21.2 cm silicon spacers at 124 K with dielectric coatings. Thermal noise (Allan) 6.5×10^{-17}. Stability at 6.5×10^{-17} for averaging times between 0.8 s to 80 s.
- [118] 2024: 20 cm silicon spacer at 10 K with crystalline coatings. Thermal noise (Allan) 4.5×10^{-18}. Stability at 1×10^{-16} at 1 s.

It is noteworthy that even the most advanced cryogenic systems are only approximately one order of magnitude better, than the ULE cavities utilized in this study. This advancement, however, is accompanied by a significant increase in system cost, particularly due to the cryostat and its associated maintenance requirements. Additionally, the system's complexity rises due to the necessity of low temperatures, which demands a more sophisticated design and management. Devices and components must be graded for use in cryogenic environments.

However, the integration of crystalline mirrors and cryogenic cavities enables the exploration of the 10^{-18} level of thermal noise, a significant advancement for next-generation optical lattice clocks, wich is however not within the scope of this thesis. A recent collaborative effort among various European institutions has resulted in the publication of a report, entitled "Guidelines for designs for ultra-stable laser with 10^{-17} fractional frequency instability" [67]. This print offers a concise overview of the most recent advancements in the pursuit of the best frequency instability. The author of this thesis is one of the co-authors, with small contribution (see Section 4.4, Publication in B.3.2), that does not originate from the ULE cavity configuration. Rather, it is the result of an additional resonator configuration that utilizes a relatively uncommon spacer material, NEXCERA, a subject that will be addressed in the next section.

3.2 NEXCERA-Based Resonator

A central subject of this thesis was the construction of a metrology system for a collaborative experiment between HHU Düsseldorf and MPIK Heidelberg on the spectroscopy of molecular hydrogen ions. The system incorporates an optical reference resonator based on the NEXCERA ceramic, which is anticipated to be competitive with ULE but has been utilized sparingly for resonators to date. As of the time of writing, there is only one other group that has used NEXCERA for ultra-stable lasers, in addition to the Institute at HHU [119, 120, 67]. NEXCERA^{TM} is an ultra-low thermal expansion ceramic with a cordierite base, produced by the company Krosaki Harima Corporation. The abbreviation "NEXCERA" is an acronym for "**N**aught **Ex**pansion **Cera**mics." Currently, there are five distinct materials in existence: N113B, N117B, **N118C**, N119C, and CD107 [121].

The resonator utilized in this thesis is based on the material N118C. The objective of this resonator, however, was not to achieve the highest attainable performance but rather to operate at a reasonably good level of approximately 10^{-14} with an emphasis on robustness and flexibility. In the initial stages of the set-up, it was also the subject of a Bachelor's thesis [122] by P. Schulte, which was advised by the author of this work. A characterization of finesse has been carried out within the framework. This data was jointly collected and is newly analyzed in this thesis.

Prior to this work, the resonator was optically contacted and placed inside a vacuum chamber by a member of the institute who had initially worked with the cavity and presented the work in [120]. The spacer in this thesis is, in fact, the exact same spacer of that work; it has merely been paired with high-finesse mirrors for a wavelength of 1.5 µm, as opposed to the previous 1064 nm. The temperature change and data collection of the ZCTE measurement, described in this study was conducted in collaboration with the same person, C. J. Kwong. However, the setup, method and

analysis of the measurement was subject of this thesis. Furthermore, the configuration of the electronics, optics, evacuation of the resonator, and PDH offset lock, in addition to the enhancement of performance, has been a focal point of this thesis.

The design process included the implementation of an offset lock technique (see Section 2.3.2) for flexible frequency tuning and the maximization of the system's robustness for transportability and operational versatility across institutions. Additionally, the system will be capable of remote control. The resonator was used as an optical reference for the search for Dark Matter in [37] (see Section 7.2, Publication in Appendix B.1.2), and as a reference in the characterization of the OPO in [68] (see Section 8.3, Publication in Appendix B.2.2). Further, its exceptional long-term stability will be reported in Section 6. As mentioned in the preceding section, the instability, linewidth, and drift of the NEXCERA locked light is also part of the guideline paper [67].

3.2.1 Geometry and the Thermal Noise Floor

The resonator is shaped biconically, with a length of 12 cm, and is composed of two FS mirrors with dielectric coatings for 1.5 µm and ULE compensation rings. The radius of the rim is measured at 45 mm, while the radii of the end faces are determined to be 15 mm. The radius of the center bore hole is measured at 5 mm. The lower radius of the end faces is used to approximate the thermal noise floor in the cylindrical model. However, this effect is only marginal when it comes to the values. The material's Young modulus is 140 GPa [121], the loss angle is estimated to fall within the range of $\phi_{nex} = 1.9 \times 10^{-5}$ and 3×10^{-5} [123, 67] for N117B. The precise thickness of the coating is not known, but it is estimated to fall within the range of 5–10 mm.

Table 3.4 presents the lower and upper bounds of the thermal noise floor, derived from the loss angle and coating thickness uncertainty. The thermal noise floor has been calculated to be approximately 2×10^{-16} level in terms of Allan deviation. This is comparable to that of an identical cavity based on a ULE spacer. NEXCERA is mechanically stiffer but exhibits a larger loss angle. However, the dominant contribution to the thermal noise floor comes from the coating and mirror substrates. In fact, an identical ULE-based resonator with the same mirrors would have a thermal noise floor $2-5\,\%$ higher than that of the NEXCERA resonator. Thus, for room-temperature systems, the two materials are quite similar in performance. Moreover, the noise floor of the NEXCERA cavity is found to be 2.6 and 3.4 times higher than that of the 30 cm long ULE-based resonators discussed earlier—a difference primarily due to cavity length rather than spacer material.

Floor	$\nu_0^{-1}\sqrt{S_{f,th}(f)}\left[\frac{1}{\sqrt{\text{Hz}}}\right]$	$\mathcal{L}_{db,th}\left[\frac{\text{dBc}}{\text{Hz}}\right]$	$\nu_0^{-1}\sigma_{A,th}$	$\nu_0^{-1}\sigma_{M,th}$
Low	$2.0 \times 10^{-16}\, f^{-1/2}$	$-31\,\frac{\text{dBc}}{\text{Hz}} + 10\log 10\left(f^{-3}\text{Hz}^3\right)\,\frac{\text{dBc}}{\text{Hz}}$	2.3×10^{-16}	1.8×10^{-16}
High	$2.6 \times 10^{-16}\, f^{-1/2}$	$-29\,\frac{\text{dBc}}{\text{Hz}} + 10\log 10\left(f^{-3}\text{Hz}^3\right)\,\frac{\text{dBc}}{\text{Hz}}$	3.1×10^{-16}	2.4×10^{-16}

Table 3.4: Thermal noise floor of the employed N118C resonator, including FS mirrors with dielectric coatings. The "low" and "high" noise floors are determined by the range of loss angles that have been established for the spacer material N117B.

3.2.2 Experimental Apparatus

The resonator is positioned vertically within a vacuum chamber, which contains an inner heat shield that is actively stabilized by TECs and a temperature sensor that is set to the experimentally determined ZCTE of 17.8 °C. The ion pump [Agilent Technologies] is maintaining the pressure level at 7×10^{-7} mbar. The cavity is held in place by support posts located within the heat shield, while the vacuum chamber itself is supported by an additional three posts positioned on top of a small (approximately 30 mm by 60 mm) optical breadboard. A 45 ° mirror enables in-coupling to the resonator. The chamber is equipped with two windows that permit the entry and exit of light. The schematic of the setup is presented in Figure 3.15.

A fiber laser [NKT Photonics E15] operating at a wavelength of 1.5 µm is directed through a fiber-coupled AOM [Gooch & Housego]. Two fiber lasers, with wavelengths of 1.534 µm and 1.561 µm respectively, are utilized interchangeably as reference lasers. Switching from one to the other takes only a few minutes. This is followed by a 99 : 1 PM TC, which divides the beam into two distinct paths. The 1 % coupling path is directed to a fiber-coupled EOM [iXBlue] and subsequently out-coupled into free space by a collimator. It is noteworthy that all mating sleeves combining fibers are PM graded, a classification that aligns with the PM rating of all fibers within the system.

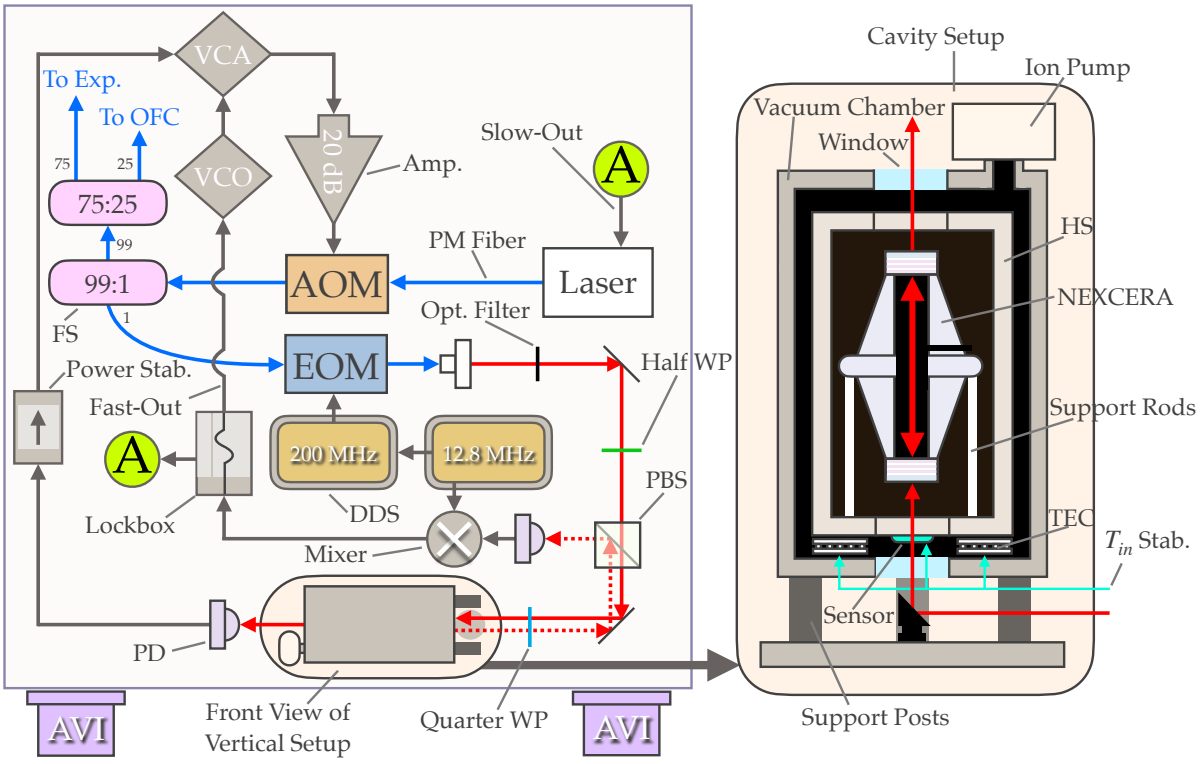


Figure 3.15: Schematic of the setup for laser stabilization (right) and the optical resonator (left). The cavity is in a vertical arrangement, but shown from the side on the setup. Electronics other than the laser are not placed on the laser breadboard, but below or on top of it. All fibers in the setup are PM, the free space path is simplified as much as possible.

The free space light propagates through an optical filter, thereby suppressing the total power by approximately 11 dB. Then, the light is separated by a half-waveplate and a PBS, where one path is directed through a quarter-waveplate towards the cavity and the other is obstructed. The back reflected light of the cavity propagates again through the quarter-waveplate before being directed to a PD [Hamamatsu, Homebuilt]. An additional PD is placed on top of the cavity to measure the transmission signal.

The mode-matching process is accomplished by the lens in the out-coupling collimator. The laser is locked by means of the offset lock technique, as previously explained. In this case, the main signal of a DDS [Homebuilt] driving an EOM is centered at 200 MHz, which is phase-modulated at 12.8 MHz. The phase-modulation output is mixed with the AC output of the reflection PD to generate the error signal, which is then sent to a lockbox after passing through a low-pass filter. The fast output of the lockbox is connected to a VCO [MiniCircuits] and amplifier [Homebuilt], which drive the AOM. Meanwhile, the slow lock is directly connected to the fiber laser modulation input. The transmission signal is routed to a basic power regulation lockbox [Homebuilt], which then controls a VCA [MiniCircuits]. The VCA in turn regulates the power between the VCO and the amplifier [Homebuilt]. This process enables the stabilization of power.

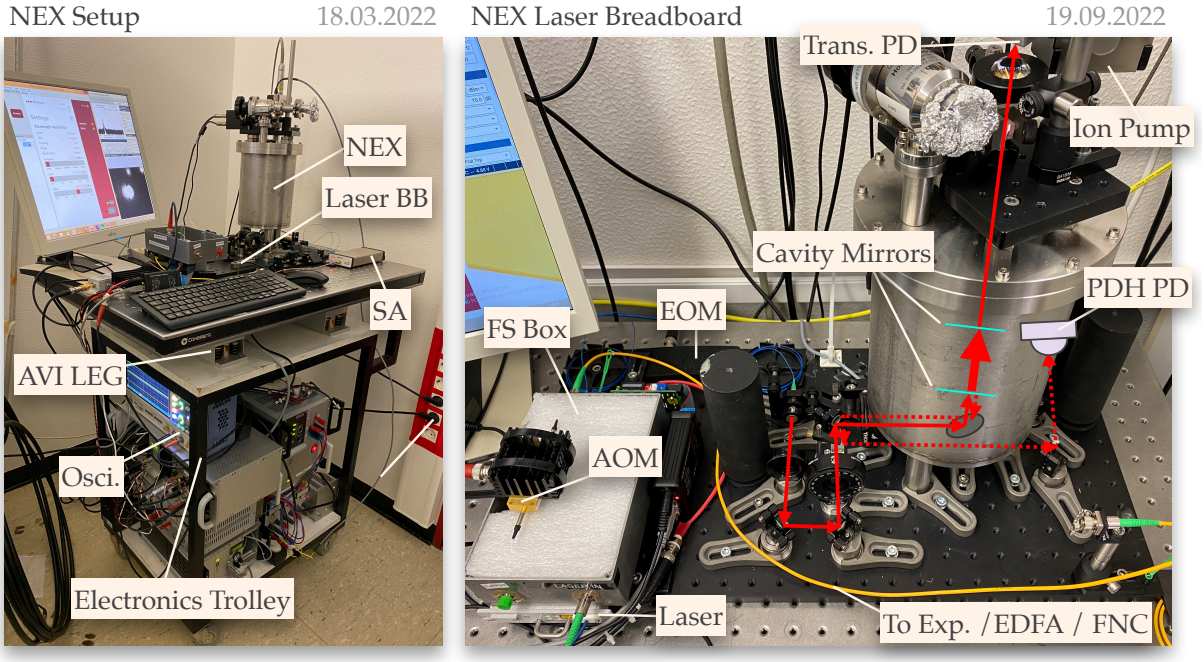


Figure 3.16: Setup of the NEXCERA resonator. The left side shows the first iteration of a portable setup including computer, electronics AVI and optics. A camera captures the transmitted light seen by the fundamental mode on the computer screen. The right side shows the laser breadboard. The TC are placed in a box with mating sleeves connected to it to simplify the overview. The AOM is placed on top of the box with a small heat sink, as it can get warm. The EOM is covered with foam.



Figure 3.17: NEXCERA system in a portable rack. The electronics are placed on top and the laser breadboard, resonator and AVI are placed on the bottom. The optical system is shielded by a plastic cover during operation. The computer screen and diagnostic tools are placed on top of the rack, allowing the system to be moved between laboratories without the need for additional equipment. The heat generated by the electrical equipment was moderate and of no concern in the air-conditioned laboratories.

The laser breadboard is affixed to a slightly larger optical breadboard, which is positioned on top of an AVI unit that is equipped with two legs. The system was designed on a small trolley

setup, with all necessary electronics situated below the optical components. Figure 3.16 presents a photograph of the setup and the cavity laser breadboard. The design philosophy was predicated on the objective of creating a bare minimum setup that is robust, transportable, and easy to maintain as the core of a metrology system. The 99 % TC output is subsequently divided into two distinct paths, with a 75 : 25 TC ratio. One output is allocated for experimental purposes, while the other serves as a reference input for an OFC. Following the configuration and characterization of the system atop the trolley, its subsequent integration into a movable rack is illustrated in Figure 3.17. This system was characterized by its portability, which enabled its utilization between laboratories at the institute. The device is powered by a single power cord that can be connected to a battery. This configuration enables the system to remain locked while it is moved. Within the confines of the rack, a wooden board is positioned at the interface between the AVI [Table Stable, 200S] and the rack, as well as between the AVI and the laser breadboard. The system is protected from air turbulence from the AC units by a plastic shield located in the front and back. The presence of black foam in front of the plastic shield may have a minor effect on acoustic influences, but its primary purpose is aesthetic. The PC, which controls the laser and is used for monitoring detectors and collecting data, is part of the electronics.

The PC's components, including the monitor, keyboard, mouse, as well as an oscilloscope [Rohde & Schwarz, RTB2004], and SA [Rohde & Schwarz, FPC 1000], are positioned on the top of the rack. This configuration ensures the system's complete self-sufficiency. In the context of high-performance applications, the necessity of an additional input, specifically an H-master connection for the DDS driving the EOM, is a matter of optionality, depending on the specific nature of the application. Note that this connection is not necessary in a classical PDH lock, as the local oscillator cancels out in the mixing process. In the offset lock, however, the main tuning frequency remains in the total frequency.

3.2.3 Resonator Properties and Laser Frequency Stability

The finesse of the cavity was measured by the ring down method. By monitoring the transmission signal of the locked laser and abruptly deactivating the lock, it is possible to measure the decay and its time constant, τ_c, of photons within the cavity. In order to obtain an accurate estimation, it is essential that the sudden loss of resonance occurs at a rate that is significantly faster than the characteristic decay. In this case, the lock was managed by an AOM with a response time of approximately 10 ns. Consequently, when the lock is deactivated, the laser rapidly loses lock and jumps away from resonance. This is due to an offset that is induced when the lock is engaged. Repeating this type of measurement by locking and unlocking the laser allows for a statistical analysis of the decay time. This analysis can be performed by plotting Equation (2.12) (see Section 2.1.1) in form of

$$I_t(t) = I_0 e^{-\frac{t}{\tau_c}} + I_{off}.$$

The time constant, τ_c, is determined by the fit. Inserting it into Equation (2.10) and (2.9) yields a value for the finesse $\mathcal{F}_{nex}$. An exemplary measurement is presented in Figure 3.18 (a). It displays the exponential decay that occurs subsequent switching off the lock.. The left plot Panel (b) shows a histogram of the evaluated finesse over 101 consecutive measurements.

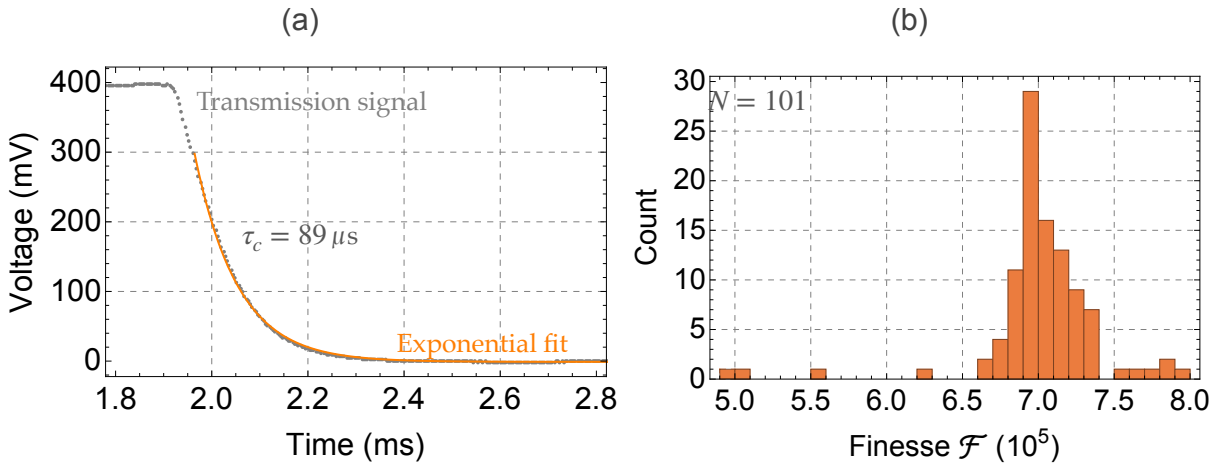


Figure 3.18: Finesse measurement of the NEXCERA cavity. (a): Single ring-down measurement (gray) including an exponential fit (orange). (b): Histogram of the evaluated finesses of 101 consecutive measurements.

The value of the finesse is estimated to be approximately $\mathcal{F}_{nex} = 7.0(4) \times 10^5$, with time constants in the order of $\tau_c \approx 90\,\text{ms}$, which is considerably larger than the response time of the AOM. The FSR of the cavity is approximately $\Delta\nu_{nex} = 1.25 \times 10^9$ Hz, which results in a cavity linewidth of approximately $\nu_{nex} = 1.8(1)$ kHz. The ZCTE temperature of the NEXCERA spacer system, comprising FS dielectric mirrors and ULE compensation rings, is approximately $T_{ZCTE,nex} = 17.8(1)\,°\text{C}$. The measurement is shown in Section 6. The performance of the NEXCERA locked laser light is part of a publication, thus both the Allan deviation and the linewidth are addressed in Section 4.4, while the long-term stability is also delineated in Section 6. However, to conclude this section, it can be summarized that the light exhibits Allan deviations below 4×10^{-15} level for averaging times between 1 s and a few hundred seconds. Further the laser linewidth was approximated to 3 Hz. The long term drift of the cavity is in the order of $10^{-18}\,\text{s}^{-1}$.

3.3 Frequency Metrology System

One central focus of the present thesis is the metrology system devised for spectroscopy experiments on molecular hydrogen ions at MPIK in Heidelberg, explicitly in the Penning trap apparatus ALPHATRAP [124]. The cryogenic single ion trap setup has been the subject of recent works on the test QED through g-factor and mass measurements [125, 126, 127, 128]. The system described in this section is supported by a grant from the Deutsche Forschungsgemeinschaft, INST 208/809-1 FUGG, project number 460457764, Dauerstrich-Lasersystem für Präzisionsexperimente an einzelnen Molekülionen, and the state of North Rhine-Westphalia.

Following the configuration of the dual ULE system within the tower configuration, and concurrently with its maintenance as a reference for the measurement campaign on HD^+, the work on the metrology setup began. The author of this thesis was responsible for procuring the necessary components, planning (based on the proposal), and setting up the system that stabilizes a transfer laser at 1.1 µm to an OFC, which is stabilized to the 1.5 µm NEXCERA locked light. The selection

Mol. Ion	Transition (μm)	Gr. state	Ex. state	Ref. Laser (μm)	Tr. Laser (μm)
HD^+	1.151, E1	(0,1)	(5,2)	–	1.151
HD^+	1.154**, E1**	**(0,0)**	**(5,1)**	–	**1.154**
HD^+	1.165, E1	(0,1)	(5,0)	–	1.165
HD^+	4.90, E2	(0,0)	(1,2)	1.534	1.168
HD^+	5.11, E1	(0,0)	(1,1)	1.534	1.180
H_2^+	4.24, E2	(0,0)	(1,2)	1.561	1.141
H_2^+	4.57, E2	(0,1)	(1,1)	1.561	1.164
H_2^+	4.58, E2	(0,2)	(1,2)	1.561	1.164
H_2^+	4.58, E2	(2,1)	(3,3)	1.561	1.164
H_2^+	4.89, E2	(1,3)	(2,3)	1.534	1.168
H_2^+	5.10, E2	(3,0)	(4,2)	1.534	1.179

Table 3.5: The rovibrational transitions are expressed as follows: $(v_g, N_g) \rightarrow (v_e, N_e)$. From the respective ground state to the excited state. The vibrational quantum number is denoted by v, and the rotational quantum number by N. The generation of the transition wavelengths is facilitated by DFG, utilizing the respective wavelengths of the reference and transfer lasers (last column). Preliminary results on the optical transition from (0,0) to (5,1) is shown in Section 8.4. E1: Electric dipole transition. E2: Electric quadrupole transition.

of wavelengths was made with consideration for the rovibrational transitions enumerated in Table 3.5. The theoretical framework can be found in [129]. Three out of five rovibrational transitions in HD^+ can be driven by a tunable laser at 1.15 – 1.17 μm; however, the other eight transitions are at mid-infrared wavelengths around 4.9 – 5.1 μm. Operating within the domain of light at these specific wavelengths poses a significant challenge, as the industrial sector, particularly in the domains of optics, lasers, fibers, and detectors, has historically focused its efforts on near infrared and telecom wavelengths. Another option is the difference frequency generation (DFG) technique, which involves three wave mixing and is characterized by the production of a photon at the difference of the frequencies of photons of shorter wavelengths [130]. A similar spectroscopy setup has been employed in [33]. A notable advantage of this approach is that the resulting wave exhibits the same stability as the inputs. Consequently, if both input waves are stabilized, the output wave will also be stable.

The proposed transitions can be covered by the combination of light at 1.5 μm and light between 1.1 – 1.2 μm. In order to optimize the device's efficiency, the wavelengths for the NEXCERA resonator were selected to be 1.534 μm and 1.561 μm, respectively. The first option was selected due to its compatibility with the Acetylene line for the Dark Matter experiment, while the second option was chosen to provide frequency stability measurements against an additional ultra-stable laser at the institute. In addition, the utilization of these wavelengths enables the comprehensive

coverage of all rovibrational transitions, incorporating a transfer laser tunable over the range of 1.141 µm and 1.180 µm, which is commercially available. The performance objectives for the spectroscopy experiments include a laser linewidth of less than 10 Hz, an instability at the 10^{-14} level, and an uncertainty of the absolute frequency at the 10^{-14} level. To this end, a metrology system, as outlined in Section 2.4.3, will be required. Prior to the initiation of the metrology system, a H-maser was transferred from HHU to the laboratory at MPIK.

The objective of this thesis was to establish the metrology system and characterize it at HHU in Düsseldorf. Subsequently, the system was to be transported to a laboratory provided by MPIK in Heidelberg. This design process involved the implementation of the fiber noise cancellation paths (50 m) of the laser light until the Penning trap setup as the systems are operated in spatially separated laboratories. The system is described in the following section and was exclusively set up by the author of this thesis. This includes the lock of the transfer laser. Additionally, the system has been configured to permit comprehensive remote control and incorporates automated self-repair routines, thereby minimizing the necessity for physical intervention. Following the relocation and configuration at MPIK Heidelberg, the OFC reference laser and FNC system remained under the author's oversight. However, the transfer laser lock and in-coupling to the trap were then executed by a colleague from the institute at HHU, I. V. Kortunov.

During the design process, the author opted to establish all optical pathways utilizing PM (and, in select instances, SM) fibers. This approach encompassed the PLL of the spectroscopy laser, FNC configurations, and beat lines. This has been implemented to guarantee the system's robustness, particularly with regard to its transportability and complexity. A noteworthy consequence relates to the configuration of the fully fiberized FNC system, wherein an optical circulator is employed to substitute for the conventional free-space PBS wave plate configuration.

3.3.1 Setup and Architecture

As previously mentioned, the experimental configuration is based on the principle of DFG, which is the process of producing longer-wavelength light by combining two shorter-wavelength sources. The resulting light exhibits properties derived from the initial lasers, including linewidth and frequency instability. Specifically, the configuration under consideration involves a fixed-wavelength fiber laser [NKT Photonics, E15] operating at either λ_R = 1.561 µm or 1.534 µm, with a thermal tuning range of 1 nm, serving as the reference laser. Furthermore, a tunable laser with a central wavelength of λ_T = 1.150 µm [Toptica, DLC TA PRO HP] and tunability spanning 100 nm functions as the transfer laser. The configuration is depicted schematically in Figure 3.19.

The reference laser is locked to the NEXCERA cavity, which serves as a foundation for the OFC [Menlo Systems, FC1500]. The CEO (f_{ceo} = 20 MHz) of the OFC is stabilized to the H-maser, which serves as the global RF reference of the system. The transfer laser is stabilized to the OFC via a PLL, ensuring a high degree of correlation between the tuning and reference lasers. This configuration enables the generation of higher wavelength light between 3.73 µm and 5.18 µm, utilizing the designated DFG module, with the fundamental stability of the NEXCERA resonator being the determining reference. Depending on the requirements, this laser can be readily substituted for any other laser as long as its wavelength falls within the output range of the OFC

and the reflectivity curve of the cavity mirrors, thereby allowing for a greater range of possibilities within the DFG. In this configuration, the two reference lasers can be interchanged within a span of minutes. The system is assembled on an optical table in a metrology laboratory, with the exception of the DFG module, which was planned to be placed in the Penning trap laboratory. Consequently, the light from the two spectroscopy lasers propagates through two 50 m long SM fibers installed between the laboratories.

As previously outlined (see Section 3.2.2), the PDH offset lock scheme is employed to stabilize the frequency, thereby enabling the tuning of the reference laser by modulating the DDS frequency driving the EOM. The system has been engineered to counteract thermal variations in the laboratory that reach the cavity, as well as the long-term drift of the spacer and any other slow perturbation. This is accomplished by utilizing a slow feedback loop that compares the locked reference laser to the H-maser, which, by design, has an exceptional long term stability. The system incorporates an auto-lock circuit loop, designed within the scope of this thesis. This loop ensures that the reference laser regains stability when the system unlocks. The device under consideration is designed to measure the transmission signal. In the event of an unlock of the light, the device tunes the frequency of the fiber laser through a voltage until it finds the mode again. PM fibers are utilized to distribute the stable laser to the OFC and through the fully PM fiberized FNC setup, which is designed to stabilize the long fiber path between the metrology system and the experiment.

The output of the OFC and the light of the reference laser are combined using an SM fiber coupler featuring polarization controllers. The repetition rate $\left(f_{rep} = 250\,\text{MHz}\right)$ of the comb is fixed by stabilizing the nearest comb mode $\left(N \approx 770 \times 10^3\right)$ via a PLL to the reference laser. In a similar manner, an additional fiberized beat, in conjunction with a supplementary PLL, is employed to stabilize the transfer laser to the OFC. The absolute frequency and respective comb tooth number of the transfer and reference lasers are measured by a wavemeter [HighFinesse, WS7].

Typically, the beat line of the OFC and a laser are achieved using a Bragg grating that filters the appropriate mode of the OFC output. The existence of many other modes has been demonstrated to result in the deterioration of the lock. In this fiberized configuration, a custom-made fiberized AOM [Gooch & Housego] centered at 1.15 µm was utilized to filter the OFC light. The efficacy of this method is attributable to the fact that the angle of diffraction can be tuned by the RF frequency (or rather wavelength). Consequently, it can be utilized to couple-in only the components of the light that are of interest. The system's design objective was to achieve maximum compactness and ease of use, featuring a solitary free-space path for mode matching into the resonator.

With the exception of two cases, all other elements are realized in PM fibers. In these two cases, SM fibers and polarization controllers are used to adjust the power in the respective beats with the comb and the transfer laser. In the dual ULE cavity system, each laser frequency was constrained to fixed resonance frequencies of the cavity, $\omega = \omega_{res}$, and could only be tuned in increments of the FSR, $\Delta\nu$. Offset locking enables the carrier wave to be adjusted through the modulation frequency. This adjustment results in $\omega_{res} = \omega \pm \Omega$, where the sign indicates the upper or lower sideband.

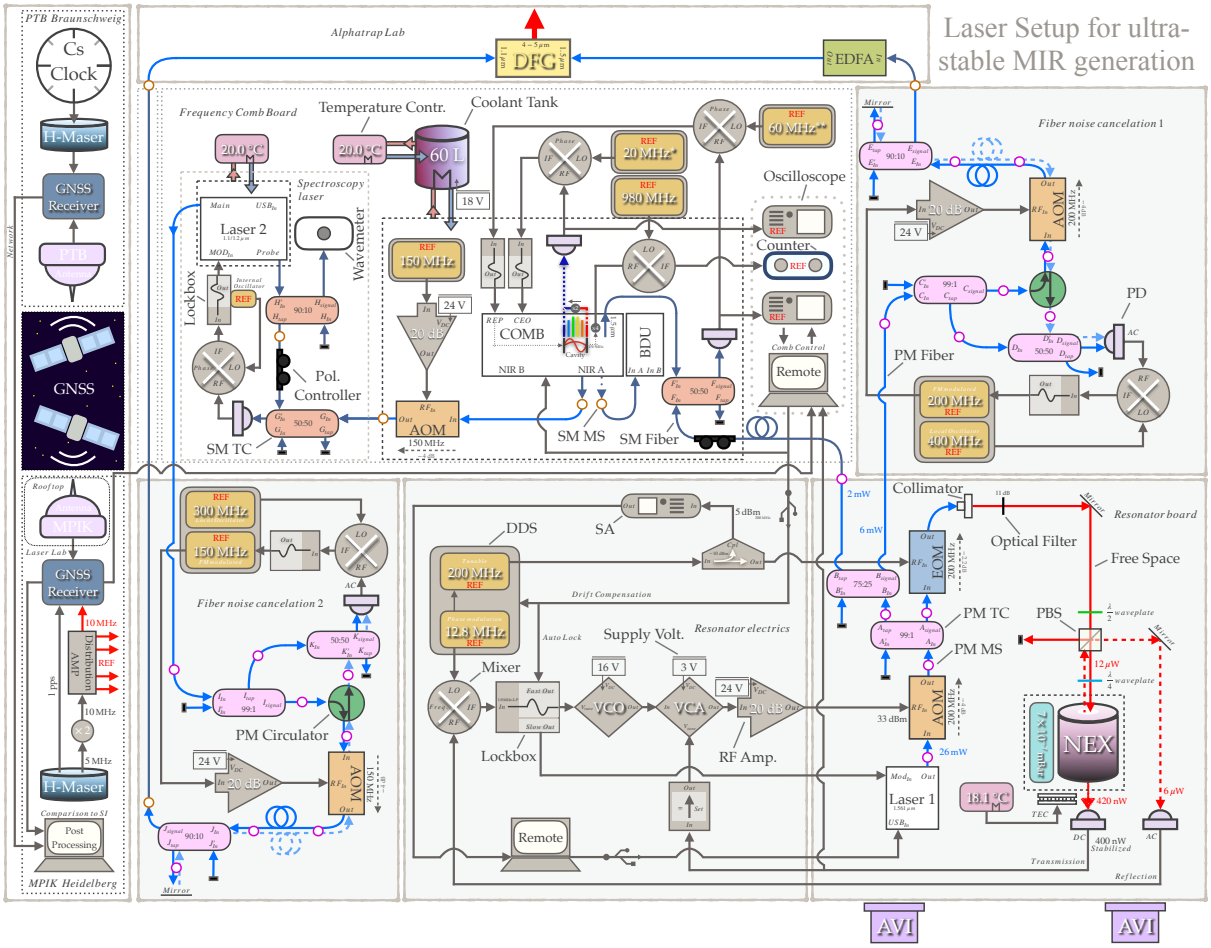


Figure 3.19: The experimental setup of the metrology system. The configuration of the resonator (NEX: NEXCERA) is illustrated in the lower right quadrant, while the associated electronic components are positioned in the adjacent box. The bottom left and top right boxes illustrate the fiberized FNC configurations for the spectroscopy lasers. The top left box illustrates the OFC, while the top center box showcases the installation in the trap laboratory. The fiberized PLL of the transfer laser illustrates the configuration as established at HHU. At MPIK, the transfer laser PLL was set up in free space by the colleague who took over it. As can be seen, the H-maser comparison from MPIK (also holds true for HHU) to GNSS via PTB is shown in the leftmost box. Acronyms used in the figure: SA, PD, PM, SM, DDS, PBS, TC, MS, AOM, EOM, EDFA, VCO, VCA and RF.

In this configuration, the DDS driving the sideband functions within a frequency range of 1 Hz and 400 MHz, with a resolution of 300 mHz, initially set to $\Omega/2\pi = 200\,\mathrm{MHz}$. The phase modulation is fixed at $\Gamma/2\pi = 12.8\,\mathrm{MHz}$, with a portion decoupled for demodulation. Consequently, while secured in place, the laser can be precisely tuned within a range of several hundred MHz. The selection of an appropriate sideband enables the adjustment of the laser frequency to a range of approximately $\Omega/2\pi = 800\,\mathrm{MHz}$, centered around the cavity mode. However, due to the phase modulation, it is not possible to tune the sideband at frequency Ω close to or below the frequency Γ. This results in a gap of size 2Γ around the cavity mode, within which the laser cannot be tuned to by the sideband. This results in a gap of $\Omega/2\pi = 400\,\mathrm{MHz}$ between the longitudinal modes. This

gap is not a fundamental limit; rather, it is a constraint imposed by the maximum output frequency of the DDS. A DDS with a frequency output of approximately $\Omega/2\pi = 600\,\text{MHz}$ would enable nearly continuous frequency tuning of the laser within the laser's thermal tuning range, which in this setup exceeds 100 GHz. A frequency change Δf_R of the reference laser, is translated to the comb according to the wavelength of the comb line. This, in turn, affects the frequency of the laser phase-locked to the comb by

$$\Delta f_T = \frac{\lambda_R}{\lambda_T} \Delta f_R. \tag{3.2}$$

Thus, the offset lock can be employed to set the transfer laser to a specific frequency, with further adjustments achievable at the target wavelength using an AOM. Figure 3.20 presents a depiction of one of the FNC systems, accompanied by a schematic representation. It is fundamentally identical to its free space counterpart, as illustrated in Figure3.4. It is based on a double pass through a fiberized AOM [Gooch & Housego] and combining a reference arm with the reflected light at the experiment. A 99 : 1 TC is utilized, where the 1 % path is employed as a reference. The main part of the light traverses a PM circulator toward the AOM and through the long fiber. The reflected light will undergo a subsequent shift due to the AOM entering the circulator from the opposite side.

Consequently, it will depart through its third port, thereby significantly suppressing any feedback to the laser. This light is combined with the reference light by another 50 : 50 TC. A 75 : 25 TC at the experiment's side is used to split light for the back reflection. A comparison with the international standard was conducted through continuous H-maser measurement using GNSS. A comparative analysis was performed on the data using the same measurement of two PTB masers that were steered against a Cs fountain clock. This was accomplished using a three-cornered hat method. The H-maser signal is distributed to all synthesizers, oscilloscopes [Rohde & Schwarz, RTB2004)] SAs [Rohde & Schwarz, FPC1000], and counters [K&K for CEO and Beats/Microsemi Phasestation for Repetition Rate] in the laboratory by using low-noise distribution amplifiers and frequency doublers from 5 MHz to 10 MHz.

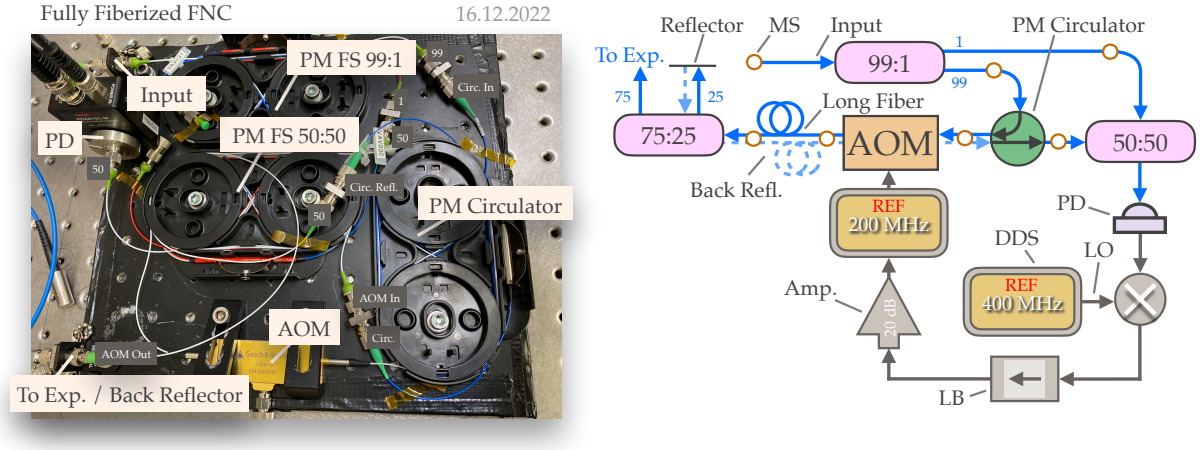


Figure 3.20: Left: Photograph of the fully fiberized FNC of one of the spectroscopy lasers. The FNC was configured on a small quadratic breadboard for the purpose of improving its transportability. Right: Schematic of the FNC system.

The concept remains unchanged during operation at HHU and MPIK; however, for operation at MPIK, a new GNSS antenna and receiver [Joseph Attenberger] had to be procured. The GNSS antenna was installed during the work on this thesis by the author and J. Morgner on top of the roof of the MPIK in Heidelberg. The repetition rate is measured by means of a high-performance frequency counter, given the limitations of absolute frequency measurement, as explained in Section 2.4.3.

The system was designed with portability in mind. While it remains stationary within a measurement campaign, it can be disassembled and reassembled with minimal effort. Due to its fiberized nature, the optical path can be reconstructed within a time frame ranging from minutes to hours. Notably, the alignment of the light to the resonator demonstrated remarkable resilience during the relocation process. The compact design of the resonator breadboard offers distinct advantages for transportation. Specifically, the operational integration from Düsseldorf to Heidelberg was accomplished in less than one week.

The H-Maser is not included in this calculation because it was relocated at an earlier time. In addition to offering high stability, the base plates of both the OFC and the transfer laser are actively water-cooled. The OFC is cooled in a two-stage system that includes a chiller and a buffer tank with a volume of approximately 60 liters. The CEO is particularly vulnerable to drift when the cooling is not engaged.

The DFG necessitates a substantial amount of input power due to its suboptimal efficiency, which is approximately 0.1 % at the level of the percentage of power output relative to the total power input. This means that a 1 W input power output results in 1 mW of power in the output wave. The transfer laser exhibits a maximum power output of approximately 1 W; however, the reference laser operates at a level of approximately 10 mW or less when reaching the trap laboratory.

Accordingly, an Erbium-doped fiber amplifier (EDFA) [Lumibird] with a maximum output of 5 W was procured for the reference light. This EDFA was subjected to rigorous testing and validation in the context of this work, which demonstrated that it does not induce linewidth broadening or increased frequency noise at a significant level. Eventually, while writing this script, the first measurements on the HD^+ ion at 1.15 µm are performed, thus the method of DFG is not yet employed. Nevertheless, the necessary devices and infrastructure, including EDFA, fiber paths, and suitable DFG modules, remain available.

During the course of the relocation process, the ion pump—which is responsible for maintaining the pressure within the resonators' vacuum chamber—was connected to a battery. The complete system was meticulously inventorized, labeled, and carefully packed prior to its transportation over the 300 km distance between the institutes via van on June 29, 2023. The comparison of the setup in Düsseldorf and MPIK is demonstrated in Figure 3.21. A photograph of the inside of the van, the day the system was moved is shown in Figure 3.22.

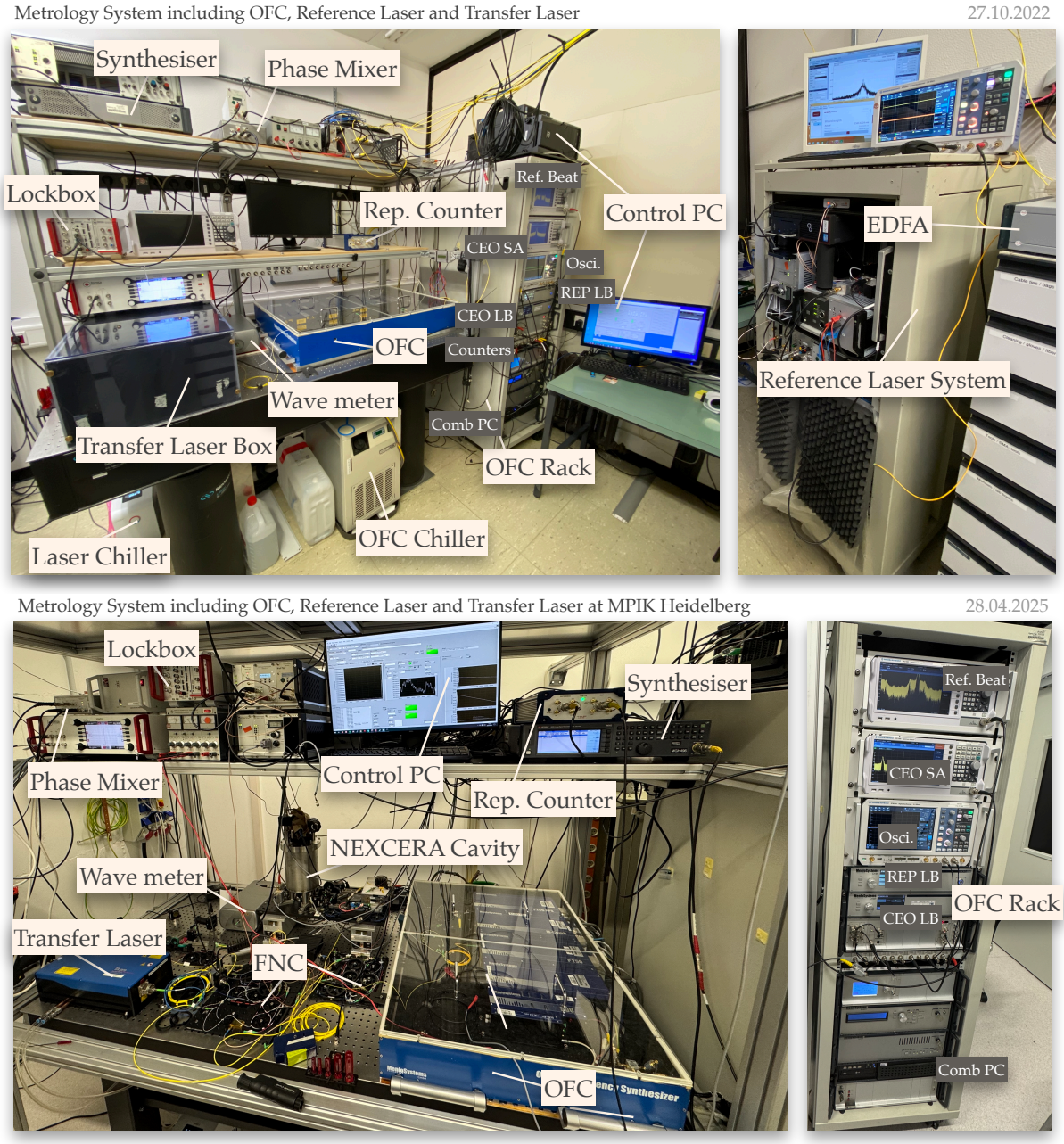


Figure 3.21: Top: Photograph of the frequency metrology system as configured at HHU in Düsseldorf. The image on the right presents a shows the OFC, transfer laser, and control PC. The rack in the left image contains the reference laser and NEXCERA cavity. The two elements are situated in the same laboratory and are connected by a short SM fiber. Bottom: The metrology system that was implemented at MPIK following the move is shown in the left image, which depicts the optical table with the OFC, the reference laser, the transfer laser, and the associated electronics. The image on the right shows the comb rack positioned adjacent to the optical table.



Figure 3.22: The metrology system was relocated from HHU Düsseldorf to MPIK Heidelberg, a distance of 300 kilometers. The van transported the FNC, OFC, and all of its electronics, the reference cavity and its electronics, as well as the transfer laser and all components necessary for beat lines. The photograph depicts, with the exception of the optical table and the H-maser, the majority of the apparatus.

However, the H-Masers are not depicted in the provided images. At HHU, it is situated in another laboratory, while at MPIK, it is located in a corner of the metrology laboratory. The optical table on which the system operates at MPIK was procured from HHU and delivered directly to MPIK at an earlier date. The software that operates the metrology system is based on a LabVIEW suite that has been developed by a former member of the institute. The OFC and the wavemeter are both equipped with dedicated software that can be managed by LabVIEW. This thesis includes an expansion of the LabVIEW tool with the following features:

- A mechanism for automatic locking of the reference laser, which re-locks the laser within seconds upon its subsequent unlocking.
- A correction for the repetition rate to ensure the proper comb tooth is utilized for the transfer laser.
- A slow lock incorporating a PID algorithm of the reference laser to the maser, employing the absolute frequency reading of the OFC and the PDH offset lock technique.
- A set frequency of the OFC reference tooth, when it is locked to the light. This frequency can be fixed, modulated, or shifted in steps of Hz level by the use of the slow lock of the previous bullet point.
- A self-regulating mechanism that, checks if the operational parameters of the OFC are accurate, including the beat sign, ensures the frequency maintains its set value.
- An error log that systematically documents a range of critical parameters, including the status of the CEO and repetition locks of the OFC, the fast and slow locks of the reference, the mode number of the comb tooth, and other relevant metrics.

The system was configured as an internal network, with the primary PC granted access to all SAs, oscilloscopes, and computers within the laboratory. The primary software application has been configured to interface with the wave meter, OFC, and reference laser. The system has been configured to stabilize itself in the event that the reference laser loses lock, thereby removing the need for human intervention. Additionally, the entire system can be operated remotely, constituting the predominant method for its maintenance. Nonetheless, over the course of the past two years, there have been numerous travels to MPIK for on-site work on the project.

3.3.2 System Characterization

Allan Deviation and Long Term Stability

The mathematical exposition of the OFC is elaborated in Section 2.4.3. The system depicted therein is precisely the system under consideration here. The instability of the measurement of the frequency counter, which is employed to measure the repetition rate and thus the absolute frequency of the laser, is shown to be limited by the H-maser instability through

$$\sigma_{R'}^2 \approx \sigma_R^2 + \sigma_m^2.$$

In this equation, $\sigma_{R'}$ is the measured Allan deviation, σ_R is the Allan deviation of the (reference) laser, and σ_m is the Allan deviation of the maser at the optical carrier frequency of the reference

laser. All deviations are expressed in terms of fractional frequency instability. Therefore, it can be concluded that the fractional instabilities of the laser and the maser contribute fully (with a weight of one) to the final measurement. Consequently, for averaging times, where the maser exhibits higher instability, the measurement is significantly constrained by this instability. This is shown in Figure 3.23. The beat between the reference laser and another cavity-stabilized laser at 1.5 µm (shown in blue) is measured concurrently with the absolute frequency of the reference laser by the OFC (orange). The blue curve already serves as a characterization of the NEXCERA locked light, with a performance below the 4×10^{-15} level at averaging times below 10 seconds. Additionally, the green line indicates a beat measurement of a comb line with one of the ULE stabilized lasers of Section 3.1, at 1064 nm.

The near-infrared (NIR) ULE-locked laser light is propagating through several meters of unstabilized fiber between the two laboratories. Please note that the green line has been adjusted to be compared at the fractional frequency scale. Due to the limited power, this beat was measured with a SA that had a resolution bandwidth of 3 Hz. This limitation results in higher frequency instability at shorter averaging times. Nonetheless, the frequency instability of a comb line evaluated by an optical beat is superior to the instability of the comb when constructed form the measured repetition rate, which further suggests a limitation through the H-maser.

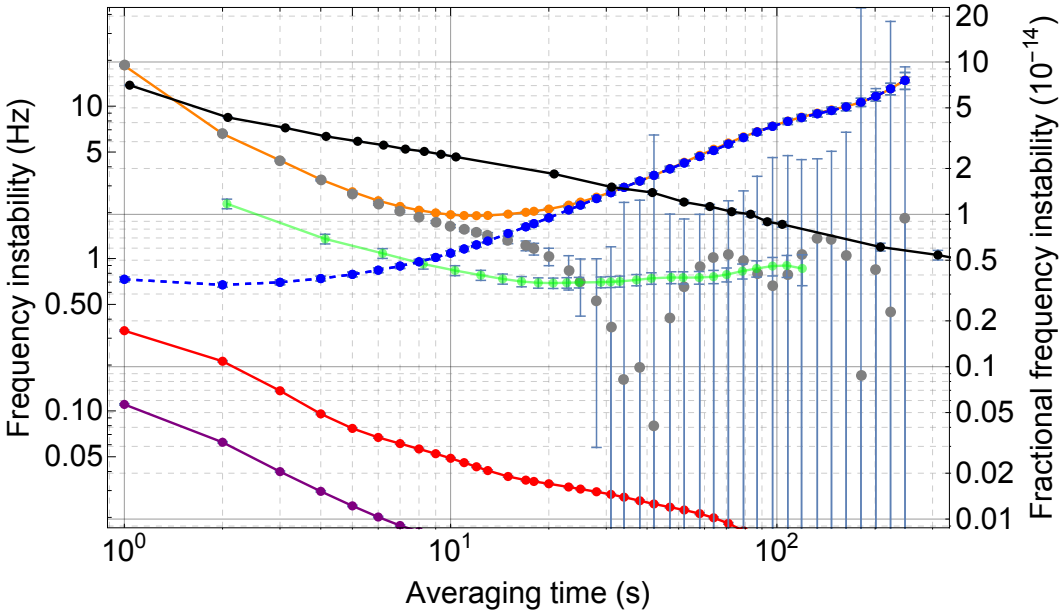


Figure 3.23: Allan deviations of the metrology system. Orange: Absolute frequency of the reference laser measured against the H-maser using the OFC. Blue: Direct beat between the reference laser and another cavity stabilized laser. Gray: Estimate of the H-maser instability using Equation (2.88) applied to the blue and orange data. Black: Measurement of the beat of the H-maser against a different H-maser. Green: Beat between a comb line and a 1064 nm laser, scaled to the reference wavelength. Red: Offset lock noise $\delta f_{ceo,lock}$. Purple: Comb lock noise $\delta f_{comb,lock}$. The blue, orange, red and purple data sets were measured simultaneously.

The frequency counter, which was utilized to measure the repetition rate, exhibited a resolution of 2×10^{-14} at one second averaging time for the applied settings. The maser stability is simulated and displayed in gray using equation (2.88) The simulated data follows the measured comb instability for times scales below 10 s but becomes noisy at a few tens of seconds. This can be explained by the precision of the data points of the Allan deviations of the blue and orange lines at larger time scales. The actual beat between the H-maser and another H-maser (specifically, the one that was transported to MPIK) is displayed in black. The noise magnitude of both Masers is comparable. The measurement was conducted in Düsseldorf during the setup process. The PLL beats of the CEO and comb lock were measured concurrently and displayed in red and purple, respectively. This procedure was implemented to verify the previously stated assertion that the PLLs do not induce additional noise to the frequency stability. As a result, the validity of Equation (2.92) is confirmed. Therefore, the frequencies of the reference laser, $\breve{f}'_r$, and the transfer laser, $\breve{f}'_l$, with respect to the international standard are given by

$$\breve{f}'_r = \begin{pmatrix} \left(f_{cb,0} + N_r\, f_{rep,0} + f_{ceo,0}\right)(1+\sigma_{si}) \\ \sqrt{\delta f_r^2 + \delta f_m^2} \end{pmatrix}, \text{ and } \breve{f}'_l = \begin{pmatrix} \left(f_{cl,0} + N_l\, f_{rep,0} + f_{ceo,0}\right)(1+\sigma_{si}) \\ \sqrt{\frac{N_l^2}{N_r^2}\delta f_r^2 + \delta f_m^2} \end{pmatrix}.$$

In this model it was used, that the transfer laser is locked to the OFC via a beat f_{cl} with the comb tooth of number N_l, while the OFC is locked through a beat f_{cb} between the comb tooth of number N_r and the reference light. The parameter σ_{si} is defined as the slowly drifting offset between the H-maser in the laboratory and the international standard at PTB. Please note that these are the measured values. The inherent instability of the reference and transfer lasers used in the interrogation of molecules is not constrained by the H-maser.

A comparison of the H-maser to PTB enables the precise measurement of the absolute frequency to a level of uncertainty of below 10^{-14}, as determined by the precision with which the instability level of the measured light at a given time scale can be evaluated in combination with the precision of the evaluated σ_{si}. While operating at MPIK, the H-maser exhibited an approximated a drift level of $5.5 \times 10^{-16}\,\mathrm{d}^{-1}$. The parameters of the setup are summarized in Table 3.6. All optical resonators undergo expansion due to the aging process. This results in a nearly linear decrease in resonance wavelength or an increase in frequency.

Furthermore, short-term fluctuations in ambient temperature can induce alterations in the resonator's length. While the resonator demonstrates instabilities in the mid 10^{-15} regime for averaging times in the order of 10 seconds, thermal effects elevate the instability above the 10^{-13} level after several hundred seconds of averaging time. This phenomenon is frequently well approximated by a linear function over time scales of an hour. The result of a linear fit to the raw data can be subtracted to reveal the underlying instability. However, this is usually done in post-processing. In contrast to the laser, the H-maser demonstrates a higher degree of instability at shorter time scales; however, it significantly surpasses the resonator at larger time scales due to its connection to a fundamental constant.

The reference laser displays instabilities in the mid 10^{-12} regime at 10^4 seconds, whereas the H-maser maintains a level of approximately 10^{-15}, which is three orders of magnitude more stable.

f_{ceo}	f_{rep}	f_{cb}	N_r	f_{cl}	N_l
20 MHz	250 MHz	±60 MHz	768×10^3	variable	1.0×10^6

Table 3.6: Parameters of the OFC: The beat f_{cl} can be variable in a range from $\pm(5-125)$ MHz, equaling half the comb mode spacings. The exact mode number N_l depends on the wavelength of the transfer laser but is approximately 10^6.

In order to capitalize on the short-term performance of the reference and the long-term stability of the maser, a feedback loop has been incorporated. The absolute frequency of the reference laser is measured by the optical OFC, which effectively measures the beat between reference light and the H-maser. This measurement is averaged over 20 seconds and corrected to a setpoint by acting on the DDS that drives the offset lock of the NEXCERA locked laser.

In this manner, the short term stability of the light locked to the resonator remains unchanged. However, long-term frequency variations and drifts are stabilized with respect to the maser. The quality of the lock can be observed in Figure 3.24. The reference light, including the drift mitigation, is measured against the other stable laser at 1.5 µm (blue), while the absolute frequency is recorded by the OFC (orange). The drift of the beat is removed. However as the NEXCERA-locked laser is steered to the H-maser, essentially the drift of latter laser is removed. Hence this system allows for the identification of individual drifts. The Allan deviation of the absolute frequency decreases to the 10^{-16} level after several hundred seconds.

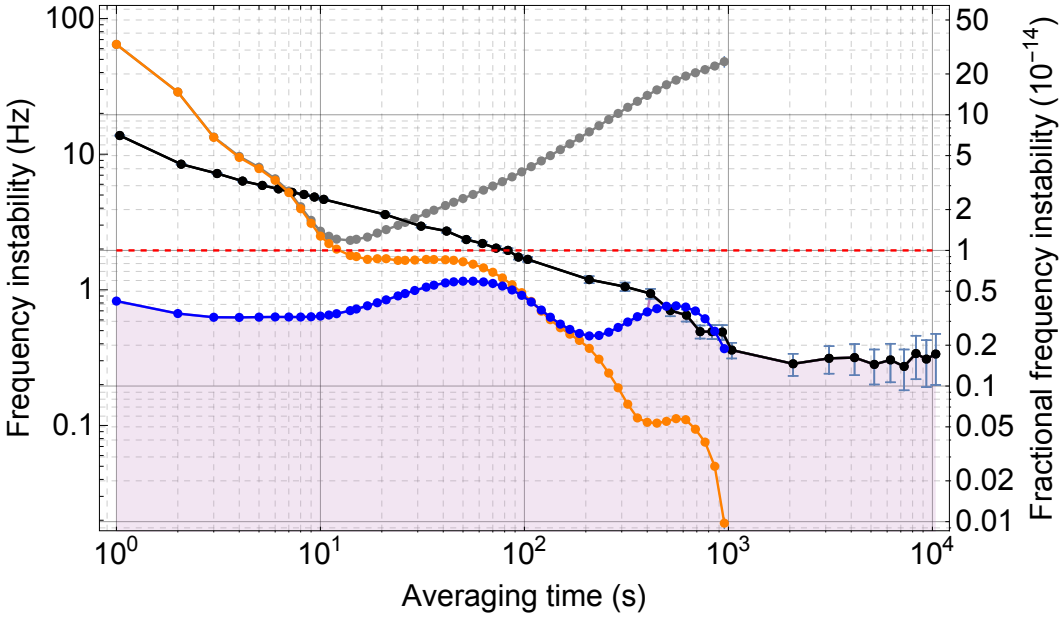


Figure 3.24: Allan deviations of the metrology system. Orange: Absolute frequency measurement of the reference laser by the OFC, thus of the reference against the H-maser. Gray: Orange data, when the DDS correction is added back to the signal. Black: H-maser stability. Blue: Simultaneous beat between the reference and another cavity stabilized laser, drift removed. The filled area below the curves the total instability of the reference laser.

Consequently, the discrepancy between the H-maser and the laser becomes negligible, resulting in the laser's convergence with the maser. The short-time instability of the orange line has been observed to exceed that of the maser instability (black curve). This limitation is imposed by the resolution of the frequency counter, which measures the repetition rate, due to a change in its settings for this specific measurement. However, the beat with the other ultra-stable laser exhibits a mid 10^{-15} level of instability at shorter time scales. With this configuration, the reference laser output and the comb lines have been short-time stabilized to the cavity and long-time stabilized to the maser, respectively. This results in an instability below 10^{-14} level (red dashed curve) at all timescales between 1 s and 10^4 s. Explicitly, the laser stability is between 2×10^{-15} and 6×10^{-15} level. Indeed, given that the maser generally exhibits an instability of below 1×10^{-14} for averaging times up to 10^5 to 2×10^5 seconds, it can be deduced that the laser would also demonstrate this instability up to this level, provided that the system remains operational. The gray curve illustrates the reference laser stability when the drift mitigation is deactivated, by reintegrating the correction signal into the data.

The absolute frequency is depicted in Figure 3.25 (a). In this instance, the comb is assigned a set point frequency with the objective of stabilizing the laser. As illustrated in magenta, the DDS correction exhibits fluctuations within a range of 4 kHz, with an additional drift of approximately 61 $\frac{\text{mHz}}{\text{s}}$ over a period of approximately 18 hours. This drift may be indicative of the thermal drift of the resonator; however, given the limited data available, such inferences would be speculative, as the observed time scale remains too brief to draw definitive conclusions. In fact, the long term drift of the NEXCERA resonator is exceptionally small and has been the key aspect of this thesis (see Section 6).

The resonator demonstrates a high degree of robustness in its lock. It has been locked for extended periods, often for months at a time, without any indication of failure or degradation. However, the longest uninterrupted period in which the OFC was locked was approximately two weeks. Due to a cross talk between the CEO and the repetition rate, the integrated slow locks of the comb are unable to be used. Consequently, the lockboxes will gradually approach the voltage limit of the respective slow lock output. Typically, the system can be locked for approximately three days before the respective lockboxes must be recentered. This recentering process is a manual procedure that requires several minutes to complete. It is performed via remote control.

The implementation of an automation process was a viable option; however, this was intentionally executed manually to ensure the system's regular monitoring. The integration of offset lock technique and drift mitigation has been achieved, enabling the frequency selection of the laser concurrently with active stabilization of the system. A shift in the laser frequency of the comb lines is achieved by modifying the setpoint or target of the drift mitigation and implementing a proper software-based feedback loop. The current DDS allows for the selection of any frequency within a 60 MHz band. The operational capacity of this band is constrained by the frequency-dependent output power of the DDS, a limitation that can be addressed through the implementation of a power stabilization technique or an alternative DDS. Figure 3.25 (b) presents a series of frequency sweeps in the order of MHz and kHz.

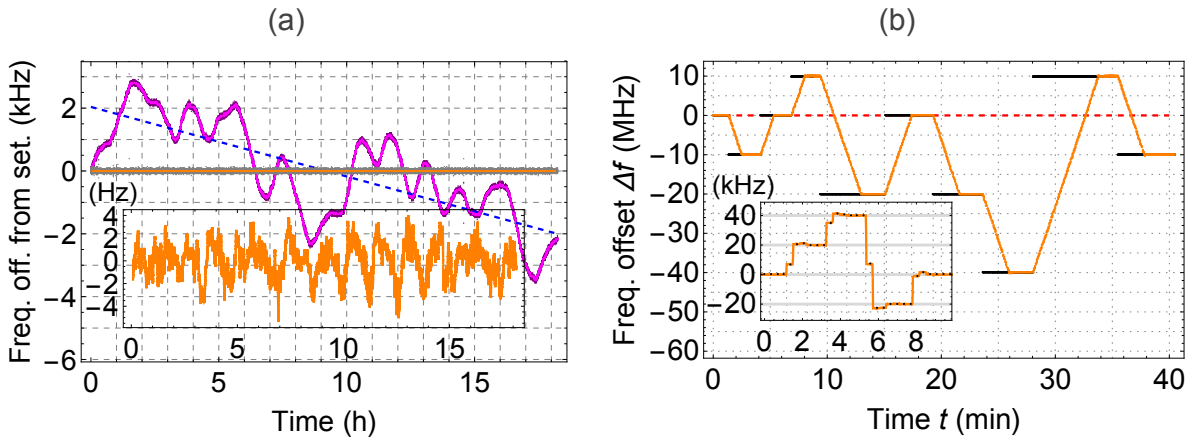


Figure 3.25: (a): Gray: The absolute frequency of the reference laser measured by the OFC. Orange: A 10 minute moving average of the gray data, also displayed in the inset. Magenta: DDS correction signal. Purple: The measurement of reference light, in conjunction with the DDS correction (Post-Processing). Blue: Linear fit over the cavity frequency variation (b) Frequency tuning of the OFC achieved through the offset lock on the EOM. The orange line illustrates the absolute frequency of the reference, as measured by the OFC. The red dashed line indicates the initial target frequency. The black lines in the large plot indicate when the target frequency is changed. Black dots in the inset indicate the frequency change of the DDS.

The absolute frequency of the reference laser was measured with the OFC, while the target frequency for the drift mitigation was changed. After applying a 50 MHz change in the target, the system was operative again within 300 s. Thus, the frequency sweep is as fast as about 150 kHz per second without losing lock. The frequency target can be tuned with a resolution of 300 mHz through the AOM, however due to the high instability of the measured absolute frequency at lower averaging times, it could only be properly measured and tuned with this resolution at over 10^3 s time scales. In this setup, the drift mitigation uses a moving average over 20 s, therefore a realistic resolution of the target switch is in the order of 2 Hz.

Automatic Restabilization of the System

A software-controlled auto-re-lock feature, actuated by stepper motors, has been installed on the lockbox of the reference resonator. This feature is intended to ensure the measurement time. The transmission signal from the resonator serves as an indicator of light stabilization. A decrease in transmission power activates an electronic circuit, which deactivates the active slow lock component of the lockbox and initiates a sweep of the laser frequency by altering the static slow lock offset through the use of a stepper motor. This process continues until the system detects a transmission signal once more. Subsequently, the motor ceases operation and the slow lock is reactivated. The slow lock offset can vary within a range of up to 1.5 GHz; however, during operation, it predominantly scans a specific band of approximately 50 MHz with a periodicity of approximately 4 s. Once the light to the resonator has been blocked or unlocked via software, the resonator lock is generally regained within this time frame.

The OFC generally attains full operational capacity within two minutes of such an event, which

involves the re-locking of the reference laser and the repetition rate, incorporating drift compensation through the H-maser. This considerably enhances the operational efficiency of the system, thereby ensuring optimal functionality during weekend and overnight periods. Errors, such as faulty locks or instabilities in the OFC or reference laser, are systematically logged and monitored by the software.

It monitors and records a total of over 50 independent signals within the comb system. The maintenance, frequency selection, and data collection functions are also remotely accessible. As illustrated in Figure 3.26, a critical failure of the system is demonstrated. At approximately the three-minute mark, the resonator lock was disrupted, preventing it from re-locking for approximately 24 seconds. Subsequently, the CEO lock was deactivated for a period of approximately six seconds. Consequently, the comb was subjected to full-scale free-running conditions, thereby simulating one of the most unfavorable potential scenarios.

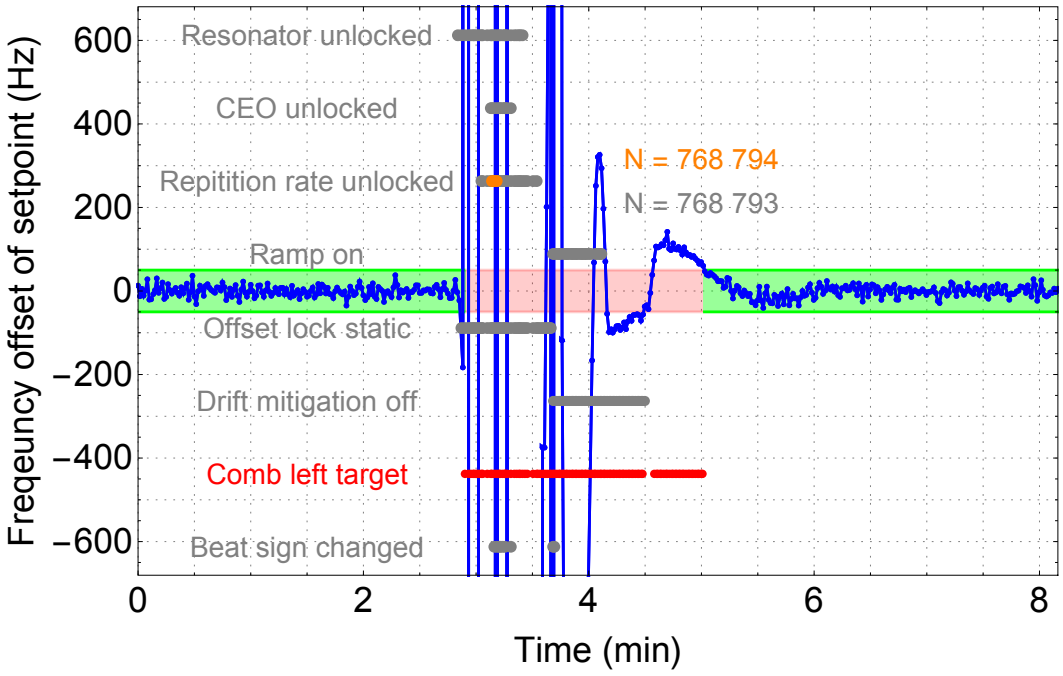


Figure 3.26: The automatic re-locking mechanism of the OFC and the NEXCERA stabilized reference laser. The blue curve indicates the absolute frequency measurement of the reference by the OFC. The green area illustrates the boundaries within which the system is considered operational. At approximately three minutes into the experiment, the reference laser's locking mechanism was remotely disrupted, and the CEO lock was manually deactivated and reactivated. This example is designed to replicate a critical failure of the system. Subsequent to this, the system autonomously re-engaged the lock with the H-maser within a span of two minutes. During that interval, the comb tooth number underwent modification and reversion to the original state. The error log is presented with its corresponding label and duration. The most significant of these is the "Comb left target". This measurement has been replicated on multiple occasions; nevertheless, this particular instance was the sole instance in which all the features of the re-lock were observed.

Subsequent to the disturbance being removed from the resonator light, the resonator exhibited a swift reacquisition of its lock within a few seconds. The repetition lock was stabilized to the reference light four seconds later, and the drift mitigation feature was immediately activated by ramping the frequency close to the set point within 20 seconds. Thereafter, the system collected data for a period of 20 seconds before fully engaging the drift mitigation and locking to the maser.

The figure also displays the mode number N_r of the repetition rate, which is fundamentally indicative of the repetition rate at which the comb oscillates in relation to the reference. In essence, the alteration of this number following a re-lock does not pose a concern. However, if it remains constant, it simplifies the work on the spectroscopy laser that is locked to the comb, as its designated comb tooth remains unchanged. It is noteworthy that the system typically locks to the same mode number, thereby maintaining a consistent repetition rate. In the event of a re-lock, there is a possibility that the system will attempt to lock to a different tooth.

However, this occurrence is often accompanied by a change in the beat sign, which is detected and corrected by the system. Consequently, the system will eventually regain its initial repetition rate. These events are infrequent, of which there is an example in the Figure. The system was restored to its previous operational state within approximately two minutes after the disruption. The measurement was conducted remotely from Düsseldorf, with the setup being operated at MPIK. The procedure is reproducible. The system was only interacted with through the artificial disturbance. The execution of the corrections was performed autonomously by the software.

A similar restabilization system was set-up within the scope of this thesis for the clock laser of the ground optical clock, at that time at PTB, that is to be compared to a space optical clock on the ISS as part of the ACES mission. There, a more sophisticated version, incorporating an applied voltage to the offset lock rather than a stepper motor, has been installed.

Comb and Laser Light Linewidths

For the measurement of the comb line width, a beat with the ultra-stable laser at 1064 nm was utilized. In total, 200 consecutive sweeps were recorded, with a RBW of 1 Hz and a sweep time of approximately 4 s, over a total time of approximately 16 min. The NIR laser was directed towards the comb via an unstabilized fiber that measured several meters in length. Figure 3.27 (a) illustrates the beats. The values presented herein represent the average of all 200 sweeps. The individual FWHMs are displayed in the inset histogram. The beat was tracked using a software program that enabled the overlaying and averaging of the sweeps. This tracking displays a similar effect to that of eliminating the slow drift; therefore, it remains subject to short-time frequency instabilities. The mean is represented by the blue data points. A Lorentzian fit over this data yielded a linewidth of 10 Hz.

This dataset closely corresponds to the system when the drift mitigation feature is engaged. The gray data exhibits equivalent mean values; nevertheless, the maximum values for each sweep are set at the same frequency. This would simulate a system of virtual frequency instability of zero, as the beat remains at a fixed position in time. This statement indicates that the lineshape of the beat is symmetric around the maximum, thereby ensuring that the average frequency of the

oscillator remains at a constant position. The data obtained from the histogram indicates that the frequency of the comb when interacting with the probe laser at a wavelength of $\lambda_p = 1064\,\text{nm}$ is approximately $\Delta f_{beat} = (7.5 \pm 3.3)\,\text{Hz}$, over a time span of 4 seconds. Over the course of approximately 16 minutes, the beat linewidth is observed to be in the order of 10 Hz, with occasional instances of short-term frequency jitter. Linewidth convolution is a complex process. However, for M uncorrelated sources, the total linewidth of the beat, denoted by Δf_{beat}, can be estimated by the sum of the individual linewidths (see Section A.5.2):

$$\Delta f_{beat} = \sum_{i=1}^{M} \Delta f_i$$

Here, the linewidth of the beat consists of the reference laser frequency Δf_r, the probe laser frequency Δf_p, the locking noise of the comb to the reference $\Delta f_{r,lock}$, and the transfer noise between the different comb lines given by the ratio of their wavelengths, such that

$$\Delta f_{beat} = \underbrace{\frac{\lambda_r}{\lambda_p}}_{\text{line transfer}} \left(\underbrace{\Delta f_r + \Delta f_{r,lock}}_{\text{comb line at } \lambda_r} \right) + \underbrace{\Delta f_p}_{\text{probe laser}} . \tag{3.3}$$

This can be used to establish limits on the linewidth of the spectroscopy laser when it is stabilized to the comb and the reference laser. The probe laser is part of a two-resonator configuration, comprising two resonators that are nearly identical for 1064 nm light.The linewidth of a beat between those lasers, employing the same method as for the blue data in Figure 3.27 (a), has been measured to be 6 Hz. In the course of the Three-Cornered Hat measurements conducted in the past (see Section 8.2), it was demonstrated that the phase noise spectra of both lasers are analogous, thereby indicating that a probe laser linewidth of $\Delta f_P = 3\,\text{Hz}$ can be assumed. The light of the probe laser undergoes broadening due to the presence of a fiber with a length in excess of 10 m between the systems. However, due to the absence of fiber noise quantification, the fiber noise is incorporated into the OFC linewidth as a conservative estimate. The resulting upper approximations for the Comb line linewidths are as follows:

$$\Delta f_{comb,1064} \approx 7\,\text{Hz}, \text{ and } \Delta f_{comb,1561} \approx 5\,\text{Hz}$$

The line at 1150 nm for the transfer laser is marginally narrower than the 1064 nm line. In addition, the PLL linewidths of CEO beat with the Maser, and the comb beat with the reference and the comb beat with the transfer laser are displayed in Figure 3.27 (b). Following the same treatment, with 40 consecutive sweeps of 1 Hz RBW, the individual linewidths are measured to

$$\begin{aligned} \Delta f_{pll,ceo} &= (0.84 \pm 0.01)\,\text{Hz} \approx 1\,\text{Hz} \\ \Delta f_{pll,ref} &= (0.98 \pm 0.06)\,\text{Hz} \approx 1\,\text{Hz} \\ \Delta f_{pll,transfer} &= (1.4 \pm 0.03)\,\text{Hz} \approx 1.5\,\text{Hz}. \end{aligned} \tag{3.4}$$

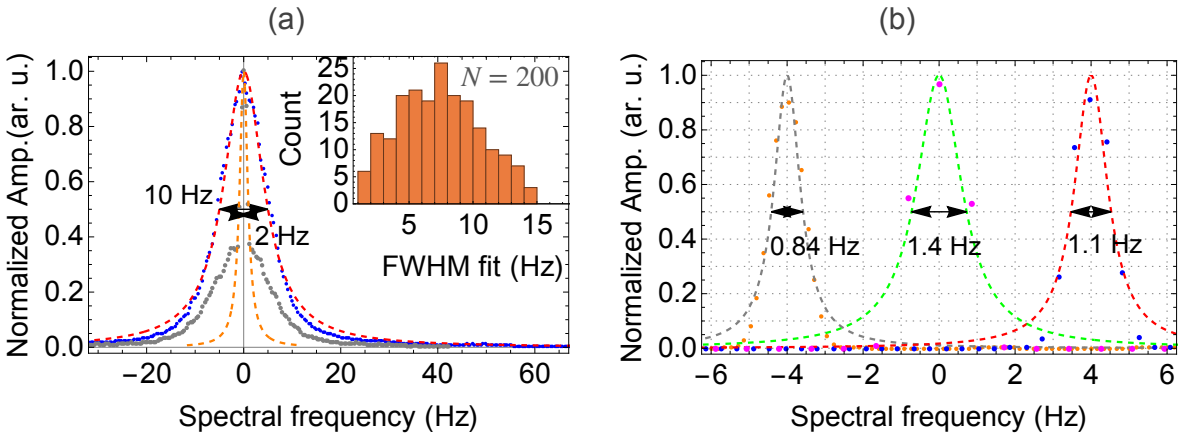


Figure 3.27: (a): Linewidth of the beat between the stabilized laser at 1064 nm and a comb line at the same wavelength. 200 consecutive sweeps of 1 Hz RBW with a sweep time of about 4 s were recorded. The software tracked the peak such that the slow drift of the beat was compensated. The blue line corresponds to the average, if all data sweeps are overlaid. The grey data corresponds to the average, if all sweeps are centered to the same frequency and then overlaid. The histogram shows the values of the fitted FWHMs of all sweeps when employing a Lorentzian function. (b): Linewidths of the three PLL loops, measured with a RBW of 1 Hz. Each line is the average of 40 consecutive sweeps. Different spans of the measurement explain the different distances of frequency bins. Orange and Gray: CEO lock. Magenta and Green: Lock of the transfer laser to the OFC. Blue and Red: Lock of the OFC to the NEXCERA reference.

It is conceivable that the linewidths are constrained by the RBW of the measurements and do not correspond to an actual broadening. Nevertheless, they can be utilized as an upper bound. Furthermore, the CEO and Comb PLL linewidths are already incorporated into the comb lines. Consequently, the only additional broadening is attributable to the PLL of the transfer laser.

Eventually, the linewidths of the laser can be conservatively approximated as 5 Hz for the reference laser and 7 Hz for the transfer laser. This includes a significant correlation to the reference laser. Utilizing the values of the histogram data, the linewidths are determined to be 2 Hz for the reference laser and approximately $3-4$ Hz for the transfer laser. In the absence of substantial linewidth broadening originating from the DFG module, the linewidth of light at MIR, particularly at 4.2 µm, is predicted to be less than 10 Hz under all circumstances.

Spectral Frequency Noise Density

The spectral purity of the OFC can be characterized by the spectral frequency noise density $S_f(f)$ of the light. It is connected to the single sideband phase noise, designated as $\mathcal{L}(f)$, with units of $\frac{\text{dBc}}{\text{Hz}}$, via

$$S_f(f) = 2f^2\, 10^{\frac{\mathcal{L}(f)}{10}}. \tag{3.5}$$

A detailed explanation is found in Section A.5.2. The phase noise is obtained through the analysis of frequency spectra, with varying spans between 500 Hz and 5 MHz, in increments of a factor of

10. These spectra are then normalized to the carrier strength and the respective RBW. The normalized spectra are finally arranged into a single plot. In Figure 3.28, the corresponding frequency noises, $\sqrt{S_f(f)}$, of all PLLs are presented (gray, purple, red), along with the comb line beat with the 1064 nm laser (blue) and the beat between the reference laser and the second laser at 1.5 µm (black). Here, it is important to note that all plots, with the exception of the one at 1064 nm, have been scaled to 1.5 µm.

Consequently, the blue line can be compared to the others on the relative scale but not on the absolute scale. The light of the 1064 nm laser was measured against a second laser at the wavelength. In general, the beat with the comb is dominated by the noise of the comb line itself, especially for higher frequencies. The peak at 1.59 MHz originates from the sideband of the PDH configuration of the NIR light. The reference light is the limitation at frequencies below 1 kHz, as demonstrated by the black line. In the case of higher frequencies, the PLL-induced noises of the repetition rate and offset locks become the predominant factor.

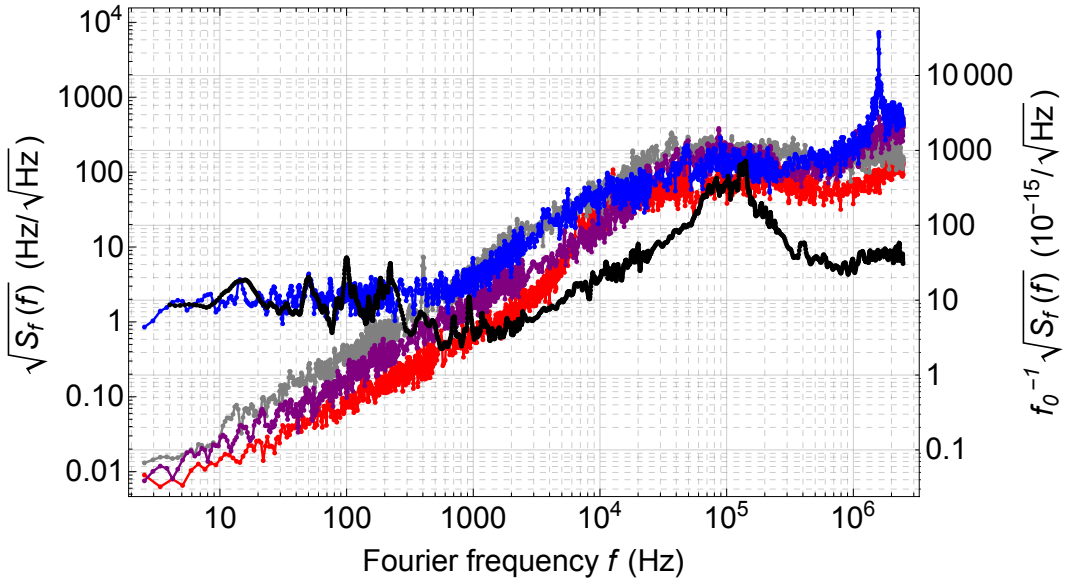


Figure 3.28: Spectral frequency noise spectra of all beats in the setup. Red: Repetition rate PLL. Gray: CEO PLL. Purple: Transfer laser PLL. Black: Beat between the reference laser and the other 1.5 µm cavity stabilized laser. Blue: Beat between one of the 1064 nm cavity stabilized lasers and the closest OFC line. The peak at 1.59 MHz originates from the PDH sideband of the 1064 nm system. All PLLs are scaled to be compared to the OFC reference light. They can be compared on the absolute and relative scale to the black line. The blue line can be compared at relative scales.

Fiber Noise Cancellation

The process of transporting light between laboratories introduces an additional source of noise, stemming from mechanical effects such as vibrations or acoustics, which manifest through the optical fiber. This effect is highly dependent on the environment and is most frequently observed at frequencies below a few kHz. The noise can be characterized and compensated for, but it is difficult to predict. In the FNC configuration, the fiber path noise is inversely mapped to the light

to generate stable light at the output in the other laboratory. To ensure the reliability of the setups, extensive testing has been conducted using fibers of lengths up to 4 km. A real-world example of the FNC for 1.5 µm of the fiber path measuring several hundred meters between two laboratories in HHU is shown in Figure 3.29 (a) and (b). In this experiment, the frequency noise and linewidths of the self-beat are measured while the FNC is off or on.

When the FNC is engaged, it is evident that both low-frequency noises and linewidth improve. The linewidth is likely constrained by the RBW of 1 Hz. Upon deactivation of the FNC, a broadening of the light's linewidth is observed, reaching hundreds of Hertz. This compensation has been demonstrated to be both robust and reproducible for any length of fiber, even under conditions of externally induced large mechanical noises. The 50 m long fiber path between the experiment and the laser laboratories is inconsequential.

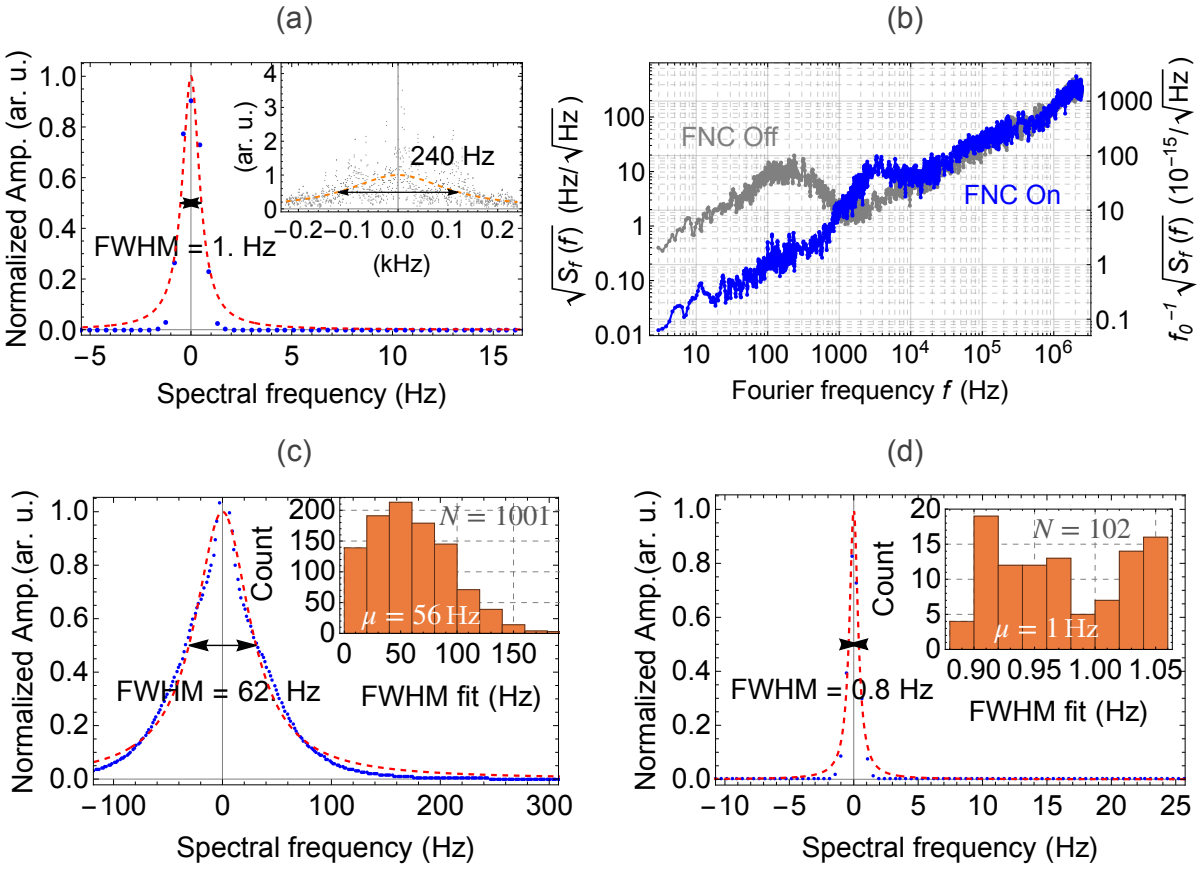


Figure 3.29: (a): Power spectra of the self beat of the 1.5 µm FNC setup for several hundred meters of fiber. Blue and red: FNC on. Gray and orange: FNC off. The dashed lines correspond to Lorentzian fits. (b): Spectral frequency noise density of the self beat of the 1.5 µm FNC setup for several hundred meters of fiber. Blue: FNC on. Gray: FNC off. (c) and (d): Power spectra of the self beat of the 1.15 µm FNC setup for the fiber path between the metrology lab and ALPHATRAP. The insets show the histogram of FWHM fits of about 10^3 and 10^2 consecutive sweeps, respectively. (c): FNC off. (d): FNC on.

It has been determined that this path will not cause a change in the linewidth of the lasers, with a maximum variation of 1 Hz when the FNC is engaged. Therefore, the light that arrives at the experiment does not exceed linewidths of 10 Hz over any given time span. Figure 3.29 (c) and (d) correspond to measurements of the fiber path of the transfer laser at MPIK to the trap laboratory when its FNC is turned off (panel (c)) and on (panel (d)). A broadening of the line width up to 60 Hz is exhibited by the 50 m long fiber. Upon activation of the FNC, the occurrence of this broadening is effectively eradicated, as evidenced by the linewidth and histogram measurements.

EDFA Noise

The intrinsic noise of the EDFA was evaluated through two distinct methodologies. A self-beat of the NEXCERA locked laser light, with one arm propagating through the EDFA, is the first of these. The frequency shift was performed on an EOM at 50 MHz. The EDFA was configured to maintain a constant power output of 50 mW. The beat was analyzed in terms of its spectrum from 10 Hz to 1 MHz, as well as its linewidth. In Figure 3.30 (a), the red curve illustrates the frequency noise density of the self-beat. The schematic is shown in Panel (c).

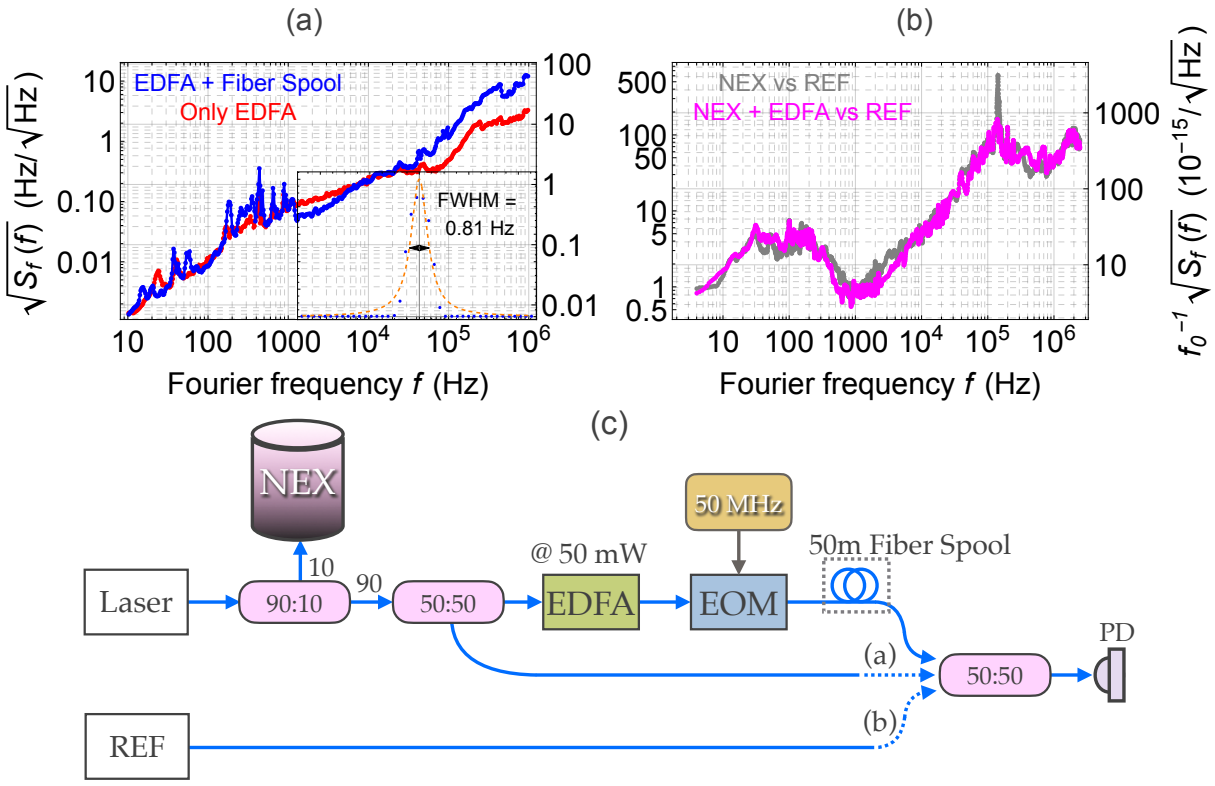


Figure 3.30: Measurement of the frequency noise induced by the EFDA and a 50 m long fiber spool. (a): Frequency noise spectrum of the self-beat of one arm propagating through the EDFA (red), and an additional fiber spool (blue). The inset shows the linewdith of the red curve, however, the linewidth of the blue curve looks identical. (b): Beat between the EDFA amplified NEXCERA-stabilized light and the reference laser (magenta) compared to the non amplified beat (gray). The peak in the gray line around 10^5 Hz was a parasitic signal that could be eliminated after that measurement.

The linewidth inset is an average of four consecutive sweeps of 1 Hz RBW and a sweep time of 4 s. Furthermore, the blue curve illustrates the self-beat of the light subsequent to its travel through a 50 m fiber path, which is coiled on a spool. It is evident that neither measurement introduces appreciable noise to the laser, particularly at lower frequencies. In panel (b), the beat between the NEXCERA locked laser and the reference laser is shown with and without amplifying the NEXCERA laser using the EDFA. Once more, no substantial alterations are discernible. This finding indicates that the EDFA does not induce a significant level of instability in the spectroscopy light.

Summary

This configuration enables the complete functionality of a frequency metrology system, incorporating cross measurements of the RF reference with other facilities, such as the PTB, and absolute frequency measurements. The results indicate frequency instabilities at the sub 10^{-14} level for averaging times ranging from 1 s and 10^5 s . These instabilities can be attributed to the short-term locking of an optical resonator and the long-term locking to an RF source. The OFC, in conjunction with any referenced light, can be tuned to any frequency within a band of 60 MHz with respect to the reference wavelength, while maintaining a locked state. In the event of larger frequency offsets, the system can be tuned to a frequency within the thermal tuning range of the reference and output ranges of the OFC. With the exception of a few tens of centimeters of free space light coupling into the optical resonator, the system is fully fiberized. FNC setups have been engineered to mitigate mechanical noises along the fiber path between the laboratories. This ensures that the light utilized for experimental purposes remains narrow and spectrally pure. The system will enable the creation of broadly tunable MIR light with linewidths in the order of 10 Hz. The system meets and surpasses the objectives outlined in the proposal, and it is currently employed in a measurement campaign on HD^+ in ALPHATRAP during the writing of this thesis (see Section 8.4).

Chapter 4

Developments in Ultra-Stable Lasers

Contributions to the field of ultra-stable lasers that have been made within the work of this thesis will be discussed in this chapter. This includes the reference and characterization of an ultra-stable OPO that was utilized as a spectroscopy laser, guidelines for the setup of ultra-stable lasers at state-of-the-art performance levels, research on transmission filtering of optical references and reduction of the frequency stability limitation due to RAM.

4.1 Mitigation of RAM below Thermal Noise

As previously outlined in Section 3.1.4, the impact of residual amplitude modulation can impose a limitation when aiming to stabilize light at or below the 10^{-16} level of fractional frequency instability. A theoretical approach, incorporating losses, has been introduced in Section 2.3.3. It can be recalled that the contribution of RAM to the fractional frequency instability of the locked light, denoted by σ_f, is expressed as:

$$\sigma_f = \frac{f_c}{\nu_0}\sigma_M, \text{ with } \sigma_M = \underbrace{M' \cos(\gamma)}_{:=M_{eff}} \begin{cases} 1 & \text{[88]} \\ \underbrace{\frac{1}{4\sqrt{\rho}}}_{\text{carr. to sb. correction}} & \text{[86]} \\ \underbrace{\frac{1}{4\sqrt{\rho}} \frac{V\rho + (1+2V)}{1-V}}_{\text{loss correction}} & \text{This work} \end{cases} \tag{4.1}$$

The impact of RAM as an effect in impurities of PHM leading to spurious AM has been a subject of extensive research. As posited by [87], the phenomenon can be attributed to the unequal strength of the individual sidebands, a consequence of the birefringence exhibited by the crystal alignment in relation to the polarizer axis. It was demonstrated that the addition of a DC voltage to the system can effectively suppress RAM, resulting in a comparable effect to that of rotating the crystal. [90] conducted an analysis of RAM due to imperfect phase modulation in the EOM. An examination of RAM can also be found in [131]. In the study by [132], the impurity of the PHM leading to AM was suppressed by active temperature stabilization, yielding a RAM level of $M_{eff} = 2.5 \times 10^{-5}$. Consequently, in [133], the combination of slow temperature stabilization of the modulator, and

fast actuation on an electro-optical crystal in front of the EOM resulted in RAM below the 10^{-6} level. As demonstrated by [134], it is possible to suppress RAM to a level below 10^{-5} by reducing photo refractive scattering due to spatial variations in the beam shape inside the EOM using a counter-propagating beam.

As demonstrated in the study by [88], the RAM was successfully reduced to the 10^{-6} level through the implementation of active suppression, which incorporated DC offset and temperature control. This study was conducted within the context of lasers stabilized to optical resonators. In [135], RAM was evaluated in the context of the PDH scheme. At that juncture, the effect had already been demonstrated to exhibit characteristics of a separated parasitic etalon effect and the birefringence effect, as previously discussed. Their effect on cavity-locked light was thoroughly investigated. Etalon effects [136] are a form of PHM/FM that manifest when light enters a material with two parallel surfaces, akin to an optical resonator. Reflections between the surfaces, such as in waveplates, EOM crystals, or in free space optical paths featuring PBS and mirrors, will convert into spurious AM.

The loss correction factor, derived in this thesis, is not entirely novel in its idea. A comparable analysis has previously been conducted in [92], wherein the effects of impedance and mode matching were examined in the context of RAM within the PDH scheme. In both cases, it is acknowledged that losses/impedance matching and coupling efficiency can have substantial impacts on RAM in the error signal. In the study by [89], the experimental findings demonstrated the capacity to reduce the RAM to a level between $(2-5)\times10^{-7}$. This translates to $(0.8-2)\times10^{-17}$ level, in terms of fractional frequency. This objective has been accomplished by modifying an EOM through the addition of wedged surfaces with respect to the input and output beam. This resulted in a separation of the propagation axes of the electromagnetic wave, which could subsequently be filtered.

Recent advancements in the field have led to significant improvements in the suppression of RAM with the lowest recorded level being between $(1-4)\times10^{-7}$, as reported by [86]. This achievement was made possible by the implementation of temperature stabilization, power stabilization, and a DC offset to the EOM. Eventually, the findings suggest that untreated RAM can act as a hindrance to the performance of state-of-the-art stable lasers. However, it is noteworthy that RAM can be suppressed to operate below the typical thermal noise floors observed in the most advanced optical references to date. Nonetheless, given the recent advancements in crystalline mirrors and cryogenic cavities, RAM may soon become a challenge once more.

This thesis will demonstrate an alternative approach to achieving RAM stability that is competitive with the most effective active and passive methods. The effectiveness of this approach is dependent upon a single parameter in the configuration: the modulation frequency. A notable aspect of the experimental configuration is the direct generation of the sidebands at the piezo of the Nd:YAG lasers, an approach that diverges from the conventional method of external EOMs. The impact of modulation frequency on RAM has been previously documented in the literature. This phenomenon has been investigated in the works of [91] and [137].

The latter work has already measured its effect on a system similar to the one described in

this thesis. Specifically, the work measured the effect on a Nd:YAG laser at 1064 nm, sideband modulated at the piezo. The findings indicated that for sidebands within the range of 500 kHz and 900 kHz, the RAM level exhibited fluctuations within the range of $4\times10^{-5}$and 5×10^{-4}, approximately spanning one order of magnitude. The system utilized in [100], a predecessor of the one used here, evaluated the effect of RAM on the fractional frequency instability to $(2-7)\times10^{-17}$ on the observed time scales of 10 s to 2000 s. This thesis presents RAM contributions below the10^{-17} level with respect to fraction frequency instability at similar time scales, without (invasive) passive or active suppression on RAM.

Accordingly, the two ULE resonator configuration outlined in Section 3.1 is hereby considered. The experimental setup is illustrated in Figure 3.1. In order to assess the effect of RAM on the error signal, a PBS separates the light into two distinct paths. One of these paths is directed towards the resonator, while the other is directed towards another PD. This RAM detector is calibrated with respect to the reflection PD utilized for the PDH scheme concerning power levels. To obtain the RAM depth, Equation (2.74) will be used:

$$M_{eff} \coloneqq M' \cos(\gamma) = \alpha_\varepsilon(V,\rho)\,\alpha_f(V,\rho)\,\frac{P_{PDH}}{P_{RAM}}\,\frac{\varepsilon_{off}}{2\varepsilon_{pp}}$$

Here, the relation of power in the carrier and sideband is $\rho = \frac{P_c}{P_s}$, and the loss correction is $V \to V(r,\delta)$. To evaluate this formalism, it is necessary to ascertain the parameters P_c, P_s, r, and δ. This objective can be accomplished by measuring the total power at the reflection detector in lock $P_{pdh,res}$ and off resonance $P_{pdh,off}$, the resonator linewidth f_c, i.e., through ring-down spectroscopy, and the peak-to-peak error signal strength, denoted by ε_{pp}, while scanning over the resonance. Assuming that the phase has been optimized while observing the error signal, thus $\phi = 0$, results in a set of four equations to be used to determine the parameters:

$$\left|\begin{array}{c} P_c + 2P_s = P_{pdh,res} \\ V(r,\delta)^2 P_c + 2P_s = P_{pdg,off} \\ -4\sqrt{P_s P_c}\,(V(r,\delta)-1) = \varepsilon_{pp} \\ \frac{\Delta\nu}{\pi}\,\frac{1-r^2\delta^2}{r\delta} = f_c \end{array}\right| \tag{4.2}$$

Please note that $\delta = 1$ would describe a lossless system. The following parameters were determined in the setup of L1 locked to C2: $\rho_{c2} = 7.2$, $\delta_{c2} = 0.999998$, and $r_{c2} = 0.999995$. The coupling efficiency is about 43 %, thus the loss parameter becomes $V_{c2} = 0.76$. This indicates that the actual RAM in resonance is approximately three-quarters of the signal measured off resonance, suggesting an inherent improvement found in the coupling into the resonator. The carrier-to-sideband strength is consistent with the observations of the beat note of the light locked to the resonator. The α_i coefficients are thus expressed as follows: $\alpha_\varepsilon = 1/3.1$ and $\alpha_f = 1/1.3$. Therefore, compared to the respective lossless ($V = 0$) coefficients it is:

$$\underbrace{\frac{\alpha_f(V_{c2},\rho_{c2})}{\alpha_f(0,\rho)} \approx 8}_{\text{frequency instability}}, \text{ and } \underbrace{\frac{\alpha_f(V_{c2},\rho_{c2})\,\alpha_\varepsilon(R_{c2},\rho_{c2})}{\alpha_f(0,\rho_{c2})\,\alpha_\varepsilon(0,\rho_{c2})} \approx \frac{1}{4}}_{\text{RAM depth}} \tag{4.3}$$

While the RAM depth is essentially lower, when losses are concerned, because a part of the measured value is already accounted for the coupling efficiency loss, the actual frequency instability is almost an order of magnitude worse. Consequently, this imposes an additional improvement for future systems. A cross-check of these parameters is illustrated in Figure 4.1. Here, the error signal is experimentally determined by locking one laser to one resonator and sending this pre-stabilized light to the other. An AOM is employed to gradually modify the frequency over the resonance of the second resonator, while concurrently measuring the DC outputs of the transmission and reflection detector. In Section 3.1.3, the measurement is discussed in the context of linewidth measurements. The red curve illustrates a simulation, not a fit, of the error signal using the experimentally determined parameters from above and Equation (2.58):

$$\begin{aligned}\varepsilon_{ram} = {} & 2\sqrt{P_s P_c}\,\Im\left[F^*(\omega)\,F(\omega+\Omega) - F(\omega)\,F^*(\omega-\Omega)\right]\cos(\phi) && \text{(b)}\\ & - M'(P_c + 2P_s)\,\Re\left[F^*(\omega)\,F(\omega+\Omega) + F(\omega)\,F^*(\omega-\Omega)\right]\cos(\phi)\cos(\gamma) && \text{(f)}\\ & - 2M' P_s \cos(\phi)\cos(\gamma) && \text{(j)}\end{aligned}$$

As previously mentioned, the Lorentzian fit over the transmission data yielded a linewidth of approximately 2 kHz, which corresponds to the value determined by the finesse measurement. A subsequent outcome of the figure was that the peak-to-peak strength of the error signal, while scanning with low amplitudes, can be compared to the actual peak-to-peak strength. This streamlines the measurement of RAM.

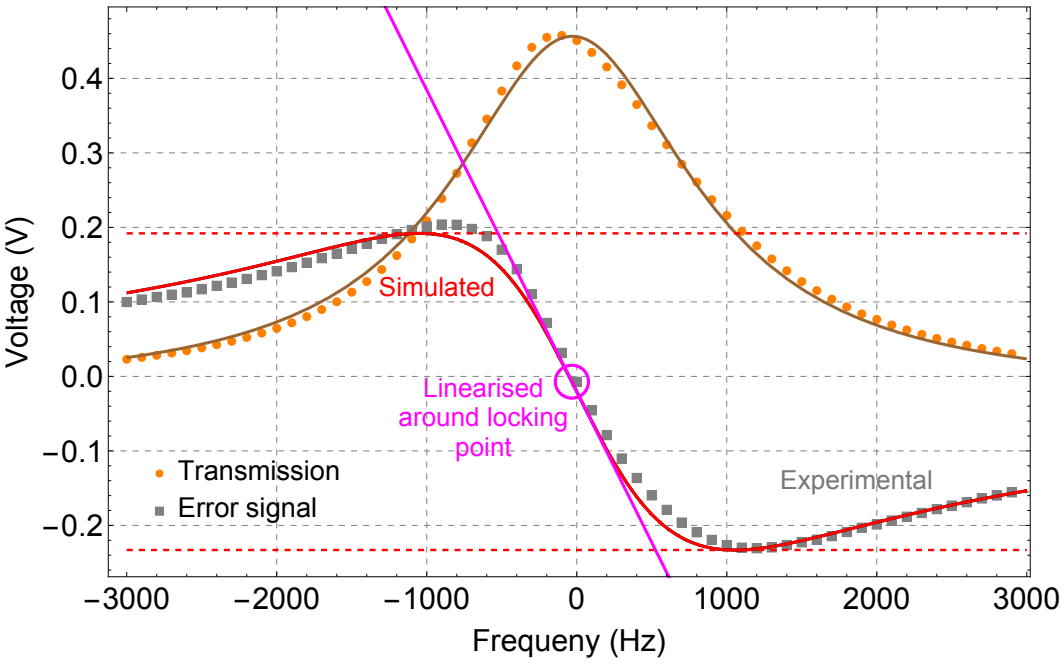


Figure 4.1: Transmission profile (orange) and error signal (gray), measured while slowly scanning pre-stabilized light over the resonance mode of the cavity. The red curve is a simulation of the error signal based on Equation. (2.58). The red dashed lines indicate the peak to peak strength based on Equation (2.67). The magenta line is the linearization around the locking point based on Equation (2.68). The brown line is a Lorentzian fit over the transmission profile.

The gray data was not obtained consequent to the parameters in Equation (4.2) but rather on a different day where phase and power have been optimized again. This finding indicates that the evaluation of the parameters is robust. The effect of RAM appears to vary at different modulation frequencies, exhibiting specific resonances. In particular, frequencies exist at which the RAM depth is minimized. The RAM depth can be evaluated by measuring the peak-to-peak strength of the error signal and the amplitude of the AC output of the reflection detector at the modulation frequency (when the laser is detuned from the cavity resonance) using a SA. For each modulation frequency (between 600 kHz and 4.2 MHz), the phase of the error signal has been optimized again. The data is displayed in Figure 4.2 (a).

This landscape indicates that modulation frequencies at 1.6 MHz introduce RAM at the 10^{-3} level, while tens of kHz away, the level is approximately 2×10^{-6}, representing an improvement of a factor of 500. The measurement was reiterated at the minimum, as illustrated in the inset of the plot. The optimal frequency was determined to be 1.6468 MHz. A similar landscape plot for C1 is presented in panel (b). However, at the optimal frequency of approximately 2.3 MHz, the system did not attain a stable and robust lock. Consequently, the frequency was reduced to 1.59 MHz, which demonstrated stability and provided an adequate RAM depth. The contribution of fractional frequency instability is displayed on the respective right axes. The interpretation of this measurement is that the estimated RAM depths lead to offsets of the locking point at the levels of 4×10^{-17} and 10^{-15} at the corresponding operating frequencies for C2 and C1.

It is important to note that for C2, the landscape surrounding the ideal frequency has been analyzed in greater detail. In this analysis, the discrepancy between the broad measurement (orange) and the most precise measurement (red) results in an order of magnitude improvement in the RAM depth. This has not been done for C1 at 1.59 MHz, which may serve as an explanatory factor for the observed discrepancy. When both orange lines are compared, the RAM depth of C1 is approximately five times greater than that of C2. Nevertheless, this instability manifests as an offset of the lockpoint. The time-dependent fluctuation of the RAM depth, in turn, yields the actual RAM contribution to the frequency instability.

In order to validate the time variation of RAM while locked to the resonator, the RAM detector was calibrated towards the PDH detector in terms of power. Subsequently, the AC signal of the RAM detector is mixed down using the same oscillator and same model mixer as for the error signal. The demodulated signal is the object of measurement by a DAQ card. The voltage can be converted into terms of power, thereby providing the time variation of ε_{off}. A comparison with the power measured by SAs at the AC output demonstrated an accurate reading of the DAQ card. The peak-to-peak strength of the error signal has been measured at multiple intervals; however, no observable change has been detected. The power of the resonator was stabilized at the transmission detector, with no discernible correlations to the RAM signal. However, given that the measured voltages are approximately 60 µV, the noise accuracy of the DAQ card becomes a salient issue, particularly at lower averaging times.

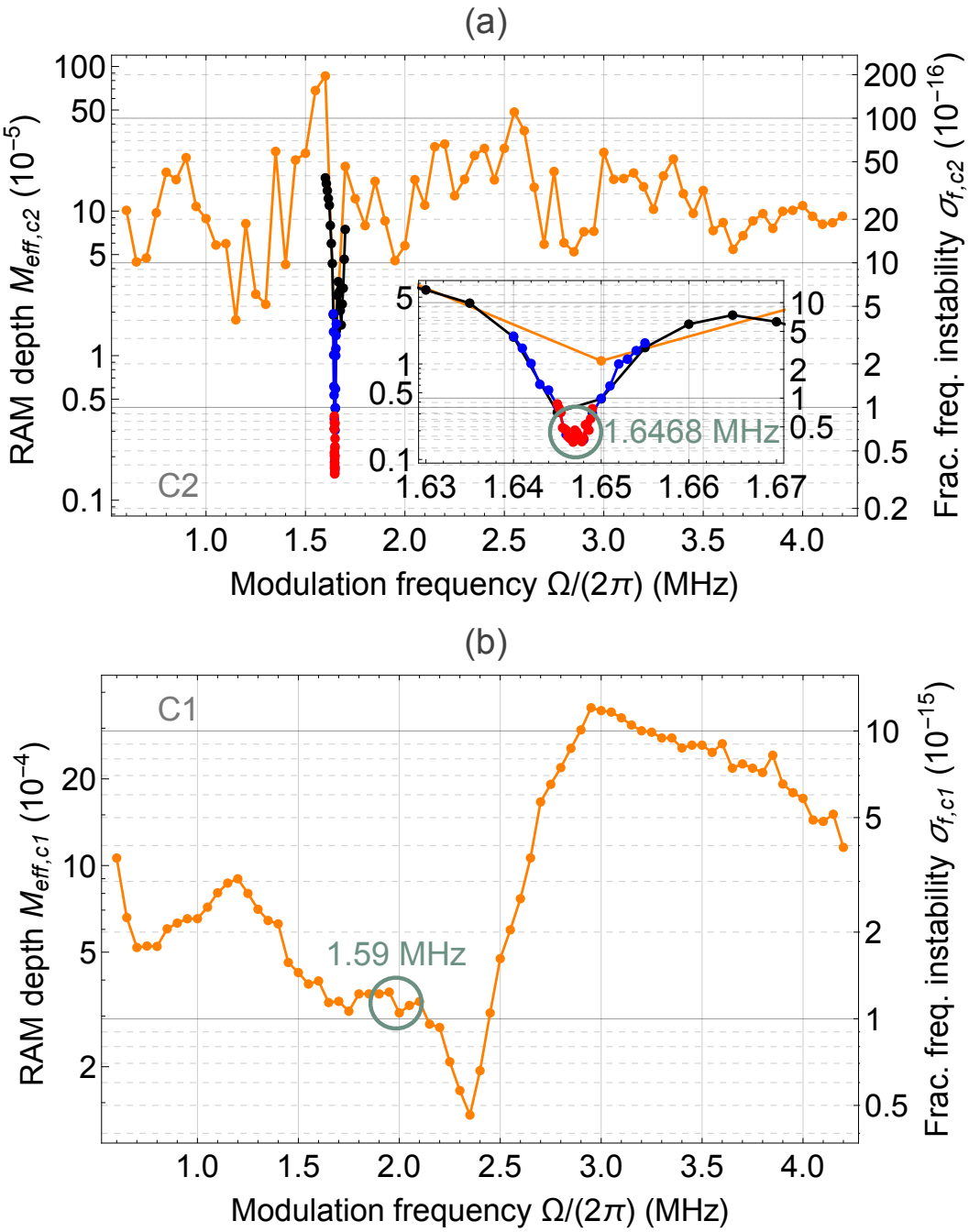


Figure 4.2: RAM depth landscape measurements on (a): C2 and (b): C1, with respect to the sideband modulation frequencies. The Inset in the upper plot shows the refined measurements around the ideal sideband frequency. The green circles indicate the actual operating frequencies for each system. Note that for C1, due to instabilities of the lock, this frequency is not equal to the optimal one. The left axis is chosen in a manner that it is directly comparable to RAM depth found in literature.

The dashed lines in Figure 4.3 represent the DAQ card noise floor of the respective measurements. For C2 (red) at time scales below 5 s, there is a possibility of a contribution resulting from the measurement itself. Nevertheless, for averaging times starting from 5 s, the RAM is at the 1×10^{-6} level, reaching down to almost 2×10^{-7} above 500 s. This contributes to fractional frequency fluctuations between $(5-10)\times10^{-18}$ level for averaging times above 5 s, which could also be the case for averaging times below if the noise of the DAQ card is considered. However, if this is not the case, RAM exhibits an upper limit at the 3×10^{-17} level at 1 s averaging time, rendering it competitive with the most advanced active (orange, [86]) and passive (magenta, [89]) compensation techniques.

For C1, the overall RAM is larger than for C2 starting from $(2-3)$ s averaging times. It peaks below the 3×10^{-17} level in terms of fractional instability reaching levels below 10^{-17} above 150 s averaging time. The gray line in the plot represents the combined limitation due to RAM in the beat of both lasers. To date, even most cryogenic resonators would not be constrained by this noise with respect to their thermal noise limit. This renders the technique suitable for application in next-generation systems. However, given the thermal noise floor of 4.5×10^{-18} of the resonator in [118], further suppression of RAM would be necessary. It is theoretically possible to enhance the RAM in this work by another factor of $7-8$ for near-perfect in-coupling to the resonator. Eventually, the beat-note between the resonators has been observed in the high to mid 10^{-16} level, approximately a factor of 5 away from the thermal noise floor at around $(1-2)\times10^{-16}$. This discrepancy is attributed to other environmental effects, such as tilts and vibrations.

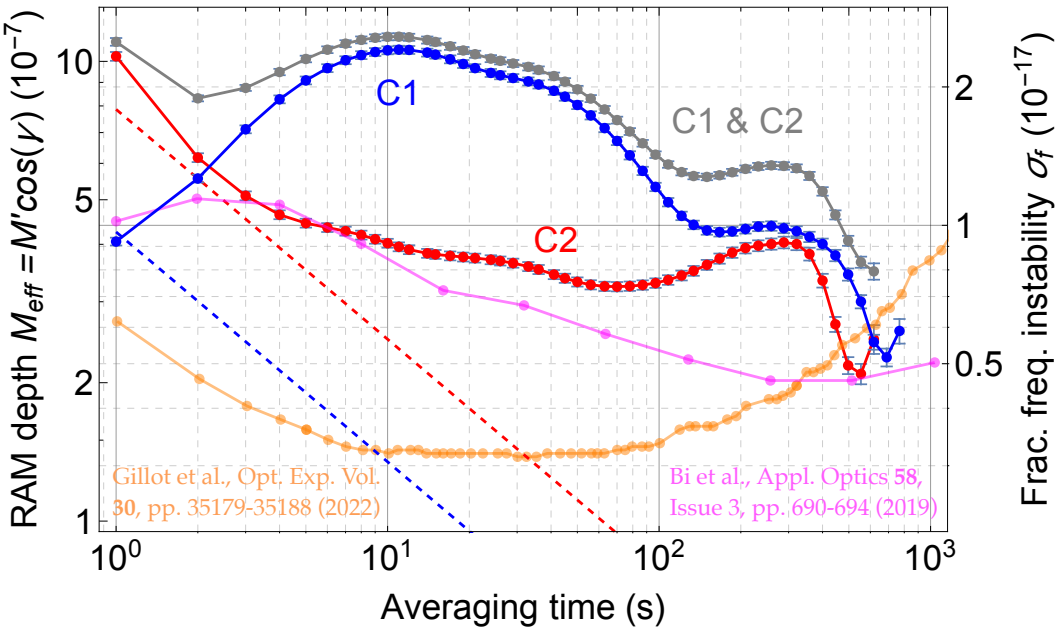


Figure 4.3: Allan deviations of the RAM depth for both cavities. Red: C2. Blue: C1. Gray: The combined effect of RAM of both resonators on the beat instability. The dashed lines show the noise floor of the DAQ card that was used to record the RAM detector signal. The magenta line shows the, to date, best passive approach to reduce RAM [89]. The orange line presents the best active suppression [86].

Summary

In conclusion, this section demonstrated a methodology for attaining a suppression ratio of RAM below 10^{-17} level in terms of fractional frequency instability. This was achieved by identifying and operating the system at its optimized modulation frequency. However, this result is specific to the employed laser type due to the particular method of sideband modulation and cannot directly be transferred to any fiber and diode laser.

4.2 Transmission Filtering: Resonators as Mode Cleaners

Thus far, it has been demonstrated that an optical reference, such as a FP type cavity, can be utilized to suppress frequency variations in time, laser linewidth, and phase noise. The time evolution of the frequency is found to be strongly dependent on the deformation of the resonator, while linewidths, and more specifically, the entire phase noise spectrum, are found to be dependent on the locking bandwidth of the PDH scheme. The magnitude of suppression, in turn, is related to the cavity linewidth. Typically, the servo bandwidth of the lock is of order 100 kHz. At higher frequencies, the cavity-locked laser is essentially free running. Nonetheless, the resonator can be utilized to suppress phase noise at frequencies above the locking bandwidth within the context of a mode cleaner (MC). In this configuration, the transmitted light of the laser will be filtered by the resonators transmission profile, determined by its linewidth.

In the study by [138], an optical resonator with a linewidth of 160 kHz was utilized as a MC, and an effect was observed and analyzed at frequencies exceeding 4 MHz. In [139], frequencies exceeding 10 MHz were analyzed with a MC with a linewidth of 1 MHz. While the effect was observable, it was found to be smaller than the theoretical prediction. Another analysis was performed with a 5 MHz wide MC in [140]. [141] utilized a high-finesse ULE resonator with a 9 kHz linewidth as the MC, and injection locked a higher power light to the relatively weak transmission signal. In the study by [142], a 2.1 MHz wide MC was utilized to achieve a 40 dB reduction in phase noise within the observed high frequency domain. In [143], the phase noise of a 6.55 kHz high finesse resonator was evaluated using the beat between transmission and incident light. A setup employing a 2.5 MHz and a 30 MHz MC was evaluated in [144].

In the study by [145], a resonator with a linewidth of 140 kHz was utilized as MC. The transmission signal of the resonator was strategically implemented as a feedback mechanism to mitigate the phase noise of the cavity-locked laser. A noteworthy contribution in this area is the work of [146], which utilizes the higher frequency components of the PDH error signal and integrates a feedforward lock on an EOM to suppress phase noise. While the latter work does not fall within the scope of resonators as MC, it aligns with the fundamental objective of the initiative. A commonality among the aforementioned works is the utilization of the transmission profile for the purpose of cleaning the phase noise spectrum. However, this utilization occurs predominantly in the context of low to medium finesse resonators, or without an emphasis on the concrete behavior at low frequencies.

A case in point is the search for dark matter, which necessitates a high degree of spectral purity. The works that will be mentioned in this thesis (see Sections B.1.1 and 7.2, Publications in

B.1.1 and B.1.2) require low-frequency fluctuations starting from Fourier frequencies of 100 Hz. In this section, an analysis of the transmission signals of the dual-resonator system described in Section 3.1 and the resonator detailed in Section 3.2 is conducted within the low-frequency domain. A comparison is made between the theoretical predicted suppression and the actual experimental data.

Dual ULE Cavity Setup

The transmission profile can be modeled by the intensity function, given by the Lorentzian shape of the cavity mode line, as expressed in Equation (2.3). Specifically, this function is expressed as

$$I(f) = \frac{\left(1-r^2\right)^2}{1-2r^2\cos\left(2\pi\frac{f}{\Delta\nu}\right)+r^4}.$$

Within this formula, the mean mirror reflectivity r and the FSR $\Delta\nu$ are utilized. For the sake of conceptual clarity, the losses are not addressed. In the case of the two-resonator ULE system, the beat between the light locked to the cavities can be analyzed and converted into its frequency noise spectrum, $S_f(f)$ (see Section A.5.2, setup in Figure 3.1). The transfer function T of the beat can be determined through experimental means by measuring the beat incident $S_{f,in}(f)$ to the cavities, and the transmission $S_{f,tr}(f)$, respectively:

$$S_{f,tr} = T^2 S_{f,in}$$

The transfer function can be expressed in terms of the individual cavity mode intensity profiles, $I_1(f)$, and $I_2(f)$, as well as the individual noise spectra, $S_{f,1}$ and $S_{f,2}$ of the respective incident light, according to the equation

$$S_{f,tr} = \left(I_1 S_{f,1} + I_2 S_{f,2}\right) \approx (I_1 + I_2) S_f. \tag{4.4}$$

Here, it was utilized that the overall noise of both cavity-locked lasers is similar, a claim that can be verified in Section 8.2. This would imply that $S_f := S_{f,1} \approx S_{f,2}$. This further simplifies the incident frequency noise to

$$S_{f,in} = S_{f,1} + S_{f,2} \approx 2S_f. \tag{4.5}$$

Inserting Equation (4.5) into (4.4), yields

$$S_{f,tr} \approx \frac{1}{2}(I_1 + I_2) S_{f,in} \Longrightarrow \frac{S_{f,in}}{S_{f,tr}} = \frac{2}{I_1 + I_2}.$$

One common approach involves the analysis of the square root of the frequency noise density, $\sqrt{S_f}$, resulting in the definition of the transfer function T of the system as follows:

$$T^{-1} = \frac{\sqrt{S_{f,in}}}{\sqrt{S_{f,tr}}} = \alpha\frac{\sqrt{2}}{\sqrt{I_1 + I_2}} \tag{4.6}$$

The parameter α was incorporated to account for a fixed factor between the spectra that was not accounted for by the cavity modes. In words, the transfer function $T(f)$ describes the suppression of the phase noise of the light in transmission of the resonator, with respect to its incident noise at a particular Fourier frequency f. The transmitted beat was measured by directing the transmitted light of both resonators to a PD in free space. For the purposes of this measurement, the power of the lasers was not stabilized, as all power was allocated to the beat. Figure 4.4 (a) illustrates the experimentally determined beats of the phase noise, with a red dashed line denoting the noise floor of the PD for the measurement of the transmitted (cyan) light. This measurement reaches that limit at approximately 10 kHz due to the low power (S/N ratio) in the transmitted light.

The black line in the figure indicates the phase noise of the incident beat. This noise is not limited at the observed frequency range due to its substantial S/N ratio. The transmitted phase noise is observed to be lower than that of the incident light, exhibiting an intriguing phenomenon beginning at low frequencies that are well within the mode linewidth. The effect of the transmission filtering is expected to become dominant for frequencies that are approximately above half the linewidth, such that they are highly suppressed due to the lineshape. In this experiment, however, a constant factor of reduction in the transmitted light is observed. A methodology for determining this is to convert the phase noise to frequency noise. Panel (b) of Figure 4.4 illustrates the inverse transfer function as given by Equation (4.6). The gray curve corresponds to the experimental data, while the red curve represents a simulation that incorporates the individual transfer functions I_1 and I_2. The parameter α was determined through a fit, yielding

$$\alpha = 3.88(4) \approx 4.$$

Notably, the measurement of the beat note of the incident light was conducted at the cavity breadboard. There are still certain path lengths and optical elements between this detector and the front mirrors of the cavities. It is plausible that this could be the underlying cause of the observed α factor.

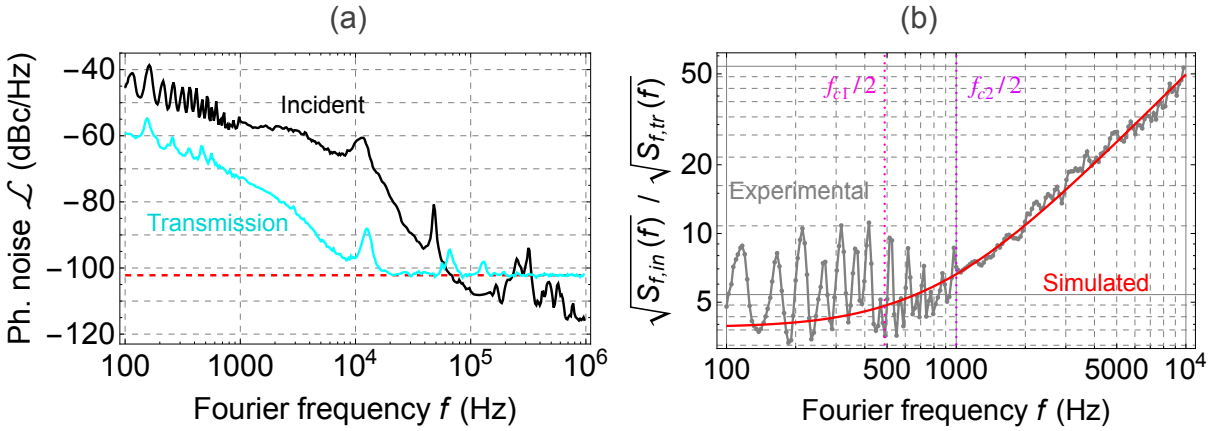


Figure 4.4: (a): Phase noise measurements were obtained for the beat between C1 and C2 for both incident and transmitted light. The red line in the figure indicates the PD noise floor of the transmission measurement. (b): A plot of the experimentally determined (gray) and theoretically simulated (red) inverse transfer function T^{-1}. The dashed lines indicate the half-cavity linewidths.

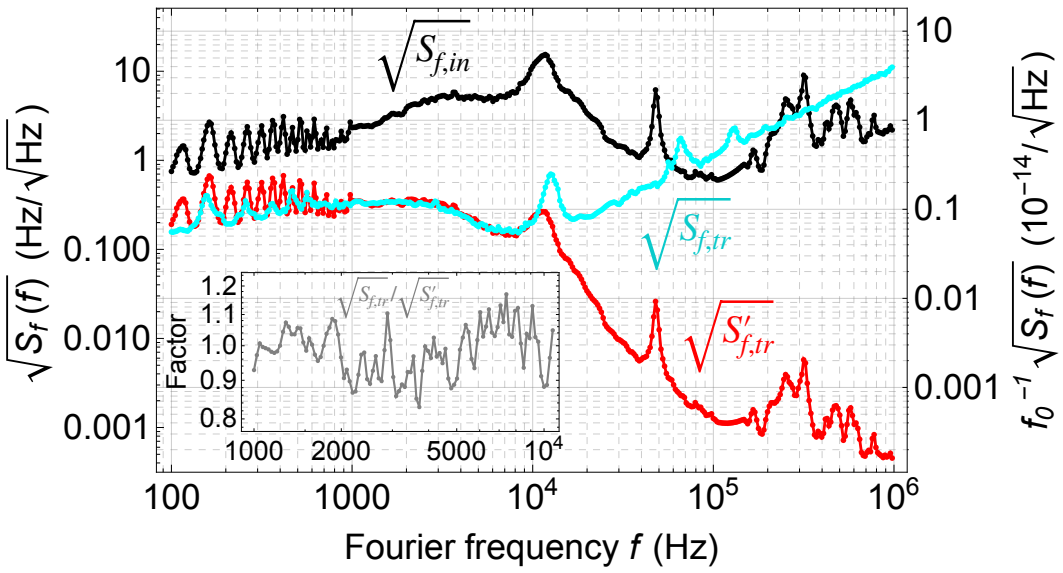


Figure 4.5: A comparison of the frequency noise of incident and transmitted light. The red line shows the theoretically predicted transmission signal when the transfer function T is applied to the black line. The cyan curve represents the experimentally measured transmission signal. In the inset, the gray line serves as a visual representation of the relation between the experimental and theoretical signal.

The simulated and experimentally determined transfer functions demonstrate a high degree of agreement specifically above half of the larger cavity linewidth $f_{c2}/2 \approx 1\,\text{kHz}$, indicated by the purple dashed line. At lower frequencies, where the filtering effect has not yet become apparent, variations between the two are discernible. Nevertheless, the overall shape remains consistent, even when accounting for the approximation made in Equation (4.4). The application of the theoretical transfer function to the incident beat data results in the predicted transmission data , $\sqrt{S'_{f,tr}}$, which is represented by the red line in Figure 4.5. The relationship between the experimental (cyan) and predicted (red) curves is displayed in the inset up to $10^4\,\text{Hz}$. It is evident that there is concurrence within a $\pm 10\,\%$ margin for the majority of the frequencies.

As a result, it can be deduced that the actual transmitted light will likely follow the red curve if the signal-to-noise ratio of the measurement is increased. However, the data does not allow for determination of the point at which other, fundamental, effects may become dominant. Nevertheless, a reduction of a factor of 50 was observed at the spectral frequency noise density at 10 kHz, even with the experimental data. This results in a phase noise suppression of 30 dB. This renders the transmitted light of high finesse resonators a valid choice for applications that require exceptional frequency noise at low frequencies (i.e., frequencies of less than 100 kHz). Indeed, between 100 kHz and 10 kHz, the frequency noise of the transmitted beat is at and below the $10^{-15}\,\text{Hz}^{-1/2}$ level. Therefore, it can be concluded that a single laser may exhibit frequency noise below $5\times10^{-16}\,\text{Hz}^{-1/2}$.

NEXCERA Cavity

An additional measurement was conducted on the NEXCERA-stabilized laser and the other ULE-stabilized 1.5 µm laser utilized for its characterization. In this configuration, the power of transmission was coupled into fibers and subsequently combined by a tap coupler to a photo diode. Both lasers had to be operational for measurement campaigns, necessitating the division of a portion of the transmission for the purpose of power stabilization. Consequently, the resultant beat frequency exhibited insufficient power to facilitate meaningful analysis. However, it was possible to measure the incident light of both cavities against the transmitted light of the other, thereby providing an opportunity to characterize the transmission filtering.

An intriguing measurement is the beat $S_{f,3,sb}$ between the incident $S_{f,3,in}$ and transmitted $S_{f,3,tr}$ light of the same resonator, here NEXCERA. In essence, this will result in the elimination of frequency noise that is present in front of the cavity, but not behind it. In the Figures 4.6 (a) and 4.7 (a), the orange curve illustrates this beat in terms of phase or frequency noise, respectively. In the frequency noise picture, this curve is small at low frequencies, within the cavity linewidth $f_{nex}/2 \approx 900\,\mathrm{Hz}$, where it represents a self-beat, but grows for larger frequencies. At 1 kHz it surpasses the transmission beat of the individual ULE-locked lasers (cyan line Figure 4.4 (a)) This is due to the still a significant common noise in the transmission and incident light around the cavity linewidth in addition to the already low level of noise at this frequency. This finding suggests the presence of a significant disparity between incident and transmitted light. Mathematically, this discrepancy can be expressed as

$$S_{f,3,sb} = S_{f,3,in} - S_{f,3,tr}.$$

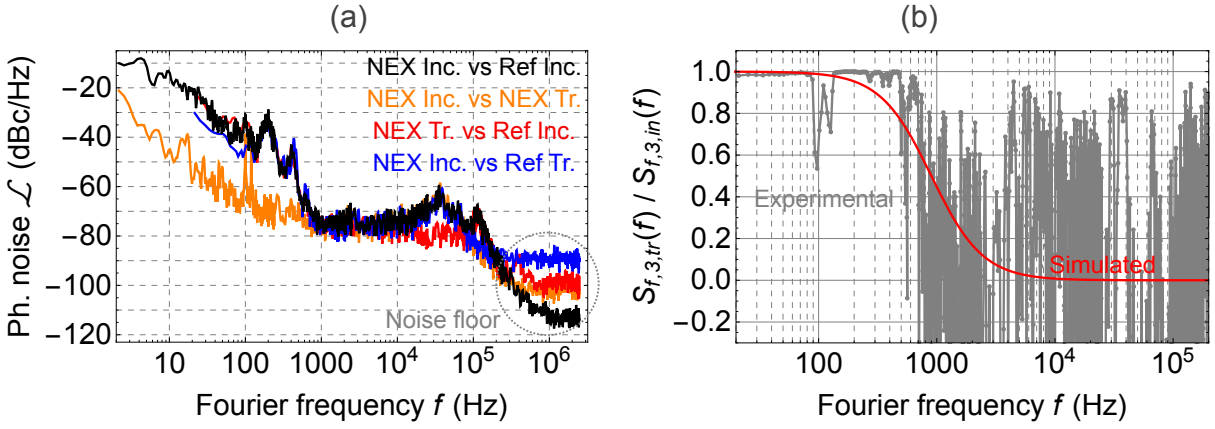


Figure 4.6: (a): Phase noise spectra of various beats between transmission and incident light of the NEXCERA (NEX) stabilised light and the ULE cavity (REF). the orange line is the "self-beat" of the NEXCERA system (b): Experimentally determination and theoretical simulation of the transfer function T^2_{nex} for the NEXCERA light. Due to the inherent limitations of the phase noise measurements, the data becomes more susceptible to noise at higher frequencies.

By re-expressing the transfer function T, through $S_{f,3,tr} = T_{nex}^2 S_{f,3,in}$, gives the expression

$$T_{nex}^2 = 1 - \frac{S_{f,3,in} - S_{f,3,tr}}{S_{f,3,in}} \approx 1 - \frac{S_{f,3,sb}}{S_{f,t}}. \tag{4.7}$$

The frequency noise of the incident light can be estimated by the noise of the beat $S_{f,t}$ between the incident light of the NEXCERA cavity and the transmitted light of the other, reference, resonator (blue curve). At lower frequencies, the latter resonator may contribute more significantly. However, this contribution disappears at higher frequencies. Consequently, no correction factor is applied in this case. Accordingly, experimental testing of the Equation (4.7) is possible through the establishment of a relationship between the frequency noise of the orange curve and the noise of the blue curve. A simulated solution of T_{nex}^2 is represented by

$$T_{nex}^2 = \frac{S_{f,3,tr}}{S_{f,3,in}} = I_3^2(f),$$

as illustrated by the red line in Figure 4.6 (b). A certain degree of congruence is evident between the simulated and experimental data. Nevertheless, the resolution and precision with which the frequency noise can be measured may impose constraints on the analytical approach. However, the conceptual notion of a modest effect in proximity to the carrier frequency, accompanied by a more pronounced suppression at greater distances, persists. The utilization of various beats aids in the identification of the origin of specific sidebands within a laser setup. Peaks at 37 kHz are evident in the blue, orange, and black curves but absent from the red curve.

This observation indicates that these peaks are part of the NEXCERA setup, as the red curve is the only one in which NEXCERA's transmitted light, consequently the highly filtered light, is utilized. The same argument holds true for the ULE resonator with regard to the peak around 113 kHz. This method would therefore enable the characterization of independent lasers without the necessity of a third system or a three-cornered hat analysis for frequencies above the cavity linewidths. Figure 4.7 (b) illustrates the theoretical transmitted frequency noise $S'_{f,3,tr}$ of the NEXCERA cavity, as depicted by the gray data. This theoretical predicted noise is calculated by applying the transfer function T^2 to the blue data, thus $S_{f,t}$. The gray curve is at $10^{-15}\,\mathrm{Hz}^{-1/2}$ level at frequencies above half the cavity linewidth.

Summary

The data from NEXCERA and the two ULE cavities demonstrate that laser light in transmission of an optical cavity can attain a level of instability in the frequency noise regime of $10^{-15}\,\mathrm{Hz}^{-1/2}$ already at relatively low frequencies (100 Hz to 1 kHz), which further benefits of the mode cleaning at higher frequencies. This property is advantageous for applications requiring exceptionally pure spectra, as it facilitates the determination and reduction of noise peaks. Furthermore, at frequencies exceeding half of the cavity line width the transmission signal acts as a low noise reference and this method essentially transforms into a two-cornered hat analysis of the frequency spectrum, thereby eliminating the necessity for a third oscillator.

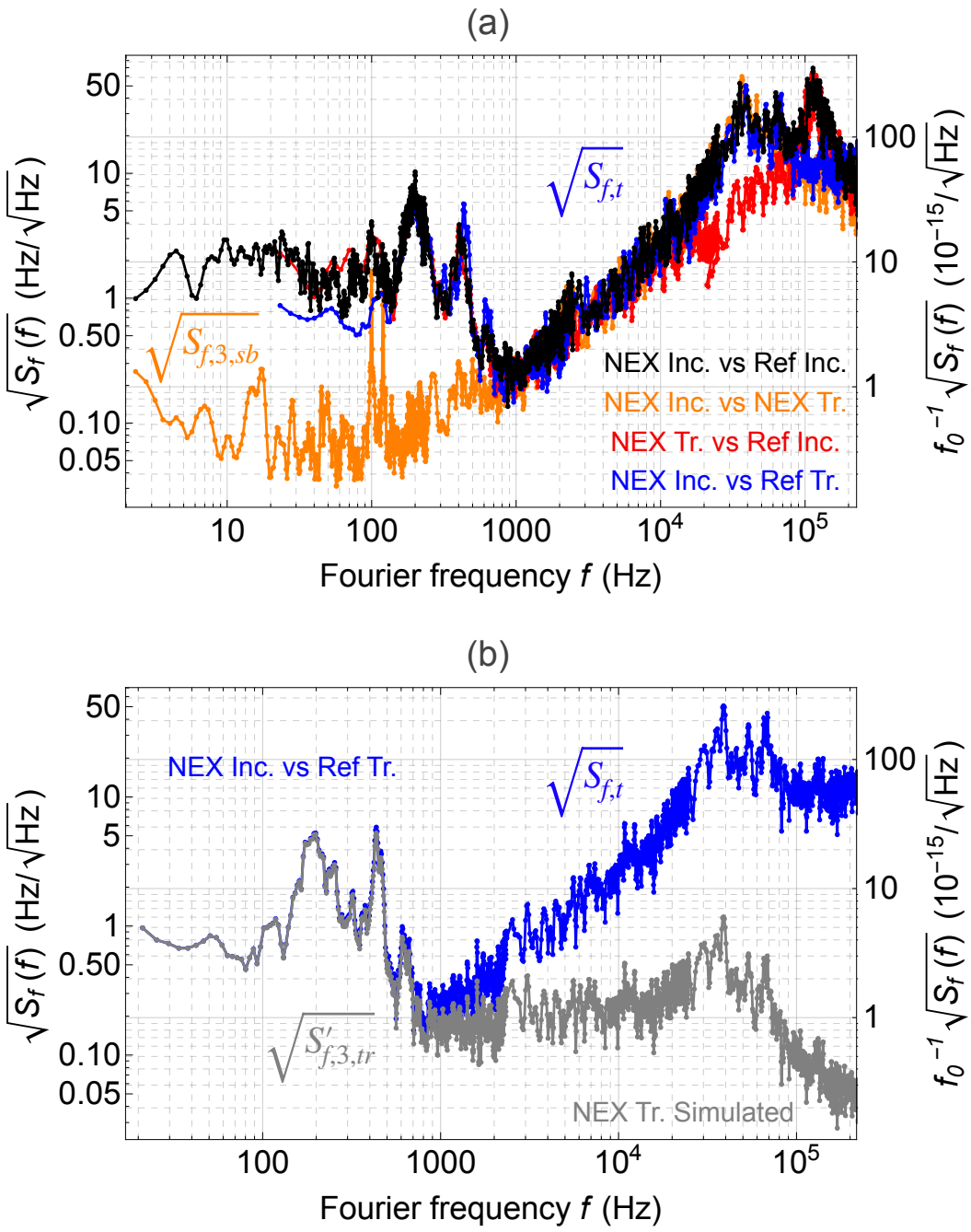


Figure 4.7: Frequency noise density for (a): the beats shown in Figure 4.6. Below half the cavity linewidth of NEXCERA, the orange line is close to a self-beat. (b): the theoretically predicted transmitted light of the NEXCERA resonator. The transfer function T was applied to the blue data because it can be estimated that NEXCERA light is the dominant factor at higher frequencies.

4.3 An Ultra-Stable Optical Parametric Oscillator

Referenced work: Schenkel et al., Metrology-grade spectroscopy source based on an optical parametric oscillator, Opt. Express 32 (2024) pp. 43350-43365 [68]. Publication in Appendix B.3.1.

In order to measure the rovibrational transition in H_2^+, [35] employed a transfer laser that was locked to an OFC (see Section 8.3). The responsibility for the transfer laser was attributed to an associate of the experiment, M. Schenkel. The OFC and, consequently, the laser were referenced to one of the ultra-low frequency (ULE)-based dual resonators described in this thesis (see Section 3.1). The novelty: The transfer laser is an optical parametric oscillator (OPO), which is a device that converts light of a pump frequency, ω_p, into a signal, denoted by ω_s, and an idler, ω_i, output. The formalism of the OPO is expressed as:

$$\omega_p = \omega_i + \omega_s.$$

This concept was employed to generate light that is capable of being tuned over a wide range and can be stabilized. The pump laser operated at a fixed wavelength of 1064 nm during all experimental phases. Conversely, the idler and signal frequencies were capable of being tuned. The idler wave typically exhibits wavelengths in the order of 2 µm and above. Stabilization of this wave can be achieved through frequency doubling or wavelength halving. These stabilization techniques involve the use of SHG and locking the light to an OFC via a PLL. Therefore, mid-infrared light could be utilized for experimental purposes while also capitalizing on the stability of the reference of the OFC.

The novelty of an ultra-stable OPO was emphasized in this referenced work. In order to characterize the performance of the OPO, its stabilized light was evaluated by another OFC, namely the NEXCERA-based metrology system (see Section 3.3). Therefore, the light of the OPO could be characterized by an independent frequency comb with an individual reference laser. The sole shared oscillator was the H-Maser, which was measured in relation to the PTB against the standard time. The performance of the frequency comb, NEXCERA resonator, and ULE-stabilized light has been thoroughly delineated in this thesis; therefore, further exploration will not be pursued here.

Additionally, the publication contains a sufficient number of measurements and analyses to evaluate the performance of the OPO at a technical level, rendering additional characterization redundant at this point. The author of this thesis contributed to the obtaining and evaluation of the data. The reference laser for the comb to which the OPO is locked, as well as the setup for the second OFC with its reference, which were utilized for the characterization in the publication, were designed, set up, and operated by the author of this thesis.

4.4 Guidelines for Ultra-Stable Lasers at the 10^{-17} Level

Referenced work: Barbarat et al., Guidelines for designs for ultra-stable laser with 10^{-17} fractional frequency instability, arXiv (2025) [67]. Publication in Appendix B.3.2.

A report on the developments of next-generation ultra-stable lasers was published, and it included a section characterizing NEXCERA as an alternative to ULE glass. The analysis specifically concentrated on the utilization of NEXCERA as a spacer material. This was achieved by determining its loss angle and characterizing its stabilization of light to two high finesse resonators. One of these resonators was the 12 cm resonator utilized in this study (see Section 3.2). The objective of the manuscript was to provide a concise overview of the guidelines necessary to achieve a level of 10^{-17} stability for resonator-stabilized lasers.

In this regard, a presentation of the NEXCERA laser's top Allan deviations and Linewidth measurements indicate the upper limits for the thermal noise floor of the material. Figure 4.8 presents the Allan deviation of the laser, which was measured against a second 1.5 µm cavity stabilized laser in the laboratory. In this section, a data set is presented for the Allan deviation, which differs from the data set presented in the manuscript. However, this does not alter the conclusions of the analysis.

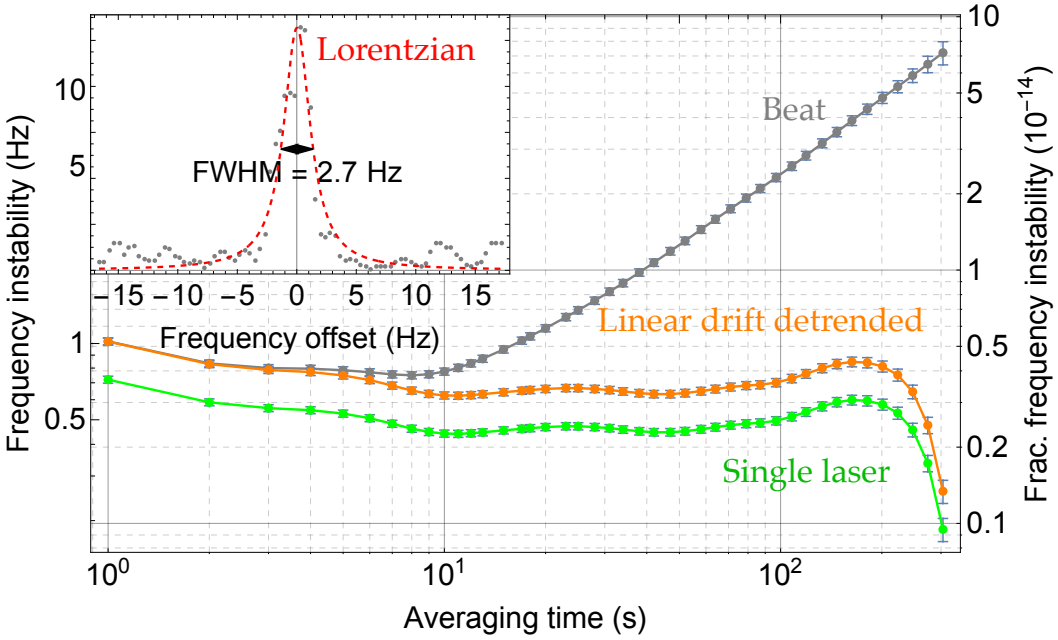


Figure 4.8: Allan deviation and linewidth measurements of the NEXCERA stabilized laser in comparison to other ultra-stable lasers. The line-width measurement is normalized such that the ordinate is rendered irrelevant. The orange line in the graph represents the data of the gray line, with the linear drift of the measurement being subtracted. The green line represents an approximation of a single laser, under the assumption that both lasers contribute equally. The Allan deviation was measured against a laser at 1.5 µm, while the linewidth was measured against a laser at 1064 nm using the OFC, which was stabilized to NEXCERA.

The Allan deviation is based on a beat at the optical frequency of the NEXCERA locked light at 195 THz, while the linewidth was measured at a comb line (stabilized to NEXCERA) at 282 THz, against one of the dual cavity lasers presented in this thesis (see Section 3.1). The total linewidth (FWHM of a Lorentzian fit) was measured to below 3 Hz. Therefore, it can be argued that the linewidth of the NEXCERA laser is amplified by approximately $\frac{282}{195} \approx 1.4$ at the comb line frequency. Additionally, the locking noise of the comb is also present in this beat. The reference laser at 282 THz exhibited a linewidth of the order of 1 Hz, suggesting that the NEXCERA laser in this particular measurement also exhibited a linewidth of the order of 1 Hz at its own optical frequency.

A conservative upper limit of the thermal noise floor is approximately at the 3×10^{-15} level, as indicated by the detrended beat (orange) at 10 s averaging time. This is attributable to the fact that the instability contribution of the individual lasers is unknown and the sharp decline in Allan deviation on longer time scales may be a mathematical artifact. However, under the supposition that both lasers contribute to the same extent, a reasonable estimation for the limit of the frequency instability of a single laser (green) would be at the 2×10^{-15} level. This would be an order of magnitude above the theoretical determined thermal noise floor for this cavity and an identical ULE-based cavity. Given the straightforward configuration of a single heat shield on a compact breadboard, absent tilt stabilization and acoustic shielding, this level of stability is noteworthy.

Chapter 5

Non-Cryogenic Fiber Ring Resonator

The concept of fiber rings has existed for decades. SFRRs with a finesse of 80 have been previously documented in [147]. The method of a DFRR and several fiber rings as a frequency filter using the transmission profile is demonstrated in [148]. The stabilization of a fiber ring to light, by the use of a piezo actuator, has been demonstrated in [149]. In this study, the fiber ring was utilized to transfer the frequency stability of light. Mirroring silicon filters have been documented in the literature, specifically in the works of [150, 151, 152]. These studies have primarily focused on the application of these filters in the domain of frequency filters or frequency modulators.

The works of [153, 154] are the first on this list to actively stabilize light to a FRR in the application of an opto-electronic oscillator to create a 10 GHz RF wave. In their work, the researchers obtained a measurement of thermal sensitivity that corresponded to $6.8 \times 10^{-6}\,\mathrm{K}^{-1}$. Spiral resonators have been demonstrated to attain short-term stability levels of 3.9×10^{-13} at an averaging time of 400 µs, as reported by [155]. In the works of [156, 157], a laser was stabilized to a fiber ring. The former reports a linewidth narrowing down to 60 kHz, and the latter shows an improvement at short-term fluctuations below 1 s averaging time to 1.5×10^{-12} level.

[158] present a report on a 4 m long FRR locked laser with a linewidth as low as 2.8 kHz for short time scales, which is susceptible to thermal drift over longer time scales. Consequently, [159] demonstrated an enhancement of 40 dB in the spectral phase noise density when a free-running laser was stabilized to a 2 m long fiber ring at frequencies below 1 kHz.

The most ambitious advancement in the field is the 120 m long cryogenic FRR reported on in [160]. This FRR is based on a Corning® Clear Curve® [161, 162] fiber and has an operating wavelength of 1.5 µm. The ZCTE temperature was found to be 3.55 K, with a short-term instability of 10 kHz, approximately $< 10^{-10}$ level. The frequency drift was measured to be less than 10^{-9} over a period of 16 hours.

Consequently, the utilization of fiber rings in the domain of frequency filtering has gained significant recognition, and their exploration as potential optical references for lasers has begun to gain traction. Nevertheless, even the most advanced systems demonstrate a lack of competitiveness when confronted with established optical references at the 10^{-15} level of frequency instability. A key challenge in addressing this issue is the necessity to further minimize losses within the fiber

rings.

The novel approach of this thesis is to establish a fiber ring resonator in a configuration of a DFRR, with a ZCTE temperature at room temperature, or that can be attained by conventional TEC elements. This would result in a long-term stable optical reference for lasers that is both inexpensive and robust, and would be simple to utilize. It is conceivable that, depending on the precision level of the application, they could eventually become a valid competition to wave meters or optical cavities. This is particularly salient in instances where short-term instabilities are not a factor. Nevertheless, enhancing the system with regard to losses and shielding it more effectively from external disturbances may prove to enhance the stability of free-running lasers by orders of magnitude without incurring significant expenses. In addition, consistent with the spirit of [160], the employment of an enhanced resonator within a cryogenic environment could render it a suitable candidate for the applications of optical lattice clocks..

The scope of this thesis includes the design, planning, procurement of components, set up, and characterization of a DFRR. Further, light locked to the resonator via the PDH technique is analyzed. The design was intended to serve as a proof of principle for the concept of thermal insensitivity at specific temperatures and as a prospective alternative to optical resonators in applications that could also benefit from the low-frequency noise of long optical fibers, such as the search for UDM.

This study was undertaken within the project “Verbundprojekt: Hybrid-Integrierte und frequenzstabilisierte Laser zur betriebssicheren Manipulation ultrakalter Atome für transportable Systeme (ISABELLA). Teilvorhaben: Erforschung, Charakterisierung und Anwendungsdemonstration eines transportablen ultrastabilen Uhrenlasers mit einer Frequenzinstabilität im unteren 10^{-17} Bereich auf Basis von kryogenen optischen Resonatoren”, supported by VDI and the Bundesministerium für Bildung und Forschung. FKZ:13N16061.

The future objective of the system is to establish a linear fiber resonator in a manner analogous to that of an optical resonator, incorporating Bragg gratings. However, for the preliminary tests, a DFRR configuration was methodically planned and designed. At the time, a project on dark matter was included in a proposal with a target performance level of $2\times10^{-16}\,\mathrm{Hz}^{-1/2}$ at frequencies ranging from 100 Hz to 1 MHz. The design of the fiber ring was performed with this potential application in mind. A multitude of configurations were simulated in regard to finesse, linewidth, and free spectral range capabilities. The DFRR configuration, as depicted in Section 2.1.4, was utilized in combination with TCs from different manufacturers and variable fiber lengths. Ultimately, the set up and characterization of the DFRR were also components of a Bachelor’s thesis, [163]. This thesis was overseen by the author of the present work, and the proper credit will be attributed throughout the section.

5.1 Concept and Design

The theoretical framework is found in Section 2.1.4 and 2.2.4 Important fiber parameters for the SMF-28 fibers for light at 1.5 µm are given in 2.1. The company Corning is responsible for the

production of this particular fiber type [164], which is subsequently distributed to other companies, including Thorlabs, Gooch & Housego, etc. which then utilize the fiber type to manufacture a variety of products, such as TCs, among other fiber optics. In order to optimize the performance of the laser light, it was hypothesized that a combination of the thermal noise floor of the fiber and the transmission filtering through the cavity linewidth would be necessary. Consequently, the initial configuration of the system was determined to be a two-splitter arrangement. Nonetheless, while the free spectral range of the system is fixed and given by the round-trip path length of the resonator, the linewidths and, by extension, the finesse are strongly bound to the losses in the system. On the one hand, the thermal noise floor decreases with larger fibers, while on the other hand, the linewidth is smaller in shorter fiber resonators due to the reduced attenuation due to the fiber path. In the context of two ideal TCs that exhibit no losses, the condition $\gamma_0 = \gamma_1 = 0$ is satisfied, and the signal path splitting approaches 100 %, it can be deduced that the finesse of the system is constrained by the fiber length by

$$\mathcal{F} \approx 1.5 \times 10^5 \, \frac{\mathrm{m}}{L}. \tag{5.1}$$

This is derived from dividing the FSR by Equation (2.27), where it has been used that the system is designed for 1.5 µm in SMF-28 fibers with an attenuation of $0.18\,\mathrm{dB\,km^{-1}}$. The expression in Equation (5.1) is valid for fiber lengths of approximately $L \lesssim 10^4\,\mathrm{m}$. In order to attain the requisite noise level of $2 \times 10^{-16}\,\mathrm{Hz^{-1/2}}$ at a few 100 Hz below the carrier, a fiber path length of more than $7 \times 10^3\,\mathrm{m}$ would be necessary for a room temperature setup, or approximately $3 \times 10^3\,\mathrm{m\,m}$ at 120 K. A length of approximately 100 m of fiber would be required at a temperature of 4 K, which aligns with the system in [160]. Therefore, even within a cryogenic environment, the maximum attainable finesse of the system is approximately $\mathcal{F} \approx 1.5 \times 10^3$.

This is followed by the MSs, which represent the next limiting factor. These components are frequently characterized by an insertion loss of less than 0.5 dB (i.e. specified in the catalog of Thorlabs). The implementation of three mating sleeves, connecting the TCs to the long fiber, would result in a reduction of the maximum finesse of a 100 m long system to approximately $\mathcal{F} \approx 17$. By splicing the TCs together with a nominal loss of 0.0 dB, thereby removing one MS, it is possible to increase the finesse up to 26. Nevertheless, the utilization of MSs imposes a substantial constraint on the system's performance, as a mere loss of 0.1 dB across three MSs would fail to attain a finesse of 100. In a high-performance system, it is advised to splice all interfaces.

Another salient aspect is the bandwidth of the lock of the laser to the resonator. For even the longest optical resonators, the FSR is several 100 MHz, while the locking bandwidth is at the order of 10^5 Hz. Fiber resonators have the capacity to attain lengths of several kilometers, a property that will significantly reduce the FSR of the system. A system with a 7 km long fiber will exhibit an FSR of 30 kHz. This will limit the locking bandwidth of the PDH setup to that level and create resonances at its harmonics.

These resonances may add to the frequency noise. Adding blind spots to the locking circuits is not impossible; however, this would require the implementation of blind spots at every harmonic of the FSR. Consequently, this approach would render itself obsolete at higher frequencies. A

γ_0 (%)	Splitter 1	Splitter 2	f_D (kHz)	$\mathcal{F}$	S/N(dB)	Tr.(%)
8.6	50 : 50	50 : 50	679	3.0	11	49
	50 : 50	75 : 25	514	4.0	22	33
	50 : 50	90 : 10	446	4.6	25	15
	50 : 50	99 : 1	404	5.0	16	0.68
7.9	75 : 25	50 : 50	514	4.0	3.9	33
	75 : 25	75 : 25	363	5.6	6.3	27
	75 : 25	90 : 10	299	6.8	8.6	13
	75 : 25	99 : 1	260	7.9	11	0.65
8.3	90 : 10	50 : 50	446	4.6	1.3	15
	90 : 10	75 : 25	299	6.8	2.1	13
	90 : 10	90 : 10	237	8.7	2.7	7.1
	90 : 10	**99 : 1**	**198**	**10**	**3.4**	**0.38**
6.3	99 : 1	50 : 50	404	5.0	0.050	0.68
	99 : 1	75 : 25	260	7.9	0.078	0.65
	99 : 1	90 : 10	198	10	0.10	0.38
	99 : 1	99 : 1	160	13	0.13	0.022

Table 5.1: A DFRR of length 100 m formed by combining commercially available TCs. The bold data corresponds to the system employed in this study. The S/N value is indicative of the signal-to-noise ratio at the PDH output. γ_0 is the global loss in power of the TC corresponding splitting ratio indicated in column 'Splitter 1', which is also valid for the identical ratio in the column 'Splitter 2'. The Tr. column represents the maximum peak transmission in resonance with respect to the incident power.

100 m long fiber exhibits an FSR of 2 MHz, which is sufficiently large to occupy the entire spectrum for the referenced UDM experiment.

In addition to the fibers, the splitting ratio of the TCs must be selected. Table 5.1 presents a comprehensive overview of the four most commonly utilized commercial TC ratios: 50 : 50 [165], 75 : 25 [166], 90 : 10 [167], and 99 : 1 [168]. In the table, the total loss of the initial splitter is displayed in the leftmost column. Evidently, the losses are occurring at the 8 % level. The table presents the linewidth, finesse, and signal-to-noise (S/N) ratio of the signal at the PDH output. Additionally, it illustrates the transmitted power relative to the incident power.

The latter is critical for analyzing the transmission signal of the system, while the S/N ratio of the PDH signal is a pivotal characteristic for the locking circuit and performance. A notable observation is the influence of the order of splitters on this property. In the PDH scheme, the

lower splitting ratio initially yields a superior S/N ratio in the output, attributable to the increased coupling of incident light to this output. This must be acknowledged during the configuration of the resonator.

All other properties are independent of the order of the TCs. The peak transmitted power is a critical for evaluating the extent to which the transmitted signal can be measured. Nonetheless, there is invariably a leakage from the incident light in the transmission, which contains unsuppressed noise. The maximum is achieved with two 50 : 50 TCs, which generate a plateau of 10 % incident power in the transmission, assuming losses and mating sleeves are taken into account. Furthermore, to ensure optimal performance of the lock and effective filtering through the mode, it is essential to minimize the cavity linewidth. As demonstrated in Figure 5.1 (a), the lowest possible linewidth is achieved for high splitting ratios of both TCs and a low resonator length.

Two aspects of this case are particularly noteworthy. Firstly, it should be noted that diminishing returns are observed for higher splitting ratios. A plot of a setup containing two 99.9 : 0.1 TCs would be visually congruent with the one for 99 : 1 splitters. This phenomenon can be attributed to the fact that insertion loss becomes the predominant constraint. It is evident that high-end TCs with total losses lower than $\gamma_i < 1\,\%$ may have the capacity to surpass that limit. Secondly, divergence between systems will eventually occur at a specific length of the resonator when the loss due to the fiber length becomes dominant.

The plot in Figure 5.1 (b) is based on Equation (2.27) and presents the frequency dependence of the frequency noise at 100 Hz in the frequency domain. Here, the system was simulated at a temperature of 300 K. The key finding of this section is that the performance of a fiber ring is contingent on the losses of the TCs, with suboptimal performance occurring at lengths in the 10 km range. The linear configuration of a fiber resonator, employing the use of mirrors, Bragg gratings, or coatings at the fiber's ends, can enhance the Finesse and consequently the linewidth. However, this configuration results in a reduction of the FSR by a factor of two, as the light is required to travel twice the length of the fiber path.

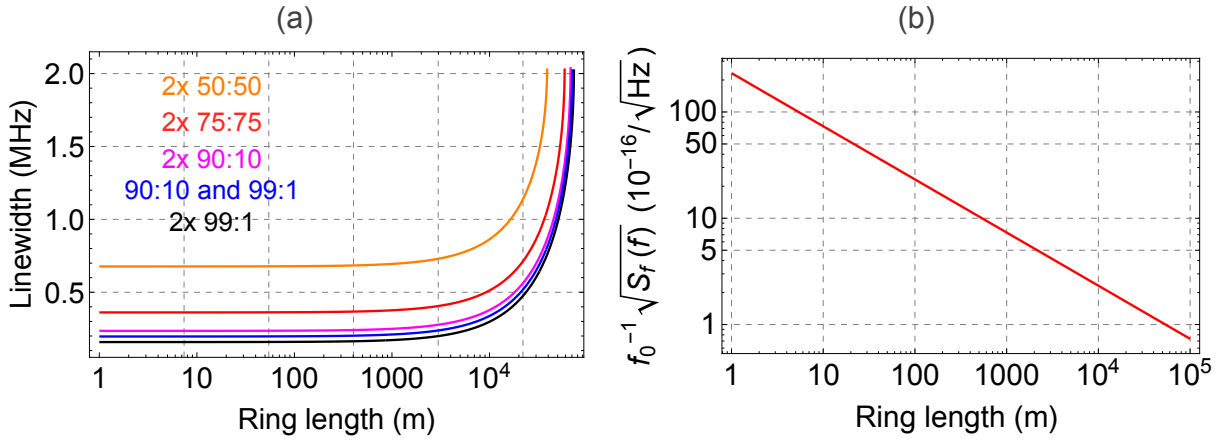


Figure 5.1: The design parameters of the DFRR depending on the ring length. (a): Resonator linewidth for various TC combinations. (b) The thermal noise floor at 100 Hz in the frequency domain for a fiber at 300 K.

Linear Fiber Resonator

In the event that an application necessitates an ultra-narrow linewidth in conjunction with a minimal thermal noise floor, yet does not impose a stringent restriction on the FSR, a viable solution might involve the utilization of a 1 km long fiber equipped with two Bragg coatings at each mirror, featuring reflectivities exceeding 99.2 %.

Subsequently, the FSR of the system would be approximately 1×10^5 Hz, which is sufficient for a stable lock. The linewidth would be 2 kHz, which is competitive with ultra-high finesse optical resonators, despite the fact that the finesse of the fiber resonator is only at the order of 50. The thermal noise floor at room temperature would be considerably large at $f_0^{-1}\sqrt{S_{f,th}(f)} \propto 6 \times 10^{-15} f^{-1/2}$, but could be reduced to below $10^{-15} f^{-1/2}$ level at cryogenic temperatures below 10 K.

The initial tests for this thesis involved the configuration of a fiber ring resonator in a dual splitter configuration. This configuration included one 90 : 10 TC and one 99 : 1 TC, with a long fiber between them of length 100 m. The TCs were spliced together, however for flexibility, the long fiber was connected by MSs.

5.2 Thermal Properties and Resonator Design

Thermal variations in T along the fiber path will have effects on the refractive index n as well as the length of the fiber. For the SMF-28 fibers, the following holds at room temperature: $\frac{dn}{dT} = 9.2 \times 10^{-6} \alpha_{fib} = 5.5 \times 10^{-7}\ \nu_0\,\mathrm{K}^{-1}$ and $\alpha_{fib} = 5.5 \times 10^{-7}\ \nu_0\,\mathrm{K}^{-1}$ [79]. In this context, the symbol α_{fib} denotes the CTE of the fiber glass. The values presented herein are applicable to systems maintained at room temperature and exhibit minimal variation, even at subzero temperatures [169]. In the context of this thesis, the effective coefficient of thermal expansion α_{eff} is defined by

$$\nu_0^{-1}\alpha_{eff} = \frac{dn}{dT} + n\nu_0^{-1}\alpha_{fib}.$$

The second term is responsible for the optical path length change, given by $n\alpha_{fib}$, due to the propagation medium being non-vacuum, specifically fiber glass, thus it is $\nu_0^{-1}\alpha_{eff} \approx 10^{-5}\,\mathrm{K}^{-1}$. Even in a well-maintained environment with thermal variations in the 10 µK range, thermally induced frequency instabilities at the 10^{-10} or 20 kHz level can occur.

Additionally, the ZCTE of silica-based fibers is likely to be in closer proximity to that of silica itself at cryogenic temperatures. In the work of [169], an expected ZCTE at −250 °C was reported for SMF-28 fibers, and a ZCTE at −80 °C was reported for hollow-core fibers (HCFs). The thermal sensitivity, as defined in this paper, is represented by the quantity S_φ , which is converted to the parameters in this thesis through

$$S_\varphi = \frac{2\pi}{\lambda}\nu_0^{-1}\alpha_{eff} \Longleftrightarrow \nu_0^{-1}\alpha_{eff} = \frac{\lambda S_\varphi}{2\pi}.$$

Specifically, within the temperature range of −50 °C and +50 °C, the CTE of the fiber is observed to vary from $7 \times 10^{-6}\,\mathrm{K}^{-1}$ to $1 \times 10^{-5}\,\mathrm{K}^{-1}$ in a good linear approximation.

The objective of the configuration in this thesis was to develop a simple resonator that exhibits optimal performance at a minimal maintenance standard. Additionally, the configuration is characterized by a ZCTE within the aforementioned temperature range, which can be stabilized by conventional TEC elements. In the course of research, the company Linden Photonics was identified as a provider of specialized tubing for fibers, yielding an effective CTE with positive and negative signs [170, 171]. In addition, the fibers feature the company's patented crystal polymer jacketing and demonstrate comparable geometries and properties to those of SMF-28 fibers, including mode field diameter, cladding diameter, and refractive index. The fiber attenuation is of the order of a $\alpha_L < 0.35\,\mathrm{dB\,km^{-1}}$. While this loss is substantially larger than the previously expected $0.18\mathrm{dB\,km^{-1}}$, it is comparatively negligible within the present configuration.

Under the assumption that light, at speed c_n, travels through a fiber of length L_0, the time required for this process, t_0, is given by $t_0 = L_0 c_n^{-1}$. If the fiber undergoes expansion, for example, due to temperature fluctuations, the light will require a slightly longer duration to propagate through it. The time delay, Δt_1, is given by the length change, ΔL_1 through $\Delta t_1 = \Delta L_1 c_n^{-1}$. Accordingly, the normalized time delay per unit length of the fiber is subsequently expressed as:

$$\frac{\Delta t_1}{L_1} = \frac{\Delta L_1}{L_1} c_n^{-1} = \nu_0^{-1} \alpha_{eff,1} T c_n^{-1}.$$

In this equation, the definition of the CTE as the relative length change per unit temperature $\nu_0^{-1}\alpha_{eff} = \Delta L/(LT)$ has been inserted.

The company Linden Photonics provided data on the delay time, with respect to a reference temperature, of two fiber spools with opposite sing in their CTE at room temperature, as well as the total length of each fiber spool. The delay was measured at five different temperatures for each fiber. The resulting data is presented in Figure 5.2 (a). The objective of this thesis was to formulate a fiber with an effective CTE of zero at room temperature. Consequently, the slope of a linear fit through the data can be utilized to express the path delay time per unit temperature and unit length, β, as follows:

$$\beta_1 = \frac{\Delta t_1}{L_1 T} = \nu_0^{-1} \alpha_{eff,1}\, c_n^{-1}.$$

It was determined that the fiber spools exhibited relative path length delays of $\beta_1 = +4.25(6)\,\frac{\mathrm{fs}}{\mathrm{mK}}$ and $\beta_2 = -11.4(8)\,\frac{\mathrm{fs}}{\mathrm{mK}}$. To create a fiber with net zero path length delay, fiber lengths of both spools can be combined/spliced together, where ρ is the fraction of the fiber with positive path length delay and $(1-\rho)$ the fraction of the fiber with negative path length delay with respect to the total fiber length. Subsequently, the ratio $\rho : (1-\rho)$, was evaluated, resulting in

$$\nu_0^{-1}\alpha_{eff} = 0 = \rho\nu_0^{-1}\alpha_{eff,1} + (1-\rho)\,\nu_0^{-1}\alpha_{eff,2} = c_n(\rho\beta_1 + (1-\rho)\beta_2),$$

which is solved to

$$\rho = \frac{\beta_2}{\beta_2 - \beta_1}.$$

For this particular set of fibers, this ratio is 73.8 : 27.2, such that the company was asked to splice together a long fiber following this ratio with a total length of 100 m. This unique fiber served as the foundation for the DFRR. Furthermore, a 10 m fiber with a marginally deviating ratio was procured for experimental purposes.It is salient to note that the system is engineered to exhibit ZCTE at ambient temperature in the absence of additional fibers. However, the TCs utilized in this study will be based on standard SMF-28 fibers, which exhibit reduced ZCTEs at cryogenic temperatures. Consequently, the combination of the special fiber and the TCs will result in a shift of the effective ZCTE to slightly lower temperatures. It is conceivable that this effect could have been compensated by a different ratio of fibers. However, the option to add Bragg coatings and create a linear resonator was wanted to be kept open. In such a configuration, the sole contributor to the CTE would be the special fiber.

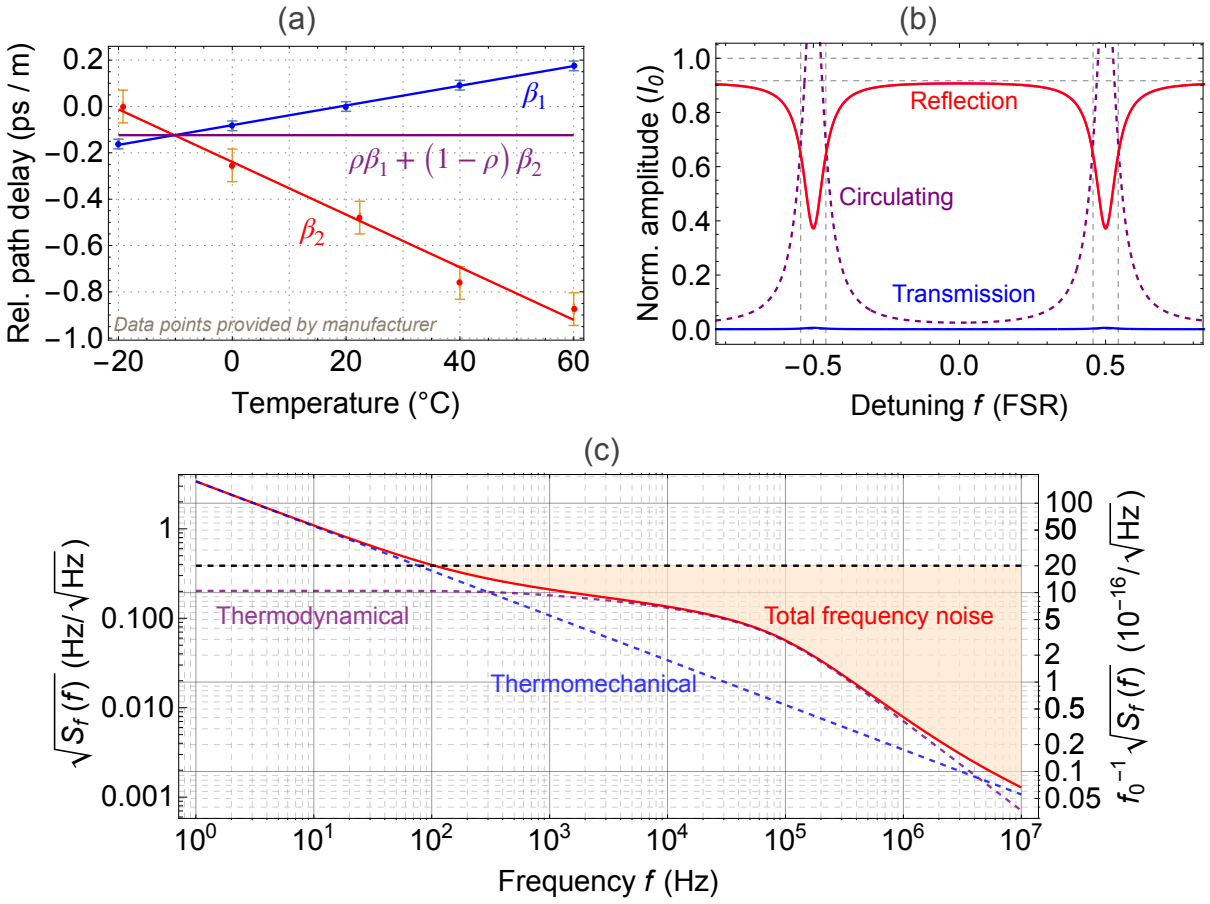


Figure 5.2: The DFRR modeled through the use of two commercial TCs (90 : 10 and 99 : 1) and a 100 m long special fiber positioned between them. (a): The effective CTE is derived from the time delay, which is expressed as a function of the unit length and the unit temperature. The blue and red lines represent linear fits over the data provided by the company. The purple line indicates the target. The error bars are estimated based on the fit and are not part of the raw data. (b) Simulation of the intensities inside the resonator (circulating), as well as in the PDH output (reflection) and transmission. (c): Simulation of the thermal noise floor of the ring resonator at approximately 247 K.

In order to mitigate this effect in the fiber ring, the TCs were shortened and spliced together during the process. This was done to remove the effect of one MS, thereby ensuring that the ring's path length through the splitters is less than 1 m. Consequently, the total length of the ring is estimated to fall within the range of 100 m and 101 m. In summary, the design process of the resonator has been outlined and concluded, yielding the following simulations of the systems shown in Figure 5.2 (b). and (c). The signal used for the PDH lock exhibits a single-to-noise ratio of 3.4 dB, with a maximum transmission output of approximately 0.4 %. The FSR of the system is estimated to be in the range of $\Delta\nu = 2.03\,\mathrm{MHz}$ to 2.05 MHz, contingent upon the specific length of the resonator. Given a linewidth of approximately 175 kHz, the system exhibits a finesse of approximately $11 - 12$. The system was simulated for two MSs and two splices, with a nominal losses of 0.1 dB. The thermal noise floor is $f_0^{-1}\sqrt{S_{f,th}(f)} \propto 1.8 \times 10^{-14} f^{-1/2}$ for the thermomechanical contribution, where the thermodynamical part becomes dominant between 300 Hz and approximately 4 MHz in the frequency domain. At a frequency of 100 Hz, the noise level is simulated at below $2 \times 10^{-15}\,\mathrm{Hz}^{-1/2}$ for all subsequent frequencies illustrated by the black dashed line and the orange fill area in the plot. The temperature of the simulation is set at 247.15 K, a foreshadowing that will be addressed in greater detail subsequently.

5.3 Experimental Apparatus

The process of stabilizing laser light to a fiber resonator is analogous to the conventional method of locking to an optical cavity. The light of a fiber laser [NKT Photonics, E15] at 1.5 µm propagates through a fiber-coupled AOM [Gooch & Housego] and EOM [iXBlue]. Subsequently, it is connected to the input port of the DFRR. Consequently, the PDH output is transmitted to a photodiode [Thorlabs], whose AC output is mixed with a signal from the local oscillator, which is producing the sideband modulation. The resulting error signal is low-pass filtered and transmitted to a lockbox [Homebuilt], which fast output is then sent to the frequency modulation (FM) input of the DDS [Homebuilt], driving the AOM.

However, in numerous instances, the fast lock of the system did not engage properly, and the lock was performed solely by the slow modulation, modulating the laser current. The light that is transmitted by the DFRR is directed to an additional TC, where it is combined with the 1.5 µm ULE-stabilized laser that was utilized for the characterization of the NEXCERA cavity. The NEXCERA resonator was already at MPIKMax- at that time. The measurement of the beat signal is performed through the utilization of various instruments, including an oscilloscope [Rohde & Schwarz, RTB2004], and a SA [Rohde & Schwarz, FPC1000]. These devices are referenced to the H-maser to ensure accuracy in signal analysis. The experimental setup is illustrated in Figure 5.3.

During the configuration and preliminary evaluation of the temperature sensitivity of the fiber, it became evident that the CTE exhibited a decrease at temperatures lower than the ambient temperature. Therefore, an array of methodologies was employed to achieve progressively lower effective temperatures at the fiber ring. Eventually, a classical TEC configuration consisting of four elements connected to a stainless steel heat reservoir was employed to stabilize the temperature of a copper box containing the fiber resonator. As illustrated in the top left pictures of Figure 5.4, the wiring on the spool and the top view of the open copper box are depicted.

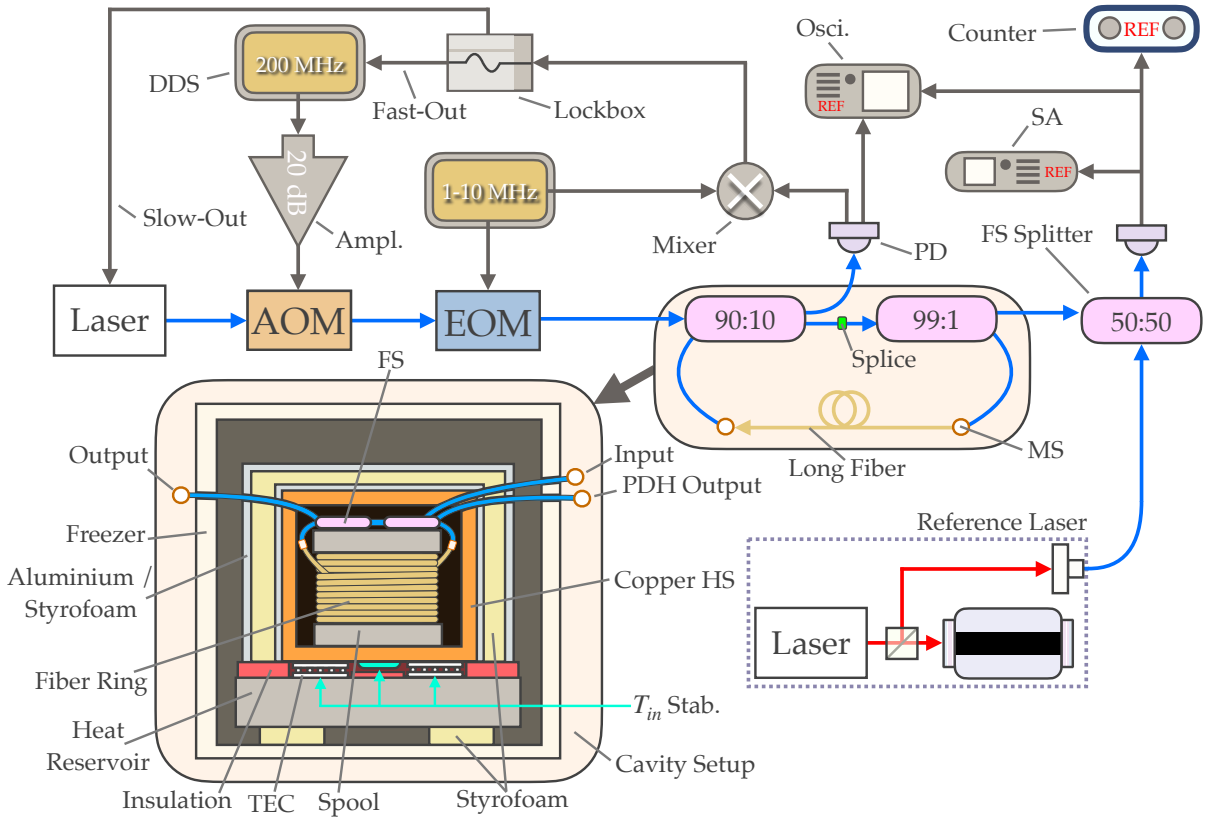


Figure 5.3: The schematic illustrates the configuration employed for the stabilization of light to a fiber ring resonator through the utilization of the PDH technique as well as a profile cut of the resonator inside the freezer. Throughout the course of the experiment, the frequency driving the EOM was systematically varied. The transmission of the DFRR was once again measured in comparison to the ULE-stabilized laser (reference laser) at 1.5 µm, which was utilized to characterize the NEXCERA-stabilized laser.

The copper box contains a lid and was configured in a manner that allows access to the input and two output ports. The exterior of the box is lined with aluminum foam, which serves the additional purpose of insulating the resonator. This is illustrated in the top right photograph. The structure is encased by a layer of thick foam, followed by an additional aluminum foam layer, as depicted in the two bottom left images. The PID controller, when utilized to regulate the Peltier elements, demonstrated an inability to attain stability beyond a range of approximately zero degrees Celsius within a standard ambient temperature setting.

However, data indicated that the ZCTE of the system, if it exists, remains below this threshold. In addition to the in-loop sensor, four supplementary sensors were utilized to assess the temperatures at the interior of the lid of the copper box, at the fiber center inside the box, the heat reservoir, and the ambient temperature of the freezer.

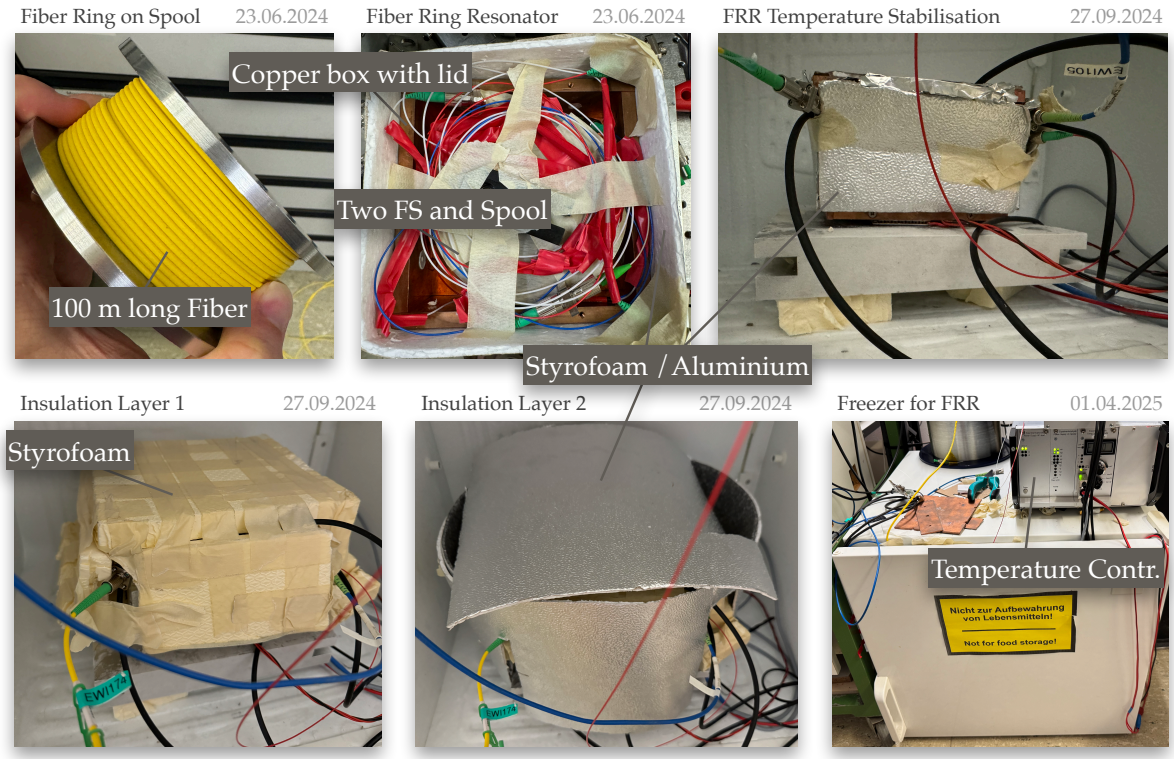


Figure 5.4: Photographic documentation of the DFRR. The 100 m long fiber is displayed in the top left corner of the figure. The resonator itself is positioned within a copper enclosure that is actively temperature-stabilized inside a freezer. The implementation of foam layers, including the thicker yellow foam and aluminum foam sheets, serves the purpose of additional insulation.

Consequently, the entire apparatus was initially positioned in a refrigerator and subsequently in a freezer to significantly reduce the ambient temperature and alleviate the loads on the Peltier elements. The heat reservoir was separated from the bottom of the freezer by insulation foam.

Subsequently, an additional layer of insulation was incorporated between the heat reservoir and the base of the copper box. This modification was implemented to mitigate heat transfer. The sheet was designed with specific apertures for the integration of the Peltier elements and the temperature sensor of the PID loop. This configuration enabled the measurement of stabilized temperatures as low as −33 °C, which was deemed to be sufficiently low.

A photograph of the freezer and the PID controller can be found in the image located in the lower right corner. The configuration of the electronics and laser apparatus is illustrated in Figure 5.5. At the top, the computer, oscilloscope, lockbox, and SA are positioned. At the base, the laser configuration is displayed, including the fibered, EOM, and AOM.The system was partially set up and characterized in collaboration with M. Castelein [163] within the scope of his Bachelors thesis.

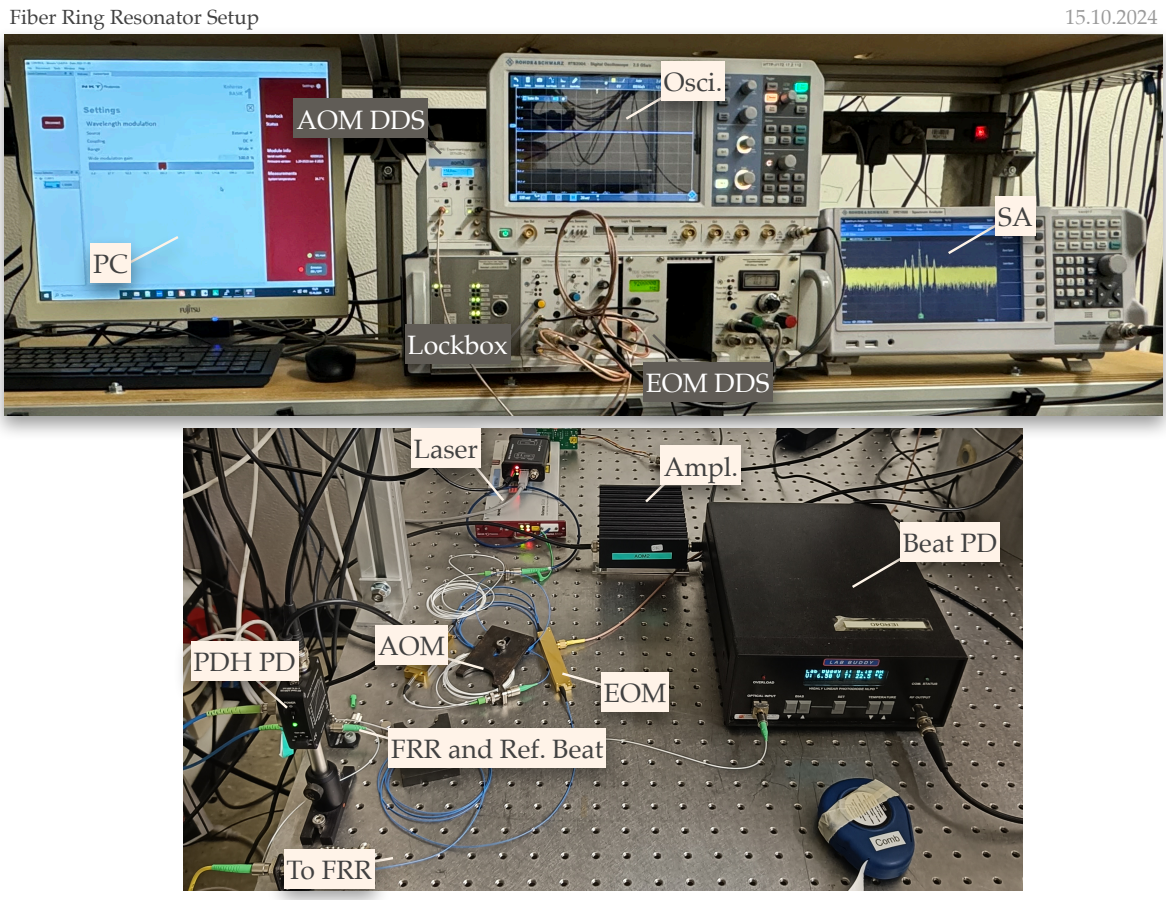


Figure 5.5: Photographs of the electronic configuration utilized for the purpose of locking laser light to the fiber ring. In the top image, the shelf designated for the electronics is displayed. The bottom image illustrates the optical configuration, which is comprised of a fiber laser, EOM, and AOM.

5.4 Resonator Characterization

Initially, it was necessary to confirm the finesse, free spectral range, and cavity linewidth. For the purpose of evaluation, the laser was locked to the FRR, and the beat with the ULE stabilized laser was observed. Given the low FSR of 2 MHz, it is feasible to scan and measure the power of the modulation sidebands in the beat. This process enables the determination of the transmission profile's structure. Provided that the laser is locked to the DFRR, its frequency instability is inconsequential. This is due to the fact that the sidebands will remain at a constant distance from the stabilized mode. This method was used to generate the data illustrated in Figure 5.6. The gray datapoints in this figure represent the average power of the upper and lower sidebands. The red, blue, and orange curves represent the pure Lorentzian fits of form

$$I(f) = \frac{A}{2\pi} \frac{f_D}{(f - f_0)^2 + \left(\frac{f_D}{2}\right)^2}.$$

Measurement	f_D (kHz)	$\Delta\nu$ (MHz)	$\mathcal{F}$	L
Red	300(7)	8.184(2) / 4 ≈ 2.046	6.8	100.64
Blue	392(16)	10.199(3) / 5 ≈ 2.040	5.2	100.94
Orange	223(6)	8.175(2) / 4 ≈ 2.044	9.2	100.75
Black	262(16)	2.023(8)	7.7	101.78

Table 5.2: Extraction of the parameters gained from the fits shown in Figure 5.6. The resonator linewidth, FSR, finesse and resonator length are determined.

The linewidth of the mode can be obtained directly from the fit parameter f_D. Additionally, the FSR $\Delta\nu$ is linked to the offset frequency, f_{off}, via $\Delta\nu = m\, f_{off}$,where m signifies the (offset) number of longitudinal modes in relation to the locked one. The orange and red line correspond to $m = 4$, while the blue line corresponds to $m = 5$. The black dashed curve illustrates the theoretical transmission profile that has been fitted to the data, which is of form

$$I_{tr} = \frac{\left(1-\gamma_0-\delta_0^2\right)\left(1-\gamma_1-\delta_1^2\right)\delta_m^2}{1+2\delta_1'\delta_0\delta_s\cos\left(\frac{2\pi}{\Delta\nu}f\right)+\delta_1'^2\delta_0^2\delta_s^2} = \frac{A}{1+2w\cos\left(\frac{2\pi}{\Delta\nu}f\right)+w^2}.$$

This function enables the direct extraction of the FSR and the linewidth through

$$f_D = \Delta\nu - \arccos\left(\frac{1-4w+w^2}{2w}\right)\frac{\Delta\nu}{\pi},$$

with $w = \delta_1'\delta_0\delta_s = \delta_1\delta_0\delta_L\delta_m^3$. The results of the four fits, including the resulting finesse and fiber lengths, are displayed in Table 5.2. The result from the transmission profile demonstrates the most variation in relation to the others, a circumstance that is probably due to the asymmetric nature of the data concerning the modes. As demonstrated by the individual fits, the blue curve yields a substantially larger linewidth than the red one.

In addition, the total fiber ring is estimated to be approximately 101 m based on the configuration. An alternative approach for estimating the FSR involves observing the error signal during modulation frequency tuning. It has been demonstrated that when the sideband frequency attains a multiple of the FSR, the error signal becomes eliminated. Nevertheless, it is not possible to perform this task while the laser is locked, as this would cause frequency variations that could potentially disrupt the system.

Still, in that particular instance, the FSR was estimated to be 2.04(1) MHz, a value that aligns with the previous findings of the present analysis. It is estimated that the resonator has a linewidth of approximately 3×10^5 Hz, an FSR of 2.04 MHz, and a finesse of approximately 7. The linewidth of the resonator is too large to accurately measure the phase noise filtering of the system. This is due to the fact that the effects of the filtering will appear far away in the frequency spectrum with respect to the free running laser linewidth (10 kHz).

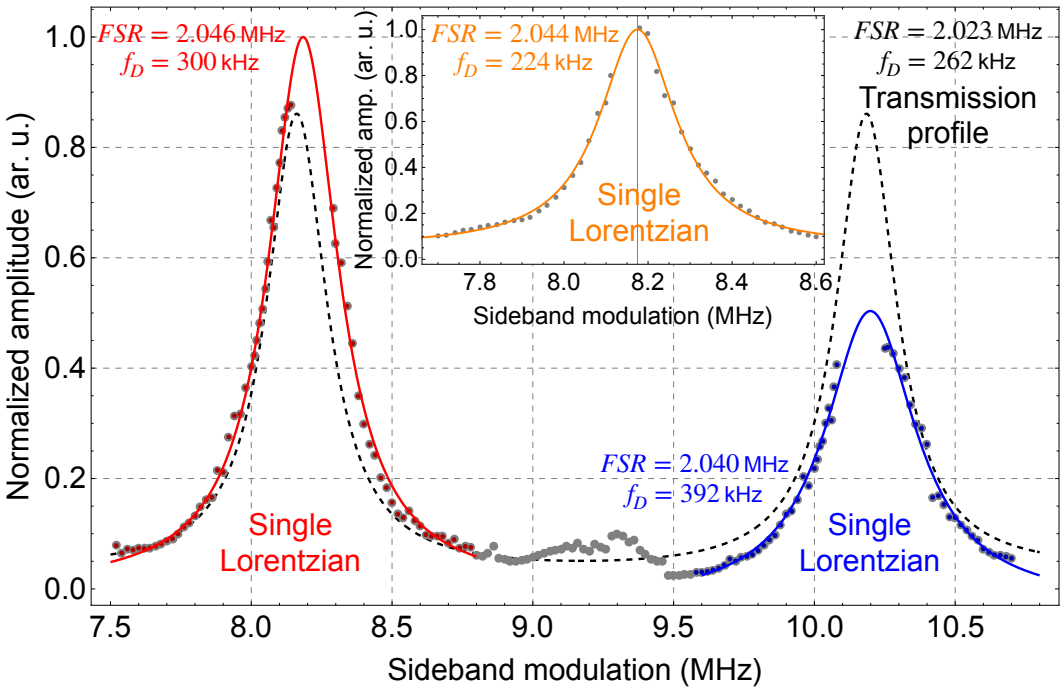


Figure 5.6: Measurement of the transmission profile of the DFRR. The power of the upper and lower PDH sideband was measured upon variation of their frequency while the laser was locked to the DFRR. the gray data is the mean of both sidebands. The red, blue and orange lines are Lorentzian fits, while the black dashed line is a fit of the transmission profile function.

Additionally, the signal-to-noise ratio of the beat would not allow for such measurement. The final parameters deviate from the initial design with regard to the linewidth and finesse. Consequently, the finesse is elevated by a factor of about 1.7. This deviation may be attributed to the losses within the system. The theoretical values, with a splice positioned between the splitters and two mating sleeves with losses of 0.8 dB, result in a loss parameter w_{th} that is comparable to the best-estimated measurement in this study, which is the orange curve, representing an experimental value $w_{exp} \approx 0.670$.

The ZCTE temperature was evaluated in a manner consistent with the NEXCERA resonator (see Section 6) by changing the temperature and observing the frequency change in the beat. The time constant of the resonator to accept a temperature change was in the order of a few hundred seconds. However, it should be noted that the actual temperature change may require a longer time period to manifest. The data is displayed in Figure 5.7. The ZCTE temperature T_{ZCTE}, as determined by a quadratic fit, (see Section 2.2.2, Equation (2.33)), is $T_0 = -28.2\,°\mathrm{C}$.

This value is slightly lower than the estimates derived from alternative methods, which concluded with a final result of $-29(2)\,°\mathrm{C}$. Consequently, the temperature at which the resonator was stabilized was approximately $-29\,°\mathrm{C}$. The curvature of the fit is approximately $(T - T_{ZCTE})^{-1} \frac{d\nu}{dT} = -4.0(2) \times 10^{-8}\,\mathrm{K}^{-2}$, which is about a factor of 25 steeper than that of ULE [172, 102] and approximately four times larger than that of NEXCERA [119, 120].

Further, it is just slightly more than twice as large than the curvature of the CTE of cryogenic silicon cavities at 124 K [59]. The findings of this study demonstrate that the thermal characteristics of a basic fiber ring resonator can be benchmarked against contemporary optical resonators, with slightly more stringent criteria for temperature stabilization. Additionally, the ZCTE has been determined to be lower than the targeted value. This is likely attributable to the fraction of the fiber ring that is part of the standard TCs. However, temperatures of −30 °C are not considered cryogenic and can be managed with less complex setups. This development also creates the possibility of designing fiber rings in a manner that incorporates the TCs, thereby maintaining the ZCTE at ambient temperature.

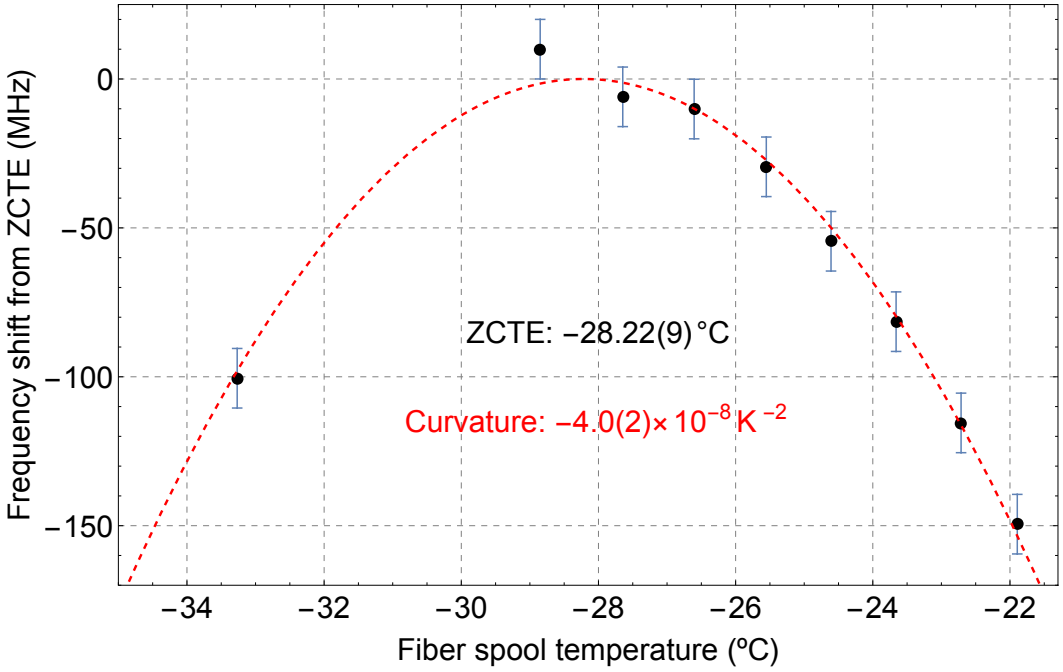


Figure 5.7: ZCTE measurement of the DFRR. The red dashed line is a quadratic fit over the data points. The ZCTE was determined by changing the temperature at the resonator and measuring the resulting frequency difference in beat with the ultra-stable reference. The instability and drift of the reference is negligible with respect to the observed frequency changes.

5.5 Laser Frequency Stability and Thermal Sensitivity

The linewidth of the laser was measured from the beat with the ULE-stabilized laser. This measurement was performed using a SA. The reference light is conservatively at the 10^{-14} level in terms of frequency stability and 10 Hz level linewidth. This is negligible in comparison to the FRR, as elaborated now. The result is illustrated in Figure 5.8. A total of 93 consecutive sweeps were monitored and individually fitted by a Lorentzian function. The estimated linewidth of DFRR-locked laser was approximately 4 (2) kHz. The free-running lasers have linewidths of approximately 12 kHz, suggesting that there has been a discernible enhancement in the DFRR lock. It stands as a generally valid rule of thumb that, under typical operating conditions, the laser linewidth of a well-locked laser is expected to be approximately 10^3 times smaller than that of the cavity linewidth.

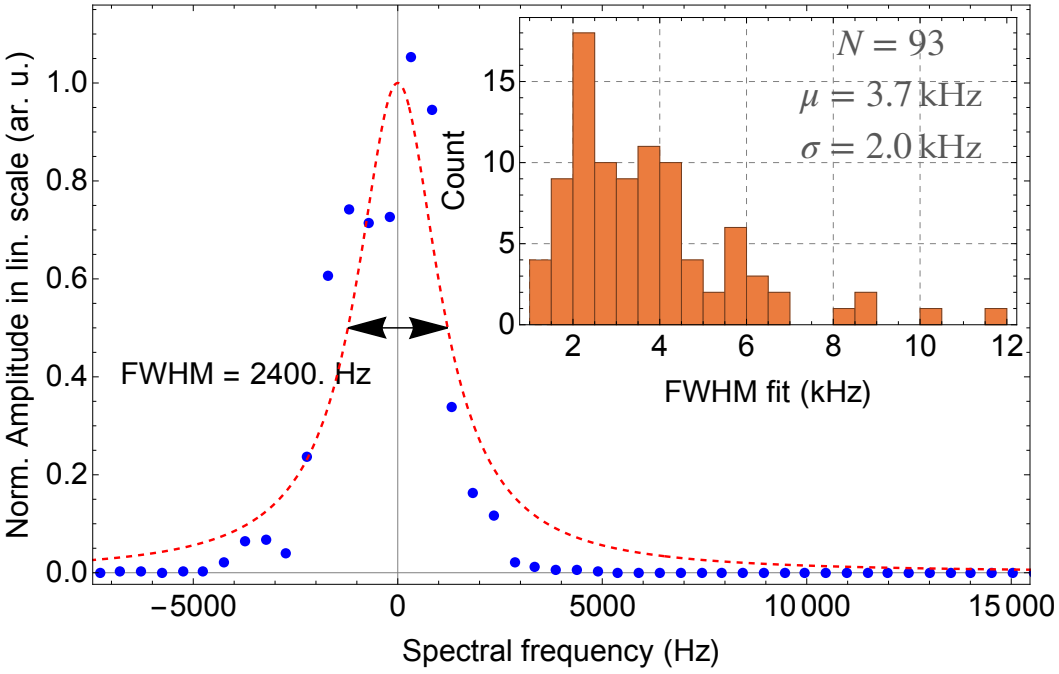


Figure 5.8: Measurement of the laser linewidth locked to the DFRR against the ultra-stable laser at 1.5 µm. The linewidth is reduced by a factor of 4 – 5 with respect to the free-running laser. The red dashed line indicates the Lorentzian fit. The histogram and statistics of the FWHM fit values of 93 consecutive measurements is shown in the inset.

In this particular instance, the ratio approaches a factor of 100. However, this may be partially explained by the limited fast lock locking bandwidth of less than 20 kHz and the high frequency instability of the system. Nevertheless an effect is observed, which can be enhanced by ring resonators with reduced losses. In the subsequent measurement, the fiber ring was set to −28.7 °C at the temperature controller, and the thermal sensitivity of the locked laser light was analyzed. The temperatures measured at the four sensors are displayed in Figure 5.9 (a). In this configuration, the colors serve to denote the four distinct positions. Of these, three are situated on the fiber spool, specifically at the top, center, and bottom. The remaining position is located within the environment, particularly on the heat reservoir utilized for the TEC elements. The oscillation, with a time period ranging from 40 to 45 minutes and observable in all sensors, is attributable to the freezer. The pump is activated at regular intervals in order to regulate the internal temperature. When it is off, the freezer gradually warms up internally until the pump is once again activated.

The oscillation is pronounced at the sensor measuring the heat reservoir, and it is also evident at the top and center of the fiber spool. The temperature at the base of the spool remains relatively consistent due to its proximity to the in-loop sensor, which serves to stabilize the system, as well as the effective insulation in this area. Panel (b) illustrates the beat signal of a synchronous measurement of temperature and frequency, which was obtained by tracking the peak in a fixed spectrum using a SA. Here, only the slow lock output of the lockbox was engaged. The oscillation of the freezer is also clearly discernible. Nonetheless, a pronounced drift in frequency is not evident.

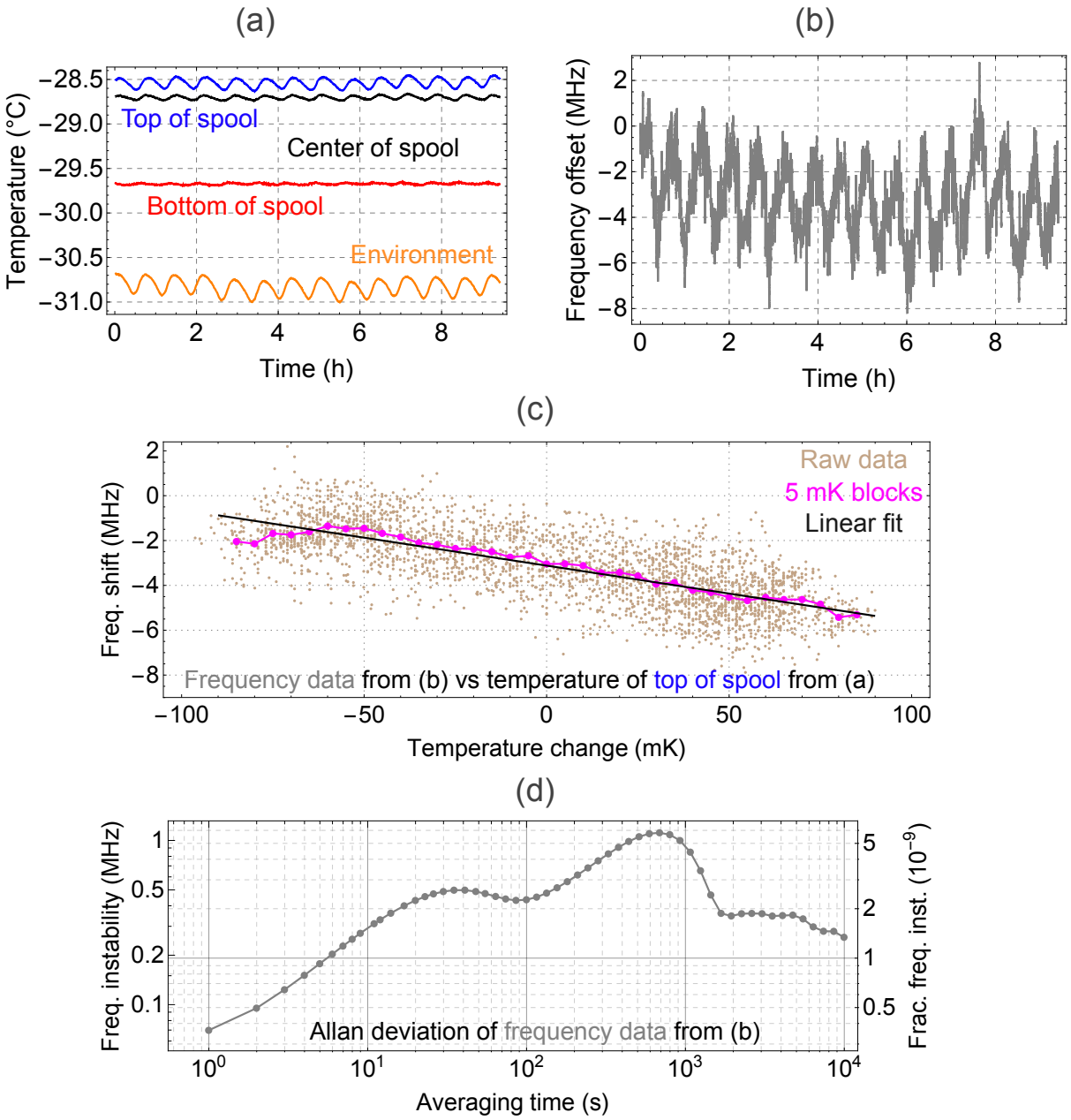


Figure 5.9: Long term performance and temperature sensitivity of the DFRR. (a): Temperature reading of all four sensors surrounding the resonator. (b) Beat-note measurement of the DFRR with another ultra-stable laser at 1.5 µm. (c): Correlation of the frequency and temperature data of the sensor on top of the spool, including a linear fit to obtain the temperature sensitivity. The magenta line depicts an average over the frequency data over blocks of 5 mK. (d): Allan deviation of the data shown in panel (b). The bump at a few hundred seconds is correlated to the periodic temperature variation in the freezer.

Correlating the frequency to the temperature sensor located on the uppermost portion of the fiber spool results in the plot displayed in panel (c). The temperature data was adjusted to coincide with the frequency spectrum, necessitating a shift of approximately 1250 s. The brown data points

Sensor	$\nu_0^{-1}\alpha_{eff}\,(10^{-7}\,\mathrm{K}^{-1})$	$\alpha_{eff}\,(10^{-7}\,\mathrm{MHz\,K}^{-1})$
Top of spool	−1.30(3)	−25
Center of spool	−3.16(6)	−61
Bottom of spool	−8(16)	−150
Environment / Heat reservoir	−0.62(2)	−12

Table 5.3: Evaluated CTEs of the DFRR with respect to different locations of the temperature sensors. The CTE is given in terms of fractional and absolute frequency.

represent the raw, correlated data, while the magenta line indicates an average of blocks of 5 mK. The black line represents a linear fit over the raw data. The slope of the curve is an estimate of the effective CTE of the resonator with respect to the temperature measured at the top sensor. Analyses of this kind have been conducted for all other sensors; the results are displayed in Table 5.3. The actual CTE of the DFRR with respect to the temperature of the fiber will fall between the numbers for the three sensors located in proximity to the spool. Specifically, the top and center sensors will be used, as the bottom one is very close to the in-loop sensor.

The lowest estimate of the CTE of the FRR with respect to the temperature at the bottom of the spool is $\nu_0\alpha_{eff} \approx 1.3 \times 10^{-7}\,\mathrm{K}^{-1}$, which would be a factor of 50–80 better than that of a SMF-28 fiber at temperatures between −50 °C and +50 °C. In addition, this would indicate that the fiber is approximately 5 K from the actual ZCTE. This enables the potential for enhancement in terms of temperature sensitivity. Concurrently, it substantiates the concept underlying the fiber ring resonator. The final piece of characterization is the instability of the locked light in terms of its Allan deviation, as illustrated in Panel (d). The Allan deviation shows a minimum of 7×10^5 Hz at 1 s averaging time, corresponding to a level below 4×10^{-10} level. The instability has a peak at approximately 7×10^2 seconds, which corresponds with the oscillation of the freezer. On longer time scales, at an averaging time of 10^4 s, the system demonstrates stability at the low 10^{-9} level, which is nearly 50 times lower than the typical observed drift of that laser type. Consequently, the fiber ring may already demonstrate an enhancement in laser stability over extended periods.

Summary

A novel fiber ring resonator has been designed, set up, and characterized with a ZCTE at temperature that can be achieved with common TEC elements. A special fiber has been utilized to increase the ZCTE with respect to SMF-28 fibers by nearly 220 K , exhibiting a curvature of comparable steepness to that of cryogenic silicon cavities. The laser-locked light exhibits thermal sensitivities that are approximately 50 times smaller than those of a SMF-28 fiber at the same temperature. Furthermore, the linewidth and long-term stability of the locked laser have been determined to be 4 kHz and 10^{-9} level, at 10^4 s averaging time, respectively. These parameters are strongly limited by the system being several Kelvin away from the actual ZCTE and variations in the environmental temperature. The enhancement of temperature stabilization, the implementation of a lock, and the mitigation of losses in the fiber resonator bear the potential to yield highly cost-effective, long-term stable systems that could potentially rival the stability of wavemeters.[86]

Chapter 6

Ultra-Low Drift of a Room-Temperature Reference

The following section is written in a style such that it can be transferred into a draft for a manuscript. The temperature changes of the ZCTE measurement shown herein were performed in collaboration with C. J. Kwong. Note that in the following text, ν_0 is the optical carrier frequency of the light and f_0 is a frequency offset. This chapter focuses on the measurement of the lowest long-term drift ever recorded in a room-temperature optical reference.

Introduction

In recent decades, ULE has emerged as a favored spacer material due to its low thermal sensitivity, which is accessible at or near room temperature and its low thermal noise profile capable of enhancing the frequency stability of laser light. Nevertheless, glasses (an amorphous material) and ceramics (a micro-crystalline material) experience long-term, environmentally independent deformations due to complex internal structural changes related to their absolute temperature. This phenomenon has been the subject of extensive research in the field, particularly in the context of glasses, as outlined in [173]. The structural deformation results in a modification of the optical path length within the resonator, which in turn leads to a slow frequency drift of the resonance modes. This, in turn, is transferred to the stabilized light. In this category, ULE glass has been demonstrated to be an excellent choice, exhibiting drifts of the order and below

$$D = \nu_0^{-1}\, d\nu/dt = 10^{-15}\,\mathrm{s}^{-1},$$

for light at typical optical carrier frequencies ν_0 of around a few hundred THz. Best-in-class values in terms of the fractional frequency drift are in the order and slightly below $D = 4.7 \times 10^{-17}\,\mathrm{s}^{-1}$ ('NPL' in Figure 6.1.) [174, 172, 119, 175, 176]. In contrast, cryogenic setups using silicon spacers [71, 63, 117, 64, 66] can reach low to mid $10^{-19}\,\mathrm{s}^{-1}$ level, offering an improvement of two orders of magnitude compared to room-temperature systems. In particular, recent developments have achieved drifts of $(1.4 - 3.7) \times 10^{-20}\,\mathrm{s}^{-1}$ ('HHU-1' and 'HHU-3' in Figure 6.1.) [63, 66], respectively, thereby further widening the gap between cryogenic and room-temperature graded resonators.

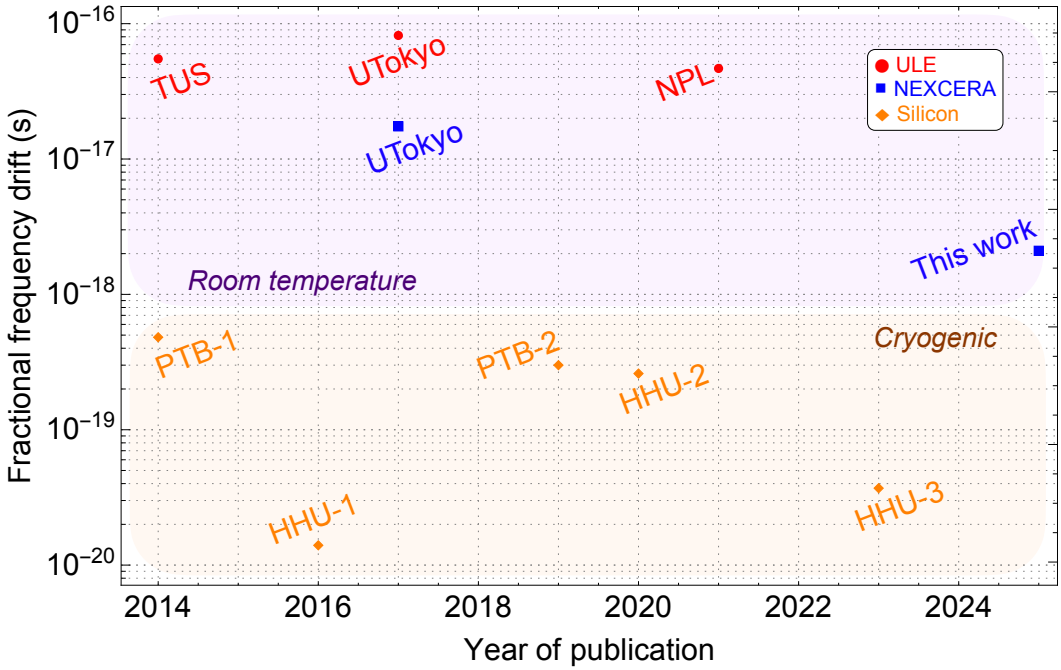


Figure 6.1: Recent results on optical cavities with ultra-low drift. TUS: [172], UTokyo: [119], NPL: [176], PTB-1: [71], PTB-2: [117], HHU-1: [63], HHU-2: [64], HHU-3: [66]

Nevertheless, the cost, space, and workload related efforts to set up cryogenic systems, as well as the difficulty to achieve low short-term instability strongly affected by vibrations inside the cryostats are still significant factors that draw toward the room-temperature variants. NEXCERA [177], is a poly-crystalline oxide ceramic spacer material that has been shown to have properties competitive with ULE. Ito et al. demonstrated a NEXCERA spacer that exhibits drifts of $4.9\,\mathrm{mHz\,s^{-1}}$ $\left(1.8\times10^{-17}\,\mathrm{s^{-1}}\right)$ [119], ('UTokyo' in Figure 6.1.).

This section provides a study of the long-term performance of an NEXCERA-based optical resonator, which constitutes the core component of the metrology system designed for single-ion spectroscopy on molecular hydrogen ions in Penning traps. The resonator frequency was measured over a period of 550 days and its drift is compared to the SI standard of frequency.

Context

The laser system was designed, developed and characterized at HHU Düsseldorf and subsequently transported by van (300 km) to MPIK Heidelberg in summer 2023 for a joint research initiative on precision spectroscopy on single molecular hydrogen ions in the Penning trap ALPHATRAP [124]. The measurements reported here were performed after the system was re-installed and hosted there. This context is important to be repeated here, in that transportation (and therefore time-dependent mechanical forces applied to the resonator) is a common scenario for how such a piece of equipment comes into operation in a research lab. The characterization of the drift was performed using metrology infrastructure (lasers, frequency comb, H-maser, GNSS receiver, antenna, computers and software) that was also transported from HHU to MPIK. Infrastructure for remote access of the system was provided by MPIK.

Reference Cavity and Laser Stabilization

The NEXCERA spacer (see Section 3.2) of type N118C was procured in 2016 and was initially utilized with ULE mirrors for 1064 nm, the results of which can be found in [120]. Subsequently, the mirrors were replaced with fused silica mirrors for 1.5 µm, on which ULE compensation rings are connected. The optical contacting was performed in-house. The system was operated in a semi-stationary manner, with intermittent movement between laboratories, and was used for experimentation at HHU [68, 37] until its transportation to MPIK Heidelberg. The resonator has a standard bi-conical shape connected via a centre rim with a larger diameter of 45 mm. The NEXCERA spacer has an inner bore hole with diameter of 1 cm, which can be evacuated by the use of a smaller, radial, bore hole connected to it and establishes the 12 cm long optical path. Two high reflectivity fused silica dielectric mirrors are optically contacted by us to the spacer. The finesse of the resonator was evaluated to approximately $\mathcal{F} \approx 7 \times 10^5$ through a ring-down measurement on the transmission signal. The cavity is arranged vertically in an evacuated vacuum chamber. A pressure level of 7×10^{-7} mbar is maintained by an ion pump.

In order to provide a stable thermal environment, the resonator is surrounded by an aluminum heat shield which is actively temperature stabilized by TECs and a temperature sensor on the bottom base plate of the resonator. A PID controller stabilizes the resonator to its experimentally determined ZCTE temperature at 17.8 °C. The experimental setup is shown in Figure 6.2. A fiber laser at 1.5 µm is locked to the cavity by an offset lock technique, where a phase-modulated sideband at f_{DDS}, generated by a waveguide EOM, is acting as carrier for the PDH technique [84, 85]. In this setup, the sideband frequency originates from a DDSwith a tunable center frequency at f_{DDS} = 200 MHz which is phase-modulated by a fixed internal signal at 12.8 MHz. An AOM is used both as a fast frequency actuator and for power regulation on the transmission of the resonator. In addition to the fast lock on the AOM, slow frequency variations of the laser are compensated by a slow lock through the modulation input of the laser.

The total power sent to the cavity is approximately 10 µW. The coupling efficiency to the TEM_{00} mode is 35 % on resonance relative to the total incident light power. This efficiency is reasonably high, considering that half of the incident power cannot be coupled into the resonator due to the inherent nature of the offset lock. The in-coupling optics, laser, waveguides and resonator are placed on a small breadboard, which is decoupled from the optical table by an AVI.

Optical Frequency Measurement

For the purpose of absolute frequency measurement, an OFC is employed (see Section 3.3). The OFC is phase-locked The resonator-locked laser through a beat between the laser and the closest mode in the OFC spectrum. The CEO is locked to a H-maser which also references oscillators, spectrum analyzers and frequency counters in the laboratory. This is achieved through a distribution amplifier and frequency doubler at one of the 5 MHz outputs of the H-Maser. In addition, the frequency of the laboratory H-maser is continuously compared to international standard at PTB Braunschweig through GNSS. It is compared to the respective frequencies of two masers in PTB Braunschweig that are steered towards the local Cs-clock.

Apart from the in-coupling to the resonator, the system is completely fiberized. A local Ethernet splitter connects computers, spectrum analyzers and oscilloscopes, forming a local network that can be accessed remotely. The resonator, OFC and lasers can be controlled, in part by home-built and in part by commercial software, making the system almost entirely controllable and serviceable from virtually anywhere. The following parameters can be controlled remotely: the frequency, power, and emission status of the reference laser; the output frequency of the DDS driving the EOM; as well as the slow and fast lock status, including the slow lock offset. For the OFC, the mode-locking, repetition rate, and CEO frequency can be adjusted via software, and both locking and unlocking functions are accessible. The OFC output modules are also software-controllable. Additionally, comparison of the laboratory hydrogen maser with the Cs-steered masers at PTB can be performed remotely. Data can be transmitted between the system and the remote login computer. Beats can be observed in real-time on spectrum analyses that are connected to the internal network.

The OFC and resonator also feature self-caring routines, such as an automated re-lock accounting for events that can lead the reference laser to fall out of lock and the necessary subroutines that stabilize the frequency comb to the set-point frequency.

Drift measurement and compensation

Since the NEXCERA resonator exhibits a small drift, it is actively compensated. The control system works as follows. The long term stability is achieved by comparing the NEXCERA-stabilised laser frequency with the H-maser frequency through the OFC. Here, a slow feedback loop, takes the average of the difference of the measured frequency against a set point frequency f_{set} over a time period of 20 seconds. This is interpreted as an error signal and compensated by a digital PID controller at a rate of 1 Hz. The frequency of the measured light f'_{laser} is therefore gradually stabilized by the lock to the maser to the fixed frequency f_{set}. Corrections to the cavity drift through a long term stable reference such as an H-maser in combination with an OFC have been demonstrated in [178].

Here, the drift compensation is achieved by acting on the frequency f_{DDS} of the phase-modulated sideband through a DDS as indicated in Figure 6.2. Thus, the OFC, as well as the resonator locked light, benefit from the short-term stability of the cavity and the long-term stability of the H-maser, resulting in stable light for experimentation that does not suffer middle-term frequency variations induced on the cavity spacer, such as temperature fluctuations or tilts. Consequently, the compensation frequency f_{comp} provided by this system contains information regarding the behavior of the cavity spacer (and mirrors), thereby facilitating the identification and evaluation of the long-term drift of the cavity.

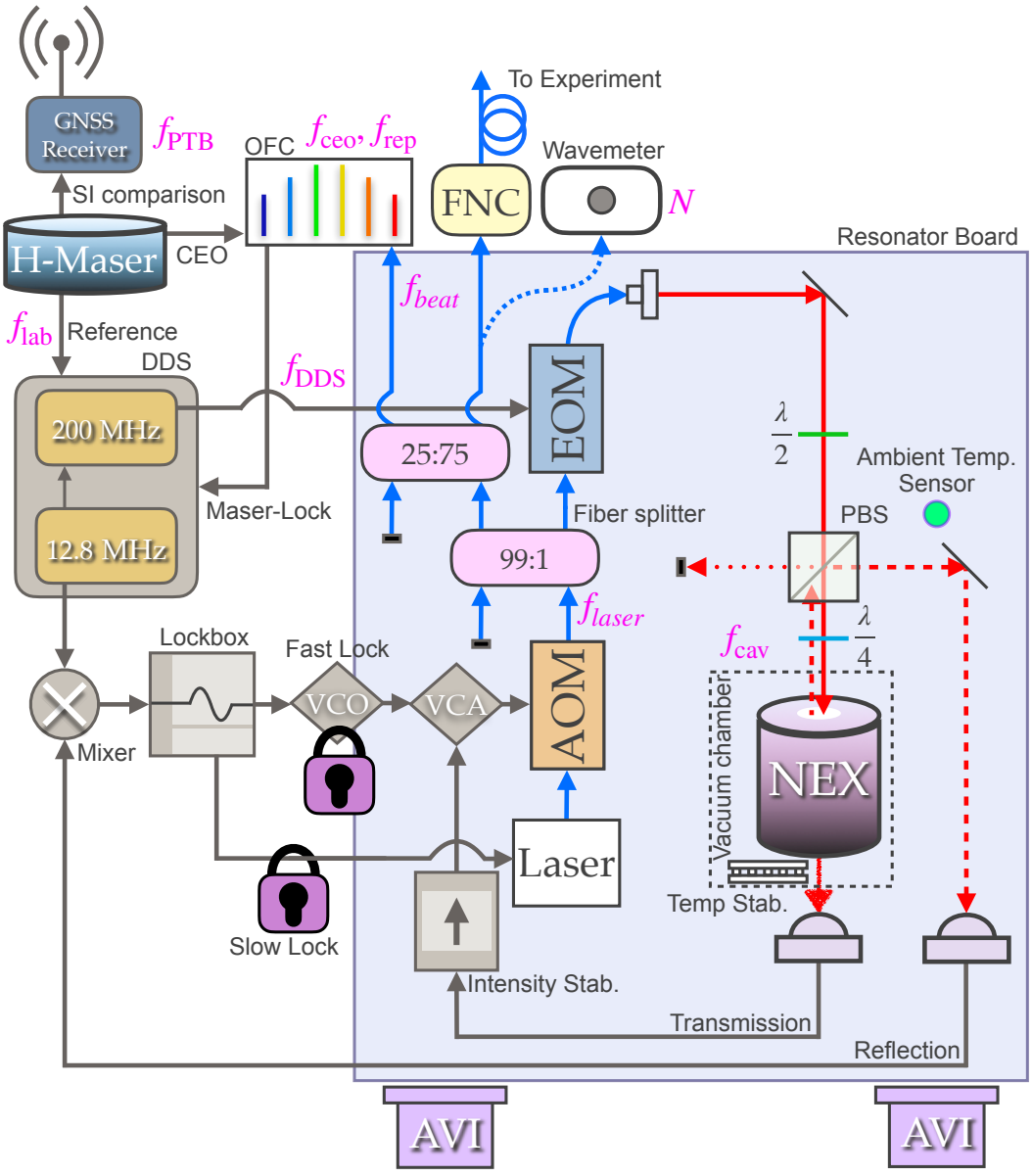


Figure 6.2: Schematic of the experimental setup. The VCO and VCA are employed for the fast lock and power stabilization of the laser light by modulating the AOM. The slow lock directly acts on the laser current. The light is stabilized to the NEXCERA resonator by the offset lock technique and slowly steered towards the H-maser by comparison via the OFC through a slow feedback loop.

Independent laser systems have demonstrated that this technique does not induce any measurable impact on short-term stability, but rather enhances long-term stability [68]. This was achieved by measuring the direct beat between the NEXCERA-locked laser and another ultra-stable laser while the drift mitigation was engaged.

Absolute Frequency Measurement

The laser light f_l that is shifted by the AOM frequency is beat with the N-th comb line, closest to the light. This beat frequency is denoted by f_{beat}. The comb modes are equally spaced by the repetition rate f_{rep} with the first mode not beginning at zero frequency but at an offset frequency f_{ceo}. This offset is arising from the phase shift between carrier and envelope between pulses in the pulse train of the OFC due to the difference between group and phase velocity between consecutive pulses. The absolute frequency of the light entering the OFC can be calculated by

$$f_{laser} = f_{beat} + N\, f_{\mathrm{rep}} + f_{\mathrm{ceo}} \tag{6.1}$$

The mode number N is determined by measuring the same light with a wavemeter that has a significantly better resolution than the repetition rate. The actual frequency of the cavity mode f_{cav} is calculated by adding the frequency f_{DDS}, of the synthesizer driving the EOM for the offset lock with the sign of the respective sideband, yielding

$$f_{\mathrm{cav}} = f_{laser} + f_{\mathrm{DDS}}. \tag{6.2}$$

The frequencies f_{beat}, f_{ceo} and f_{rep} are measured by counters that are referenced to the H-maser f_{maser}. The DDS is also referenced to it. For the frequency counters, this signal is considered to be exactly 10 MHz. However, we wish to determine the cavity frequency with respect to the international standard of frequency. This is achieved through comparison of this H-maser with masers at f_{PTB} in PTB via common-view GNSS. The PTB masers are steered to the international standard of frequency. Denoting the absolute frequency offset by $\delta f_{\mathrm{ref}} = f_{\mathrm{PTB}} - f_{\mathrm{lab}}$, then $\sigma_{\mathrm{ref}} = \frac{\delta f_{\mathrm{ref}}}{f_{\mathrm{PTB}}}$ is the fractional corrections to the laboratory reference f_{lab}. Thus, if a counter in our lab measures a value f_i', or a DDS provides such a frequency, the correct – SI-referenced – value f_i is found by

$$f_i' = f_i + \frac{f_i}{f_{\mathrm{PTB}}}\delta f_{\mathrm{ref}} = f_i\,(1+\sigma_{\mathrm{ref}})\,. \tag{6.3}$$

Equation (6.1) illustrates that the absolute frequency of the light stabilizing the comb mode, is determined by the summation of three distinct contributions. These components are measured using counters, with the H-maser serving as the standard reference. Consequently, each frequency must be corrected according to Equation (6.3). Thus,

$$f_{cav} = (1+\sigma_{\mathrm{ref}})^{-1}\left(f_{cav}' + f_{\mathrm{DDS}}'\right). \tag{6.4}$$

The laser frequency is corrected by the digital lock so that the frequency value measured by the comb with respect to the maser is maintained equal to a preset numerical value

$$f_{laser}' = f_{\mathrm{set}}'. \tag{6.5}$$

The discrepancy between the H-Maser and the PTB is represented by an offset frequency, which translates to $f_{\mathrm{off}} = \sigma_{\mathrm{ref}} f_{\mathrm{set}}$ at the laser frequency. The exact value of the offset has still to be determined however the drift of the H-maser could be estimated at approximately $-6\times10^{-16}\,\mathrm{d}^{-1}$ or $-7\times10^{-21}\,\mathrm{s}^{-1}$ with respect to the Cs-clock steered maser. Further, it translates to an overall drift of approximately 40 Hz yr^{-1} of the offset frequency.

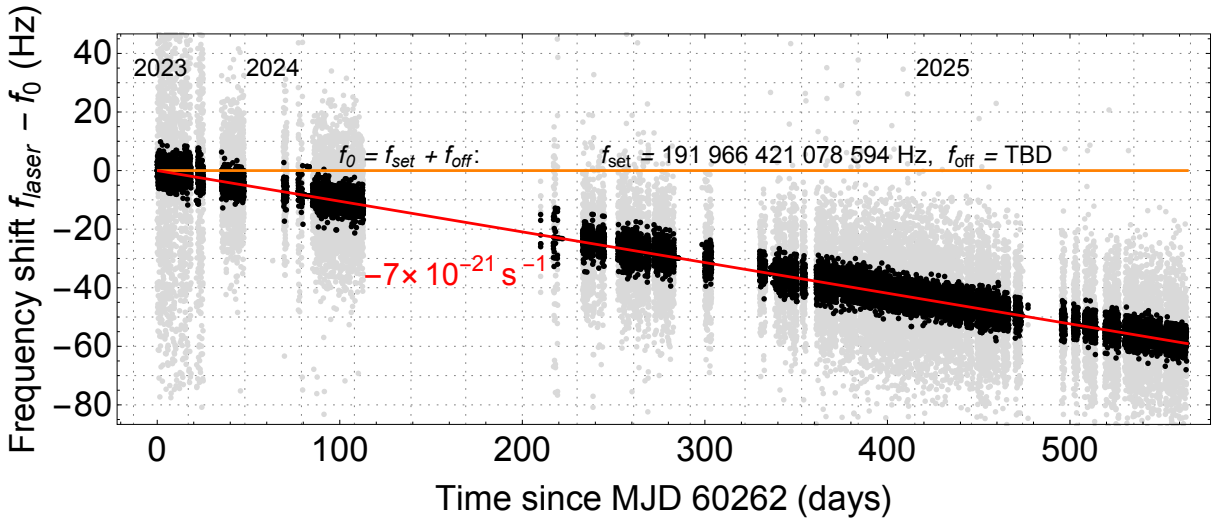


Figure 6.3: Grey: Measurement of the laser light frequency used to lock the comb-mode measured through the OFC. The absolute frequency f_{laser} of the cavity-stabilized laser, frequency-shifted by the AOM in order to maintain a constant preset frequency with respect to the H-maser (Equation (6.5)). It is obtained from f'_{laser} by applying the correction f_{off} that is still to be determined. Still the drift is approximately known. Black: a 20 second moving average over the grey data. A linear fit of the black data is shown as red line. This is corresponds to the estimate of the drift of our maser with respect to the international frequency standard. The orange line indicates the set frequency

During recording, the measured frequency, f'_{laser}, exhibited no drift around the set frequency. However, as illustrated in Figure 6.3, due to the slow drift of the H-Maser the actual frequency f_{laser} of the light underwent a downward drift. The data was collected at a sample rate of 1 Hz. However, due to the substantial size of the total files, every hundredth data point was considered in the analysis. Furthermore, in order to reduce the size of the plot, the data was further reduced such that two adjacent data points are spaced by 10 minutes. This also holds true for the data shown in Figure 6.5. The drift is indicated by the red line. The raw data, represented in grey, is constrained in its resolution by the counter utilized to measure the repetition rate in the first month. Subsequently, the H-Maser's short-term instability contributes to the limitation of the data. The black data, representing a 20 s moving average of the grey data, provides a more refined representation of the frequency fluctuations.

ZCTE Temperature of the Resonator

The coefficient of thermal expansion was determined by variation of the temperature of the resonator (heat shield) between two values T_1, T_2 and measuring the resulting cavity frequency shift $\Delta f_{\mathrm{cav}}(t,T_1,T_2)$ over time relative to the maser frequency. An individual measurement and a corresponding exponential fit

$$\Delta f_{\mathrm{cav}}(t,T_1,T_2) = \Delta f_{T_1\to T_2}\left(e^{-t/\tau}-1\right) \tag{6.6}$$

are shown in the inset of Figure 6.4. Here, τ is the time constant of the exponential function and $\Delta f_{T_1\to T_2}$ is the total frequency shift for the respective temperature variation, hence when $t\to\infty$.

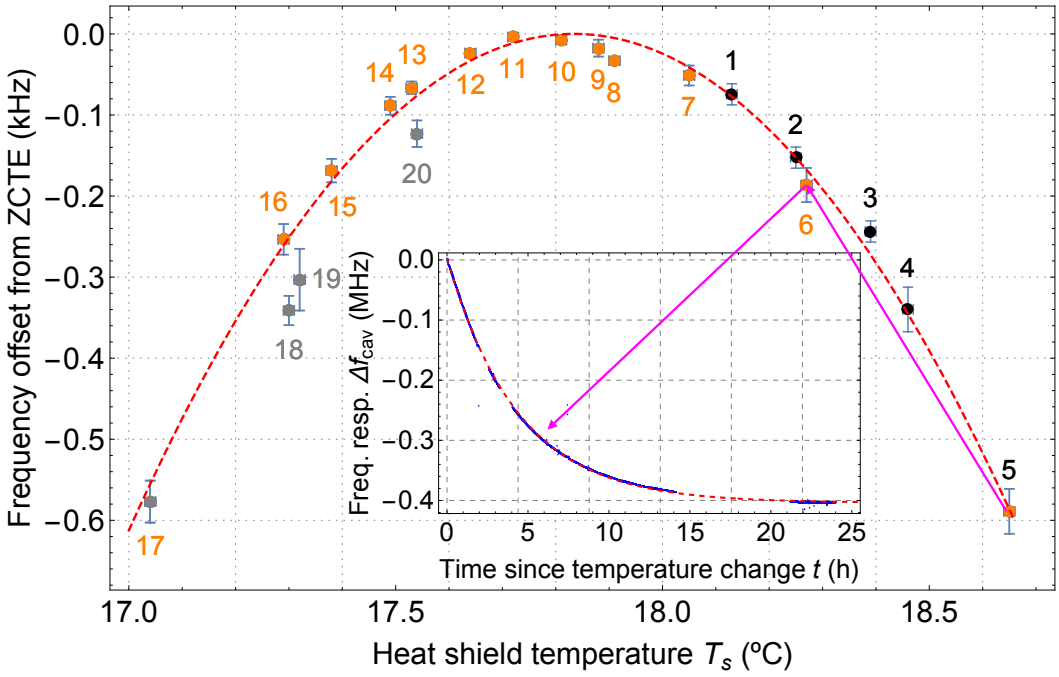


Figure 6.4: The ZCTE measurement of the NEXCERA N118C resonator. The inset illustrates the frequency response (blue) of the resonator during a single temperature change of the heat shield from $T_1 = 18.65\,°\mathrm{C}$ to $T_2 = 18.27\,°\mathrm{C}$, as indicated by the magenta arrows ($5 \longrightarrow 6$). In this instance, the blue line represents an exponential fit, yielding a time constant of approximately four to five hours. The ZCTE, as determined by the quadratic fit (illustrated by the red dashed curve), was found to be $17.83\,°\mathrm{C}$. The data points designated as 18, 19, and 20 were not included in the final analysis. The black, orange, and gray data points are indicative of the direction of change in temperature.

A total of seventeen measurements were taken, with approximately one day between each measurement. Each data point in Figure 6.4 is the result of measurement corresponding to a single temperature change. The plot shows the determined frequency shifts in dependence of the respective target temperature exhibiting a quadratic behavior which can be modeled by

$$\Delta f_{\mathrm{cav}}\,(t \to \infty, T_z, T_s) = \nu_0\,\beta\,(T_s - T_z)^2\,. \tag{6.7}$$

The experimentally determined ZCTE temperature is at $T_z = 17.83\,(1)\,°\mathrm{C}$ with a fractional frequency curvature of

$$2\beta = -9.0\,(2) \times 10^{-9}\,\mathrm{K}^{-2}$$

The β value is approximately 20 % larger and the ZCTE temperature is approximately 5 K lower than found in [120] for this same spacer with, at that time, ULE mirrors. Further, our curvature is more than twice as large as estimated in [179] $\left(3.86\,(3) \times 10^{-9}\,\mathrm{K}^{-2}\right)$. In that work, the ZCTE temperature $(16.4\,(1)\,°\mathrm{C})$ was within 1.5 K of the present value. In comparison to ULE, the β coefficient of our NEXCERA resonator is approximately a factor of six larger (see. e.g. [172], $\beta_{\mathrm{ULE}} = 1.5 \times 10^{-9}\,\mathrm{K}^{-2}$). It should be noted that our β value is still approximately twice lower compared to a silicon cavity at 124 K $(1.71\,(1) \times 10^{-8}\,\mathrm{K}^{-2}$ [59]).

Long-Term Variation of the Resonator Frequency

As illustrated in Figure 6.5, the frequency of the resonator is shown in the blue data points. The data has undergone adjustments at four specific points, indicated by magenta circles. The initial two events are associated with a change in the resonator's internal power, due to the replacement of the power stabilization unit. The timing of these events is marked by the first circle, indicating the moment power stabilization was deactivated, and the second circle, denoting its reactivation. It is observed that during these periods, the internal power within the resonator exhibited elevated levels, resulting in deviations in the data of 90 kHz and −70 kHz, respectively. These frequency shifts occurred over time scales of hours, which could be distinguished from long-term drift effects.

Consequently, a decision was made to compensate for these deviations in the data by manually removing the frequency shifts. The bar in the bottom of the plot indicates the time, at which the intensity stabilization was engaged. The other three events exhibited comparable jumps of 45 kHz, −55 kHz and 27 kHz, respectively, which may have been caused by active work on the system at those times. These frequency shifts were also removed from the data. In this particular instance, the slope of a linear regression (red) over the data for the duration of intensity stabilization is utilized to evaluate the drift, yielding a value of approximately $400\,\mu\mathrm{Hz\,s^{-1}}$ $\left(D = 2.07(2)\times10^{-18}\,\mathrm{s^{-1}}\right)$. This excludes data between the days MJD 60 278 and MJD 60 331 in terms of the modified Julian date (MJD)

To eliminate uncertainties introduced by frequency corrections, a linear fit was performed over the longest uninterrupted time interval. During the 176 days following MJD 60 601, when the system operated without perturbations, the fit (cyan) yields a drift estimate of $D = 2.03(4)\times10^{-18}\,\mathrm{s^{-1}}$, consistent with the results of the previous analysis within the statistical uncertainties. However, it should be noted that throughout the total measurement period, clear day-to-day variations in frequency were observed, which may potentially distort the calculated drift rates. To mitigate this, a further analysis is performed by comparing the resonator's ambient temperature variations $\Delta T = T_{\mathrm{am}} - T_0$ from the a temperature T_0 at the beginning of a measurement with its frequency variations $\Delta f_{\mathrm{cav}}(T_{\mathrm{am}},T_0) = f_{\mathrm{cav}} - f_0$. Figure 6.6 (a), demonstrates the relationship between these variations over a period of two months, with a spacing of 30 seconds between data points in frequency and temperature.

It should be noted that in this instance, the time variation in the OFC measurement and the maser time-dependent drift correction have not been applied, as their negligible size renders them inconsequential. The grey data represent individual frequency and temperature pairs, when the points are averaged over a window of 200 seconds, while the orange line indicates an average over the grey data over blocks of 10 mK, representing the sensor's resolution. The orange curve can be interpreted as the remaining temperature sensitivity of the cavity $f_0\,\gamma(\Delta T_{\mathrm{am}})$ with respect to ambient temperature variations which can also be applied to the raw frequency to generate a compensated frequency f_c that estimates its behavior decoupled from temperature given by

$$f_c = f_{\mathrm{cav}} - f_0\,\gamma(\Delta T)\,\Delta T. \tag{6.8}$$

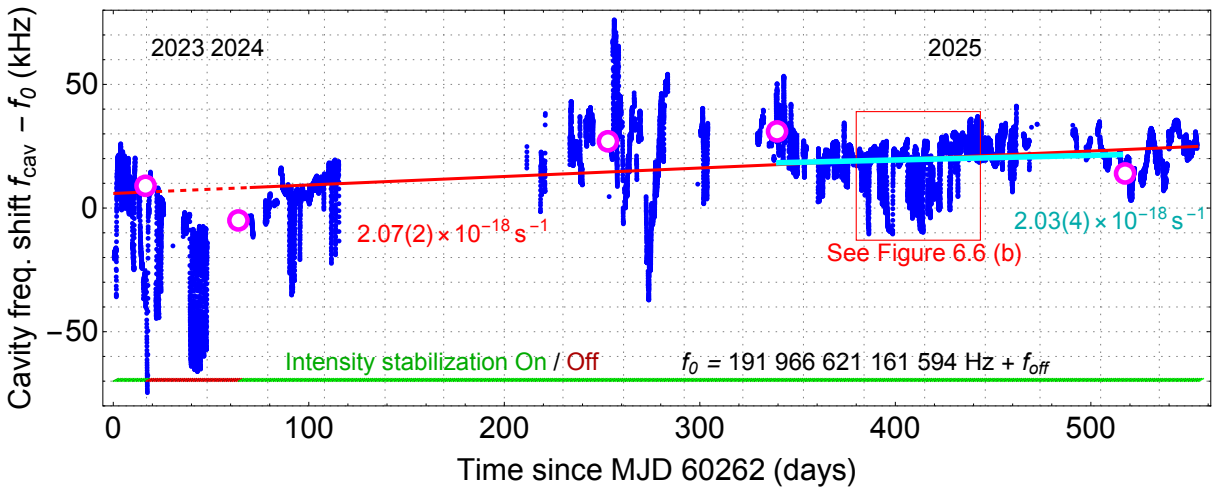


Figure 6.5: The long-term measurement of the cavity frequency. The blue line shows the cavity mode drift obtained from Equation (6.4). The red line shows a linear fit over the blue data for the time period the intensity stabilization was on. The magenta circles indicate the times when significant immediate frequency shifts of several 10 kHz were observed in the data. The horizontal red/green line at the bottom of the graph indicates the time interval during which the intensity stabilization was engaged. The cyan line is a fit over the longest time period that the frequency was uncorrected for (176 days).

The frequency and temperature data of the two-month measurement are represented by the blue and magenta lines in Figure 6.6 (b), respectively. It was evident that a time delay of approximately 24 minutes existed between a change in temperature and the subsequent effect on the resonator frequency. To facilitate further analysis, the frequency has been aligned by this time delay to coincide with the corresponding temperature change. The carrier frequency of the laser light is $\nu_0 \approx 192.967\,\mathrm{THz}$. The cyan line in the central panel of Figure 6.6 (b) represents the compensated frequency when Equation 6.8 is applied with $\gamma(\Delta T)$ being the orange data curve from Figure 6.6 (a).

The top and bottom panel show the frequency and temperature measurements during that time period, respectively. It is evident that a correlation between temperature variations and laser frequency exists, which could be partially removed during the analysis. However, due to the averaging processes in the sensitivity curve as well as its uncertainty and the non-perfect synchronicity of the thermal response of the cavity to temperature variations, the cyan data may still include effects due to temperature.

Despite the rudimentary approach, a linear fit over the resulting compensated frequency results in a drift of $D = 2.1\,(1) \times 10^{-18}\,\mathrm{s}^{-1}$. The elevated statistical uncertainty with respect to the other two values for the drift may be due to the not perfectly linear appearance of the compensated frequency data. Nonetheless, the drift over the whole data set (18 months), the longest uncompensated data set (6 months), and over the temperature decorrelated data set (2 months) all agree within their statistical uncertainties.

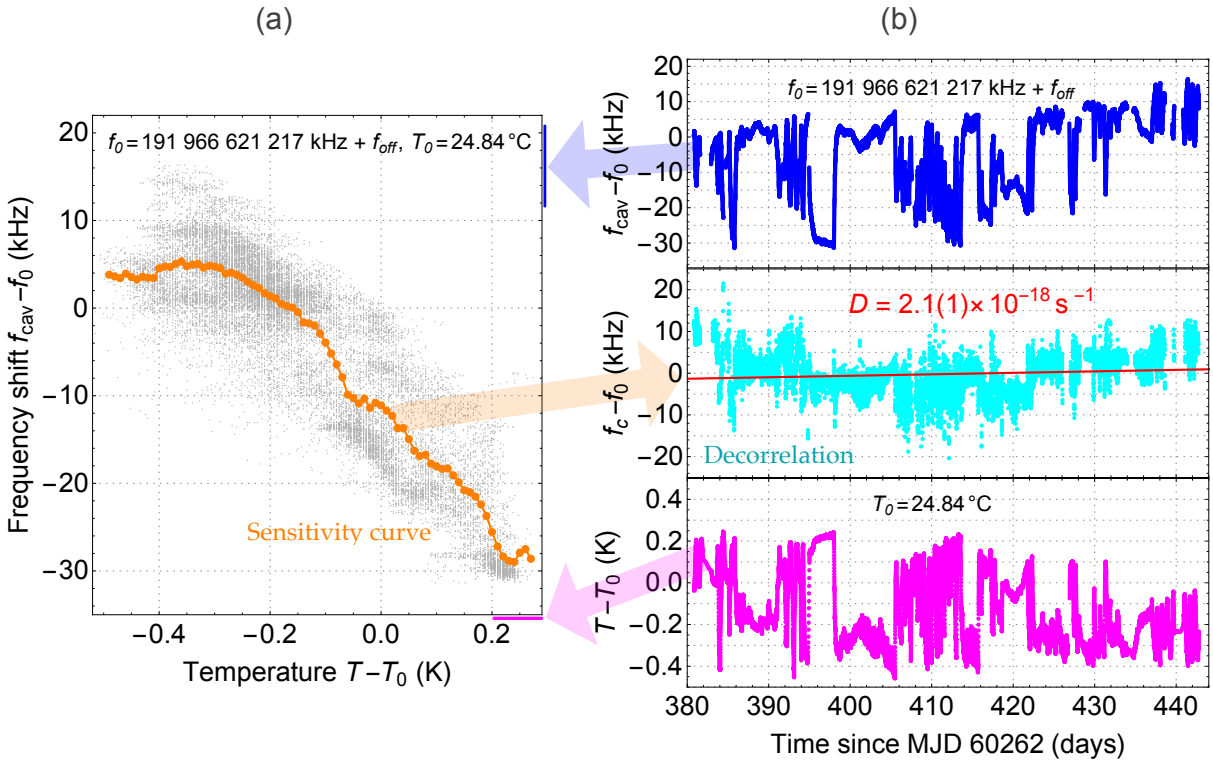


Figure 6.6: (a): Correlation of cavity mode frequency variations with ambient temperature. Grey: Plot of frequency changes over corresponding temperature variations. Orange: Average of grey data in blocks of size 10 mK. (b): Top: Frequency of the resonator mode over a period of two months. Middle: Corrected frequency after decorrelating the temperature variations by Equation (6.8). The red line is a linear fit over the data. Bottom: Ambient temperature data over the same time period. The data has been further parsed in order reduce the plot size.

Comparative Analysis

The characterization of the thermal properties of the resonator enables a comparative analysis of various configurations of cavities, substrates, and compensation rings, which is shown in Table 6.1. The table presents the length, ZCTE temperature, and corresponding β coefficients. In addition, the estimated aging drift of the respective system is provided together with the time frame of evaluation.

A distinction is made between room temperature and cryogenic systems. A notable observation is that the highest recorded temperatures were observed in the NEXCERA and ULE combinations, occurring at and slightly above ambient room temperature. It is also noteworthy that a configuration of FS mirrors and ULE compensation rings exhibits a 20 K difference between ULE and NEXCERA spacers of similar length. Additionally, the configuration of the NEXCERA spacer and ULE rings exhibits an approximate ZCTE of 15 K larger than that of a full ULE configuration. This finding suggests that NEXCERA possesses a significantly higher ZCTE temperature compared to ULE, thereby rendering it more suitable for utilization in conjunction with FS mirrors. Indeed, the resonator described in this work is unique in that it is the only one of this set that features FS mirrors at a temperature that is not close or even below 0 °C.

Spacer	L (cm)	Substrate	Rings	T_z	-2β	$-\Delta L/L$
Room Temperature				°C	$10^{-9}\,\mathrm{K}^{-2}$	$10^{-17}\,\mathrm{s}^{-1}$
ULE [29]	8.4	ULE	None	8.5 / 9	1.9	N/A
ULE [29]	8.4	ULE	None	7 / 7.5	1.4	N/A
ULE (H) [172]	10	ULE	None	−3.3	1.5	5.5 (2 mo)
ULE (V) [172]	7.75	ULE	None	22.4	1.6	16
ULE [119]	7.75	ULE	None	26.5	1.1	6.7 (2 mo)
ULE [72]	10	FS	ULE	1.18	2.3	N/A
ULE [103]	30	FS	ULE	−0.11	1.9	N/A
ULE [102]	30	FS	ULE	−0.85	1.9	N/A
ULE [176]	5	FS	ULE	N/A	N/A	4.7 (2 mo)
NEXCERA [119]	7.75	ULE	None	26.6	4.9	1.7 (2 mo)
NEXCERA [120]	12	ULE	None	22.9	7.6	55 (2 mo)
NEXCERA	12	FS	ULE	17.83	9.0	**0.21 (18 mo)**
DFRR	10^4	None	None	−28.2	40	N/A
Cryogenic				K	$10^{-9}\,\mathrm{K}^{-2}$	$10^{-20}\,\mathrm{s}^{-1}$
Silicon [59]	21	Silicon	None	124	17	N/A
Silicon [71]	21	Silicon	None	124	N/A	49 (2 mo)
Silicon [63]	25	Silicon	None	N/A	N/A	1.4 (5 mo)
Silicon [64]	5	Silicon	None	3.5	8.5×10^{-3}	26 (2 mo)
Silicon [66]	19	Silicon	None	1.6 – 4.0	N/A	3.7 (6 mo)

Table 6.1: A comparison of thermal properties in different resonator configurations. The initial two ULE resonators are comprised of two ULE blocks, each equipped with two cross-resonators. The ZCTEs contained within a given block are represented adjacent to one another. The first NEXCERA resonator is composed of N117B material, while the subsequent two are composed of N118C. A distinction is made between room temperature and cryogenic systems. The table presents a summary of the length, the substrate material, the compensation rings, the ZCTE temperature, the CTE coefficient 2β, and the long-term drift $\Delta L/L$. The bold systems are described in this thesis. The DFRR is the fiber ring resonator.

The lowest length drift of any material at room temperature, to the best of knowledge, has been observed in the NEXCERA cavity. The value is approximately $2.1\times10^{-18}\,\mathrm{s}^{-1}$ over a time period of 550 days. This represents an improvement of almost an order of magnitude compared to previous measurements on the NEXCERA material and more than a factor of 20 compared to the lowest drifts reported to date on ULE-type resonators. Further, the gap between this result and some of

the most advanced cryogenic resonators is less than an order of magnitude. It is also only a factor of four larger than in the cryogenic system in [71], and is only two orders of magnitude away from the best cryogenic systems [63, 66].

In addition, it is approximately 300 times larger than the drift of the H-Maser, which is estimated to be approximately $-7 \times 10^{-21}\,\mathrm{s}^{-1}$. However, given the simplicity of the resonator setup, which yields a total frequency drift at the order of 12 kHz per year at the optical carrier frequency, the material is a reasonable long-term reference for applications aiming for a 10^{-10} level of frequency uncertainty.

In the final analysis, the remarkably minimal drift, the more accessible ZCTE temperature, and the equivalent or lower thermal noise floor all serve to establish NEXCERA as a competitive spacer material to ULE. However, this is accompanied by a factor of twice the steeper CTE curvature, which increases the requirements on the temperature stability.

Chapter 7

Search for Dark Matter in the Fourier Domain

The UDM is modeled as a scalar field $\phi(t)$ [57, 180]. Due to the extremely low mass of the particles, their Compton wavelength, defined as $\lambda_C = h/mc$, is exceedingly large. This results in a significant overlap of the wavelengths of these particles, which complicates their analysis and treatment as distinct entities. The UDM field is expressed as follows:

$$\phi(t) = \phi_0 \sin(2\pi f_C t)$$

The amplitude, ϕ_0, is assumed to remain constant within the confines of the experiment. The oscillation of the field is determined by the Compton frequency

$$f_C = \frac{m_{udm} c^2}{h} = \frac{E_{udm}}{h},$$

with the speed of light c, the Planck constant h, and the energy of the UDM E_{udm}. The mass of UDM is generally expressed through its energy. Typically, in the case of UDM, masses well below 1 eV are of concern. This hypothesis suggests that the UDM exhibits a weak coupling with masses and the electromagnetic field, resulting in oscillations in fundamental constants (FCT) such as the electron or nuclear masses m_e and m_N or the electron charge e. Consequently, this would also lead to oscillations in the fine structure constant α_0. Therefore, by probing a vibrational transition that is sensitive to those FCT, one can search for their oscillations.

In this experiment, an ultra-stable laser is utilized to interrogate a fixed point at the flank of a molecular absorption line through a vapor cell. The concept is illustrated in Figure 7.1. The output signal of the cell is then directed towards a photo detector. If balanced detection is employed, this signal is subtracted to the signal on a detector measuring the unperturbed laser signal to reject common mode noise.

According to the classical perspective, in an unperturbed environment, the difference signal should be at a constant amplitude. This results in a spectral noise density that yields a Dirac delta at the carrier frequency. Consequently, the amplitude is zero at all other frequencies in the Fourier domain, thus there are no sidebands at higher frequencies.

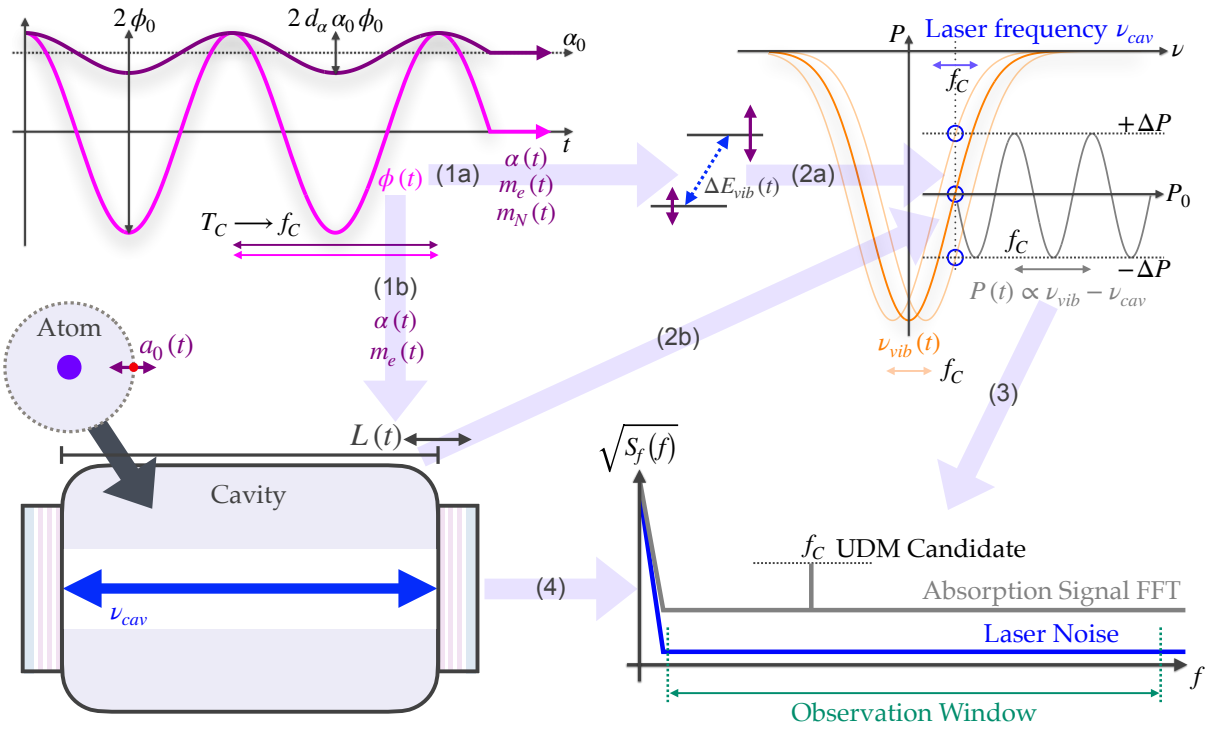


Figure 7.1: The concept guiding the search for UDM in this context. The UDM scalar field (magenta) oscillates at the Compton frequency f_C (with a time period T_C), which couples to FCTs, here represented by the fine structure constant, α (purple). The FCTs will exhibit an oscillation itself, the strength of which is determined by the respective coupling constants d. (1a): Oscillations in α, m_e, and m_N lead to oscillations in the vibrational electronic energy levels. (1b): Oscillations in the Bohr radius a_0, thus in α and m_e lead to oscillations in the cavity length. (2a): The oscillation of the transition energy is translated to the molecular transition frequency, ν_{vib} (orange). (2b): The change of the cavity length induces an oscillation in the locked laser frequency. Oscillations in the difference $\delta\nu = \delta\nu_{vib} - \delta\nu_{cav}$ are transferred to the amplitude of the absorption signal (gray) at the laser frequency (blue circles) at the flank of the transition. (3) and (4): A Fourier transform of the detected signal will manifest a sideband at the UDM frequency, f_C, under conditions wherein the laser noise (blue) (and that of the apparatus) is sufficiently low to allow for its resolution. The depicted laser noise is typically evaluated using beats with light locked to other optical cavities, where the UDM contribution would be common mode.

However, in practice, the signal will still exhibit noise arising from the electronics, measurement apparatus, and laser light. Nevertheless, in the presence of an oscillating scalar field that couples to the FCT, the fine structure constant will undergo a transformation:

$$\alpha\,(t) = \alpha_0\,(1 + d_\alpha \phi_0 \sin(2\pi f_C\, t))\,.$$

In this context, the quantity α_0 is understood to be its value in the absence of a scalar field. The parameter d_α represents the coupling strength between the UDM and the fine structure constant. The same description models oscillations in the electron and nuclear masses with the coupling coefficients d_e and d_N, respectively. The fractional frequency variation due to coupling with dark

matter can be described by

$$\frac{\delta\nu_j}{\nu_j} = R_\alpha^{(j)}\frac{\delta\alpha}{\alpha_0} + R_{m_e}^{(j)}\frac{\delta m_e}{m_e} + R_{m_N}^{(j)}\frac{\delta m_N}{m_N},$$

where the parameter j describes either the molecular transition or the cavity length and $R_k^{(j)}$ is the sensitivity factor of the respective FCT k. While the energy levels of the transition are sensitive to all three FCTs, the cavity length is connected to the Bohr radius a_0 which is expressed as $L \propto a_0 = \hbar(m_e c\alpha_0)^{-1}$. Therefore, for the cavity it is $R_\alpha^{(cav)} = R_{m_e}^{(cav)} = 1$, and it reads

$$\frac{\delta\nu_{cav}}{\nu_{cav}} = \frac{\delta\alpha}{\alpha_0} + \frac{\delta m_e}{m_e}.$$

In the molecule on the other hand, the transition frequency is given by the energy difference of the states with vibrational quantum number v, which are given by

$$E_{vib}(v) = hc\underbrace{\frac{\alpha_0^2 m_e c}{2h}}_{R_\infty}\left(v+\frac{1}{2}\right)\gamma\sqrt{\frac{m_e}{\mu_N}},$$

within the Born-Oppenheimer approximation. Here, R_∞ is the Rydberg constant and the constant γ depends on the electronic state. The reduced nuclear mass μ_N is expressed by

$$\mu_N = \frac{m_e m_N}{m_e + m_N}.$$

The sensitivity of the molecular transition frequency to the fine structure constant is therefore $R_\alpha^{(vib)} = 2$, while $R_{m_e}^{(vib)} = 1 - R_{m_N}^{(vib)}$ are dependent on the electronic state. Eventually, the measured quantity is the difference between the molecular transition and cavity locked light $\delta\nu = \delta\nu_{vib} - \delta\nu_L$, thus

$$\begin{aligned}\frac{\delta\nu}{\nu_0} &= \Delta R_\alpha\frac{\delta\alpha}{\alpha_0} + \Delta R_{m_e}\frac{\delta m_e}{m_e} + \Delta R_{m_N}\frac{\delta m_N}{m_N}\\ &= \frac{\delta\alpha}{\alpha_0} - R_{m_N}^{(vib)}\frac{\delta m_e}{m_e} + R_{m_N}^{(vib)}\frac{\delta m_N}{m_N}.\end{aligned} \tag{7.1}$$

In this context $\nu_0 = \nu_{cav} \approx \nu_{vib}$ is the optical carrier frequency of the light corresponding to the vibrational transition frequency. The respective sensitivity factors for the cavity and examined vibrational transitions are summarized in Table 7.1. Equation (7.1) shows the concept of the UDM detector. Two cavity stabilized lasers will always exhibit a vanishing contribution from dark matter in the beat frequency due to the identical sensitivities. By comparing the cavity to a molecular transition, a non zero signal contribution in $\delta\nu\,\nu_0^{-1}$ would be expected. Consequently, this will result in an oscillation, which can be observed on the photo detector. This is due to the fact that the amplitude, $P(t)$, of the absorption line at the laser frequency, ν_{cav}, will now vary in time. The spectral frequency noise density, $\sqrt{S(f)}$, is evaluated by performing a fast Fourier transform (FFT) on the signal after the photodetector. Consequently, a sideband at the oscillation frequency, f_C, emerges.

Sensitivity	Cavity	Iodine [36]	Acetylene [37]
R_α	1	2	2
R_{m_e}	1	0.94	0.532
R_{m_N}	0	0.06	0.468

Table 7.1: Sensitivity factors of the employed detectors for the search for UDM. In particular the sensitivity R_{m_N} is of interest when comparing both molecular transitions. The measurement of $\delta\nu\,\nu_0^{-1}$ in the Acetylene transition is eight times more sensitive to oscillations in the electron and nuclear masses than in the Iodine transition.

Therefore, the molecular absorption is compared to the cavity locked laser, implying that a high spectral purity of the light will benefit the resolvable noise floor. The sampling rate of the detector imposes an upper frequency limit on the range of frequencies that can be examined. The duration of the measurement can be utilized to average down, thereby enhancing the visibility of potential static sidebands in the spectral noise density. In the subsequent two publications, the constraints imposed by the experimental setup result in an observed window ranging from 10 Hz and 100 kHz in the Fourier domain. In this particular range, high-performance, ultra-stable lasers exhibit a remarkable degree of alignment with the optical reference, attributable to the narrow linewidth and servo bandwidth of the locked light. With regard to mass, the configurations enable the examination of prospective UDM couplings ranging from 4×10^{-14} eV to 4×10^{-10} eV.

In order to probe higher energies, it is necessary to consider two factors. Firstly, in order to achieve a faster sampling rate of the signal, additional measures must be taken. Secondly, the stability of the light must be ensured as the frequency range leaves the locking bandwidth. The utilization of cavities as mode cleaners has been demonstrated in Section 4.2. The detectors were operated by R. Oswald. The responsibility of the author of this thesis was to prepare and maintain a spectrally pure light source that was used to interrogate absorption lines in iodine and acetylene, respectively, for the purpose of searching for UDM at the given energy scales. The theoretical analysis and treatment of the results is the scope of other works; here, the performance of the light in the context of its phase noise will be displayed.

7.1 Search for Dark Matter in Iodine

Referenced work: Oswald et al., Search for Dark-Matter-Induced Oscillations of Fundamental Constants Using Molecular Spectroscopy, Physical Review Letters 129 (2022) pp. 031302 [36]. Publication in Appendix B.1.1.

The ULE resonators, when installed in Lab1 (see Section 3.1), were utilized in a measurement campaign that sought to search for UDM in oscillating fundamental constants. The laser light, locked to C2, was directed towards a setup where a transfer laser operating at 1064 nm was phase locked to it, and its frequency was doubled through a process known as second-harmonic generation (SHG). This light, at 532 nm, is transmitted through a gas cell containing iodine gas,

while the frequency is stabilized at the flank of one of the absorption lines of the gas. The measurement of the transmitted light of the cell is achieved through the utilization of a balanced detector, which serves to calculate the ratio of the transmitted light to the incident light. Subsequently, the resulting signal is analyzed in its frequency domain.

Initially, the setup, which included the vapor cell, was placed in a different laboratory than the ULE resonators. The two were connected by a fiber that ran several hundred meters.The implementation of the FNC configuration was indeed possible; however, this process resulted in a significant reduction in the light's power, thereby it was inactive during the measurement process. Additionally, the laser frequency was analyzed at frequencies greater than 100 Hz. In this case, the focus was not on the linewidth and low frequency performance of the laser, which renders the FNC superfluous.

An analysis of the performance of the light has been conducted and the results are presented in Figure 7.2. The beat between the lasers locked to C1 and C2 respectively is indicated by the blue line. Furthermore, a measurement of the fiber noise was carried out, whereby the light of the laser locked to C1 was transmitted through the long fiber, reflected back, and then beat with the light stabilized to C2, as illustrated in gray. The performance of the PLL has been measured on the PLL beat between the transfer laser and the reference laser. The result of this measurement is shown in red. The black line signifies the combination of the gray and red curve, thereby yielding an upper estimation of the frequency noise limit due to the laser through the cell.

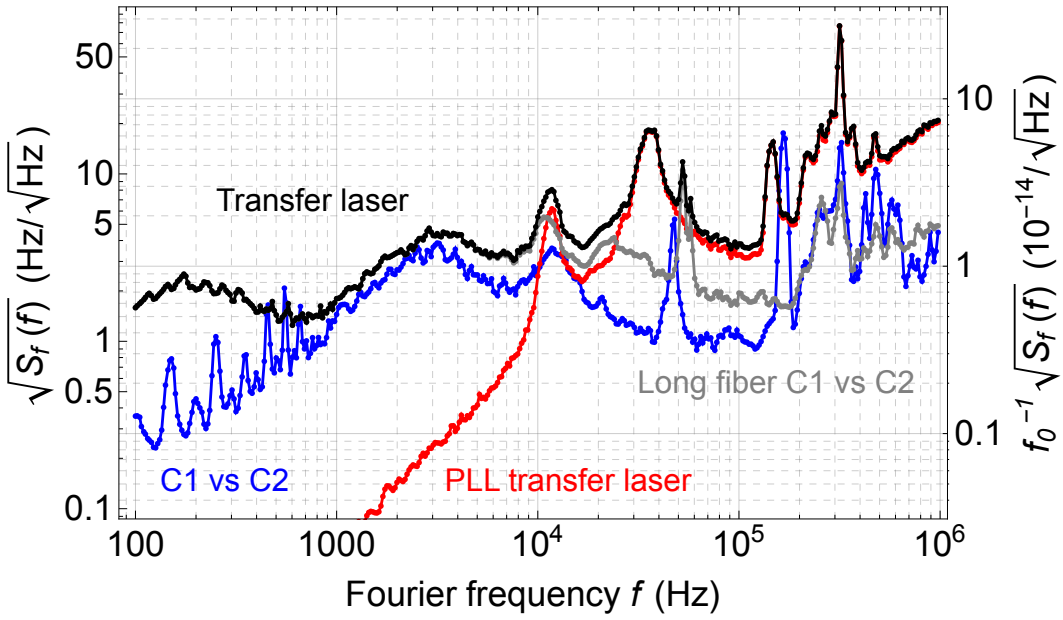


Figure 7.2: The spectral frequency noise density of the transfer laser (black) interrogating the vibrational transition in the iodine experiment. It is estimated from the beat of the reference laser with the second ULE stabilized laser (blue), the PLL (red) of the transfer laser, and the fiber noise (gray).

The black data set constituted the basis for the analysis in the referenced work, which revealed that detector noise remained the primary limiting factor. However, the laser light exhibited a deviation of less than an order of magnitude, underscoring the significance of ultra-stable light for precise measurements. The performance of the transfer laser was found to be below the $2 \times 10^{-14}\,\mathrm{Hz}^{-1/2}$ level when evident sidebands were removed from the PLL around $10^4\,\mathrm{Hz}$ and $3-4\times10^4\,\mathrm{Hz}$. Here, it can already be seen that the use of a PLL is introducing significant noise at higher frequencies above $10^5\,\mathrm{Hz}$, while the performance of the beat between the ULE lasers remains at the low to mid $10^{-14}\,\mathrm{Hz}^{-1/2}$ level up to 1 MHz in the Fourier domain.

7.2 Search for Dark Matter in Acetylene

Referenced work: Oswald et al., Search for oscillating fundamental constants using a paired detector and vibrational spectroscopy, Phys. Rev. D 111 (2025) pp. 055003 [37]. Publication in Appendix B.1.2.

In a manner analogous to the experiment on UDM in iodine, an experiment was set up to search for UDM and oscillating fundamental constants in acetylene, as it has an increased sensitivity. In contrast to the previous configuration, which necessitated SHG on NIR light, this time the acetylene line frequency was approximately 1.53 µm. Consequently, the metrology system (see Section 3.3), incorporating the NEXCERA resonator (see Section 3.2), was engineered to facilitate the integration of a laser at the designated wavelength as a reference light source.

Furthermore, a cross-correlation analysis was conducted through the implementation of two independent experiments. These experiments incorporated a gas cell, photo detectors, and a reference laser, thereby ensuring the reliability and precision of the analytical process. The NEXCERA-based laser was utilized as the reference standard for one of the systems, while the other system operated using another ULE-stabilized laser operating at 1.53 µm. It is the same laser that was utilized during the characterization phase of the NEXCERA-based metrology system.

For the purposes of this referenced work, the focus was exclusively on the frequency noise of the laser light, spanning frequencies between 10 Hz and 100 kHz. This narrowed the scope to a particular range, thereby diminishing the significance of Allan deviations. The linewidth of the light, however, is increasingly important at the lower limit. The measurements for the publication were conducted while the NEXCERA resonator and metrology system were operating in HHU.

The performance of both lasers is illustrated in Figure 7.3. Here, the frequency noise was measured as shown in Section A.5.2, by analyzing five independent sweeps of the spectral power density for different frequency spans and RBW and converting into frequency noise. The instability persists at the $10^{-14}\,\mathrm{Hz}^{-1/2}$ level for frequencies ranging from 10 Hz to $10^4\,\mathrm{Hz}$, exhibiting a rise to nearly $10^{-12}\,\mathrm{Hz}^{-1/2}$ at $10^5\,\mathrm{Hz}$ due to the bandwidth limitation of the VCOs.

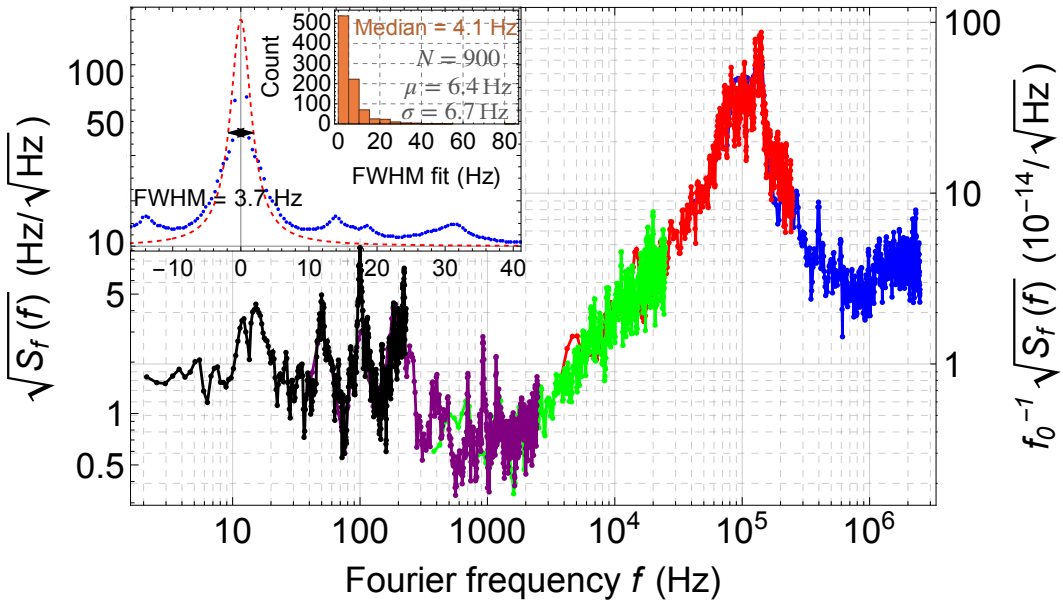


Figure 7.3: The spectral frequency noise density of the beat between the NEXCERA laser and the ULE laser operating the UDM detectors. The inset illustrates the line width measurement that was obtained over a series of 900 consecutive sweeps, with an RBW of 1 Hz. The histogram provides the fit parameter for each individual sweep. The peaks at around 100 kHz are due to the locking bandwidths of both PDH setups.

The linewidth of the beat is also displayed in the inset. A total of 900 consecutive sweeps of 1 Hz RBW and sweep times of approximately 4 seconds were analyzed. The blue curve indicates the mean of the overlap of all sweeps, with the drift of the beat having been previously removed. The red curve represents a Lorentzian fit over this data set, yielding a linewidth of approximately 4 Hz. This finding aligns with the median of all individually analyzed sweeps. Nevertheless, the mean is marginally elevated at 7 Hz, as the presence of outliers during the measurements is observed. Eventually, the frequency noise was estimated to be between one and two orders of magnitude below the detected signals. As a result, the measurement was not limited by the light, but the necessity of ultra-stable lasers was warranted.

Chapter 8

Precision Spectroscopy of Molecular Hydrogen Ions

The complexity of a bound system increases as one progresses from atoms to molecules, with the presence of two nuclei and a single electron in the specific case of diatomic MHIs. MHIs represent a pivotal area of research at HHU. An exposition of MHI, encompassing its historical development in research, theoretical underpinnings, and experimental nature, has been provided in [44]. This work serves as the foundational reference for the present section. The molecular structure is depicted in Figure 8.1 (a). In this particular instance, the focus will be on the heteronuclear molecule HD^+, which is composed of a proton, a deuteron, and an electron.

The three-body problem is a notoriously challenging analytical problem, with its solution to energy being the subject of extensive research, i.e. in [181]. The nuclei are maintained in the center by the electron, which exerts a force that draws them together. Additionally, the motion of the electron keeps it from colliding into one of the nuclei. The incorporation of the additional third particle introduces an additional degree of freedom into the system. In order to illustrate this concept, one may consider an elliptical trajectory of an electron, with the nuclei placed at the foci of the ellipse.

In this scenario, the center of mass or charge remains unperturbed under two distinct conditions: first, a combined rotation of the nuclei around the center; and second, a vibration along their axis. The potential of the electronic ground state, $^1\Sigma^+$, is shown in Figure 8.1 (b). It can be modeled using a repulsive potential between the nuclei and an attractive potential between the electron and each nucleus. In this configuration, $R = \left|\boldsymbol{r}_p - \boldsymbol{r}_d\right|$ represents the distance between the two nuclei.

A comparison can be made between this model and the potential of a harmonic oscillator (HO) $V_{ho} \propto x^2$, particularly in the vicinity of the dip region of the potential at $R = 2a_0$, where a_0 is the Bohr radius. As a result, similar to the HO, vibrational states of distinct energy are obtained. In a similar fashion, the motions and energies in a diatomic molecule bound by the electronic potential are not arbitrary. Rather, they are subject to certain rules that result in a quantization of possible energies. The quantum numbers in question are vibrational v, with quantum number values of $v = 0, 1, \ldots$, and rotational N, with quantum number values of $N = 0, 1, \ldots$.

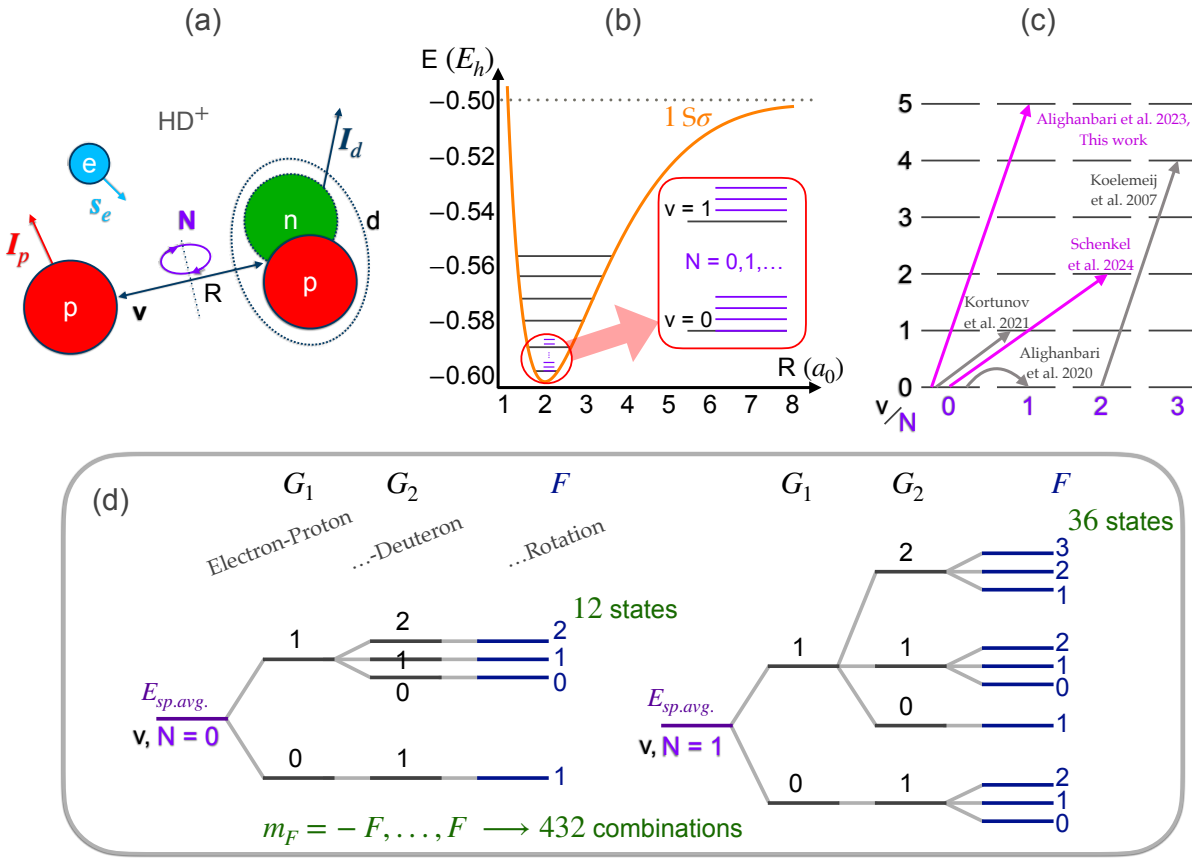


Figure 8.1: The following is a collage of characteristics of the MHI HD^+: The energy levels are not to scale. (a): The molecule's schematic structure (n: neutron, p: proton, e: electron) encompasses spins, vibrations, and rotational quantum numbers. (b): A plot of the potential of the $^1\Sigma^+$ electronic state. The energy is measured in units of $E_h = 1\,\text{Hartree}$ and plotted against the nuclear distance R, which is expressed in units of the Bohr radius a_0. The inset provides a magnified view of the well of the potential, which in turn illustrates the vibrational and rotational states of the nucleus. (c): The energy diagram in the $1\,\text{S}\sigma$ electronic state, with a focus on quantum numbers $v \leq 5$ and $N \leq 3$. The gray lines represent the works of [32, 33], while the magenta lines denote the measurements of [34, 35]. Additionally, a two photon-transition was measured in [49], from $(0,3) \longrightarrow (4,2) \longrightarrow (9,3)$. The author of this thesis made a direct contribution to the magenta lines. (d): The fine structures of the $(0,0)$ and $(5,1)$ states, including the (electron-proton)-deuteron and rotational coupling parameters G_1, G_2 and F for a zero magnetic field. The $(0,0)$ state has 12 sub-states, whereas $(5,1)$ is comprised by 36 Zeeman sub-levels given by the projection spin-coupling number m_F. Diagrams in (d) are not to scale.

Solving the Schrödinger equation quickly demonstrates the limitations of the analytical approach, thereby indicating that the rovibrational energies, $E_{v,N} \longrightarrow E$, cannot be simply extracted. The precise calculation method is intricate and beyond the scope of this thesis. An energy level diagram is shown in Figure 8.1 (c). It should be noted that the ensuing discussion will exclusively address the $^1\Sigma^+$ state as it is the only stable bound state. Notably, if the nucleus distance diverges, the system will eventually dissociate into one of the nuclei and the 1S state of (heavy) hydrogen with an energy of $-0.5\,\text{Hartree} \approx -13.6\,\text{eV}$.

Moving from the general description of the rovibrational energy levels, laser spectroscopy can be used to probe the energy difference between two states. In a two level system of two specified energy states, designated as ground state g and excited state e, which are characterized by a predetermined set of quantum numbers, that difference, denoted by ΔE can be expressed in terms of the frequency, ν_{ph} of a photon of equivalent energy:

$$\Delta E = E_e - E_g = E_{ph} = h\nu_{ph} \Longleftrightarrow \nu_{ph} = \frac{\Delta E}{h}.$$

This transition can thus be examined by tuning a laser to the appropriate frequency, ν_{ph} and subsequently observing the response of the molecule. In order to accurately probe the transition, it is essential that the laser exhibit instability that is comparable to, or better than, the natural linewidth γ of the excited state which was derived in Section A.5.1). In summary, it is a measure for its life time $\tau = \gamma^{-1}$.

However, under the assumption of a transition in the HD^+ molecule in the $^1\Sigma^+$ electronic state interrogated in resonance by a narrow linewidth $\left(\nu_{ph}^{-1} f_c = 10^{-13}\right)$, and with a highly stable $\left(\nu_{ph}^{-1}\sigma_f = 10^{-14}\right)$ laser at frequency ν_{ph}, the transition energy can be evaluated experimentally. In order to compare it to theory, not considering any systematic effects in the measurement yet, two corrections have to be introduced:

- Firstly, perturbation theory is employed to calculate the energies, utilizing relative orders of the fine structure constant, α^k. This approach encompasses the calculation of relativistic and quantum electrodynamic (QED) contributions. These correction terms f_{corr} can result in shifts in frequency with an order of magnitude of $\nu_{ph}^{-1} f_{corr} = 10^{-9}$. This frequency is also designated as the spin average frequency, denoted by $\nu_{ph} \longrightarrow \nu_{sp.avg.}$.
- Secondly, the (hyper)fine splitting of the transition has not yet been examined. Moreover, in contrast to the hydrogen atom with two spin quantum numbers, there are now four angular momenta that can couple: the proton spin $\hat{\boldsymbol{I}}_p$, the deuteron spin $\hat{\boldsymbol{I}}_s$, the electron spin $\hat{\boldsymbol{s}}_e$, and the rotational momentum $\hat{\boldsymbol{N}}$, here displayed as (vector) operators. This model requires the extension of the Hamiltonian, incorporating a range of coupling terms that collectively generate the fine structure of a particular electronic and rovibrational energy state.

The hyperfine splittings in small magnetic fields can be described by the quantum numbers $G_1 = \left|s_e - I_p\right|, \ldots, s_e + I_p$ for the electron-proton spin coupling, and $G_2 = |G_1 - I_d|, \ldots, G_1 + I_d$, including the deuteron spin. The total structure is thus expressed as $F = |G_2 - N|, \ldots, G_2 + N$, accounting for the nuclear rotation. An overview of all possible states for $N = 0$ and $N = 1$ is provided in Table 8.1 and illustrated in Figure 8.1 (d). In this case, the spin quantum numbers $I_p = 1/2$, $s_e = 1/2$, and $I_d = 1$ were utilized. It is now possible to select a transition of interest and determine the appropriate theoretical frequency of the transition. Subsequently, the molecule can be interrogated with photons at the selected frequency. However, in order to probe the molecular ion at the location of a laser beam with high precision in the transition frequency, it is necessary to first trap it and subsequently cool it. In the contributions addressed in this thesis, two distinct types of ion traps were utilized to perform spectroscopy.

G_1	G_2	$F(N=0)$	$F(N=1)$
0	1	1	0,1,2
1	0	0	1
	1	1	0,1,2
	2	2	1,2,3

Table 8.1: The fine splitting of the rovibrational states in the electronic $1S\sigma$ state of HD^+. A state is fully characterized by a specific set of quantum numbers, denoted by (v,N,G_1,G_2,F). In this table, the explicit states for $(v,N=0)$ and $(v,N=1)$ are presented.

8.1 Ion Trapping and Cooling

The Linear RF Quadrupole Trap

In contrast to neutral particles, ions possess a charge. In the following, the distinction between molecular ions and mononuclear ions is not made explicit. Moreover, in the explanation, ion-ion interactions will be ignored. This property can be utilized to confine the ions' motion by applying forces that can couple to the charge. For instance, the electric force experienced by a particle of charge Q due to the presence of an electric field $\boldsymbol{E}$, given by the gradient of a potential $\Phi(\boldsymbol{r})$, is expressed as follows:

$$\boldsymbol{F}_{el} = Q\boldsymbol{E} = -Q\,\nabla\Phi$$

The potential $\Phi(\boldsymbol{r})$ is the spatial variation of an applied voltage U_0. A preliminary concept that may be considered is the application of six static, thus DC, voltages to confine the ion in all three spatial dimensions. However, Earnshaw's theorem posits that it is not possible to trap ions through the utilization of static electric fields alone. This limitation stems from the inherent dynamics of the particles, which invariably find escape routes along an axis. An explanation for this phenomenon is that every static field exerts an outward force on the particle, propelling it toward the trap center while simultaneously repelling it from the center. Fundamentally, it emerges from the Maxwell equations, that forbid the formation of a three-dimensional electrostatic potential minimum.

However, the Maxwell equations do not forbid the creation of a time-averaged electric minimum. This can be achieved by the incorporation of RF voltages, which generate oscillating electric fields. Consider a system composed of four metallic rods, which are connected to a voltage source U_{qd} that is characterized by a static U_{dc} and an alternating component with an amplitude U_{ac} and a frequency of Ω, given by

$$U_{qd} = U_{dc} - U_{ac}\cos(\Omega t)\,.$$

The electrodes are arranged in a quadratic configuration, with the $z-$axis oriented parallel to all of them. The transverse axes intersect in the center, between the rods. The transverse axes are tilted such that there are two rods along each. The configuration of the system is illustrated in Figure 8.2 (a), which presents a frontal perspective along the $z-$axis. The voltages applied to the electrodes aligned along one axis are in phase, but are phase-shifted by π with respect to the electrodes aligned along the other axis. This configuration will result in the formation of a RF quadrupole potential,

wherein two electrodes will exert a pulling force, while the remaining two electrodes will apply a pushing force on the charged particle. Accordingly, this potential must also fulfill Gauss law, which states that the divergence of the electric field is equal to zero in free space $\nabla \cdot \boldsymbol{E} = 0$, thereby resulting in no charge density. Consequently, this leads to the Poisson equation, $\nabla^2 \Phi = 0$. Therefore, the potential can be expressed as follows:

$$\Phi(\boldsymbol{r}) = U_{qd} \frac{x^2 - y^2}{2r_0^2}$$

Here, r_0 is the distance between each electrode and the trap center, which, in this design, is defined as the intersection of the transverse axes. Solving Newton's equation of motion

$$m\ddot{\boldsymbol{r}} = -Q \nabla \Phi(\boldsymbol{r}),$$

for a particle of charge Q and mass m, will ultimately result in the Mathieu equations

$$\frac{d^2u}{d\tau^2} + (a_u - 2q_u \cos(2\tau))\, u = 0. \tag{8.1}$$

Here, $\tau = \Omega t/2$ and $u = x, y$ were substituted. In addition, the respective a and q parameters are given by the following equations:

$$a \coloneqq a_x = -a_y = \frac{4QU_{dc}}{mr_0^2\Omega^2} \text{ and } q \coloneqq q_x = -q_y = \frac{2QU_{ac}}{mr_0^2\Omega^2}$$

Solving Equation (8.1) will yield specific boundaries for the a and q parameters. These boundaries can be visualized in a stability diagram, as illustrated in Figure 8.2 (b). In this figure, the blue lines indicate the area for which motion along the $x-$axis is stable, and the magenta shaded part indicates the stable y motion. It is only in the region where both intersect that a stable motion of the particle in the transverse directions will occur, resulting in its trapping along those two axes. In most cases, the stability regions are characterized by relatively small values of a and q, resulting in corresponding U_{dc} and U_{ac} voltages that are also smaller.

It should be noted that the parameters are contingent upon the geometry of the trap. This geometry is characterized by the parameters r_0, Ω, U_{dc} and U_{ac}. Additionally, the charge-to-mass ratio of the particle, Q/m, plays a significant role in determining the parameters. This approach enables the implementation of such a system as a mass filter, facilitating stable motions for the desired particles and unstable motions for undesirable ratios. In order to describe the actual motion of the trapped ion, it is necessary to separate the electric field into its static and oscillatory parts:

$$\boldsymbol{E}(\boldsymbol{r},t) = \boldsymbol{E}_0(\boldsymbol{r},t) + \boldsymbol{E}_\Omega(\boldsymbol{r},t)$$

These parts can be Taylor expanded for small displacements $\Delta\boldsymbol{r}$ from the trap center. Performing this and subsequently filtering the slowly varying terms will result in the pseudo potential, Φ_{ps}, for the particle. In the context of the one-dimensional x motion in the mass filter, this is expressed as

follows:

$$\Phi_{ps}(x) = \left(\frac{U_{dc}}{2r_0^2} + \frac{Q}{4m\Omega^2}\frac{U_{ac}^2}{2r_0^2}\right)x^2 = \frac{m\Omega^2}{8}\left(a_x + \frac{q_x^2}{2}\right)x^2.$$

Solving the equation of motion for this case yields

$$\begin{aligned} m\ddot{x} &= -Q\frac{d}{dx}\Phi_{ps}(x) \\ \Longleftrightarrow \ddot{x} &= -\omega_x^2 x. \end{aligned}$$

In a manner analogous to a mass on a spring, a force is exerted that acts linearly against its displacement. Consequently, a harmonic oscillation with the characteristic secular frequency, ω_x, is observed. The solution of motion is then of form $x(t) = x_0\cos(\omega_x t + \varphi_x)$. Analogously, the frequency along the other transverse axis, y, can be derived. In summary, the particle's motion $\boldsymbol{r}_{tot}(t) = \boldsymbol{r}(t) + \Delta\boldsymbol{r}(t)$ is described by the following equations:

$$x_{tot}(t) = x_0\cos(\omega_x t + \varphi_x) - \frac{q}{2}\cos(\Omega t), \text{ with } \omega_x = \frac{\Omega}{2}\sqrt{a + \frac{q^2}{2}}$$

$$y_{tot}(t) = y_0\cos\left(\omega_y t + \varphi_y\right) + \frac{q}{2}\cos(\Omega t), \text{ with } \omega_x = \frac{\Omega}{2}\sqrt{-a + \frac{q^2}{2}}$$

The particle's trajectory is elliptical (or circular) in the transverse plane, characterized by slow secular frequencies that are modulated by a fast micromotion. This micromotion is determined by the frequency of the RF field.

Finally, to confine the particle in the z-axis, a static electric field is applied by adding end caps to the electrodes that are connected to a DC voltage U_{ec}. This results in the addition of a term, $\Phi(z) = \kappa U_{ec} z^2$, to the total three-dimensional potential. Nevertheless, in order to fulfill the Poisson equation, it is necessary to incorporate a compensation term of the form $-\frac{1}{2}\kappa U_{ec}\left(x^2 + y^2\right)$. This will result in a slight modification to the transverse secular motions, which are expressed as follows:

$$\omega_x = \frac{\Omega}{2}\sqrt{a - a_{ec} + \frac{q^2}{2}},\ \omega_y = \frac{\Omega}{2}\sqrt{-a - a_{ec} + \frac{q^2}{2}}, \text{ and } \omega_z = \frac{\Omega}{2}\sqrt{2a_{ec}}, \text{ with } a_{ec} = \frac{4\kappa}{\Omega^2}\frac{Q}{m}U_{ec}$$

The motion of a particle in the RF trap employed at HHU is described by this model, including the micromotion. The schematic of the three-dimensional trap is shown in Figure 8.2 (c). The RF trap is of the linear Paul trap type. For his invention of the RF quadrupole mass spectrometer and its subsequent application to trap ions, a field subsequently developed by the scientific community [182, 183, 184, 185], Wolfgang Paul was awarded the Nobel Prize in 1989.

Typical secular frequencies in this specific geometry of the quadrupole RF trap, employed at HHU, are at the order of some $\omega_{x,y,z} \approx (2\pi)\,100\,\text{kHz}$, while the RF frequency is at the order of $\Omega \approx (2\pi)\,10\,\text{MHz}$. The process of trapping particles, such as Be^+, begins with the heating of a solid in an oven, which results in the sublimation of particles. These sublimated particles are then directed towards the center of the trap. Others, such as HHUs, are already in gas phase an can

be connected by a gas tank. An electron gun may be employed to ionize the particles. Typical trap depths are larger than the kinetic energy of the hot particles, thereby facilitating the trapping process. Nevertheless, additional cooling is required. The temperature distribution of particles will lead to a distribution of the photon frequencies that can drive the transition. This is due to the Doppler-shift of a particle moving along the axis of the light. The hotter the particle(s), the broader the range of possible absorptions resulting in a broadened linewidth of the transition. A well-established method involves laser cooling, as demonstrated in the works [186, 187, 188]. This pioneering approach led to the Nobel Prize award in 1997, jointly recognizing Steven Chu, Claude Cohen-Tannoudji, and William D. Phillips for their contributions. By driving a specific transition in the particle with a laser of matching frequency, slightly red-detuned to account for the Doppler shift, the net momentum transfer between absorbed photon and ion will always be along the wave vector of the cooling laser.

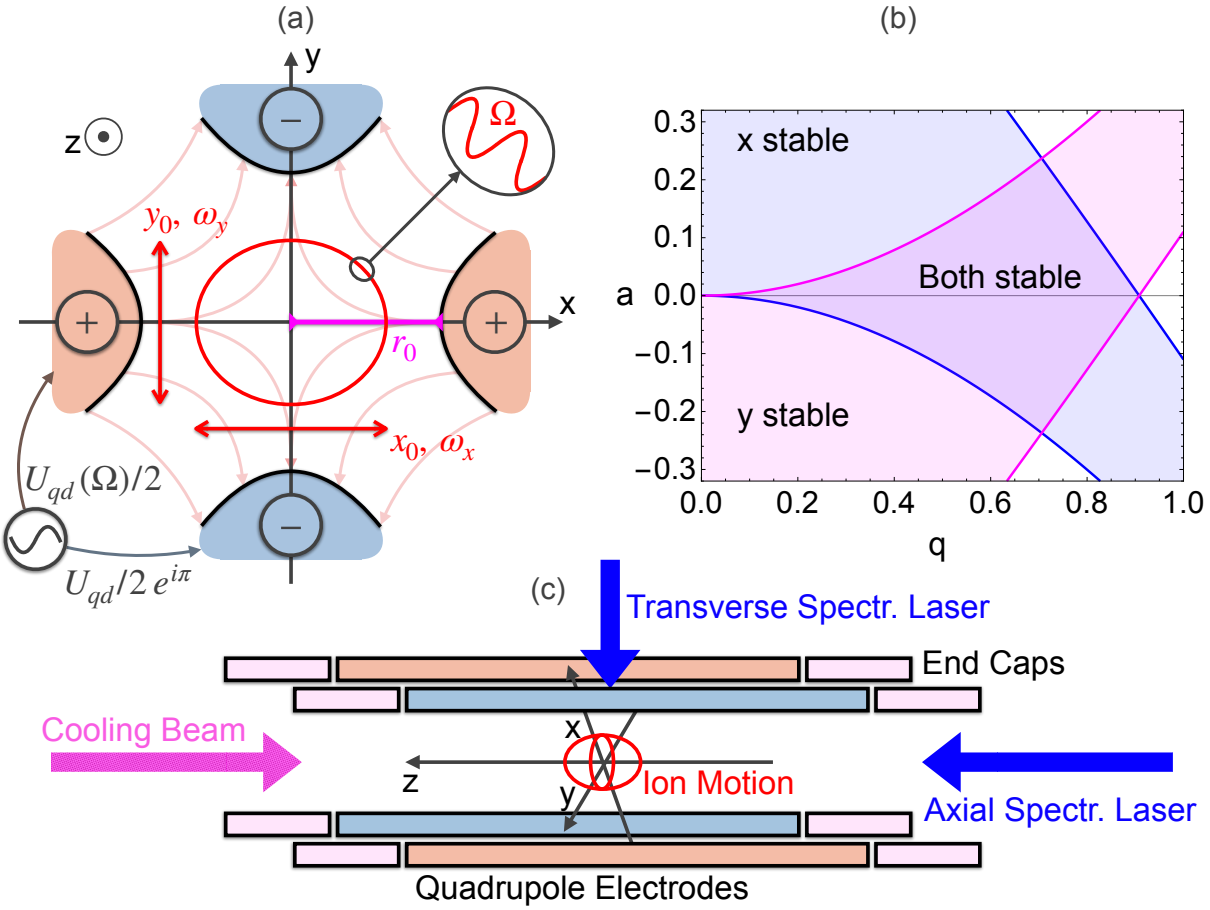


Figure 8.2: Schematic of a linear Paul trap as employed at HHU. (a): The profile of the trap along the quadrupole electrodes. The positive and negative signs demonstrate a specific point in time. The electrodes are connected to phase-shifted outputs of an oscillating voltage. the motion of the particle is indicated by the red circle, with the micromotion indicated in the zoom. (b): The stability diagram of the mass filter motion for small values of a and q. (c): The three-dimensional trap including end cap electrodes connected to a DC voltage. The direction of the cooling laser and two different spectroscopy lasers is indicated.

However, the photon resulting from spontaneous emission will propagate in a random direction. Accordingly, following a series of absorption and emission processes, the particle will undergo deceleration along the propagation direction of the laser. One may assume that a total of six lasers are required to cool a particle in a trap. However, due to thermalization occurring within the trap, resulting in the distribution of the particle's kinetic energy being evenly dispersed across all spatial directions, a single beam is sufficient.

Laser cooling is contingent upon a closed transition loop, thereby ensuring that the particle does not reach an energy state that would impede the cooling process, such as through spontaneous decay or spurious polarizations. In such cases, the implementation of a repumper laser may be deemed necessary to drive the particle into an energy state that is part of the laser cooling transition. For example, the Beryllium ion Be^+ exhibits a cooling transition $^2S_{1/2} \longrightarrow {}^2P_{3/2}$ at 313 nm, with $(F = 2, m_F = 2) \longrightarrow (F = 3, m_F = 3)$, with a single repumper laser for the state $(F = 1, m_F = 1)$, facilitating its cooling process. The temperature limit of this cooling stage is defined by the natural linewidth of the cooling transition, which establishes the Doppler limit. For low laser intensities, the Doppler limit is expressed as

$$T_D = \frac{\hbar\gamma}{2k_B}.$$

The derivation can be achieved by applying the equipartition theorem to the dynamic equilibrium velocity of the particles due to the constant heating and cooling from the spontaneous emission and absorption processes. In this equation, k_B denotes the Boltzmann constant and $\hbar$ is the reduced Planck constant. The natural linewidth of the cooling transition in Be^+ is approximately $\gamma = (2\pi)\,19.4\,\text{MHz}$, which corresponds to the Doppler limit temperature of 0.5 mK. It can be interpreted as the mean kinetic energy, thus velocity, thus Doppler frequency shift, of the particles, when the cooling reaches a steady state.

Note: The textbook "Laser Cooling and Trapping" [189] by H. J. Metcalf and P. van der Straten serves as a comprehensive reference for the subject matter. In addition to providing a thorough overview, the text includes tables that present crucial characteristics, such as natural linewidths, saturation intensity, and scattering cross-sections. Nonetheless, the emphasis is on neutral atom traps. The book "Charged Particle Traps" [190] by F. G. Major, V. N. Gheorghe, and G. Werth, provides a comprehensive examination of ion traps, as well as employed cooling methods, with a particular focus on Paul and Penning traps.

A laser, interrogating the molecules axially, will therefore be operating in the Doppler-broadened regime. In such a case, the transition lines are broadened due to the temperature distribution of the particles limiting the spectroscopy resolution. For RFs, this broadening is at the MHz level [35].

The performance of spectroscopy in a Doppler-broadened regime hinges upon the confinement of ions with respect to the axis of the spectroscopy laser. In the case of the quadrupole trap, the highest confinement is achieved radially when the ion(s) are aligned along the axial axis. If they are confined such that their displacement along the axis is much smaller than the wavelength of the interrogation laser along the same axis the system is operating in what is referred to as the Lamb-Dicke regime [191]. Along the $x-$axis, it is characterized by the condition $\eta = k x_0 \ll 1$. Here, η is the Lamb-Dicke parameter, k the wave vector of the light and x_0 the particles oscillation

amplitude. For an interrogation laser along the $x-$axis it can be written in the form

$$\eta = \sqrt{\frac{\omega_r}{\omega_x}},$$

where $\hbar\omega_r$ represent the recoil energy, acquired by an ion at rest when it absorbs a photon of momentum $\hbar k$. The frequency ω_x defines the quantized energy spacing of the states in the harmonic potential, which confines the particle along the transverse $x-$axis. In this regime, the kinetic energy of trapped Beryllium ions will correspond to temperatures of approximately 20 µK. This would result in observable transition lines that are more narrow in nature, particularly with respect to an interrogation along the axial direction, which is not within in the Lamb-Dicke regime.

Molecules, in contrast to atoms, possess a more intricate energy level diagram due to the presence of rovibational energy states, which complicates the determination of the necessary number of repumper lasers. Instead, the method of sympathetic cooling is employed to achieve motional cooling of the molecules [192, 193, 194, 195]. This approach is also employed in the trap at HHU. The MHIs and a Beryllium cloud are loaded into the trap. Typically, a couple thousand of the atoms and a few hundred MHIs are present, the latter being lighter and thus situated in the center of the trap. This results in the formation of cigar-shaped clusters, wherein the MHI are aligned along the trap axis. The cigar shape is emerging from the confinements along the axes signifying why spectroscopy along the transverse axes can be within the (Lamb-)Dicke regime.

The Be^+ ions interact with the MHI through collisions, thereby exchanging momentum and maintaining a thermal steady state. While the Be^+ ions are subjected to cooling, they undergo recurrent heating due to the elevated temperature of the MHIs. This induced heat is subsequently extracted from the system through continuous laser cooling. Consequently, the MHI are cooled by Beryllium. The efficiency of the momentum transfer depends on the mass ratio between the particles. In the case of HD^+ (3 u) and Be^+ (9 u), this ratio is 1 : 3 which is significant, but still advantageous compared to many other atoms such as Mg^+(24 u) or Ca^+(40 u).

The apparatus described herein has been utilized at HHU for the purpose of sympathetic cooling and spectroscopy of rovibrational transitions in strings of HD^+ and H_2^+ molecules [196, 193, 32, 33, 34, 35, 41]. In these instances, the spectroscopy is of a destructive nature. A dissociation laser is shone in the trap. This laser selectively dissociates the MHIs that are in the excited rovibrational state by driving them into the continuum, therefore generating $H^{(+)}$ and $D^{(+)}$ particles that will leave the trap. The result is a decrease in the amount of MHIs. This signal proportional to the number of MHIs can be measured by secular excitation of the MHIs which will heat up the cluster of Be^+ ions.

While the cooling laser is at fixed, red-detuned, frequency, the fluorescence signal of the Beryllium ions will change when their temperature distribution changes. Eventually, the loss of MHIs through dissociation is measured in a reduced fluorescence signal of the Be^+ ions upon secular excitation of the molecules. This has to be compared to background losses and can be used to determine transition linewidths by measuring the ion loss at different laser frequencies. To suppress BBR induced rotational transitions due to the room temperature environment, lasers are employed for

rotational cooling in the $v = 0$ state of the MHI (HD^+) cluster to increase the population in the rovibrational ground state.

In particular, the transition from $(0,0) \longrightarrow (5,1)$ in the HD^+ system is accompanied by the utilization of a dissociation laser operating at a wavelength of 266 nm. However, as explained, this process entails the loss of ions, rendering them unsuitable for further experimental use. Consequently, the necessity arises to load new ions into the trap to resume experimental operations. In scenarios where multiple 100 MHIs can be interrogated concurrently, this approach ensures a feasible measurement time. However, in a single ion system, this method compromises the efficacy of data collection for statistical analysis. The development of a trap single ion quadrupole RF trap at HHU [197], aims, among applications such as quantum logic spectroscopy, to achieve non-destructive spectroscopy.

Ultimately, the trap is operational without the application of a magnetic field to confine the particles, in contrast to the second trap that will be described subsequently. However, this does not imply the absence of a magnetic field at the location of the ions. The Earth's magnetic field, with a strength of some 20 µT, exerts an influence on the magnetic quantum numbers m_F, giving rise to a splitting of these quantum numbers as observed in the Zeeman effect. This shift can be, and is, controlled by employing compensation coils around the trap to counteract, or increase, the magnetic field at the position of the ions.

The Static Field Penning Trap - ALPHATRAP

Earnshaw's theorem stipulates the impossibility of trapping an ion through the exclusive use of static electric fields. However, the implications of a static magnetic field remain to be elucidated. Assuming a homogeneous magnetic field $\boldsymbol{B}$ oriented along the $z-$axis, a particle of charge Q and velocity v will experience the Lorentz force $\boldsymbol{F}_l = Q\,\boldsymbol{v} \times \boldsymbol{B}$. Accordingly, the force will cause the particle to execute a circular motion along the xy-plane, or radially, as expressed by the Newton's equation of motion:

$$\left| \begin{array}{c} \ddot{x} = \omega_c \dot{y} \\ \ddot{y} = -\omega_c \dot{x} \end{array} \right|, \text{with } \omega_c = \frac{QB}{m}$$

Here, the cyclotron frequency, denoted by ω_c characterizes the oscillatory behavior in the xy-plane. The application of a static electric field results in the confinement of the particle in all three directions. As in the Paul trap, the form of the potential generating the field must still satisfy the Poisson equation: $\nabla^2\Phi = 0$. Consequently, it is described by a static quadrupole potential

$$\Phi = \frac{U_0}{2d^2}\left(z^2 - \frac{\left(x^2 + y^2\right)}{2}\right).$$

The parameter d is determined by the geometry of the trap, which involves the inner radius r_0 of the ring electrode and the distance between the trap center and the endcap z_0. It is calculated by

$$d = \sqrt{\frac{z_0^2 + r_0^2}{2}}.$$

The force exerted on the ion is thus expressed as $\boldsymbol{F} = Q(\boldsymbol{E} + \boldsymbol{v} \times \boldsymbol{B})$, where $\boldsymbol{E} = -\nabla\Phi$. The complete system of equations of motion for this force yields the following set of motions:

$$\left| \begin{array}{c} \ddot{x} - \omega_c \dot{y} - \frac{\omega_z^2}{2} x = 0 \\ \ddot{y} + \omega_c \dot{x} - \frac{\omega_z^2}{2} y = 0 \\ \ddot{z} + -\omega_z^2 z = 0 \end{array} \right|, \text{with } \omega_c = \frac{QB}{m}, \text{ and } \omega_z = \sqrt{\frac{QU_0}{md^2}}.$$

The axial motion is a decoupled differential equation, meaning that its oscillation is fully described by the secular axial frequency ω_z. The coupled differential equations along the radial direction can be solved by employing the decoupling ansatz $\ddot{\xi} = x + iy$ and $\ddot{\varepsilon} = x - iy$, thus

$$\ddot{\xi} + i\omega_c \dot{\xi} - \frac{\omega_z^2}{2} \xi = 0$$

$$\ddot{\varepsilon} - i\omega_c \dot{\varepsilon} - \frac{\omega_z^2}{2} \varepsilon = 0.$$

The solution of these equations $\left(\text{i.e. } \tilde{\xi} = e^{i\omega_{1/2} t}\right)$ yields a new set of frequencies along the transverse plane given by

$$\omega_{1,2} = \frac{\omega_c}{2} \pm \sqrt{\left(\frac{\omega_c}{2}\right)^2 - \frac{\omega_z^2}{2}}.$$

This can be evaluated as a small magnetron frequency ω_m and a reduced cyclotron frequency ω_c' given by the expressions

$$\omega_m \coloneqq \omega_2 = \frac{\omega_c}{2} - \sqrt{\left(\frac{\omega_c}{2}\right)^2 - \frac{\omega_z^2}{2}}, \text{ and } \omega_c' \coloneqq \omega_1 = \omega_c - \omega_m.$$

Physically, the ion will undergo drift in its cyclotron motion, given by the slow magnetron motion, resulting in a reduced cyclotron frequency. The system is also referred to as a Penning trap, illustrated in Figure 8.3, an appellation derived from Franz Michel Penning [198], the inventor of a vacuum ion gauge. This innovation was subsequently built upon by Hans Georg Dehmelt [199], who shared the Nobel Prize in 1989 with Paul, in recognition of their seminal contributions to the field.

The Penning trap ALPHATRAP [124] at MPIK Heidelberg is a large, complex experimental apparatus, that contains multiple Penning traps. The ALPHATRAP apparatus is managed by the research team at MPIK Heidelberg and was designed to investigate highly charged ions. It is also part of a collaborative effort with HHU Düsseldorf involving spectroscopy of MHIs. The metrology system, which is detailed in Section 3.3, was developed specifically for this project.

In the context of a molecular ion such as HD^+ in ALPHATRAP, the typical values for the trap frequencies are of order $\omega_m \approx (2\pi)\,10\,\text{kHz}$, $\omega_c' \approx (2\pi)\,20\,\text{MHz}$, and $\omega_z \approx (2\pi)\,650\,\text{kHz}$. The cyclotron motion is determined by the magnetic field, which, in the ALPHATRAP, is generated by solenoid coils operating in a liquid helium-cooled state within a warm borehole magnet. This configuration attains a field strength at the coils of 4 T.

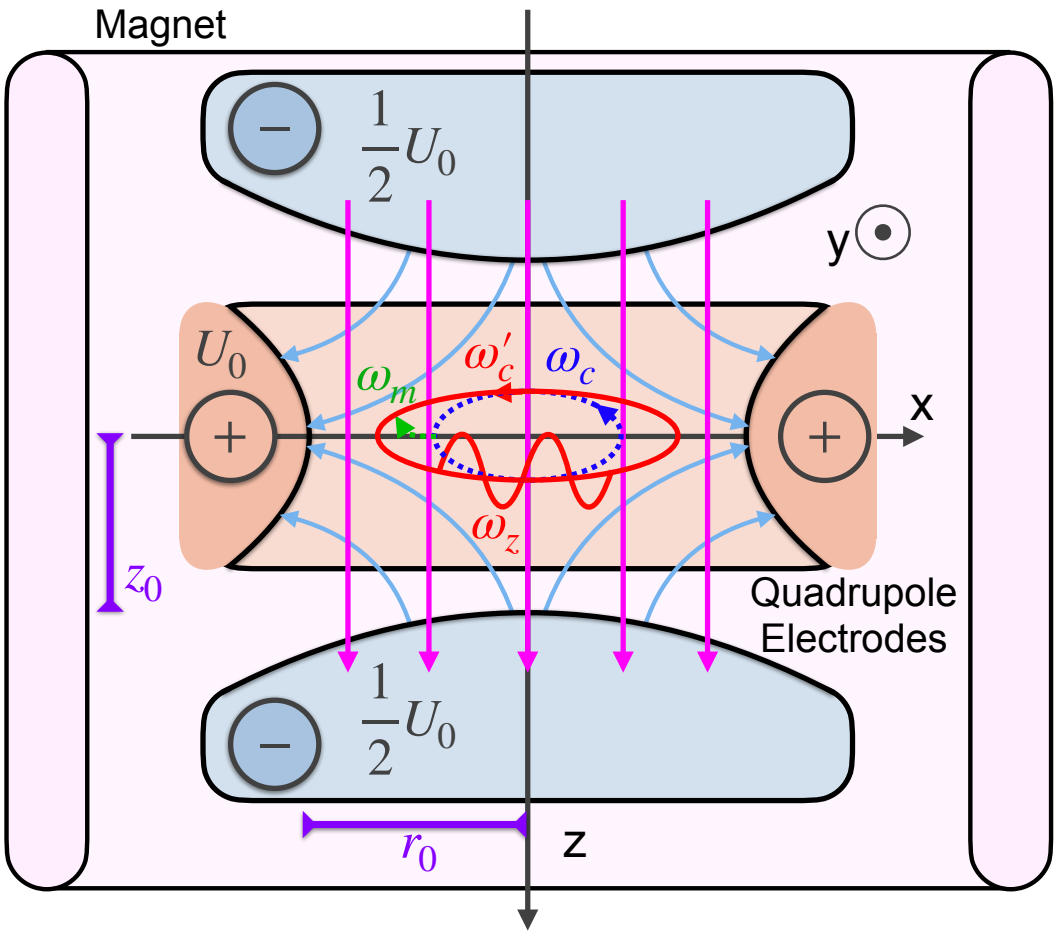


Figure 8.3: Schematic of the profile of a hyperbolic Penning trap. The magenta arrows indicate the magnetic field lines, while the blue arrows depict the static quadrupole field lines. The motion of the ion is indicated by the red circle in the center that is modulated by the axial frequency. The magnetron drift is indicated by the green arrow, the unperturbed cyclotron motion by the blue one. The electrodes are applied to trap positively charged particles, where the upper and lower electrode will pull on the particle.

The trap chamber is situated within a cryostat that is composed of two stages. The removable inner cryostat, which is maintained at a temperature of 4 K, is encased within a liquid nitrogen-cooled cryostat that is set to a temperature of 77 K. The motion of the ion itself is cooled in two ways. The axial motion is subject to resistive cooling through the use of a resonant LC circuit [200, 201, 202], including a low noise amplifier, designed at the resonant frequency of the axial motion, ω_z. This circuit is connected to the trap electrodes, which in turn couple to the axial motion of the ion.

The current generated by the moving charge is picked up by the circuit, which consequently starts to resonate and heat up, thereby extracting energy from the ion. The dissipation of this heat will eventually result in the cooling down of the particle. Along the transverse axes, the ion is cooled by using the coupling of the radial modes to the axial and resistively cool these sidebands [203]. The Paul trap, with its magnetic fields of strength 10 μT, exhibits a Zeeman splitting of a

rovibrational state that can be fit into a band of some 100 kHz. In comparison, the Penning trap possesses a magnetic field that is more than 10^5 times stronger.

This results in the decoupling of the spins of the internal components of the ion within the static field trap, thereby enabling them to precess independently around the magnetic field. This phenomenon is referred to as the Paschen-Back regime [204]. The ALPHATRAP is partially operating in the Paschen-Back regime, where the electron spin decouples. The hyperfine structure of the 12 fundamental combinations of the three spin states of the rovibrational (0,0) state in HD^+ in ALPHATRAP, at a magnetic field of approximately 3.9 T, was thoroughly examined using MW excitation [205].

This concept can be further elaborated by considering the strong magnetic field's interaction with the magnetic dipole moment $\boldsymbol{\mu}$ of a particle, which is defined by the particle's spin. Note that the following is a simple description to account for the concept of determining the $g-$factor in single particle systems, the actual Hamiltonian, eg. for HD^+ is complex and contains many terms.

The interaction Hamiltonian, $\hat{H}_{spin}$, is the result of the spin orientation in the magnetic field, which consequently gives rise to a magnetic potential, given by

$$\hat{H}_{spin} \propto -\hat{\boldsymbol{\mu}} \cdot \boldsymbol{B}, \text{ with } \hat{\boldsymbol{\mu}} = -g_e \mu_B \frac{\hat{\boldsymbol{s}}}{\hbar}, \text{ and } \mu_B = \frac{e\hbar}{2m_e}.$$

In this equation, μ_B denotes the Bohr magneton, while g constitutes the g-factor, a concept of notable significance in the realm of atomic physics. For electrons and protons, two spin orientations can be observed; up and down. The deuteron exhibits an additional orientation. The interaction Hamiltonian for a particle can be described by incorporating a term of unit frequency, ω_l, which is given by:

$$\hat{H}_{spin} \propto -g_e \frac{e}{2m_e} \hat{\boldsymbol{s}} \cdot \boldsymbol{B} = -\hat{s}_{\parallel B} \omega_l, \text{ with } \omega_l = \frac{g_e}{2} \frac{e}{m_e} B.$$

This frequency is known as the Larmor spin-precession frequency, which can directly be related to the cyclotron frequency. This relationship is key to extracting the g factor for a particle of charge Q, which is

$$g = 2 \frac{\omega_l}{\omega_c} \frac{m_e}{m} \frac{Q}{e}.$$

In the event that a single electron is trapped and observed, its g_e-factor can be calculated by determining the ratio of the measured Larmor and cyclotron frequencies

$$g_e = 2 \frac{\omega_l}{\omega_c}.$$

In practice, the reduced cyclotron frequency is measured. Consequently, the magnetron and axial frequencies must also be measured to reconstruct the cyclotron frequency, or ω_c via the invariance theorem [206]. The magnetic moment of the spin also results in a force in a magnetic field. The magnitude of this force is expressed as

$$\boldsymbol{F}_{spin} = \nabla (\hat{\boldsymbol{\mu}} \cdot \boldsymbol{B}).$$

In the context of a magnetic field of strength B oriented along the z-axis, the driving force is

$$F_z = \hat{\mu}_z \frac{dB}{dz} \overset{e^-}{=} \mp \frac{1}{2} g_e \mu_B \frac{dB}{dz}. \tag{8.2}$$

Measurements on mass ratios and g-factors in penning traps include the works [125, 126, 128]. As indicated in the right side of Equation (8.2), the force was evaluated for the electron, with the two spin orientations $m_s = \pm 1/2$. The presence of a magnetic potential would result in the generation of a force that is spin orientation dependent. This, in turn, would introduce an additional term into the equation of motions, thereby inducing a change in the axial frequency.

However, this can only be true if the magnetic field is actually varying along z. If it is homogenous, the force will vanish, thus a spin flip in the electron would not be detectable in a change of the axial frequency. This issue has been previously addressed by Dehmelt, who incorporated the continuous Stern-Gerlach method into the trap [207]. The magnetic field can be modified by introducing a quadratic magnetic inhomogeneity, represented by the equation $[A] = \mathrm{Tm}^{-2}$ around the trap center. This modification leads to a transformation of the magnetic field

$$B(z,r) = B + Az^2.$$

The magnetic bottle exhibits a nonzero force, resulting in a change in the axial frequency when the electron spin flip orientation changes. This process unveils a remarkable property of the system: the ability to non-destructively detect states by employing an induced electron flip, driven by an electron spin resonance transition (ESR). Its application in the context of spectroscopy will be further delineated in Section 8.4. The utilization of this instrument considerably enhances the measurement efficiency, as the ion can be recycled.

Nevertheless, the magnetic field gradient will also couple to the other field-dependent frequencies, yielding complex systematic effects in the trap. While this tool is useful for **analyzing** spins, for **precision** spectroscopy, a well-known ultra-homogenous field is generally preferred. Therefore, contemporary Penning traps, such as ALPHATRAP, are based on a two-trap solution that incorporates the analysis trap (AT) and the precision trap (PT). The ion can be moved in between adiabatically. A schematic representation of the system is provided in Figure 8.4.

ALPHATRAP employs cylindrical electrodes forming the trapping potential, with a ring-electrode at each center, with upper and lower correction as well as end cap electrodes surrounding the ring-electrode. The PT contains two more correction electrodes than the AT. The central electrode in the AT is responsible for the magnetic bottle. The molecules are prepared for the Penning trap using electron-beam ion traps (EBIT)s that are not further discussed. However, important features of the system include the preparation of molecules with a long life time of many weeks and months as well as the external injection of the ions into the trap.

Significant advancements in the domain of Penning traps involve the utilization of these traps for the capture of antiparticles, specifically antiprotons. These antiprotons can be produced at the CERN facility and subsequently employed in crucial tests of CPT symmetries, [208, 209, 210, 211].

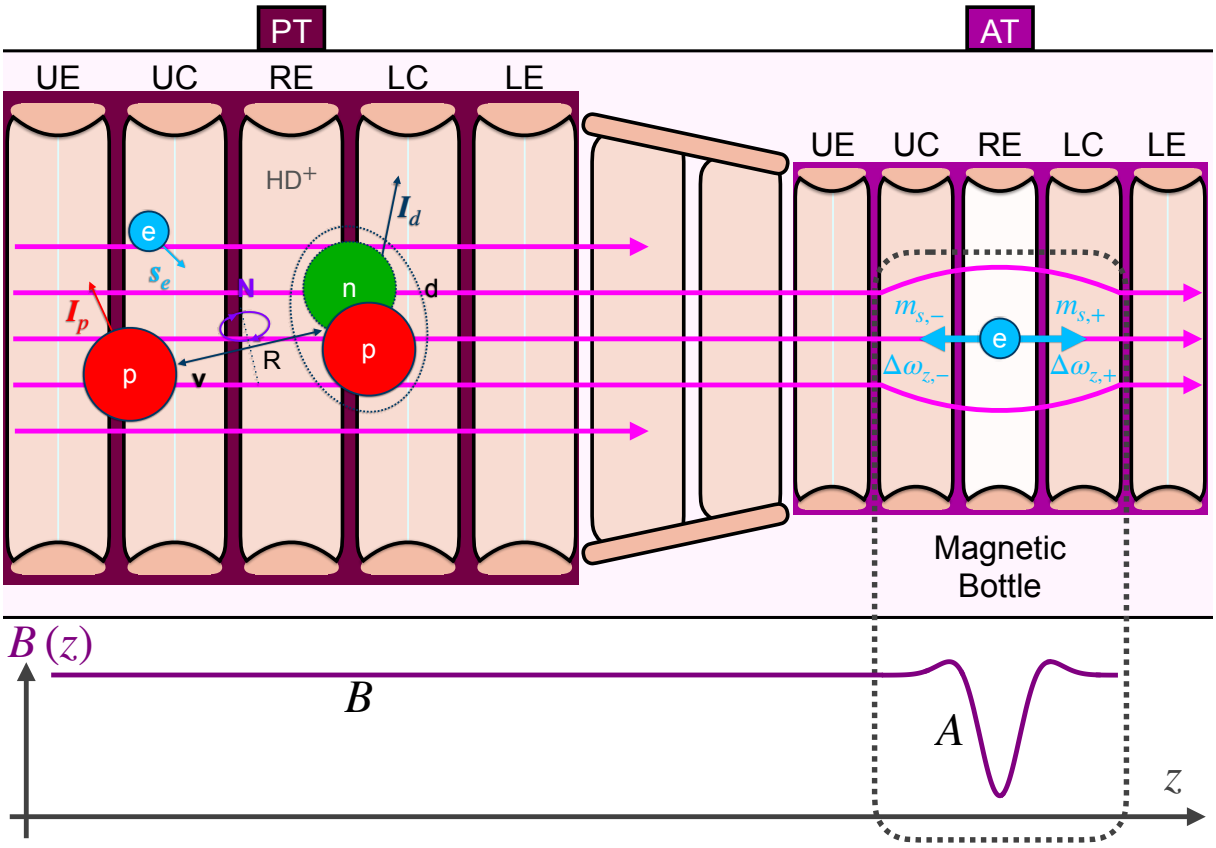


Figure 8.4: Schematic presentation, not to scale, of the AT and PT in ALPHATRAP. The electrodes are separated into upper and lower endcap electrodes (UE/LE) and upper and lower correction electrodes (UC/LC) with a ring electrode in the center (RE). The endcap electrodes are split into two distinct electrodes, which is also the case for the correction electrodes in the PT. The ring electrode in the AT is responsible for the inhomogeneity in the magnetic field strength along the $z-$axis, shown in the plot below, enabling the continuous Stern-Gerlach effect for spin flip detection. The electron in the AT illustrates the continuous Stern-Gerlach effect, there the axial frequency depends on the spin orientation. The HD^+ molecule in the PT is in reality in confined in the center of the respective ring electrode. The length of the PT and AT are approximately 2 cm and 0.6 cm respectively. The corresponding diameters of the inner electrodes are 18 mm and 6 mm.

Furthermore, recent studies have demonstrated the feasibility of transporting antiprotons in a portable Penning trap apparatus [212]. This perspective offers a promising outlook for the future, as it paves the way for the generation of anti- MHIs, particularly anti-H_2^+, which can subsequently be utilized for advanced testing of CPT symmetries as in the (anti) proton-to-electron mass ratio [43].

Systematic Shifts in the Spectroscopy Frequency

Once the MHI has been trapped and cooled, and the theoretically spin-averaged frequency, $\nu_{sp.avg.}$, has been evaluated, experimentation on the target transition can be performed. Nonetheless, the measured frequency of the laser interrogating the molecule must be methodically corrected for

systematic effects. The ensuing discourse will address the following effects and estimate an order of magnitude to their contributions:

Upon the absorption of a photon by a particle, a momentum transfer ensues. Consequently, the conservation of energy and momentum is a prerequisite for the successful excitation of the system. In a system such as the linear Paul trap at HHU, where a sting of many MHI is examined, the recoil energy of the absorbed photon will change the motional state. This is possible as many motional modes exist. The exciting photon must carry an elevated frequency with respect to the transition, in order to carry the necessary energy E_r to drive the transition and to account for the recoil. This recoil energy, depends on the momentum of the absorbed photon and the mass of the ions. For a single particle that is strongly confined, such as in ALPHATRAP, or that is in the Lamb-Dicke regime in the Paul trap, thus no adjacent motional modes, this recoil is strongly suppressed. In those cases, no correction to the measured frequency is necessary. In the case of the rovibrational $(0,0) \longrightarrow (5,1)$ transition in HD^+ ($\lambda \approx 1\,\mu m$), the frequency correction, applicable in [34], is approximately $\Delta f_r \approx -50\,kHz$. The salient point to note is that this quantity is invariably negative, as the photon is required to carry additional energy.

In addition, as elucidated in Section 2.4.3, the local frequency reference in the laboratory may not be consistent with the international standard. In a multitude of high-precision applications, including the present one, the laboratory reference is a H-maser. The masers within this work of frequency f_m exhibit frequency offsets with respect to SI that are of the order of $(f_m - f_{si})/f_{si} \approx 10^{-11}$, which translate to shifts in the photon frequency of approximately $\Delta f_m \lesssim 5\,kHz$. This offset can either be actively corrected or, as in this case, addressed through post-processing. Fundamentally, the sign can be either positive or negative.

The AC Stark shift is defined through second-order perturbation theory of the transition dipole moment. The energy shift [213] of the respective state is calculated by the transition strength and the detuning. The total transition shift is defined as the difference between the energy shifts in both states. It arises within the presence of a detuned and rapidly oscillating EM wave, such as the light itself used in spectroscopy, which induces energy shifts in the states of the transition. This is also referred to as the light shift. The Stark shift depends on the intensity of the spectroscopy light, the polarizability of the states and the transition strength. It is noteworthy that in a Paul trap with RF electric fields oscillating at approximately 10 MHz, an AC Stark shift can be induced. In the context of the aforementioned transition in HD^+ in the Paul trap, the total AC Stark shift was estimated to be approximately $\Delta f_{ls} \approx 0.1\,kHz$ for the light shift and approximately $\Delta f_{rf} \approx 1\,kHz$ for the trap shift [34].

Within both trap types, DC electric fields are also present, which induce energy level shifts by coupling to the static polarizability of the molecule. This, in turn, alters the transition frequency yielding the DC stark shift. In the transition that was examined in the Paul trap, it is presumed that the shift is negligible. However, due to the inherent statistical uncertainties, it was assumed to be below the level of $\Delta f_{dc} \approx 0.1\,kHz$.

A related systematic is the black-body radiation (BBR) shift, which essentially induces Stark shifts due to BBR. Radiation of temperature T reaches the ion and acts on it static polarizability,

for instance, through the spectroscopy light window (ALPHATRAP), or if the trap itself is at room temperature (HHU Paul trap). This shift has been modeled and simulated and was estimated to be well below the mHz level for the examined rovibrational states [214].

Ultimately, the magnetic fields present in both types of traps will induce shifts due to Zeeman splitting. In the context of the Paul trap, the magnetic field, which typically is of order 10 µT, causes a degeneracy of the energy levels into their magnetic quantum numbers, m_F. Consequently, these effects can be regarded as corrections to the designated transition frequency. In the Penning trap, the ultra-stable 4 T magnetic field will fundamentally cause the same effect, but at a larger scale. This effect is part of the actual energy level structure of the ion in its rovibrational state and in a specific magnetic field.

Further, higher-order effects and diamagnetic shifts, which are proportional to B^2, emerge in strong magnetic fields and are thus considered a subject of investigation. As of the present moment, the calculations are being carried out [215]. A preliminary result for this particular transition is at the order of $5\,\mathrm{kHz\,T^{-2}}$, thus around 80 kHz level in the Penning trap.

Eventually, the exact systematic shift budget has to be measured in a case by case scenario and have to be carefully addressed. This section is not meant to give an exact value of the systematics but to explain their origin and give an estimation of their magnitude. An conceptual examination of the recoil and Stark shifts is also performed in [189].

8.2 Spectroscopy of HD^+ in a Linear Paul Trap 1

Referenced work: Alighanbari et al., Test of charged baryon interaction with high-resolution vibrational spectroscopy of molecular hydrogen ions, Nature Physics 19 (2023) 1263–1269 [34]. Publication in Appendix B.2.1.

In the initial phase of this thesis, a configuration for three-cornered hat (TCH) analysis was established. This configuration was utilized to characterize the two ULE resonators (see Section 3.1), as well as an additional reference laser that was employed to stabilize an OFC and spectroscopy laser for experimentation on the rovibrational transition $(0,0) \longrightarrow (5,1)$ in HD^+. The results of the Allan deviation and linewidth of this reference laser (Ref), as presented in the publication, are the product of the TCH measurement conducted by the author of this work. The reference system is composed of a Nd:YAG laser with an output wavelength of 1064 nm stabilized to a 10 cm long, high finesse $\left(\mathcal{F} = 4 \times 10^5\right)$ cavity based on a ULE spacer and FS mirrors, as described in [72].

The configuration is illustrated in Figure 8.5. At that time, both ULE resonators were situated in Lab 1. The reference laser was located in another laboratory, which was sent to the dual cavity laboratory by a fiber that spanned several hundred meters. Therefore, a FNC station was installed at the reference laser to mitigate the broadening at low Fourier frequencies. The beats were measured by three identical frequency counters that were synchronized to a sub-second level and read out by a LabVIEW software. The beats between the ULE resonators, C1 and C2, $f_{C1,C2}$, were created separately on the laser breadboard.

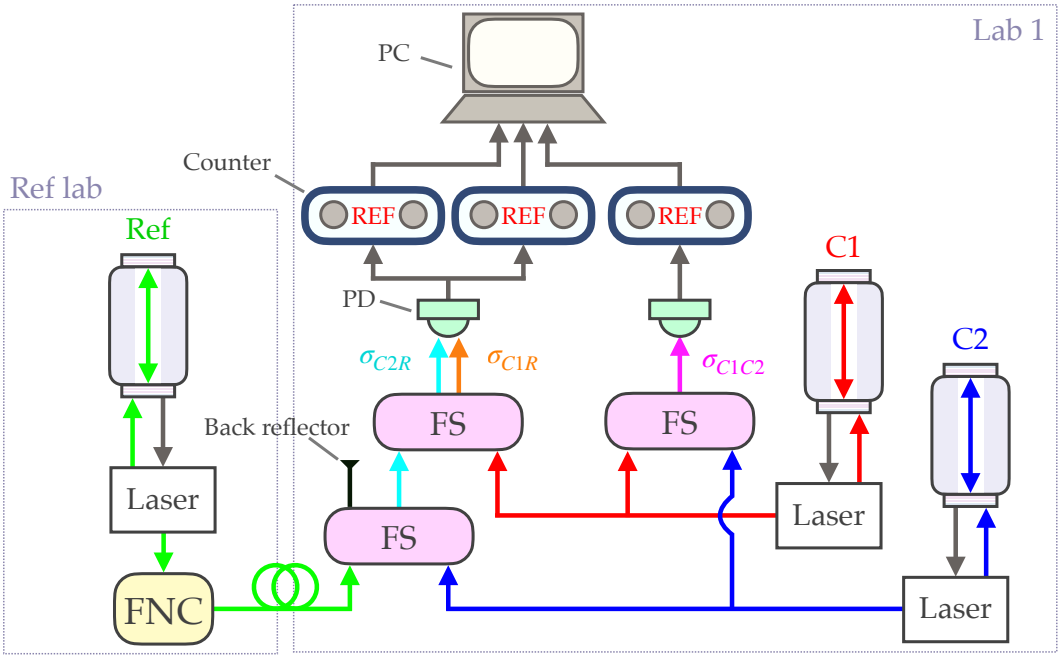


Figure 8.5: The following schematic illustrates the configuration employed for the recording of beats between three resonators in order to perform a TCH analysis. The reference light is propagating through a fiber with a length of several hundred meters, compensated by a FNC setup. The counters are referenced against the H-maser. FS: Fiber Splitter.

Conversely, the individual beats, C1 vs. Ref $f_{C1,R}$ and C2 vs. Ref $f_{C2,R}$, were generated by overlapping all three lights and sending them to a single PD. The individual beats were measured at 30 MHz and 70 MHz using a separate counter, with the appropriate band-pass filters applied. The measurement setup required several weeks of optimization to ensure the accurate and reliable collection of data. The results for the linewidths, as measured by a spectrum analyzer with an RBW of 122 mHz, are displayed in Figure 8.6. Here, it is evident that the linewidth of the plots (b) and (c) was constrained by the reference laser at approximately $2-3$ Hz, as the beat between the ULE cavities, C1 and C2, was as low as 0.6 Hz.

The data displayed in panel (b) has been published in the referenced work. It was crucial to estimate the performance of the spectroscopy light interrogating the ions to have a linewidth of less than 10 Hz when noises of the OFC and fiber paths were added. The determination of the Allan deviation was achieved through the concurrent recording of the time trace of all three beats with a gate time of 1 second, for a total duration of approximately 6 hours. The time trace and the corresponding Allan deviations are displayed in Figure 8.7 (a). The plot shows that both measurements taken against the reference laser were significantly constrained by said laser. The individual beats are determined by the following equations:

$$f_{C1,C2} = f_{C2} - f_{C1},\ f_{C1,R} = f_R - f_{C1} \text{ and } f_{C2,R} = f_{C2} - f_R.$$

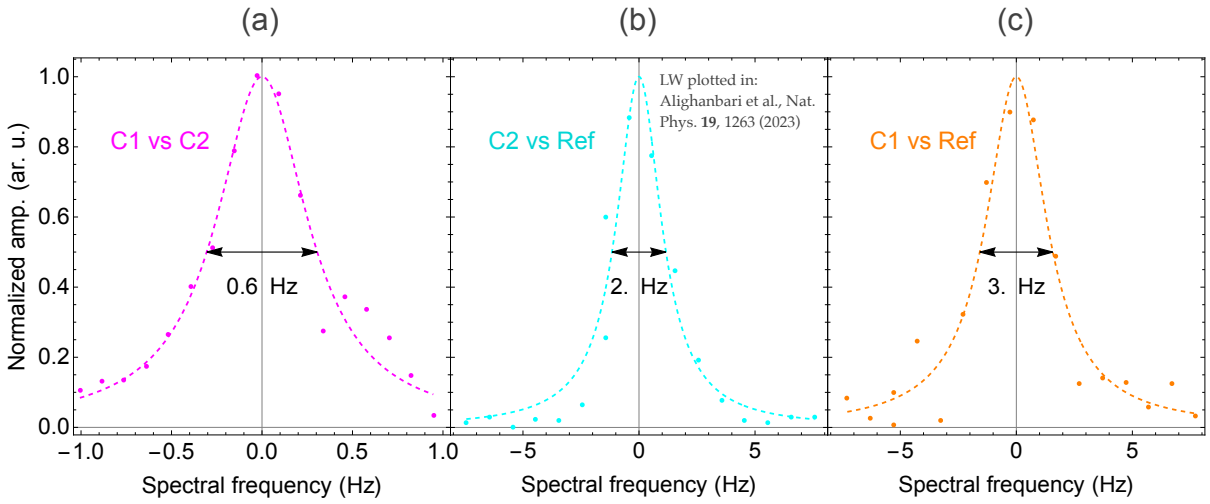


Figure 8.6: The linewidths correspond to the beats that were measured with an RBW of 122 mHz. (a): C1 vs. C2. (b): C2 vs. Ref. (c): C1 vs. Ref. The dashed line in the respective plots signifies the Lorentzian fit, with the fitted FWHM indicated in each.

The summation of the individual beat measurements with the reference is mathematically equivalent to a cancellation of the former, thereby yielding the beat between the ULE resonators:

$$f_{C2,R} + f_{C1,R} = f_{C2} - f_{C1} = f_{C1,C2}. \tag{8.3}$$

A visual representation of this calculation is provided by the gray data in the Allan deviation plot. It is evident that this method is effective for averaging times greater than 10 s, with an increase in deviation at lower time scales. This can be attributed to the presence of asynchronous behavior in the data, which is predominant at lower time scales. However, this is not a concern in the context of the TCH analysis. In essence, the Allan variance of a beat between oscillators i and j is mathematically equivalent to the sum of the individual Allan variances given by:

$$\sigma_{ij}^2 = \sigma_i^2 + \sigma_j^2$$

This relationship can be extended to

$$\sigma_{ij}^2 + \sigma_{jk}^2 = \sigma_i^2 + \sigma_k^2 + 2\sigma_j^2,$$

when a beat is introduced between oscillator j and a third oscillator, k. From a mathematical perspective, the information of oscillator j can be extracted by calculating

$$\sigma_j^2 = \frac{1}{2}\left(\sigma_{ij}^2 + \sigma_{jk}^2 - \sigma_{ik}^2\right).$$

This describes the conceptual framework of the TCH analysis. In order to obtain information regarding all three frequencies, it is necessary to measure and analyze all three beats.

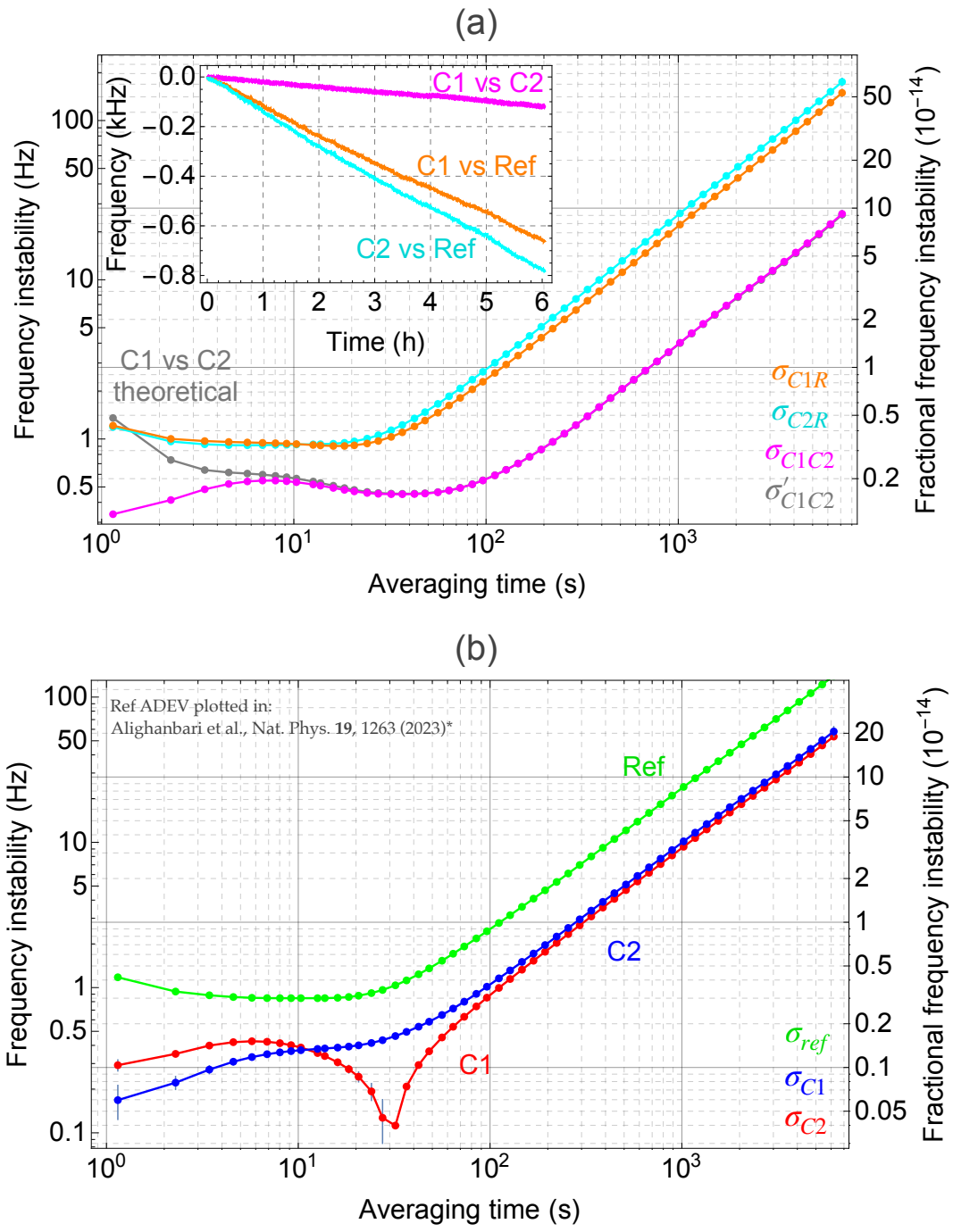


Figure 8.7: (a): Allan deviations observed for each of the three individual beats. Orange and cyan are the beats between the respective ULE resonator and the reference. Magenta is the beat between both ULE resonators. The inset illustrates the time trace of all three measurements. The gray Allan deviation is defined as the theoretically estimated beat derived from the other two via Equation (8.3). (b): TCH analyses of the Allan deviations following Equation (8.4). The reference laser demonstrates noticeably greater instabilities in comparison to the individual ULE resonators.

The resulting system of equations is expressed as follows:

$$\begin{vmatrix} \sigma^2_{C1C2} = \sigma^2_{C1} + \sigma^2_{C2} \\ \sigma^2_{C1R} = \sigma^2_{C1} + \sigma^2_{Ref} \\ \sigma^2_{C2R} = \sigma^2_{C2} + \sigma^2_{Ref} \end{vmatrix} \Longrightarrow \begin{vmatrix} \sigma^2_{C1} = \frac{1}{2}\left(\sigma^2_{C1C2} + \sigma^2_{C1R} - \sigma^2_{C2R}\right) \\ \sigma^2_{C2} = \frac{1}{2}\left(\sigma^2_{C1C2} + \sigma^2_{C2R} - \sigma^2_{C1R}\right) \\ \sigma^2_{Ref} = \frac{1}{2}\left(\sigma^2_{C1R} + \sigma^2_{C2R} - \sigma^2_{C1C2}\right) \end{vmatrix}. \tag{8.4}$$

The result of this analysis is illustrated in Figure 8.7 (b). It is evident that the reference laser exhibits a high degree of similarity with its the respective beats depicted in Panel (a). Furthermore, both ULE resonators display a level of instability two to three times lower than that observed in the reference laser. The green data, representing the Allan deviation of the reference, has been plotted in the publication. It should be noted that at that time, the standard Allan deviation was still employed; however, here, the modified Allan deviation has been utilized.

This approach yields only a marginal impact on the data, ultimately resulting in a similar overall outcome. The evaluation of the performance of the spectroscopy light to mid 10^{-15} level necessitated the collection of this data, which was constrained to the reference laser frequency instability. A third and final analysis was conducted to examine the frequency noise of the beats. These measurements were obtained by a spectrum analyzer, which was configured to measure Fourier frequencies ranging from 10 Hz to 1 MHz.

The primary objective of this analysis was to assess the performance of the FNC system that had been implemented at the time in addition to the noises of the individual lasers. The data is displayed in Figure 8.8. The magenta curve corresponds to the beat between the ULE resonators in Lab 1. Cyan and orange correspond to the respective beats with the reference, when the FNC is activated. The blue and brown colors correspond to the beats when the FNC is deactivated.

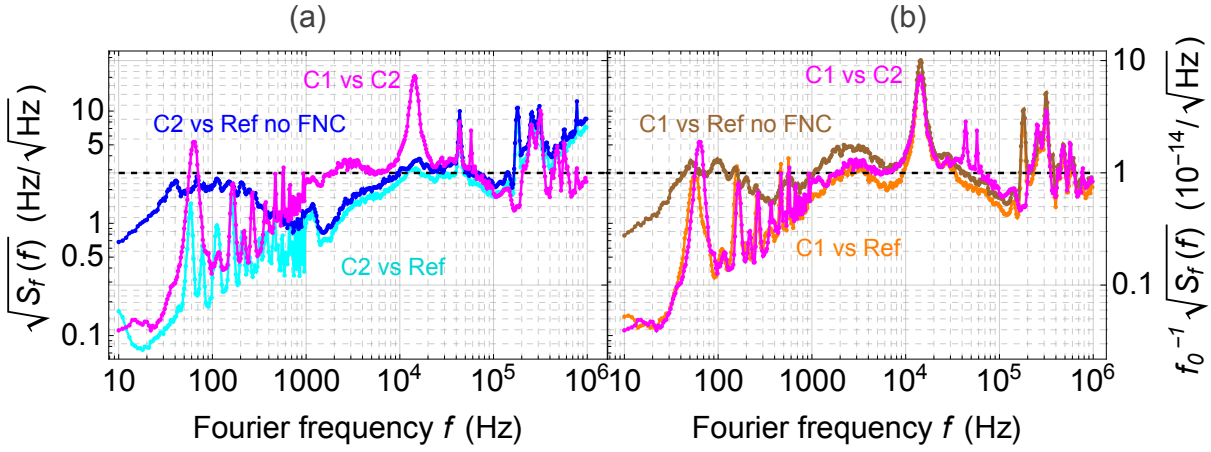


Figure 8.8: Frequency noise measurements were obtained for all three beats while the FNC of the reference light was alternated between on (cyan and orange) and off (blue and brown). The gray dashed line indicates the $10^{-14}\mathrm{Hz}^{-1/2}$ level of white noise. The magenta curve represents the beat between the dual cavities in Lab 1.

This data set provides insights into the potential origins of the sidebands observed in the beat between C1 and C2, suggesting possible contributions from the resonator setups. As an example, consider the peak at 14.3 kHz that is not present in the beat between C2 and the reference, such that it can be denoted to the setup of C1. The FNC appears to have an extensive effect for Fourier frequencies up to 1 kHz, which agrees with the fundamental idea that light is more insensitive to very fast vibrations or changes inside of an optical fiber. Nevertheless, the introduced noise can exhibit an order of magnitude larger levels for lower frequencies, thereby significantly degrading the linewidth of the beat.

8.3 Spectroscopy of HD^+ in a Linear Paul Trap 2

Referenced work: Schenkel et al., Laser spectroscopy of a rovibrational transition in the molecular hydrogen ion H_2^+, Nature Physics 20 (2024) 383–388 [35]. Publication in Appendix B.2.2.

Initially, following the relocation of the dual ULE resonator to the tower setup in Lab 2 (see Section 3.1.2), the objective was to rotate the components to acquire data for the isotropy of light test. However, given the exceptional stability of the system, it was utilized as a reference for an OFC, thereby serving as the basis for spectroscopy light used for the measurement of the rovibrational transition $(v = 0, N = 0) \longrightarrow (2,2)$ in HD^+.

During the measurement campaign, the laser tower, housing the cavities, was closed and exclusively utilized and maintained by the author as the comb reference. A FNC was implemented to ensure the stability of the fiber pathway spanning approximately 10 mm between the laser and the comb. Eventually, the light for nine out of twelve lines of HD^+ E2 transitions that were measured and presented in the publication were measured with the OFC referenced to the laser locked to cavity C1. The following presentation will illustrate the performance of the system during that period.

The linewidth was evaluated from 90 consecutive sweeps, with each sweep lasting approximately 4 seconds. The measurements were obtained using a spectrum analyzer with an RBW of 1 Hz. In Figure 8.9, the orange data illustrates the overlaid data from all sweeps. The sweeps were not re-centered, such that the orange line also includes any drift of the beat during the time. A Lorentzian fit to this data yields a linewidth of 5.7 Hz. During the measurement period, the center frequency exhibited a drift of approximately 11 mHz/sweep, which corresponds to a frequency change of roughly 45 mHz/s. The total drift over the measurement period was found to be nearly 1 Hz. This may elucidate the discrepancy between the mean value of 5.0 Hz when each sweep is analyzed independently. The histogram is displayed in the inset.

A visual representation of the system's long-term performance is provided in Figure 8.10. An inset is provided, which displays the detrended beat data along with a 100 s moving average. The blue curve represents the Allan deviation of the raw beat signal, incorporating the drift. The Allan deviations of the detrended signal are represented by red and black, respectively, and the latter approximates a single laser. The thermal noise floor of the cavities, with respect to the beat, is displayed in cyan.

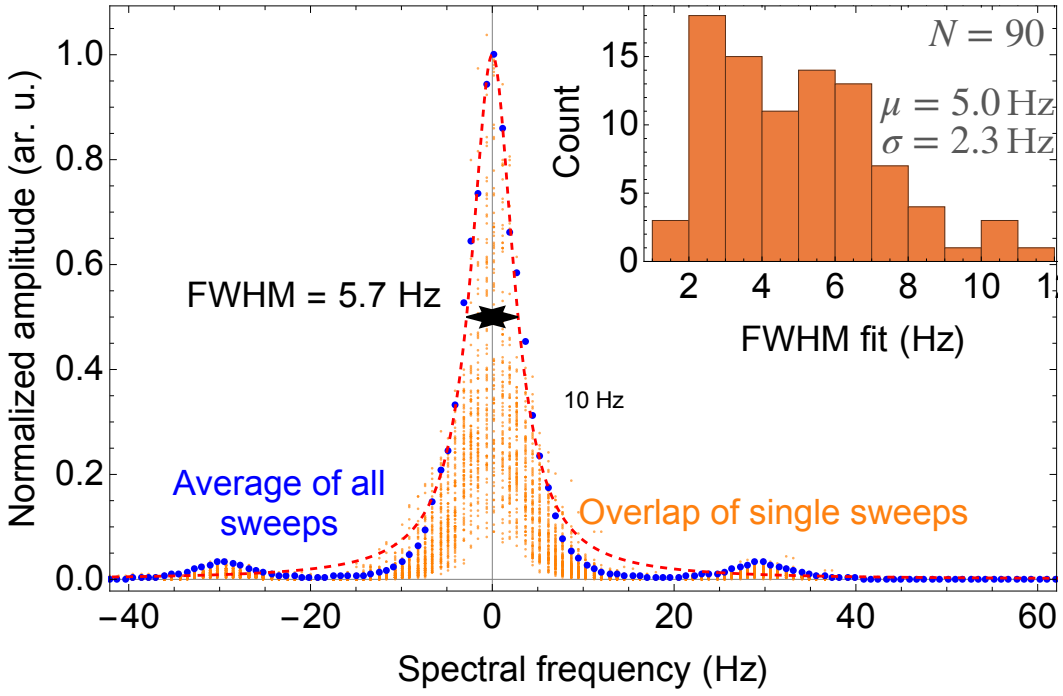


Figure 8.9: The linewidth measurement of the beat conducted during while the setup was operating within the tower. The orange data points represent individual sweeps, while the blue data points represent the average of all sweeps when overlapped. The red dashed line is a Lorentzian fit over the blue data. The histogram of all FWHMs of the 90 individual sweeps is displayed in the inset.

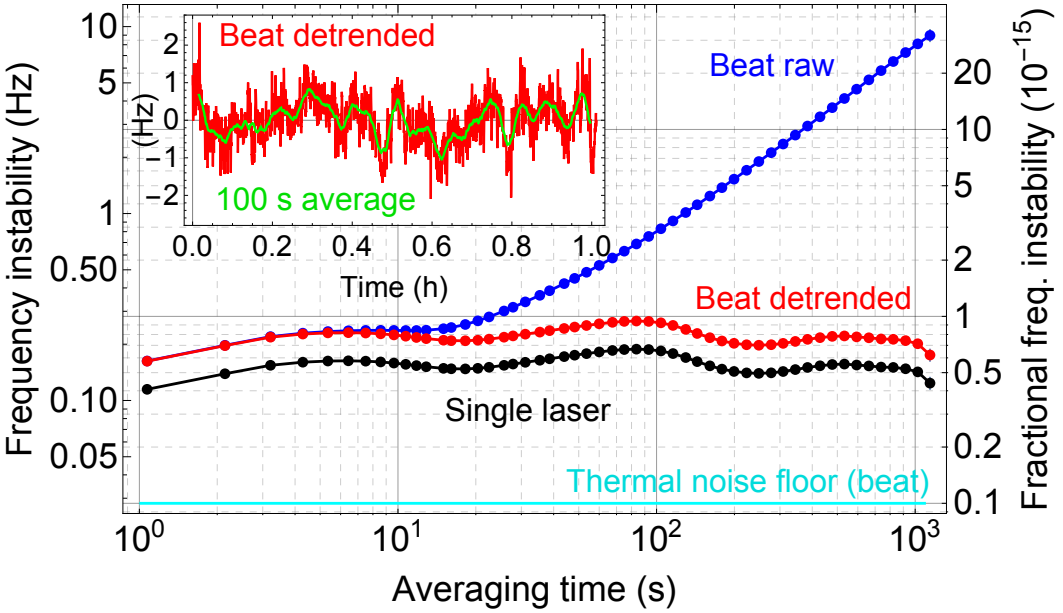


Figure 8.10: Allan deviations of the ULE-based resonator system while it was employed for the spectroscopy. The blue curve corresponds to raw data. When drift is removed, the performance of a single laser (black) was at the mid 10^{-16} level, with an upper limit in the beat (red) at below 1×10^{-15}.

The performance is indicative of the period during which the setup was operational within the closed tower. On larger time scales, the OFC was steered against the H-maser in the laboratory, thereby countering the drift of the ULE locked laser. Consequently, the short-term instability is of particular interest. On all observed time scales, detrending the drift, the beat shows an upper limit below 1×10^{-15} level, with an approximation of a single laser close to the mid 10^{-16} level.

8.4 Spectroscopy of HD^+ in ALPHATRAP

This section constitutes an exception in that it does not refer to a publication. This is due to the preliminary nature of the results presented. For the joint experimentation on molecular hydrogen ions in the Penning trap ALPHATRAP, the metrology system described in Section 3.3 was transported and set up at MPIK Heidelberg. The light of the spectroscopy was directed through a FNC to an in-coupling breadboard situated beneath the trap. The setup of the in-coupling breadboard as well as the integration of the spectroscopy lock with the ALPHATRAP software was achieved by I. V. Kortnuov. The operation of the trap was conducted by the colleagues at MPIK (M. Bohman, F. Heiße and S. Sturm). The reference laser and cavity, FNC and CTE were setup and maintained by the author of this work.

As illustrated in Figure 8.1 (d), the rovibrational level$(v, N = 0)$ state is comprised of a total of 12 Zeeman sub-levels. In the case of $(v', N' = 1)$, this number increases to 36. This results in a total of 432 potential candidates for transitions. Which option should be selected? To begin with, the transition from the initial state of $(0,0) \longrightarrow (5,1)$ will be examined, as this transition possesses an optical transition frequency of 259 THz. This frequency can be achieved by modern laser systems and can be stabilized using an OFC and optical reference.

The strength of a transition from a ground state $|0\rangle$ to an excited state $|1\rangle$ is determined by the Rabi frequency Ω_{01}. In particular, during continuous interrogation of the transition of laser light with the electric field $\boldsymbol{E}(\boldsymbol{r},t)$ at exactly the transition frequency, it is

$$\hbar\Omega_{01} = \left|\left\langle 1 \left| \hat{H}_{int} \right| 0 \right\rangle\right|. \tag{8.5}$$

The Rabi frequency is a measure of the population in, or probability of the particle to be in, the ground or excited state at a given time. Conversely, if the value is higher, it signifies that the transition is more probable within the specified time window, thus leading to the term "stronger." The interaction Hamiltonian $\boldsymbol{H}_{int}$ [216], can be expressed as follows:

$$\begin{aligned}
\hat{H}_{int} = -e\,\boldsymbol{r}\cdot\boldsymbol{E}(\boldsymbol{r},t) &= -e\,\boldsymbol{r}\cdot\left[\boldsymbol{E}(0,t) + (\boldsymbol{r}\cdot\nabla)\boldsymbol{E}(0,t) + \frac{1}{2}(\boldsymbol{r}\cdot\nabla)^2\boldsymbol{E}(0,t) + \ldots\right] \\
&= \underbrace{-e\,\boldsymbol{r}\cdot\boldsymbol{E}(0,t)}_{\text{Dipole - E1}} \underbrace{-e\,\boldsymbol{r}(\boldsymbol{r}\cdot\nabla)\boldsymbol{E}(0,t)}_{\text{Quadrupole - E2}} \underbrace{-\frac{e}{2}\boldsymbol{r}\cdot(\boldsymbol{r}\cdot\nabla)^2\boldsymbol{E}(0,t)}_{\text{Octupole - E3}} \\
&= \hat{H}_{E1} + \hat{H}_{E2} + \hat{H}_{E3}.
\end{aligned}$$

It is the interaction between the EM wave and the electron of charge e at its position $\boldsymbol{r}$ relative to the center of mass of the molecule. The multipole expansion of the external electric field gives rise to

a variety of interaction terms, which are designated according to the specific multipole expansion. The three terms of interest that emerge are the result of possible transitions given by the dipole (E1), quadrupole (E2), and octupole (E3) Hamiltonians. The evaluation of transition strengths in Equation (8.5) can be achieved through

$$\hbar\Omega_{01} = \left|\left\langle 1\left|\hat{H}_{int}\right|0\right\rangle\right| = \left|\left\langle 1\left|\hat{H}_{E1}+\hat{H}_{E2}+\hat{H}_{E3}\right|0\right\rangle\right|. \tag{8.6}$$

Upon examination of the respective Hamiltonians of the E1, E2, and E3 terms, using the derivative of a classical planar wave $\boldsymbol{E}(\boldsymbol{r},t) = \boldsymbol{E}_0 e^{-i(\boldsymbol{k}\cdot\boldsymbol{r}-\omega t)}$, the following proportionalities can be found:

$$\begin{aligned} H_{E1} &\propto e\,r \\ H_{E2} &\propto e\,\lambda^{-1}r^2 \\ H_{E3} &\propto e\,\lambda^{-2}r^3 \end{aligned}$$

It is evident that higher-order multipoles scale with $\lambda^{-1}r$. In the context of the molecule it is $r \approx 10^{-10}\,\mathrm{m}$, and the optical wavelength is of the order of $\lambda \approx 10^{-6}\,\mathrm{m}$. Consequently, the E2 and E3 transitions will exhibit a decrease in intensity by 10^{-4} and 10^{-8}, respectively, in comparison to the E1 transitions. Therefore, in a molecule that permits dipole transitions, E1 is generally favorable. This is the case for the HD^+ molecule because the deuteron and proton generate a shift of the center of charge with respect to the center of mass of the molecule. For instance, the presence of identical nuclei in H_2^+ renders it incapable of exhibiting an electric dipole moment. In particular, using the previously introduced quantum numbers to represent the states, Equation (8.6) becomes

$$\hbar\Omega_{ge} = \left|\left\langle v',G_1',G_2',N',F',m_F'\left|\hat{H}_{E1}+\hat{H}_{E2}+\hat{H}_{E3}\right|v,G_1,G_2,N,F,m_F\right\rangle\right|.$$

The Wigner-Eckart theorem posits that the potential transitions in multipoles impose constraints on the permissible variations in angular momentum. Defining $\Delta F = F' - F$ and $\Delta m_F = \Delta m_F' - \Delta m_F$, these rules are:

$$\begin{aligned} \mathrm{E1} &\longrightarrow \Delta F = 0,\pm1 \text{ and } \Delta m_F = 0,\pm1 \\ \mathrm{E2} &\longrightarrow \Delta F = 0,\pm1,\pm2 \text{ and } \Delta m_F = 0,\pm1,\pm2 \\ \mathrm{E3} &\longrightarrow \Delta F = 0,\pm1,\pm2,\pm3 \text{ and } \Delta m_F = 0,\pm1,\pm2,\pm3 \end{aligned}$$

Notably, the transition $F = F' = 0$ is forbidden. This knowledge can now be used to find all physically possible transitions. An overview of the number of the examined possible dipole transitions is provided in Table 8.2. This results in a total of $2\times83+94 = 260$ candidates for possible E1 transitions. To identify the relevant ones, a closer look at the angular momentum change during the full transition is necessary. The rotational quantum number is designed to undergo a change of one unit, expressed as a shift in angular momentum. This increase in angular momentum must be expressed in the projections of the contributors to the coupled momentum, given by

$$\Delta m_F = \Delta m_s + \Delta m_{I_p} + \Delta m_{I_d} + \Delta m_N.$$

In the case that $\Delta m_F = 0$, at least two spin or momentum projection numbers must be changed to yield a net zero. In the absence of alterations, the conservation of angular momentum would not be upheld. However, as expressed in the Hamiltonian, there is no coupling between the spins of

Δm_F	+1	0	−1
M	83	94	83

Table 8.2: Number M of possible E1 transitions within the $(v,0) \longrightarrow (v',1)$ transition, filtered by the respective change Δm_F.

the molecule and the EM wave. Consequently, outcomes involving any spin projection change are significantly suppressed relative to transitions in which the angular momentum increases (or decreases) by one unit of the rotational projection, m_N. In the case of Delta $\Delta m_F = 0$, it is evident that still at least one spin projection must undergo a change in conjunction with the rotational projection.

Nevertheless, under the condition that $\Delta m_F = \pm 1$, it is feasible to conserve all spin projections. This is accomplished by modifying $\Delta m_N = \pm 1$, which will yield the most probable transitions. In practice, this necessitates the utilization of light with circular polarization, which induces the respective change in the magnetic moment. In particular, linearly polarized light (π) drives $\Delta m_F = 0$, while clockwise circular polarization (σ^+) and counterclockwise polarization (σ^-) drive $\Delta m_F = +1$ and $\Delta m_F = -1$, respectively. The elimination of linearly polarized light to provide the strongest possible transitions results in a reduction to 166 candidates. Eliminating all transitions at which $\Delta F > \pm 1$, as these transitions are inherently weak, results in 142.

However, given the utilization of only a single circular polarization at a time, and the high symmetry between the two, the number of candidates is further reduced to 71. It is important to note that these transitions also include those at which it is $\Delta m_N = 0$, where the other spin projections account for the angular momentum change. Therefore, upon filtration to only include transitions in which all spins are conserved, the number of viable candidates is reduced to 12. This argument alone inherently filters the 12 possible transitions. However, the small intermezzo gives an understanding of the complex energy diagram and possible transitions therein. This can be helpful to understand the decay of the particle in a specific state, or candidates for BBR transitions

The rewriting of the set of quantum numbers into a set given by $\left(v,N,m_s,m_{I_p},m_{I_d},m_N\right)$, enables the display of all possible transitions in Table (8.3). This decoupling of spins is a natural consequence of the strong magnetic field in the Penning trap. The table also displays the calculated frequency shifts, Δf_{epd}, of the respective transition frequency ν_{epd}, with respect to the spin-averaged one of the rovibrational transition:

$$\nu_{epd} = \nu_{sp.avg.} + \Delta f_{epd}$$

In this context, the indices signify the electron, proton, and deuteron spins, respectively. It can be observed that all 12 potential transitions for the specific case of σ^- polarization are confined within a frequency band with an approximate width of 100 MHz. Typically, when an ion is loaded into ALPHATRAP, all spin states can be determined, i.e. m_s, m_{I_p}, m_{I_d} and m_N. Subsequent to this, the spectroscopy light can be detuned to the calculated offset frequency, and an attempt can be made to drive the transition. What remains to be elucidated is the detection scheme that would enable the determination of a successful optical transition. In order to proceed with this matter, it is necessary to consider a few additional factors.

m_s	m_{I_d}	m_{I_p}	$m_N\,(N=0)$	$m'_N\,(N=1)$	$\Delta f_{epd}\,(\Delta m_N=-1)$
		$+1$	0	$-1,1$	$-25.9230\,\mathrm{MHz}$
	$\mathbf{+\frac{1}{2}}$	**0**	**0**	**−1**, 1	**−17.7879 MHz**
$\mathbf{+\frac{1}{2}}$		-1	0	$-1,1$	$-9.7021\,\mathrm{MHz}$
		$+1$	0	$-1,1$	$+26.7510\,\mathrm{MHz}$
	$-\frac{1}{2}$	0	0	$-1,1$	$+34.8961\,\mathrm{MHz}$
		-1	0	$-1,1$	$+43.0084\,\mathrm{MHz}$
		$+1$	0	$-1,1$	$+67.5241\,\mathrm{MHz}$
	$+\frac{1}{2}$	0	0	$-1,1$	$+59.3698\,\mathrm{MHz}$
$-\frac{1}{2}$		-1	0	$-1,1$	$+51.2274\,\mathrm{MHz}$
		$+1$	0	$-1,1$	$+13.9643\,\mathrm{MHz}$
	$-\frac{1}{2}$	0	0	$-1,1$	$+5.8121\,\mathrm{MHz}$
		-1	0	$-1,1$	$-2.3414\,\mathrm{MHz}$

Table 8.3: All possible transitions that conserve spin orientations. The right column displays the offset from the spin averaged frequency $\nu_{sp.avg} = 259.762\,97\,\mathrm{THz}$ for transitions that drive $\Delta m_N = -1$. The calculations were performed and provided by S. Schiller. The values are calculated for a magnetic field strength of $B = 38413.3900\,\mathrm{G}$ using μ_B, g_p and g_d from CODATA2022, g_{rot} from [217], $g_{(5,1)}$ from [218] and vibrational corrections from [219] and $g_{(0,0)}$ from the ALPHATRAP experiment.

The ion favors energetically low levels, allowing it to remain at the $(v = 0, N = 0)$ state for extended periods. In the event that the system is excited to the $(5,1)$ state by means of a forceful excitation, and the presence of the laser is subsequently disabled, the system will ultimately decay back into the $(0,0)$ state. This process occurs through a sequence of spontaneous decays, with the most probable decays occurring at $\Delta v = -1$ and $\Delta N = \pm 1$, resulting in lower energies. Simulations performed by I. V. Kortunov have demonstrated that the probability of the particle decaying into the $(0,1)$ state prior to reaching the rovibrational ground level is high, exceeding 50 %, distributed to the sub-states with $m_N = 0$ and $m_N = \pm 1$. In addition, the lifetime of this rovibrational state is approximately 140 s. Therefore, following a successful optical transition, an electron spin resonance (ESR) can be attempted on the particle while in the state of $(v = 0, N = 1, m_N = +1)$.

This transition can be driven by an RF wave with a frequency that is tuned to induce a change $\Delta m_s = \pm 1$ in the electron spin orientation. The ESR of the $m_N = +1$ sub-state is selected for its distinct frequency and minimal overlap with an ESR in the rovibrational ground state. This overlap in the AT arises from the magnetic bottle and temperature of the molecule. In the PT, this overlap would be essentially zero. This is of particular significance, as the successful ESR transition serves as an indicator for the successful optical transition. Consequently, an ESR in the ground state would

result in a false positive detection. In the specified configuration of ALPHATRAP, the probability of a single ESR flipping the electron spin is approximately 50 %, with an estimated time requirement of 10 seconds, accounting mostly for the readout. Therefore, the detection scheme was designed to encompass a total of 10 consecutive attempts at driving an ESR. In the event that the ion was found to be in the specific state of (0,1) at a given moment in time, there is a high probability that this will be discernible in the ESR. Additionally, it aligns with the approximately two-minute life time of the state. The ESR detection process is conducted within the AT, wherein a change in the electron's spin orientation is quantifiable through the variation in the axial frequency of the particle.

Accordingly, one possible scheme for an on/off measurement is as follows:

1. Two counters should be initiated: one to enumerate the number of measurements $M_m = 0$, and another to record the observed electron spin flips $M_e = 0$.

2. The ion must be prepared in the rovibrational ground state (0,0).

3. The individual spins m_s, m_{I_p} and m_{I_d} of the nuclei and electron must be determined. Typically, the nuclear spins are well-known and the electron spin is prepared in the desired state. Then, the laser must be tuned to the respective transition frequency $\nu_{sp.avg.} + \Delta f_{epd}$.

4. The ion is then subjected to a 20 second interrogation with laser light, at a fixed frequency, after which the laser is shuttered off.

5. A total of 10 consecutive attempts are to be made to drive an ESR in the respective $\left(0,1,m_s,m_{I_p},m_{I_d},1\right)$ state.

   (a) In the event that a successful ESR is observed, the spin flip counter M_e is to be incremented by one.

   (b) In the absence of ESR, no further action is required.

6. The measurement counter, M_m, is to be incremented by one, and the process is to be repeated from step 4. If it was the last laser interrogation, it is stopped here.

The individual steps are also illustrated in Figure 8.11. At the conclusion of a measurement series, the fraction $p_{sf} = M_e M_m^{-1}$ provides the percentage of observed spin flips observed for a laser frequency $\nu_{sp.avg.} + \Delta f_{epd}$, thereby yielding the spin flip probability. Repeating the same measurement but at a frequency that is considered to be off resonance will result in a plot as shown in Figure 8.12 (a). In this particular case, the off resonance frequency was chosen to be the spin averaged frequency, $\nu_{sp.avg.}$. A compelling indication that the optical transition from the state of $(0,0) \longrightarrow (5,1)$ has been successfully driven is provided when

$$p_{sf}\left(f_{sp.avg.} + \Delta f_{epd}\right) \gg p_{sf}\left(f_{sp.avg.}\right).$$

In other words, when a substantial number of spin flips are observed in the "on" resonance state as opposed to the "off" state. These effects are clearly observable in the figure.

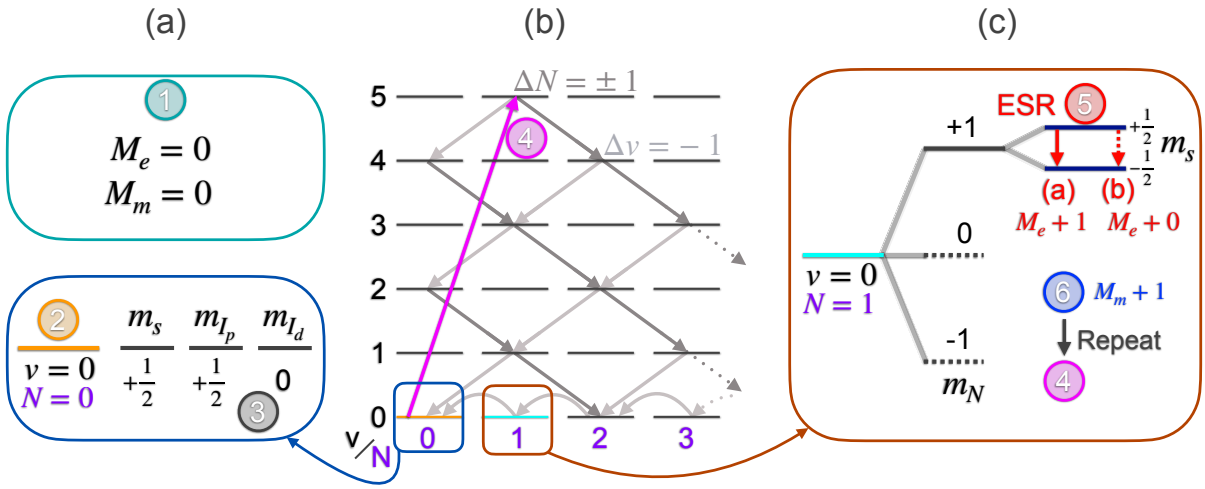


Figure 8.11: Measurement scheme for the on/off measurement of the rovibational $(0,0,1/2,1/2,0,0) \longrightarrow (5,1,1/2,1/2,0,-1)$ transition in HD^+. (a): The first three steps of the scheme involving the preparation of the ion in the ground state and the determination of the spin orientations. (b): Step 4: Interrogation of the molecule with light either on or off resonance (magenta). The subsequent decay has a high probability for the molecule to stay in the $(0,1,1/2,1/2,0,1)$ state that has a lifetime of approximately 140 s. (c): Step 5: Attempts to drive the $(0,1,1/2,1/2,0,1) \longrightarrow (0,1,-1/2,1/2,0,1)$ ESR transition (red), yielding either a positive (straight) or negative (dashed) result. The diagrams are not to scale.

The $(0,0,1/2,1/2,0,0) \longrightarrow (5,1,1/2,1/2,0,-1)$ optical transition was interrogated with a frequency detuning of $\Delta f_{epd} = -17.7879\,\text{MHz}$. Subsequently, ESRs from the $(0,1,1/2,1/2,0,1) \longrightarrow (0,1,-1/2,1/2,0,1)$ state were attempted. The off-resonance signal yielded a spin-flip probability of $2-3\,\%$. At the predicted resonance frequency, the probability is approximately $20\,\%$ At adjacent frequencies of 150 kHz, the spin flip probability is approximately 12–15 %.

In the most recent developments—occurring just days before the submission of this thesis—a candidate optical transition with a width of a few kilohertz was identified. A preliminary analysis of the high-resolution data was carried out by S. Sturm (MPIK, videoconference, 20 June 2025). As the data are still under internal review at the time of writing, they are not included in this thesis.

The findings indicate with high confidence that this represents the first detection of an optical rovibrational transition in a single molecule. It is important to emphasize rovibrational, as rotational spectroscopy has previously been performed at NIST and reported by [50]. Panel (b) displays the duty cycle of the OFC and reference laser during the period since the start of data collection on the ion. The red areas indicate times at which the OFC was not operating at the target frequency and stability. The green line indicates a moving average of 10 minutes. The comb has been operational for slightly less than 80 % of the total measurement period. The 18 h long measurement in Panel (a) was obtained within the initial 10 d, a period during which the OFC remained fully operational.

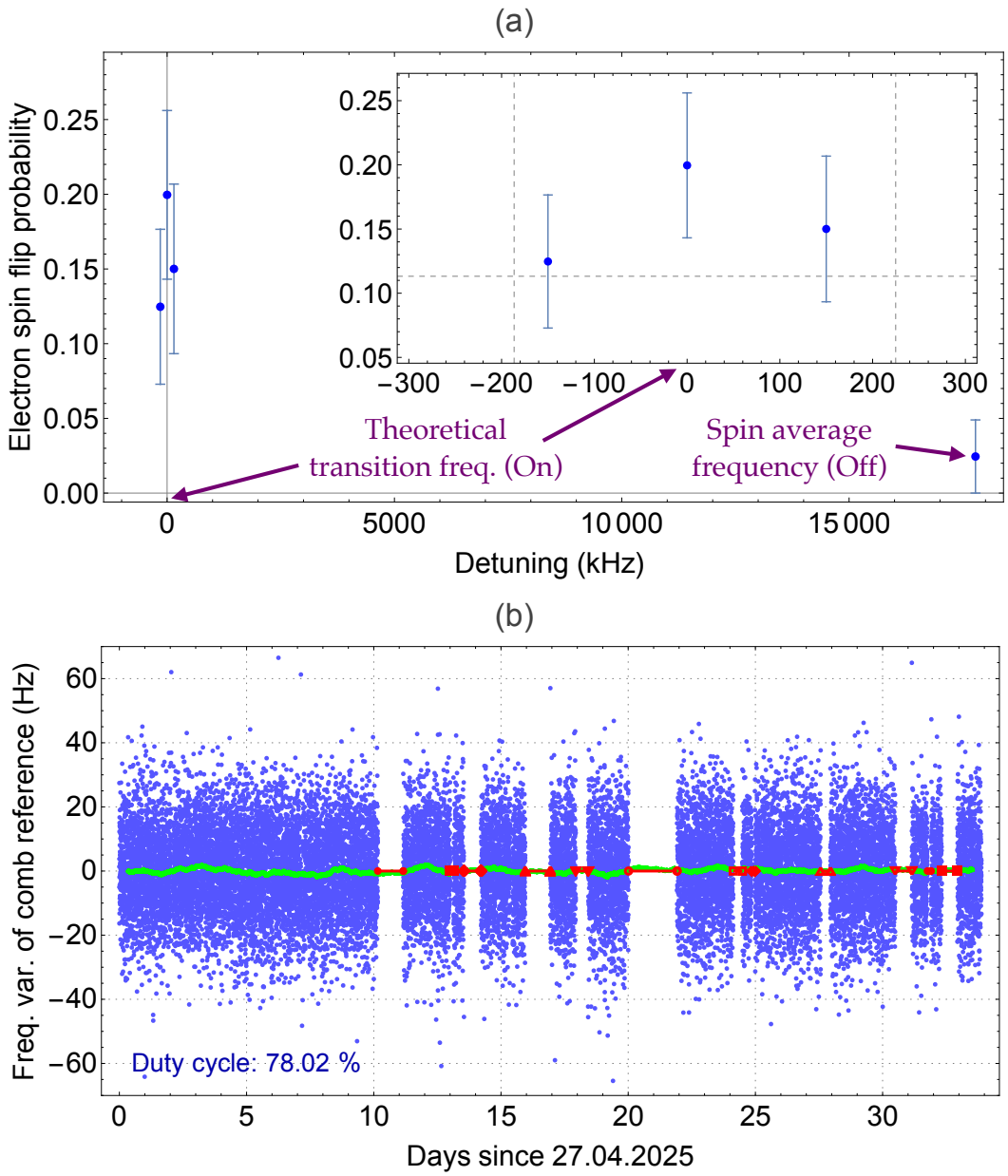


Figure 8.12: (a). First detection of an optical rovibrational transition in a single molecule. The "On" measurement was performed at the predicted theoretical transition frequency, while the "Off" measurement was conducted at the spin averaged frequency $\nu_{sp.avg.}$. The data points at ±150 kHz around the "On" signal indicate a more complex structure around it. (b): The duty cycle of the reference laser, and the OFC, which stabilize the spectroscopy light. Specifically, the reference laser frequency, as measured by the OFC, is displayed. The green data is a 10 min moving average of the blue data, the precision of which is constrained by the limitations of the frequency counter. The red lines indicate times at which the OFC was not deemed operational for the spectroscopy.

Within the trap, the occurrence of a spontaneous nuclear spin flip is a possibility. This can be measured and addressed by adjusting the spectroscopy laser to a new offset frequency, denoted as Δf_{epd}. This kind of event tends to occur at the order of once per day. The spectroscopy laser can be tuned within a band of approximately 80 MHz while locked, thereby enabling direct addressing of a significant number of nuclear spin flips. The implementation of this was performed by I. V. Kortunov.

Nevertheless, it is essential to acknowledge that these measurements were conducted in the AT, not the PT, thereby constraining the achievable resolution of the measurement. Furthermore, sidebands resulting from the axial motion of the ion, which is nearly perfectly parallel to the EM wave propagation vector, will result in a Doppler-like broadening of the spectrum. Additionally, sidebands of the magnetron and cyclotron motion may emerge due to the imperfection angles of the wave vector with respect to these devices. As is customary, the response will entail the collection of additional data. However, the preliminary results are encouraging.

Chapter 9

Summary and Outlook

Summary

This thesis presents a comprehensive didactic overview of ultra-stable lasers, starting from the fundamentals of electromagnetic waves and progressing through theoretical and practical aspects. Original derivations and calculations are provided alongside established concepts, laying a foundation suitable for future expansion into a tutorial-style publication, especially with the inclusion of state-of-the-art results.

A dual-cavity system with 30 cm long ULE spacers was developed, achieving a fractional frequency instability of 10^{-16} and an optical linewidth at the Hz level. The spectral frequency noise density remained at or below $10^{-14}\,\mathrm{Hz}^{-1/2}$ between 10^{-3} Hz and 1 MHz. This light served as a reference for rovibrational spectroscopy of cold, trapped HD^+ [35] and for UDM searches via Iodine spectroscopy [36]. It was also used to characterize the laser employed in high-resolution spectroscopy of cold, trapped HD^+ [34], thus fulfilling Objective A and part of Objective C set in Chapter 1.

A compact and robust optical reference based on a NEXCERA spacer achieved a frequency instability of 10^{-15}. The system exhibited spectral noise densities below $10^{-14}\,\mathrm{Hz}^{-1/2}$ (2 Hz to 10^4 Hz) and below $10^{-12}\,\mathrm{Hz}^{-1/2}$ up to 1 MHz. This system supported a second UDM detection experiment [37], completing Objective C.

A frequency metrology system based on the NEXCERA cavity and a frequency comb, including a tunable transfer laser, was developed for rovibrational spectroscopy of HD^+. Fully fiberized and portable, it included remote control, automation, and re-locking functionalities, enabling high duty cycle operation. It was tested across multiple institutions and corrected against international frequency standards (PTB Braunschweig), thereby fully addressing Objective B.

This system enabled the first-ever on/off rovibrational signal detection from a single HD^+ ion in the ALPHATRAP Penning trap. It also facilitated the characterization of an ultra-stable OPO [68] used in spectroscopy [35], where the OPO's comb was referenced to one of the 30 cm ULE-locked laser mentioned above.

Aging drift of just $2.1 \times 10^{-18}\,\mathrm{s}^{-1}$ was measured on a room-temperature resonator, the lowest ever recorded. RAM suppression in the dual-cavity setup reached instabilities below 10^{-17} in one cavity and combined levels below 3×10^{-17}, rivaling top-tier methods in the literature.

An analysis on using optical references as mode cleaners for frequencies above cavity linewidth demonstrated improved noise suppression below $10^{-15}\mathrm{Hz}^{-1/2}$, relevant to UDM searches.

A novel fiber-based ring resonator featuring a ZCTE temperature of around $-30\,^{\circ}\mathrm{C}$, 220 K above typical cryogenic values, was developed and characterized. This system may offer a long-term, cost-effective alternative to commercial wavemeters, fulfilling Objective D.

Finally, the NEXCERA resonator's performance contributed to European guidelines for achieving 10^{-17} level instability in ultra-stable lasers [67].

Outlook

The dual-cavity system was designed for experiments testing the isotropy of light. Rotating and monitoring the cavities could tighten constraints on Lorentz invariance and potentially test CPT symmetry. Implementing active tilt stabilization may further improve frequency stability.

The fiber ring resonator is still in early development. Its performance could be significantly enhanced through better temperature control near its ZCTE point, higher finesse, and improved shielding from external disturbances. Future research may explore ZCTE temperatures closer to room temperature ($\sim 20\,^{\circ}\mathrm{C}$). Linear resonators also offer a promising, cost-effective path toward linewidths comparable to the best optical references.

Stabilizing higher-power lasers using low-power signals transmitted through optical resonators could reduce phase noise in specific frequency domains. This approach may advance dark matter searches or other applications requiring ultra-pure spectral light. Such techniques might enable stability beyond the thermal noise limit, opening new frontiers for ultra-stable laser research.

The ongoing measurement campaign at MPIK Heidelberg holds promise for detailed comparisons between experiment and theory. Beyond the milestone on/off rovibrational measurement on HD^+, future work could probe relativistic and QED corrections to spin-averaged frequencies. Comparative spectroscopy on H_2^+ and eventually anti-H_2^+ may enable CPT tests in Paul or Penning traps, contributing to searches for physics beyond the Standard Model.

The metrology system developed here is robust, remotely controlled, and transportable, allowing rapid deployment across different laboratories. Its modular design permits adaptation to various wavelengths and applications, potentially sparking numerous collaborative research initiatives.

NEXCERA has proven competitive with ULE glass, offering lower aging and a slightly better thermal noise floor. Although its ZCTE temperature is higher, it demands somewhat stricter temperature stability compared to ULE. Despite this, it remains an attractive and cost-effective choice for long-term local optical references, potentially replacing H-masers in some applications. While

its drift is still about two orders of magnitude higher, well-controlled cavities may drift as little as 6×10^{-11} per year, sufficient for many uses.

As ultra-stable lasers become crucial to an expanding range of applications, ongoing research to push fractional frequency instability lower remains vital. This field will continue to be at the forefront of precision measurement science.

Appendix A

From Wave to Metrology: A Tutorial

The content of this paragraph now appears in the main thesis text (beginning of Chapter 2) as it forms a critical part of the theoretical framework. This note serves as a placeholder for its original appendix location.

Appendix A contains fundamental theoretical descriptions and derivations that, while essential, are too elementary or textbook-like for inclusion in the main body of the thesis. These include the descriptive frameworks of dielectric mirrors, GBs, optical fibers, lasers, Allan deviations, frequency and phase noise, RF components, wavemeters, and OFCs.

A.1 Foundations of Light: Waves and Interfaces

This subsection is concerned with the mathematical description of planar EM waves. In particular, it explores the behavior of electric and magnetic fields at interfaces and the resulting expressions for reflection and transmission in a mathematical sense. This results in the delineation of high reflectivity mirrors, with a particular emphasis on dielectric mirrors, and, subsequently, a rudimentary exposition of linear FP optical resonators. The following textbooks are relevant to the subjects introduced in this section: [220, 221, 222, 223].

A.1.1 Light as a Wave: Electromagnetism and Polarization

The electric field of an EM wave, denoted by $\boldsymbol{E}$ with amplitude E_0, can be mathematically described by a complex exponential function, given by

$$\boldsymbol{E} = E_0 \hat{\boldsymbol{p}} e^{-i(\boldsymbol{k_n} \boldsymbol{r} + \omega t)}, \tag{A.1}$$

with the imaginary unit i. In this context, the propagation of the wave in space $\boldsymbol{r}$ is indicated by the wave vector $\boldsymbol{k}_n$. The relationship between the wave vector and the wavelength λ_n is expressed as $k_n = \frac{2\pi}{\lambda_n}$. The propagation of the wave through time, denoted by t, is characterized by the radial frequency, ω, which is connected to the frequency ν of the wave as $\omega = 2\pi\nu$. Such, Equation (A.1) can be expressed as follows:

$$\boldsymbol{E} = E_0 \hat{\boldsymbol{p}} e^{-2\pi i \left(\frac{1}{\lambda_n} \hat{\boldsymbol{k}} \boldsymbol{r} + \nu t \right)}$$

The wave equation $\frac{d^2}{dt^2}\boldsymbol{E} = c_n^2 \Delta \boldsymbol{E}$ (derived in Equation (A.43) in Section A.2.1) can be applied to the electric field. This provides an expression for the velocity c_n of the wave, which is defined by its frequency and wavelength as

$$c_n = \lambda_n \nu.$$

In this setting, c_n and λ_n represent the speed of light and wavelength, respectively, within a medium of propagation. The medium's refractive index, denoted by n, the speed of light in a vacuum c_0, defined by the electric and magnetic constants ε_0 and μ_0, is expressed as $c_0 = \frac{1}{\sqrt{\varepsilon_0 \mu_0}}$. Specifically, it is

$$c_n = \frac{c_0}{n} = \frac{\lambda_0}{n} \nu,$$

where λ_0 signifies the vacuum wavelength of the light. The quantity $\hat{\boldsymbol{p}}$ is defined as the polarization vector of the electric field, illustrating the direction of oscillation. It is normalized through $|\hat{\boldsymbol{p}}| = 1$, thereby establishing the strength of the electric field as a function of its amplitude, $E_0 = |\boldsymbol{E}|$. Both magnetic and electric fields have a polarization, which is not arbitrary. The relationship between the fields is expressed by the speed of light, given by

$$|\boldsymbol{B}| = \frac{|\boldsymbol{E}|}{c_n}, \tag{A.2}$$

where $\boldsymbol{B}$ represents the magnetic field. Moreover, it holds $\boldsymbol{k} \parallel \boldsymbol{E} \times \boldsymbol{B}$. Consequently, the field polarizations are found to be orthogonal to each other and to the direction of propagation at any given moment. If the wave exhibits a continuous rotation around the propagation axis, it is designated

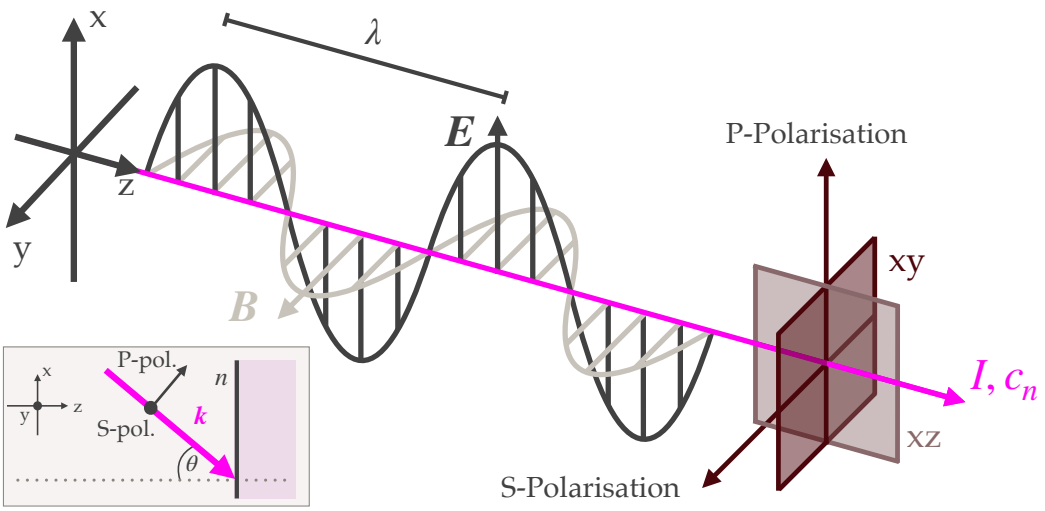


Figure A.1: Presentation of an EM wave propagating along the z-axis. The electric and magnetic fields are perpendicular to each other. In this configuration, the wave is characterized as $p-$polarized with respect to the electric field. The parameter I indicates the intensity of the light.

as circularly polarized. This arises from the observation that the field vector undergoes a spiral movement. Therefore, in the event that the fields exhibit oscillatory behavior along a fixed axis, the wave is defined as linearly polarized.

Specific optical components possess the capacity to interact with light, thereby altering its polarization. This interaction can manifest in a variety of ways, including the rotation of the polarization or the transition between linear and circular polarization. The subsequent discussion in Section A.3 will address select components in greater detail. In the majority of the applications examined in this thesis, linearly polarized light is utilized. It can be divided into two components: the $s-$polarization axis and the $p-$polarization axis.

In the case that light propagates along the $z-$axis towards a surface in the $xy-$plane, the direction of the resulting beams will remain in the $xz-$plane. In this particular instance, the axis that is oriented perpendicularly (in German, "**s**enkrecht") with respect to the $xz-$plane is designated as the $s-$polarization axis. Conversely, the parallel (in German, "**p**arallel") axis, which remains perpendicular to $\boldsymbol{k}$, is identified as the $p-$polarization axis, as illustrated in Figure A.1. The definition of "polarization" as the oscillation of an electric or magnetic field is not of consequence. However, it is generally accepted that the electric field is the primary metric for measuring polarization, which is a consequence of energy transport along the electric field. In the case of the incident light, the polarization vector is expressed as follows:

$$\hat{\boldsymbol{p}} = \hat{\boldsymbol{p}}_E = \begin{pmatrix} p_p \\ p_s \\ 0 \end{pmatrix}$$

In the figure, the electric field is $p-$polarized, with the magnitude of the electric field expressed by $p_p = 1$. In consideration of the propagation of light within the $xz-$plane, the angle of incidence, θ,

is the angle between $\boldsymbol{k}$ and the $z-$axis, as illustrated in the inset of Figure A.1. Here, the electric field is expressed as follows:

$$\boldsymbol{E} = \begin{pmatrix} E_x \\ E_y \\ E_z \end{pmatrix} = E_0 \begin{pmatrix} \cos(\theta)\, p_p \\ p_s \\ \sin(\theta)\, p_p \end{pmatrix} e^{-2\pi i \left(\frac{1}{\lambda_n} (\sin(\theta)x + \cos(\theta)z) + \nu t \right)} \tag{A.3}$$

It is noteworthy that the polarization factors, p_p and p_s, are real but can be negative, provided that $p_p^2 + p_s^2 = 1$. Eventually, the polarizations establish a basis for the electric fields, given by

$$\begin{pmatrix} E_x \\ E_y \\ E_z \end{pmatrix} \longrightarrow \begin{pmatrix} \boldsymbol{E}_p \\ E_s \end{pmatrix},$$

with $E_s = E_y$ and $\boldsymbol{E}_p = \begin{pmatrix} E_x \\ E_z \end{pmatrix}$. This presentation of the electric field is of particular relevance for the study of processes that are explained in the following sections and chapters. Furthermore, the polarization of the magnetic field, $\hat{\boldsymbol{p}}_B$ is expressed as

$$\hat{\boldsymbol{p}}_B = \begin{pmatrix} -\cos(\theta)\, p_s \\ p_p \\ -\sin(\theta)\, p_s \end{pmatrix}.$$

For linear polarization, it is important that the condition $\hat{\boldsymbol{p}}_E \cdot \hat{\boldsymbol{p}}_B = 0$ is maintained under all circumstances, given that the fields are perpendicular to each other.

A.1.2 Boundaries of Light: Matching Fields at Interfaces

In order to comprehend the behavior of EM waves, as formulated by Equation (A.3), when they propagate from one medium with refractive index n_1 to another of index n_2, it is necessary to employ the Maxwell equations to establish boundary conditions. Each of the four identities can be utilized to establish a continuity equation for specific directions of the fields. The Maxwell equations are as follows:

$$\nabla \cdot \boldsymbol{E} = \frac{\rho}{\varepsilon_0} \tag{A.4}$$

$$\nabla \cdot \boldsymbol{B} = 0 \tag{A.5}$$

$$\nabla \times \boldsymbol{E} = -\frac{\partial}{\partial t} \boldsymbol{B} \tag{A.6}$$

$$\nabla \times \boldsymbol{B} = \mu_0 \left(\boldsymbol{J} + \varepsilon_0 \frac{\partial}{\partial t} \boldsymbol{E} \right) \tag{A.7}$$

The initial two equations can be identified as Gauss' law, while the third equation is Faraday's law. The final identity can be attributed to Ampere's law. Considering the surface of interaction to be the $xy-$plane, the initial two equations can be utilized to establish boundaries for the components of the fields perpendicular to the surface. Conversely, the subsequent two equations can be employed to determine the parallel components, which are of particular relevance in the following calculation

of reflection and transmission coefficients. The integral form of Equation (A.6) is expressed as follows:

$$\oint_S \boldsymbol{E} \cdot d\boldsymbol{s} = -\frac{\partial}{\partial t} \int_A (\boldsymbol{B} \cdot \hat{\boldsymbol{n}}_A)\, dA \tag{A.8}$$

Faraday's law of induction stipulates that a changing magnetic field that is normal ($\hat{\boldsymbol{n}}_A$) to a loop S of area A induces an electric field along the loop. This is an example of the following phenomenon: a changing current through a wire generates a magnetic flux, which in turn induces an electric field. With regard to the propagation of light through two media, the law is illustrated in Figure A.2. The normal vector denoted by $\hat{\boldsymbol{n}}_A$, is distinct from the refractive index, n. In this scenario, the closed loop is perpendicular to the interaction surface, resulting in equal amounts in both mediums one and two. The long side of the loop along the $x-$axis of length Δx is parallel to the surface, whereas the short side of length Δz along the $z-$axis is perpendicular to it. The center of the coordinate system is set at the point of impact between the wave and the surface. As Δz approaches 0, the loop approaches the surface from both directions until it is in contact with it. The left side of the integral containing the electric field becomes

$$\lim_{\Delta z \to 0} \oint_S \boldsymbol{E} \cdot d\boldsymbol{s} = \oint_{\Delta x} (\boldsymbol{E} \cdot \hat{\boldsymbol{x}})\, dx,$$

where the closed integral now exclusively includes the long axis. In particular, if the field is divided into two parts, $\boldsymbol{E}_1$ in medium one and $\boldsymbol{E}_2$ in medium two, The calculation is expressed as follows:

$$\begin{aligned}
\lim_{\Delta z \to 0} \oint_S \boldsymbol{E} \cdot d\boldsymbol{s} &= \int_{-\Delta x/2}^{\Delta x/2} (\boldsymbol{E}_1 \cdot \hat{\boldsymbol{x}})\, dx + \int_{\Delta x/2}^{-\Delta x/2} (\boldsymbol{E}_2 \cdot \hat{\boldsymbol{x}})\, dx \\
&= \int_{-\Delta x/2}^{\Delta x/2} E_1 \cos(\theta_1)\, p_p e^{i\phi(t_0)} dx + \int_{-\Delta x/2}^{\Delta x/2} E_2 \cos(\theta_2)\, p_p e^{i\phi} dx \\
&= (E_1 \cos(\theta_1) - E_2 \cos(\theta_2))\, e^{i\phi} p_p \Delta x \\
&= \left(E_{1,\parallel} - E_{2,\parallel}\right) p_p \Delta x
\end{aligned}$$

In this equation, the electric field in Equation (A.3) has been inserted. At the surface the wave must be continuous, thus the exponential terms for both electric fields will become the same phase factor. Specifically, given that the spatial coordinates are zero at that particular point in time t_0, the phase factor is given by $\phi = -2\pi i \nu t_0$. Eventually, the final expressions for the electric fields are the components of the respective waves $E_{j,\parallel,p}$ that are parallel to $p-$polarized light and parallel to the surface of interaction. These will be abbreviated as

$$E_{j,\parallel,p} = E_j \cos\left(\theta_j\right) e^{i\phi} p_p. \tag{A.9}$$

The absence of a component along $s-$polarization is attributable to the perpendicular orientation of these components with respect to the closed loop. However, if the loop were to be laid in the $yz-$plane instead and of length Δy, upon Δz approaching zero, the formalism would become $(E_1 - E_2)\, e^{i\phi} p_s \Delta y$. It does not include the angle of propagation, as the light is still propagating in the $xz-$plane. Therefore, $s-$polarization is defined as being entirely parallel to the surface of

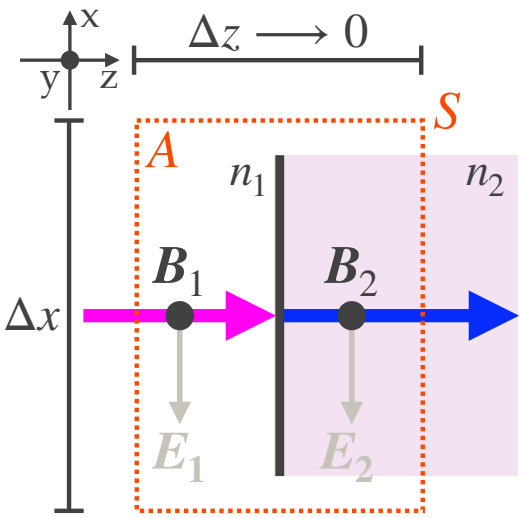


Figure A.2: Faraday's law of induction, as it applies to EM waves propagating through a surface separating two media with disparate refractive indices. The orange dashed rectangle indicates the closed loop of circumference S and area A.

interaction and it can be expressed as

$$E_{j,\parallel,s} = E_j e^{i\phi} p_s, \tag{A.10}$$

and subsequently

$$\lim_{\Delta z \to 0} \oint_S \boldsymbol{E} \cdot d\boldsymbol{s} = \left(E_{1,\parallel} - E_{2,\parallel}\right) p_s \Delta y.$$

The total electric field $E_{1,\parallel}$ parallel to the surface can be constructed through the polarizations, such as:

$$\begin{aligned} E_{1,\parallel}^2 &= E_{1,\parallel,p}^2 + E_{1,\parallel,s}^2 \\ &= E_{1,\parallel}^2 p_p^2 + E_{1,\parallel}^2 p_s^2 = E_{1,\parallel}^2 \end{aligned}$$

Accordingly, the description of the left side of Equation (A.8) is deemed complete and has been solved for any direction of the electric field amplitude. The right-hand side, which contains the magnetic field, is expressed as follows:

$$\begin{aligned} \lim_{\Delta z \longrightarrow 0} \left(-\frac{\partial}{\partial t} \int_A (\boldsymbol{B} \cdot \hat{\boldsymbol{n}}_A)\, dA \right) &= \lim_{\Delta z \longrightarrow 0} \left(-\frac{\partial}{\partial t} \int_{-\Delta x/2}^{\Delta x/2} \int_{-\Delta z/2}^{\Delta z/2} B_\perp dx dz \right) \\ &= \lim_{\Delta z \longrightarrow 0} \left(-\frac{\partial}{\partial t} B_\perp \Delta x \Delta z \right) = 0 \end{aligned}$$

This solution is elementary. The magnetic field is perpendicular to the area A of the loop, so it is independent of x or z. When the length Δz vanishes, so does A, and thus the integral becomes zero. Eventually, the expression is derived by integrating both sides of Faraday's law. The result is

expressed as follows:

$$\left(\left(E_{1,\parallel} - E_{2,\parallel}\right) p_p \Delta x\right)^2 + \left(\left(E_{1,\parallel} - E_{2,\parallel}\right) p_s \Delta y\right)^2 = 0$$

$$\Longrightarrow \left(E_{1,\parallel} - E_{2,\parallel}\right)^2 \left(\Delta x^2 + \Delta y^2\right) = 0$$

Ultimately, it can be demonstrated that $E_{1,\parallel} = E_{2,\parallel}$. Therefore, it can be concluded that the electric field components that are parallel to the surface of interaction between media are continuous. This is applicable to all components of the electric fields within the specified medium. A similar approach can be employed in the context of Amperes' law for the magnetic field

$$\nabla \times \boldsymbol{B} = \mu_0 \left(\boldsymbol{J} + \varepsilon_0 \frac{\partial}{\partial t} \boldsymbol{E}\right).$$

Here, the primary distinction lies in the additive term of the injection current, $\boldsymbol{J}$. This term is zero when an EM wave propagates through a dielectric medium. Consequently, the formalism undergoes a simplification, resulting in the expression:

$$\nabla \times \boldsymbol{B} = \mu_0 \varepsilon_0 \frac{\partial}{\partial t} \boldsymbol{E}$$

This is equivalent to Faraday's law. Therefore, it can be concluded that the magnetic fields will also be equivalent, i.e., $B_{1,\parallel} = B_{2,\parallel}$. In particular, the magnetic field is composed of the following individual components:

$$B_{j,\parallel,p} = -B_j \cos\left(\theta_j\right) e^{i\phi} p_s \tag{A.11}$$

$$B_{j,\parallel,s} = B_j e^{i\phi} p_p. \tag{A.12}$$

It is important to understand that the $p-$polarization of the magnetic field belongs to an $s-$polarized electric field and vice versa, and that the parameters p_s and p_p give the orientation of the polarization of the electric field. These properties are instrumental in the subsequent derivation of the reflection and transmission coefficients across the surface.

A.1.3 Reflection and Transmission: The Fresnel View

The propagation of electromagnetic (EM) waves through a medium of refractive index n_1 towards another medium of refractive index n_2 will result in the phenomenon of reflection and refraction at the boundary surface. In the case of a perfectly smooth boundary, these processes can be described qualitatively using Huygens' Law and in quantitative terms using Snellius' Law for the refraction process:

$$n_1 \sin(\theta_1) = n_2 \sin(\theta_2), \tag{A.13}$$

where θ_1 is the incident angle with respect to the normal to the surface and θ_2 is the corresponding refracted angle. In the context of dielectric mirrors and resonators, described in this work, it is of interest to quantify the fractions R and T, defined as $R = \frac{P_R}{P_0}$ and $T = \frac{P_T}{P_0}$, by which light of incident power P_0 is reflected or refracted, respectively. In the following, the term "transmission" will be utilized to denote the phenomenon of refracted light. The description of these fractions is facilitated by the application of the magnetic and electric fields, as described by the Fresnel equations, which

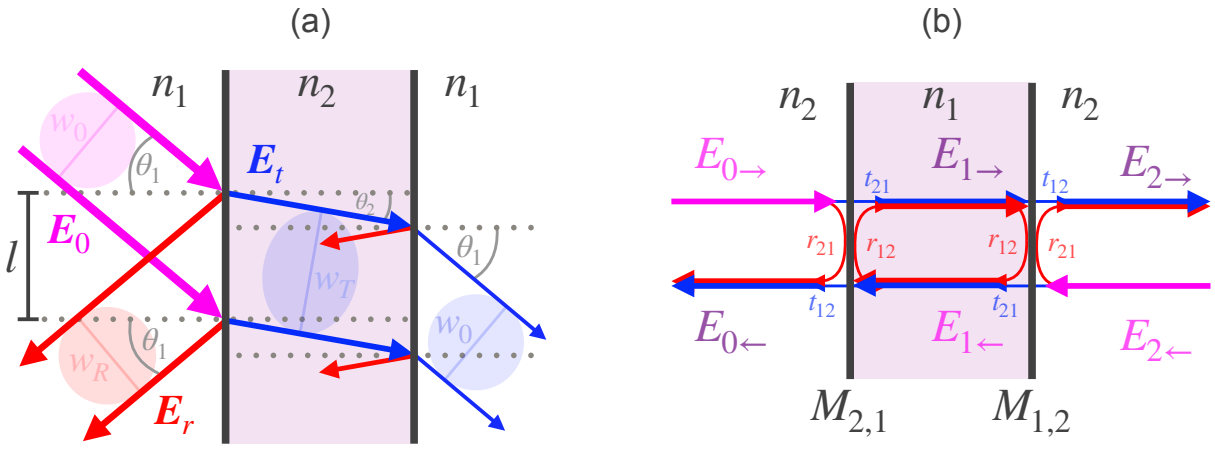


Figure A.3: (a): Visual depiction of refraction (transmission) and reflection of the electric fields of a cylinder-like ray propagating through a medium. (b): Presentation of the coefficients of the transfer matrix. The magenta beams represent the incident beams that are propagating towards the system. The total reflected and transmitted beams are comprised of components from both of them.

are derived in this chapter: Power is defined as the energy over time. This concept can also be expressed as the intensity and surface area through the following equation:

$$P_j = \frac{dW_j}{dt} = I_j A_j$$

The intensity of an EM wave is proportional to the square of the electric field, given by

$$I_j = \frac{1}{2} c_0 n_j \varepsilon_0 \left| \boldsymbol{E}_j \right|^2 . \tag{A.14}$$

The fundamental principle of energy conservation stipulates that the total energy of a system must remain constant. This translates to the following equation: $W_0 = W_R + W_T$. Therefore, conservation dictates $P_0 = P_R + P_T$ and consequently

$$R + T = 1. \tag{A.15}$$

In conclusion, this formalism in terms of intensity is expressed as

$$I_0 A_0 = I_R A_R + I_T A_T, \tag{A.16}$$

with a circular beam spot area $A_j = \frac{\pi w_j^2}{4}$, depending on the beam waist w_j of the light at the interaction surface, which is $A = \frac{\pi l^2}{4}$ as illustrated in Figure A.3 (a). This concept is equally applicable to the Gaussian beam presentation of light, as opposed to the ray picture, a topic that is elaborated upon in Section A.2.2. In the context of an incident and reflected beam, the relevant trigonometric function is given by $\cos(\theta_1) = \frac{w_0}{l} = \frac{w_R}{l}$. For a transmitted beam, on the other hand, the corresponding trigonometric function is $\cos(\theta_2) = \frac{w_T}{l}$. Thus, given the circular nature of the incident and reflected beams in cross-section, the transmitted beam is elliptical due to the refraction angle being

confined to a single axis. Therefore, it is $A_T = \pi \frac{w_T}{2} \frac{w_0}{2}$. Inserting the areas into Equation (A.16), results in the following expression:

$$\begin{aligned} I_0 w_0^2 &= I_R w_0^2 + I_T w_0 w_T, \\ \Longleftrightarrow I_0 \cos(\theta_1) &= I_R \cos(\theta_1) + I_T \cos(\theta_2) \end{aligned}$$

Substituting the previously defined quantity (A.14) into (A.16) yields the following result:

$$n_1 \cos(\theta_1) |\boldsymbol{E}_0|^2 = n_1 \cos(\theta_1) |\boldsymbol{E}_r|^2 + n_2 \cos(\theta_2) |\boldsymbol{E}_t|^2$$

Therefore, the transmission and reflection coefficients, denoted by t and r, respectively, for the reflected E_r and transmitted E_t electric fields, which are defined by $E_r = r\,E_0$ and $E_t = t\,E_0$, are connected to the power-coefficients by the following relations:

$$R = \frac{P_R}{P_0} = \frac{|\boldsymbol{E}_r|^2}{|\boldsymbol{E}_0|^2} = |r|^2, \text{ and } T = \frac{P_T}{P_0} = \frac{n_2}{n_1} \frac{\cos(\theta_2)}{\cos(\theta_1)} \frac{|\boldsymbol{E}_t|^2}{|\boldsymbol{E}_0|^2} = \frac{n_2}{n_1} \frac{\cos(\theta_2)}{\cos(\theta_1)} |t|^2 \tag{A.17}$$

The parameters r and t are complex numbers. In some literature they are defined as reals necessitating a complex phase to describe their effect on the electric field. E_0 is defined as the electric field amplitude of the incident light. The derivation of these coefficients relies on the presentation of the electric fields from the preceding subsection. In this representation, an incident beam propagates at an angle of θ_1 relative to the $z-$axis inside the $xz-$plane. The beam interacts with a smooth surface in the $xy-$plane, as illustrated in Figure A.4. The resulting reflected and transmitted beams are also propagating inside the $xz-$plane under the angles θ_1 and θ_2 to the $z-$axis, respectively. The angle of reflection corresponds to the incident angle. According to the expressions derived earlier, the components of the electric and magnetic field that are parallel to the surface can be expressed as follows:

$$E_{0,\parallel} + E_{r,\parallel} = E_{t,\parallel} \tag{A.18}$$

$$B_{0,\parallel} + B_{r,\parallel} = B_{t,\parallel} \tag{A.19}$$

The left side of the panel in the figure illustrates components in a medium of refractive index n_1, while the right side corresponds to fields in a medium of n_2. The absolute value of the field of wave j is expressed by: $\left|\boldsymbol{B}_j\right| = B_j$ and $\left|\boldsymbol{E}_j\right| = E_j$. To begin with, for pure $s-$polarization, the electric fields are determined by inserting Equation (A.10) into (A.18) to obtain the total electric field $E_0 + E_r = E_t$. The magnetic fields are derived from Equations (A.11) and (A.19), which yield the following relationship:

$$(B_0 - B_r)\cos(\theta_1) = B_t \cos(\theta_2) \tag{A.20}$$

It is important to use the appropriate signs in this equation, as the reflected beam propagates in the opposite direction of the incident and transmitted beams. Substituting Equation (A.2) into (A.20) to convert magnetic to electric fields and expressing E_t by Equation (A.18) results in the following formalism:

$$n_1 E_0 \cos(\theta_1) - n_1 E_r \cos(\theta_1) = n_2 E_0 \cos(\theta_2) + n_2 E_r \cos(\theta_2)$$

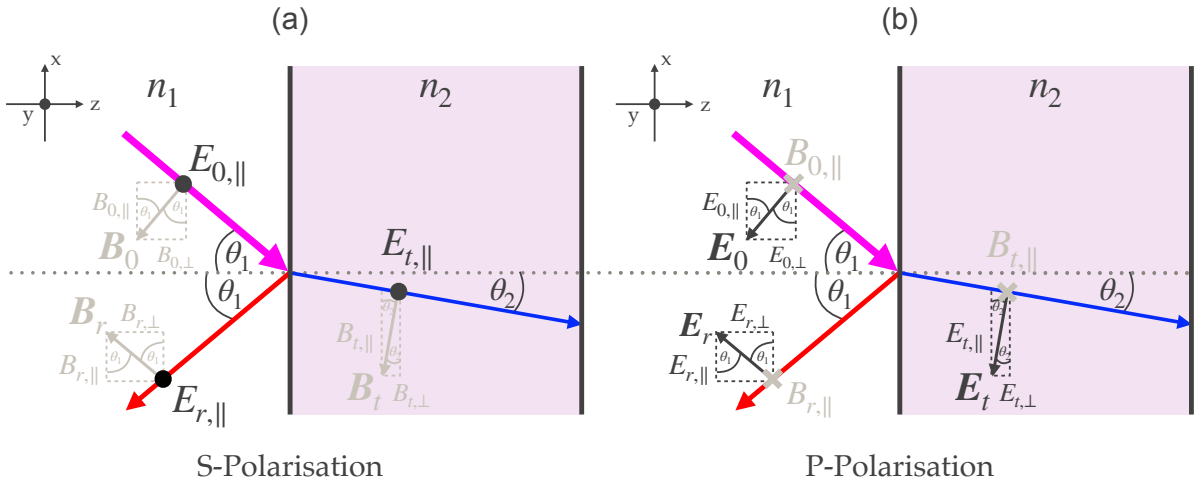


Figure A.4: The phenomenon of reflection and transmission of an EM wave that propagates from one medium to another interacting with a smooth surface. In regard to the plane of reflection, the following polarized electric fields are distinguished: (a) S-polarized electric field, and (b) P-polarized electric field.

Subsequently, the reflection coefficient r_s for $s-$polarized light can be expressed as follows:

$$r_s := \frac{E_r}{E_i} = \frac{n_1\cos(\theta_1) - n_2\cos(\theta_2)}{n_1\cos(\theta_1) + n_2\cos(\theta_2)}. \tag{A.21}$$

Performing the same analyses, yet inserting Equation (A.18) for E_r yields the following equation:

$$n_1 E_0\cos(\theta_1) - n_1(E_t - E_0)\cos(\theta_1) = n_2 E_t\cos(\theta_2)$$

Then, the transmission coefficient t_s for $s-$polarized light is:

$$t_s := \frac{E_t}{E_i} = \frac{2n_1\cos(\theta_1)}{n_2\cos(\theta_2) + n_1\cos(\theta_1)} \tag{A.22}$$

In analogy for pure $p-$polarized light, the formalisms for the electric and magnetic field components are:

$$(E_0 - E_r)\cos(\theta_1) = E_t\cos(\theta_2) \text{ and } B_0 + B_r = B_t$$

This leads to reflection and transmission constants for p-polarization given by

$$r_p := \frac{E_r}{E_i} = \frac{n_1\cos(\theta_2) - n_2\cos(\theta_1)}{n_1\cos(\theta_2) + n_2\cos(\theta_1)}, \text{ and } t_p := \frac{E_t}{E_i} = \frac{2n_1\cos(\theta_1)}{n_1\cos(\theta_2) + n_2\cos(\theta_1)}, \tag{A.23}$$

In this specific instance, these constants are real, thereby enabling the presentation of the absolute value as a square. Then, the total coefficients r and t for the electric fields are derived as follows:

$$r^2 = r_s^2 p_s^2 + r_p^2 p_p^2 \text{ and } t^2 = t_s^2 p_s^2 + t_p^2 p_p^2 \tag{A.24}$$

Therefore, upon combining the Equations in (A.17) and (A.24), the result is:

$$\begin{aligned} R+T &= r^2 + \frac{n_2}{n_1}\frac{\cos(\theta_2)}{\cos(\theta_1)}t^2 \\ &= \underbrace{\left(r_s^2 + \frac{n_2}{n_1}\frac{\cos(\theta_2)}{\cos(\theta_1)}t_s^2\right)}_{=1} p_s^2 + \underbrace{\left(r_p^2 + \frac{n_2}{n_1}\frac{\cos(\theta_2)}{\cos(\theta_1)}t_p^2\right)}_{=1} p_p^2 = p_s^2 + p_p^2 \overset{\text{A.1.1}}{=} 1 \end{aligned}$$

This demonstrates that the intensity is conserved, as indicated by Equation (A.15) that states $R+T = 1$. If light propagates along the z-axis, such that $\theta_1 = 0$, the incident, transmitted, and reflected light are congruent, resulting in $A_0 = A_R = A_T$, $T = \frac{n_2}{n_1}t^2$. The reflection and transmission coefficients for field and intensity, or power, are reduced to the following:

$$\text{Electric field:} \quad r_s = r_p = \frac{n_1 - n_2}{n_1 + n_2} = r \text{ and } t_s = t_p = \frac{2n_1}{n_1 + n_2} = t$$

$$\text{Intensity:} \qquad R = \frac{(n_1 - n_2)^2}{(n_1 + n_2)^2} \text{ and } T = \frac{n_2}{n_1}\frac{4n_1^2}{(n_1 + n_2)^2}$$

In general, when light propagates in medium m and interacts with a surface in medium j, the coefficients can be expressed as follows:

$$r_{mj} \coloneqq r\left(n_m, n_j\right) = \frac{n_m - n_j}{n_m + n_j} = -r\left(n_j, n_m\right) \coloneqq -r_{jm} = r_{jm}e^{i\pi}, \tag{A.25}$$

and

$$t_{mj} \coloneqq t\left(n_m, n_j\right) = \frac{2n_m}{n_m + n_j} = \frac{n_m}{n_j}\frac{2n_j}{n_m + n_j} = \frac{n_m}{n_j}t\left(n_j, n_m\right) \coloneqq \frac{n_m}{n_j}t_{jm}. \tag{A.26}$$

(A.25) shows that a phase jump of π occurs when light propagates in a medium with a lower optical density than that of the reflecting surface. Subsequently, the power coefficients are derived as follows:

$$R_{mj} = r_{mj}^2 = \left(-r_{jm}\right)^2 = R_{jm} \text{ and } T_{mj} = \frac{n_j}{n_m}t_{mj}^2 = \frac{n_m}{n_j}t_{jm}^2 = T_{jm}, \tag{A.27}$$

and

$$R_{mj} + T_{mj} = 1 = r_{mj}^2 + \frac{n_j}{n_m}t_{mj}^2. \tag{A.28}$$

The Equations presented in Equation (A.27) demonstrate that the power coefficients are independent of the direction of travel, thereby allowing for interchangeability of the indices. The coefficients that are identified in this context are considered constant properties of the given layer. They are determined exclusively by the respective refractive properties, which may depend on parameters such as the wavelength of the interacting light.

A.1.4 Layered Insight: The Transfer Matrix Method

The investigation thus far has focused on a single beam propagating from one side. However, the system becomes more complex when incident beams from both sides are considered. This is

illustrated in Figure A.3 (b). For this purpose, the notation undergoes an adjustment to the following form:

$$E_{j\rightarrow} = t_{mj}E_{m\rightarrow} + r_{jm}E_{j\leftarrow}$$
$$E_{m\leftarrow} = t_{jm}E_{j\leftarrow} + r_{mj}E_{m\rightarrow},$$

The parameters m and j represent the respective medium and the arrows $\rightarrow$ and $\leftarrow$ denote the propagation direction of the electric field. The general matrix describing the transformation of the electric field is of form

$$\boldsymbol{M}_{mj} = \begin{pmatrix} M_{11} & M_{12} \\ M_{21} & M_{22} \end{pmatrix},$$

with the coefficients

$$t_{jm} = \frac{1}{M_{22}},\ r_{mj} = -\frac{M_{21}}{M_{22}},\ r_{jm} = \frac{M_{12}}{M_{22}} \text{ and } t_{mj} = \frac{M_{11}M_{22} - M_{12}M_{21}}{M_{22}} = \frac{\det\left(\boldsymbol{M}_{mj}\right)}{M_{22}}. \tag{A.29}$$

Therefore, given the established relationship between the coefficients of a single layer, the system of equations for that layer, describing the change from $\boldsymbol{E}_m$ to $\boldsymbol{E}_j$ is expressed as

$$\boldsymbol{E}_j = \boldsymbol{M}_{mj}\boldsymbol{E}_m = \begin{pmatrix} E_{j\rightarrow} \\ E_{j\leftarrow} \end{pmatrix} = \frac{1}{t_{jm}} \begin{pmatrix} 1 & r_{jm} \\ r_{jm} & 1 \end{pmatrix} \begin{pmatrix} E_{m\rightarrow} \\ E_{m\leftarrow} \end{pmatrix}, \tag{A.30}$$

where the transfer matrix $\boldsymbol{M}_{mj}$, which is exclusively dependent on the surface of interaction, is defined as

$$\boldsymbol{M}_{mj} = \frac{1}{t_{jm}} \begin{pmatrix} 1 & r_{jm} \\ r_{jm} & 1 \end{pmatrix} = \frac{n_m}{n_j}\frac{1}{t_{mj}} \begin{pmatrix} 1 & -r_{mj} \\ -r_{mj} & 1 \end{pmatrix}. \tag{A.31}$$

In this context, the arrangement of the indices is of significance. Specifically, the coefficients that are of the form t_{mj} and r_{mj} are the true coefficients of the matrix of form $\boldsymbol{M}_{mj}$. If the matrix is configured in a manner that results in the main diagonal being equal to 1, the coefficients can be directly interpreted. If this is not feasible, Equation (A.29) must be utilized. Further, the determinant and adjunct properties of the matrix of a single layer are as follows:

$$\det\left(\boldsymbol{M}_{mj}\right) = \frac{n_m}{n_j} \text{ and } \operatorname{adj}\left(\boldsymbol{M}_{mj}\right) = \frac{1}{t_{jm}} \begin{pmatrix} 1 & -r_{jm} \\ -r_{jm} & 1 \end{pmatrix}$$

The inverse of the matrix is

$$\boldsymbol{M^{-1}}_{mj} = \frac{1}{\det\left(\boldsymbol{M}_{mj}\right)} \operatorname{adj}\left(\boldsymbol{M}_{mj}\right) = \frac{n_j}{n_m}\frac{1}{t_{jm}} \begin{pmatrix} 1 & -r_{jm} \\ -r_{jm} & 1 \end{pmatrix} \tag{A.32}$$

$$= \frac{1}{t_{mj}} \begin{pmatrix} 1 & r_{mj} \\ r_{mj} & 1 \end{pmatrix} = \boldsymbol{M}_{jm}. \tag{A.33}$$

When an additional layer is incorporated adjacent to the primary layer, the entire system can be expressed as the product of the individual transfer matrices. Consequently, for any configuration of

N layers, thereby resulting in $N+1$ surfaces of interaction, the total matrix $\boldsymbol{M}_{tot}$ becomes

$$\boldsymbol{M}_{tot} = \prod_{s=0}^{N} \left(\boldsymbol{M}_{mj}(\phi_m)\right)_s .$$

The dependence of ϕ is indicative of the phase of the electric field at the layer subsequent to its transmission through the designated propagation medium. The matrix for this case is derived from

$$\begin{vmatrix} E_{j\rightarrow}e^{i\phi} = t_{mj}E_{m\rightarrow}e^{i\phi} + r_{jm}E_{j\leftarrow}e^{-i\phi} \\ E_{m\leftarrow}e^{-i\phi} = t_{jm}E_{j\leftarrow}e^{-i\phi} + r_{mj}E_{m\rightarrow}e^{i\phi} \end{vmatrix},$$

where the phase is added for light that propagates from left to right and subtracted for light traveling from right to left. The final transfer matrix is expressed as follows:

$$\boldsymbol{M}_{mj}(\phi) = \frac{n_m}{n_j}\frac{1}{t_{mj}} \begin{pmatrix} 1 & -r_{mj}e^{-2i\phi} \\ -r_{mj}e^{2i\phi} & 1 \end{pmatrix}$$

In the case that the phase is equal to a multiple of π, indicated by an integer b, this expression is equivalent to the standard transfer matrix, as outlined in Equation (A.31). If the phase is a multiple of $\frac{\pi}{2}$, it can be expressed as an index-exchanged matrix with a pre-factor that is proportional to the ratio of the refractive indices. Both cases are demonstrated in the following equations:

$$\boldsymbol{M}_{mj}(b\pi) = \frac{1}{t_{jm}} \begin{pmatrix} 1 & r_{jm} \\ r_{jm} & 1 \end{pmatrix} = M_{mj}(0), \tag{A.34}$$

and

$$\boldsymbol{M}_{mj}\left(b\frac{\pi}{2}\right) = \frac{n_m}{n_j}\frac{1}{t_{mj}} \begin{pmatrix} 1 & r_{mj} \\ r_{mj} & 1 \end{pmatrix} = \frac{n_m}{n_j} M_{jm}(0). \tag{A.35}$$

This presentation provides a foundation for comprehending more intricate configurations of reflective surfaces, including dielectric mirrors and resonators, which will be addressed in the following section.

A.1.5 Mirrors of Light: The Physics of Dielectric Coatings

State-of-the-art frequency stabilization is commonly achieved by employing standing wave FP-type resonators, which essentially consist of two high-reflectivity mirrors positioned at a distance L from each other. Examples of such mirrors include dielectric and crystalline models. In this thesis, exclusively dielectric mirrors are treated. They consist of a substrate, which serves as the foundation, and a dielectric coating, which achieves ultra-high reflectivity.

Typically, the light enters from an ambient medium, such as air or a vacuum, of refractive index n_0 towards a layer of high refractive index n_1. Subsequently, the wave propagates through multiple layers of alternating refractive indices, n_1 and n_2, where n_2 exhibits a smaller refractive index than n_1, as illustrated in Figure A.5. Thereafter, it penetrates the substrate medium, n_3, from a layer of medium n_2. The surfaces between the layers exhibit nearly-perfect parallelism. As illustrated in the figure, the light is depicted as propagating at an angle to illustrate the effects.

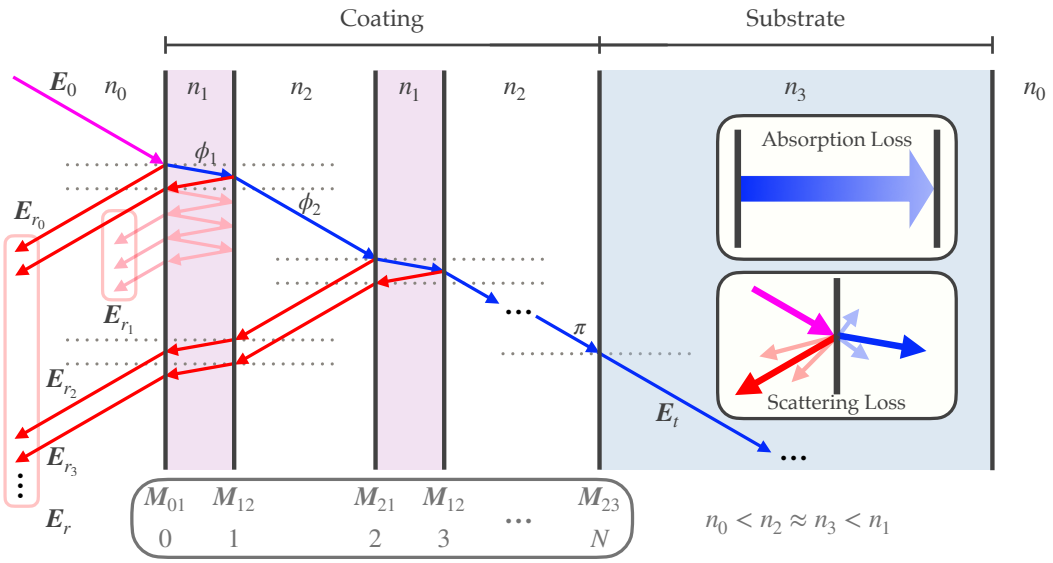


Figure A.5: Schematic representation of a dielectric mirror, including the first two alternating layers of the coating. This schematic visually illustrates the constructive interference of light as it travels different paths. The role of the incident angle is to enhance visual clarity. The magenta line represents the incident beam, red and blue are the components constituting the reflected, and transmitted beams respectively.

However, for the purpose of the calculation and in idealized reality, light is emitted perpendicular to the surface. The arrangement of the coated layers can be conceptualized as a single mirror with an incident light E_0 and a reflected part E_r into the incident medium, as well as a transmitted part E_t into the substrate. The thickness of each layer is determined by the design wavelength. This configuration comprises $N+1$ surfaces, with a total of N layers of coating. The design is such that N is even, and there are $\frac{N}{2}$ layers of each medium. The total reflected field, E_r, is the sum of a manifold of individual reflections and can be expressed as follows:

$$E_r(N) = \sum_{m=0}^{N} E_{r_N}$$

In the context of a single layer of refractive index n_1 separating mediums n_0 and n_2, the total reflected field can be formulated as the sum of the partial beams $E_r(N=1) = E_{r_0} + E_{r_1}$. Therefore, for the part reflected at the first surface, it can be shown that

$$E_{r_0} = r_{01}E_0 = r_{10}e^{i\pi}E_0. \tag{A.36}$$

In this equation, the reflection coefficient is written in the form that the index of the higher refracting medium comes first. In this manner, the sign is positive, thereby simplifying its addition to the other beams. Consequently, the phase shift of π becomes discernible. The electric field components in E_{r_1} are more complex due to the reflection of light within the medium by both surfaces. At each incidence of reflection at the surface towards medium zero, a portion of the transmitted light is added to the total reflected light. This is analogous to the concept of a resonator, as will be

demonstrated further on. The summation of the electric fields is expressed as follows:

$$\begin{aligned} E_{r_1} &= t_{01}r_{12}t_{10}e^{2i\phi_1}E_0 + t_{01}r_{12}r_{10}r_{12}t_{10}e^{4i\phi_1} + \dots \\ &= \frac{1-r_{10}^2}{r_{10}}E_0\left(\sum_{m=0}^{\infty}\left(r_{10}r_{12}e^{2i\phi_1}\right)^m - 1\right) \\ &= \left(1-r_{10}^2\right)\frac{r_{12}e^{2i\phi_1}}{1-r_{10}r_{12}e^{2i\phi_1}}E_0 \end{aligned} \tag{A.37}$$

The final row of the equation presents the geometric series, which can be solved by the identity,

$$\sum_{m=0}^{\infty} q^m = \frac{1}{1-q}.$$

The round trip factor inside medium one is given by $q = r_{10}r_{12}e^{2i\phi_1}$, where each subsequent beam is reflected once at medium zero and once at medium two. This results in an optical path length (OL) phase that is twice the single-path length phase ϕ_1 inside medium one. A dielectric mirror, also known as a Bragg mirror, is a device designed to enhance reflectivity, thereby increasing the intensity and electric field amplitude of the total reflected light. The objective is to maximize the ratio of reflected light to the incident light

$$\frac{P_r}{P_0} = \frac{|E_r|^2}{|E_0|^2},$$

to achieve optimal performance. In the context of a single layer, it is maximized with respect to ϕ_1 by calculating:

$$\frac{1}{|E_0|^2}\frac{d}{d\phi_1}\left(|E_r(N=1,\phi_1)|^2\right) \stackrel{!}{=} 0 \Longleftrightarrow \sin(2\phi_1)\left(1+2r_{10}^2r_{12}^2-r_{12}^2\right) \stackrel{!}{=} 0 \tag{A.38}$$

In accordance with the prevailing definition, the value of r_{mj} is constrained by the interval $0 \leq r_{mj}^2 \leq 1$. In the scenario where the sine term is not equal to zero, it is necessary to satisfy the equation

$$r_{10}^2 = -\frac{r_{12}^2+1}{2r_{12}^2}. \tag{A.39}$$

However, this is incompatible with the requirement that the left side of Equation (A.39) be zero or positive, because the right side will always be negative. Therefore, it can be concluded that the sine term in Equation (A.38) must be equal to zero. The following identity can then be derived for the phase ϕ_1:

$$2\phi_1 = \pi b \Longleftrightarrow \phi_1 = \frac{\pi b}{2}$$

Here, $b \in \mathbb{Z}$ is an integer number. In order to understand whether a maximum or minimum occurs, it is necessary to calculate the second derivative. It follows

$$\frac{1}{|E_0|^2}\frac{d^2}{d^2\phi_1}\left(|E_r\left(N=1,\phi_1\right)|^2\right)\Big|_{\phi_1=\frac{\pi b}{2}} \begin{cases} >0 & \text{even } b \\ <0 & \text{odd } b \end{cases},$$

which demonstrates that a maximum occurs if b is odd. Assuming the premise that light travels the shortest possible distance, the smallest reasonable number is $b = 1$. This ultimately leads to the phase relationship of $\phi_1 = \frac{\pi}{2}$. To elaborate, the light that is reflected once at the interface between mediums one and two will undergo a phase shift of π with respect to the incident light E_0. However, the light reflected at the first surface also experiences this phase shift due to the reflection coefficient, meaning that both beams will positively interfere. Consequently, each subsequent beam in the chain would undergo an alternating sequence of destructive and constructive interference, as each beam would individually experience an additional shift in the phase of π. The phase can be presented as a relation between the wavelength λ, and the OL. The OL is determined by the refractive index and the thickness d_1 of the coating layer:

$$\phi_1 = 2\pi\frac{n_1 d_1}{\lambda} \Longleftrightarrow \underbrace{n_1 d_1}_{\text{OL}} = \frac{\lambda}{4}$$

Consequently, when light traverses the medium of n_1, it undergoes a shift that is equivalent to one-quarter of its wavelength. This same analysis can be applied to the subsequent layer of medium two. This process yields

$$\begin{aligned} E_{r_2} &= t_{01}t_{12}r_{21}t_{21}t_{10}e^{2i(\phi_1+\phi_2)}E_0 + t_{01}t_{12}r_{21}r_{21}r_{21}t_{21}t_{10}e^{2i(\phi_1+2\phi_2)}E_0 + \ldots \\ &= \frac{n_0 n_2}{n_1^2}t_{10}^2 t_{12}^2 r_{21}e^{2i(\phi_1+\phi_2)}\sum_{m=0}^{\infty}\left(r_{21}^2 e^{2i\phi_2}\right)^m E_0 + O \\ &= \left(1-r_{10}^2\right)\frac{\left(1-r_{12}^2\right)r_{12}e^{2i\phi_2}}{1-r_{12}^2e^{2i\phi_2}}\underbrace{e^{2i\phi_1+i\pi}}_{=1} + O. \end{aligned}$$

In this context, the symbol O denotes the beams that are reflecting again within medium one, thereby generating a formalism analogous to Equation (A.37). Furthermore, the beams that are reflected at the interface between mediums one and two partially enter medium two again, thereby contributing to the complexity of the cascade. Nevertheless, the main beam in E_{r_2} is of the same form as E_{r_1}, yielding the following result:

$$\phi_2 = 2\pi\frac{n_2 d_2}{\lambda} \Longleftrightarrow n_2 d_2 = \frac{\lambda}{4}$$

The relationship between the OLs within medium one and two is then expressed as:

$$n_1 d_1 = n_2 d_2 = \frac{\lambda}{4} \text{ and } \phi_1 = \phi_2 = \frac{\pi}{2}$$

The second layer, therefore, introduces an additional phase shift of π to the beam, resulting in a net phase shift of 3π to the initial beam due to the phase "flip" that occurs at the interface between mediums two and one. Hence, all three beams—the incident beam, the first beam reflected in medium one, and the first beam reflected in medium two—are interfering constructively. Pursuing this approach would, in principle, generate a formalism for the total reflected field. However, the complexity of the method increases exponentially with each layer. An elegant alternative is provided by the transfer matrices. Under the assumption that all layers are considered as a single entity, the incident field E_0, the total reflected field E_r, and the total transmitted field E_t are predicted to align with the values indicated in Equation (A.30), given by

$$\begin{pmatrix} E_t \\ 0 \end{pmatrix} = \prod_{s=0}^{N} \left(\boldsymbol{M}_{mj}(\phi)\right)_s \begin{pmatrix} E_0 \\ E_r \end{pmatrix}.$$

Given the absence of incident light from the side of the substrate, the total matrix $\boldsymbol{M}_C$ of form

$$\boldsymbol{M}_C = -\frac{n_3}{n_0}\frac{1}{t_c}\begin{pmatrix} 1 & -r_c \\ -r_c & 1 \end{pmatrix},$$

will consequently yield the reflection and transmission coefficients, denoted as r_c and t_c, respectively, for the coating. The expansion of the matrix will result in the presence of multiple phase factors, depending on the medium through which the light propagates. The initial matrix will function as the reference, and consequently, it will not comprise a phase due to the propagation length. The light will travel $\frac{N}{2}$ times from medium one to medium two, including phase ϕ_1, and $\frac{N}{2}-1$ times from medium two to medium one, including phase ϕ_2. The latter occurs once less due to the fact that the ultimate interaction happens between a layer of medium two and the substrate, which is medium three. The transfer matrix for the coating is therefore

$$\begin{aligned}
\boldsymbol{M}_C &= \boldsymbol{M}_N(\phi_N)\boldsymbol{M}_{N-1}(\phi_{N-1})\ldots\boldsymbol{M}_0(\phi_0) \\
&= \boldsymbol{M}_{23}(\pi)\left(\boldsymbol{M}_{12}\left(\frac{\pi}{2}\right)\right)^{\frac{N}{2}}\left(\boldsymbol{M}_{21}(\pi)\right)^{\frac{N}{2}-1}\boldsymbol{M}_{01}(0) \\
&= \boldsymbol{M}_{23}\left(\frac{n_1}{n_2}\boldsymbol{M}_{21}\right)^{\frac{N}{2}}\left(\boldsymbol{M}_{21}\right)^{\frac{N}{2}-1}\boldsymbol{M}_{01}.
\end{aligned}$$

Accordingly, employing Equation (A.31) and inserting the values for the phases results in:

$$\boldsymbol{M}_C = \boldsymbol{M}_{23}\left(\frac{n_1}{n_2}\right)^{\frac{N}{2}}\left(\boldsymbol{M}_{21}\right)^{N-1}\boldsymbol{M}_{01}$$

Performing the extensive calculus, the total matrix $\boldsymbol{M}_{21}$ for the layers of medium one and two is given by the expression:

$$\left(\frac{n_1}{n_2}\right)^{\frac{N}{2}}\left(\boldsymbol{M}_{21}\right)^{N-1} = \left(\frac{n_1}{n_2}\right)^{\frac{N}{2}}\frac{n_1^{N-1}+n_2^{N-1}}{2n_1^{N-1}}\begin{pmatrix} 1 & \frac{n_1^{N-1}-n_2^{N-1}}{n_1^{N-1}+n_2^{N-1}} \\ \frac{n_1^{N-1}-n_2^{N-1}}{n_1^{N-1}+n_2^{N-1}} & 1 \end{pmatrix}$$

Following the incorporation of the initial and final surfaces of interaction, the resulting total matrix for the coating is expressed as

$$\boldsymbol{M}_C = \frac{n_0}{n_3}\frac{n_3 n_1^N + n_0 n_2^N}{2n_0 (n_1 n_2)^{\frac{N}{2}}}\begin{pmatrix} 1 & -\frac{n_0 n_2^N - n_3 n_1^N}{n_3 n_1^N + n_0 n_2^N} \\ -\frac{n_0 n_2^N - n_3 n_1^N}{n_3 n_1^N + n_0 n_2^N} & 1 \end{pmatrix}.$$

This results in the total reflection and transmission coefficients from medium one to medium three through all layers being

$$r_c = \frac{n_0 n_2^N - n_3 n_1^N}{n_3 n_1^N + n_0 n_2^N} \text{ and } t_c = \frac{2n_0 (n_1 n_2)^{\frac{N}{2}}}{n_3 n_1^N + n_0 n_2^N}.$$

The sum of the total (Fresnel) power-coefficients is once again equivalent to one, as evidenced by $R_c + T_c = r_c^2 + \frac{n_3}{n_0} t_c^2 = 1$. In the final step of the system's construction as a mirror $\boldsymbol{M}_M$, the substrate material must be incorporated by multiplying its matrix, $\boldsymbol{M}_S = \boldsymbol{M}_{30}$, to the coating:

$$\boldsymbol{M}_M = \boldsymbol{M}_S \boldsymbol{M}_C = \underbrace{\frac{n_0}{n_0}\frac{n_3 n_1^N + n_3 n_2^N}{2n_3 (n_1 n_2)^{\frac{N}{2}}}}_{1/t_m}\begin{pmatrix} 1 & \underbrace{-\frac{n_0 n_3 n_2^N - n_0 n_3 n_1^N}{n_0 n_3 n_1^N + n_0 n_3 n_2^N}}_{r_m} \\ -\frac{n_0 n_3 n_2^N - n_0 n_3 n_1^N}{n_0 n_3 n_1^N + n_0 n_3 n_2^N} & 1 \end{pmatrix}$$

In this particular use case, given that the incident and final medium are the same, the power transmission coefficient is simplified such that

$$R_m + T_m = r_m^2 + t_m^2 = 1.$$

This is also evident in the determinant, which is expressed as $\det(M_M) = 1$. The enhancement factor of this setup can be understood by examining a real-life example. In particular, for a wavelength of 1.5 µm, a configuration may comprise a fused-silica (FS) (SiO_2) substrate with a refractive index of $n_3 = 1.4446$ [224, 225], silicon dioxide or quartz glass (SiO_2), chemically identical to FS, with a refractive index of $n_2 = 1.4446$ [224, 225], and titanium dioxide (TiO_2) with a refractive index of $n_1 = 2.0576$ [226]. Assuming that light travels inside a vacuum with $n_0 = 1$ and that there are $N = 24$ layers, the reflectivity would already reach 99.94 with a total coating thickness of 5.3 µm. In this instance as well, it is evident that the substrate and medium two exhibit a high degree of similarity in their respective refractive indices.

In comparison, the individual reflectivities are $R_{12} = 6.7\,\%$, $R_{23} = 0\,\%$ and $R_{03} = 3.3\,\%$, thereby emphasizing the substantial enhancement in total reflectivity. These coatings are typically broadband, which can be measured by the wavelength-dependent refractive index. This property ensures that the coatings maintain a high level of reflectivity, even if the actual wavelength is several 10 nm away from the designed wavelength. The refractive indices were obtained from the refractive index database [227], which summarizes and displays the results of research and, in some instances, includes numerical data provided by the authors of books and publications. The corresponding works that the database utilizes are cited after the respective refractive index. In this particular

context, the configuration of a mirror for 1.5 µm was selected, as it is, next to 1064 nm, one of the two predominant wavelengths that are examined in this thesis. Additionally, it is considered to be one of the fundamental wavelengths in the domain of optical telecommunications and is widely recognized as an industrial standard.

A.1.6 Light Trapped in Time: Standing Wave Resonators

The content of this section now appears in the main thesis text (Section 2.1.1) as it forms a critical part of the theoretical framework. This note serves as a placeholder for its original appendix location.

A.1.7 Imperfect Realities: Understanding Optical Losses

The content of this section now appears in the main thesis text (Section 2.1.2) as it forms a critical part of the theoretical framework. This note serves as a placeholder for its original appendix location.

A.2 Gaussian Optics: Beams, Fibers, and Cavities

As previously discussed, resonators function as instruments employed for the confinement of light of distinct frequencies. Frequency stabilization is achieved through the utilization of the resonator's modes as a reference point. However, a prerequisite for understanding this is a more thorough discussion of the spatial geometry of light. This is of particular importance in the laboratory setting, where it plays a critical role in guiding light in either free space or within waveguides, such as optical fibers. The ensuing subsection aims to describe the Gaussian beam (GB), employing both visual and mathematical methodologies. This section will also demonstrate how this spatial geometry influences the design process of a resonator. An additional set of modes is introduced, with reference not to frequency but to spatial profile. Moreover, within the present scope, the incorporation of fibers into this section as a flexible medium for light propagation is a pragmatic approach, as they are described based on the identical mathematical framework. The following textbooks provide comprehensive analyses of the subject: [228, 229, 230, 231, 232]. Note that in this section, r will be employed to describe a spatial coordinate, R is used for a radius, f is used for focal lengths, and in the context of modes n is an enumerating integer.

A.2.1 Intensity in Focus: Transverse Profiles and the Helmholtz Equation

Until this point in the work, EM waves were considered to be planar, with a homogeneously infinite propagation rate in space. In reality, particularly in the case of lasers, the intensity of the light is tightly focused. Assuming the propagation axis to be z, the light can be regarded as exhibiting circular symmetry in the transverse ($xy-$plane) direction. This is frequently posited as a model by linear rays and is employed in classical geometrical optics. However, a more natural approximation would be for the electric field to follow a Gaussian distribution, with a maximum amplitude at the center and a gradual decline towards the edges. Therefore, the wave remains virtually present throughout space, although the majority of its energy is confined to a finite area of radius w. This

radius is defined such that the intensity $I(w)$ of the light at the edges is equivalent to $\frac{I(w)}{I_c} = e^{-2}$ of the amplitude I_c in the center. The total expression for the intensity is thus

$$I(r) = I_c e^{-2\frac{r^2}{w^2}},$$

with $r^2 = x^2 + y^2$ describing the transverse profile. Elliptical profiles constitute a significant aspect of GBs; nevertheless, for the sake of simplicity, the circular shape is employed hereinafter. To calculate the total power, P, integration over the entire transverse area, A, is necessary, resulting in

$$P = I_c \int_A e^{-2\frac{r^2}{w^2}} dA = I_c \int_0^\infty \int_0^{2\pi} r e^{-2\frac{r^2}{w^2}} dr\, d\varphi = \frac{\pi}{2} w^2 I_c. \tag{A.40}$$

This will provide a comprehensive formalism for the transverse intensity of the light at a specific point along its propagation axis in either polar (r, φ) or Cartesian (x, y) coordinates, based on

$$I(r) = P \frac{2}{\pi w(z)^2} e^{-2\frac{r^2}{w(z)^2}}.$$

The following calculations were derived using the Cartesian system. The beam radius, $w(z)$ is considered as a function of the direction of propagation, z. This will become clear in the further below. Then, substituting $P = \frac{\pi}{2} w_0^2 I_0$ due to power conservation, if w_0 and I_0 are the respective beam waist and intensity at $z = 0$, the formalism becomes

$$I(x, y, z) = I_0 \frac{w_0^2}{w(z)^2} e^{-2\frac{x^2+y^2}{w(z)^2}}.$$

The starting point along z is not specified in the given formula and is set to zero for the sake of clarity and convenience in the subsequent calculus. In a more general context, the offset value z_0 can be set at a later point. This method further suggests that $I_c(z)$ is also a function of z. However, it is important that this does not interfere with the calculation performed in Equation (A.40). It is still assumed that the beam preferably propagates in a specified direction, namely the $z-$axis. Thus, the electric field is given by

$$\boldsymbol{E}(x, y, z) = E_0 \hat{\boldsymbol{p}} \frac{w_0}{w(z)} e^{-\frac{x^2+y^2}{w(z)^2}} e^{i\phi(x,y,z)} e^{-ikz}, \tag{A.41}$$

with

$$I_0 = \frac{1}{2} c_0 \varepsilon_0 |E_0|^2.$$

The electric field is, in essence, the complex square root of the intensity, with a degree of freedom resulting in a phase ϕ, which vanishes when the absolute value is calculated. The subsequent derivations will yield the actual formalisms for $w(z)$ and ϕ. These formalisms will result in a well-known and applicable approximation of EM waves, which is necessary to describe a manifold of processes. It is a prerequisite for an EM wave to satisfy the wave equation (Section A.1.1) in order to be considered a valid solution. This is a consequence of the fundamental laws of electromagnetism, which are shown in Section A.1.2 through the Maxwell equations. The wave equation is derived as follows: According to Faraday's law, as expressed in Equation (A.6), the application of

the rotational operator to both sides of the equation yields a result of

$$\nabla \times (\nabla \times \boldsymbol{E}) = \nabla \times \left(-\frac{\partial}{\partial t} \boldsymbol{B} \right). \tag{A.42}$$

The equation can be solved on both sides. Beginning on the left-hand side, the equation can be simplified by utilizing a property of the nabla operator. Consequently, Gauss's law for electric fields, as presented in Equation (A.4), is incorporated, resulting in the following equation:

$$\text{l.h.s of (A.42)} = \nabla \times (\nabla \times \boldsymbol{E}) = \nabla (\nabla \cdot \boldsymbol{E}) - \nabla^2 \boldsymbol{E} = \nabla \frac{\rho}{\varepsilon_0} - \nabla^2 \boldsymbol{E}$$

On the right-hand side, the time derivative and space-dependent nabla operator are interchanged, and Amperes' law from Equation (A.7) is applied:

$$\text{r.h.s of (A.42)} = \nabla \times \left(-\frac{\partial}{\partial t} \boldsymbol{B} \right) = -\frac{\partial}{\partial t} (\nabla \times \boldsymbol{B}) = -\mu_0 \frac{\partial}{\partial t} \left(\boldsymbol{J} + \varepsilon_0 \frac{\partial}{\partial t} \boldsymbol{E} \right).$$

Eventually, through the usage of nearly all Maxwell equations, the wave equation is derived:

$$\left(-\nabla \frac{\rho}{\varepsilon_0} - \mu_0 \frac{\partial}{\partial t} \boldsymbol{J} \right) + \nabla^2 \boldsymbol{E} - \mu_0 \varepsilon_0 \frac{\partial^2}{\partial t^2} \boldsymbol{E} = 0$$

In the context of a wave propagating in a vacuum or any dielectric medium, the terms within the parentheses are shown to vanish, given the absence of fluctuating charges and, consequently, currents. The result of this calculation will be the standard form of the wave equation given by

$$\nabla^2 \boldsymbol{E} - \frac{1}{c_0^2} \frac{\partial^2}{\partial t^2} \boldsymbol{E} = 0. \tag{A.43}$$

In particular, for a wave with a specified propagating direction, the electric field may be described as the combination of a classical planar wave and a space-dependent form factor, $u(\boldsymbol{r})$, given by

$$\boldsymbol{E} = u(\boldsymbol{r}) E_0 \hat{\boldsymbol{p}} e^{-i(\boldsymbol{k}\boldsymbol{r} + \omega t)}. \tag{A.44}$$

The time derivative leads to a factor of ω^2, with the property $\omega = k\,c$, k being the wavenumber and c the speed of light. As the final expressions become more extensive, indices for propagation medium are excluded. The wave equation is modified to the following form:

$$\left(\nabla^2 + k^2 \right) \boldsymbol{E}(\boldsymbol{r}) = 0 \tag{A.45}$$

This equation is known as the Helmholtz equation. Inserting Equation (A.44) into the Helmholtz equation, finally simplifies to

$$\nabla^2 u(\boldsymbol{r}) - 2ik \frac{\partial}{\partial z} u(\boldsymbol{r}) = 0.$$

The function $u(\boldsymbol{r})$ adds a layer of complexity to the system that is necessary to describe waves that are not completely planar. In fact, assuming that the ray changes slowly along its propagation axis, so that the beam radius $w(z)$ changes slowly, its curvature is small. Mathematically, it is

approximated by

$$\left|\frac{\partial^2}{\partial z^2}u(\boldsymbol{r})\right| \ll 2ik\left|\frac{\partial}{\partial z}u(\boldsymbol{r})\right|.$$

The GB becomes a candidate for a solution of the system. This approach is called the slowly varying envelope approximation and leads to the paraxial Helmholtz equation

$$\nabla_\perp^2 u(\boldsymbol{r}) - 2ik\frac{\partial}{\partial z}u(\boldsymbol{r}) = 0.$$

In this context, the transverse Laplacian is defined as $\nabla_\perp^2 = \frac{\partial^2}{\partial x^2} + \frac{\partial^2}{\partial y^2}$. Assuming the GB formalism of Equation (A.41), which still essentially describes a light "tube", the form function u is

$$u(x,y,z) = \sqrt{\frac{2}{\pi}}\frac{1}{w(z)}e^{-\frac{x^2+y^2}{w(z)^2}}e^{i\phi(x,y,z)}. \tag{A.46}$$

As written here, this system describes semi-planar waves. In the case of $\frac{\partial}{\partial z}w(z) = 0$, they are essentially perfect plane waves in a pure cylinder, since there is no spatial dependence on z that can lead to a curvature of the wavefront. However, this special case is not accurate enough to solve for the phase factor $\phi(\boldsymbol{r})$. It can be obtained by inserting Equation (A.46) into the paraxial Helmholtz equation. Following the mathematical steps, the following expression remains:

$$\begin{aligned} i\frac{\partial^2\phi}{\partial x^2} + i\frac{\partial^2\phi}{\partial y^2} - \left(\frac{\partial\phi}{\partial x}\right)^2 - \left(\frac{\partial\phi}{\partial y}\right)^2 - \frac{4i}{w^2}\left(x\frac{\partial\phi}{\partial x} + y\frac{\partial\phi}{\partial y}\right) \\ +4\frac{x^2+y^2}{w^4} - \frac{4}{w^2} - 4ik\frac{\partial w}{\partial z}\frac{x^2+y^2}{w^3} + 2k\frac{\partial\phi}{\partial z} + \frac{2ik}{w}\frac{\partial w}{\partial z} = 0. \end{aligned}$$

In this context, the condition that the equation be equal to zero is equivalent to the requirement that both the imaginary and real parts vanish independently of each other. This is due to the fact that $\phi, w, k \in \mathbb{R}$. This condition can be expressed in the form of a system of two equations, given by

$$\left|\begin{array}{ll} i\frac{\partial^2\phi}{\partial x^2} + i\frac{\partial^2\phi}{\partial y^2} - \frac{4i}{w^2}\left(x\frac{\partial\phi}{\partial x} + y\frac{\partial\phi}{\partial y}\right) - 4ik\frac{\partial w}{\partial z}\frac{x^2+y^2}{w^3} + \frac{2ik}{w}\frac{\partial w}{\partial z} = 0 & (a) \\ -\left(\frac{\partial\phi}{\partial x}\right)^2 - \left(\frac{\partial\phi}{\partial y}\right)^2 + 4\frac{x^2+y^2}{w^4} - \frac{4}{w^2} + 2k\frac{\partial\phi}{\partial z} = 0 & (b) \end{array}\right|. \tag{A.47}$$

Upon rearranging the initial line, (a), the equation can be further subdivided into two distinct equations (a_1) and (a_2). This is motivated by the reasonable assumption that $\phi \propto r^2$, a combination of comparison of the terms and an educated guess. From this assumption it can be deduced that $\frac{\partial^2\phi}{\partial x^2} = const.$ and $x\frac{\partial\phi}{\partial x} \propto x^2$. The new set of equations becomes

$$(a) \rightarrow \left|\begin{array}{ll} \frac{\partial^2\phi}{\partial x^2} + \frac{\partial^2\phi}{\partial y^2} = -\frac{2k}{w}\frac{\partial w}{\partial z} & (a_1) \\ x\frac{\partial\phi}{\partial x} + y\frac{\partial\phi}{\partial y} = -k\frac{\partial w}{\partial z}\frac{x^2+y^2}{w} & (a_2) \end{array}\right|. \tag{A.48}$$

Given the symmetry of the intensity profile in the transverse coordinates, it is reasonable to infer that the phase profile also exhibits this symmetry. Subsequently, Equation (A.48) results in the

following conditions for the phase:

$$\phi = -\frac{1}{2}\frac{k}{w}\frac{\partial w}{\partial z}x^2 + C_{yz}, \text{ and } \phi = -\frac{1}{2}\frac{k}{w}\frac{\partial w}{\partial z}y^2 + C_{xz} \tag{A.49}$$

The constants C_{jk} are defined through $\frac{d}{dl}C_{jk} = 0$. In this equation, l, j, and k represent any combination of the coordinates x, y, and z. These formalisms also fulfill Equation (A.48) (a_2), agreeing with the assumptions for the time being. Inserting the formulas in Equation (A.49) for the transverse derivatives in Equation (A.47) (b), solving for ϕ gives the expression:

$$\phi = -\left(x^2 + y^2\right)\int\left(\frac{2}{kw^4} - \frac{k}{2w^2}\left(\frac{\partial w}{\partial z}\right)^2\right)dz + \int\frac{2}{kw^2}dz + C_{xy} \tag{A.50}$$

An examination of the formalisms in A.49 reveals the absence of any transverse proportionalities that are independent of the variable z, thereby ensuring that C_{xy} is zero. This conclusion is substantiated by the already complete nature of the z dependences in Equation (A.50). As a result, Equation (A.50) is indeed complete in all three coordinates. A comparison of the three equations reveals the following relationship:

$$\int\left(\frac{2}{kw^4} - \frac{k}{2w^2}\left(\frac{\partial w}{\partial z}\right)^2\right)dz = \frac{1}{2}\frac{k}{w}\frac{\partial w}{\partial z}$$

When integrated over z, this relationship becomes:

$$\frac{2}{kw^4} - \frac{k}{2w^2}\left(\frac{\partial w}{\partial z}\right)^2 = \frac{k}{2}\frac{\partial}{\partial z}\left(\frac{1}{w}\right)\frac{\partial w}{\partial z} + \frac{k}{2}\frac{1}{w}\frac{\partial^2 w}{\partial z^2} \tag{A.51}$$

Equation (A.51) is a complex differential equation. The solution of this can be derived to

$$w(z) = w_0\sqrt{1 + \left(\frac{z}{z_r}\right)^2}, \tag{A.52}$$

The parameter w_0 denotes the beam waist at $z = 0$, and z_r is a degree of freedom that is fixed by inserting this solution into the differential equation given by

$$\frac{2}{kw^4} - \frac{k}{2w^2}\left(\frac{w_0^2 z}{z_r^2 w}\right)^2 = -\frac{k}{2}\frac{z w_0^2}{z_r^2 w^3}\frac{w_0^2 z}{z_r^2 w} + \frac{k}{2}\frac{1}{w}\left(\frac{w_0^2}{z_r^2 w} - \frac{w_0^4 z^2}{z_r^4 w^3}\right) \Longleftrightarrow z_r = \frac{k w_0^2}{2}.$$

Eventually, the phase is fully derived and can be expressed as

$$\phi = -\frac{k\left(x^2 + y^2\right)}{2R(z)} - \psi(z). \tag{A.53}$$

The function $R(z)$ is defined by

$$R(z) = w(z)\left(\frac{\partial w(z)}{\partial z}\right)^{-1} = z\left(1 + \frac{z_r^2}{z^2}\right), \tag{A.54}$$

and the z dependent phase term $\psi(z)$ is given by

$$\psi(z) = \arctan\left(\frac{z}{z_r}\right). \tag{A.55}$$

The final complete solution for the electric field of a beam with a Gaussian transverse beam shape is thus obtained by inserting the phase term in Equation (A.53) into Equation (A.41):

$$\boldsymbol{E}_{00}(x,y,z) = A_{00}\hat{\boldsymbol{p}}\frac{w_0}{w(z)}e^{-\frac{x^2+y^2}{w(z)^2}}e^{-i\frac{k\left(x^2+y^2\right)}{2R(z)}}e^{i\psi(z)}e^{-ikz} \tag{A.56}$$

This describes the simplest transverse electromagnetic (TEM_{00}) mode, wherein the indices "00" denote the transverse beam shape. In this particular instance, the beam shape is a single circle or ellipse. The amplitude of the electric field is now given by the factor A_{00}, which must not be confused with the total electric field $\boldsymbol{E}_{00}$. Those formalisms, which are derived entirely from mathematics, possess a profound physical significance:

The beam is characterized by a minimum beam waist, w_0, which gradually increases along the propagation axis in both directions. This phenomenon can be attributed to the diffraction of light. Huygen's law for elementary spherical waves in a double or single slit experiment can be employed to provide a visual explanation, which is illustrated schematically in Figure A.6. In this configuration, two coherent elemental waves of the same wavelength and phase are positioned at a distance of $2w_0$ on the $x-$axis. The propagating axis $z-$exhibits a symmetrical location at the centered between the EM waves. In the event that the OL difference between the sources S_1 and S_2 is equivalent to an integer multiple of the wavelength λ, the waves will interfere in a constructive manner. In this particular instance, the first orders of constructive interference are indicated by the magenta lines that connect the intersections of wavefronts between S_1 and S_2. The magenta lines form hyperbolas with both its foci at the origins of the elemental waves. The difference Δr in distance between the optical paths r_1 and r_2 is given by $|\Delta r| = r_2 - r_1 = \lambda$. This will conclude in the formalism of a hyperbola given by

$$\frac{x^2}{a} - \frac{z^2}{b} = 1 \overset{GB}{\equiv} \frac{w(z)^2}{w_0} - \frac{z^2}{z_r}. \tag{A.57}$$

In this formalism, a denotes the distance of the vertex of the hyperbola to the center of the coordinate system, which is equivalent to the beam waist parameter w_0 of the Gaussian beam. The parameter b is the distance between the vertex and the asymptotes of the hyperbola wings for large distances. This is, not merely by a coincidence, the same length z_r that was previously derived. The x-coordinate can be expressed as the beam radius, $w(z)$, which can be obtained by rearranging Equation (A.57) to yield the exact same expression as found in Equation (A.52). Therefore, the diffraction of the beam can be compared to the propagation of light in its most elemental form.

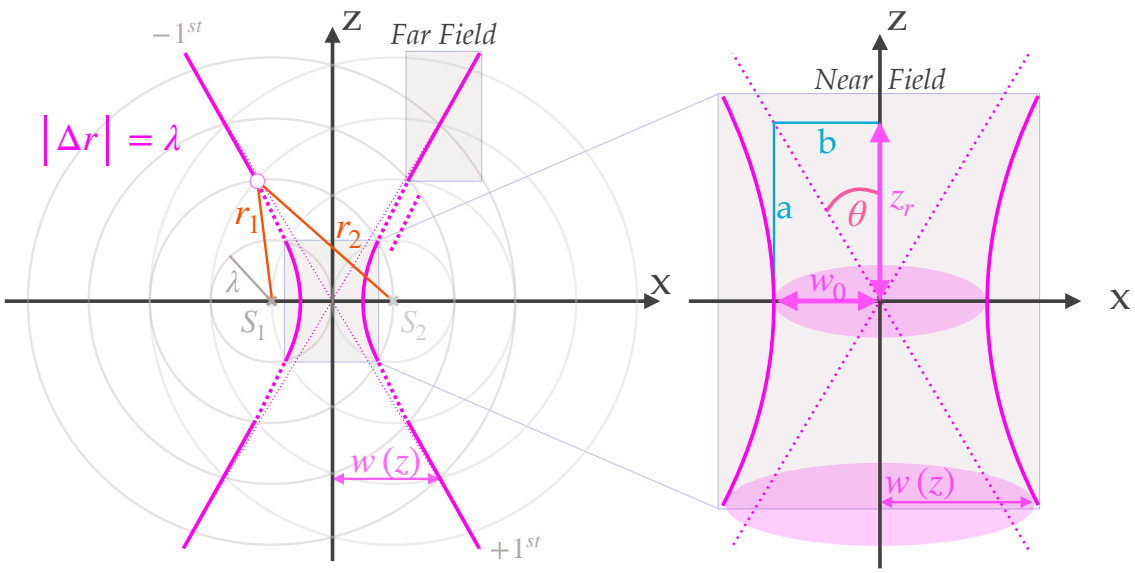


Figure A.6: The geometric representation of the cross-section of a Gaussian beam in the $xz-$plane is presented as two hyperbolas, illustrating the interference of two elementary waves. This representation is employed to explain the diffraction phenomenon. The far-field regime is indicated in the hyperbola arm, while the near-field regime is displayed in the zoom on the right side.

A more thorough examination of this subject reveals the necessity to consider the near-field and the far-field, both of which have been previously investigated by Fresnel, Sommerfeld and Fraunhofer, respectively. Indeed, the Fraunhofer diffraction is the method by which the intensity profile in the single slit experiment is explained. A closer look at z_r reveals that it denotes the distance from the waist at which the beam radius has increased by a factor of $\sqrt{2}$, i.e., $w(z_r) = \sqrt{2}w_0$. This is a characteristic referred to as the Rayleigh length of a GB. Within, and close to, the Rayleigh length, the near-field (nf) regime is dominantly applicable, whereas the far-field (ff) regime is typically describing the beam at distances $z \gg z_r$. In particular it is

$$w(z \gg z_r) \approx \frac{z}{z_r} \Longrightarrow w_{ff}(z) = \frac{2}{kw_0^2} z.$$

The divergence angle Θ of the beam can be described by twice the angle θ of one of the asymptotes of the hyperbola to its propagation axis. The latter can be derived from the far-field beam radius and is expressed as

$$\sin\theta = \frac{w_{ff}(z)}{z},$$

where this angle is typically small, as the envelope of the beam varies slowly. Hence, the trigonometric function is approximated as

$$\theta \approx \frac{w_{ff}(z)}{z} = \frac{2}{kw_0^2} = \frac{\lambda}{\pi w_0^2}.$$

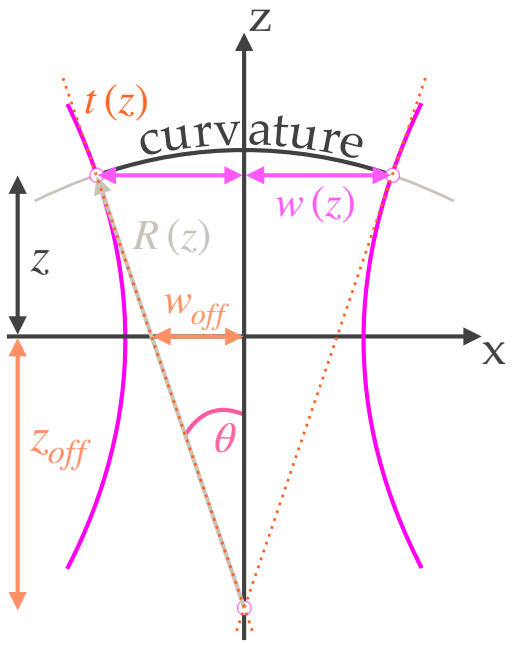


Figure A.7: The radius of curvature of the wavefronts along a single transverse propagational plane in the near-field regime. The function $t(z)$ is the tangent with respect to the GB profile at the indicated wavefront.

Therefore, the total divergence angle is equivalent to

$$\Theta = 2\theta = \frac{2\lambda}{\pi w_0^2}.$$

The function $R(z)$, given in Equation (A.54), is defined by the beam radius at a specific position along the propagation axis z, and its derivative. it gives an expression for the radius of curvature of the wavefront at that particular point. The explanation for that claim can be demonstrated through the use of geometry. Assuming the wavefronts to be approximated by spheres, thus circles in the transverse propagation planes, the radius of curvature is given by

$$\cos(\theta) = \frac{z + z_{off}(z)}{R(z)} \Longleftrightarrow R(z) \approx z + z_{off}(z). \tag{A.58}$$

In this equation, z is the distance between wavefront and beam waist, and z_{off} denotes the distance between the beam waist and the center of the hypothetical circle. Within the calculation it was used that the angle θ is small, such that $\cos(\theta) \approx 1$. In general, the derivative of a curve at a particular point z' is defined as the slope of its tangent $t(z', z)$ at that specific point, expressed as

$$t(z', z) = \left.\frac{dw(z)}{dz}\right|_{z'} z + w_{off}.$$

The term w_{off} describes the beam radius offset along the transverse axis. This offset can be determined by examining the property that the tangent and beam waist meet at z'. This yields the

equation

$$w(z') = t(z',z') \Longleftrightarrow w_{off}(z') = w(z') - \left.\frac{dw(z)}{dz}\right|_{z=z'} z'. \tag{A.59}$$

The value z_{off} is determined by the intersection of the tangent with the propagation axis, which occurs when $t\left(z', z_{off}\right) \stackrel{!}{=} 0$. This results in an expression for the offset as

$$z_{off}(z') = -w_{off}\left(\left.\frac{dw(z)}{dz}\right|_{z'}\right)^{-1}. \tag{A.60}$$

The insertion of Equations (A.59) and (A.60) into Equation (A.58) will yield the expression that was previously identified in Equation (A.54). The procedure is as follows:

$$R(z) = z - z_{off}(z) = z + \left(w(z) - \frac{dw(z)}{dz} z\right)\left(\frac{dw(z)}{dz}\right)^{-1} = w(z)\left(\frac{dw(z)}{dz}\right)^{-1}$$

Therefore, the physical meaning of the function is equivalent to the radius of curvature of the wavefront. Eventually, the model of the GB incorporates a phase term

$$\psi(z) = \arctan\left(\frac{z}{z_r}\right),$$

which is zero for $z = 0$ and converges to $\psi(z \gg z_r) = \frac{\pi}{2}$ in the far-field regime as demonstrated in Figure A.8 (a). In addition, at the precise Rayleigh length, this phase becomes $\psi(z_r) = \frac{\pi}{4}$. The mathematical form of the phase is derived from the integral

$$\psi(z) = \frac{2}{k}\int \frac{1}{w(z)^2} dz.$$

In the distance, well beyond the beam waist minimum, originating from negative infinity, the wavefront curvatures, denoted by $k = R(z)^{-1}$ approximate zero as they grow with z^{-1}, resulting in an infinite radius. In this limit, the electric field phase will propagate linearly with ikz, akin to a regular plane wave. As the light approaches w_0, the convergence bends the curvature due to diffraction, thereby creating a bottleneck in which the electric field undergoes a non-linear compression in phase. The non-linear growth rate of the phase attains its maximum at the point of maximum curvature, which corresponds to $-z_r$. Subsequently, the growth will proceed in a linear fashion until it attains the beam waist minimum at $z = 0$. Thereafter, the system will undergo a relaxation phase, accompanied by a decline in growth, initially at a gradual rate and subsequently at a precipitous decline after the point $+z_r$ is reached. Subsequent to this, the curvature of the phase will undergo a slow gradual accumulation, until such time as the beam can once again be approximated as a plane wave. The total phase shift in this scenario is

$$\psi_\infty = \frac{2}{k}\int_{-\infty}^{\infty} \frac{1}{w(z)^2} dz = \pi.$$

The specific value of π is attributed to the geometry of the GB waist. This is particularly evident in the hyperbolic behavior and the subsequent compression of the wavefronts. The function $\psi(z)$

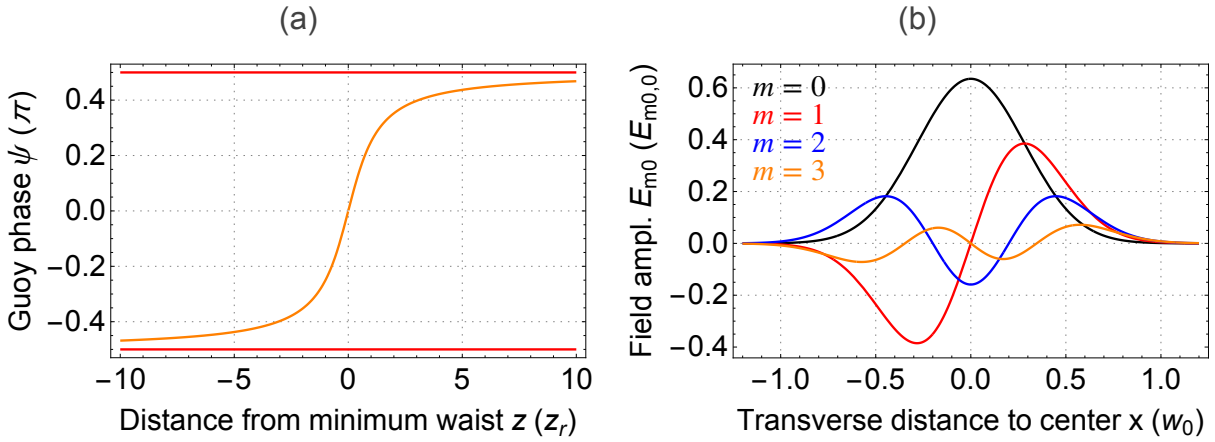


Figure A.8: (a): A plot of the Guoy phase $\psi(z)/\pi$ along the propagation axis, expressed in units of the Rayleigh length, z_r. The red lines represent the values $\pm\frac{\pi}{2}$, to which the phase converges. (b): A simulation of the electric field amplitude at $z = 0$, which corresponds to the minimum beam waist, for a selection of TEM_{m0} modes. These modes are plotted against the transverse coordinate x, expressed in units of w_0. In all cases, the minimum beam waist was $w_0 = 400\,\mu\mathrm{m}$, and the wavelength was set to $\lambda = 1\,\mu\mathrm{m}$. From left to right: TEM_{00}, TEM_{10} TEM_{20} and TEM_{30}. The electric field amplitudes are normalized such that all beams contain the same total power P.

is also referred to as the Guoy phase. It is particularly significant in scenarios where light is either confined or focused in a finite manner. This marks the completion of the fundamental GB, also referred to as the fundamental mode, for an intensity profile of a perfect circle. This model is adequate for comprehending and explaining the spatial shape of light in this thesis. However, it is crucial to acknowledge two variations. Firstly, the beam's shape can be elliptical, meaning that instead of a constant radius r, which would fulfill the property $x^2 + y^2 = r^2$, here are the semi-major g and semi-minor h axes with

$$\frac{x^2}{g^2} + \frac{y^2}{h^2} = 1.$$

Secondly, a more drastic mathematical change is represented by higher-order modes TEM_{mn} in contrast to fundamental mode (TEM_{00}), which include more complex geometries in the transverse cross-section. The index m designates the number of zero-crossings of the intensity along one axis, while n indicates the number of zero-crossings along the other axis. The notation "00" for a circle is therefore explicable. Derivation of higher-order modes is achieved through modification of Equation (A.46) by

$$u(x,y,z) \longrightarrow u_n(x,z)\,u_m(y,z),$$

where each transverse coordinate possesses a function that depends on n or m, respectively, specified by the Hermite polynomials

$$H_m(x) = (-1)^m e^{x^2} \frac{d^m}{dx^m} e^{-x^2} \text{ and } H_n(y) = (-1)^n e^{y^2} \frac{d^n}{dx^n} e^{-y^2}.$$

This provides the general solution for any Gaussian TEM_{mn} mode of amplitude A_{mn}, given by

$$\boldsymbol{E}_{mn}(x,y,z) = A_{mn}\hat{\boldsymbol{p}}\,H_m\left(\frac{\sqrt{2}x}{w(z)}\right)H_n\left(\frac{\sqrt{2}y}{w(z)}\right)\frac{w_0}{w(z)}e^{-\frac{x^2+y^2}{w(z)^2}}e^{-i\frac{k\left(x^2+y^2\right)}{2R(z)}}e^{i\psi_{mn}(z)}e^{-ikz}. \tag{A.61}$$

The phase factor $\psi_{mn}(z)$ depends on the mode and is expressed as

$$\psi_{mn}(z) = (m+n+1)\arctan\left(\frac{z}{z_r}\right),$$

which can be written as the multiplication of the fundamental Guoy phase and a factor that depends on higher order modes as $\psi_{nm}(z) = \phi_{nm}(z)\psi(z)$. In this context it is $\phi_{nm} = (m+n)\arctan\left(\frac{z}{z_r}\right)$. The GB can then be separated into two components: one component describing the fundamental mode and another component describing higher-order modes through Hermite functions:

$$\boldsymbol{E}_{mn}(x,y,z) = \underbrace{\frac{A_{mn}}{A_{00}}H_m\left(\frac{\sqrt{2}x}{w(z)}\right)H_n\left(\frac{\sqrt{2}y}{w(z)}\right)e^{i\phi_{mn}(z)}}_{\text{Hermite}}\underbrace{\boldsymbol{E}_{00}(x,y,z)}_{\text{Gaussian}}$$

This explains the rationale behind the utilization of the somewhat unconventional notation for the amplitude and electric fields in the context of the fundamental mode. In the context of power conservation, the following assertion is made: When a beam undergoes a change in mode while concurrently maintaining the same energy, its amplitude A_{mn} has to satisfy:

$$P = \int_A I\,dA = \frac{1}{2}c_0\varepsilon_0\int_A |\boldsymbol{E}_{mn}(x,y,z)|^2\,dA = \frac{1}{2}c_0\varepsilon_0\,|A_{mn}|^2\int_A \left|\hat{\boldsymbol{E}}_{mn}(x,y,z)\right|^2 dA$$

$$\Longleftrightarrow |A_{mn}| = \sqrt{\frac{2P}{c_0\varepsilon_0\int_A \left|\hat{\boldsymbol{E}}_{mn}(x,y,z)\right|^2 dA}}$$

A superficial examination of Hermite polynomials may lead to the supposition that they are rather complex. However, upon further scrutiny, they ultimately describe a simple polynomial chain. The highest occurring exponent of the argument is equivalent to the index, and these polynomials exclusively contain odd or even exponents with alternating signs. The manipulation of the fundamental Gaussian mode by these polynomials results in the acquisition of zero crossings and negative amplitudes of the electric field. This leads to the emergence of more than a single peak in the field, as illustrated in Figure A.8 (b), and therefore intensity, without compromising the overall Gaussian characteristics. This shape does not need to follow radial or diagonal symmetry but only transverse. This is given by the integer indices m and n which may be different from each other leading to a manifold of possible intensity patterns which can be realized in a simple way by using standing wave resonators, which will be discussed within the scope of cavity stability later on.

The calculus for these higher-order modes and the derivation of the Hermite polynomials, as well as the specific form of their argument, have not been specifically addressed in the scope of this thesis as they were not part of the experimental work. For all beams propagating through

space that were examined in this thesis, including those inside resonators, which will be discussed in greater detail subsequently, the fundamental mode was the objective shape as well as the mode employed. Nevertheless, higher-order modes constitute an integral component of the comprehension of GB. These modes can be readily observed in reality, as they are not merely theoretical constructs. Consequently, to reach a comprehensive conclusion on this subject, they are presented here. The spatial profile of a selection of modes is represented by a simulation in Figure A.9. In the laboratory, such beam profiles can be detected through direct imaging if the camera is situated within the beam's path in free space. The measurement of the transverse profile, via camera, along the propagation direction, can be used to simulate the spatial geometry of the laser light.

A.2.2 The Ray Matrix Method: Understanding the $q-$Parameter

The shape of the GB can be fully described by its beam radius $w(z)$ and curvature $R(z)$ at a point z. As indicated by Equation (A.56), a characteristic function, $q(z)$, can be extracted that fully describes this beam shape at any point without resorting to the entire electric field formalism. This objective can be accomplished through two exponential factors of the electric field, which are

$$\boldsymbol{E}(x,y,z) \propto e^{-\frac{x^2+y^2}{w(z)^2}} e^{-i\frac{k\left(x^2+y^2\right)}{2R(z)}} = e^{-i\frac{k}{2}\frac{\left(x^2+y^2\right)}{q(z)}}.$$

Therefore, the function $q(z)$ is reduced to a compact form containing the beam radius and the wavefront curvature:

$$\frac{1}{q(z)} = \frac{1}{R(z)} - i\frac{2}{kw(z)^2} \tag{A.62}$$

The insertion of Equation (A.54) and (A.52) into Equation (A.62) yields the final expression for the q-parameter $q(z)$. Notably, this expression can be simplified to one of the most fundamental forms, comprising solely the propagation variable and the Rayleigh length. Furthermore, in the event that the minimum beam waist, w_0, is not located at $z = 0$, but rather at a previously specified offset value, $z = z_0$, the expression must be modified accordingly and it follows

$$q(z) = (z - z_0) + iz_r. \tag{A.63}$$

This offset z_0 becomes especially of interest, when a beam is manipulated by optics like a lens along its path. In that case, the q-parameter of the final beam is different of the initial one. In order to describe the change of the parameter in space, specifically going from q_j to a beam with q_l can again be done using a transfer matrix approach. A common description of classical one dimensional and linearly propagating rays $\boldsymbol{r}$ is formulated by

$$\boldsymbol{r}_l = \boldsymbol{M}_{jl}\boldsymbol{r}_j \Longrightarrow \begin{pmatrix} r_l \\ \theta_l \end{pmatrix} = \begin{pmatrix} A & B \\ C & D \end{pmatrix} \begin{pmatrix} r_j \\ \theta_j \end{pmatrix}. \tag{A.64}$$

In this context, the matrix $\boldsymbol{M}_{jl}$ is defined by the optical component responsible for manipulating the light. The parameter r denotes the transverse height of the beam with respect to the optical axis, and θ indicates its propagation angle with respect to the optical axis. The symbol shares its designation with half the divergence angle of the GB; this occurrence is not mere coincidence. All of these parameters are specified at the location of the component. In this context, it is postulated

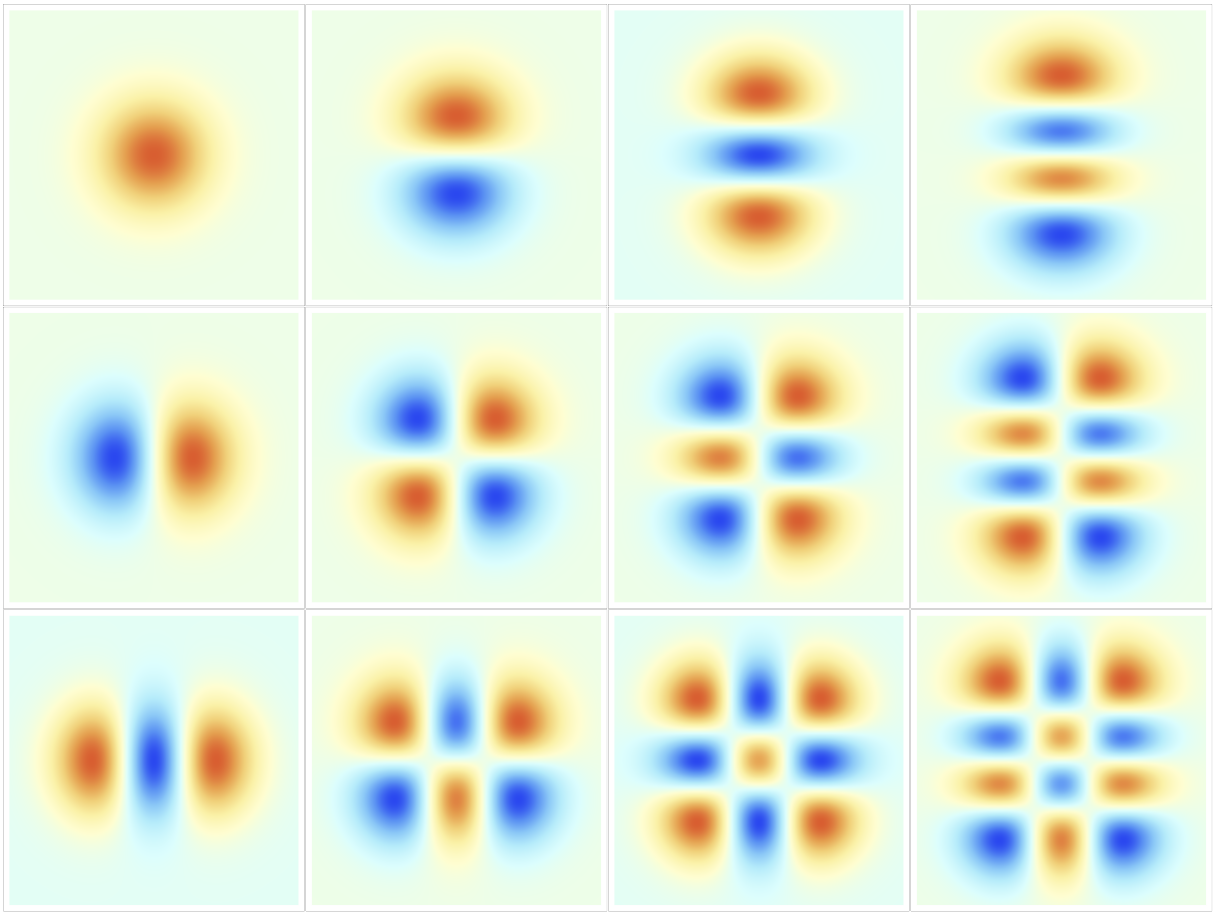


Figure A.9: The following simulation is of the transverse cross-section of GBs, at $z = 0$, which is equivalent to the position of the minimum beam waist, for a selection of TEM modes. In all cases, the following assumptions were made: $w_0 = 400\,\mu\text{m}$, and $\lambda = 1\,\mu\text{m}$. The modes were normalized to carry the same power. The integer n, ranging from left to right, denotes the number of zero crossings along y, here in ascending order from zero to three. The left top mode is congruent with the fundamental beam. The integer m, ranging from zero to two, denotes the number of zero crossings of intensity along x. Blue or red coloration indicates the sign of the electric field amplitude, while the saturation shows its strength.

that the component is perpendicular to the optical axis, with the GB traveling parallel to it. This concept can be extrapolated to GB as well, under the condition that the ray describes the transverse envelope. Consequently, the beam waist is equivalent to $r = w(z)$. In this particular instance, the angle relative to the propagation axis is determined by the slope of the beam waist at the specified position, given by the relation $\tan(\theta) \approx \theta = \frac{dw_j(z)}{dz}$. In particular, it is

$$r_j = w_{0,j}\sqrt{1+\left(\frac{z}{z_{r,j}}\right)^2} \text{ and } \theta_j = z\frac{w_{0,j}}{z_{r,j}^2\sqrt{1+\left(\frac{z}{z_{r,j}}\right)^2}}, \tag{A.65}$$

in the instance of the initial beam. The matrix in Equation (A.64) constitutes the following system of equations:

$$\left|\begin{array}{ll} r_l = Ar_j + B\theta_j & (a) \\ \theta_l = Cr_j + D\theta_j & (b) \end{array}\right| \tag{A.66}$$

Upon inserting the respective expressions for r and θ of Equation (A.65), and subsequently dividing Equation (A.66) (a) by (b), under the assumption that (b) is not equal to zero, the expression

$$\frac{z_{r,l}^2}{z} + z = \frac{A\left(\frac{z_{r,j}^2}{z}+z\right)+B}{C\left(\frac{z_{r,j}^2}{z}+z\right)+D},$$

is yielded. This formalism establishes a correlation between the beam curvature radius of the incident beam and that of the resulting beam. This can also be expressed by the real part of q^{-1} by

$$R_l = \frac{AR_j+B}{CR_j+D} = \Re\left[\frac{1}{q_l}\right]^{-1} = \frac{A\Re\left[\frac{1}{q_j}\right]^{-1}+B}{C\Re\left[\frac{1}{q_j}\right]^{-1}+D}.$$

At this point it is needed to provide a rationale for this discourse. A classical ray is characterized by its height and slope, which determines its propagation angle. The incorporation of the hyperbolic function of the beam waist in the context of a GB results in a unique description of the beam, whereby its wavefront curvature or radius serves as the primary defining characteristic. In the event that such a scenario were to be true, the imaginary part of the $q-$parameter would be rendered superfluous, and the system could be fully described by R. However, the issue arises from the fact that the wavefront radius does not follow a unidirectional growth pattern.

The beam radius decreases from a theoretical infinity to its minimum when approaching the beam waist, and subsequently, it increases back to theoretical infinity. However, the curvature is equal to zero for both the case far away from the beam waist and at the beam waist but with a maximized curvature at the Rayleigh length. Therefore, the information regarding the beam width can no longer be extracted from curvature alone. The placement of the optical element, specifically its position relative to the Rayleigh length, is of particular significance. This is due to the fact that the radius and curvature of the wavefronts are not uniquely associated with a particular beam waist.

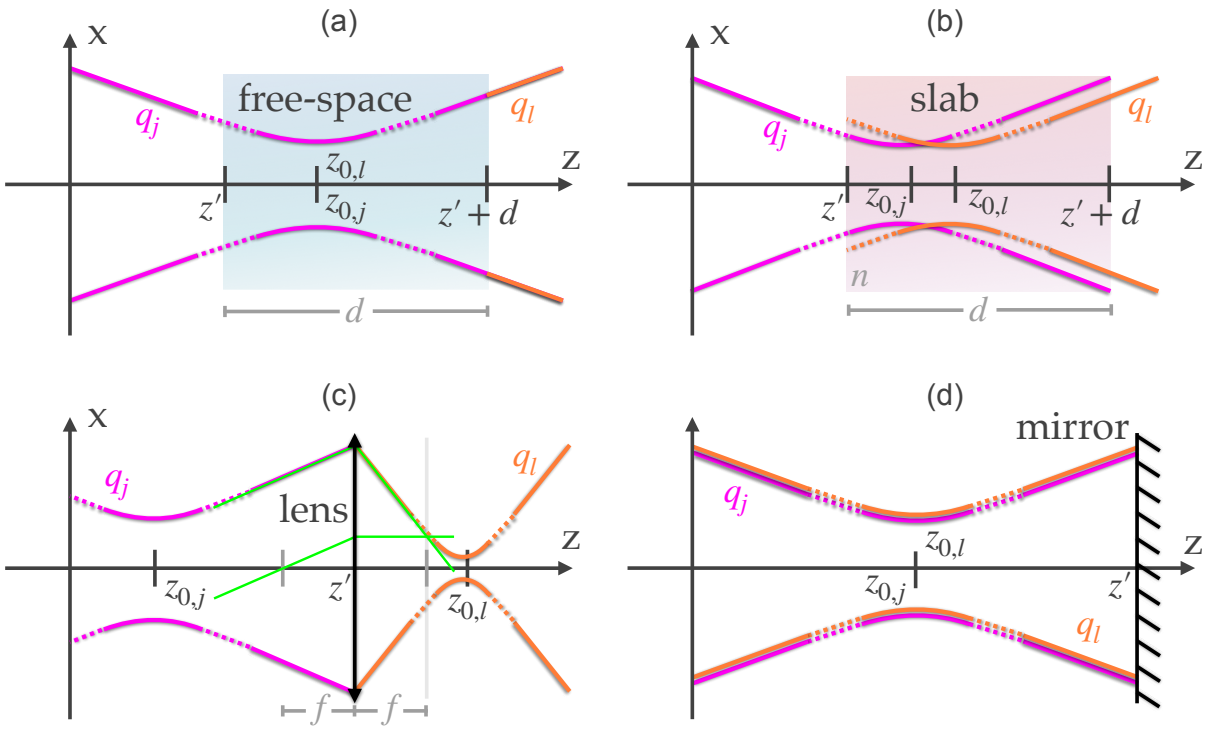


Figure A.10: GB manipulation by selected optical components. The magenta line signifies the incident mode, while the orange curve provides a visual representation of the resulting beam. The following four phenomena are to be considered: (a): Propagation through free space of length d. (b): Propagation through a slab of length d with refractive index n. (c): Propagation through a thin lens of focal length f. (d): Reflection on a flat mirror. The beams are overlapping but offset for the sake of clarity.

The resolution to this issue is straightforward. It has been previously observed how the real part of the $q-$parameter is transformed by the matrix formalism. Consequently, the imaginary part can be added to the real part to yield

$$\left(\Re\left[\frac{1}{q_l}\right]+i\Im\left[\frac{1}{q_l}\right]\right)^{-1}=\frac{A\left(\Re\left[\frac{1}{q_j}\right]+i\Im\left[\frac{1}{q_j}\right]\right)^{-1}+B}{C\left(\Re\left[\frac{1}{q_j}\right]+i\Im\left[\frac{1}{q_j}\right]\right)^{-1}+D}.$$

The final formula for the $q-$parameter transformation through an optical element, derived based on the classical ray matrix approximation, and enhanced to the GB model, is as follows:

$$q_l=\frac{Aq_j+B}{Cq_j+D} \tag{A.67}$$

In the context of this study, the primary free-space optical elements employed for the manipulation of light include mirrors for directional changes, lenses for focusing, and waveplates, frequently utilized in conjunction with polarizing beam splitters (PBS), to modulate the power and polarization of light along specific pathways (see Figure A.10). The simplest case, free space propagation,

provides a clear illustration of the invariance of the GB characteristics. Nevertheless, the resulting beam is offset from the original by the propagation distance, d. For the purpose of a clear origin, the initial beam is given by

$$q_j = z - z_{0,j} + iz_{r,j},$$

where z_0 is the position of the minimum beam waist $w_{0,j}$. Therefore, when free space propagation commences at z' the evolution of the $q-$parameter is

$$q_l(z'+d) = z'+d-z_{0,l}+iz_l = \left(z'-z_{0,j}+iz_{r,j}\right)+d = q_j(z')+d = \frac{(1)\,q_j(z')+(d)}{(0)\,q_j(z')+(1)}. \tag{A.68}$$

Trivially, the $q-$parameter for any position z, reasonably with $z \geq z'+d$ for the resulting beam, is given by

$$q_l(z) = z - z_{0,j} + iz_{r,j}.$$

The notation of the numbers in parentheses in Equation (A.68) has been inspired by the textbook written by Nagourney [229], as it is a convenient way to determine the matrix parameters, hence for free space it is

$$\boldsymbol{M}_{fs} = \begin{pmatrix} 1 & d \\ 0 & 1 \end{pmatrix}. \tag{A.69}$$

The scenario becomes slightly more intricate when a thin lens of focal length f is positioned at a distance z'. In the model of a classical ray, emitted by an object, the evolution is described by the thin lens equation

$$\frac{1}{a_j} + \frac{1}{a_l} = \frac{1}{f},$$

where a_j is the distance between the object and the lens, and a_l denotes the distance from the lens to the resulting image. In the case of a GB, the distances can be arranged to be equivalent to the radius of curvature of the individual beams, such that

$$\frac{1}{R_j} - \frac{1}{R_l} = \frac{1}{f}.$$

In this particular instance, the parameter a_l is negative, a consequence of the configuration of the system. This arises from observing the left side of the initial beam and the right side of the resulting beam. Employing the same rationale employed in the matrix formalism, the total $q-$parameter undergoes the following transformation:

$$\frac{1}{q_j} - \frac{1}{q_l} = \frac{1}{f} \Longleftrightarrow q_l = \frac{(1)\,q_j+(0)}{\left(-\frac{1}{f}\right)q_j+(1)} \tag{A.70}$$

The latter part in Equation (A.70) is written in a manner that facilitates the derivation of the transfer matrix for a thin lens. This transfer matrix is given by

$$\boldsymbol{M}_{tl} = \begin{pmatrix} 1 & 0 \\ -\frac{1}{f} & 1 \end{pmatrix}. \tag{A.71}$$

In order to obtain the resulting $q-$parameter at the position of the lens $q_l(z')$ in the form $q_l(z') = z' - z_{0,l} + iz_{r,l}$, the evaluation of Equation (A.70) is necessary. It follows:

$$\begin{aligned} q_l(z') &= \left(-\frac{1}{f} + \frac{1}{R_j(z')} - i\frac{2}{kw_j(z')^2}\right)^{-1} \\ &= \underbrace{\frac{\left(z'-z_{0,j}\right)f^2 - f\left(z'-z_{0,j}\right)^2 - fz_{r,j}^2}{\left(f-z'+z_{0,j}\right)^2 + z_{r,j}^2}}_{z'-z_{0,l}} + i\underbrace{\frac{f^2 z_{r,j}}{\left(f-z'+z_{0,j}\right)^2 + z_{r,j}^2}}_{z_{r,l}}. \end{aligned}$$

This formalism provides an explicit calculation for the beam waist minimum, $w_{0,l}$, which is

$$w_{0,l} = \sqrt{\frac{2z_{r,l}}{k}} = \sqrt{\frac{2f^2 z_{r,j}}{k\left(f-z'+z_{0,j}\right)^2 + kz_{r,j}^2}}. \tag{A.72}$$

This is depicted in the plot in Figure A.11 (a) expressed in units of $w_{0,j}$ and depending on the focal length f relative to the distance between the lens and the initial minimum beam waist. The illustration presents three curves, each corresponding to a distinct distance measured in units of the initial Rayleigh length, $z_{r,j}$. It is noteworthy that the lens, if positioned close to the initial beam waist, will exclusively focus the beam spot until the focal length diverges. However, when positioned at a greater distance, the lens can either focus or expand the spot size, a phenomenon that is contingent upon the focal length. Furthermore, the position of the minimum beam waist of the resulting beam can be either before or after the focal length of the lens, and it can even be on the left side of the lens, thus virtual. This is illustrated in the plot in Figure A.11 (b), again for the three curves in units of $z_{r,j}$.

The subsequent optical element, which is also the most prevalent one, is the mirror. A spherical mirror's behavior is analogous to that of a lens. However, the focal length, f_m, is equivalent to half the radius of curvature, R_m, of the mirror. The sign of the radius is contingent upon the mirror's convex or concave nature. Flat mirrors are particularly useful in modifying the propagation direction of a beam. In this instance, the matrix is simply

$$\boldsymbol{M}_m = \begin{pmatrix} 1 & 0 \\ 0 & 1 \end{pmatrix}, \tag{A.73}$$

as $R_m \to \infty$. This results in the trivial connection $q_l(z') = q_j(z')$ with no beam along z after the position z' of the mirror. It should be noted that mirrors are frequently positioned at an angle relative to the beam, thereby resulting in a presentation of the $q-$parameter that is slightly more complex. This presentation includes the inclusion of a second axis that constitutes the plane of propagation, which ideally remains parallel to the optical axis itself. Nevertheless, this does not modify the GB characteristics; rather, it introduces an angle in a two-dimensional plane. Certain components, such as PBSs and wave plates, can be described as slabs of a specific thickness. The influence of these objects on the polarization of light has not yet been considered; thus far, the geometry of the beam has been the sole element under review. Their effect on the beam is analogous to that of free-space

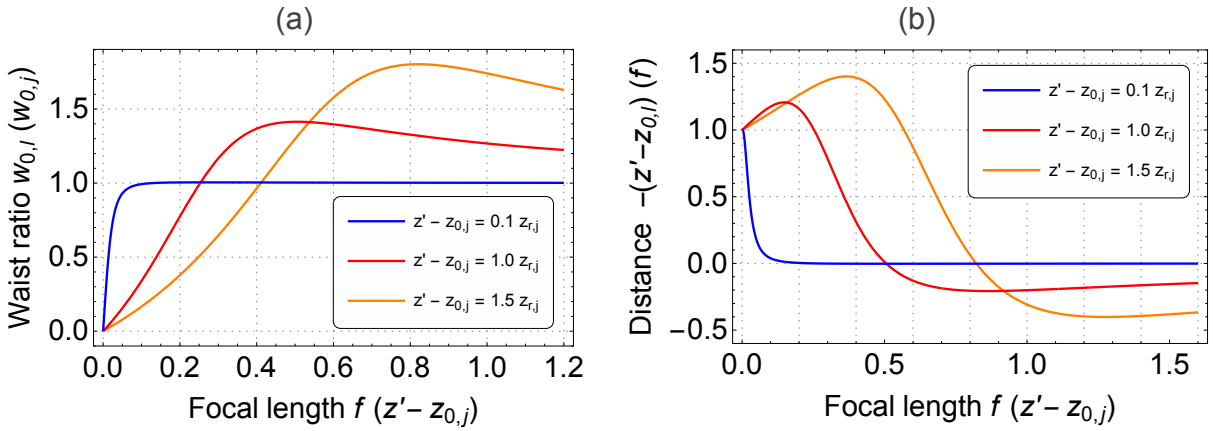


Figure A.11: (a): A GB propagating through a thin lens. The minimum beam waist ratio $w_{0,l}/w_{0,j}$ is plotted in dependence of the focal length, f, measured in units of the distance between the incident minimum beam waist and the lens. (b): The plot depicts the ratio of the distance between the lens and the minimum beam waist of the resulting beam to the focal length, with respect to the focal length. The incident light has a beam waist of $w_{0,j} = 400\,\mu$m, and the wavelength of the light is $1\,\mu$m.

propagation. However, it is important to consider the refractive index, n, of the slab. Therefore, the value of the transfer matrix of a slab $\boldsymbol{M}_s$ is

$$\boldsymbol{M}_s = \begin{pmatrix} 1 & d/n \\ 0 & 1 \end{pmatrix}. \tag{A.74}$$

The four matrices presented in the Equations (A.69), (A.71), (A.73) and (A.74), which are also illustrated in Figure A.10, facilitate the execution of nearly all calculations in the context of the geometry of laser light propagation through free space optics necessary for this thesis. Complementary, the follwing section entails a comprehensive examination of light propagation through optical fibers. A notable property of these transformation matrices is their unimodular nature, which implies that $\det(\boldsymbol{M}) = 1$. Therefore, it can be deduced that the final matrix describing an array of optical elements will also be unimodular, as they are merely the product of unimodular matrices.

A.2.3 Guiding Light: The Basics of Optical Fibers

In the current theoretical framework, the propagation of light is assumed to occur in a vacuum or in a single medium with a refractive index of n. In such scenarios, manipulating the direction of light's propagation poses a significant challenge. The utilization of mirrors is a viable method to achieve this objective; however, they can pose challenges when it comes to practical implementation, particularly in scenarios where transmitting the signal over extended distances is desired. To this end, the implementation of optical fibers is requisite. These waveguides, which will be discussed in greater detail subsequently, are capable of confining the electric field of a beam within predefined boundaries. In this manner, a fiber can be arranged along extended pathways, allowing for reasonable flexibility while maintaining the transmission of light from one location to another.

To achieve this objective, there are several concepts that have been posited; however, the one that is most common and the one that will be used within this work is the step index optical fiber. It utilizes the effect of total internal reflection in order to establish a lossless propagation of light within the fiber.

The structure of a step index optical fiber is composed of the following elements: The core of the fiber is a cylinder of a specific width and material that functions as a propagation medium for light. This component possesses a refractive index of n_1. Surrounding this cylinder is a ring cylinder composed of a distinct material, designated as the "cladding" with n_2. When light is coupled into the core at an angle θ relative to the optical axis through the center of the core, it will reflect and refract, as explained in Section A.1.3. Specifically, the refraction is governed by Snellius's law, which stipulates that:

$$n_1 \sin(\theta_1) = n_2 \sin(\theta_2). \tag{A.75}$$

In this equation, the index refers to the different mediums separated by the interface. If θ_2 becomes parallel to the surface of the process, light will only be reflected, and refraction will not occur. This is called total internal reflection. It appears when the angle of incidence is larger than or equal to the critical angle, denoted by θ_c, which is given by

$$n_1 \sin(\theta_c) = n_2 \sin\left(\frac{\pi}{2}\right) \Longleftrightarrow \theta_c = \arcsin\left(\frac{n_2}{n_1}\right).$$

Light is usually coupled into a fiber using air or a vacuum. This makes the refractive index n_0 of the environment smaller than the guiding materials, which are usually some kind of glass. However, this means that for the largest accepted input angle, denoted by the symbol θ_{max}, for light that travels from the outside medium into the core, the following relationship is true:

$$n_0 \sin(\theta_{max}) = n_1 \sin\left(\frac{\pi}{2} - \theta_c\right) = n_1 \sin\left(\frac{\pi}{2} - \arcsin\left(\frac{n_2}{n_1}\right)\right) = n_1 \sqrt{1 - \frac{n_2}{n_1^2}} = \sqrt{n_1^2 - n_2^2} := NA.$$

The numerical aperture NA (NA) is a quantity that determines the accepted angles of light entering from a given external material into a fiber. It is larger, the larger the difference of refractive indices between core and cladding. Conversely, an increase in numerical aperture, which results in a steeper incident angle, corresponds to an enhancement in the fiber's sensitivity to bends. It is important to note that a fiber does not resemble a rigid rod; rather, it is a flexible cable that functions as a conduit for light by guiding it along a path that is susceptible to numerous and rather aggressive changes in direction. As the radius of the bend increases, the tangent at the point of reflection undergoes a rotation, thereby decreasing the effective incident angle to the normal to the tangent. The potential for refraction within the fiber is thereby introduced. Indeed, according to the NA's definition, each bend will invariably result in a specific degree of refraction, as the critical angle, θ_c, is already fixed.

However, the losses of a bend of given radius will be larger for steeper incident angles, as these angles result in a greater number of refractions inside the curve. Conversely, for more shallow angles, the losses will be smaller. The concept is illustrated in Figure A.12 for rays that

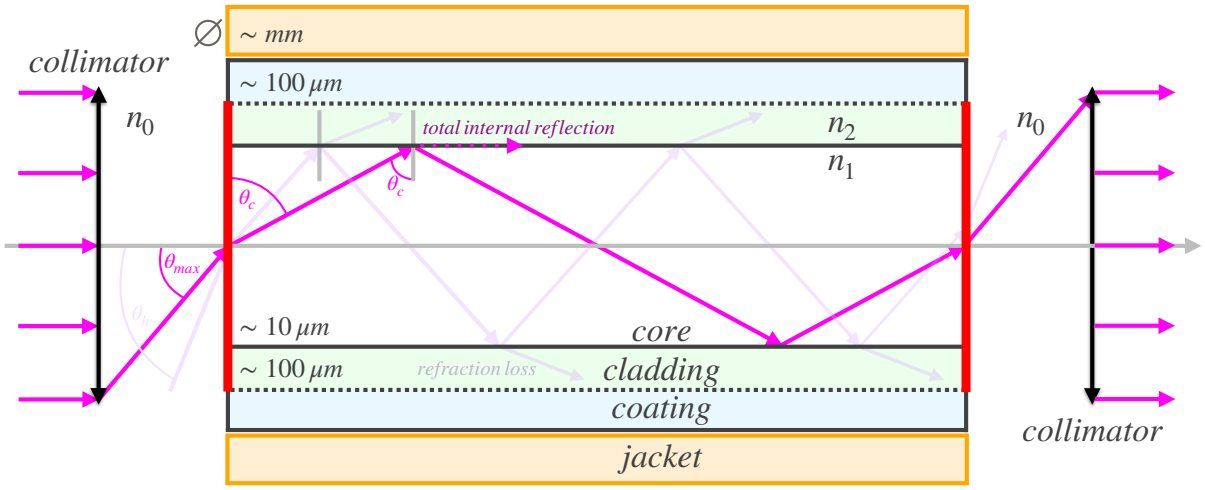


Figure A.12: The concept of an optical step index fiber. Light is focused by a lens, known as a collimator, towards the tip of the fiber (red). Photons will fully reflect at the interface between the cladding (green) and the core (white) within the core, provided that the incident angle falls below or remains equal to the maximum incident angle, θ_{max}. At angles of greater magnitude, refraction losses into the cladding will be experienced. The application of a protective coating (blue) and jacket (yellow) serves to preserve the integrity of the fiber.

are collimated at a single focal point, where the optical axis intersects the core. This is an effective method for illustrating the accepted angles and NA of a fiber. In the ray picture, light that is perfectly parallel to the fiber would not be guided by it and would propagate freely. In actuality, a minimal incident angle is employed to guarantee that light propagates through the fiber in an optimal manner.

The range of typical core diameters is from 8 µm and 25 µm, with claddings reaching up to 125 µm. A coating material with a diameter of approximately 250 µm is affixed to the cladding of the optical fiber, thereby enhancing its flexibility. A protective layer, in the form of a jacket with diameters in the order of millimeters, is finally added. The distal ends of the fiber are typically equipped with a ferrule connector (FC), which can vary in configuration. Two of the most prevalent forms are physical contact (PC) and angled physical contact (APC). These components are typically designated as FC/PC or FC/APC, and their primary function is to couple light into and out of the fiber, or to connect two separate fibers. This is achieved by utilizing a mating sleeve (MS), which adjusts the fiber tips to ensure seamless light transmission from one tip to the other.

In this work, the majority of utilized fiber connectors are of the FC/APC variety, a choice that is predicated on the fact that the additional angle of 8° results in a substantial diminution of the optical return loss experienced by light that is reflected back to the source, in contrast to the scenario observed with FC/PC, which features a flat surface. Nevertheless, when considering the approximation to reality, it is not rays that interact with the fiber; rather, it is GBs that possess a finite, non-zero width. In order to obtain a more precise description of the propagation process through a fiber, it is essential to consider the EM wave characteristics. The electric field and its

corresponding modes that can propagate through a fiber are determined by the Helmholtz equation

$$\left(\nabla^2 + k_n^2(\boldsymbol{r})\right)\boldsymbol{E}(\boldsymbol{r}) = 0,$$

where the wavenumber is dependent on the respective refractive index of the material of the fiber. In the case of the cylindrical geometry, the refractive index $n(r)$ depends on the radial coordinate, thus

$$\left(\nabla^2 + \left(\frac{2\pi}{\lambda\, n(r)}\right)^2\right)\boldsymbol{E}(\boldsymbol{r}) = 0.$$

Inserting the wavenumber for the light in a vacuum, $k = \frac{2\pi}{\lambda}$ results in

$$\left(\nabla^2 + k^2 n^2(r)\right)\boldsymbol{E}(\boldsymbol{r}) = 0. \tag{A.76}$$

In a manner analogous to the GBs, the electric field can be described by a predominantly planar wave comprising geometric functions, depending on the fiber's confinement. It can be written as

$$\boldsymbol{E}(\boldsymbol{r}) = u_l(\varphi)\, u_m(r)\, E_0 \hat{\boldsymbol{p}}\, e^{-i(\beta z - \omega t)}, \tag{A.77}$$

where cylindrical coordinates are introduced to align with the boundaries of the waveguide. The functions $u_l(\varphi)$ and $u_m(r)$ are dimensionless and only dependent on their respective variable. The propagation constant has undergone a transformation from k to β, due to the disparate materials through which the modes will propagate. At this stage, the expression for β remains unknown and has to be derived during the process. The indices l and m are analogous to the potential Hermite-Gaussian modes in free space. They are integers, denoting the zero crossings of the electric field amplitude in the azimuthal and radial directions, respectively. Inserting Equation (A.77) into (A.76), which is expressed in cylindrical coordinates, the following equation is obtained:

$$\frac{1}{r}\frac{d}{dr}\left(r\frac{d\boldsymbol{E}(\boldsymbol{r})}{dr}\right) + \frac{1}{r^2}\frac{d^2\boldsymbol{E}(\boldsymbol{r})}{d\varphi^2} + \frac{d^2\boldsymbol{E}(\boldsymbol{r})}{dz^2} + k^2 n^2(r)\boldsymbol{E}(\boldsymbol{r}) = 0$$

The equation is simplified after the insertion of the explicit form of the electric field in Equation (A.77), yielding the following result:

$$\frac{1}{u_m(r)}\frac{1}{r}\frac{d}{dr}\left(r\frac{du_m(r)}{dr}\right) + \frac{1}{u_l(\varphi)}\frac{1}{r^2}\frac{d^2u_l(\varphi)}{d\varphi^2} + k^2 n^2(r) - \beta^2 = 0. \tag{A.78}$$

The refractive index of the fiber in the radial direction is determined by the core and the cladding, respectively. This yields in a step function around the radius of the core, r_c, hence giving the system the name "step index" fiber. The refractive index is modeled as follows:

$$n(r) = \begin{cases} n_1 & r \le r_c \\ n_2 & r > r_c \end{cases}$$

To proceed, it may be advantageous to employ an elegant feature of the fiber. The term $u_l(\varphi)$ describes the azimuthal field in the cross section of the fiber. It is evident that the electric field

is constrained to a single value at any point on a circle of radius r. Consequently, the field must be periodic by 2π. Moreover, the full field must exhibit l zero crossings during one complete rotation around this circle. This enables the function to be described by $e^{il\varphi}$. Nevertheless, it is necessary for the intensity profile to also contain the angle φ, such that the dependence does not vanish immediately when the absolute value of the electric field is taken. Therefore, the following equation can be established:

$$u_l(\varphi) = \cos(l\varphi). \tag{A.79}$$

The integration of this formalism into Equation (A.78) and reordering of it will result in the equation for the core

$$r^2 \frac{d^2 u_m(r)}{dr^2} + r \frac{du_m(r)}{dr} + \left(\alpha_m^2 r^2 - l^2\right) u_m(r) = 0, r \leq r_c, \tag{A.80}$$

with $\alpha_m^2 = k^2 n_1^2 - \beta_m^2$. This is analogous to the Bessel equation $u_m(r) = J_l(r)$, if $\alpha_m = 1$. This equation can be solved by the first-order Bessel function $J_l(r)$ given by

$$J_l(r) = \sum_{j=0}^{\infty} \frac{(-1)^j}{j!\,\Gamma(j+l+1)} \left(\frac{r}{2}\right)^{2j+l}, \tag{A.81}$$

where the Gamma function is defined as $\Gamma(z) = \int_0^\infty t^{z-1} e^{-t} dt$. The derivation of these functions will require a significant degree of mathematical sophistication. While the subject is undoubtedly intriguing, it may exceed the scope of the present work. Nevertheless, it is advantageous to have been privy to the origins of Bessel functions, as opposed to merely presenting them as a solution. Substituting $r' = \alpha_m r$ and inserting the solution $u_m(r) = A_m J_l(\alpha_m r)$ with the property

$$\frac{dJ_l(\alpha_m r)}{dr} = \frac{dJ_l(\alpha_m r)}{d(\alpha_m r)} \frac{d(\alpha_m r)}{dr} = \alpha_m \frac{dJ_l(r')}{dr'},$$

will yield the differential equation

$$r'^2 \frac{dJ_l^2(r')}{dr'^2} + r' \frac{dJ_l(r')}{dr'} + \left(r'^2 - l^2\right) J_l(r') = 0.$$

The parameter A_m is the mode normalization factor. Therefore, the function $J_l(\alpha_m r)$ is a solution to the wave equation for the radial component of the electric field in the core. The intermediate electric field in the core can be expressed by

$$\boldsymbol{E}_{core}(\boldsymbol{r}) = A_m J_l\left(\alpha'_m r_n\right) \cos(l\varphi) E_0 \hat{\boldsymbol{p}} e^{-i(\beta z - \omega t)},$$

where $\alpha'_m = \alpha_m r_c$, such that the field can be expressed in the radial component relative to the core radius, thus $r_n = \frac{r}{r_c}$. As photons are known to travel exclusively within the core, a continuous and exponential decline in the electric field within the cladding is inevitable. In addition, the function must be continuous at $r_n = 1$ and must also satisfy the Bessel equation

$$r^2 \frac{d^2 u_m(r)}{dr^2} + r \frac{du_m(r)}{dr} - \left(\gamma_m^2 r^2 + l^2\right) u_m(r) = 0, r \geq r_c, \tag{A.82}$$

with $\gamma_m^2 = -\left(k^2 n_2^2 - \beta_m^2\right)$. It is important to note that the signs have undergone a slight rearrangement. The function in Equation (A.82) can also be solved by a typical Bessel function. However, the requirement that it drops exponentially necessitates the consideration of the modified Bessel function of second order, $K_l(\gamma_m r)$, as a valid solution. The field in the cladding then becomes

$$\boldsymbol{E}_{clad}(\boldsymbol{r}) = B_m K_l\left(\gamma'_m r_n\right)\cos(l\varphi)\, E_0 \hat{\boldsymbol{p}}\, e^{-i(\beta z - \omega t)},$$

witch $\gamma'_m = \gamma_m r_c$. The initial step in ensuring continuity is to ensure that both fields coincide at the boundary surface. This objective can be achieved by incorporating a normalization factor, which is expressed as the respective Bessel function, at the position of the boundary. The comprehensive formalism of the electric field in a fiber is expressed as follows:

$$\boldsymbol{E}_{lm}(\boldsymbol{r}) = A_{lm}\hat{\boldsymbol{p}}\, e^{-i(\beta z - \omega t)}\cos(l\varphi)\, C_{lm} \times \begin{cases} \frac{J_l(\alpha'_m r_n)}{J_l(\alpha'_m)} & r_n \leq 1 \\ \frac{K_l(\gamma'_m r_n)}{K_l(\gamma'_m)} & r_n > 1 \end{cases} \tag{A.83}$$

In this equation, A_{lm} represents the global mode depending field amplitude, and $C_{lm} \coloneqq \frac{J_l(\alpha'_m)}{J_l(0)}$ is the normalization constant. The latter is necessary due to the fact that Bessel functions are not inherently normalized to one, in contrast to the Gaussian distribution. In this formalism (Equation (A.83)), the core and cladding fields will match if $r_n = 1$. The identity

$$\alpha'^2_m + \gamma'^2_m = r_c^2 k^2\left(n_1^2 - n_2^2\right) \coloneqq V^2 \Longleftrightarrow V = \sqrt{\alpha'^2_m + \gamma'^2_m} \tag{A.84}$$

is of particular interest and will be elaborated upon subsequently. In order to satisfy the second continuity requirement and finalize the fields, it is requisite that the slope of the electric field match the core radius. The requirement stipulates that

$$\left.\frac{d}{dr}\,\frac{J_l\left(\alpha'_m \frac{r}{r_c}\right)}{J_l(\alpha'_m)}\right|_{=r_c} \stackrel{!}{=} \left.\frac{d}{dr}\,\frac{K_l\left(\gamma'_m \frac{r}{r_c}\right)}{K_l(\gamma'_m)}\right|_{r=r_c}. \tag{A.85}$$

The following four identities of the Bessel functions are introduced:

$$\frac{d}{dr}J_l\left(\alpha'_m \frac{r}{r_c}\right) = \frac{\alpha'_m}{2r_c}\left(J_{l-1}\left(\alpha'_m \frac{r}{r_c}\right) - J_{l+1}\left(\alpha'_m \frac{r}{r_c}\right)\right)$$

$$\frac{d}{dr}K_l\left(\gamma'_m \frac{r}{r_c}\right) = -\frac{\gamma'_m}{2r_c}\left(K_{l-1}\left(\gamma'_m \frac{r}{r_c}\right) + K_{l+1}\left(\gamma'_m \frac{r}{r_c}\right)\right)$$

$$J_l\left(\alpha'_m\right) = \frac{\alpha'_m}{2l}\left(J_{l-1}\left(\alpha'_m\right) + J_{l+1}\left(\alpha'_m\right)\right)$$

$$K_l\left(\gamma'_m\right) = \frac{\gamma'_m}{2l}\left(K_{l-1}\left(\gamma'_m\right) - K_{l+1}\left(\gamma'_m\right)\right)$$

The utilization of them in Equation (A.85), serves to simplify the final expression necessary to fully solve for the electric field in the fiber to

$$\frac{\alpha'_m J_{l-1}\left(\alpha'_m\right)}{J_l\left(\alpha'_m\right)} = -\frac{\gamma'_m K_{l-1}\left(\gamma'_m\right)}{K_l\left(\gamma'_m\right)}. \tag{A.86}$$

The Equations (A.84) and (A.86) form a system of equations that can be used to find solutions for possible modes in an optical fiber. It is given by

$$\left| \begin{array}{c} \frac{\alpha'_m J_{l-1}(\alpha'_m)}{J_l(\alpha'_m)} = -\frac{\gamma'_m K_{l-1}(\gamma'_m)}{K_l(\gamma'_m)} \\ V = \sqrt{\alpha'^2_m + \gamma'^2_m} \end{array} \right|. \tag{A.87}$$

The quantity V, also called the $V-$parameter, is determined by the fiber and the light that is coupled into it. An alternative approach to identifying the solutions is solving the equation

$$\frac{\alpha'_m J_{l-1}\left(\alpha'_m\right)}{J_l\left(\alpha'_m\right)} = -\frac{\sqrt{V^2 - \alpha'^2_m} K_{l-1}\left(\sqrt{V^2 - \alpha'^2_m}\right)}{K_l\left(\sqrt{V^2 - \alpha'^2_m}\right)}, \tag{A.88}$$

for the parameter α'_m.For a given azimuthal mode l, it is possible that there exist multiple solutions. These solutions are then numbered sequentially, by the number m, denoting the mode number. These solutions describe the roots of the Bessel functions, particularly the zero crossings of the electrical field along the radial axis. This characterizes the linearly polarized LP_{lm} modes in the fiber, where l and m are integers, with the first possible mode being the LP_{01}. A selection of modes is shown in Figure A.13. In essence, they can also be considered TEM modes. However, in the context of waveguides, the existence of transverse electric (TE) and transverse magnetic (TM) modes is predicated on the presence of strong boundaries. In such cases, it is observed that the respective field is not perpendicular to the direction of propagation. This is particularly evident in strongly guided geometries and necessitates sophisticated treatment. The optical fiber under consideration exhibits a tendency to guide light weakly. This can be attributed to the presence of a relatively small discrepancy in refractive index between the core and the cladding of the fiber. This enables the hypothesis that hybrid modes, which include modes with transverse electric and magnetic fields, can propagate. Consequently, this results in a fixed linear polarization of the light in the waveguide.

In addition, upon substituting the expressions for α_m and γ_m, the V-parameter can be expressed in terms of the MIR, wavelength of the light, and core radius as follows:

$$V = \frac{2\pi}{\lambda} r_c NA$$

For a given fiber, thus fixed materials and radii, the $V-$parameter undergoes modification solely in relation to the utilized light. A noteworthy observation during the resolution of Equation (A.88) is the revelation that the number of solutions exhibits a direct correlation with V. Specifically, it was found that there exists a solitary solution for values of $V_{cutoff} \lesssim 2.405$, which corresponds to the LP_{01} mode. The application of this effect is twofold: first, it can be used to ensure the presence of high-order modes; second, it can be used to ensure single-mode operation of the fiber. For latter,

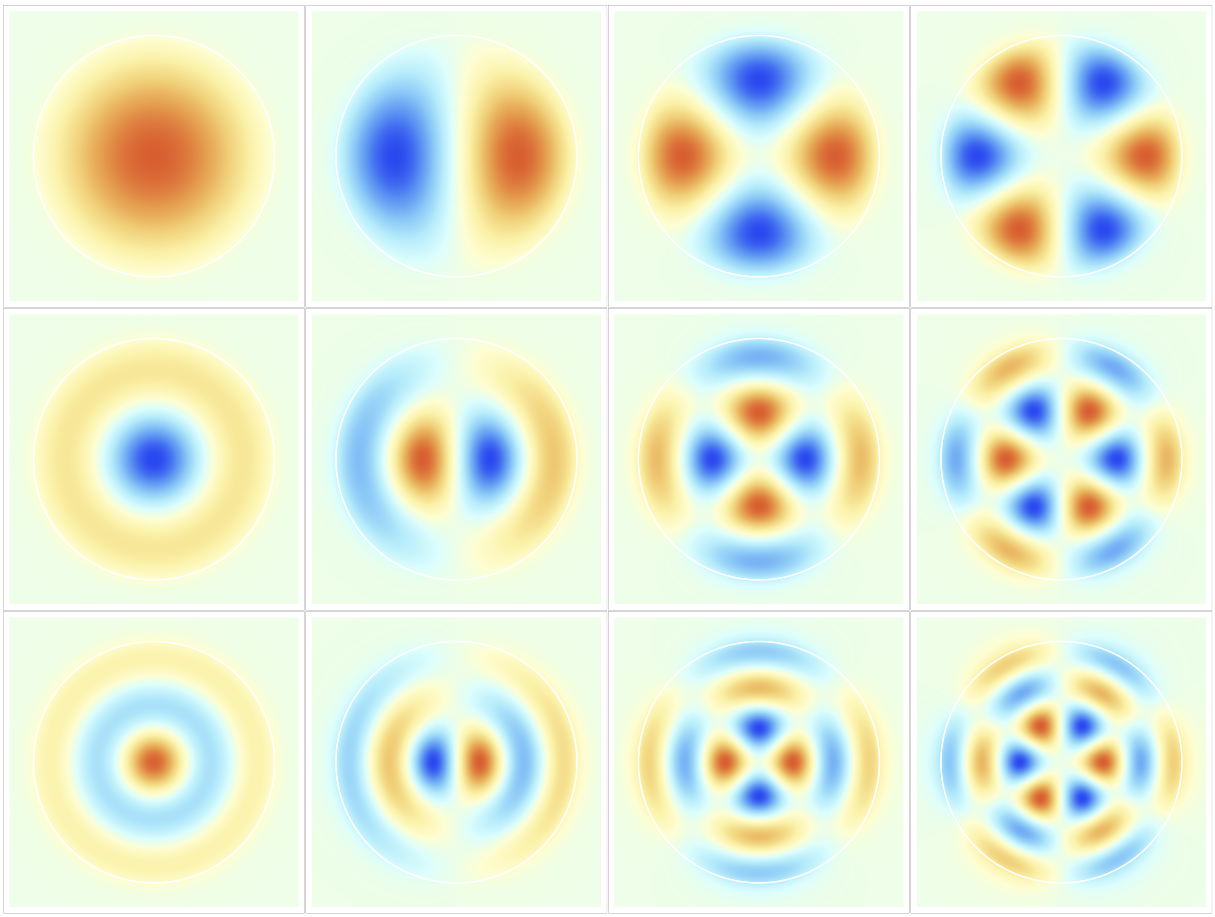


Figure A.13: Simulation of the electric field of the transverse cross-section of light in a fiber at $z = 0$ for some LP_{lm} modes. The fiber is a SMF-28 single mode (SM) fiber designed for light at 1.5 µm with a cutoff wavelength of approximately 1300 nm. The light that is coupled into the fiber has a wavelength of 213 nm which is necessary for this specific multi-mode operation. The core radius is indicated by the white line. Blue or red coloration indicates the sign of the electric field amplitude, while the saturation shows its strength.

the prerequisite is: the wavelength of the coupled light must be greater than or equal to the cutoff wavelength, $\lambda \geq \lambda_{cutoff}$. The propagation of higher order modes is dependent on the respective $V-$parameter at a given wavelength. The presence of light with a shorter wavelength facilitates the propagation of an increasing number of higher order modes. In comparison, most LP and TEM modes differ in shape, such that coupling a high-order free space mode into any fiber mode will result in some form of loss and inconvenience as their intensity profiles do not match.

This issue is effectively addressed by employing the respective fundamental modes, which exhibit a high degree of similarity. Indeed, the power and shape of the fundamental fiber mode demonstrate a close correspondence with the Gaussian mode, provided that the minimum beam waist is marginally larger than the core radius and situated at the fiber tip. In the event that the beam waist of theGB is smaller or larger, solely the portion of the GB that fits into the fiber mode will be guided through the fiber. Additionally, the beam divergence may not conform to the accepted

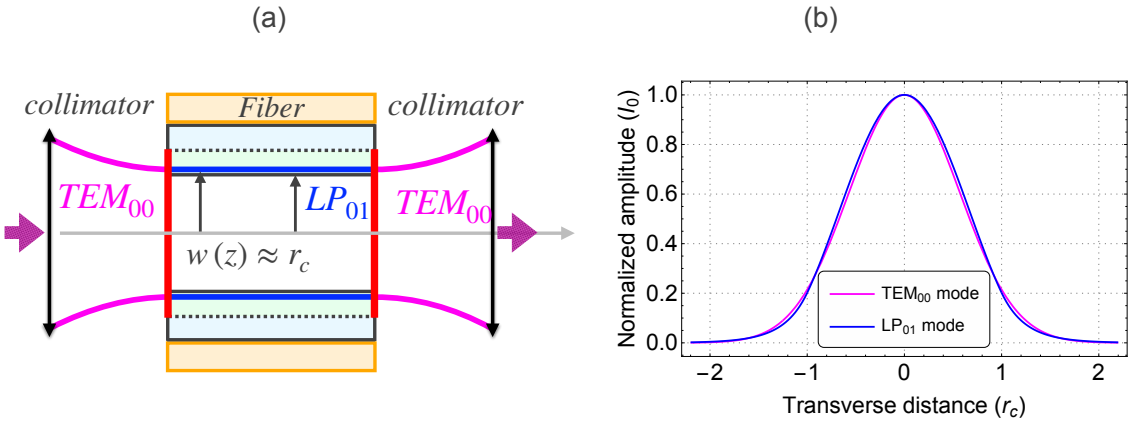


Figure A.14: The process of coupling a TEM_{00} mode into an LP_{01} mode of an SMF-28 SM fiber. The light has a wavelength of 1.5 µm. The beam waist is of an ideal size to maximize the overlap integral. For this configuration, this is the case at $w_0 = 1.14\,r_c$. (a): Schematic representation of the process. (b): A simulation of the intensity along the radial direction.

range of angles if the beam waist is particularly narrow. The numeric coupling efficiency, δ_{CE}, is derived as the ratio of the overlap between the power of the intensity profiles and the power of the individual fundamental profiles, that is,

$$\delta_{CE} = \frac{P^2_{overlap}}{P_{TEM} \cdot P_{LP}}.$$

Assuming the minimum beam waist and position of the tip of the fiber at $z = z_0$, the formalism becomes

$$\begin{aligned}\delta_{CE}(w_0) &= \frac{\left(\frac{1}{2}c_0\varepsilon_0 \int_0^{2\pi}\int_0^{\infty} \boldsymbol{E}_{TEM}\cdot\boldsymbol{E}^*_{LP} r\,dr\,d\varphi\right)^2}{\frac{1}{2}c_0\varepsilon_0 \int_0^{2\pi}\int_0^{\infty} |\boldsymbol{E}_{TEM}|^2 r\,dr\,d\varphi \cdot \frac{1}{2}c_0\varepsilon_0 \int_0^{2\pi}\int_0^{\infty} |\boldsymbol{E}_{LP}|^2 r\,dr\,d\varphi} \\ &= \frac{\left(\left|\frac{J_l(\alpha'_m)}{J_l(0)}\right|^2 \left(\int_0^{r_c} r e^{-\frac{r^2}{w_0^2}} \frac{J_l(\alpha'_m r_n)}{J_l(\alpha'_m)} dr + \int_{r_c}^{\infty} r e^{-\frac{r^2}{w_0^2}} \frac{K_l(\gamma'_m r_n)}{K_l(\gamma'_m)} dr\right)\right)^2}{\frac{w_0^2}{4}\cdot\left(\int_0^{r_c} r \left|\frac{J_l(\alpha'_m r_n)}{J_l(\alpha'_m)}\right|^2 dr + \int_{r_c}^{\infty} r \left|\frac{K_l(\gamma'_m r_n)}{K_l(\gamma'_m)}\right|^2 dr\right)}.\end{aligned}$$

The solution of this equation, maximized with respect to w_0, for a SMF-28 fiber and an input wavelength of 1.5 µm is approximately $\delta_{CE,max} \approx 99.6\,\%$. This is also illustrated in Figure A.14. In this particular instance, the beam waist has been determined to have a value of $w_0 \approx 1.14\,r_c$. These values are subject to slight variation depending on the wavelength and the type of fiber. However, under general principles, an optimized coupling is achieved when the beam waist at the fiber tip is approximately equivalent to the core radius of the fiber. From a technical standpoint, the specific type of beam waist is inconsequential, provided the dimensions align. However, the divergence of the beam at the fiber's entrance, θ_{TEM}, must align with the NA. Consequently, for any position z',

it must be

$$\theta_{TEM} \leq \theta_{max} \Longleftrightarrow \arctan\left(\left.\frac{dw(z)}{dz}\right|_{z=z'}\right) \leq \arcsin\left(\frac{\sqrt{n_1^2 - n_2^2}}{n_0}\right),$$

with $w(z') \approx r_c$. Typically, collimators equipped with fixed or adjustable lenses are employed to couple free space light into fibers. In practice, the occurrence of in-coupling is typically in the range of 70 % of the incident light power that passes through the fiber, due to imperfections in the mode shapes or clipping of light.

A.2.4 Keeping Light In: Conditions for Cavity Stability

Given the knowledge acquired on GBs, it is now appropriate to undertake a more thorough examination of the resonator described in Section 2.1.1. The light within a resonator of length L will travel multiple times between the mirrors, thereby interfering with each other. The initial mode that couples into the cavity is designated as the resonator mode, q_1. The process is analogous to the earlier matching of the Gaussian and fiber modes. It is crucial that the light inside the resonator always matches the resonator mode. In the event of a change in the characteristics of the mode due to a reflection at a mirror or the propagation through the resonator, the total interference will undergo an exponential decrease with the number of round-trips in relation to the mismatch of the modes. In the context of a stable resonator, this is contingent upon the principle of self-consistency. That is to say, the shape of the mode inside is fixed in order to generate a maximum overlap to maintain the standing wave. In the context of the q-parameter evolution, shown in Equation (A.67), the self-consistency is expressed as

$$q_1 = \frac{Aq_1 + B}{Cq_1 + D}.$$

The solution to this equation for q_1^{-1} can be found by utilizing the relationship of unimodularity, which states that $AD - BC = 1$, such that it follows

$$\frac{1}{q_1} = \underbrace{\frac{D-A}{2B}}_{1/R(z_1)} \pm \underbrace{\frac{1}{2B}\sqrt{(A+D)^2 - 4}}_{-2i/kw^2(z_1)}. \tag{A.89}$$

In this equation, z_1 denotes the initial point of the system, which in this case is the front mirror of the resonator. Equation (A.89) allows for a comparison of beam waist and radius of curvature. It is evident that a non-zero beam waist can only exist when the term in the square root is negative, such as

$$|A + D| < 2, \tag{A.90}$$

which is called the stability criteria of a standing wave resonator. The radius of curvature and beam waist are then

$$R(z_1) = \frac{2B}{D-A} \text{ and } w(z_1) = \sqrt{\frac{4|B|}{k\sqrt{4 - (A+D)^2}}}, \tag{A.91}$$

where the absolute value $|B|$ evolves from the fact that only the square root of the total positive term is taken. In order to obtain explicit values for the matrix entries, it is necessary to configure the resonator matrix $\boldsymbol{M}_{res}$. A standard standing wave FP resonator is composed of two mirrors and two free space propagations between them for a complete round trip from and to the front mirror. The result of this calculation is as follows:

$$\begin{aligned}\boldsymbol{M}_{res} &= \underbrace{\begin{pmatrix} 1 & 0 \\ -\frac{2}{R_1} & 1 \end{pmatrix}}_{\text{mirror 1}} \underbrace{\begin{pmatrix} 1 & L \\ 0 & 1 \end{pmatrix}}_{\text{free-space}} \underbrace{\begin{pmatrix} 1 & 0 \\ -\frac{2}{R_2} & 1 \end{pmatrix}}_{\text{mirror 2}} \underbrace{\begin{pmatrix} 1 & L \\ 0 & 1 \end{pmatrix}}_{\text{free-space}} \\ &= \begin{pmatrix} 1-\frac{2L}{R_2} & L+L-\frac{2L^2}{R_2} \\ \frac{4L}{R_1R_2}-\frac{2}{R_1}-\frac{2}{R_2} & 1+\frac{4L^2}{R_1R_2}-\frac{4L}{R_1}-\frac{2L}{R_2} \end{pmatrix}.\end{aligned}$$

Please note that the radii of the mirrors, R_1 and R_2, must not be confused with the radii of curvature at the mirrors' positions, $R(z_1)$ and $R(z_2)$, respectively. A frequent replacement is the g-parameters

$$g_1 = 1-\frac{L}{R_1} \text{ and } g_2 = 1-\frac{L}{R_2}, \tag{A.92}$$

thereby yielding the final form

$$\boldsymbol{M}_{res} = \begin{pmatrix} 2g_2-1 & 2g_2L \\ \frac{2}{L}(2g_1g_2-g_1-g_2) & 4g_1g_2-2g_2-1 \end{pmatrix}. \tag{A.93}$$

Subsequently, the stability criteria from Equation (A.90) for the two-mirror standing wave resonator is modified to $|4g_1g_2-2|<2$. An investigation of both cases for the sign of the absolute value ultimately resulted in the following conclusion:

$$0 < g_1g_2 < 1.$$

In some literature one finds the relationship $0 \leq g_1g_2 \leq 1$, where the boundaries are also mathematical solutions. However, these boundaries are characterized by a vanishing beam waist, a feature that is not consistent with realistic physical scenarios. An illustration of the stability criteria is shown in Figure A.15 (b). Inserting the explicit forms of both g-parameters from Equation (A.92) will yield

$$L < R_1+R_2 < \frac{R_1R_2}{L}+L,$$

and in particular, the following expressions will be true:

$$R_1+R_2 > L \text{ and } \frac{R_1R_2}{L} > 0$$

Latter formalism demonstrates that, given the non-negativity of the length, the utilization of either two convex or two concave mirrors is necessary. Any combination of them is strictly prohibited. Nonetheless, the initial equation must be positive and exceed L. This stipulation is only met if both radii are positive. Consequently, for the standing wave resonator, it is necessary to employ two concave mirrors that are oriented in the direction of the respective light. This can be explained by considering the self-consistency of the light inside the resonator. The radius of curvature at the

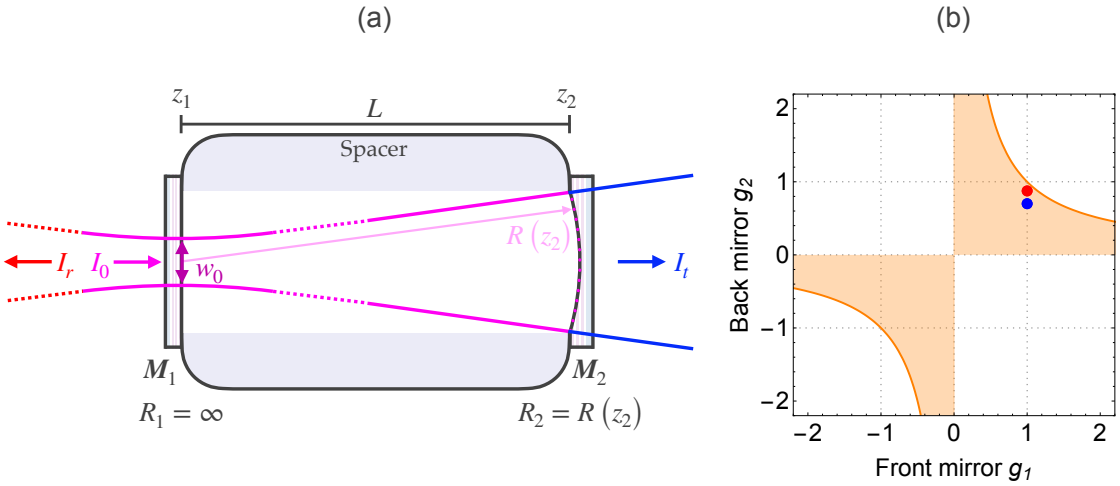


Figure A.15: The design of an optical resonator illustrating two key aspects: (a): the ability to replicate the mode within the resonator and (b): the application of stability criteria. The red (Section 3.2.3) and blue (Section 3.1.3) dots denote the actual working points for the resonators utilized in this study.

position of a mirror must conform to its curvature. It is possible for this to occur if the beam waist minimum is present at any point within the resonator, including at the mirrors. In the event that the waist is outside of the resonator, the curvature sign will not align with at least one mirror, thereby significantly reducing the coupling efficiency in the resonator mode. Upon revisiting Equation (A.91) and inserting Equation (A.93), it can be concluded that

$$R(z_1) = \frac{L}{g_1 - 1} = -R_1 \text{ and } w(z_1) = \sqrt{\frac{4|2g_2L|}{k\sqrt{4-(4g_1g_2-2)^2}}}.$$

In addition, the $q-$parameter at the second mirror is determined by a single free-space propagation of length L, as illustrated by

$$\frac{1}{q_2} = \frac{1}{q_1}\frac{1}{1+\frac{1}{q_1}L}.$$

The resolution of this rather protracted algebraic equation results in

$$R(z_2) = \left(\frac{1}{L} - \frac{g_1g_2}{L} - \frac{g_2}{R_1}\right)^{-1} = R_2 \text{ and } w(z_2) = \sqrt{\frac{2}{k}\frac{LR_1g_1}{(L+R_1g_1)\sqrt{g_1g_2-g_1^2g_2^2}}}.$$

The radii of curvature reveal $R(z_1) = -R_1$ and $R(z_2) = R_2$, thereby substantiating the claim that the minimum beam waist must be situated within the resonator. In the event that one of the mirrors is flat (i.e., the front mirror), thereby resulting in an infinite radius of curvature, the beam waist minimum must be at the location of the front mirror. Subsequently, the curvature of the second mirror must align with the wavefront curvature of the light at a distance L from the first mirror. Such a resonator is depicted in Figure A.15 (a). The efficacy of this configuration is rooted in

its ability to streamline the mode matching to the resonator mode by ensuring the position and size of the beam waist at the front mirror. This can be accomplished through the use of one or several lenses, carefully shaping the beam to achieve the desired results. For a specific geometry and wavelength, the beam waist at the front mirror must correspond to

$$w(z_1) \coloneqq w_{res} = \sqrt{\frac{L\lambda\left|1-\frac{L}{R_2}\right|}{\pi\sqrt{\frac{L}{R_2}-\frac{L^2}{R_2^2}}}}. \tag{A.94}$$

In the present study, three standing resonators were utilized, of which two, identical ones, are 30 cm long and designed for 1064 nm wavelengths, and one is 12 cm long and designed for 1.5 µm wavelengths. The front mirrors exhibit a flat profile, while the rear mirrors possess radii of curvature measuring 1 m and 2 m, respectively. The working points in the stability diagram are indicated in panel (b) of the figure. Here, the blue dot corresponds to the 30 cm long resonator, and the red dot to the 12 cm long one. The respective beam waist values at the front mirrors are calculated to be $w_{res,1064} \approx 394\,\mu\text{m}$ and $w_{res,1561} \approx 405\,\mu\text{m}$.

A.2.5 Mode Matching: Efficient Coupling Between Beams and Cavities

With the resonator in place and the relevant theory established, any incident light that closely approximates the fundamental GB can be coupled into the cavity. A straightforward approach would be the single-lens mode-matching, however, in space-restricted systems, the use of multiple lenses can enhance compactness. The disadvantage of this approach is that it is more sensitive to misalignments and results in a more complex system. In the single-lens case, the concept could be as follows. Initially, laser light propagates through a fiber with a collimator at the end. This ensures that the beam waist at the output is well-defined, as it is given by the core radius of the fiber in combination with the focal length of the collimator.

Commercial collimators are instruments that are typically, not exclusively, characterized by the location and size of the beam waist, w_c, at which light will leave the collimator and enter free space. By establishing the position of this beam waist at $z_0 = 0$ and denoting the position of the front mirror of the resonator as z_1, it is possible to position a lens at any point z_l between these two points. The propagation matrix for this configuration is as follows:

$$\boldsymbol{M}_{mm} = \underbrace{\begin{pmatrix} 1 & z_m \\ 0 & 1 \end{pmatrix}}_{\text{free-space}} \underbrace{\begin{pmatrix} 1 & 0 \\ -\frac{1}{f} & 1 \end{pmatrix}}_{\text{lens}} \underbrace{\begin{pmatrix} 1 & z_l \\ 0 & 1 \end{pmatrix}}_{\text{free-space}} = \begin{pmatrix} 1-\frac{z_m}{f} & z_r + z_l - \frac{z_m z_l}{f} \\ -\frac{1}{f} & 1-\frac{z_l}{f} \end{pmatrix}$$

In this equation $z_m = z_1 - z_l$ represents the distance between the lens and the front mirror. The transformation of beam parameters $q_0 = iz_{r_0}$ and $q_1 = iz_{r_1}$ is expressed as

$$q_1 = \frac{A_{mm}q_0 + B_{mm}}{C_{mm}q_0 + D_{mm}},$$

which yields the identity

$$\underbrace{iz_{r_1}f - iz_{r_1}z_l - ifz_{r_0} + iz_{r_0}z_m}_{=0} = \underbrace{fz_m + fz_l - z_m z_l - z_{r_0}z_{r_1}}_{=0}. \tag{A.95}$$

The parameters q_0 and q_1 correspond to the beams at the collimator and front mirror, respectively. All parameters are physical lengths; consequently, they are considered real. Imaginary and real parts of a complex number are inherently disconnected. Consequently, for the Equation (A.95) to be true, it is necessary that both sides of the equation equal zero. This process results in the establishment of the system of equations

$$\left| \begin{array}{ll} f = \frac{z_{r_1}z_l - z_{r_0}z_m}{z_{r_1} - z_{r_0}} & (a) \\ f = \frac{z_m z_l + z_{r_0}z_{r_1}}{z_m + z_l} & (b) \end{array} \right|. \tag{A.96}$$

Inserting Equation (a) into (b) and subsequent rearrangement of the resulting expression yields the formalism

$$z_l(z_m) = \sqrt{z_{r_0}\left(z_{r_1} - z_{r_0} + \frac{z_m^2}{z_{r_1}}\right)}, \tag{A.97}$$

which in turn affords a function that characterizes the position of the lens and the distance between the collimator or incident beam waist and the cavity mirror. Inserting Equation (A.97) into (A.96) (a) yields an expression for the focal length $f(z_m)$ given by

$$f(z_m) = \frac{z_{r_1}\sqrt{z_{r_0}\left(z_{r_1} - z_{r_0} + \frac{z_m^2}{z_{r_1}}\right)} - z_{r_0}z_m}{z_{r_1} - z_{r_0}}. \tag{A.98}$$

In general, the number of solutions is infinite. However, for any given distance between the collimator and the lens, the remaining two parameters are uniquely fixed. The two functions in (A.97) and (A.98) are plotted in Figure A.16. No upper limit exists for the total distance $z_m + z_l$; however, a minimum is required for the existence of real solutions. The minimum can be determined through the observation of the square root in Equation (A.97). This root must be equal to or greater than zero in order to ensure the existence of a physically reasonable solution. In particular, given that z_l is monotonous in z_m, the exact minimum $z_{m,min}$ is thereby established as

$$z_{r_0}\left(z_{r_1} - z_{r_0} + \frac{z_{m,min}^2}{z_{r_1}}\right) = 0 \Longleftrightarrow z_{m,min} = \sqrt{z_{r_1}z_{r_0} - z_{r_1}^2}.$$

In this case, the positive solution for $z_{m,min}$ is considered, as it concerns only configurations in which the cavity and collimator are positioned on opposite sides of the lens. In the event that $z_l = 0$, the positioning of the lens at the waist of the beam may prove to be impractical if it is too close to the collimator. Nevertheless, the total minimum distance between the incident waist and cavity and

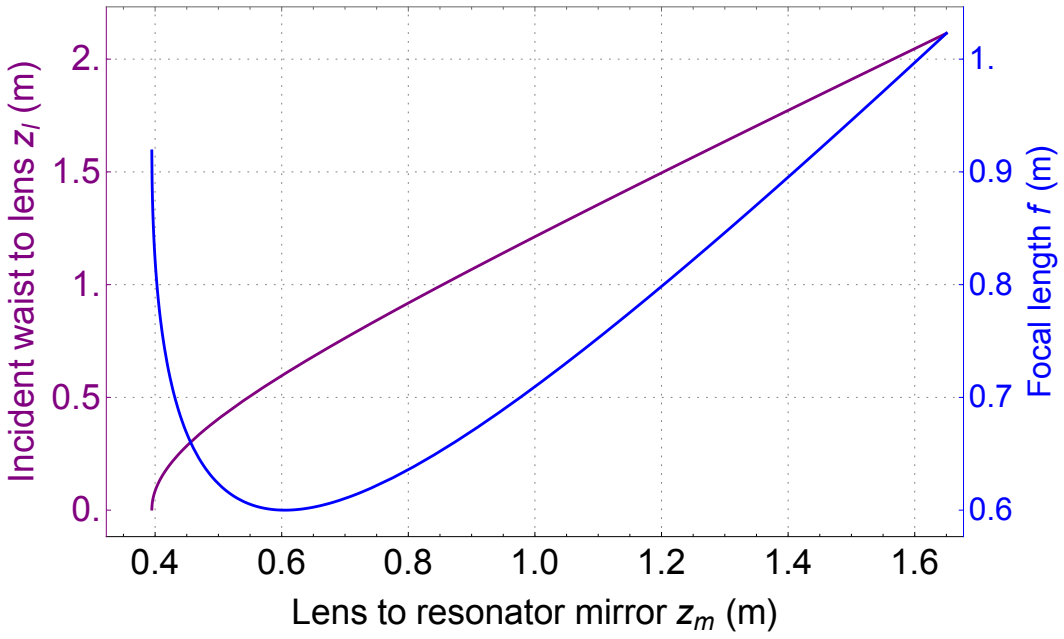


Figure A.16: Simulation of the distance between the incident beam waist and the lens (purple, Equation (A.97)) and the focal length (blue, Equation (A.98)) as a function of the lens-to-cavity distance. The functions are associated with a real-world example. If the incident waist of 520 µm for light of wavelength 1064 nm must be matched with the beam waist of 394 µm at the resonator.

the focal length of the lens required to achieve this objective are given by

$$z_1\left(z_{m,min}\right) = \sqrt{z_{r_1} z_{r_0} - z_{r_1}^2}, \text{ and } f\left(z_{m,min}\right) = -\frac{z_{r_0}\sqrt{z_{r_1} z_{r_0} - z_{r_1}^2}}{z_{r_1} - z_{r_0}}.$$

The minimum distance is not associated with the minimized focal length, which is calculated by

$$\frac{df\left(z_m\right)}{dz_m} = \frac{z_{r_0}}{z_{r_1} - z_{r_0}}\left(\frac{z_{m,fmin}}{\sqrt{z_{r_0}\left(z_{r_1} - z_{r_0} + \frac{z_{m,fmin}^2}{z_{r_1}}\right)}} - 1\right) \stackrel{!}{=} 0,$$

yielding the result

$$z_{m,fmin} = \sqrt{\frac{z_{r_0} z_{r_1}^2 - z_{r_1} z_{r_0}^2}{z_{r_1} - z_{r_0}}} \Longrightarrow f_{min} = \sqrt{\frac{z_{r_0} z_{r_1}^2 - z_{r_1} z_{r_0}^2}{z_{r_1} - z_{r_0}}} = z_{m,fmin}.$$

This is reasonable given that the minimum focal length is specified as the distance between the lens and the mirror. In this particular instance, the lens is oriented in such a manner that it directly focuses on the mirror. In the event that the beam is well collimated, a rapid in-coupling may be achieved by employing any lens with a focal length of $f \geq f_{min}$ and positioning it at a distance

f from the cavity. It is noteworthy that commercial lenses are frequently available in a range of distinct focal lengths. Therefore, in order to construct a compact system with optimal functionality, it is necessary to first determine the value of $f\left(z_{m,min}\right)$ and subsequently identify the catalogue lens with the closest focal length, thus $f_{catalogue} \leq f\left(z_{m,min}\right)$. Subsequently, z_l and z_m can be calculated for the specified lens.

A.2.6 A Quick Note on Cavity Modes

In the context of free-space light, the fundamental Gaussian mode is typically observed. In addition, as previously determined, the arrangement of SM fibers directs the propagation of light in a manner that can be approximated by the fundamental mode. In the context of an optical resonator, the optimal coupling is contingent upon the congruence between the resonator mode and the incident light's shape. However, minor inclinations with respect to the cavity axis can result in the accumulation of higher-order modes within the resonator.

These phenomena can be readily observed during the transmission of the cavity using a camera. Higher-order modes do not necessarily compromise the system's performance; indeed, there are certain aspects in which they could be argued to be superior to the fundamental mode. Resonators are also among the most prevalent methods for generating Hermite-Gaussian modes. Nevertheless, in practice, the generation of a fundamental mode in the resonator is often desired. This is due to the fact that it is the simplest mode with the highest degree of symmetry, which is easiest to find and reproduce.

This is especially true when considering that the intensity profiles of higher-order modes can be confused, as well as the best achievable coupling efficiency due to the mode overlap with the incident beam. In order to couple the majority of the transmitted light into a fiber, it is essential that the fundamental mode be utilized. Within the laboratory setting, the process of in-coupling is accomplished through the strategic alignment of two or more mirrors, which collectively ensure the precise orientation of light waves into and within the cavity.

A.3 Optical Components: Routing, and Modulating Light

As part of the present thesis, a variety of optical elements are employed. These components can be categorized into two distinct groups: free-space and fiber coupled components. Some of these devices function passively, while others require the use of an electrical driver. To this point, the discussion has centered on the introduction and explanation of lenses, mirrors, and small slabs of materials of a particular refractive index in the context of their interaction with light.

The utilization of collimators within the domain of optical fibers, which are technically lenses, is primarily aimed at the precise coupling of light into or out of a fiber. Another elementary component is the beam splitter (BS), which is essentially a mirror with a coating that is not designed to maximize reflection. Rather, it is designed to maintain reflection and transmission within specific design parameters. The following subsection will provide an overview of the most commonly employed optical components within the scope of this work.

This text provides an introduction to waveplates and PBSs, as well as to their combined use in the division of specific fractions of light into disparate paths. The following discussion will introduce the concepts of acousto-optic and electro-optic effects, which serve to shift or modulate the frequencies of EM waves. Subsequently, a discussion will ensue regarding the integration of fiber optic components, with a particular emphasis on fiber couplers, and their application in establishing a fiber-based ring resonator. Interesting literature includes [233].

A.3.1 Directing Polarized Light: Wave Plates, Isolators, and Beam Splitters

As previously mentioned in Section A.1.1, the polarization axis of an EM wave is determined by the orientation of the electric field's oscillation axis. This is a consequence of the energy transport along the electric field. Specialized optical components can be utilized to modify or separate the polarization components of the light. In this work, the focus is on waveplates and PBSs, which operate on the principle of birefringence. A birefringent crystal is characterized by the presence of two distinct axes, each with a different refractive index.

The velocity of light propagating through a crystal is dependent on the direction of its movement relative to the crystal's refractive index. When light moves parallel to the lower refractive index, its velocity is higher in comparison to its velocity when moving parallel to the higher refractive index. This is referred to as the "fast" and "slow" axes, respectively. Consequently, both components undergo a relative phase shift after traversing the medium. This phase shift directly impacts the polarization of the light. In the context of a wave propagating along the z-direction, the formalism governing this wave is expressed as

$$\boldsymbol{E}(\boldsymbol{r},t) = E_0 \boldsymbol{J} e^{-i(\boldsymbol{k_n} \boldsymbol{r} + \omega t)}, \text{ with } \boldsymbol{J} = \alpha \boldsymbol{p}, |\boldsymbol{J}| = 1.$$

In this equation, ω is the frequency of the wave, k indicates the wave number, and $\boldsymbol{J}$ denotes the Jones vector, which describes the propagation of the field amplitude along the horizontal (p) and vertical (s) axis. This is represented by its polarization $\boldsymbol{p}$ and a complex factor α. As the light traverses a wave plate, the manipulation of the polarization axes is characterized by the Jones matrix $\boldsymbol{M}$, which is dependent on the polarizer. The resulting Jones vector $\boldsymbol{J}_1$ thus expressed as $\boldsymbol{J}_1 = \boldsymbol{M} \cdot \boldsymbol{J}_0$. In the specific case of a half-wave plate $\left(\boldsymbol{M}_{\lambda/2}\right)$ and a quarter-wave plate $\left(\boldsymbol{M}_{\lambda/4}\right)$, for which the fast axis and the horizontal axis align, and the initial light is characterized by

$$\boldsymbol{J}_0 = \boldsymbol{p}_0 = \begin{pmatrix} p_p \\ p_s \end{pmatrix},$$

the respective Jones matrices and transformations to $\boldsymbol{J}_1$ are given by

$$\boldsymbol{M}_{\lambda/2} = -i \begin{pmatrix} 1 & 0 \\ 0 & -1 \end{pmatrix} \longrightarrow \boldsymbol{J}_1 = -i \begin{pmatrix} p_p \\ -p_s \end{pmatrix}, \tag{A.99}$$

and

$$\boldsymbol{M}_{\lambda/4} = e^{-i\pi/4} \begin{pmatrix} 1 & 0 \\ 0 & i \end{pmatrix} \longrightarrow \boldsymbol{J}_1 = \frac{1}{\sqrt{2}}(1-i) \begin{pmatrix} p_p \\ i p_s \end{pmatrix}. \tag{A.100}$$

The electric field that propagates through the half-wave plate can be presented by a linearly polarized light, illustrated in Figure A.17 (a), with a global phase shift of $-\frac{\pi}{2}$, expressed as

$$\boldsymbol{E}(\boldsymbol{r},t)_{\lambda/2} = E_0 \hat{\boldsymbol{p}}_{\lambda/2} e^{-i(\boldsymbol{k_n r}+\omega t+\frac{\pi}{2})}, \text{ with } \hat{\boldsymbol{p}}_{\lambda/2} = \begin{pmatrix} p_p \\ -p_s \end{pmatrix}.$$

The polarization vector is rotated by an angle equal to twice the incident angle, θ_0, between the polarization vector $\boldsymbol{p}$ and the fast axis. This may be demonstrated through the observation of light propagation along the z-axis, with the polarization vector positioned in the $xy-$plane. The angle towards the fast axis is congruent to the angle between p_p and the $x-$axis. In regard to the incident light, it holds

$$\cos(\theta_0) = \frac{p_p}{|\boldsymbol{p}|} \sin(\theta_1) = \frac{p_s}{|\boldsymbol{p}|},$$

whereas for the resulting beam it is

$$\cos(\theta_{\lambda/2}) = \frac{p_p}{|\boldsymbol{p}|} \sin(\theta_{\lambda/2}) = -\frac{p_s}{|\boldsymbol{p}|}.$$

This yields $\theta_{\lambda/2} = -\theta_0$, for the angle of the polarization vector after traversing the the half-wave plate $\theta_{\lambda/2}$, which results in a total rotation of $2\theta_0$. Nonetheless, the light propagating through the half-wave plate continues to exhibit linear polarization. A half-waveplate that is adjustable and rotatable, with its orientation perpendicular to the propagation direction, serves as a tool for actively tuning and setting the polarization vector of linearly polarized light. The effect of the quarter-waveplate on the beam's polarization is less apparent.

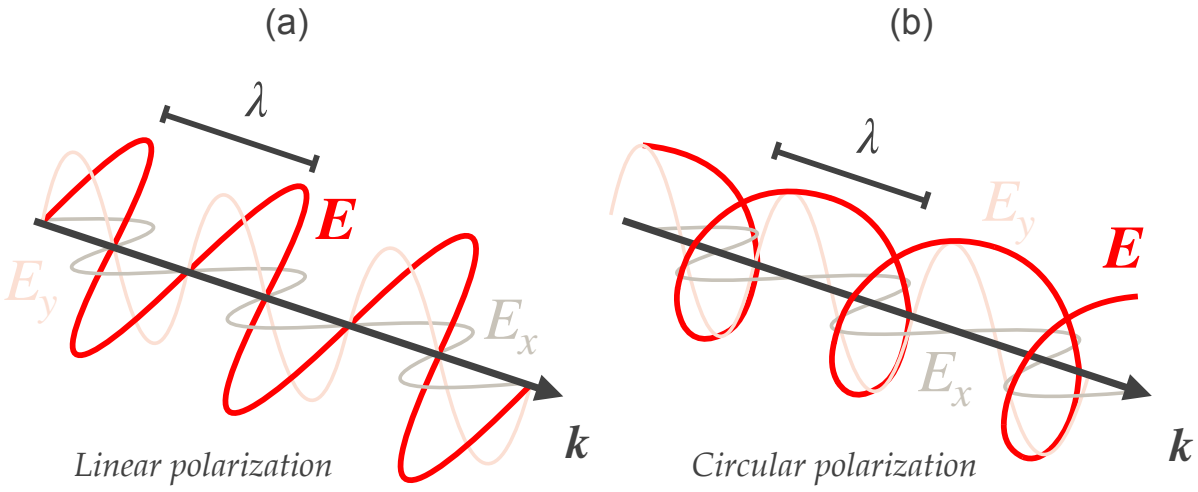


Figure A.17: Presentation of the total electric field and polarization axes, which are the result of the combination of the horizontal and vertical components. (a): Linearly polarized light, therefore the components E_x and E_y are in phase. (b): Circularly polarized light, in particular with a phase shift of $\frac{\pi}{2}$ between the electric field components.

The division of the polarization into its real and imaginary components results in

$$\boldsymbol{E}(\boldsymbol{r},t)_{\lambda/4} = E_0 \frac{1}{\sqrt{2}} \begin{pmatrix} p_p \\ p_s \end{pmatrix} e^{-i(\boldsymbol{k_n r}+\omega t)} + E_0 \frac{1}{\sqrt{2}} \begin{pmatrix} -p_p \\ p_s \end{pmatrix} e^{-i\left(\boldsymbol{k_n r}+\omega t-\frac{\pi}{2}\right)}.$$

The physical field is the real part of this expression, which is given by:

$$\Re\left[\boldsymbol{E}(\boldsymbol{r},t)_{\lambda/4}\right] = \Re\left[E_0\right] \frac{1}{\sqrt{2}} \left(\begin{pmatrix} p_p \\ p_s \end{pmatrix} \cos(\boldsymbol{k_n r}+\omega t) + \begin{pmatrix} -p_p \\ p_s \end{pmatrix} \sin(\boldsymbol{k_n r}+\omega t) \right)$$

When plotting the electric field vector of this, a spiral along the propagation axis is obtained. The circular polarization is illustrated as in Figure A.17 (b), the rotation of the polarization by a waveplate is shown in Figure A.18 (a). A noteworthy observation is the transformation of previously circularly polarized light into a linear polarization state when it propagates through a quarter-waveplate. According to the formalism, the equation

$$\boldsymbol{E}(\boldsymbol{r},t)_{\lambda/4} = E_0 \frac{1-i}{2} \left(\begin{pmatrix} p_p \\ ip_s \end{pmatrix} e^{-i(\boldsymbol{k_n r}+\omega t)} + \begin{pmatrix} -p_p \\ ip_s \end{pmatrix} e^{-i\left(\boldsymbol{k_n r}+\omega t-\frac{\pi}{2}\right)} \right),$$

can be reduced to

$$\boldsymbol{E}(\boldsymbol{r},t)_{2\times\lambda/4} = E_0 \hat{\boldsymbol{p}}_{\lambda/2} e^{-i\left(\boldsymbol{k_n r}+\omega t+\frac{\pi}{2}\right)}.$$

This indicates that two quarter-waveplates positioned behind each other are equivalent to a single half-waveplate. Quarter-waveplates are utilized in a variety of applications, including the generation of linear polarized light and the rotation of the polarization of linearly polarized light reflected off a mirror. This occurs due to the fact that light propagates twice through the waveplate. It is not feasible to achieve this outcome with a half-waveplate, as the two propagations through it will result in the same polarization vector as the incident light.

A PBS is an optical component that functions by manipulating the polarization of light, as illustrated in Figure A.18 (b). This glass cube is characterized by an angled surface with a particular dielectric coating. Specifically, $s-$polarized light undergoes full reflection, whereas $p-$polarized light transmits through the cube. Consequently, linearly polarized light is partitioned into two components, with the power ratio contingent on the incident polarization angle in relation to the axes of the PBS.

In the case of linearly polarized light, a PBS is employed in conjunction with a half-waveplate in the incident beam to regulate the power distribution. In the case that light is reflected back towards PBS, it will retrace the same path it initially took. This indicates that reflected light will undergo reflection once more, and transmitted light will pass through again. This can be mitigated by rotating the polarization of the back reflected beam by $90°$. In this manner, the $s-$ and $p-$polarization will exchange places.

This objective can be accomplished by strategically positioning a quarter-waveplate with an angle of $\frac{\pi}{4}$ between its fast axis and the optical axis, posterior to the PBS. Consequently, the polarization angle of the initially transmitted light through the PBS undergoes a double $45°$ shift

after the back reflection, allowing it to be reflected inside the PBS. This configuration enables the occurrence of overlap between the incident light and the back-reflected light.

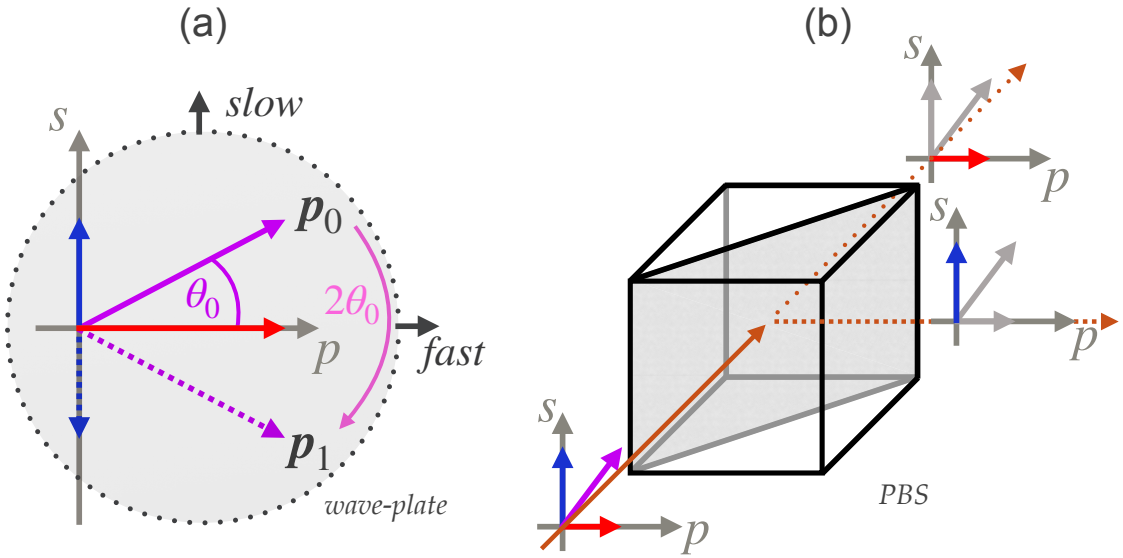


Figure A.18: (a): The rotation of the polarization is depicted for the scenario in which the fast axis of the waveplate is aligned along the horizontal axis. This illustration is applicable to a single propagation of a half-waveplate or two propagations through a quarter-waveplate. (b): The illustration shows a PBS or polarizing beam splitter cube, which functions by dividing light of specific polarization into two filtered beams, thereby presenting the respective component of polarization.

A different method for rotating the polarization of light can be achieved by utilizing the Faraday effect. A dielectric material of a given length L, when subjected to an external magnetic field, such as one created by a permanent magnet of equal length, exhibits a specific optical phenomenon characterized by the occurrence of a birefringent pattern. Linearly polarized light can be expressed as a superposition of two circularly polarized beams, where the field of one is clockwise and the other is counterclockwise rotating along the propagation axis.

In this geometry, the magnetic field $\boldsymbol{B}$ is aligned parallel to the direction $\boldsymbol{k}$ of the light. Subsequently, the velocity of one of the circularly polarized beams comprising the light will be decelerated with respect to the other, thereby inducing a phase shift at the material's limits. Subsequent to the absence of the magnetic field, the resultant light exhibits linear polarization, albeit with a rotation of $\theta_f = V\,|\boldsymbol{B}|\,L$ with respect to the horizontal axis. The Verdet constant, V, which is material-dependent and can assume positive or negative values, governs this rotation.

A suitable use case is illustrated by a Faraday isolator, as depicted in Figure A.19. In this configuration, the system is engineered to rotate the light of the design wavelength by an angle of $\theta_f = \frac{\pi}{4}$ after a single propagation. A PBS positioned at the front of the apparatus ensures that only a single polarization of light exits the dielectric material. A second PBS, situated behind the magnetic field tilted by θ_f, will fully transmit this light further. However, any light that propagates in the opposite direction will first be filtered by the tilted PBS, rotated by another θ_f, and enter the initial PBS, which is tilted by $2\theta_f = \frac{\pi}{2}$.

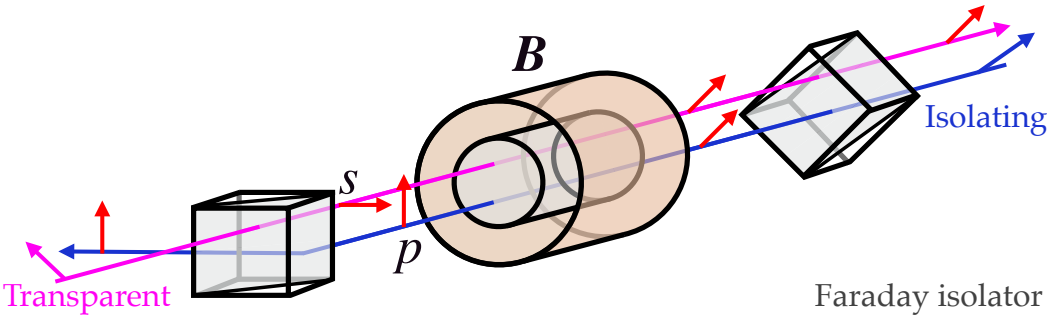


Figure A.19: The conceptual model of an optical isolator, which is predicated on the Faraday effect. The blue and magenta lines represent beams propagating from opposite directions.

This PBS will not transmit light at all; rather, it will reflect it completely. Such a system is designated a Faraday isolator, as it permits the transmission of light of a specific polarization while effectively blocking light from any counterpropagating polarization. With regard to the application of waveplates, linear polarizers are frequently utilized to filter specific polarizations from an incident light. These crystals possess a distinct structural configuration that facilitates the transmission of electric field components perpendicular to the crystal's axis, while components parallel to the axis are absorbed. The utilization of these filters, in conjunction with their specific orientation, is an effective method for selecting a particular polarization. However, it should be noted that this approach is accompanied by a loss of power from all other polarization components.

A.3.2 Steering with Sound: The Acousto-Optic Modulator

A critical element in the manipulation of light is the modulation of its amplitude or frequency, which can be achieved through two primary methods: a constant value or a periodic oscillation. A device capable of performing either of these tasks is known as an acousto-optic modulator (AOM). This device utilizes the acousto-optic effect, whereby the propagation of sound waves through a crystal generates a periodically changing refractive index $n(\boldsymbol{r},t)$ that affects light propagating through the same crystal. The refraction index is expressed as

$$n(\boldsymbol{r},t) = n_c + \Delta n\, e^{-i(\boldsymbol{k}_s\cdot\boldsymbol{r}-\omega_s t)}.$$

In this equation, the refractive index of the crystal, n_c, the amplitude of the refractive index change, Δn, and the sound wave wavenumber and angular frequency, $\boldsymbol{k}_s$ and ω_s, respectively, are considered. The sound wave is generated by a piezoelectric crystal, which vibrates in response to an applied electric field. The interaction of optical light with sound waves, of speed c_s, can be modeled as an interaction between photons and phonons, thereby conceptualizing the sound wave as a lattice in a solid. As is customary, the conservation of energy W and momentum p must be satisfied, therefore it is

$$W_1 = W_0 + W_p \text{ and } \boldsymbol{p}_1 = \boldsymbol{p}_0 + \boldsymbol{p}_p.$$

In this equation, the incident photon has index 0, and the diffracted photon has index 1. The phonons are represented by the index p. The energy is denoted by frequency ν_i and momentum by

wave vector $\boldsymbol{k}_i$ through $W_i = h\nu_i$ and $\boldsymbol{p}_i = h\boldsymbol{k}_i$. Here, h is the Planck constant. Thus, it is

$$\nu_1 = \nu_0 + \nu_p \text{ and } \boldsymbol{k}_1 = \boldsymbol{k}_0 + \boldsymbol{k}_p.$$

In consideration of the incident light propagating towards the wavefront of the sound wave at an angle of incidence θ_m, between them and $|\boldsymbol{k}_i| = k$, the explicit formalism for the momentum of the sound wave is derived. The formalism can be expressed as

$$\begin{pmatrix} -\sin(\theta_m) \\ \cos(\theta_m) \end{pmatrix} k_1 = \begin{pmatrix} \sin(\theta_m) \\ \cos(\theta_m) \end{pmatrix} k_0 + \begin{pmatrix} -1 \\ 0 \end{pmatrix} k_p, \tag{A.101}$$

and ultimately simplifies to

$$\sin(\theta_m) = \frac{\lambda_1}{2\lambda_p}. \tag{A.102}$$

The bottom row of Equation (A.101) provides the value of $k_1 = k_0$, and the wavenumber $k_i = \frac{2\pi}{\lambda_i}$ was inserted. Furthermore, energy conservation results in a modification of the frequency, mathematically expressed as $\Delta\nu = \nu_1 - \nu_0$. This quantity is directly proportional to the phonon frequency:

$$\Delta\nu = \nu_p. \tag{A.103}$$

In an AOM, numerous rays of incident light interact with multiple wavefronts of the sound wave. In order to maximize the power in the resulting beam, it is necessary that the diffracted beams interfere constructively. Therefore, the OL difference d between two rays diffracted at adjacent layers must be a multiple of half wavelengths. That is to say, $d = m\frac{\lambda_0}{2}$, where m is an integer. This relationship can be further expressed as $\sin(\theta_m) = \frac{d}{\lambda_s}$, where θ_m is the incident angle and λ_s is the wavelength of the sound. This relationship provides the spacing between the layers. This results in the Bragg condition for maximized diffracted intensity of

$$\sin(\theta_m) = m\frac{\lambda_0}{2\lambda_s}. \tag{A.104}$$

The concept of the AOM is illustrated in Figure A.20. A comparison of Expression (A.104) with Equation (A.102) reveals a connection between the phonon and sound wavelength and frequency. Specifically, it is $\lambda_p = \frac{\lambda_s}{m}$, and $\frac{c_s}{\nu_p} = \frac{c_s}{m\nu_s}$. In conclusion, the frequency shift undergone by the diffracted light is determined by $\Delta\nu = m\nu_s$, where m denotes the order of light corresponding to the specific Bragg angle θ_m.

However, not all light undergoes diffraction; a portion of it will transmit undisturbed by the sound frequency. The intensity ratio, denoted by σ, between the diffracted intensity, I_d, and the incident intensity, I_0, is expressed as

$$\sigma = \frac{I_d}{I_0}.$$

This ratio varies in proportion to the radio frequency RF signal power, that is responsible for generating the sound wave. As the power increases, the degree of light diffraction concomitantly rises. An AOM's efficacy is regarded as high when $\sigma \approx 80\,\%$ of the light is diffracted. The modulators under consideration are found in two forms: the first is found in free space, and the second is

fiber-coupled. The latter is typically built in such a way that only the first-order diffracted light is coupled into the fiber. Free space models permit the tuning of higher-order diffractions, and the entirety of the light can be utilized for further experimentation. However, the alignment process is critical. The typical frequency values for AOMs for light in the optical or infrared spectrum range from 80 MHz to several 100 MHz. It bears mentioning that the Bragg angle is dependent upon the sound wave frequency, denoted by the symbol ν_s.

A modulation of this frequency can result in alterations in the power and direction of the diffracted light. However, these changes may be negligible if the modulation frequency is sufficiently low. One method of counteracting this involves the implementation of a double pass through the AOM. In this configuration, light that has undergone diffraction once is reflected by a mirror and subsequently coupled through the AOM once more. The resulting beam is shifted by twice the sound frequency but overlays the incident light. Consequently, it is insensitive to changes in the Bragg angle and the actual sound frequency. The material and geometry of the AOM also do not permit all possible values for ν_s; rather, a band is centered around the carrier, where diffraction efficiency, thus σ, drops if the sound frequency drifts away from the central value. AOMs are utilized in this thesis for the purpose of rapidly modulating the frequency and amplitude of a given beam.

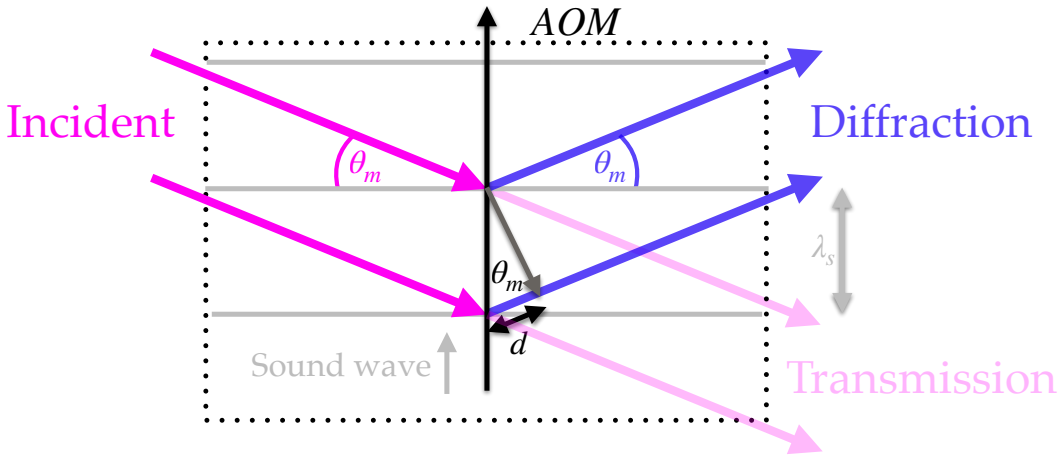


Figure A.20: The figure illustrates the conceptual model of an AOM. Incident light interacts with the various wavefronts of a sound wave train. Maximum diffraction occurs when the angle, θ_m, results in constructive interference among individual beams. In the absence of perturbations, a certain degree of light transmission is observed.

A.3.3 Modulating Light with Voltage: The Electro-Optic Effect

Another common method for modulating the frequency of light is through the electro-optic effect, which typically involves the use of Pockels cells. Assuming the $z-$axis to be the axis along which light propagates towards and through a crystal, a time-varying electric field driven by an RF voltage can induce a change in the refractive indices along the transverse axes. In considering the incident light

$$\boldsymbol{E}_{in} = E_0 \hat{\boldsymbol{p}} e^{-i(k_n z - \omega t)},$$

where $z = 0$ denotes the input of the crystal and $z = L$ signifies the output, the electric fields of the beams at these positions are

$$\boldsymbol{E}_{in} = E_0 \hat{\boldsymbol{p}}_{in} e^{i\omega t} = E_0 e^{i\omega t} \left(p_x \hat{\boldsymbol{e}}_x + p_y \hat{\boldsymbol{e}}_y \right),$$

and

$$\boldsymbol{E}_{out} = E_0 e^{-i\left(k_{n_x} L - \omega t\right)} p_x \hat{\boldsymbol{e}}_x + E_0 e^{-i\left(k_{n_y} L - \omega t\right)} p_y \hat{\boldsymbol{e}}_y .$$

The parameters k_{n_x} and k_{n_y} are the wave vectors that depend on the different refractive indices of the transverse axis j, $n_j(t)$ where latter is defined as

$$n_j(t) = n_c + \Delta n_j \left| \boldsymbol{E}_{RF} \right| . \tag{A.105}$$

In this context n_c is the crystal's unperturbed refractive index, and the electric field $\boldsymbol{E}_{RF}$, induced by an alternating voltage of frequency Ω, is given by

$$\boldsymbol{E}_{RF} = \frac{\boldsymbol{U}_{RF}}{d} = \boldsymbol{A}_{RF} \cos(\Omega t) . \tag{A.106}$$

The length d denotes the distance between the electrodes, while $A_{RF} = |\boldsymbol{A}_{RF}|$ is the electric field amplitude. The factor Δn_j is indicative of the strength with which the corresponding crystal axis responds to the electric field in terms of its optical properties. The insertion of Equation (A.106) into (A.105) , with $\alpha_j = \Delta n_j A_{RF}$, results in

$$n_j(t) = n_c - \alpha_j \sin(\Omega t) .$$

The wave vectors can then be described by

$$k_{n_j} = \frac{2\pi}{\lambda} n_j(t) = \frac{2\pi}{\lambda} n_c - \frac{2\pi}{\lambda} \alpha_j \sin(\Omega t) = k_c - \frac{2\pi}{\lambda} \alpha_j \sin(\Omega t),$$

yielding an electric field at the output described as

$$\boldsymbol{E}_{out} = E_0 e^{-ik_c L} e^{i\omega t} \left(e^{i\frac{2\pi}{\lambda}\alpha_x L \sin(\Omega t)} p_x \hat{\boldsymbol{e}}_x + e^{i\frac{2\pi}{\lambda}\alpha_y L \sin(\Omega t)} p_y \hat{\boldsymbol{e}}_y \right). \tag{A.107}$$

In the context of pure phase modulation, it is rational to align the axis of the electric field with one of the crystal axes. This alignment results in the elimination of one of the terms in Equation (A.107), thereby simplifying the equation. Assuming the polarization is oriented along the x-axis, with $p_x = 1$, the resultant equation is

$$\boldsymbol{E}_{out} = E_0 e^{i\omega t} e^{i\beta \sin(\Omega t)} e^{-i\phi_c} \hat{\boldsymbol{e}}_x .$$

In this equation, the quantity $\beta = \frac{2\pi}{\lambda}\alpha_x L = 2\pi \Delta n_j \frac{L}{\lambda} A_{RF}$ is defined as the phase modulation depth of the light by the electric field and material properties. The constant phase shift $\phi = k_c L$ is the shift that the light experiences by an unperturbed crystal, in particular if no field is applied. The concept of the modulator is illustrated in Figure A.21. Polarizers positioned in front of and behind the cell frequently serve to ensure that the appropriate polarization enters and exits the modulator. However, slight misalignments of the polarization, slow variations of the refractive index of the crystal due to

temperature, and etalon effects due to reflections inside the crystal on the transverse surfaces can all lead to unwanted changes of the field amplitude. This bears a resemblance to phase modulation (PHM), albeit in the amplitude domain. Any amplitude modulation (AM) can be described by an oscillation of the electric field amplitude at a given AM frequency Ω' and AM depth M'. This AM depth may also include a phase, which is described by γ. The total expression for the electric field E_1 subsequent to the phase modulator or electro-optic (phase) modulator (EOM) is therefore

$$E_1 = E_0 \left(1 + \underbrace{M' e^{i\gamma} \sin(\Omega' t)}_{\text{AM}} \right) e^{i\omega t} \underbrace{e^{i\beta \sin(\Omega t)}}_{\text{PM}} e^{ikz}. \tag{A.108}$$

This will become a salient point when the stabilization of light to an optical resonator is explained. The role of the PHM part is of particular significance in Section (2.3). The PHM and AM parts are also crucial for elucidating the effect that is detailed in Section (2.3.3). In this particular instance, the coordinate system has been set to the output of the modulator. This adjustment has been made so that any additional phase that might be attributed to the crystal is not taken into account. The amplitude E_0 has been rescaled from $E_0 \rightarrow E_0(1 + M')$ to conform to the AM formalism.

Consequently, a comparison with the incident electric field is no longer applicable. In essence, the power throughput of an EOM is comparably inefficient due to the occurrence of in-coupling, absorption, and scattering losses. These losses have the capacity to diminish the output power to a level that is substantially below the initial value, at the order of fifty percent of the incident power. As with AOMs, EOMs are also available in a variety of types, with the option of fiber coupling.

Furthermore, EOMs have the capacity to be designed as polarization or intensity modulators. The term "waveguide" is frequently used in the context of EOMs, when a rigid and narrow notch is edged along the propagation axis in the crystal.

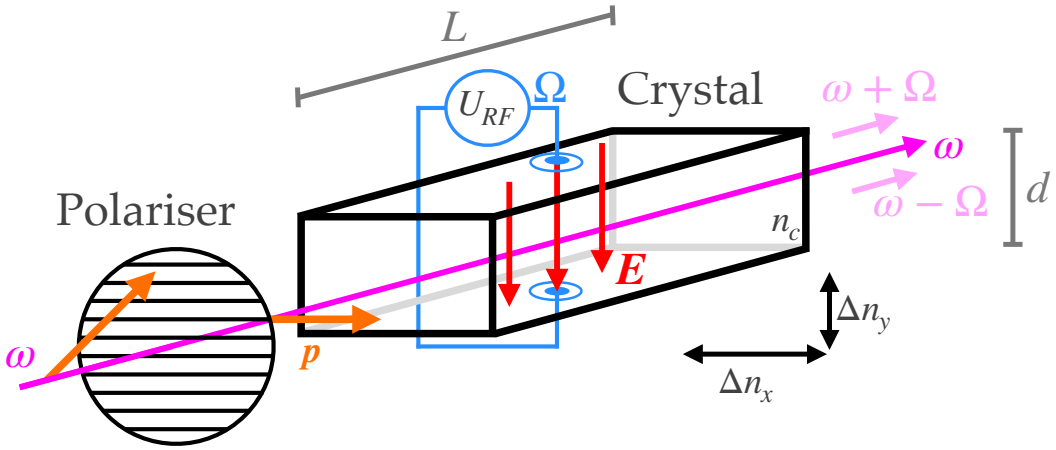


Figure A.21: The concept of an EOM as a phase modulator. The incident light is filtered in such a manner that only the polarization parallel to the main axis of the crystal is able to propagate through it. The RF voltage induced electric field is the driving force behind the change in the refractive index. In turn, the output light is modulated by the frequency of the RF voltage.

Its purpose is to guide the wave in a strict confinement, which results in a reduced voltage that is necessary to generate an equivalent effect on the light if propagating through the "large" crystal. Within the scope of this work, the focus lays on EOMs as phase modulators. To comprehend the essence of PHM, it is necessary to introduce the following identity:

$$e^{i\omega t}e^{i\beta\sin(\Omega t)} = e^{i\omega t}\sum_{l=-\infty}^{\infty} e^{il\Omega t}J_l(\beta) \tag{A.109}$$

The quantity J_l denotes the previously (Section A.2.3, Equation (A.81)), defined Bessel function of the first order. Depending on the modulation depth, the existence of terms presenting light of frequencies $\omega \pm l\Omega$ is predicated, where l designates the order of the respective sideband. In most cases, the objective is to generate a single set of sidebands. Consequently, the modulation depth is configured to a low level, thereby ensuring that Bessel functions of higher order become negligible. The implementation of

$$J_{-l}(z) = (-1)^l J_l(z),$$

along with the definition of $E_c = J_0(\beta)E_0$ and $E_s = J_1(\beta)E_0$, for the electric field amplitudes of the carrier and sidebands, results in

$$\begin{aligned} E_1 &= \left(1 + M'e^{i\gamma}\sin(\Omega' t)\right)E_0 e^{i\omega t}e^{i\beta\sin(\Omega t)} \\ &\approx \left(1 + M'e^{i\gamma}\sin(\Omega' t)\right)\left(\underbrace{E_s e^{i\omega t}}_{\text{carrier}} + \underbrace{E_s e^{i(\omega t+\Omega t)}}_{\text{upper sb.}} - \underbrace{E_s e^{i(\omega t-\Omega t)}}_{\text{lower sb.}}\right). \end{aligned} \tag{A.110}$$

Therefore, in a manner analogous to an AOM, the EOM modulates the frequency by adding or subtracting the driver frequency, denoted by Ω, to the carrier. However, in contrast to the AOM, all three beams exist in the same beam and not in spatial separation.

A.3.4 Directing Light: Fiber Types, Splitters, and Circulators

The content of this section now appears in the main thesis text (Section 2.1.3) as it forms a critical part of the theoretical framework. This note serves as a placeholder for its original appendix location.

A.3.5 Light in a Loop: Principles of Fiber Ring Resonators

The content of this section now appears in the main thesis text (Section 2.1.4) as it forms a critical part of the theoretical framework. This note serves as a placeholder for its original appendix location.

A.4 Essential Electronics: Lasers, RF, and Feedback Systems

The EM wave is a property that has been employed in all calculations in the preceding sections. Prior to delving into the intricacies of frequency analysis and stabilization, it is fundamental to

establish a foundation in the origin of coherent light. In this context, it is reasonable to provide an explanation for the typical electronic devices utilized to measure light and manipulate and adjust frequencies not directly on the wave, but in post-processing. Literature, especially on the topic of lasers, is [231, 234, 232, 235], while PID feedbacks are in depth explained in [236, 237, 238].

A.4.1 Coherent Light: How Lasers Work

Monochromatic light has been a constant presence up to this point. Nevertheless, the generation of EM waves that are sufficiently powerful and resonate at a precise frequency necessitates specific preparation. This is not only a theoretical matter; it is also of practical importance in its real-world implementation. There are three primary types of lasers. Solid-state lasers, diode lasers, and fiber lasers, which are all based on the same principle: a pump source prepares atoms in a gain medium into the excited state, denoted as $|e\rangle$, which forms the laser transition with the ground state, denoted as $|g\rangle$. While this ground state does not correspond to the general ground state in terms of energy, it is the lower state of the two-level system, with the energy difference given by the expression $\Delta E = h\nu$, where h is Planck's constant and ν is the laser frequency.

Through spontaneous emission, a photon of frequency ν is emitted and further interacts with other atoms in one of two ways. It can either be absorbed by an atom which is in state $|g\rangle$ or drive a stimulated emission process by interacting with an atom in state $|g\rangle$. In the first scenario, the photon vanishes; in the latter a total of two photons of ν are generated, which can initiate a sequence of stimulated emissions, thereby amplifying the light within the gain medium. In order for the net gain of this amplification, denoted by α, to exceed zero, the stimulated emission processes must outweigh the absorptions. This can be demonstrated by accounting for the probabilities, p_e and p_g, with which the atom is in the excited or ground state, respectively. It follows that

$$\begin{aligned}\alpha = \frac{N_1 - N_0}{N_0} &= \frac{N_{stim} p_e + N_{abs} p_g}{N_0} - 1 \\ &= 2p_e - 1,\end{aligned}$$

where N_0 denotes the number of incident photons and N_1 is the number of the resulting photons. With $N_{stim} = 2$ being the amount of photons after a stimulated emission process and $N_{abs} = 0$ after the absorption respectively, it follows the relation

$$\alpha > 0 \Longleftrightarrow p_e > \frac{1}{2}.$$

In a two-level system that exhibits no loss, the probabilities add up to 100 %, given the condition that $p_e + p_g = 1$. Consequently, to achieve any amplification of light, the number of atoms in the excited state must exceed the number of atoms in the ground state, a phenomenon referred to as population inversion. It is important to note that this is inherently impossible in a two-level system, as demonstrated by examining the rate equation

$$\dot{p}_e(t) = \underbrace{-\gamma p_e(t)}_{\text{spont. em.}} \underbrace{-\sigma F(t) p_e(t)}_{\text{stim. em.}} + \underbrace{\sigma F(t) p_g(t)}_{\text{absorption}}, \tag{A.111}$$

which relates the time-dependent change in the population probability of the excited state in relation to the three fundamental processes. The term $-\gamma p_e(t)$ corresponds to the decrease due to spontaneous emission, $-\sigma F(t)p_e(t)$ corresponds to the decrease resulting from the stimulated emission, and $\sigma F(t)p_g(t)$ signifies the increase because of absorption. The quantity γ is the inverse of the mean lifetime of the excited state; consequently, it can be interpreted as the spontaneous emission rate. $F(t)$ is the photon flux density, which can be expressed as $F(t) = \frac{I}{\hbar\omega}$, where I is the intensity of the interacting photons and $\nu = 2\pi\omega$ is their frequency. The parameter $\sigma = \sigma(\omega)$ is the scattering cross section of the stimulated emission and the absorption process. The frequency-dependent cross section $\sigma(\omega)$, can be expressed as follows:

$$\sigma(\omega) = \frac{\sigma_{res}}{1 + \left(2\frac{(\omega-\omega_0)}{\gamma}\right)^2}$$

In this formalism, $\sigma_{res} = \frac{\lambda_0^2}{2\pi}$ is the cross-section when the photons' frequency is in resonance with the transition frequency, ω_0. In context of a steady state in thermal equilibrium, thus $\dot{p}_e(t) = 0$, and under the assumption of a constant photon flux density $F(t)$, Equation (A.111) reduces to the following equation:

$$0 = -\gamma p_e - \sigma F p_e + \sigma F p_g$$

Solving for p_e and using the expression for flux and cross section yields

$$p_e = \frac{1}{2}\frac{s_0}{1 + s_0 + \left(2\frac{\delta}{\gamma}\right)^2}.$$

Here, $\delta = \omega - \omega_0$ is the detuning of the frequency of the incident photon to the transition, and $s_0 = \frac{I}{I_{sat}}$ is the saturation parameter where $I_{sat} = \frac{\pi c h}{\lambda_0^3}\gamma$ is the saturation intensity. The probability of being in an excited state is maximized for large saturation parameters and when the photons are in resonance. However, it converges to $p_{e,max} = \frac{1}{2}$, which is insufficient for population inversion. The resolution to this issue can be achieved through the implementation of modifications to the system, specifically by introducing one or more additional states. These can be utilized to extract atoms from the ground state and subsequently store them, thereby generating the requisite imbalance. Figure A.22 presents a schematic representation of a conventional four-level system, which is employed in a Nd:YAG solid-state laser.

In this model, a state below the ground state is designated as the "floor state" $|f\rangle$, while a state above the excited state is referred to as the "pump state" $|p\rangle$. A pump, which can be a flash tube for a solid-state laser, emits light that is absorbed by the gain medium and into state $|p\rangle$. This state undergoes non-radiative decay to $|e\rangle$ through phonon interaction. Subsequently, a spontaneous emission from the state of $|e\rangle$ to the state of $|g\rangle$ instigates the avalanche, where another non-radiative decay from the state of $|g\rangle$ to the state $|f\rangle$ finalizes the cycle. The gain medium is sandwiched between a high reflective mirror and a partially reflective mirror. This configuration allows the photons to bounce inside the gain medium, thereby increasing the amplification of light inside before enough light has been accumulated to detect the photons leaving the partial mirror.

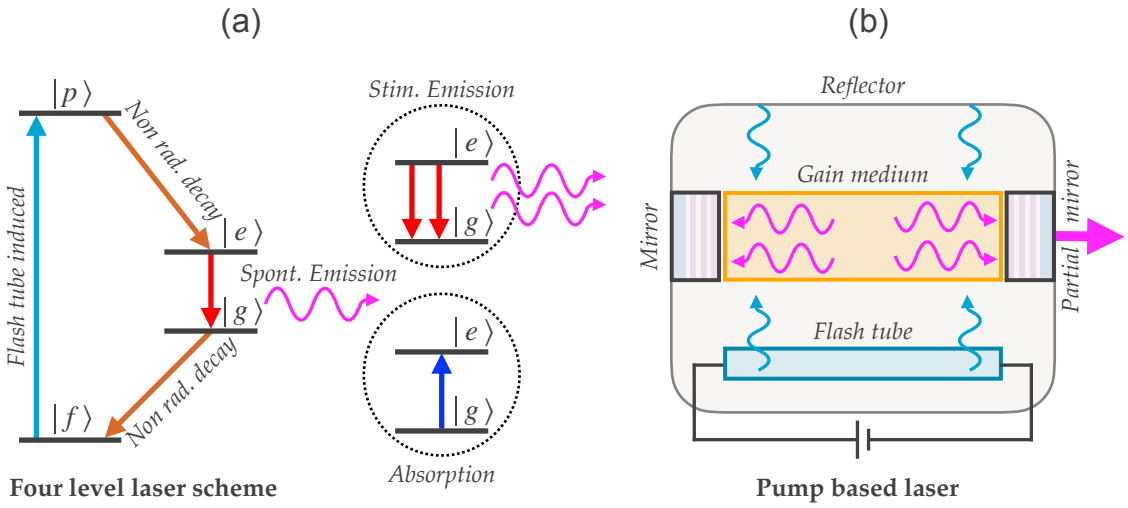


Figure A.22: As illustrated in figure (a), the concept of the level diagram is demonstrated in a four-level laser. Similarly, figure (b) shows the concept of a solid-state laser, in which the pump can be a flash tube.

The high intensity of in-phase photons of the same frequency results in the phenomenon known as "light amplification by stimulated emission of radiation", or, laser. A reflector is positioned around the gain medium and flash tube to redirect pump light that was not absorbed by the gain medium.

An alternative method for constructing a laser involves the use of semiconductors. In this configuration, two slabs of materials are positioned such that one is p-doped (electron holes) and the other is n-doped (electrons are over-saturated). These slabs sandwich an active area with the gain medium. The application of a direct current (DC) voltage will result in the generation of an electron current from the n-type to the p-type doped region through the active area. In this process, the atoms within the active area are excited by the electrons.

Subsequent to this step, the process remains unchanged in comparison to the solid state laser. Semi-conductor-based lasers are also referred to as diode lasers. In essence, fiber lasers employ a laser diode, utilizing the emitted light as a pump to amplify the power within a fiber-based resonator. The pump light is inserted into the cladding of the fiber and excited the atoms in the doped core, thereby initiating a photon avalanche within the core itself. In many instances, the fibers in question possess two distinct cladding layers, wherein the light is induced within the inner cladding layer.

Bragg gratings are utilized to maintain the internal confinement of light within the fiber, where one side is again exhibiting a partial reflective nature. In the case of a fiber laser, the pump light of the diode is typically of a different wavelength than the resulting laser light. This results in a three-state level diagram. Figure A.23 shows a schematic of diode and fiber lasers. In principle, the distinguishing feature of lasers is the manner in which they are pumped.

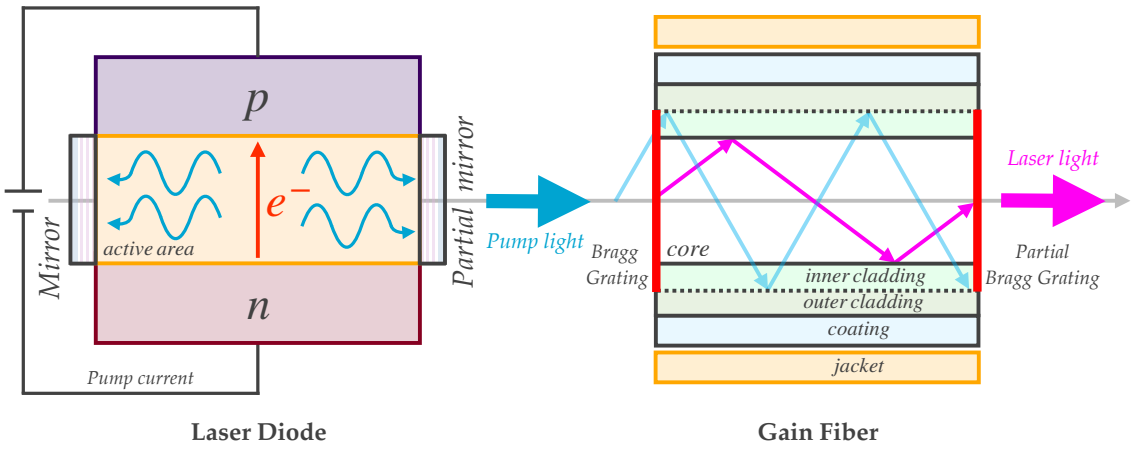


Figure A.23: The following schematics illustrate a fiber laser, which is essentially a diode laser if the fiber is disregarded. In the diode, the pump is defined as the electron stream between the doped materials. In the fiber, the pump is defined as the optical light inserted into the cladding, i.e., through a diode.

A.4.2 RF Electronics: Signals at High Frequencies

The subsequent passage will provide a brief overview of the frequently utilized electrical devices employed in the scope of this work within the laboratory to measure or manipulate light.

Photodiode

A photodiode is a type of semiconductor that functions as a light detector. When light of a certain wavelength is absorbed by the surface of the photodiode, the photodiode's electrons are excited from the valence band to the conducting band. This excitation generates an electrical current that is proportional to the intensity of the incident light. This current can be measured and converted into a voltage. The utilization of electrical amplifiers is frequently employed to augment the input voltage of a diode. Any incident light with the electric field of form $E_1 = A_0 e^{i\omega_1 t}$ will result in an intensity of $I \propto |A_0|^2$, which is unaffected by the frequency of the photons. However, if a second beam of $E_2 = A_0 e^{i\omega_2 t}$ is overlapped at the photodiode thereby generating a beat signal, the total electric field is

$$\begin{aligned} E_{beat} = E_1 + E_2 &= A_0 e^{i\omega_1 t} + A_0 e^{i\omega_2 t} \\ &= 2A_0 \cos\left(\frac{\omega_1 - \omega_2}{2} t\right) e^{i\frac{\omega_1+\omega_2}{2} t}. \end{aligned}$$

Therefore, oscillating components are observed with the average frequency of both beams, as well as an envelope of the averaged difference. The intensity of the beat is expressed by

$$\begin{aligned} I_{beat} &= 4\,|I_0|^2 \cos^2\left(\frac{\omega_1 - \omega_2}{2} t\right) \\ &= \underbrace{2\,|I_0|^2}_{\text{DC}} + \underbrace{2\,|I_0|^2 \cos(\Delta\omega t)}_{\text{AC}}. \end{aligned}$$

The quantity $f_b = \frac{\Delta\omega}{2\pi} = \frac{1}{2\pi}|\omega_2 - \omega_1|$ is defined as the beat frequency. The intensity is found to contain a non-oscillating static component and a component oscillating with the beat frequency. The diode does not directly measure the intensity; rather, it measures the optical power P, which is equivalent to the energy per unit time. This relationship is expressed as $P \approx IA$, where A is the transverse area, and it is wanted that A contains the majority of the beam's energy. Naturally, in scenarios where the beam spot exceeds the dimensions of the photodiode, a proportion of the power may be clipped. However, under the assumption of a constant beam spot size, the intensity is proportional to the electrical voltages generated by the detector. Consequently, the intensity components are proportional to a DC voltage for the static part and an alternating current (AC) voltage that carries the beat information.

In this instance, the assumption was made that both waves possess equivalent amplitudes. However, it is important to note that, in reality, the AC components may exhibit considerably reduced power levels. Photodiodes are distinguished by their bandwidth, which determines the frequency range over which AC components are resolved before the diodes' sensitivity declines sharply. The bandwidth in question may be considered to range from that of DC diodes to that of diodes capable of observing signals up to GHz levels. It should be noted that a wave frequently exhibits multiple distinct frequency components. In particular, noise can be interpreted as sidebands at the noise frequency. Therefore, a single laser wave at photodiode will still lead to an observable spectrum, not including the carrier itself. In a combination with an amplifier the diode becomes a photo detector (PD)

DDS

Another method for generating an alternating electric frequency signal is through the use of a direct digital synthesizer (DDS). In this method, a reference oscillator, such as a quartz crystal, generates an RF voltage by means of the piezoelectric effect. The crystal undergoes a transformation in response to an applied voltage, subsequently relaxing upon the removal of the stimulus. In the presence of an AC) voltage, the quartz will undergo mechanical vibrations at its resonant frequency. This process induces a current, which subsequently generates an RF voltage that can be utilized as a reference. The resonance frequencies of crystals range from kHz to MHz levels, depending on the material and geometry of the crystals. It has been demonstrated that the reference frequency, f_{ref}, can be utilized to generate any other frequency, provided that certain constraints are considered. In a DDS, the phase accumulator ϕ with bit depth N is defined as follows:

$$\phi(f_{out}) = \frac{f_{out}}{f_{ref}} 2^N$$

utilized to generate an RF frequency at f_{out} by converting this phase to the respective amplitude. Subsequently, the amplitude is converted by a digital-to-analog converter (DAC), thereby generating the output sine wave.

RF Frequency Mixer

An RF mixer is a device that takes two RF signals as input and generates an output that consists of the difference or sum of both waves. The power of the electric wave j is denoted by P_j, and

the mixing process will yield the output power P_{IF} (intermediate frequency). In most cases, the objective is to modify the frequency ω of the main signal, P_{In}, by an amount equal to the frequency ω_{LO} of the reference signal, referred to as the local oscillator (LO), denoted by P_{LO}. The mixer multiplies the signals, which can be described as follows:

$$P_{IF} = P_{In} \times P_{LO} = P_0 \sin(\omega t) \times P_{LO} \sin(\omega_{LO} t + \phi)$$

The parameter ϕ is the phase between the inputs, thus, the signals of their respective powers P_0 and P_{LO}. Applying the appropriate trigonometric identity

$$\sin(\omega t)\sin(\omega_{LO} t + \phi) = \frac{1}{2}\left[\cos((\omega - \omega_{LO})t - \phi) - \cos((\omega + \omega_{LO})t + \phi)\right],$$

and by the use of a low pass filter that cuts off oscillations at $\omega + \omega_{LO}$, the total power at the output is expressed as

$$P_{IF,\sin} = \frac{P_0 P_{LO}}{2} \cos(\Delta\omega t - \phi).$$

In the event that the initial light oscillates as a cosine rather than a sine, the identity

$$\cos(\omega t)\sin(\omega_{LO} t + \phi) = \frac{1}{2}\left[\sin(\omega_{LO} t + \phi - \omega t) - \sin(\omega_{LO} t + \phi + \omega t)\right],$$

in combination with the low pass filter leads to the total power

$$P_{IF,\cos} = \frac{P_0 P_{LO}}{2} \sin(-\Delta\omega t + \phi).$$

RF mixers are utilized in frequency metrology laboratories for a variety of applications, including frequency stabilization, a topic that will be addressed in Section 2.3. In the specific instance when $\Delta\omega = 0$, that is, when the local oscillator and input signal are of the same frequency, the power is proportional to $P_{IF,\cos} \propto \sin(\phi)$ and $P_{IF,\sin} \propto \cos(\phi)$, respectively. When implemented in this configuration, the mathematics concerning frequencies can be simplified as

$$f_{IF} = f_{IN} \otimes f_{LO} \coloneqq |f_{IN} - f_{LO}|,$$

where the operator $\otimes$ is defined as a combination of the mixer and the appropriate low-pass filters.

VCO

A voltage-controlled oscillator (VCO) is a device that takes a tunable DC voltage, U_t, and transforms it into a RF voltage by using LC and/or RC loops to generate a frequency, f_{VCO}, following

$$f_{VCO} = f_0 + \beta_f U_t,$$

where the conversion factor β_f is typically approximately linear. The base frequency f_0 of the oscillator is given at the supply voltage U_{sp}. VCOs have the capacity to be centered at various frequencies, exhibiting substantial tuning ranges. This attribute renders them as practical instruments for the modulation of EOMs or AOMs. Nevertheless, the stability of the frequency is contingent

upon the stability of the tuning voltage, which is ordinarily less stable than that of a quartz in a DDS. Consequently, the latter is more frequently utilized to drive static frequencies. A primary advantage of a VCO is its rapid response time, which results in a considerably higher bandwidth. This attribute makes them superior in applications that can leverage this bandwidth, as will be demonstrated subsequently.

VCA

A voltage-variable attenuator (VCA) is an electrical device that functions by attenuating an input power P_{in} based on the tuning voltage that is applied to it. Subsequently, the output power P_{out} is estimated to be approximately

$$P_{out} = \left(\beta_A \frac{U_t}{U_{max}} + \beta_{min}\right) P_{in}.$$

The device has been engineered to block all power except for a fraction β_{min}, which is given by the condition that there is no voltage present. The attenuation is gradually decreased until it is minimized when $U_t = U_{max}$ is at its maximum voltage, where the total throughput is $\beta_{max} = \beta_A + \beta_{min}$. VCAs can be utilized to stabilize and modulate amplitudes, including the driving signal of an AOM, which in respect modulates the amplitude of the light diffracting within the AOM.

A.4.3 Feedback Control: The PID Framework

In a multitude of applications, it is requisite to stabilize a variable to a fixed set value. A tangible example of this would be the temperature of a material, while an abstract example would be the frequency of an EM wave. In any event, the conceptual framework underlying the stabilization scheme remains unaltered. The time-varying parameter $y(t)$ is to be measured and compared against the desired set value u_0. The creation of an error signal, $e(t) = y_0 - y(t)$, is universally practical due to the fact that $y(t) = y_0$ if $e(t) = 0$. This property ensures that the stabilization mechanism is independent of the set point, thus allowing for its application in a general manner. Additionally, the error signal is sign sensitive.

The direction in which $y(t)$ must be tuned can be determined by observing the sign of $e(t)$. The effectiveness of the stabilization process necessitates the inclusion of a sensor that quantifies the value of $y(t)$ over time, in tandem with an actuator capable of adjusting the parameter. This actuator can be illustrated by a Peltier/TEC element, which modifies the temperature of a copper plate attached to it. The current of the parameter value is compared to the set point, and the magnitude of the resulting error is used by the actuator to drive the parameter towards the set point. The most straightforward implementation is the proportional (P) loop, in which the signal $u(t)$ that is added to the parameter is given by the following equation:

$$u_p(t) = K_p e(t).$$

The coefficient K_p is the linear gain factor. In a system where the changes in $y(t)$ over time are negligible for the purpose at hand, this method is an adequate way to stabilize the system. In such

circumstances, it is reasonable to hypothesize that K_p will approximate one. When the time variation of y becomes significant, $u_p(t)$ will become a limit. The steady-state error is a fundamental issue because the compensation can only function when an error is measured that is not zero. This results in periods of instability, during which the parameter may deviate or undergo significant fluctuations. Noises in the system, arising from the sensor or electronics, will also create an offset in the output value relative to the actual set point. Increasing the gain factor, K_p, has been demonstrated to be a viable method for decreasing the steady-state error, provided that certain boundaries are respected. However, it is important to note that this approach can also lead to the introduction of oscillations around the setpoint. In any event, an additional element is incorporated into the control signal $u(t)$ in such a system, as depicted by the following equation:

$$u_i(t) = K_i \int_0^t e(\tau)\, d\tau = K_p \frac{1}{T_i} \int_0^t e(\tau)\, d\tau$$

The function $u_i(t)$ is defined as the integration of the error over a specified time period t, with the weighting coefficient K_i. However, it is generally accepted practice to maintain K_p as a global gain factor. Consequently, the coefficient T_i can be interpreted as a time gain factor. The integrator's (I) primary benefit is that it enables compensation even in the absence of a current error, thereby ensuring the integrity of the output. In order to enhance the stability of the system, an additional "derivative" (D) term is incorporated. It is designed to quantify the slope of the current error and predict its future behavior. It is given by $u_d(t)$, following

$$u_d(t) = K_d \frac{de(t)}{dt} = K_p T_d \frac{de(t)}{dt}.$$

In this case, the coefficient K_d is the respective gain parameter. It can be expressed as the multiplication of a time gain T_d and the global gain K_p. The final control function is derived by adding all three terms:

$$u(t) = K_p \left(e(t) + \frac{1}{T_i} \int_0^t e(\tau)\, d\tau + T_d \frac{de(t)}{dt} \right)$$

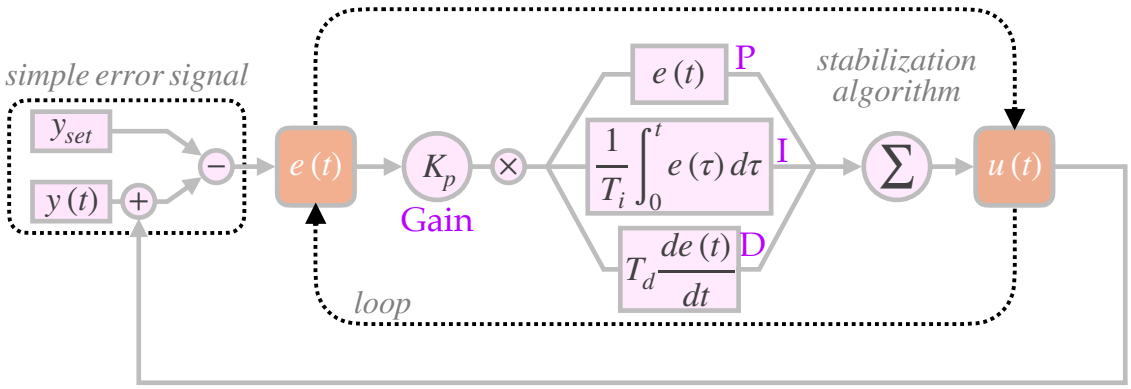


Figure A.24: The following schematics illustrate a standard PID controller, featuring simple error signal generation. The loop comprises the continuous measurement of $e(t)$ and the subsequent compensation by $u(t)$.

This is the conventional and well-established formalism for describing proportional-integral-derivative (PID) controlled loops, the purpose of which is to stabilize any parameter to a set point. The concept is also illustrated in Figure A.24. In this thesis, a multifold of control systems is implemented, all of which are based on this concept. The range of options extends from simple power stabilizations, incorporating only a fundamental proportional and integrator element, to complex frequency stabilizations, encompassing proportional, derivative, and multiple integrator stages. An investigation into the theoretical descriptions and optimization algorithms of PID emerges as a worthwhile exercise, given the lack of a universally applicable solution to all problems.

A.5 Optical Stability and Noise – From Linewidth to Limits

The ensuing subsection will direct its attention toward an evaluation of laser light. The investigation begins with the introduction of two critical characteristics of EM waves: linewidth and lineshape. Subsequently, the broader spectrum surrounding the carrier frequency is analyzed in the phase noise regime. This analysis is complemented by the examination of time variation in the Allan deviation picture. This knowledge will be used to explain different categories of noise types and how to distinguish them. Subsequently, the utilization of optical resonators for the purpose of stabilizing light will be examined, prior to an in-depth discussion of the fundamental limitation of optical FP resonators: the thermal noise floor. Notable textbooks on this subject include the works of [232, 239, 240, 241]. This section will also feature real-world data to describe the different analysis methods.

A.5.1 Linewidth and Phase: Laser Stability Fundamentals

The laser has been regarded as a sort of magical device, capable of producing a stream of coherent photons at a single frequency. The occurrence of monochromatic behavior would result in the formation of a delta peak at the carrier frequency, denoted by ν_j, as depicted in the Fourier picture. In the context of statistical physics, the total power P_j of a delta peak is determined by the photon flux per unit time, which is expressed as the differential rate of change of the number of photons, or $\frac{dN}{dt}$. The power is given by

$$P_j = \frac{dN_j}{dt} h\nu_j,$$

as it is equivalent to the energy, or the number of photons at this frequency per unit time. This assumption is predicated to the premise that all other frequency components are of zero power, which is a crude approximation in reality. In a broader context, the total power, P, of laser light can be modeled as the sum of all individual photons, with their respective frequencies, per unit time. This objective can be achieved through the implementation of two distinct methodologies. The first method involves the calculation of a sum. The second method involves the integration of all possible frequency components:

$$P = \sum_{j=0}^{\infty} \dot{N}_j h\nu \rightarrow P = h \int_0^{\infty} \dot{N}(\nu)\, \nu \, d\nu$$

This formalism constitutes the foundational framework for the characterization of key terms such as "noise," "stability," and "linewidth." In a laser, photons are generated by stimulated emission through a transition from an excited state to a ground state. Nevertheless, the occurrence of this effect is not immediate. In consideration of the population in the excited state, the intensity of the emission at any given time is determined by the transition probability and the current population in the state. This is a classical decay that can be modeled using an exponential function and a characteristic decay time, τ, or frequency, $\gamma = \tau^{-1}$. Accordingly, the corresponding electric field $\boldsymbol{E}_{|e\rangle}$ in the excited state is then given by

$$\boldsymbol{E}_{|e\rangle}(\boldsymbol{r},t) = E_0 \boldsymbol{p} e^{-i(\boldsymbol{k_n} \boldsymbol{r} + \omega_0 t)} e^{-\frac{1}{2}\frac{t}{\tau}}.$$

As one is interested in the power of photons of certain frequency ω, the electric field has to be transformed from time domain to frequency by a Fourier transform. The resulting field $\boldsymbol{E}_{|e\rangle}(\boldsymbol{r},\omega)$ is given by

$$\begin{aligned}\boldsymbol{E}_{|e\rangle}(\boldsymbol{r},\omega) &= \int_0^\infty \boldsymbol{E}_{|e\rangle}(\boldsymbol{r},t)\, e^{i\omega t} dt = E_0 \boldsymbol{p} e^{-i\boldsymbol{k_n}\boldsymbol{r}} \int_0^\infty e^{\left(-\frac{\gamma}{2} + i(\omega-\omega_0)\right)t} dt \\ &= E_0 \boldsymbol{p} e^{-i\boldsymbol{k_n}\boldsymbol{r}} \frac{1}{\frac{\gamma}{2} + i(\omega_0 - \omega)}.\end{aligned}$$

The intensity of light is determined by the absolute square of the electric field and the corresponding pre-factors. In addition, incorporating the normalization property $\int_{-\infty}^{\infty} I_{|e\rangle}(\omega)\, d\omega = 1$ results in the total intensity being

$$I_{|e\rangle}(\omega) = \frac{1}{\pi} \frac{\frac{\gamma}{2}}{\left(\frac{\gamma}{2}\right)^2 + (\omega - \omega_0)^2},$$

thereby defining a Lorentzian curve. This line indicates that laser light is not merely a delta peak at the carrier frequency of the transition, but rather a Lorentzian peak with a FWHM of $f_{tr} = \gamma\,(2\pi)^{-1}$ around this carrier. This observation explains why γ is also referred to as the natural linewidth of the transition. According to the theory, the picture of the laser as a true monochromatic device is invalidated, as its inherent nature comprises frequency components that span an array of frequencies. Nevertheless, the linewidth may be negligible, depending on the application. Both, the gain medium and the amplification cavity exert an influence on the light. Furthermore, a Lorentzian shape is exhibited around the resonance frequency of the resonator, which is designed to be compatible with the transition frequency. As established in an earlier chapter, the linewidth f_c of light transmitting through the resonator is given by

$$f_c = \frac{\Delta\nu}{\pi} \arccos\left(1 - \frac{\left(1 - r^2\right)^2}{2r^2}\right).$$

The FSR is given by $\Delta\nu = \frac{c_n}{2L}$ and the mean reflection coefficient of both mirrors is r. In many instances, the linewidth resulting from the transition is considerably smaller than that of the cavity $f_{tr} \ll f_c$, thereby preventing the resonator from functioning as a filter. In a perfectly stable environment, the light benefits from this reduced linewidth and the high amplification gain achieved through the resonator. Nevertheless, in actuality, the OL of light is subject to the influence of a

multitude of environmental factors. The cavity length itself is vulnerable to contraction-expansion effects through thermal variations, mechanical vibrations, acoustics, or tilts. As a consequence, the resonance frequency of the resonator will undergo a drift in accordance with its length. This, in turn, will affect which photons will be amplified by the resonator. This effect is also present inside the gain medium itself, where local refractive index variations will have the same effect as well as any influences that change the energy difference of the transition. Depending on the frequency of the respective disturbance, in combination with the observation time, it will manifest in one of three ways: as a drift of the frequency, a broadening of the linewidth, or sidebands around the carrier frequency. The term "observation time" is pivotal in this context, as the effects described above are essentially manifestations of the same phenomenon, albeit on disparate time scales.

The **linewidth** of a system can be measured over a range of time scales. For instance, on a scale of a few µs, the linewidth of a specific system may be measured to be 1 Hz. However, when the same system is measured over a longer time span, such as several seconds, the linewidth can be measured at a kHz level. This can be attributed to the definition of the term, which is the frequency width in which a specific portion (typically half) of the total power of the light is contained. However, given that power is defined as energy per unit time, it is important to explicitly state the time scale in order to accurately interpret the value of power. A drift of the carrier wave of magnitude 1 Hz / s, may also be regarded as a component of the linewidth, provided that an averaging period of one day is observed. It may be reasonable to omit any definitions and simply treat light by measuring all the components of its power across the entire frequency domain over a sufficiently long period to encompass all appearing (periodic) effects on it.

The power spectrum is widely regarded as one of the most consistent methods for investigating the properties of light. However, it is generally not feasible to measure power at an infinitesimally small frequency bin. Consequently, the power is typically presented as the power spectral density. In this case, the power of the light along a frequency segment or sideband of a fixed width is observed and averaged. The result is then normalized to this width, which is also called the resolution bandwidth (RBW). Often, these diagrams are referred to as **phase or frequency noise**, depending on the presentation of the ordinate.

Another analysis method, which characterizes the frequency stability of the light, treats the properties on longer time scales in the time domain. The mean frequency of the light, that is to say, the center of the total power distribution measured over a constant gate time, is determined through temporal observation. This will result in a trace that demonstrates the impact of slower effects on light and the introduction of drift effects or oscillations on time scales that exceed the gate time. It is indeed possible to measure slow oscillations in the frequency domain and vice versa. However, drifts of the central peak, or carrier, of the light will skew the phase noise and blur information below that time scale. Therefore, in particular in the subject of ultra-stable lasers, for scales that exceed approximately 1 s (thus below 1 Hz), the time domain is more conducive and facilitates one of the most frequently utilized analytical treatments for oscillator stabilities: the **Allan deviation**.

Additionally, it is technically challenging to measure RBW below 1 Hz and to create gate times that are much faster than 1 s. This results in a natural separation between the time and frequency domains. Eventually, phase noise, frequency stability, and linewidth are three terms that are

synonymous. However, they are employed to describe the behavior of light on short, medium, or long time scales, depending on the power distribution on said time scale. No laser is without imperfection; in reality, there are sidebands present at all frequencies, stemming from the non-zero Lorentzian and the black body radiation in the form of EM waves in the gain medium, mirrors, or other materials. Additionally, the presence of electrical circuits has the potential to induce noise in the measurement device. This also includes the inherent shot-noise limit of the PD itself. However, in many cases, this noise floor is remarkably minimal, thus allowing it to be disregarded for the intended purpose. However, if these conditions are no longer met, it is the system has to be characterized with greater care.

A.5.2 Tracking Jitter: Measuring Phase and Frequency Noise

The spectral phase noise density $\mathscr{L}_{dB}$ is frequently quantified in units of $\frac{\text{dBc}}{\text{Hz}}$ using a spectrum analyzer (SA). It is obtained from the relative root mean square (RMS) power between a sideband $P_S(f)$ and the carrier P_C. The sideband power is measured in a frequency band of width Δf, at a frequency offset f from the carrier frequency ν_0 (or from f_b of a beat) in the frequency domain. One possible method of obtaining this would be to perform a Fourier analysis of the output from the beat detector. However, an SA is a tool that has been developed for the purpose of measuring the power spectrum in the frequency domain. This is achieved by making a comparison between the probe light and an internal or external oscillator.

The measurement of a spectrum is illustrated in Figure A.25 (a), its spectral phase noise density in (b). The SA is scanning the beats between the signal and the oscillator within an interval around the carrier, which is referred to as the span. For a specific frequency bin, the signal is filtered by the SA through a bandpass filter of width Δf, which is equivalent to the RBW. A satisfactory methodology for ascertaining whether the RBW exceeds or lies beneath the linewidth of the light is to examine its lineshape. As previously established, the majority of pure EM waves exhibit a Lorentzian-like shape (in the context of stabilized light), while electrical bandpasses demonstrate Gaussian behavior.

The powers P_{dB} are measured in units of dBm. In order to calculate a power density p, it is necessary to establish a relationship between the power at a sideband and the resolution bandwidth of the measurement. In linear scale P_{lin}, with units of watts (W), the calculation of power density p_{lin} per unit bandwidth (1 Hz) can be achieved by dividing the power by the bandwidth resolution. Thus, it is

$$p_{lin} = \frac{P_{lin}}{\Delta f}, \tag{A.112}$$

which is of unit $\frac{\text{W}}{\text{Hz}}$. The conversion of the power and the power density from linear to logarithmic scales are given by

$$P_{dB} = 10\log_{10}\left(\frac{P_{lin}}{\text{mW}}\right)\text{dBm, and } p_{dB} = 10\log_{10}(p_{lin})\,\frac{\text{dBm}}{\text{Hz}}. \tag{A.113}$$

Inserting the power density in Equation (A.112) into (A.113) leads to:

$$p_{dB} = 10\log_{10}\left(\frac{\text{Hz}}{\Delta f}\frac{P_{lin}}{\text{mW}}\right)\frac{\text{dBm}}{\text{Hz}} = \frac{P_{db}}{\text{Hz}} - 10\log_{10}\left(\frac{\Delta f}{\text{Hz}}\right)\frac{\text{dBm}}{\text{Hz}} \tag{A.114}$$

The phase noise density at a specific Fourier frequency is defined as the power density difference between the sideband and the carrier, expressed as

$$\begin{aligned}\mathscr{L}_{dB} := \Delta p_{db}(f) = &\frac{P_{dB,S}(f) - P_{dB,C}}{\text{Hz}}\frac{\text{dBc}}{\text{dBm}} \\ &- 10\log_{10}\left(\frac{\Delta f}{\text{Hz}}\right)\frac{\text{dBc}}{\text{Hz}}.\end{aligned} \tag{A.115}$$

It should be noted that the power $P_{dB,S}$ is the average of the upper and lower sidebands. For reference, a measurement of $\mathscr{L}_{dB}$ of the beat between two 1064 nm lasers is illustrated in Figure A.25. The linear scale of the phase noise density, denoted by $\mathscr{L}_{lin}$, can be calculated using the following relation:

$$\mathscr{L}_{dB} = 10\log_{10}\left(\mathscr{L}_{lin}\frac{\text{Hz}}{\text{rad}^2}\right)\frac{\text{dBc}}{\text{Hz}} \text{ and } \mathscr{L}_{lin} = 10^{\left(\frac{\mathscr{L}_{dB}}{10}\frac{\text{Hz}}{\text{dBc}}\right)}\frac{\text{rad}^2}{\text{Hz}} \tag{A.116}$$

This quantity is in units of $\frac{\text{rad}^2}{\text{Hz}}$. In literature the following relation is frequently used:

$$\mathscr{L} = \frac{1}{2}S_\phi \tag{A.117}$$

Therefore, a relative power difference of 3 dB exists between S_ϕ and the phase noise density $\mathscr{L}$.

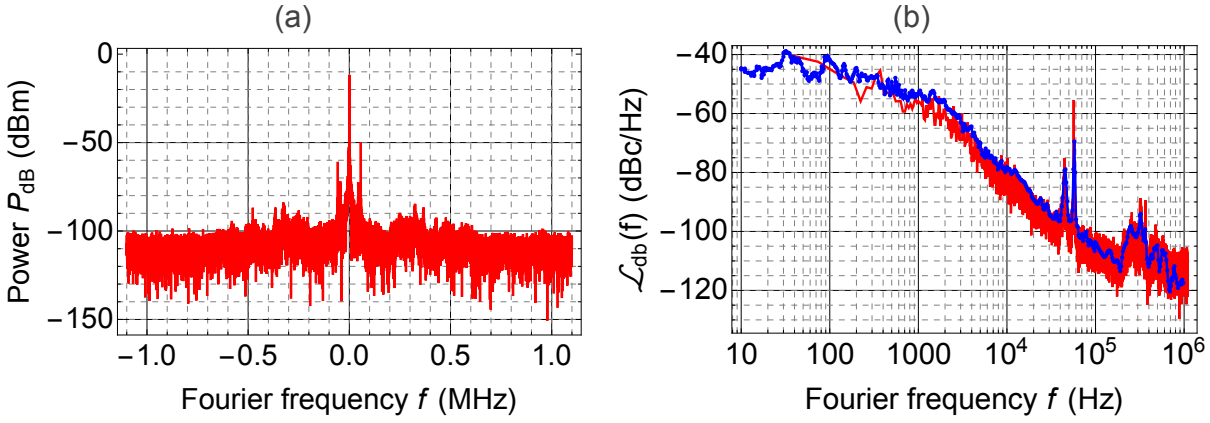


Figure A.25: (a): Power spectrum in a 2.2 MHz band of the beat between two 1064 nm lasers, measured at a RBW of 30 Hz. The beat carrier frequency is $f_b \approx 111$ MHz. The carrier power is $P_C \approx -11.75$ dBm. The plotted data is parsed to reduce the file size. (b): The SSB spectral phase noise density $\mathscr{L}_{dB}$ of the beat for Fourier frequencies between 10 Hz and 1 MHz, is measured using the SA. The beat carrier frequency is $f_b \approx 111$ MHz. The blue line was measured using the internal phase noise tool of the SA. The red line in this plot was generated by applying Equation (A.114) and (A.115) to the red data. in plot (a).

This discrepancy can be elucidated as follows: The quantity $\mathscr{L}$ is defined as the single sideband (SSB) spectral phase noise density, where only amplitudes or powers of sidebands at a single side of the carrier are of concern. The quantity S_ϕ is the double side band (DSB) spectral phase noise density. Its concept revolves around the principle that the summation of noise amplitudes is necessary for both upper and lower sidebands at an equivalent offset f within the frequency domain. Therefore, the factor of two is employed to compensate for this issue. It is also commonplace to plot the square root of the linear spectral phase noise density, denoted by $\sqrt{S_\phi}$, in $\frac{\text{rad}}{\sqrt{\text{Hz}}}$. This is correlated to the square root of the spectral frequency noise density $\sqrt{S_f}$, in units $\frac{\text{Hz}}{\sqrt{\text{Hz}}}$, which can be calculated by

$$\sqrt{S_f(f)} = f\sqrt{S_\phi(f)}. \tag{A.118}$$

Conventionally, the quantity S_f is designated as the spectral frequency noise density. However, it is also customary to examine its square root. This value is derived by multiplying the respective Fourier frequency to the square root of the DSB spectral phase noise density. Substituting Equation (A.116) into the identity (A.117) demonstrates the method for converting the phase noise of the SA or a discrete Fourier transform (DFT) into frequency noise:

$$\sqrt{S_f(f)} = \sqrt{2\times 10^{\left(\frac{\mathscr{L}_{dB}}{10}\frac{\text{Hz}}{\text{dBc}}\right)}}\,\frac{f}{\sqrt{\text{Hz}}} \tag{A.119}$$

To obtain the fractional root spectral frequency noise density, expressed in units $\sqrt{\text{Hz}}^{-1}$, it is necessary to divide the given quantity by the optical carrier frequency ν_0, hence

$$\nu_0^{-1}\sqrt{S_f(f)} = \sqrt{2\times 10^{\left(\frac{\mathscr{L}_{dB}}{10}\frac{\text{Hz}}{\text{dBc}}\right)}}\,\frac{f}{\nu_0}\frac{1}{\sqrt{\text{Hz}}}. \tag{A.120}$$

In this thesis, the quantity $\sqrt{S_f(f)}$ is typically plotted on the left $y-$axis, while $\nu_0^{-1}\sqrt{S_f(f)}$ is plotted on right one, as illustrated in Figure A.26 for the laser beat. In the context of beats, wherein two noisy oscillators contribute to the signal, the noise of one oscillator can be estimated by dividing the density S_f by a factor of two or, respectively, multiplying a factor of $1/\sqrt{2}$ on the square root of S_f. This assumption was made under the premise that both oscillators exhibited comparable noise levels. Additionally, the beat can be recorded as a voltage using a data acquisition card (DAQ).

In instances where the beat frequency is less than the measurement process's sample rate, the beat signal can be resolved through Fourier analysis. The blue and red traces in the figures are not identical due to differences in sampling rates and averaging times used in their respective measurements. The blue trace is averaged more stringently, which makes it appear thinner. In the context of signal analysis, the Fourier transformation v_s of a list of data points u of length n (amplitude, i.e., unit volts) of a signal, measured with a sampling rate γ, can be expressed as follows:

$$v_s = \frac{1}{n^{(1-a)/2}}\sum_{r=1}^{n} u_r e^{2\pi i b(r-1)(s-1)/n}, \text{ with } \frac{1}{n^{(1-a)/2}} \overset{a=-1}{=} \frac{1}{n} \tag{A.121}$$

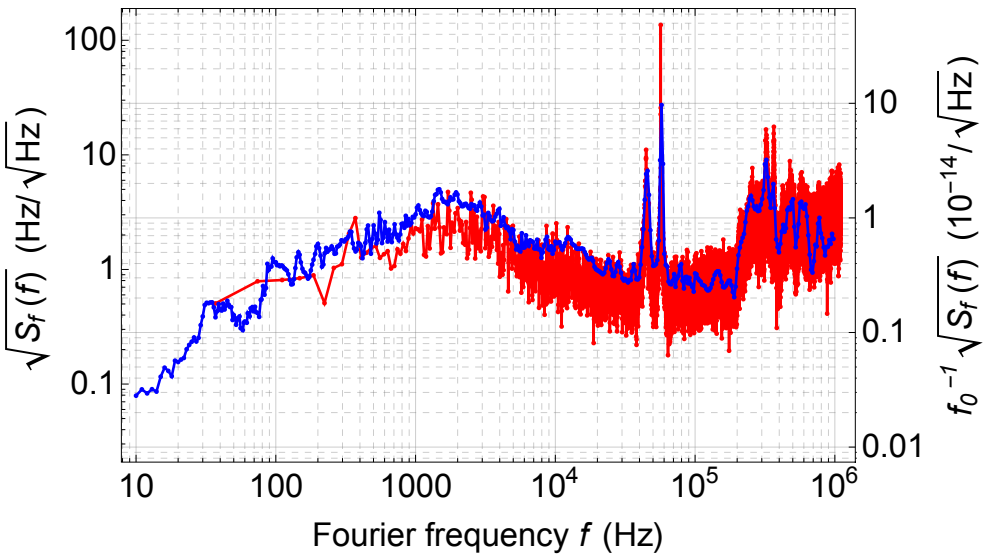


Figure A.26: The root spectral frequency noise density of the beat between two 1064 nm lasers computed via Equations (A.119) and (A.120) from the phase noise data obtained by the SA. The optical carrier frequency of the system is $f_0 := \nu_0 = 281.76\,\text{THz}$. The red and blue lines correspond to the respective data shown in Figure A.25.

The elements of v_s will carry the unit of u, thus volts. For $a = -1$, v_s is the DFT of u. Furthermore, the quantity b has the capacity to conjugate the list. The power spectrum can be obtained by calculating the magnitude of twice the Fourier transform of the signal, $P_V(f) = |2v_s(f)| = 2\sqrt{v_s(f)v_s^*(f)}$. The corresponding Fourier frequency has an increment of $df = \frac{\gamma}{n} = \frac{1}{\tau}$ where the first frequency is the inverse of the measurement time τ. In order to convert this voltage to the logarithmic scale, one has to calculate

$$P_{dB} = 10\log_{10}\left[\frac{1000}{\text{V}}\frac{P_V^2}{50}\right]\text{dBm}.$$

The factor of 50 in the logarithm is derived from the conversion of volts to watts, which is performed using the impedance of the input. In most cases, the impedance is 50 Ω. Subsequently, one may continue with the application of Equation (A.115) in the same manner as previously outlined. It is important to note that the resolution bandwidth of the spectral phase noise density undergoes a change when an averaging filter is applied. A comparison of the data acquired with a DAQ card and the SA in terms of the power spectrum is illustrated in Figure A.27 (b). In Figure A.28, the corresponding spectral frequency noise densities are presented.

Ultimately, the primary technique employed in this thesis involves the analysis of the power spectrum of light across various intervals, typically with a ratio of RBW to span of 1 : 500. These power spectra are then processed to calculate phase and frequency noises, which are subsequently integrated to generate a comprehensive representation of the signal. The device employed for this purpose is the FPC1000 SA from Rohde and Schwarz, which is externally referenced to a high-quality RF signal from a Hydrogen maser, which will be explained in Section 2.4.2.

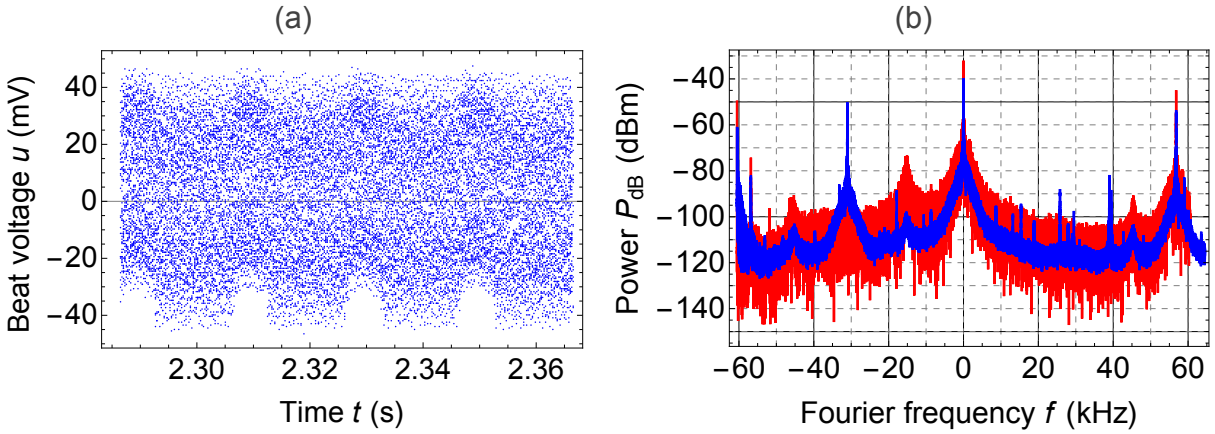


Figure A.27: (a): The beat signal of the 1064 nm lasers was measured with a DAQ card with a sample rate of 250 kHz. The plotted data shows a small section to reduce file-size. (b): The blue line shows the corresponding power spectrum obtained through a Fourier transformation of the beat signal. The data has been averaged. The red line is a power spectrum, directly obtained from the SA, with an RBW of 10 Hz. The beat signal was mixed down using a DDS to a frequency of 60.5 kHz.

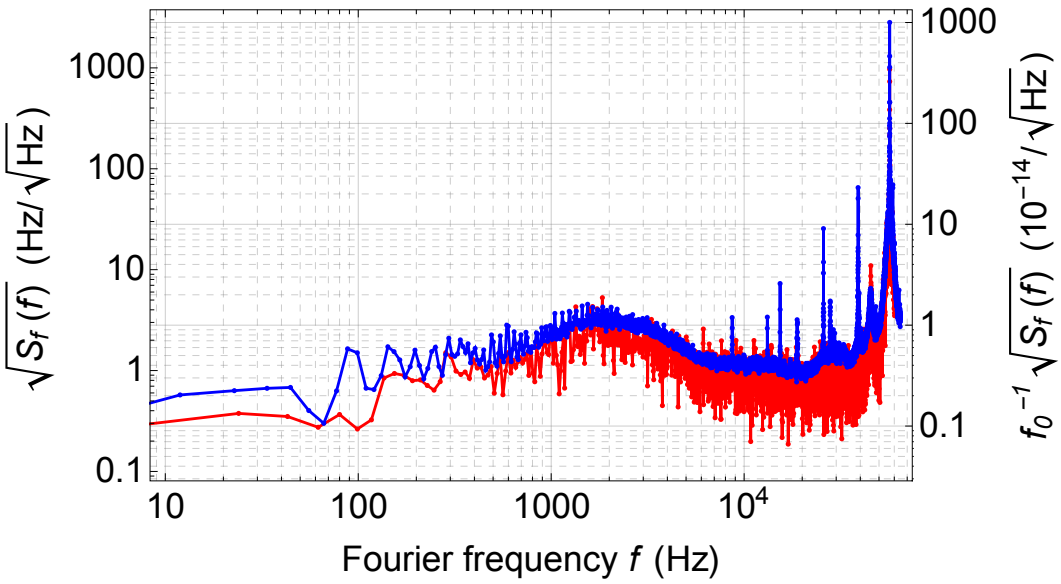


Figure A.28: Frequency noise densities obtained from the data shown in Figure A.27. The blue line represents the beat measured with the DAQ card, while the red line is derived from the SA data. For the blue line, solely the upper sidebands were utilized.

The total intensity of a beat is mathematically given by the sum of the individual electric fields of the EM waves, thus

$$I_{tot} \propto |E_1(t) + E_2(t)|^2 .$$

The intensity of the beat I_{12}, specifically the component oscillating at the difference frequency, is given by the term which is the product of the electric fields E_1 and E_2, and takes the form:

$$I_{12} \propto \left|E_1(t)\,E_2^*(t)\right|^2 = \left|\int_{-\infty}^{\infty} E_1(\omega')\,E_2^*(\omega-\omega')\,d\omega'\right|^2 \approx \int_{-\infty}^{\infty} \left|E_1(\omega')\,E_2^*(\omega-\omega')\right|^2 d\omega'.$$

$$\Longleftrightarrow I_{12} = \int_{-\infty}^{\infty} I_1(\omega')\,I_2(\omega-\omega')\,d\omega' \tag{A.122}$$

Here, two things happened. First, the convolution theorem was employed which states that the multiplication of, here, electric fields in the time domain are given by the respective convolution integral in the Fourier domain. Then the assumption was made that the waves have Lorentzian spectral profiles, typical for ultra-stable lasers. Under this assumption, the phase correlations between the fields are negligible, allowing the overlap integrals to vanish. As a result, the absolute square can be brought inside the integral, effectively reducing the expression to a convolution of intensity spectra. Eventually, the power spectrum of the beat between two laser waves is modeled by the convolution of the respective lineshapes which are, in case of Lorentzians, given by

$$I_1(\omega) = \frac{1}{\pi}\frac{\frac{\gamma_1}{2}}{\left(\frac{\gamma_1}{2}\right)^2+(\omega-\omega_1)^2}, \text{ and } I_2(\omega) = \frac{1}{\pi}\frac{\frac{\gamma_2}{2}}{\left(\frac{\gamma_2}{2}\right)^2+(\omega-\omega_2)^2}.$$

The convolution integral in Equation (A.122), is then solved to

$$\begin{aligned} I_{12} &= \int_{-\infty}^{\infty} I_1(\omega')\,I_2(\omega-\omega')\,d\omega' \\ &= \ldots = \frac{1}{\pi}\frac{\frac{\gamma_1+\gamma_2}{2}}{\left(\frac{\gamma_1+\gamma_2}{2}\right)^2+(\omega-(\omega_1+\omega_2))^2}. \end{aligned}$$

While the FWHM linewidth f_c of a single laser is given by

$$I_1(\pi f_c) = \frac{1}{2}I_1(0) \Longleftrightarrow f_c = \frac{\gamma_1}{2\pi},$$

the linewdith $f_{c,12}$ of the beat is then calculated by

$$f_{12} = \frac{\gamma_1+\gamma_2}{2\pi}.$$

This demonstrates that the linewidths add, as the convolution of two Lorentzian functions yields another Lorentzian with a full width at half maximum (FWHM) equal to the sum of the individual linewidths. As previously mentioned, this is a valid approximation for many systems, as Lorentzian line shapes frequently arise in resonator mode profiles and in lasers stabilized to high-finesse cavities. Throughout this thesis, analyses involving the addition of linewidths typically assume Lorentzian profiles; however, similar treatments can also be extended to other spectral shapes, such as Gaussian or Voigt profiles, with appropriate modifications. In particular, the linewidth of the beat presented in the Figures A.25, A.26, A.27 and A.28 is shown in Figure 8.6. There, a Lorentzian fit over the data is performed yielding a significant agreement.

A.5.3 Long-Term Fluctuations: Allan Deviation Analysis

The time domain measurement tool is the Allan deviation, which quantifies the fluctuations of frequency measurements adjacent in time, spaced by t. Typically, a frequency counter counts the occurrence of cycles of an oscillation at a given gate time, τ_0, which is given by a local oscillator serving as a reference. One cycle constitutes the complete repetition of the signal wave, which can be measured through the zero crossings of the phase variable, $\phi(t)$. The quantity of cycles N is determined by the number of times the phase has completed a full period of 2π between the final phase, denoted by ϕ_N, and the initial phase, denoted by ϕ_0. Therefore, N is calculated as follows: $N = \frac{\Delta\phi}{2\pi} = \frac{\phi_N - \phi_0}{2\pi}$. In general, frequency $\nu(t)$ is expressed as cycles per unit time. In the context of a frequency counter, this translates to the phase difference after the progression of each gate time:

$$\nu(t) = \frac{dN}{dt} = \frac{1}{2\pi}\frac{d\phi}{dt} \longrightarrow \nu_i(\tau) = \frac{\phi(t+\tau) - \phi(t)}{2\pi\tau_0}$$

Here, the index i is used to enumerate the series of phase or frequency values, respectively. Therefore, if the conclusion of one frequency measurement corresponds to the initiation of the subsequent cycle, the frequency array can be expressed as $(i\tau_0, \nu_i)$ for $i \in [0, N-1]$. Then, N corresponds to the total number of frequencies and $t = i\tau_0$ represents the real time. The difference $\delta\nu_i$ between two adjacent frequencies can be calculated by $\delta\nu_i = \nu_{i+1} - \nu_i$. For the sake of clarity, the time dependency t is not carried. Important statistical elements to analyze the fluctuations are the arithmetic mean $\mu = \frac{1}{2}\langle\delta\nu_i\rangle$ and variance $\sigma_A^2 = \frac{1}{2}\left\langle(\delta\nu_i + \mu)^2\right\rangle$, which are defined by

$$\mu = \frac{1}{2}\langle\delta\nu_i\rangle = \frac{1}{2}\frac{1}{N-1}\sum_{i=0}^{N-2}\delta\nu_i = \frac{1}{2(N-1)}\sum_{i=0}^{N-2}(\nu_{i+1} - \nu_i),$$

and

$$\sigma_A^2 \coloneqq \frac{1}{2}\left\langle(\delta\nu_i + \mu)^2\right\rangle = \frac{1}{2}\frac{1}{N-1}\sum_{i=0}^{N-2}\delta\nu_i^2 = \frac{1}{2(N-1)}\sum_{i=0}^{N-2}(\nu_{i+1} - \nu_i)^2\,. \tag{A.123}$$

The factor of two is applied to account for the mean distance between both frequencies. In this particular instance, the mean value is susceptible to the sign of the fluctuations and, under certain circumstances, can reach a value of zero. Therefore, as is the case in the majority of statistical processes, the mean square displacement or variance is a competent analysis method. This method is not sensitive to the direction of the fluctuation. The Equation (A.123) is the Allan variance, and its square root, $\sigma_A(\tau)$ is also referred to as the standard Allan deviation (ADEV) or two-sample deviation for the averaging time τ. The inclusion of μ in the variance is intended to eliminate the comparison of the variation to its mean value. Rather, it is intended to compare the variation to zero fluctuation, as the primary interest lies in the absolute stability of the signal, as opposed to the extent to which it deviates from its typical value. The Allan deviation is depicted as a function of time, thereby enabling the extraction of the total number M of frequencies that are spaced by the time $\tau = j\tau_0$ by

$$M' = \frac{T}{\tau} = \frac{T}{j\tau_0} = \frac{T}{j\tau_0} = \frac{N}{j}, \tag{A.124}$$

where T is the total measurement time, which is inherently a multiple of the gate time, τ_0. However, it is necessary to round M' up to ensure the accuracy of the resulting M, which is the mean of the new list of frequencies. For instance, a measurement of $T = 11\,\mathrm{s}$ with a gate time of $\tau_0 = 1\,\mathrm{s}$ second is analyzed for an averaging time of $\tau = 2\,\mathrm{s}$. In this case, $j = 2$, and consequently, $N = 11$, and $M = 6$. Equation (A.124) would result in M' being equal to 5.5, thereby causing the sum to conclude at a value of 5. Therefore, an expression that accounts for this behavior is given by

$$M = \frac{N-1}{j} + 1,$$

and the final computations of the ADEV σ_A are

$$\sigma_A^2(\tau_0) = \frac{1}{2(N-1)} \sum_{i=0}^{N-2} (\nu_{i+1} - \nu_i)^2, \text{ and } \sigma_A^2(j\tau_0) = \frac{1}{2\left(\frac{N-1}{j}\right)} \sum_{i=0}^{\frac{N-1}{j}-1} \left(\nu_{(i+1)j} - \nu_{ij}\right)^2. \tag{A.125}$$

The value j is a natural integer starting from one. However, ADEV plots are typically shown on a double logarithmic scale, such that the individual entries of j are often not linearly spaced, but logarithmically. In addition, an alternative to the Equation (A.125) exists. This alternative involves the analysis of distinct closed blocks of frequencies. It is referred to as the overlapped Allan deviation σ_O (ODEV). The ODEV first averages the frequency difference in blocks $\overline{\nu}_i$ of length j. Then, it sums over this mean square displacement for all possible occurring blocks:

$$\overline{\nu}_i = \frac{1}{j} \sum_{k=0}^{j-1} \nu_{i+k} \longrightarrow \sigma_O^2(j\tau_0) = \frac{1}{2(N-2j+1)} \sum_{i=0}^{N-2j} \left(\overline{\nu}_{i+j} - \overline{\nu}_i\right)^2$$

The summation concludes at $N-2j$, as the frequency averages are derived from sums of length j. The final value considered is represented by the index $N-2j+j+j-1 = N-1$, which corresponds to the final index of the total series. With regard to the individual frequency entries, the ODEV is expressed as follows:

$$\sigma_O^2(j\tau_0) = \frac{1}{2j^2(N-2j+1)} \sum_{i=0}^{N-2j} \left(\sum_{k=i}^{i+j-1} \left(\nu_{i+j} - \nu_i\right) \right)^2$$

Evidently, the ODEV enhances the quantity of samples for elevated averaging times $\tau = j\tau_0$, resulting in a more uniform curve. In this work, however, an alternative variant is employed. The modified Allan deviation (MDEV), σ_M, is a metric that characterizes the frequency fluctuation of an oscillator when its signal is overlapped by three samples instead of two. The MDEV can be expressed as

$$\sigma_M^2(j\tau_0) = \frac{1}{2(N-3j+1)} \sum_{i=0}^{N-3j} \left(\overline{\nu}_{i+2j} - \overline{\nu}_{i+j} + \overline{\nu}_i\right)^2.$$

The primary benefits of one variance over the other can be discerned by examining the potential noises in a system and the manner in which they are manifested. Allan deviation and phase noise

are elegantly connected by the following relation

$$\sigma_A^2(\tau) = 2\int_0^{f_{lim}} S_f(f)\underbrace{\frac{\sin^4(\pi\tau f)}{(\pi\tau f)^2}}_{G(\tau,f)} df, \tag{A.126}$$

which can be derived by observing the interconnection between the time domain and the frequency domain, as both are related to each other by the Fourier transformation. Here, the frequency noise is integrated over the specified frequency domain up to an upper boundary f_{lim}, incorporating a filter function $G(\tau, f)$ that accounts for the dependence on the averaging time τ and the appropriate transformation to accurately convert the noises. The oscillation is characterized by a damped squared oscillation with local maxima at $\tau = \left(m + \frac{1}{2}\right)\frac{1}{f}$ for integer numbers m. An example of an Allan deviation measurement is shown in Figure A.29.

The Allan deviation picture demonstrates that each data point corresponds to an individual integral, given by the actual value of τ. In addition, the upper bound is ideally $f_{lim} = \infty$. However, in reality, it is always limited by the measurement devices. If the predominant portion of the light's power is concentrated within this interval, the approximation becomes reasonable.

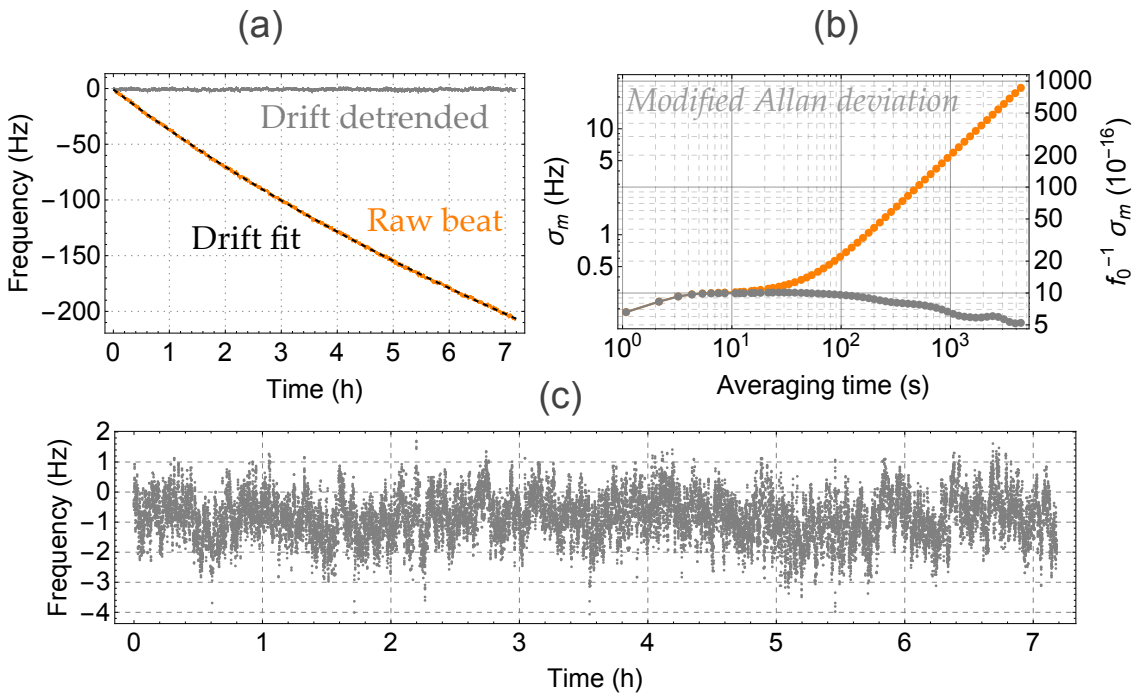


Figure A.29: Measurement of the beat of two lasers with a wavelength of 1064 nm. (a): Time trace of the beat, where a function (black), here an exponential, is fitted to the raw data (orange) to estimate the slow frequency drift. (b): MDEV of the raw data (orange) and of the detrended curve (grey) showing the underlying instabilities. (c) A zoom of the detrended line of the time trace.

A.5.4 Understanding the Spectrum: Types of Noise

In the course of the analysis of an oscillator and its stability, typical behaviors can be identified and classified into categories. The nature of these noises varies depending on the slope of the phase noise, frequency noise, and Allan deviations. A taxonomic classification typically leads to six distinct types, as will be subsequently explained. Figure A.30 shows a compilation of their visualization in frequency and phase noise spectra, as well as in the modified Allan deviation. The present chart draws considerable inspiration from two sources: first, the chart developed by Enrico Rubiola [239]; and second, the handbook on frequency stability as established by NIST [234]. In addition, Table A.1 provides a comprehensive overview of the slope of each noise in the respective picture.

Frequency Drift

The slow, long-term, directional change in the mean or peak frequency of an oscillator is referred to as its drift. The time trace is represented by the orange curve in Figure A.30 (d), which is typically the most straightforward noise type in terms of recognition in the time trace. Several factors may induce this, including slow thermal variations leading to an expansion or contraction of the laser gain medium, or aging of the materials leading to the same effect. As is customary, all noise is invariably classified according to the time at which it is observed. While day-to-day variations due to laboratory temperatures may be perceived as oscillations on a macroscopic level, they can be interpreted as drifts within time scales of an hour.

Allan deviations are a useful tool for the analysis of drifts; however, they can lead to a smearing effect in phase and frequency noise. Therefore, it is generally advisable to select sweep times for subsequent methods in a manner that ensures the peak frequency does not drift significantly compared to the established frequency domain. Furthermore, drift effects can be dominant in comparison to other noises, resulting in a clean line in the Allan deviation. Therefore, it is common practice to detrend the drift of the time trace, which can be linear, exponential, or polynomial depending on the system, in order to expose the underlying frequency fluctuations.

Random Walk

In the context of classical mechanics, the motion of a particle can be described as a trajectory that is determined by a series of discrete steps in a random direction. When these steps are taken at a constant interval, the resulting trajectory is referred to as a random walk. This is observed in the natural world through the phenomenon of Brownian motion, which describes the random motion of minute particles suspended in a liquid.

Additionally, it is evident in the process of photon scattering when photons collide with matter. The spontaneous emission of photons, characterized by distinct energies and random directions, can also be addressed within this framework. A salient property of random walks is that the mean displacement over extended periods is equivalent to zero, and the mean square displacement is used to characterize it. In the domain of oscillators, this random walk can be characterized by a fixed fluctuation frequency accompanied by a randomized sign. This is referred to as "brown" or "red" noise.

Flicker Frequency

Flicker frequency noise is frequently referred to as pink noise and $1/f$ noise. Flicker frequency noise demonstrates a decreasing amplitude in the frequency noise spectrum, $S_f(f)$. It is predominantly characterized by low-frequency phenomena, such as thermal or mechanical stress applied to a material. Equation (A.126) presents an intriguing property concerning flicker noise. When the frequency noise is expressed by $\sqrt{S_f(f)} = A_f f^{-1/2}$ the ADEV is a constant value given by

$$\sigma_A(\tau) = \sqrt{2\int_0^\infty A_f^2 f^{-1} \frac{\sin^4(\pi\tau f)}{(\pi\tau f)^2} df} = \sqrt{2\ln(2)} A_f \approx 1.2\, A_f. \tag{A.127}$$

Here, A_f is the frequency noise amplitude in units of Hz. In terms of the MDEV, this conversion is given by

$$\sigma_m(\tau) = \frac{27\ln(3) - 32\ln(2)}{8} A_f \approx 0.97\, A_f. \tag{A.128}$$

Therefore, the flicker frequency noise exhibits a constant slope in the Allan deviation picture of amplitude that is comparable to A_f. This type of noise establishes the fundamental limit for modern-age frequency stabilization, a topic that is discussed in greater detail in the paragraphs on the thermal noise floor of optical resonators within this section.

White Frequency and Color Presentation

One of the most well-known noise types is characterized by the presence of sidebands of constant power across the entire (idealized) frequency spectrum. This inherent property of the noise explains its slopes in the frequency and phase noise domains. In the frequency-time trace, the model would consist of a true random frequency in a fixed frequency band at any given point in time. At this stage, the distinction between the noises becomes challenging to discern with the unaided eye. The name can be compared to the fact that the combination of all visible colors, when equally mixed together, results in the appearance of white.

In this context, the equal amount is represented by the amplitude in the frequency noise picture, whereas the colors represent all possible frequencies in the Fourier spectrum. The term "pink noise" for flicker frequency is also explained by this. In this case, the lower frequency components are more substantial, resulting in a pink tint when compared to the color palette. Additionally, within the frequency noise spectrum, the spectrum of Brownian noise exhibits a pronounced curvature, characterized by a left-skewed distribution proportional to $\left(S_f(f) \propto f^{-2}\right)$, indicating a pronounced tendency towards red or brown colors.

Flicker Phase and White Phase

Flicker frequency noise possesses a $1/f$ slope in the frequency noise spectrum. In contrast, flicker phase noise exhibits a similar slope in the phase noise spectrum, thereby demonstrating a proportionality between the two forms of noise. This proportionality can be expressed as $\mathscr{L}_{lin}(f) \propto f^{-1}$. This corresponds to a slope of $S_f(f) \propto f^1$, such that white phase noise could be designated as blue frequency noise, given its propensity to exhibit faster oscillations. In a similar manner, white phase

noise exhibits a constant contribution across the entirety of the phase noise spectrum, analogous to white frequency noise in the frequency noise spectrum $S_f(f)$. This is equivalent to a slope of $S_f(f) \propto f^2$, which can be designated as purple frequency noise. In general, it is challenging to differentiate between the last three noise types in the time trace. This challenge is also evident in the Allan deviation, as the ADEV is incapable of distinguishing between white phase and flicker phase noise. The MDEV is a superior metric in this context because it has the capability to differentiate between the various noise types presented here.

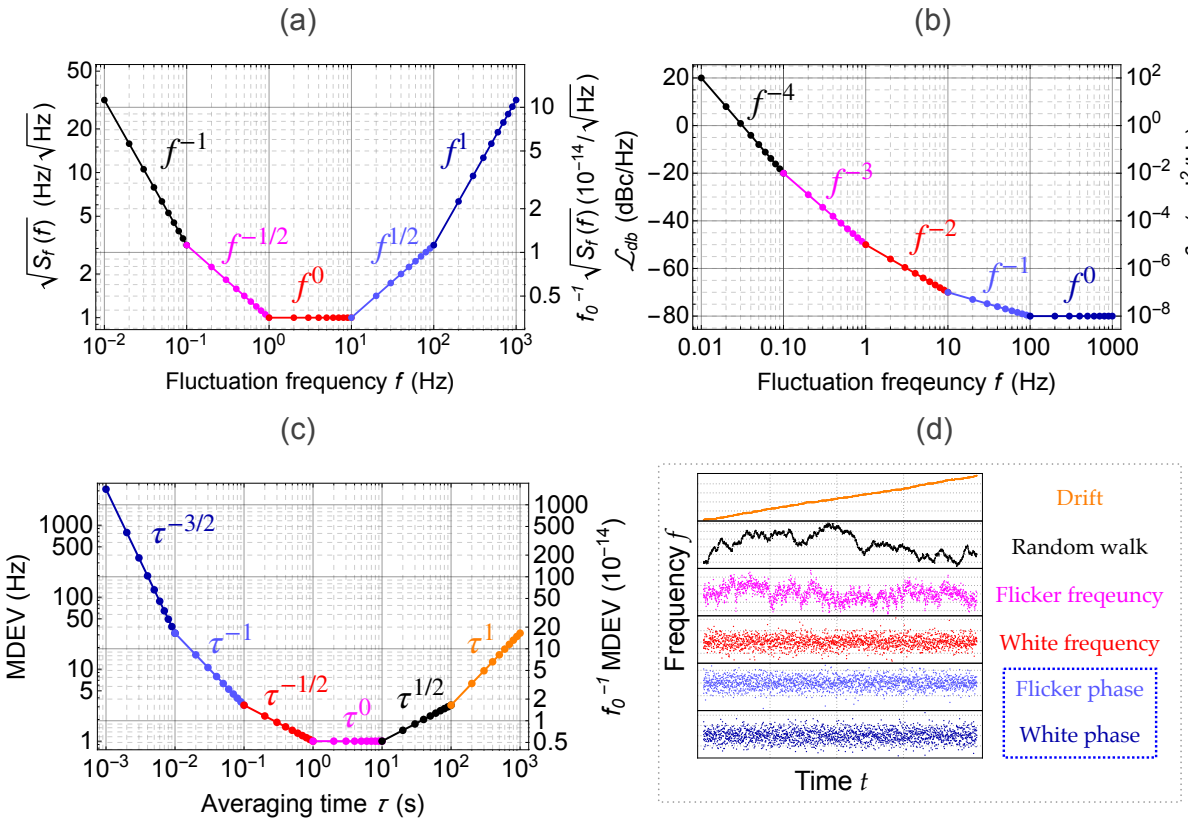


Figure A.30: The following collage illustrates the distribution of noise types across different domains. The frequency noise is illustrated in (a), the phase noise spectrum is displayed in (b), and the Allan deviations are presented in (c). The time trace of all noises is illustrated in (d) through simulations in Mathematica. In this case, the drift and the initial two noises can be distinguished with relative ease through visual means. However, the subsequent three noises present a greater challenge in this regard. In particular, flicker phase and white phase noise will demonstrate equivalent slopes in the ADEV, yet the MDEV will continue to differentiate between them, rendering the latter preferable. This figure constitutes a modest tribute to the comprehensive analysis presented in Enrico's chart [242].

Noise Type	α of $\sigma_m(\tau) \propto \tau^\alpha$	α of $\mathscr{L}_{lin}(f) \propto f^\alpha$	α of $\sqrt{S_f(f)} \propto f^\alpha$
Frequency drift	1	–	–
Random walk	$1/2$	-4	-1
Flicker freq.	0	-3	$-1/2$
White freq.	$-1/2$	-2	0
Flicker phase	-1	-1	$1/2$
White phase	$-3/2$	0	1

Table A.1: An overview of the noise types associated with the three predominant analysis methods for oscillators: The MDEV, and the spectral phase and frequency noise densities.

A.5.5 Anchoring Light: Resonators as Optical References

The content of this section now appears in the main thesis text (Section 2.2.1) as it forms a critical part of the theoretical framework. This note serves as a placeholder for its original appendix location.

A.5.6 Beating Drift: Thermal Expansion and Shielding

The content of this section now appears in the main thesis text (Section 2.2.2) as it forms a critical part of the theoretical framework. This note serves as a placeholder for its original appendix location.

A.5.7 Fundamental Limits: Thermal Noise in Resonators

The content of this section now appears in the main thesis text (Section 2.2.3) as it forms a critical part of the theoretical framework. This note serves as a placeholder for its original appendix location.

A.5.8 Fundamental Limits: Thermal Noise in Optical Fibers

The content of this section now appears in the main thesis text (Section 2.2.4) as it forms a critical part of the theoretical framework. This note serves as a placeholder for its original appendix location.

A.6 Stabilizing Light: The Pound-Drever-Hall Technique

The content of this section now appears in the main thesis text (Section 2.3) as it forms a critical part of the theoretical framework. This note serves as a placeholder for its original appendix location.

A.6.1 The Core Principle: Phase Modulation and Error Signals

The content of this section now appears in the main thesis text (Section 2.3.1) as it forms a critical part of the theoretical framework. This note serves as a placeholder for its original appendix location.

A.6.2 Offset Locking: Tuning the Frequency Gap

The content of this section now appears in the main thesis text (Section 2.3.2) as it forms a critical part of the theoretical framework. This note serves as a placeholder for its original appendix location.

A.6.3 Residual Amplitude Modulation: Limitations and Corrections

The content of this section now appears in the main thesis text (Section 2.3.3) as it forms a critical part of the theoretical framework. This note serves as a placeholder for its original appendix location.

A.7 Frequency Metrology: Measuring Light with Precision

The content of this section now appears in the main thesis text (Section 2.4) as it forms a critical part of the theoretical framework. This note serves as a placeholder for its original appendix location.

A.7.1 Mode-Locked Lasers: The Foundation of Frequency Combs

Consider the fiber laser model depicted in Section A.4.1. It was established that the pump light induces in the outer cladding of a double-clad fiber stimulates the emission of photons in the inner cladding. The energy distribution of these photons is determined by the gain medium. Typical materials used in this field include Ytterbium (1.1 µm) and Erbium (1.5 µm), which emit photons at their given center frequency ω_0 with bandwidths ω_{bw} of several terahertz on the order of 10 nm or more in terms of wavelength. In the context of continuous-wave operation, the fiber geometry is selected with Bragg gratings, ensuring the emission of an almost monochromatic target wave. However, when a fiber of length L is utilized within a standing wave resonator that has a round-trip length of $L_{rt} = 2L$, it enables the propagation of multiple longitudinal modes of the fundamental. This will result in a series of modes that are distinct in frequency ω_m (wavenumber k_m) and overlap with one another:

$$\begin{aligned} \omega_m &= \omega_0 + m\,2\pi\frac{c_m}{2L} \\ &= \omega_0 + m\,\Delta\omega \end{aligned} \tag{A.129}$$

Here, $c_m = \frac{c_0}{n(\omega_m)}$ is the speed of light in the gain medium of the fiber, and $\Delta\omega = 2\pi\frac{c}{2L}$ is the angular FSR of the resonator. The integer number $m \in [-M, M]$ is used to identify the respective mode. In this context, it is designed with frequency ω_0 at the center. Therefore, ideally it would be $M = \infty$.

In practice, the number of modes of sufficient power is determined by the relationship between the bandwidth of the gain medium and the mode spacing, $\Delta\omega$, with typical orders of

$$O\left(\frac{\omega_{bw}}{\Delta\omega}\right) \gtrsim 10^5,$$

Negative frequencies are not considered as they are not existing, thereby establishing a fundamental, lower, limit for M. The electric field component $E_s(t,\omega_m)$ of a single mode in the resonator can be expressed by

$$E_s(t,\omega_m) = E_{0,m} e^{i(\omega_m t - k_m z + \phi_m)}, \tag{A.130}$$

with the phase ϕ_m being an individual phase of every mode, as well as the mode field amplitude $E_{0,m}$. The electric field $E_p(t,z)$ of the light that accumulates within the resonator is the sum of all constituent elements. Consequently, under ideal conditions, it is

$$E_p(t,z) = \sum_{n=-\infty}^{\infty} E_s(t,\omega_m), \tag{A.131}$$

which is regarded as a light pulse in the time domain. Inserting Equation (A.130) into (A.131), yields

$$E_p(t,z) = \sum_{n=-\infty}^{\infty} E_{0,m} e^{i\omega_m t} e^{-ik_m z} e^{i\phi_m}. \tag{A.132}$$

The pulse is characterized by its rapid internal oscillation, given by the carrier frequency, denoted by the symbol ω_0, and its slowly varying envelope, arising from the summation of the individual components. In reality, dispersion occurs when numerous frequency components propagate in a medium. This stems from the fact that the refractive index $n(\omega)$ is not constant in frequency. This will result in disparate propagation speeds within the resonator, as indicated by the following equation:

$$\frac{c_m}{n(\omega)} = \frac{c_0}{n_0} + \delta v_m$$

In this context, $v_{ph} \coloneqq \frac{c_0}{n_0}$ is defined as the speed of the carrier wave, also known as the phase velocity. The term δv_m is used to denote the dependence of the frequency on the cavity mode number. Eventually, for the sake of simplicity, the frequency can be expressed in the form

$$\omega_m = \omega_0 + m\,2\pi\frac{v_{ph}}{2L} + 2\pi\frac{1}{2L}\left(v_{ph} - v_{gr}\right), \tag{A.133}$$

where the group velocity, v_{gr}, plays a fundamental role in dictating the overall velocity of the envelope. The frequency can be expressed in a different manner by establishing two new angular frequencies: the repetition rate, denoted by ω_{rep}, and the carrier-envelope offset (CEO), denoted by ω_{ceo}. Then, Equation (A.133) can be expressed as

$$\omega_m = \omega_0 + m\,\omega_{rep} + \omega_{ceo}, \text{ with } \omega_{ceo} = 2\pi\frac{1}{2L}\left(v_{ph} - v_{gr}\right), \text{ and } \omega_{rep} = 2\pi\frac{v_{ph}}{2L}. \tag{A.134}$$

The repetition rate is equivalent to the free spectral range defined at the carrier frequency. The carrier envelope offset, on the other hand, contains the dispersion component, which is determined

by the offset between the carrier wave and the envelope. It is noteworthy that the following salient relation exists between the two frequencies:

$$\omega_{ceo} = \omega_{rep}\left(1 - \frac{v_{gr}}{v_{ph}}\right)$$

This identity implicates that the CEO vanishes if carrier and envelope travel at equal speeds. Inserting the frequencies of Equation (A.134) into the pulse Formalism (A.132), yields

$$E_p(t,z) = e^{i\omega_0 t} e^{i\omega_{ceo} t} \sum_{n=-\infty}^{\infty} E_{0,m} e^{im\omega_{rep} t} e^{-ik_m z} e^{i\phi_m}.$$

Assuming the pulse propagates inside the resonator, it will reflect between the mirrors. A part of the pulse will be transmitted through the output mirror after it finishes a full round trip. Accordingly, the subsequent discussion will presume the pulse to be situated at the position of the output mirror. This can be regarded as $z = 0$, given the spatial periodicity of the frequency components. The pulse, at this point, can then be simplified to

$$E_p(t) = e^{i\omega_0 t} e^{i\omega_{ceo} t} \sum_{n=-\infty}^{\infty} E_{0,m} e^{im\omega_{rep} t} e^{i\phi_m}. \tag{A.135}$$

The repetition rate and CEO can be expressed in terms of times through $\omega_{rep} = \frac{2\pi}{T_{rep}}$ and $\omega_{ceo} = \frac{2\pi}{T_{ceo}}$, where T_{rep} is the time between two consecutive pulses equal to the roundtrip time inside the resonator. Furthermore, T_{ceo} is defined as the time at which the internal phase of the fast oscillation of the carrier wave reproduces. In the event that the electric field amplitudes of the individual modes are equal, thus $E_{m,0} = E_{s,0}$, it can be deduced that, $E_{p,0} = (2M+1)E_{s,0}$. The parameter $E_{s,0}$ is defined as the non-mode-dependent power in a single mode.

In Figure A.31, three consecutive pulses from a pulse train are shown. In this pulse train, five modes, thus $M = 2$, with identical amplitudes, are propagating inside the resonator. The phase $\phi_m = m\Delta\phi$ of each mode is fixed, with a phase difference of $\Delta\phi = \pi/2$ between each mode. As can be observed, a small, limited number of modes are capable of generating the pulse. The intensity of the pulse train in the time domain is given by

$$I_p(t) = I_{p,0}\left|E_{p,n}(t)\right|^2, \tag{A.136}$$

with $I_{p,0} = \frac{1}{2}c_0\varepsilon_0\left|E_{p,0}\right|^2$. The quantity $\left|E_{p,0}\right|^2$ is the squared electric field amplitude of the total pulse, and $\left|E_{p,n}(t)\right|^2$ is the normalized electric field, with respect to this amplitude. In the event of equivalent electric field amplitudes, it is $I_{p,0} = (2M+1)^2 I_{s,0}$, thereby indicating that the intensity undergoes an increase in proportion to the square of the overlapping modes. Figure A.32 (a), illustrates the intensity of the previously described pulse train, in addition to the intensities of two additional pulse trains. The only difference between these pulse trains is the number of interfering modes. Furthermore, panel (b) presents two pulse trains that are identical in all respects, but ϕ_m, with $M = 50$. The phase difference between the interfering modes is constant ($\phi_m = m\Delta\phi$) for one pulse train (gray) and fully randomized ($\phi_m \in [0, 2\pi]$) for the other (orange).

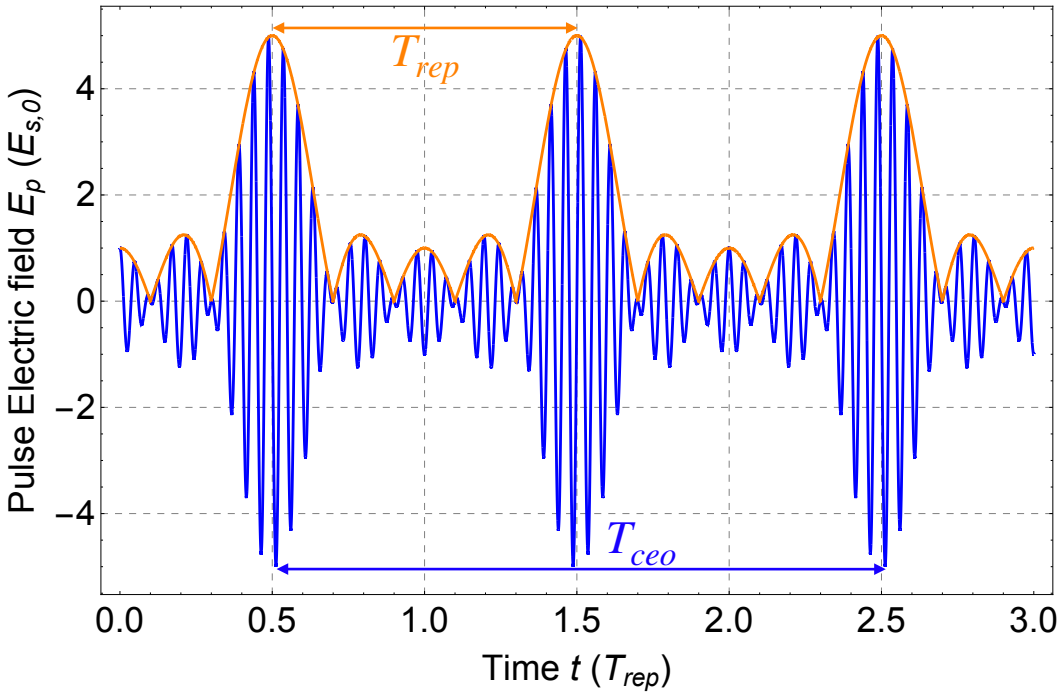


Figure A.31: The plot illustrates the electric field of a pulse train in the time domain, as delineated by Equation (A.135). The orange line signifies the absolute value of the electric field, thereby describing the envelope. In contrast, the blue line represents the real part, which highlights the rapid internal oscillations. The pulse is composed of five modes of equal electric field amplitude, including the carrier. These modes exhibit a phase shift of $\Delta\phi = \pi/2$ relative to their adjacent counterparts. The CEO frequency was set to half the repetition rate to visualize its effect, as the phase of the internal oscillation will reproduce every other pulse.

The images presented herein serve to illustrate two distinct phenomena. Firstly, as the number of modes increases, the pulse becomes more sharp and shorter without altering other characteristics, such as the pulse-to-pulse interval. Furthermore, the phase transition between modes is a critical factor in the viability of a pulse train. In particular, it should be either zero or constant. In the event of slight variations, the result will first be a decreasing amplitude before the pulse peak vanishes into the noise. In the event that the mode-to-mode phase is fixed, the laser is in a mode-locked state. This state is a prerequisite for the operational functionality of a pulsed laser. In the limit of a high number of modes, $M \gg 10$, it is sufficient to approximate the shape of a single pulse in the time domain by a Gaussian distribution through the function

$$E_p = E_{p,0} e^{-\left(2\frac{t}{\tau_p}\right)^2},$$

where the time constant τ_p is determining the $1/e$ pulse length in the intensity picture. A simulation of the intensity of two typical pulses with a repetition rate of $\Delta\omega = (2\pi)\,20\,\mathrm{MHz}$, a CEO frequency of $\omega_{ceo} = (2\pi)\,250\,\mathrm{MHz}$ and $M = 10^5$ is shown in Figure A.33. In one case, the field amplitude of

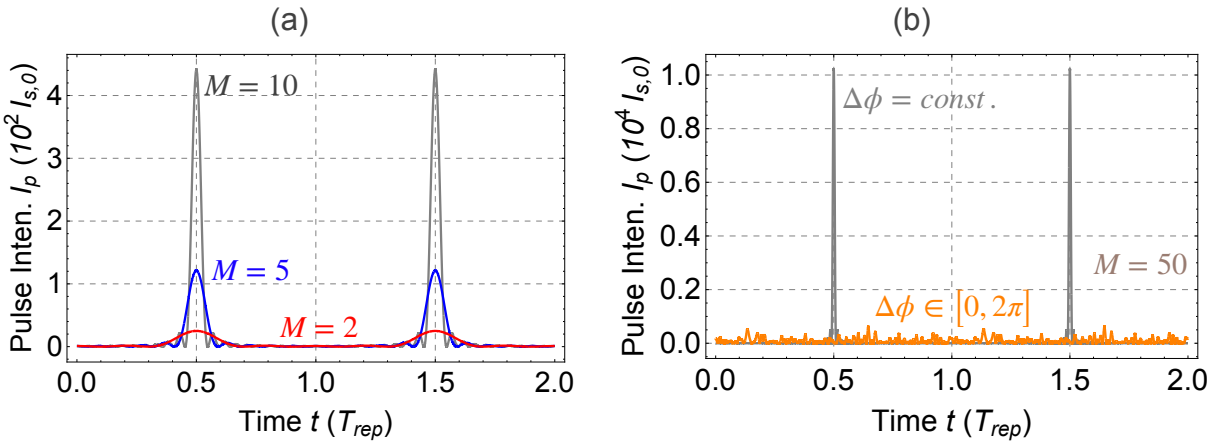


Figure A.32: The plots illustrate pulse intensities in the time domain, according to Equation (A.136), in relation to the intensity of a single mode component, $I_{s,0}$, under the assumption that all modes possess equal electric field amplitudes. (a): The figure displays two pulses of the pulse train when the train is simulated for three different fixed amounts of modes. As the mode count increases, the peak intensity and sharpness of the pulses increase accordingly, resulting in shorter pulses. (b): The simulation illustrates two pulses of a pulse train for $M = 50$ in the case of a constant mode to mode phase ϕ_m, thus in mode-locked state, (gray) and a fully randomized phase (orange).

all modes are equal in strength, yielding the pulse field amplitude

$$\text{Figure } A.33 \text{ (a)} : E_{p,0} = (2M+1)\, E_{s,0}, \tag{A.137}$$

whereas the second scenario demonstrates a Gaussian profile of the electric field amplitudes around the carrier frequency through

$$\text{Figure A.33 (b)} : E_{p,0}(m) = E_{s,0} e^{-\left(2\frac{\omega_m - \omega_0}{\omega_{bw}}\right)^2}. \tag{A.138}$$

The second model (Gaussian amplitude) incorporates the frequency band of the emitted photons within the gain medium. In the simulation, the relation $\omega_{bw} = \frac{\omega_M}{2}$ was utilized. Increasing the number of modes beyond this does not have a significant visual impact on the plot. Assuming that all modes possess equivalent strengths, a Gaussian fit over the pulse will yield the pulse length τ_p, which is contingent upon the number of modes and the time interval between pulses. This results in the following equation:

$$E_{p,0} = (2M+1)\, E_{s,0},\ \tau_p \approx \frac{0.52}{(2M+1)} T_{rep}$$

In the event that the mode strength is distributed according to a Gaussian shape, the pulse width will widen due to the reduced contribution of modes to the pulse. Consequently, the pulse shape will closely resemble the Gaussian function. The pulse length, denoted by τ, can be expressed alternatively in terms of its FWHM, which is calculated as $\tau = \sqrt{\ln 2}\tau_p$. The pulse can be further analyzed in the frequency domain, $\widetilde{E}_p(\omega)$, by performing a Fourier transformation of the electric

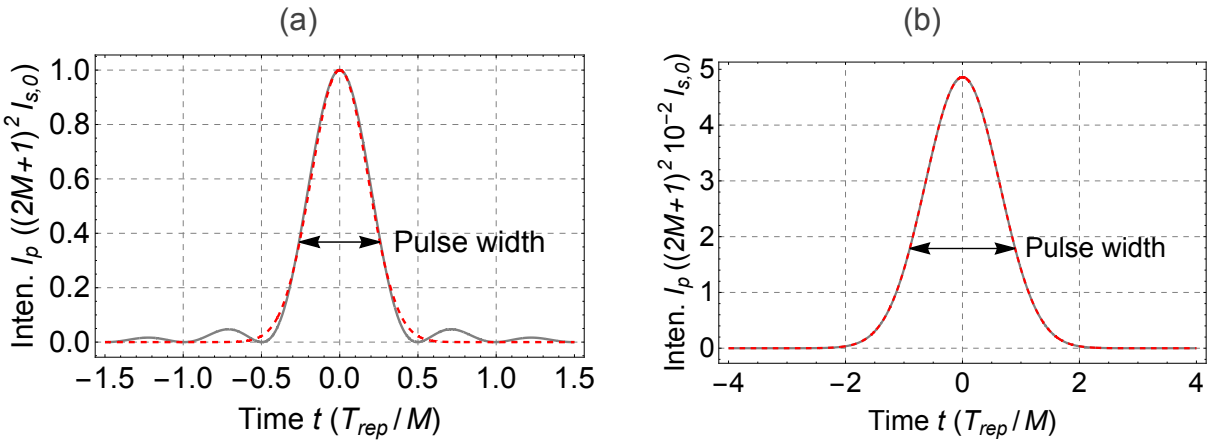


Figure A.33: The intensity of a single pulse in the time domain via Equation (A.136) (gray). (a): The intensity of the pulse is calculated for the case that all modes have an equal electric field amplitude (see Equation (A.137)). (b): The pulse intensity for a Gaussian field amplitude distribution surrounding the carrier (see Equation (A.138)). In both images, the red dashed line represents a Gaussian fit over the pulse.

field in the time domain through the formalism:

$$\widetilde{E}_p(\omega) = \int_{-\infty}^{\infty} E_p(t)\, e^{-i\omega t}\, dt \tag{A.139}$$

Substituting Equation (A.135) into (A.139) and rearranging the terms results in the expression

$$\widetilde{E}_p(\omega) = \sum_{n=-\infty}^{\infty} E_{0,m} e^{i\phi_m} \int_{-\infty}^{\infty} e^{i\left(\omega_0 - \omega + m\omega_{rep} + \omega_{ceo}\right)t}\, dt.$$

The integral of the exponential term is well-known and can be solved by the Dirac delta function, δ_D, which is defined as

$$\delta_D(\omega - \omega_0) = \frac{1}{2\pi} \int_{-\infty}^{\infty} e^{i(\omega-\omega_0)t}\, dt = \begin{cases} 0, & \omega \neq \omega_0 \\ \infty, & \omega = \omega_0 \end{cases}.$$

This will ultimately result in the expression of the electric field in the frequency domain as follows:

$$\widetilde{E}_p(\omega) = 2\pi \sum_{n=-\infty}^{\infty} E_{0,m} e^{i\phi_m} \delta_D\left(\omega'_m\right) \tag{A.140}$$

In this formalism, the argument of the Delta function is given by $\omega'_m = \omega_0 - \omega + m\,\omega_{rep} + \omega_{ceo}$. In the mode-locked state, the quantity $\widetilde{E}_p(\omega)$ is zero everywhere except when $\omega'_m = 0$. Consequently, non-vanishing components only exist when the following relation is satisfied:

$$\omega = \omega_0 + m\,\omega_{rep} + \omega_{ceo} \tag{A.141}$$

The Dirac delta is characterized by its infinitely sharp and large nature at the argument. However, in reality, the components possess a finite width and amplitude. Consequently, the discrete Delta function $\overline{\delta}_D$, defined as

$$\overline{\delta}_D(\omega-\omega_0)=\begin{cases}0, & \omega\neq\omega_0\\ 1, & \omega=\omega_0\end{cases},$$

is employed to provide a more accurate representation of reality. Therefore, the amplitude of the discrete modes is given by the respective electric field amplitude $E_{0,m}$. The application of a Gaussian distribution to model the field amplitudes results in the establishment of the formalism:

$$\widetilde{E}_p(\omega)=2\pi\widetilde{E}_{0,0}e^{-\left(2\frac{\omega m-\omega_0}{\omega_{bw}}\right)^2}\overline{\delta}_D\left(\omega'_m\right)e^{i\phi_m}$$

The intensity of the pulse train is expressed in the Fourier picture as follows:

$$\widetilde{I}_p(\omega)=(2\pi)^2\widetilde{I}_{p,0}\left|\widetilde{E}_{p,n}(\omega)\right|^2$$

The intensity of the pulse is defined as $\widetilde{I}_{p,0}=\frac{1}{2}c_0\varepsilon_0\left|\widetilde{E}_{0,0}\right|^2$, thus the squared field amplitude $\left|\widetilde{E}_{p,n}(\omega)\right|^2$ is normalized with respect to $\left|\widetilde{E}_{0,0}\right|^2$. A simulation of the Fourier components is displayed in Figure A.34. In this figure, the orange line signifies the Gaussian profile of the frequency component distribution within the gain medium. The magenta peaks represent the distinct components of the pulse, which collectively form what is referred to as an OFC. The gray bars represent the pulse, under the assumption that all components possess equivalent strength. The simulation is conceptual in nature; it is evident that a mere five modes are accommodated within the bandwidth, ω_{bw}, which is considerably lower than that of a real-world example. The total number of modes, $M'=2M+1$, generating the pulse can be estimated by

$$M'=\frac{\omega_{bw}}{\omega_{rep}}.$$

Titanium-sapphire (Ti:Al_2O_3 or simply Ti:Sa) lasers are recognized for their substantial bandwidth, which is commonly in the range of 800 nm, and their capacity to generate ultra-fast pulses with durations τ ranging from $O(\tau)=10^1-10^2$ fs, with $O(M')=10^6$. This results in the generation of a pulse with modes or lines ranging from 680 nm up to 960 nm. A variety of gain media can be utilized to generate broad output spectra across a range of central frequencies. Nonlinear processes leading to spectral broadening can be utilized to generate a broader output range of the pulsed laser. This range can extend up to $2f$, where f denotes the lowest frequency. Notably, the carrier frequency, designated as $\omega_0=2\pi f_0$, is not arbitrary but rather represents a mode frequency with a specific mode number, N_0, such that

$$f_0=N_0f_{rep}+f_{ceo}.$$

The frequency difference f_b (beat) between a probe laser light of frequency f_l and the closest comb tooth or mode can be measured on a PD. Subsequently, the absolute frequency of the laser light can

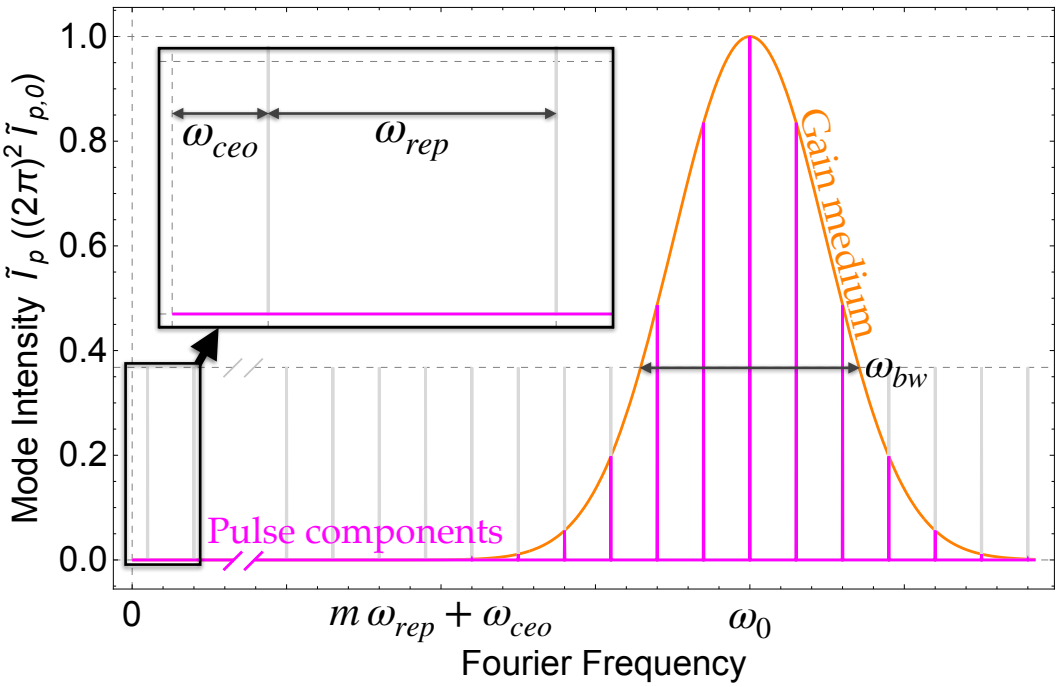


Figure A.34: This figure illustrates the intensity profile in the frequency domain of the optical frequency comb. The application of the Fourier transform to the time domain of a pulsed laser results in the generation of equally spaced, distinct frequency components. The spacing of these comb 'teeth' is dictated by the repetition rate, with the initial spacing determined by the CEO frequency. The orange curve signifies the general emission bandwidth of the gain medium, while the magenta lines denote the resulting standing wave frequency modes. The gray bars represent the structure of the gain medium in the case of an infinite bandwidth.

be reconstructed by means of the OFC characteristics through the formalism

$$f_l = f_b + N_l\, f_{rep} + f_{ceo}. \tag{A.142}$$

The integer number N_l denotes the respective closest comb tooth. The frequencies f_{ceo}, f_{rep} and f_b can be measured by frequency counters. In particular, the CEO can be determined by the beat between the frequency doubled $N-$th tooth against the tooth with mode number $2N$, such that it follows

$$f_N = N\, f_{rep} + f_{ceo},\; f_{2N} = 2N\, f_{rep} + f_{ceo} \Longrightarrow 2f_N - f_{2N} = f_{ceo}. \tag{A.143}$$

The repetition rate can be directly measured by splitting a part of the pulsed laser and sending it to a PD. The integration of a band-pass or low-pass filter around the anticipated repetition rate is essential, as the pulse-generated light contains the interference of all individual modes.

The final element necessary to calculate the absolute frequency of a probe laser of frequency f_l, is the mode number N_l, which must be determined using a separate tool capable of evaluating the absolute frequency of light. This tool is the wavemeter described in Section (A.7.3).

A.7.2 Noise Cancellation: Stabilizing Light Through Fibers

The content of this section now appears in the main thesis text (Section 2.4.1) as it forms a critical part of the theoretical framework. This note serves as a placeholder for its original appendix location.

A.7.3 Wavelength Meters: Measuring Optical Frequencies

The underlying principle of any interferometer is to divide a beam of light into two distinct paths, which are subsequently reunited. The resulting beat of the recombined light carries the information regarding the different OLs traversed. A typical configuration is a Michelson interferometer, where, in modern applications, laser light is split into two orthogonal paths by a beam splitter, where both beams then reflect at mirrors and subsequently recombine in the beam splitter. The resulting light can then be measured by means of a PD. The employment of a PBS in conjunction with quarter-waveplates is a method of optimizing the intensity along all paths. Figure A.35 illustrates the fundamental principle.

The OL difference will manifest as a visible difference in the beat, where the intensity is maximized due to constructive interference when the OL is a multiple of half wavelengths, as established prior. The apparatus can be utilized to investigate material characteristics, such as surface structures, refractive indices, or, as in this configuration, to ascertain wavelengths. The initial configuration of the mirrors is such that the intensity of the light at the detector is maximized.

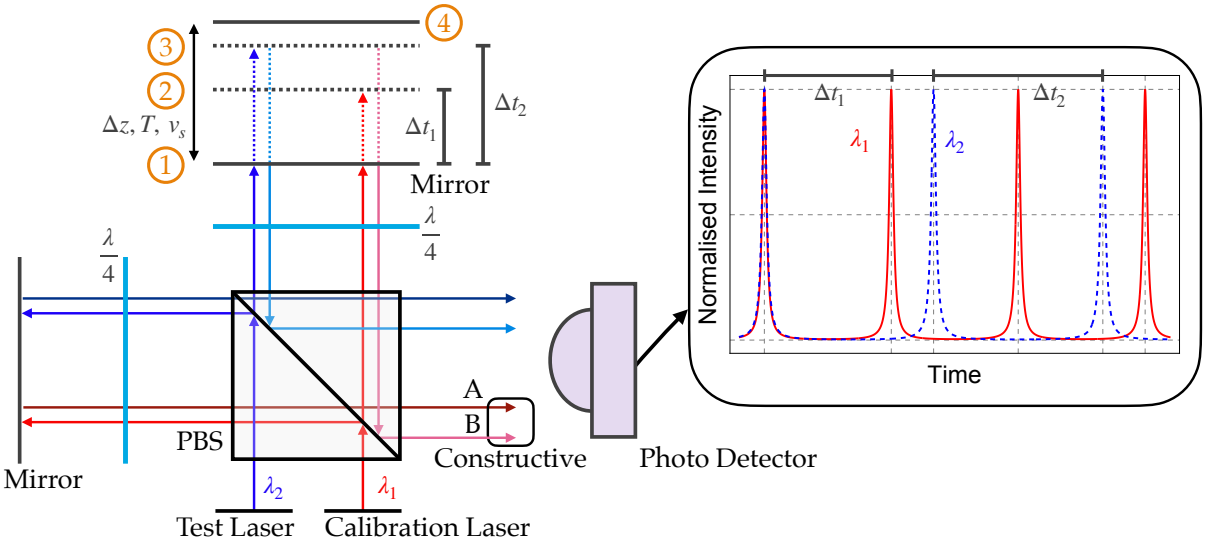


Figure A.35: The wavelength meter is based on a Michelson interferometer. The red lines signify the calibration light, while the blue line denotes the tested laser. The top mirror oscillates between positions 1 and 4, as indicated by the orange circles. Constructive interference for both lasers occurs at position 1 (typically those are different, but for the sake of simplicity in the sketch). The next constructive interference for the respective light occurs at positions 1 and 2. The intensity of both signals in the time domain is represented on the right side of the figure.

This results in an OL difference $\Delta OL_0 = m\frac{\lambda_i}{2}$, where m is an integer. At a specific time t_0, one of the mirrors undergoes an oscillatory movement with an angular frequency Ω, moving back and forth from the beam splitter. Subsequently, the temporal progression of the OL is dictated by

$$\Delta OL(t) = 2\frac{\Omega}{2\pi}(t - t_0)\, n\Delta z = 2\frac{n}{v_s}(t - t_0),$$

where Δz is the amplitude of the oscillation, v_s is the angular velocity of the mirror, and n is the refractive index of the propagation medium. The following moment in time that constructive interference will occur is denoted by t_i, thus it is

$$\Delta OL(t_i) = 2\frac{\Omega}{2\pi}(t_i - t_0)\, n\Delta z \stackrel{!}{=} (m+1)\frac{\lambda_i}{2}.$$

Calculating the difference $\Delta OL(t_i) - \Delta OL_0$ and substituting $\Delta t_i = t_i - t_0$ yields the equation

$$\Delta t_i = \frac{v_s}{4n}\lambda_i.$$

Accordingly, the intensity at the PD will exhibit peaks separated by the time interval, Δt_i. Maintaining a constant value for v_s and establishing a correlation between the time intervals between constructive interferences from two distinct lasers results in the following conclusion:

$$\lambda_2 = \frac{\Delta t_2}{\Delta t_1}\lambda_1. \tag{A.144}$$

It is possible to determine the time, Delta Δt_1, and calibrate the interferometer by taking into account a well-known wavelength, λ_1. Consequently, the wavelength of another light λ_2 can be determined by measuring the time Δt_2, as indicated by Equation (A.144). This process serves as a fundamental principle underlying the operation of a device known as a wavelength meter. The resolution of a wavelength meter is generally inferior to that of a contemporary frequency comb. Nevertheless, it can be adequate for determining the mode number N of the comb tooth that is nearest to the tested laser light. Therefore, it is critical that the resolution of the wavelength meter (short: wavemeter) is sufficient to resolve the repetition rate.

A viable alternative to the scanning mirror interferometer, which is characterized by its absence of moving parts, is the Fizeau interferometer. This particular interferometer is frequently employed in modern wavelength meters. In this configuration, light propagates towards a beam splitter, undergoes reflection, and subsequently travels through an inclined slab towards a mirror. At the front of the slab, the light is partially reflected partially propagates towards the mirror, where it is reflected. Once more, the utilization of a PBS in conjunction with wave plates can effectively redirect interfering beams towards a charge-coupled device (CCD) camera. The concept is illustrated in Figure A.36. The two arms of the interferometer are determined by the two reflected beams (front of slab and mirror). The OL difference of light of wavelength λ_i can be evaluated by

$$\Delta OL_i = 2(n_s d + n z_i).$$

In this equation, n_s denotes the refractive index of the slab, and d signifies its thickness. The distance z_i is measured from the beam's location after the beam splitter to the point at which the light is reflected by the slab. In contrast to before, the interferometer exhibits a spatial dependence

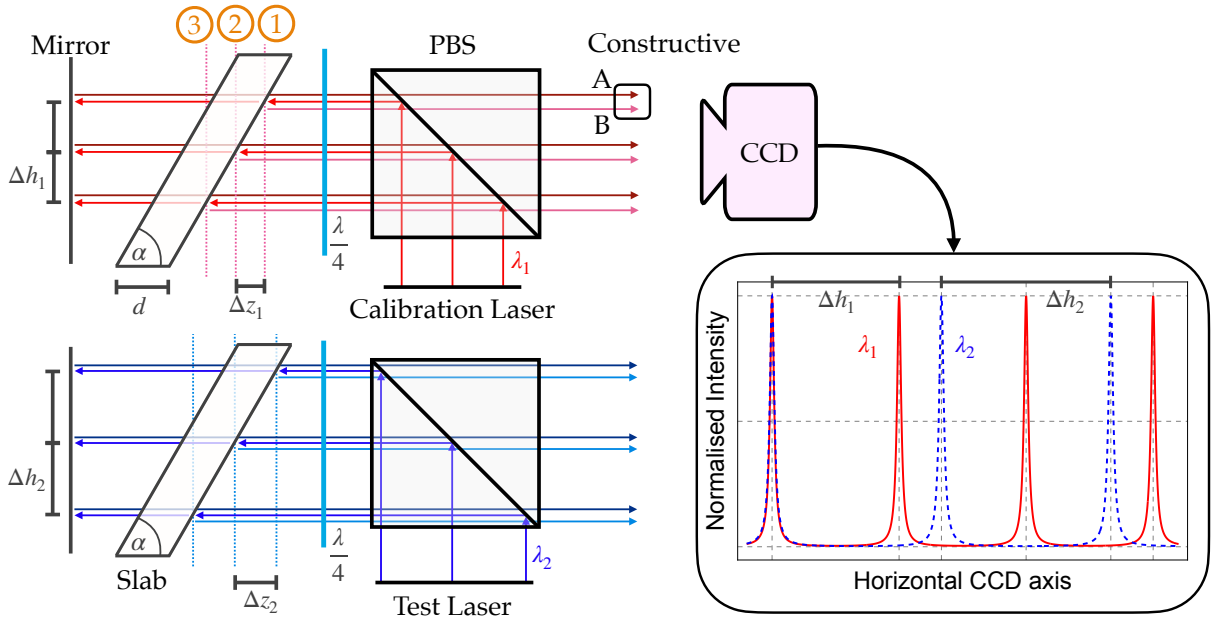


Figure A.36: Red lines denote the calibration laser light, while blue indicates the tested light. Constructive interference is observed at the camera when light is reflected at the slab at positions 1, 2, and 3. The spatial intensity, in this case along the axis parallel to the mirror, is displayed on the right.

on the path length difference, as opposed to a temporal dependence. The occurrence of constructive interference is dependent upon the height of the beam relative to the optical axis that is orthogonal to the mirror. For two spatial adjacent fringes, calculating the path length difference $\Delta OL_i - \Delta OL_0$ of constructive interference observed at positions z_0 and z_i of the beams with $\Delta z = z_i - z_0$, it follows

$$\Delta z_i = \frac{\lambda_i}{4n}.$$

The distance Δh_i between the fringes is given by the angle α of the slab with respect to the optical axis, thus

$$\Delta h_i = \tan(\alpha)\Delta z_i.$$

Eventually, similar to the Michelson interferometer, the formalism to determine the wavelength λ_2 of a tested light is given by

$$\lambda_2 = \frac{\Delta h_2}{\Delta h_1}\lambda_1.$$

Calibration of the system is essential, as previously discussed. This calibration is achieved by introducing light of a known wavelength, designated as λ_1, and subsequently measuring the distance of constructive interferences. This measurement is typically conducted using a CCD camera. Modern Fizeau-based wavemeters have the capacity to measure with a precision of 10 MHz when properly calibrated. A calibration light is typically an HeNe laser. With repetition rates in the

order of 100 MHz, the mode number N can be reliably determined. A software-based algorithm is employed to fit a suitable function to the spatial intensity distribution. This process enables the calculation of the wavelength of the test laser with respect to the calibrated data.

Due to the impact of environmental factors, it is necessary to perform regular recalibrations to ensure the maintenance of precision. Nevertheless, the resolution attainable in measuring light can be significantly superior, reaching an order of magnitude of 100 kHz or less. In instances where a long-term stability requirement is not a prerequisite of the application, and where the highest short-term stability and precision requirements are not essential, a wavelength meter can be utilized as a reference for laser light. This may be the absorption spectroscopy of transitions with linewidths at the order of several 100 MHz, where it is necessary to maintain the laser at resonance.

A.7.4 Long-Term References: Hydrogen Masers and GNSS

The content of this section now appears in the main thesis text (Section 2.4.2) as it forms a critical part of the theoretical framework. This note serves as a placeholder for its original appendix location.

A.7.5 Putting It All Together: Frequency Analysis and Measurement

The content of this section now appears in the main thesis text (Section 2.4.3) as it forms a critical part of the theoretical framework. This note serves as a placeholder for its original appendix location.

Appendix B

Publications and Contribution

The appendix comprises a total of six publications, to which the creator of this work is either an author or has made a significant contribution, either by providing data or tools for measurement, as indicated in Table B.1. In addition, the appendix includes the two works of non-authorship.

Year	Topic	Journal	Status
2022	Dark matter research on Iodine	Physical Review Letters	Published
2024	Stable lasers - Spectroscopy grade OPO	Optics Express	Published
2025	Stable lasers - Guidelines for 10^{-17} level	arXiv	Published
2025	Dark matter research on Acetylene	Physical Review D	Published

Table B.1: The following is a list of publications that employ the developments discussed in this thesis. The creator of this thesis is a co-author of all publications.

Here, the contribution is partially given in the respective acknowledgements. These are the works on molecular spectroscopy on HD^+ in 2023 and molecular spectroscopy on HD^+/H_2^+ in 2024, both published in Nature Physics. The publications are divided into three primary categories: dark matter research, molecular spectroscopy, and ultra-stable lasers.

B.1 Ultra-Light Dark Matter

B.1.1 Search for Dark Matter Using Iodine Spectroscopy

Title:
Search for Dark-Matter-Induced Oscillations of Fundamental Constants Using Molecular Spectroscopy

Authors:
R. Oswald, A. Nevsky, **V. Vogt**, S.Schiller, N.L. Figueroa, K. Zhang, O. Tretiak, D. Antypas, D. Budker, A.Banerjee and G.Perez

Status / Year: ..... Published / 2022

Journal: .....Physical Review Letters

DOI: 10.1103/PhysRevLett.129.031302

Licence: .....Creative Commons Attribution 4.0 International license.

Statement of Copyright:
"Copyright © 2011 by American Physical Society. All rights reserved.

Individual articles are copyrighted by the APS, as indicated on each article.

Individual articles may be downloaded for personal use; users are forbidden to reproduce, republish, redistribute, or resell any materials from this journal in either machine-readable form or any other form without permission of the APS or payment of the appropriate royalty for reuse."

Reuse policy for dissertation:
"[...] the author has the right to use the article or a portion of the article in a thesis or dissertation without requesting permission from APS, provided the bibliographic citation and the APS copyright credit line are given on the appropriate pages."

My Contribution:
I was responsible for setting up and operating the cavity system, which provided the ultra-stable reference light for experiment A. I created the schematic in Fig. 1, developed in collaboration with coauthors, in the main text and the setup sketch in Figure 1 in the supplemental material. I also plotted the data shown in Fig. 2 in the main text and Figure 2 in the supplemental material. Additionally, I have plotted the data in Figure 3 of the supplemental material, where I have also provided the measured data for the magenta and green lines constituting the frequency noise density of the reference light. See Section 7.1.

Search for Dark-Matter-Induced Oscillations of Fundamental Constants Using Molecular Spectroscopy

R. Oswald, A. Nevsky, V. Vogt, and S. Schiller*
Institut für Experimentalphysik, Heinrich-Heine-Universität Düsseldorf, 40225 Düsseldorf, Germany

N. L. Figueroa, K. Zhang,† O. Tretiak, and D. Antypas‡
Johannes Gutenberg-Universität Mainz, 55128 Mainz, Germany
and Helmholtz-Institut, GSI Helmholtzzentrum für Schwerionenforschung, 55128 Mainz, Germany

D. Budker
Johannes Gutenberg-Universität Mainz, 55128 Mainz, Germany Helmholtz-Institut,
GSI Helmholtzzentrum für Schwerionenforschung, 55128 Mainz, Germany
and Department of Physics, University of California, Berkeley, California 94720, USA

A. Banerjee and G. Perez
Department of Particle Physics and Astrophysics, Weizmann Institute of Science, Rehovot, Israel 7610001

(Received 2 November 2021; revised 7 April 2022; accepted 2 June 2022; published 15 July 2022)

A possible implication of an ultralight dark matter field interacting with the standard model degrees of freedom is oscillations of fundamental constants. Here, we establish direct experimental bounds on the coupling of an oscillating ultralight dark matter field to the up, down, and strange quarks and to the gluons, for oscillation frequencies between 10 and 10^8 Hz. We employ spectroscopic experiments that take advantage of the dependence of molecular transition frequencies on the nuclear masses. Our results apply to previously unexplored frequency bands and improve on existing bounds at frequencies >5 MHz. We also improve on the bounds for coupling to the electromagnetic field and the electron field, in particular spectral windows. We identify a sector of ultralight dark matter and standard model coupling space where the bounds from equivalence principle tests may be challenged by next-generation experiments of the present kind.

DOI: 10.1103/PhysRevLett.129.031302

Introduction.—There are strong theoretical reasons to assume that fundamental constants (FC) are, in fact, dynamical and can be described as expectation values of scalar fields (see Ref. [1] for a review). Temporal evolution of these fields results in a time variation of the "constants" that can be searched for at the precision frontier (see, for example, review Ref. [2]). If a scalar field constitutes ultralight dark matter (UDM) [3,4] with sub-electron-volt mass, then its amplitude oscillates at its Compton frequency, $f_\phi = m_\phi c^2/h$, where m_ϕ is the scalar-particle mass, c is the speed of light in vacuum, and h is Planck's constant.

Two theoretical proposals relevant to this study have been put forward. In the first, the UDM mass is protected by an approximate scale-invariance symmetry [3]. In the second, UDM is an axionlike particle, whose mass is protected by an approximate shift symmetry according to the Goldstone theorem [5] that is broken, together with the combined charge-parity invariance [6,7], by two independent sectors [8]. This model is inspired by the relaxion paradigm [9]. In both frameworks, dark matter (DM) couples to the standard-model (SM) fields either due to the fact that the couplings break scale invariance [10] or via mixing with the Higgs [6], resulting in time-varying FC. An additional theoretical approach, that also leads to time-varying FC, is based on discrete symmetries [11,12].

As neither observations nor theoretical arguments can constrain the DM-particle mass [13], broadband searches are particularly motivated. Note that the preferred region of the model of Refs. [8,14] is $m_\phi \gtrsim 10^{-11}$ eV $\sim$ kHz, the frequency range studied here. Above roughly 10^{-18} eV, the most stringent constraints on time-varying UDM have been provided by equivalence-principle (EP) tests of gravity (see Ref. [15] and references therein). Here, we argue that there is a sense in which the bounds arising from direct DM searches are independent from any single EP test.

Published by the American Physical Society under the terms of the Creative Commons Attribution 4.0 International license. Further distribution of this work must maintain attribution to the author(s) and the published article's title, journal citation, and DOI. Funded by SCOAP³.

Using this insight we show how the EP bounds on UDM models can be challenged by atomic and molecular experiments in the near future. Prior to discussing direct searches for scalar UDM, we introduce the phenomenology of EP tests.

EP tests are conveniently expressed in terms of the Eötvös parameter, $\eta_{\rm EP}^{\rm exp} \equiv 2|\vec{a}_A - \vec{a}_B|/|\vec{a}_A + \vec{a}_B|$, that is sensitive to the differential acceleration ($\vec{a}$) of two test bodies, A and B (see Ref. [16], for example). The parameter can be expressed in terms of the relevant DM couplings to the SM fields d_i [see Eq. (1)]. One defines the "dilatonic charge" of a body, $Q_i^X = \partial \ln m_X/\partial \ln g_i$, m_X being the mass of the body X and g_i a FC. Then,

$$\eta_{\rm EP}^{\rm exp} \propto \sum_{i,j} (\Delta Q)_i^{\rm exp} d_i \times Q_j^{\rm source} d_j,$$

with the dilatonic charge difference $(\Delta Q)_i^{\rm exp} \equiv Q_i^A - Q_i^B$.

In contrast to EP-violating acceleration searches, direct scalar-UDM experiments probe observables arising from the dependence of atomic transition energies, the length of solid objects, or the refractive indices of materials on the FCs. For a review, see, for example, Ref. [17], for proposals, see Refs. [18–27], and for experiments providing bounds on FC oscillations, see Refs. [28–37]. While atomic experiments are sensitive to variation of the electron mass m_e but are almost insensitive to changes in nuclear masses m_N, molecular experiments probe for variation of both. EP tests probe nuclear masses and are largely insensitive to m_e. Thus, EP tests and oscillating FC experiments are complementary to each other, as we further discuss below.

Moreover, the level of FC oscillations might be enhanced at frequencies $f_\phi \geq 1$ kHz due to the presence of UDM halos around Earth and Sun [38] exhibiting increased DM density and coherence time. Such enhancement would not apply to fifth-force experiments, as in these, the test masses exchange virtual DM particles, a process independent of the background DM density. Recently, searches for FC oscillations were extended to frequencies $f_\phi > 1$ Hz [29,30,34,35].

While oscillations of the fine-structure constant α and m_e have received substantial attention, here, we focus on "nuclear" FCs: the quantum chromodynamics (QCD) energy scale $\Lambda_{\rm QCD} \simeq 0.33$ GeV, and the masses of the light quarks $m_{u,d,s}$. These determine m_N. Here, we employ molecular spectroscopy to search for oscillations in these FCs over a large frequency range, with a fractional sensitivity of $10^{-14} - 10^{-15}$.

Theoretical model.—To illustrate the interaction of a sub-electron-volt scalar field ϕ with SM fields, we write the low-energy effective Lagrangian as

$$\mathcal{L}_{\rm eff} \supset -\frac{\phi}{M_{\rm Pl}}\left(\sum_X d_{m_X} m_X \bar{X} X - \frac{d_\alpha}{4} F^2 + \frac{d_{g_s}\beta(g_s)}{2g_s} G^2\right). \quad (1)$$

Here, $X = e, u, d, s$ are the fermion fields with mass m_X, $F^2 = F^{\mu\nu}F_{\mu\nu}$, $G^2 = \frac{1}{2}{\rm Tr}(G^{\mu\nu}G_{\mu\nu})$, $F_{\mu\nu}$, and $G_{\mu\nu}$ are the electromagnetic field and gluon field strength, respectively, d_j are dimensionless coupling constants, and $M_{\rm Pl} = \sqrt{\hbar c/(8\pi G_N)} = 2.4 \times 10^{18}$ GeV is the Planck mass. The parameter g_s is the strong-interaction coupling constant, $\alpha_s \equiv g_s^2/4\pi$. The function $\beta(g_s)$ describes the evolution ("running") of the coupling constant with energy, via the renormalization-group equation $\beta(g_s)/(2g_s) = -(11 - 2n_f/3)\alpha_s/8\pi$, with n_f being the number of dynamical quarks.

As a consequence of the UDM-SM couplings in Eq. (1), the SM constants acquire a dependence on the scalar field [18],

$$m_X(\phi) = m_X\left(1 + d_{m_X}\frac{\phi}{M_{\rm Pl}}\right), \quad (2)$$

$$\alpha(\phi) \simeq \alpha\left(1 + d_\alpha \frac{\phi}{M_{\rm Pl}}\right), \quad (3)$$

$$\alpha_s(\phi) \simeq \alpha_s\left(1 - \frac{2d_{g_s}\beta(g_s)}{g_s}\frac{\phi}{M_{\rm Pl}}\right). \quad (4)$$

The QCD scale $\Lambda_{\rm QCD}$ depends on g_s through the renormalization-group equation and dimensional transmutation (see, for example, Ref. [39]). Thus, the variation of $\Lambda_{\rm QCD}$ can be written in terms of the variation of α_s as

$$\frac{\partial \ln \Lambda_{\rm QCD}}{\partial \phi} = -\frac{g_s}{2\beta(g_s)}\frac{\partial \ln \alpha_s}{\partial \phi} = \frac{d_{g_s}}{M_{\rm Pl}}. \quad (5)$$

The mass of a nucleus m_N is the sum of the nucleon masses, strong and electromagnetic binding energy. Neglecting the small electromagnetic binding energy proportional to α, the nucleon mass depends on $\Lambda_{\rm QCD}$, and $m_{u,d,s}$ [16,40]. The variation of m_N can be related to variation of FCs as [41]

$$\frac{\delta m_N}{m_N} = 0.873\frac{\Delta\Lambda_{\rm QCD}}{\Lambda_{\rm QCD}} + 0.084\frac{\Delta\hat{m}}{\hat{m}} + 3\times 10^{-4}\frac{\Delta\delta m}{\delta m} + 0.043\frac{\Delta m_s}{m_s}, \quad (6)$$

where $\hat{m} \equiv (m_u + m_d)/2$ is the mean mass of the up and down quarks and $\delta m \equiv m_u - m_d$ is the mass difference. Note that, for the contribution of m_s to the nucleon mass, we have used the lattice QCD result [41]. Combining this result with Eqs. (2) and (5), we find

$$\frac{\delta m_N}{m_N} = 0.878\hat{Q}_N \cdot \vec{d}\frac{\phi(t)}{M_{\rm Pl}}, \quad (7)$$

with $\vec{d} \equiv (d_\alpha, d_{m_e}, d_{g_s}, d_{\hat{m}}, d_{\delta m}, d_{m_s})$ and $\hat{Q}_N \approx (0, 0, 0.994, 0.096, 3\times 10^{-4}, 0.049)$ defined to be a unit-length vector.

Assuming that ϕ is a viable UDM candidate, it can be treated as a classical oscillating field,

$$\phi(\vec{x},t) \approx m_\phi^{-1}\sqrt{2\rho_{\rm DM}^{\oplus}}\sin\left[m_\phi(t+\vec{\beta}_\oplus\vec{x})\right], \tag{8}$$

with $\rho_{\rm DM}^{\oplus}$ and $\vec{\beta}_\oplus$ being the UDM density and its typical velocity on the surface of Earth, respectively. Gravity-based measurements yield a weak direct bound on $\rho_{\rm DM}^{\oplus}$ (see, for instance, Refs. [38,42,43]).

We consider various scenarios for the properties of the DM around Earth. In the standard scenario where UDM constitutes a Galactic halo [44], with $\rho_{\rm DM}^{\oplus} \equiv \rho_{\rm DM}^{\rm G} \simeq 0.3\ {\rm GeV/cm^3}$ and $\beta_\oplus c \simeq 220\ {\rm km/s}$, it is reasonable to assume that during the UDM virialization process around the Galaxy, different patches or quasiparticles obtain random phases. This results in the UDM field-amplitude admitting stochastic fluctuations around its commonly assumed value [45–48]. For additional models, see Ref. [49].

Experimental approach.—Atomic clocks can be used to search for oscillations of the proton mass and the nuclear g factor. However, the operation mode of the clocks imposes $f_\phi \lesssim 1$ Hz. An alternative approach is spectroscopy of molecules [60,61]. Their transition frequencies depend on changes in the rotational and vibrational energy. Here, we focus on the latter. The vibrational energy $\hbar\omega_{\rm vib}$ of a diatomic molecule containing two nuclei N_1, N_2 scales approximately as $E_{\rm Ryd}\sqrt{m_e/\mu}$, where $\mu = m_{N_1}m_{N_2}/(m_{N_1}+m_{N_2})$ is the reduced nuclear mass. Thus, molecular transitions with a change of vibrational energy are sensitive to the nuclear mass $m_{N_i} \propto m_N$. Furthermore, their dependence on m_e is enhanced beyond the scaling $E_{\rm Ryd} \propto m_e$.

In a spectroscopy apparatus a quantum system having a resonance frequency $\nu^{(1)}$ is interrogated by the wave of frequency $\nu^{(2)}$ from an oscillator tuned to the proximity of $\nu^{(1)}$. The oscillator is often stabilized to another reference (atomic ensemble or cavity). The spectrum of the frequency deviation $\Delta\nu(t)/\nu = [\nu^{(1)}(t) - \nu^{(2)}(t)]/\nu$ is measured. The dependence of a frequency $\nu^{(i)}$ on a particular FC g may be characterized by the fractional derivative $R_g^{(i)} = d\ln\nu^{(i)}/d\ln g$. A modulation $\delta g/g$ results in a fractional frequency modulation $\delta\nu/\nu = (R_g^{(1)} - R_g^{(2)})\delta g/g$. Therefore, a key experimental parameter is the differential sensitivity $\Delta R_g = R_g^{(1)} - R_g^{(2)}$.

Apparatus and operation.—We carry out two experiments, A and B (Fig. 1) [49], in which for $\nu^{(1)}$ we use an electronic transition of molecular iodine (I_2) between the ground electronic state X and the excited electronic state B [62]. In apparatus A we perform saturation spectroscopy on the transition $R(56)32\text{-}0$ at 532 nm ($v=0$, $v'=32$), with sensitivity $R_N^{(1,A)} \simeq -0.06$. In apparatus B, absorption spectroscopy is implemented on the transition is $R(122)2\text{-}10$ at 725 nm ($v=10$, $v'=2$) [63], with $R_N^{(1,B)} \simeq 0.07$. In both experiments, the interrogating oscillator is a laser (frequency $\nu^{(2)}$). Apparatus A employs a Nd:YAG laser frequency-stabilized to a reference cavity. The detected modulation frequency range covers 10 Hz to 100 kHz. For this configuration and frequency range, $R_\alpha^{(2)} = 1$, $R_e^{(2)} = 1$ [49]. In apparatus B, the laser is a Ti:sapphire laser and frequencies in the range 100 kHz–100 MHz are considered. This range being above the acoustic cutoff frequency of the laser $f_2^{(B)} \simeq 50$ kHz [30], the frequency $\nu^{(2,B)}$ is essentially independent of the FCs [64].

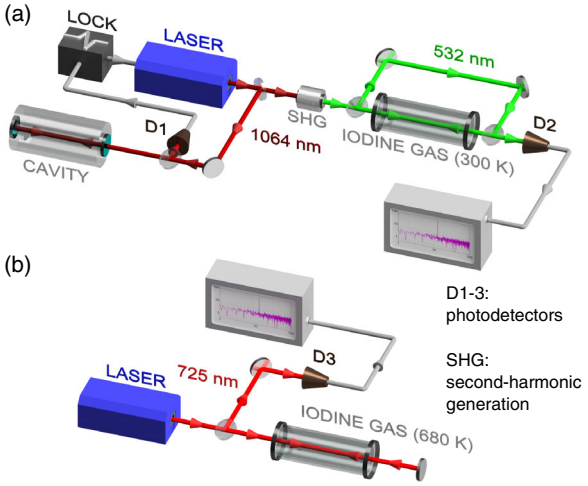


FIG. 1. The two molecular iodine experiments: (a) A; (b) B.

Summarizing, experiments A and B provide sensitivity to α, m_e, and m_N. For experiment A, $\Delta R_\alpha^{(A)} \simeq 2-1=1$, $\Delta R_e^{(A)} = (1-R_N^{(1,A)})-1 \simeq +0.06$, $\Delta R_N^{(A)} = R_N^{(1,A)} - 0 \simeq -0.06$. For experiment B, $\Delta R_\alpha^{(B)} \simeq 2$, $\Delta R_e^{(B)} = (1-R_N^{(1,B)}) - 0 \simeq +0.93$, and $\Delta R_N^{(B)} = R_N^{(1,B)} - 0 \simeq 0.07$.

In both experiments, the instantaneous frequency deviation $\Delta\nu$ is converted into a voltage signal $V^{(k)}(t) = D^{(k)}\Delta\nu^{(k)}(t)$, with the discriminators $D^{(k)}$ being system parameters, and $k = A, B$. This allows obtaining the spectrum of the fractional frequency variation $\delta\nu^{(k)}/\nu^{(k)}$. The time-varying FC ($\alpha$, m_e, and m_N) contribute to the variation according to

$$\frac{\delta\nu^{(k)}}{\nu^{(k)}} = \Delta R_\alpha^{(k)}\frac{\delta\alpha}{\alpha} + \Delta R_e^{(k)}\frac{\delta m_e}{m_e} + \Delta R_N^{(k)}\frac{\delta m_N}{m_N}. \tag{9}$$

Search for oscillating fundamental constants.—In the experiments, the lasers are tuned to the iodine transitions and the signals $V^{(k)}(t)$ are recorded. From these records the periodograms are calculated [49]. In experiment A, the obvious peaks in the periodogram [49] were investigated and identified as being of technical origin, in part by shifting the laser frequency away from the resonance and repeating the measurement. This left no obvious candidate UDM signals. We do not give limits for these excluded intervals, that have widths of 5 Hz or smaller. From the

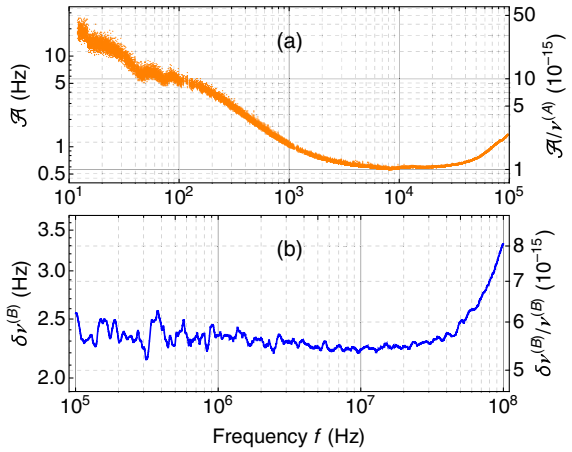


FIG. 2. (a) Experiment A. Spectral amplitude $\mathcal{A} = \sqrt{\mathrm{PSD}_F/T}$ of the scaled discriminator signal $\Delta\nu^{(A)}(t) = V^{(A)}(t)/D^{(A)}$. PSD_F is the optimally filtered power spectral density, with a filter adapted to signals having the same linewidth f/Q_0, $Q_0 \simeq 1 \times 10^6$, as standard Galactic halo UDM. The width of the orange band corresponds to the mean of $\mathcal{A} \pm \sigma(f)$. (b) Experiment B. The bound (95% confidence level) on fluctuations of the signal $\Delta\nu^{(B)}(t) = V^{(B)}(t)/D^{(B)}$.

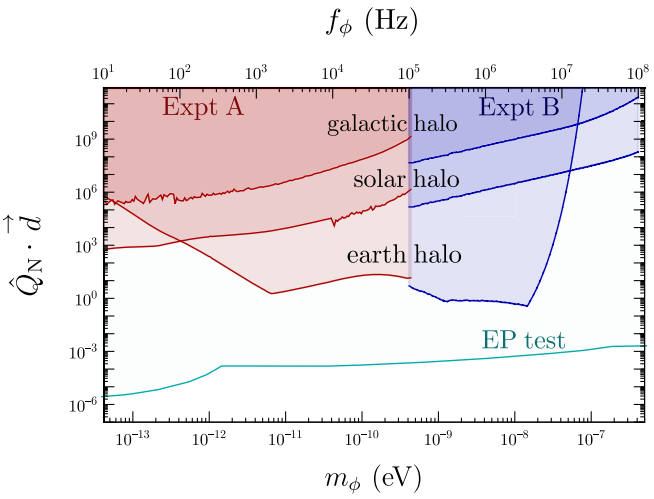


FIG. 3. Exclusion plot of the combination of couplings to the QCD sector, $\hat{Q}_N \cdot \vec{d} = 0.994 d_{g_s} + 0.096 d_{\hat{m}} + 3 \times 10^{-4} d_{\delta m} + 0.049 d_{m_s}$. Turquoise line: fifth-force–EP-violation experiments [66–70].

periodogram, the upper limit of the coupling parameters d_g was determined using the analysis of Ref. [52]. The (model-dependent) spectral amplitude of the recorded signal is shown in Fig. 2(a) [49].

In experiment B, the voltage $V(t)$ was measured with the laser frequency tuned either on the slope of the I_2 resonance, or off resonance, alternating between these UDM-sensitive and insensitive acquisition modes to account for spurious signals due to sources other than UDM. The corresponding periodograms were computed and continuously averaged. The periodogram difference between the on- and off-resonance acquisition modes was also computed and averaged over a 60-hr-long run. This spectrum will contain power in excess of statistical noise in the presence of FC oscillations, and it is subsequently investigated for UDM detection. A number of candidate peaks were identified having power in excess of a 95% detection threshold, that was computed considering the "look elsewhere" effect [65]. All spurious signals were checked in auxiliary experiments and eventually attributed to technical noise. The postinspected spectrum is used to obtain a constraint for $\delta\nu^{(B)}/\nu^{(B)}$ Fig. 2(b) [49].

Models and bounds.—We analyze the experimental data within the three mentioned models that differ in terms of the UDM field amplitude and its coherence time $\tau_{\mathrm{coh}} = 1/[\omega_\phi (v_{\mathrm{vir}}/c)^2]$:

$$\tau_{\mathrm{coh}} = \begin{cases} 5.9 \times 10^5 f_\phi^{-1}, Q = 1.1 \times 10^6, \text{Galactic halo} \\ 7.1 \times 10^7 f_\phi^{-1}, Q = 9.0 \times 10^7, \text{solar halo} \\ \infty, \text{Earth halo}. \end{cases} \quad (10)$$

To derive bounds to the UDM couplings, we assume that only one of the constants m_e, α, or m_N in Eq. (9) oscillates and analyze the three cases separately [49]. In Fig. 3, we present our constraints on the combined quark and gluons couplings $\hat{Q}_N \cdot \vec{d}$ together with existing EP constraints.

Constraints on the variation of α and m_e are presented in Fig. 4, alongside the strongest previous constraints on the relevant parameter space. Astrophysical bounds on our scenario could also apply, however, these are typically weaker than those discussed here and are less robust (see Refs. [71–73] for recent discussions). For clarity, we show constraints for the standard Galactic UDM halo only. Our results cover the previously unexplored bands 10–50 Hz and 5–10 kHz, and improve on existing bounds in the ranges 0.1–0.2 MHz and 3–100 MHz.

More generally, our experiments are sensitive to the following linear combinations of the full set of couplings, defined in Eqs. (7), (9), that can be written as $\vec{Q} \cdot \vec{d} = |\vec{Q}| \hat{Q} \cdot \vec{d}$ with $|\vec{Q}^A| = 1$, $|\vec{Q}^B| = 2.21$, and the unit-length vectors

$$\hat{Q}^A \simeq (1.0, 0.06, -0.05, -0.005, -1.5 \times 10^{-5}, -0.0024),$$
$$\hat{Q}^B \simeq (0.90, 0.42, 0.027, 0.0025, 8 \times 10^{-6}, 0.0013). \quad (11)$$

We do not consider the strange quark mass contribution in the context of EP as it is complementary to the contribution of g_s, see Ref. [49]. Thus, for the following discussion of the complementarity between EP tests and UDM searches, we reduce the six-dimensional $\vec{Q}$ to five dimensions by dropping the last entry corresponding to m_s. In this space, one can find a direction $\hat{Q}^{\perp}_{\mathrm{full}}(m_\phi)$ that is

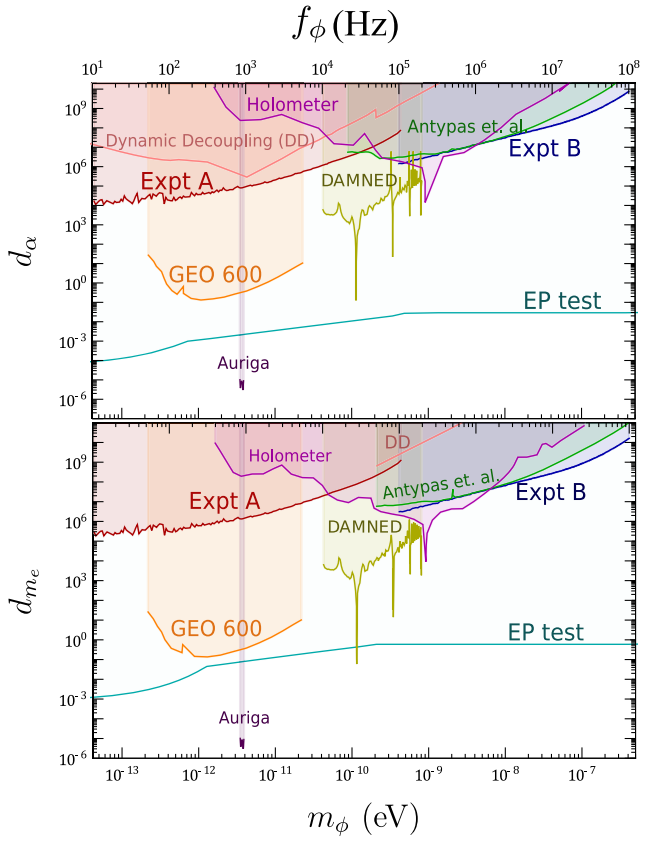


FIG. 4. Exclusion plot of the UDM couplings to α (top) and m_e (bottom). Existing constraints: shaded regions in orange [34], yellow [35], pink [29], green [64], magenta [37], and purple [74]. Fifth-force–EP tests: turquoise [66–70].

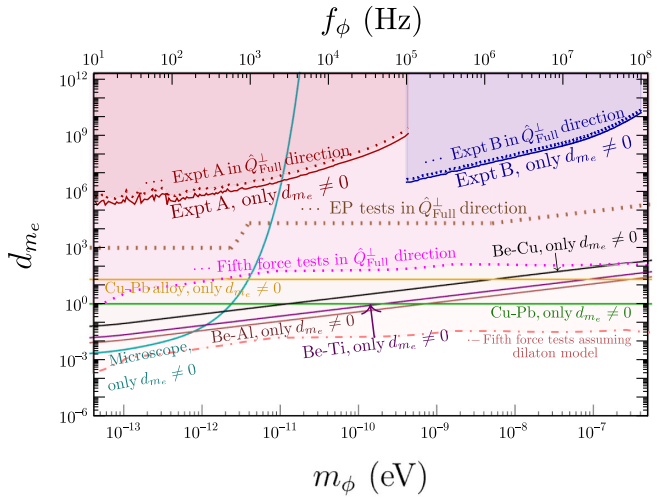


FIG. 5. Exclusion plot for d_{m_e}. The dotted lines depict the bounds for a model defined by a vector of sensitivities, $\hat{Q}^\perp_{\rm full}(m_\phi)$, that is orthogonal to the sensitivities of four leading EP test experiments [49]. Bounds from other published experiments, shown in Fig. 4, are not shown again here. The bound from the fifth-best EP test experiment in a given mass range, projected onto the $\hat{Q}^\perp_{\rm full}(m_\phi)$ direction, and further on the d_{m_e} direction, is shown as dotted brown line.

orthogonal to the best four EP-test bounds, for a given mass. For example, in the mass range of $2 \times 10^{-12} \lesssim m_\phi/\text{eV} \lesssim 5 \times 10^{-9}$, these are the Be-Al [66], Be-Ti [67], Cu-Pb [75], and Be-Cu [76] experiments, and we find $\hat{Q}^\perp_{\rm full}(m_\phi) \simeq (0.003, 0.987, 0.002, -0.001, 0.160)$. For masses above 5×10^{-9} eV, $\hat{Q}^\perp_{\rm full}$ is perpendicular to the Be-Al [66], Be-Ti [67], Cu-Pb [75], and Cu-Pb-alloy [77] sensitivity vectors, with a correspondingly modified $\hat{Q}^\perp_{\rm full}$ [49]. Models of light scalar UDM with coupling direction defined according to $\hat{Q}^\perp_{\rm full}(m_\phi) \cdot \vec{d}$ would not be constrained by these four leading EP bounds. Note that, $\hat{Q}^\perp_{\rm full}(m_\phi)$ has a substantial overlap with the d_{m_e} direction (the second entry) throughout the whole mass range. Thus, experiments that are particularly sensitive to m_e, test a sector of coupling space that the first four-best EP experiments are weakly sensitive to. In Fig. 5, we present our bounds on $\hat{Q}^\perp_{\rm full} \cdot \vec{d}$, projected (for clarity) in the d_{m_e} direction as dotted red and blue lines. The fifth-best EP bound projected onto $\hat{Q}^\perp_{\rm full}(m_\phi)$ and further on d_{m_e}, is shown by a brown dotted line. Note that we could only calculate the projection of $\hat{Q}^\perp_{\rm full}$ into the remaining fifth-best EP bound to an accuracy of 1 part in 10^3 due to the limited precision of the published test mass composition data. We find that in this sector of coupling space the bounds related to our direct UDM experiments are only two to 3 orders weaker than those from EP tests.

Furthermore, one can consider a model of a dilaton UDM, which is not constrained by the EP violating tests [18] (see Ref. [49]). A dilaton UDM would mediate a long-range Yukawa force, which can be constrained by various experiments that test for deviations from Newtonian gravity (fifth-force searches) [78]. The fifth-force bound for this model is represented by the crimson colored dot-dashed line, while for completeness in pink we also show the fifth-force bound for our model where the coupling is defined according to $\hat{Q}^\perp_{\rm full}(m_\phi) \cdot \vec{d}$ as discussed above.

Conclusion.—Our molecular-spectroscopy experiments have resulted in the first bounds on the coupling of an oscillating UDM field to the gluon and quark fields, in a broad frequency range that spans seven decades (10 Hz–100 MHz). In four windows within this range, improvements on previous limits for the coupling to the electromagnetic field and the electron field were also obtained.

A new generation of experiments, with minimization of all noise sources, long acquisition times, high sampling rates, and, possibly, multiple setups to improve statistical averaging, could improve the present limits by several orders of magnitude. Furthermore, we have argued that there is a special class of dark matter couplings where the bounds from equivalence principle tests are significantly less stringent than expected. Consequently, future

experiments of the present kind may be able to probe this class of UDM models with sensitivity competitive to EP tests.

We thank D. Kanta for help with the project, and D. Iwaschko and R. Gusek for electronics development. A. B. thanks the Galileo Galilei Institute for Theoretical Physics for the hospitality and the INFN for partial support during the completion of this work. This work was supported by the Cluster of Excellence "Precision Physics, Fundamental Interactions, and Structure of Matter" (PRISMA + EXC 2118/1) funded by the German Research Foundation (DFG) within the German Excellence Strategy (Project ID 39083149), by the European Research Council (ERC) under the European Union Horizon 2020 research and innovation program (project Dark-OST, Grant No. 695405, project YbFUN, Grant No. 947696), by the DFG Reinhart Koselleck project. The work of A. B. was supported by the Azrieli Foundation. The work of G. P. is supported by grants from BSF-NSF (No. 2019760), Friedrich Wilhelm Bessel research award, GIF, the ISF (Grant No. 718/18), Minerva, SABRA–Yeda-Sela–WRC Program, the Estate of Emile Mimran, and The Maurice and Vivienne Wohl Endowment.

*step.schiller@hhu.de
†kezhang@uni-mainz.de
‡dantypas@uni-mainz.de

[1] J.-P. Uzan, Living Rev. Relativity **14**, 2 (2011).
[2] M. S. Safronova, D. Budker, D. DeMille, D. F. J. Kimball, A. Derevianko, and C. W. Clark, Rev. Mod. Phys. **90**, 025008 (2018).
[3] A. Arvanitaki, J. Huang, and K. Van Tilburg, Phys. Rev. D **91**, 015015 (2015).
[4] P. W. Graham, D. E. Kaplan, J. Mardon, S. Rajendran, and W. A. Terrano, Phys. Rev. D **93**, 075029 (2016).
[5] F. Chadha-Day, J. Ellis, and D. J. E. Marsh, Sci. Adv. **8**, eabj3618 (2022).
[6] T. Flacke, C. Frugiuele, E. Fuchs, R. S. Gupta, and G. Perez, J. High Energy Phys. 06 (2017) 050.
[7] K. Choi and S. H. Im, J. High Energy Phys. 12 (2016) 093.
[8] A. Banerjee, H. Kim, and G. Perez, Phys. Rev. D **100**, 115026 (2019).
[9] P. W. Graham, D. E. Kaplan, and S. Rajendran, Phys. Rev. Lett. **115**, 221801 (2015).
[10] W. D. Goldberger, B. Grinstein, and W. Skiba, Phys. Rev. Lett. **100**, 111802 (2008).
[11] A. Hook, Phys. Rev. Lett. **120**, 261802 (2018).
[12] D. Brzeminski, Z. Chacko, A. Dev, and A. Hook, Phys. Rev. D **104**, 075019 (2021).
[13] G. Bertone and T. M. P. Tait, Nature (London) **562**, 51 (2018).
[14] A. Banerjee, E. Madge, G. Perez, W. Ratzinger, and P. Schwaller, Phys. Rev. D **104**, 055026 (2021).
[15] G. M. Tino, L. Cacciapuoti, S. Capozziello, G. Lambiase, and F. Sorrentino, Prog. Part. Nucl. Phys. **112**, 103772 (2020).
[16] T. Damour and J. F. Donoghue, Phys. Rev. D **82**, 084033 (2010).
[17] M. S. Safronova, Ann. Phys. (Amsterdam) **531**, 1800364 (2019).
[18] A. Arvanitaki, J. Huang, and K. Van Tilburg, Phys. Rev. D **91**, 015015 (2015).
[19] M. S. Safronova, S. G. Porsev, C. Sanner, and J. Ye, Phys. Rev. Lett. **120**, 173001 (2018).
[20] V. A. Dzuba, V. V. Flambaum, and S. Schiller, Phys. Rev. A **98**, 022501 (2018).
[21] A. Banerjee, H. Kim, O. Matsedonskyi, G. Perez, and M. S. Safronova, J. High Energy Phys. 07 (2020) 153.
[22] E. Peik, T. Schumm, M. S. Safronova, A. Pálffy, J. Weitenberg, and P. G. Thirolf, Quantum Sci. Technol. **6**, 034002 (2021).
[23] J. Manley, D. J. Wilson, R. Stump, D. Grin, and S. Singh, Phys. Rev. Lett. **124**, 151301 (2020).
[24] A. A. Geraci, C. Bradley, D. Gao, J. Weinstein, and A. Derevianko, Phys. Rev. Lett. **123**, 031304 (2019).
[25] Y. V. Stadnik and V. V. Flambaum, Phys. Rev. Lett. **114**, 161301 (2015).
[26] Y. V. Stadnik and V. V. Flambaum, Phys. Rev. A **93**, 063630 (2016).
[27] H. Grote and Y. V. Stadnik, Phys. Rev. Research **1**, 033187 (2019).
[28] K. Van Tilburg, N. Leefer, L. Bougas, and D. Budker, Phys. Rev. Lett. **115**, 011802 (2015).
[29] S. Aharony, N. Akerman, R. Ozeri, G. Perez, I. Savoray, and R. Shaniv, Phys. Rev. D **103**, 075017 (2021).
[30] D. Antypas, O. Tretiak, A. Garcon, R. Ozeri, G. Perez, and D. Budker, Phys. Rev. Lett. **123**, 141102 (2019).
[31] A. Hees, J. Guéna, M. Abgrall, S. Bize, and P. Wolf, Phys. Rev. Lett. **117**, 061301 (2016).
[32] C. J. Kennedy, E. Oelker, J. M. Robinson, T. Bothwell, D. Kedar, W. R. Milner, G. E. Marti, A. Derevianko, and J. Ye, Phys. Rev. Lett. **125**, 201302 (2020).
[33] P. Wcislo *et al.*, Sci. Adv. **4**, eaau4869 (2018).
[34] S. M. Vermeulen *et al.*, Nature (London) **600**, 424 (2021).
[35] E. Savalle, A. Hees, F. Frank, E. Cantin, P.-E. Pottie, B. M. Roberts, L. Cros, B. T. McAllister, and P. Wolf, Phys. Rev. Lett. **126**, 051301 (2021).
[36] W. M. Campbell, B. T. McAllister, M. Goryachev, E. N. Ivanov, and M. E. Tobar, Phys. Rev. Lett. **126**, 071301 (2021).
[37] L. Aiello, J. W. Richardson, S. M. Vermeulen, H. Grote, C. Hogan, O. Kwon, and C. Stoughton, Phys. Rev. Lett. **128**, 121101 (2022).
[38] A. Banerjee, D. Budker, J. Eby, H. Kim, and G. Perez, Commun. Phys. **3**, 1 (2020).
[39] M. E. Peskin and D. V. Schroeder, *An Introduction to Quantum Field Theory* (Addison-Wesley, Reading, USA, 1995).
[40] M. A. Shifman, A. I. Vainshtein, and V. I. Zakharov, Phys. Lett. **78B**, 443 (1978).
[41] P. M. Junnarkar and A. Walker-Loud, Phys. Rev. D **87**, 114510 (2013).
[42] C. J. Hogan and M. J. Rees, Phys. Lett. B **205**, 228 (1988).
[43] N. B. Anderson, A. Partenheimer, and T. D. Wiser, arXiv:2007.11016.
[44] D. J. E. Marsh, Phys. Rep. **643**, 1 (2016).

[45] J. W. Foster, N. L. Rodd, and B. R. Safdi, Phys. Rev. D **97**, 123006 (2018).
[46] G. P. Centers, J. W. Blanchard, J. Conrad, N. L. Figueroa, A. Garcon, A. V. Gramolin, D. F. J. Kimball, M. Lawson, B. Pelssers, J. A. Smiga *et al.*, Nat. Commun. **12**, 7321 (2021).
[47] M. Lisanti, M. Moschella, and W. Terrano, Phys. Rev. D **104**, 055037 (2021).
[48] A. V. Gramolin, A. Wickenbrock, D. Aybas, H. Bekker, D. Budker, G. P. Centers, N. L. Figueroa, D. F. Jackson Kimball, and A. O. Sushkov, Phys. Rev. D **105**, 035029 (2022).
[49] See Supplemental Material at http://link.aps.org/supplemental/10.1103/PhysRevLett.129.031302 for details on the experimental setups, data evaluation, and the discussion of additional models and EP tests, which includes Refs. [50–59].
[50] J. P. Turneaure, C. M. Will, B. F. Farrell, E. M. Mattison, and R. F. C. Vessot, Phys. Rev. D **27**, 1705 (1983).
[51] E. Savalle, A. Hees, F. Frank, E. Cantin, P.-E. Pottie, B. M. Roberts, L. Cros, B. T. McAllister, and P. Wolf, Phys. Rev. Lett. **126**, 051301 (2021).
[52] A. Derevianko, Phys. Rev. A **97**, 042506 (2018).
[53] A. Derevianko (private communication).
[54] M. S. Turner, Phys. Rev. D **42**, 3572 (1990).
[55] P. Touboul, G. Metris, M. Rodrigues, Y. Andre, Q. Baghi *et al.*, Phys. Rev. Lett. **119**, 231101 (2017).
[56] A. Dymarsky, Z. Komargodski, A. Schwimmer, and S. Theisen, J. High Energy Phys. 10 (2015) 171.
[57] F. Coradeschi, P. Lodone, D. Pappadopulo, R. Rattazzi, and L. Vitale, J. High Energy Phys. 11 (2013) 057.
[58] T. R. Taylor and G. Veneziano, Phys. Lett. B **213**, 450 (1988).
[59] D. B. Kaplan and M. B. Wise, J. High Energy Phys. 08 (2000) 037.
[60] D. Hanneke, B. Kuzhan, and A. Lunstad, Quantum Sci. Technol. **6**, 014005 (2021).
[61] D. Antypas, O. Tretiak, K. Zhang, A. Garcon, G. Perez, M. G. Kozlov, S. Schiller, and D. Budker, Quantum Sci. Technol. **6**, 034001 (2021).
[62] S. Gerstenkorn and P. Luc, J. Phys. France **46**, 867 (1985).
[63] S. Rakowsky, D. Zimmermann, and W. E. Ernst, Appl. Phys. B **48**, 463 (1989).
[64] D. Antypas, D. Budker, V. V. Flambaum, M. G. Kozlov, G. Perez, and J. Ye, Ann. Phys. (Amsterdam) **532**, 1900566 (2020).
[65] J. D. Scargle, Astrophys. J. **263**, 835 (1982).
[66] T. A. Wagner, S. Schlamminger, J. H. Gundlach, and E. G. Adelberger, Classical Quantum Gravity **29**, 184002 (2012).
[67] S. Schlamminger, K. Y. Choi, T. A. Wagner, J. H. Gundlach, and E. G. Adelberger, Phys. Rev. Lett. **100**, 041101 (2008).
[68] G. L. Smith, C. D. Hoyle, J. H. Gundlach, E. G. Adelberger, B. R. Heckel, and H. E. Swanson, Phys. Rev. D **61**, 022001 (1999).
[69] J. Bergé, P. Brax, G. Métris, M. Pernot-Borràs, P. Touboul, and J.-P. Uzan, Phys. Rev. Lett. **120**, 141101 (2018).
[70] A. Hees, O. Minazzoli, E. Savalle, Y. V. Stadnik, and P. Wolf, Phys. Rev. D **98**, 064051 (2018).
[71] R. Budnik, H. Kim, O. Matsedonskyi, G. Perez, and Y. Soreq, Phys. Rev. D **104**, 015012 (2021).
[72] W. DeRocco, P. W. Graham, and S. Rajendran, Phys. Rev. D **102**, 075015 (2020).
[73] N. Bar, K. Blum, and G. D'Amico, Phys. Rev. D **101**, 123025 (2020).
[74] A. Branca, M. Bonaldi, M. Cerdonio, L. Conti, P. Falferi, F. Marin, R. Mezzena, A. Ortolan, G. A. Prodi, L. Taffarello, G. Vedovato, A. Vinante, S. Vitale, and J.-P. Zendri, Phys. Rev. Lett. **118**, 021302 (2017).
[75] G. L. Smith, C. D. Hoyle, J. H. Gundlach, E. G. Adelberger, B. R. Heckel, and H. E. Swanson, Phys. Rev. D **61**, 022001 (1999).
[76] Y. Su, B. R. Heckel, E. G. Adelberger, J. H. Gundlach, M. Harris, G. L. Smith, and H. E. Swanson, Phys. Rev. D **50**, 3614 (1994).
[77] P. G. Nelson, D. M. Graham, and R. D. Newman, Phys. Rev. D **42**, 963 (1990).
[78] E. Fischbach and C. Talmadge, in *Proceedings of the 31st Rencontres de Moriond: Dark Matter and Cosmology, Quantum Measurements and Experimental Gravitation* (1996), pp. 443–451, arXiv:hep-ph/9606249.

Search for dark-matter-induced oscillations of fundamental constants using molecular spectroscopy: Supplemental Material

R. Oswald, A. Nevsky, V. Vogt, S. Schiller*
Institut für Experimentalphysik, Heinrich-Heine-Universität Düsseldorf, 40225 Düsseldorf, Germany

N. L. Figueroa, K. Zhang,† O. Tretiak, and D. Antypas‡
Johannes Gutenberg-Universität Mainz, 55128 Mainz, Germany and
Helmholtz-Institut, GSI Helmholtzzentrum für Schwerionenforschung, 55128 Mainz, Germany

D. Budker
Johannes Gutenberg-Universität Mainz, 55128 Mainz, Germany
Helmholtz-Institut, GSI Helmholtzzentrum für Schwerionenforschung, 55128 Mainz, Germany and
Department of Physics, University of California, Berkeley, California 94720, USA

A. Banerjee, G. Perez
Department of Particle Physics and Astrophysics,
Weizmann Institute of Science, Rehovot, Israel 7610001

I. EXPERIMENTS

A. Introduction

A molecular transition frequency can be approximated as $\nu^{(1)} = \nu_0 + \nu_{\mathrm{vib,B}} - \nu_{\mathrm{vib,X}}$, where $h\nu_0 \simeq (hc)15769\,\mathrm{cm}^{-1}$ is the difference in the electronic binding energies of the two states B and X, and $h\nu_{\mathrm{vib}}$ is the vibrational energy. Rotational energy contributions can be neglected, due to the large mass of iodine. We approximate the vibrational energies as $h\nu_{\mathrm{vib,X}} = h\omega_{\mathrm{vib,X}}(v + 1/2)$, $h\nu_{\mathrm{vib,B}} = (v' + 1/2)h\omega_{\mathrm{vib,B}}$, with the vibrational constants $\omega_{\mathrm{vib,X}} = c\,214.5\,\mathrm{cm}^{-1}$, $\omega_{\mathrm{vib,B}} = c\,125.7\,\mathrm{cm}^{-1}$. The vibrational quantum numbers in the states X and B are v and v', respectively. It is reasonable to assume that the electronic energy difference arises mostly from nonrelativistic dynamics. Then, since both electronic and vibrational energies are proportional to the Rydberg energy, we have $R_\alpha^{(1)} = 2$. The sensitivity to the electron mass is $R_{\mathrm{e}}^{(1)} \simeq 1 + (v'\omega_{\mathrm{vib,B}} - v\omega_{\mathrm{vib,X}})/2\nu^{(1)}$ and to the nuclear mass $R_{\mathrm{N}}^{(1)} \simeq -(v'\omega_{\mathrm{vib,B}} - v\omega_{\mathrm{vib,X}})/2\nu^{(1)}$. Since the vibrational energy contribution is only a small fraction of the total transition energy, $R_N^{(1)}$ is small. In the future, the value can be increased by using pure vibrational transitions [1].

Experiments A and B employ Doppler-free and Doppler-broadened I_2 transitions, respectively. The observed Doppler-free transition in apparatus A has a width of a few MHz. This width determines the frequency range over which there is significant molecular response to FC oscillations. In apparatus B, the observed Doppler-broadened transition is of the order of 1 GHz. In addition to Doppler broadening, there is significant homogeneous broadening due to collisions (as discussed below), and the molecular response is essentially constant over the 100 MHz range probed for FC oscillations.

Important features of the experimental setups are the power spectral noise densities of the fractional frequency fluctuations of the molecular reference, $S_y^{(1)}(f)$, and of the interrogating laser wave, $S_y^{(2)}(f)$. These contain contributions of technical or of fundamental origin. In order to obtain small values of $S_y^{(1)}$ it is advantageous to employ references containing a large number of particles, here a substantial gas volume.

B. Experiment A

Apparatus.

The scheme of the experiment is shown in Fig. 1a. The spectroscopy was performed on the a1 hyperfine structure component of the R(56)32-0 electronic transition. The oscillator interrogating the iodine gas is a Nd:YAG laser (laser 1). It is frequency-doubled to 532 nm by means of a fiber-coupled nonlinear conversion module. This wave has the frequency $\nu^{(2,\mathrm{A})}$. Laser 1 is phase-locked to a laser 2 that is frequency-stabilized to a 30 cm long ultrastable high-finesse ultra-low expansion glass (ULE) resonator.

The detected frequency range covers 10 Hz to 100 kHz. The lower end of this range covers frequencies smaller than the bandwidth of the frequency lock of the laser to the cavity, $f_1^{(\mathrm{A})} = 3\,\mathrm{kHz}$. For $f < f_1^{(\mathrm{A})}$, the frequency $\nu^{(2,\mathrm{A})}$ of the wave sent to the experiment is determined by the length of the ULE cavity. As widely discussed, for a cavity, $R_\alpha^{(2)} = 1$, $R_{\mathrm{e}}^{(2)} = 1$ [2]. For $f > f_1^{(\mathrm{A})}$ the laser resonator is the element determining the frequency fluctuations. Although the resonator is monolithic and the material has a refractive index larger than unity, to

* step.schiller@hhu.de
† kezhang@uni-mainz.de
‡ dantypas@uni-mainz.de

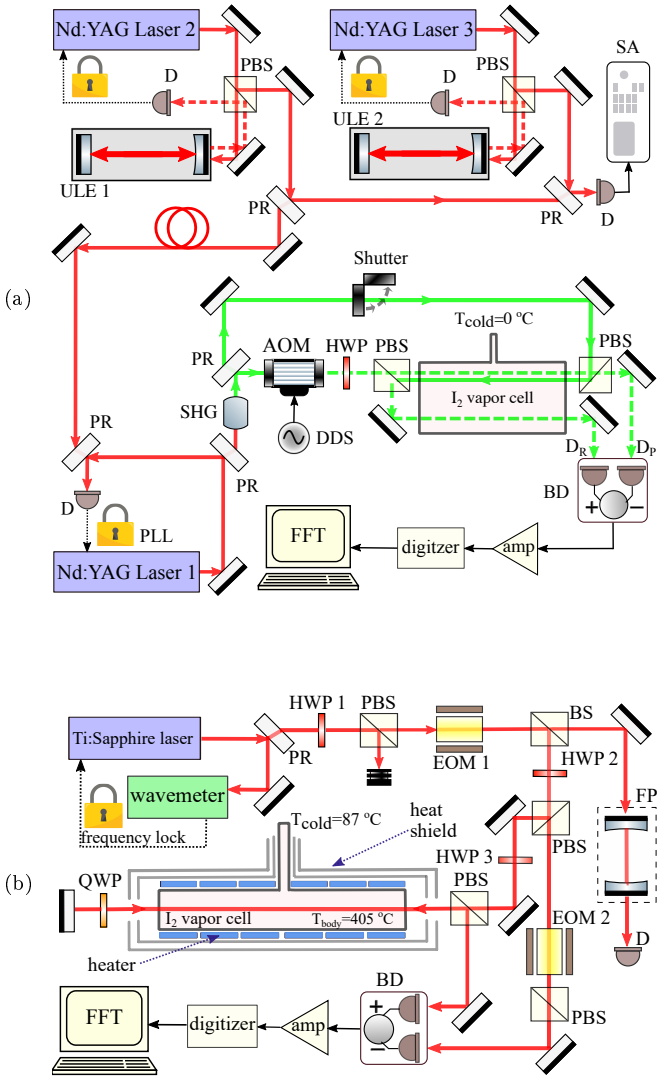


Figure 1. Experimental setups. (a) Setup for the experiment A. D: photodetector; AOM: acousto-optic modulator; SHG: second-harmonic generation; SA: spectrum analyzer; DDS: direct digital synthesizer; PBS: polarizing beam splitter; ULE: ultra-low expansion glass. BD: balanced photodetector; HWP: half-wave plate; PLL: phase-locked loop. (b) Setup for the experiment B. PR: partial reflector; PBS: polarizing beam splitter; BS: beam splitter, HWP: half-wave plate; QWP: quarter-wave plate; EOM: electro-optic modulator; D: photodetector; BD: balanced photodetector; FP: Fabry-Perot cavity. HWP 3 is mounted on a stepper motor to allow for active balancing of the detector output.

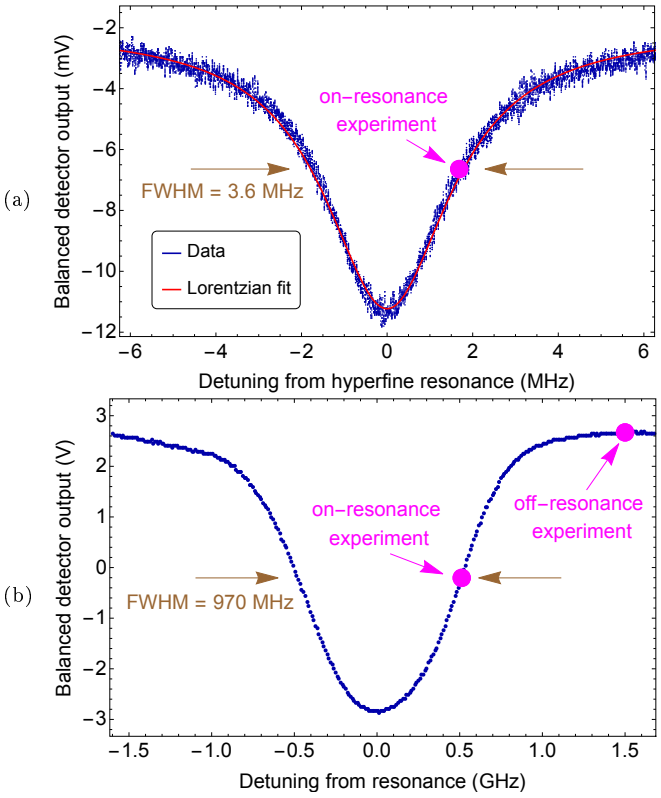


Figure 2. Spectra of iodine transitions employed in experiments A and B. (a) Doppler-free, pressure-broadened iodine transition at 532 nm in experiment A. FWHM: 3.6 MHz. Data was recorded with 1 MHz detection bandwidth and 10 ms scan time. For DM detection, the laser frequency is tuned to the operating point indicated by the magenta circle. The discriminator slope D is found from the slope of the signal at this point and the electronics' amplification factor. (b) Doppler- and pressure-broadened I_2 transition at 725 nm in experiment B. The magenta-color circles indicate the regions where the laser frequency is tuned to take data with, or without sensitivity to FC oscillations. The spectrum was recorded with 250 Hz bandwidth and 2 s scan time.

a good approximation, the same expressions for R_α, R_e hold. We neglect the effect of mechanical resonances [3].

The monolithic Nd:YAG resonator exhibits an acoustic cutoff, $f_2^{(A)} \simeq v_s/L_r \simeq 300\,\mathrm{kHz}$, where $L_r \simeq 2\,\mathrm{cm}$ is the linear dimension of the resonator and $v_s \simeq 6\times10^3\,\mathrm{m/s}$ is the speed of sound in the YAG resonator material. However, this cut-off is not relevant here because it is higher than the studied frequency range.

Approximately 30 mW of laser radiation at 532 nm is sent to the spectroscopy setup. It is split into two beams (probe and saturation) using a 20%:80% beam splitter. These are sent from opposite directions into a 30 cm-long cell filled with iodine gas (I_2). The iodine saturation pressure in the cell is maintained at about 0.04 mbar by temperature stabilization of the cell's cold finger at about 0° C using a Peltier element. The probe laser beam is frequency-shifted by 50 MHz using an AOM to prevent interference effects with the saturating beam. The counter-propagating probe and saturation beams are overlapped inside the cell allowing nonlinear saturation spectroscopy on the hyperfine structure (hfs) components of iodine rovibronic absorption lines. Saturation absorption resonances are detected in the power of the transmitted probe beam by means of a low-noise amplified photodetector D_P.

To reduce the effect of laser intensity noise we implemented balanced detection of the probe wave and a reference wave. The latter is obtained by splitting off part

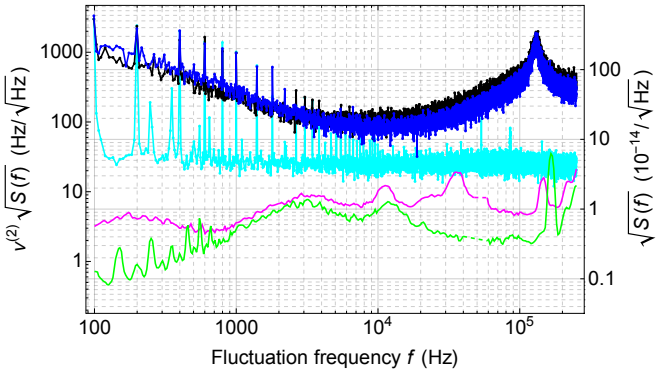


Figure 3. Noise levels in Experiment A. **Black**: total linear noise spectral density $(S_{\rm tot}(f))^{1/2}/(\nu^{(2,A)}D)$ for the detection of the relative frequency fluctuations between interrogating oscillator (laser 1) and iodine reference. The peak at 120 kHz is due to relaxation oscillations of the laser. Magenta: Estimated frequency noise of laser 1, $(S_y^{(2)}(f))^{1/2}$. A contribution to the latter is the noise of laser 2 and an estimate for it is the green trace. It is the spectral density of the frequency fluctuations of a beat between two similar cavity-stabilized lasers, one of which is laser 2, normalized to their optical frequency ($\nu^{(2)}/2 \simeq 282$ THz). Blue: total background noise of the detection process, $(S_{\rm det}(f))^{1/2}/(\nu^{(2,A)}D)$, obtained with the probe laser far detuned from the Doppler-free resonance. A contribution to the latter is the detector noise in absence of laser light, shown in cyan.

of the probe beam using a half-wave plate (HWP) and a polarizing beam splitter (PBS) in front of the cell. This reference beam is sent through the cell co-linearly with the spectroscopy probe beam, however not interacting with the saturation beam. The reference beam is detected with a photodetector D_R, similar to D_P.

The outputs of these photodetectors are subtracted in a precision differential buffer (Stanford Research Systems SRS 560). By adjusting the laser powers on the photodetectors by means of the HWP in front of the cell, the differential amplitude noise at the output of the amplifier can be reduced by about 40 dB over the bandwidth from DC to 1 MHz. This arrangement forms the balanced detector BD in the figure. The signal is further amplified by a factor of approximately 10^4 using a low-noise preamplifier. The data were acquired using a 16-bit DAQ (digital acquisition) card (National Instruments USB-6343) referenced to a Maser.

Characterization.

Figure 2a top shows one characteristic feature of the apparatus A the molecular resonance line. It is recorded by slowly scanning the frequency of the laser $\nu^{(2,A)}$ across the molecular resonance $\nu^{(1,A)}$ and acquiring the signal (voltage) change. The full width of the saturated absorption resonance was 3.6 MHz (FWHM), caused by a relatively high iodine pressure and contamination in the iodine cell. The natural linewidth of the transition is approximately 300 kHz. For DM detection, the laser 1 frequency was tuned to the half-height of the resonance by tuning the local oscillator frequency of the phase lock. Under this condition, the signal sent to the DAQ card has a sensitivity $D \simeq 1\,\text{V/MHz}$ on the laser frequency.

The second characteristic is the noise level of the apparatus. The total noise was determined by recording, for a comparatively short duration, the signal $V(t)$ when $\nu^{(2,A)}$ is kept at the operating point. (This recording was not part of the long-duration data recording, so noise presented in the following is to be regarded as typical.) The power spectral density (PSD) of $V(t)$ is denoted by $S_{\rm tot}$, having unit V^2/Hz. (In the following, we omit the superscript A in the PSDs for simplicity.) The scaled linear noise spectrum $(S_{\rm tot})^{1/2}/(\nu^{(2,A)}D)$ is shown in Fig. 3 in **black**.

We can express the total noise as arising from different contributions as

$$S_{\rm tot}(f) = (S_y^{(1)}(f) + S_y^{(2)}(f))(\nu^{(2,A)}D)^2 + S_{\rm det}(f)\,.$$

Here, $S_y^{(1)}(f)$ is the PSD of noise of the fractional molecular transition frequency (unit Hz^{-1}), $S_y^{(2)}(f)$ is the PSD of the interrogating laser (unit Hz^{-1}), and $S_{\rm det}(f)$ is the PSD of the detection noise (unit V^2/Hz).

The detection noise is due to effects such as laser amplitude noise, detector noise, electronic noise pick-up, optical feedback. These technical noises dominate over the also present fundamental noise sources, quantum fluctuations (shot noise) and thermal noises. The detection noise $S_{\rm det}(f)$ is obtained from the spectrum of the signal $V(t)$ when the laser frequency is tuned away from the Doppler-free resonance, since then the effects of $S_y^{(1)}(f)$ and $S_y^{(2)}(f)$ do not appear. The scaled detection noise $(S_{\rm det})^{1/2}/(\nu^{(2,A)}D)$ is shown in blue in Fig. 3.

The background detector noise floor, that includes the noise of the 250 kSa/s data acquisition card (DAQ, digitizer), is a contribution to $S_{\rm det}(f)$; the scaled linear noise density is shown in cyan. It was measured by blocking the laser beams impinging on D_P and D_R. By comparison with the blue trace we find it to be negligible.

An estimate of the total frequency noise of the interrogating laser 1, $S_y^{(2)}(f)$, is shown in magenta. We believe that it is negligible compared to the other noises in the experiment. It was obtained as follows. Laser 1 is phase-locked to laser 2. The frequency noise of laser 2 is determined by a beat against a similar system (laser 3). The beat linewidth is less than 1 Hz. The green trace shows the linear spectral density of frequency noise of the beat. However, because the apparatus comprising laser 2 and laser 3 is located on the same vibration isolation system, there is certain degree of common-mode noise rejection, and therefore the green curve is only an approximation to the true frequency noise of laser 2. To this noise we add the directly measured noise of the phase-lock between laser 1 and laser 2. The result is the magenta trace.

The iodine transition frequency $\nu^{(1)}$ exhibits fluctuations induced by varying environmental parameters (temperature, pressure, acoustics), a noise that is difficult to determine directly. However, because we find that

$S_{\rm det}(f)$ and $S_{\rm tot}(f)$ are of similar magnitude, we can deduce that the contribution of $S_y^{(1)}(f)$ to the total noise $S_{\rm tot}(f)$ is not major. Thus, it appears that the major noise source is residual laser intensity noise.

Data analysis and presentation.
The time series data were cropped to a duration T so that the number of data points N is equal to a power of 2. Here, $N = 2^{34}$, and $T \simeq 19\,\mathrm{h}$. The data set V_i was Fourier-transformed, i.e. the fast Fourier transform (FFT) $\tilde{V}_k$ was computed (no normalization was included). A rectangular window function was used. One frequency bin corresponds to $\simeq 15\,\mu\mathrm{Hz}$. The normalized periodogram $P_k = |\tilde{V}_k|^2/N^2$ was then obtained. The power spectral density is TP_k.

The data is presented as a filtered spectrum in Fig. 2 (a) of the main text. This spectrum was generated as follows. The overall spectral range from 10 Hz to 100 kHz was divided into intervals j whose limits were defined, in each decade, by an E48-series distribution. That is, the intervals were (10, 10.5) Hz, (10.5, 11.0) Hz,..., (95.3, 100.0) Hz, etc. For each interval $(f_{j,1}, f_{j,2})$ we consider the center frequency $f_{a,i} = (f_{j,1} + f_{j,2})/2$ as axion frequency and define a simplified DM line-shape model $L(f_{a,j}, f)$, a Lorentzian. Its quality factor $Q_0 \simeq 1 \times 10^6$ is independent of $f_{a,j}$ and thus of the considered interval j. Note that the full linewidth $f_{a,j}/Q_0$ ranges from $\simeq 10\,\mu$Hz at 10 Hz to $\simeq 100\,$mHz at 100 kHz. Thus, at the lower end of the spectrum, 10 Hz, the assumed spectral line is effectively only $\simeq 1$ frequency bins wide.

In each interval j the normalized periodogram $\{P_k\}_j$ is convoluted with the corresponding $L(f_{a,j}, f)$, yielding the optimally filtered periodogram (OFP). Its square root (ROFP) is shown, in simplified form, as orange band in Fig. 2 a of the main document. The trend of the mean of ROFP as a function of Fourier frequency f is due to various noise sources, in particular the increase for $f > 10^4$ Hz is due to laser amplitude noise.

Obvious technical noise has been removed from the ROFP by removing a 5 Hz wide frequency range around every multiple of 50 Hz ranging from 100 Hz to 15 kHz. The convolution applied to the data suppresses signals that are not representative of the expected signals of the galactic halo model. The suppression is weaker for the sun and earth halo models, that have higher signal Q factors.

Analysis of technical noise: heuristic approach.
Table I lists omitted frequency ranges that contain technical noise of substantial strength. In the following further analysis, these ranges as well as those around the 50 Hz-noise peak and its harmonics have been omitted.

A second step in the data analysis consists in checking weaker narrow-linewidth signals. We first mark any frequency bin having a signal strength above the detection limit. The latter is heuristically chosen as 3 standard deviations of the ROFP above its mean. Both standard deviation and mean are computed from the ROFP data in a small spectral window around the frequency of interest. Frequency bins that are above the threshold but within the expected lineshape of a previously marked bin will be rejected to avoid double counting. After the this procedure no candidate remained.

f (Hz)	FWHM (bin)	Q-factor (10^6)	comment
642	3	24	unknown source
1284	3	48	second harmonic
$n \times 7681$	60 to 300	8.5 to 22	laser PLL; harmonics up to 100 kHz
46091	700	0.9	laser PLL
53670	26000	0.013	laser PLL
61454	700	1.2	laser PLL

Table I. Partial list of technical noise peaks. The quality factors Q of the peaks are computed from the measured full half-widths at half maximum (FWHM).

Determination of detection limits: generalities.
The value of the DM field ϕ in SI units, at the location of the experiment, can be expressed as [3–5]

$$\phi(t) = \frac{\phi_0}{2\pi f_\phi} \sum_i \alpha_i F'(\omega_i) \cos(\omega_i t + \varphi_i)\,, \qquad (1)$$

where f_ϕ is the Compton frequency of the DM particle, $\phi_0 = \sqrt{4\pi\rho_{\rm DM} G_{\rm N}/c^2}$ is a normalized field amplitude, $\rho_{\rm DM}$ is the local DM energy density, and $G_{\rm N}$ is the gravitational constant. The dimensionless amplitudes α_i (or order unity) and phases φ_i are random numbers drawn from specific probability distributions [4]. $\{\omega_i\}$ are a set of regularly spaced angular frequencies starting at $2\pi f_\phi$ and extending over a narrow spectral window. Finally, F' is a dimensionless weighting function that takes into account the velocity distribution of the DM particles and is specific to the assumed DM model. In particular, it is characterized by a fractional full-width at half maximum, $Q^{-1} \ll 1$ (see further below). The DM spectrum is proportional to $F'(\omega)^2$. In the galactic halo DM model, $\rho_{\rm DM}^{\rm (G)} \simeq 0.3\,\mathrm{GeV/cm^3}$ and thus $\phi_0 \simeq 7 \times 10^{-16}\,$Hz.

Determination of detection limits: approach of Derevianko (2018).
For evaluation of experiment A, we apply Eq. (14) of Ref. [5]. Our 95% bound is taken as $2\hat{\sigma}_{\gamma X}^{(1)}/\Delta R_g^{\rm (A)}$, accounting for the experiment-specific sensitivities.

For the earth halo model with its infinite coherence time, there is but a single amplitude, $\alpha_1 = \sqrt{2}$, and the bound has a particularly simple expression.

In the galactic and sun halo models, the above bound holds for observations times significantly longer than the coherence time, say $T \geq 10\,\tau_{\rm coh}$. For those low DM frequencies f_ϕ for which the observation time is significantly shorter than the coherence time, $T < 0.1\,\tau_{\rm coh}$, we multiply the above expression by a factor 3, as discussed by Centers et al. [6].

In the intermediate range of observation times, $0.1\,\tau_{\rm coh} \leq T \leq 10\,\tau_{\rm coh}$, the theory of the bound has not

yet been worked out. We therefore conservatively apply the factor of 3 also in this range.

For the galactic halo model, we use the velocity values given by Foster *et al.* [4], $\sqrt{2}v_{\rm vir} = v_0 \simeq 220\,{\rm km/s}$, $v_g = v_{\rm obs} \simeq 232\,{\rm km/s}$.

The following correction to the formulae in Ref. [5] is implemented [7]: in Sec.II A, the factors "2" appearing in the definitions of d_e, d_{m_e} are replaced by "4".

C. Experiment B

Apparatus.

The apparatus of experiment B implements Doppler-broadened absorption spectroscopy in the R(122) 2-10 I_2 transition at 725 nm, and is shown in Fig. 1b. Iodine vapor is excited with ≈2 mW of light from a Ti:Sapphire laser (M squared SolsTiS) in a 10-cm long cell. The light beam is double-passed through the cell to increase the absorption signal. The cell body is maintained at ≈405 ^{o}C, sufficiently high to obtain adequate population in the electronic ground state's vibrational level with υ=10. The pressure in the I_2 cell is set to ≈30 mbar via heating of the cold finger of the cell, that is maintained to 87 °C to within ±1 °C. Balanced detection of the light transmitted through the cell is done with use of a secondary reference beam, to minimize the effects of laser amplitude noise. Small drifts in this balancing are corrected by monitoring the output of the balanced detector (Thorlabs PBD415A) and applying feedback to a stepper-motor mounted HWP (HWP 3 in Fig. 1b) to adjust the power of the beam headed to the I_2 cell. This results in suppression of laser amplitude noise by more than ×100 times. The output of the balanced photodetector is amplified ×100 times with a preamplifier (Femto HVA-200M-40-B) and is recorded with a 12-bit DAQ system (Picoscope 5244D) at a rate of 250 MSa/s. An electro-optic modulator (EOM) is used in auxiliary experiments to impose frequency modulation on the laser light, in order to measure the frequency response of the apparatus. This response may be characterized by an overall calibration function $h(f)$, which is primarily determined by the decaying response of molecules at frequencies larger than the transition's linewidth. This frequency modulation is checked with a Fabry-Perot (FP) cavity whose resonance has ≈ 150 MHz FWHM. The peak I_2 absorption corresponds to ≈ 1 absorption length for the Doppler- and pressure-broadened resonance. The transition width of ≈ 970 MHz has contributions due to Doppler (≈ 485 MHz) and collisional broadening (≈ 240 MHz). The latter is estimated from comparison of the 970 MHz width with the value ≈ 730 MHz observed at much lower I_2 pressure (≈ 3 mbar). The molecular response is essentially constant over the 100 MHz range probed for FC oscillations (the function $h(f)$ was measured to be $\simeq 1$ for all frequencies probed).

Experimental protocol.

An experimental run proceeds as follows: First, the laser frequency is swept over the I_2 resonance and the reference beam power is set to obtain a zero-crossing of the photodetector output on the side of the resonance, at the half-height of absorption feature (see Fig. 2b). Then the laser frequency is tuned to the nominal zero crossing and stabilized to the reading of a He-Ne referenced wavemeter (drift ≈ 2 MHz/h), and subsequent slow drifts of the detector output are actively compensated, as mentioned above. A time series of the amplified detector signal is recorded in a 0.1 s window once every ≈1 s (i.e. 10% measurement duty cycle), and corresponding FFT of these data are computed and the resulting periodograms, i.e. the squared magnitudes of the computed amplitudes, are continuously averaged. A flattop window is applied to the time-series data, to avoid parasitic effects in the periodograms due to the discrete nature of the computation. This windowing leads to an effective broadening of the single-bin width in the frequency domain to a resulting ≈ 37.7 Hz (It additionally reduces the integration time from 0.1 s to an effective 27 ms.). Thus, the resulting periodogram in the 100 kHz-100 MHz range consists of $N \approx 2.65{\cdot}10^6$ bins. After ≈ 200 s of data taken on the slope of the resonance, the laser frequency is detuned from resonance by 1.1 GHz, where the discriminator slope is ≈ 0, and the power of the beam headed to the I_2 cell is re-adjusted with feedback to maintain balanced detection, as mentioned above. Equal amount of data as before are taken in this FC-oscillation insensitive configuration. The corresponding periodogram is subtracted from that from data with sensitivity to FC oscillations, to minimize the impact of parasitic effects such as laser amplitude noise and instrumentation pickup. After cycling many times between the two configurations, a difference periodogram is obtained that is nearly free of parasitics and will contain power in excess of noise in the presence of FC oscillations. We henceforth refer to this as excess power spectrum (PS). We show this excess PS, produced using the data of our main 60-h-long DM run in Fig. 4.

Note that this total measurement time exceeds the coherence times of the galactic halo and solar halo models for the considered range of f_ϕ values, so that the Rayleigh probability distribution of the amplitudes α_i is fully sampled.

Check for DM candidate signals.

The excess PS of Fig. 4 is analyzed for possible FC oscillations. A DM signature would be excess power in the spectrum, above a detection threshold computed below and shown in Fig. 4. In addition to investigating such candidate signals, 'negative' peaks (i.e. with power significantly smaller than the mean background noise) are also investigated. It was established that all such peaks have technical origins and although their power in most cases is expected to cancel out in the excess PS, residual power for some of those remains. Checking the residual background power after they are accounted for, informs about potential FC oscillations in the respective frequency positions, as is the case of candidates with high excess power.

Auxiliary experiments were carried out to identify the

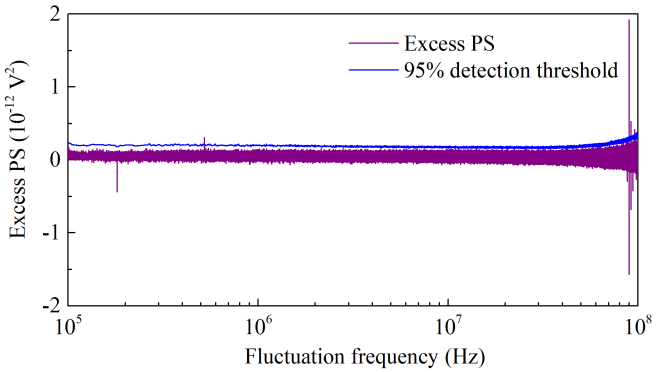


Figure 4. Excess PS and detection threshold at the 95% CL.

origin of the candidate DM and spurious peaks and measure their respective powers. These experiments were done with use of a calibrated spectrum analyzer (Keysight N9320B) to acquire spectra over 5 kHz regions around the candidate peaks. This device is more time efficient in acquiring spectra than our primary acquisition system when recording spectra over narrow frequency windows. In one set of measurements, data were acquired to check for the high-frequency-range spurious signals (above 60 MHz), alternating between acquisition with laser frequency tuned on and off the I_2 resonance. The new excess PS was found to be consistent with background noise. All spurious signals above 60 MHz were found to be due to rf apparatus pickup, since the corresponding peaks were present in the absence of light arriving at the detector. In another experiment, an EOM (EOM 2 in Fig. 1b) was used to provide improved suppression of amplitude noise in the balanced photodetection employed in the setup. This resulted in the elimination of a peak at $\approx 181\,$kHz, which was identified to be due to laser amplitude noise, as it appeared in direct measurement of the laser output light. Finally, in another experiment, the power of a peak at $\approx 523\,$kHz, only present with the laser tuned on the slope of the I_2 resonance, was identified to be laser frequency noise with the FP (see Fig. 1b). Its power was measured on the slope of the FP resonance and subtracted from the excess PS. As a result of all checks following the main 60-hr long DM run, it was established that all peaks under investigation had a technical source, and after these were accounted for in the excess PS, the residual power in the respective frequencies was consistent with background noise and below the detection threshold.

Computation of DM constraints.

Detection of FC oscillations in the excess PS of Fig. 4 is associated with power higher than noise. This noise is used to define a detection threshold $P_{\rm th}$ at the 95% confidence level, so that if a spectral feature has excess power $P_{\rm ex} > P_{\rm th}$, there is probability $p_0 = 5\%$ that it is due to statistical fluctuations. Given a noise distribution function and associated cummulative disctribution function (CDF), one can express p_0 as:

$$p_0 = 1 - {\rm CDF}(P_{\rm th}), \tag{2}$$

where ${\rm CDF}(P_{\rm th})$ represents the probability $p(P_{\rm ex} < P_{\rm th})$ that the excess power is smaller than the threshold. The Eq. (2) may be be solved for the detection threshold $P_{\rm th}$. However this determination would only be valid for an experiment investigating a single frequency bin. In experiment B, where FC oscillations are looked for in $N \approx 2.65 \times 10^6$ bins ($\approx 100\,$MHz search window consisting of $37.7\,$Hz bins), the threshold has to be raised to account for the fact that a fraction of bins ($\approx 5\%$) are expected to have power in excess of $P_{\rm th}$ [8]. This requires raising the CDF in Eq. (2) in the N^{th} power, so that:

$$p_0 = 1 - \left[{\rm CDF}(P_{\rm th})\right]^N. \tag{3}$$

The noise distribution of the excess PS of Fig. 4 was checked in many frequency bins and it was found to be well described by a Gaussian. Given this, one can solve for the threshold power $P_{\rm th}$ using the expression for the Gaussian CDF, and obtain:

$$P_{\rm th} = \sqrt{2}\,{\rm erf}^{-1}\Big\{2(1-p_0)^{1/N} - 1\Big\}\sigma + \mu \approx 5.5\,\sigma + \mu, \tag{4}$$

where μ and σ are the mean and standard deviation of the Gaussian noise. These parameters were determined throughout the spectrum of Fig. 4 by fitting the noise in consecutive 5-kHz-wide windows.

From the determined threshold $P_{\rm th}$, constraints are extracted on the frequency fluctuation $\delta\nu$. This fluctuation is given by $\delta\nu = \delta V/D$, where δV is the voltage fluctuation corresponding to the fluctuation δP in the excess PS spectrum of Fig. 4 (at the 95% confidence level: $\delta P = P_{\rm th} - \mu = 5.5\sigma$). The discriminator slope D is discussed in the main text. The quantities δV and δP are related via $\delta P = 2V_{\rm av}\delta V = 2\sqrt{P_{\rm av}}\delta V$, where $P_{\rm av} = V_{\rm av}^2$ is the averaged PS recorded with sensitivity to FC oscillations (i.e. with laser tuned to the slope of the I_2 resonance). One obtains for $\delta\nu$:

$$\delta\nu = \frac{\delta V}{D} = \frac{\delta P}{2\sqrt{P_{\rm av}}D} = \frac{5.5\sigma}{2\sqrt{P_{\rm av}}D}. \tag{5}$$

Effect of decoherence of DM field.

Before placing constraints on FC, one has to consider the effects of partial decoherence of the DM field, that if present, will result in reduced sensitivity to DM detection. In experiment B, decoherence needs to be accounted for within the galactic DM halo scenario: $\tau_{\rm coh} \simeq (6, 0.006)\,$s at $f_\phi = (10^5, 10^8)\,$Hz. Within the Solar and Earth halo scenarios, the Q-factor of the field is high enough so that there is negligible decoherence over the $27\,$ms acquisition time. In practice, a sensitivity penalty must be applied to the obtained $\delta\nu/\nu$ spectrum, to account for the decoherence during the effective 27-ms-long time interval of our data acquisition. This penalty becomes significant at a frequency $f_\phi \geq 1/27\,{\rm ms} \approx 40\,$MHz.

To compute this sensitivity loss, we considered the lineshape, $f_{\rm DM}(f)$, that arises in the lab as the laboratory moves through the virialized DM field with a velocity dispersion of $v_0 \approx 10^{-3} c_0$ (denoted above by $\sqrt{2} v_{\rm vir}$),

$$f_{\rm DM}(f) = \frac{2c^2}{\sqrt{\pi} v_0 v_{\rm lab} f_\phi} \exp\left(-\frac{2c^2}{v_0^2} \frac{f - f_\phi}{f_\phi} - \frac{v_{\rm lab}^2}{v_0^2} \right) \sinh\beta, \tag{6}$$

where $v_{\rm lab}$ (denoted v_g above) is the velocity of the laboratory in the galactic frame (232 km/s), and we have denoted

$$\beta = \frac{2 c v_{\rm lab}}{v_0^2} \sqrt{\frac{2(f - f_\phi)}{f_\phi}} \tag{7}$$

for brevity. This lineshape is proportional to the power spectral density of the DM particle and has been derived previously in Refs. [4, 5, 9, 10]. (The relationship to F' is $f_{\rm DM}(f) = F'(\omega)^2 T$.)

We had a constant frequency bin width equal to 37.7 Hz in experiment B due to the flat-top windowing in the time domain. At frequencies higher than ≈ 40 MHz the DM power spectral density will be broader than that of the bin-width, effectively leading to the power spreading over more than one point in our spectrum. We have calculated the loss due to this for different DM particle Compton frequencies, f_ϕ, by integrating the lineshape in 37.7 Hz bins and steps of 10 Hz. The maximum of these bin-integrals is then compared to the total area of the lineshape. This procedure yields the fraction of the DM power that will be observed in our spectrum. For a sense of scale, at 10 MHz the sensitivity loss because of this is $\approx 1\%$ and at 100 MHz it is $\approx 75\%$.

II. THEORY

Two additional models of DM.

In addition to the standard galactic halo model, we consider a scenario where the UDM forms a solar halo [11] with $\rho_{\rm DM}^{\oplus} = 10^5 \rho_{\rm DM}^{\rm G}$, $\beta_\oplus c = 20$ km/s, and as long as $m_\phi \gtrsim 10^{-13}$ eV the number of patches in the halo is large and we still assume that the field amplitude is stochastic.

Finally, we discuss an earth halo phenomenological model [12], where the UDM has a negligible velocity dispersion, i.e. infinite coherence time. The DM density $\rho_{\rm DM}^{\rm E}$ takes its maximally allowed value, that is a function of UDM particle mass (see Fig. 2a in the supplementary information of ref. [12]), and is enhanced compared to $\rho_{\rm DM}^{\rm G}$ by a factor increasing from 10^4 at $f_\phi = 100$ Hz to 10^{19} at $f_\phi = 3.4$ MHz. However, beyond $f_\phi \simeq 15$ MHz the ratio $\rho_{\rm DM}^{\rm E}/\rho_{\rm DM}^{\rm G}$ drops below 1.

Equivalence Principle (EP) tests.

A scalar field ϕ with mass m_ϕ would induce an Yukawa interaction between two bodies A and B in the range $\Lambda = h/m_\phi c$ that is non-universal and thus violates the equivalence principle (EP). The total potential (gravitational and Yukawa) between these two bodies can be written as

$$V = -G_{\rm N} \frac{m^{\rm A}\, m^{\rm B}}{r_{\rm AB}} \left(1 + \alpha^{\rm A} \alpha^{\rm B}\, e^{-r_{\rm AB}/\Lambda} \right), \tag{8}$$

where, $m^{\rm A}$ ($m^{\rm B}$) is the mass of body A (B), $G_{\rm N}$ is the Newtonian gravitational constant and $r_{\rm AB}$ is the distance between A and B. $\alpha^{\rm A,B}$ are the strengths of the Yukawa interaction. They measure the susceptibility of the mass to ϕ, and thus can be written as,

$$\alpha = \frac{1}{\sqrt{4\pi G_{\rm N}}} \frac{\partial \ln m(\phi)}{\partial \phi}. \tag{9}$$

In the presence of a central body (the "source") S with mass $m^{\rm S}$ at a distance r, the acceleration of a test body A can be written as

$$\vec{a}_{\rm A} = -\hat{r} \frac{G_{\rm N}\, m^{\rm S}}{r^2} \left[1 + \alpha^{\rm A} \alpha^{\rm S} \left(1 + \frac{r}{\Lambda} \right) e^{-r/\Lambda} \right]. \tag{10}$$

The Eötvös parameter, $\eta_{\rm EP}$, which measures the differential acceleration between two test bodies A and B in the presence of a source S, follows as as [13, 14]

$$\eta_{\rm EP}^{\rm Exp} \equiv 2 \frac{|\vec{a}_{\rm A} - \vec{a}_{\rm B}|}{|\vec{a}_{\rm A} + \vec{a}_{\rm B}|} \simeq (\alpha^{\rm A} - \alpha^{\rm B})\, \alpha^{\rm S} \left(1 + \frac{r}{\Lambda} \right) e^{-r/\Lambda}. \tag{11}$$

EP test experiments constrain $\eta_{\rm EP}^{\rm Exp}$ as a function of Λ. This leads to bounds on $\alpha^{\rm A,B,S}$ as a function of m_ϕ. Because $\alpha^{\rm A,B,S}$ depend on the fundamental constants (FCs) as shown in the following, a bound on $\eta_{\rm EP}$ can be converted into a bound on the coupling coefficients d_i .

FC dependence of atom mass.

To discuss how the mass of a body depends on FCs, let us start by noting that the mass of a generic atom a with atomic number $A^{\rm a}$ and proton number $Z^{\rm a}$ can be expressed as,

$$m^{\rm a} = m_N^{\rm a}(A^{\rm a}, Z^{\rm a}) + Z^{\rm a} m_e \,. \tag{12}$$

where $m_N^{\rm a}$ is the mass of the nucleus of atom a and m_e is the electron mass. The mass of the nucleus can be further decomposed as

$$m_N^{\rm a}(A^{\rm a}, Z^{\rm a}) = Z^{\rm a}\, m_p + (A^{\rm a} - Z^{\rm a})\, m_n + E_3 + E_1 \,, \tag{13}$$

where, m_p (m_n) is the proton (neutron) mass and E_3 (E_1) is the binding energy of the strong (electromagnetic) interaction. Note that E_1 is dominated by the electromagnetic effect within the nucleus [15] and thus we will ignore the electron effect on this. As m_p, m_n, E_3 and E_1 depend on the FCs, variation of the FCs would lead to a variation of nucleus and atom mass, and can be written as (we use the summation convention)

$$\frac{\partial \ln m^{\rm a}(\phi)}{\partial \phi} = \frac{\partial \ln m^{\rm a}(\phi)}{\partial \ln g_i} \frac{\partial \ln g_i}{\partial \phi} = Q_i^{\rm a} \frac{d_i}{M_{\rm Pl}} \,, \tag{14}$$

where g_i is a generic FC, and we have also implied summation over repeated indices here and below. We have

introduced the notation $Q_i^{\rm a} \equiv \partial \ln m^{\rm a}(\phi)/\partial \ln g_i$, the ith "dilatonic charge" of a body. The susceptibility of a FC to ϕ can be rewritten as $\partial \ln g_i/\partial\phi = d_i/M_{\rm Pl}$ (See Eqs. (2-5) in the main text).

For a given body, the dilatonic charges corresponding to different FCs can be given in vector form explicitly as [15] (with $(\vec{Q}^{\rm a})_i = Q_i^{\rm a}$),

$$\vec{Q}^{\rm a} \approx \quad F^{\rm a}\Big(3\times 10^{-4} - 4\, r_I + 9\, r_Z\,,\, 3\times 10^{-4} - 3\, r_I\,,\, 1\,,\, 0.1 - \frac{0.04}{(A^{\rm a})^{1/3}} - 2\times 10^6 r_I^2 - r_Z\,,\, 0.002\, r_I\Big)\,, \quad (15)$$

where here and below $\vec{X} \equiv (X_\alpha, X_{m_e}, X_{g_{\rm s}}, X_{\hat{m}}, X_{\delta m})$, with
$\hat{m} \equiv (m_u + m_d)/2$,
$\delta m \equiv m_u - m_d$,
$F^{\rm a} \equiv 931\, A^{\rm a}/(m^{\rm a}/{\rm MeV})$,
$10^4\, r_I \equiv 1 - 2Z^{\rm a}/A^{\rm a}$,
$10^4\, r_Z \equiv Z^{\rm a}(Z^{\rm a}-1)/(A^{\rm a})^{4/3}$,
where we have used $M_{\rm Pl} = \sqrt{\hbar c/(8\pi G_{\rm N})}$. Finally, the Yukawa strength of a body composed of atoms of species a is $\alpha^{\rm a} = \sqrt{2}\,\vec{Q}^{\rm a}\cdot\vec{d}$.

We do not consider the strange quark mass contribution in the context of EP tests. Thus, for discussing the complementarity between the EP tests and UDM searches, we use a 5-dimensional $\vec{Q}$, omitting the last entry corresponding to m_s, both in the main text and here.

For our experiment we can also construct an analogous $\vec{Q}$, setting $Q_i^{\rm X} = \Delta R_i^{\rm (X)}$ with X = A, B as given in the main text, with a relative sensitivity to the QCD parameters of -0.06 (0.07) in experiment A (B). So,

$$\vec{Q}^{\rm A} \;\simeq\; \big(1, 0.06, -0.05, -0.005, -2\times 10^{-5}\big)\,,$$
$$\vec{Q}^{\rm B} \;\simeq\; \big(2,\, 0.93,\, 0.06,\, 0.006,\, 2\times 10^{-5}\big)\,. \quad (16)$$

Sensitivities of EP tests.

Let us now discuss the sensitivities of the EP test experiments. In the mass region of our interest $10^{-14}\,{\rm eV} \lesssim m_\phi \lesssim 10^{-6}\,{\rm eV}$ these tests have given stronger bounds than those arising from the direct scalar DM searches. However, as we have discussed in the main text and also here, the EP tests compare the dilatonic charges of two test bodies. For instance, consider the MICROSCOPE experiment [16, 17], that provides one of the strongest EP bounds for masses below $10^{-12}\,{\rm eV}$. It is sensitive to the difference of the dilatonic charges of a platinum/rhodium alloy (90%/10%) and a titanium/aluminum/vanadium alloy (90%/6%/4%), with [15]

$$(\overrightarrow{\Delta Q}\,)^{\rm Mic} \approx 10^{-3}(-1.939\,,\, 0.031\,,\, 0.805\,,\, -2.614\,,\, -0.190)\,.$$

Alloys are treated as mixtures of pure systems. By inspecting the enclosed angles, we find that the direction of this vector in coupling space is very different than that of our experiments $\vec{Q}^{\rm A,B}$.

In our present discussion, we consider the six most sensitive EP test experiments. Apart from MICROSCOPE, these are [13, 18–21]:

$$(\overrightarrow{\Delta Q}\,)^{\rm Be-Al} \simeq 10^{-3}(-1.021, -0.021, -2.035, -5.498, 0.126),$$
$$(\overrightarrow{\Delta Q}\,)^{\rm Be-Ti} \simeq 10^{-3}(-1.566, -0.009, -2.427, -7.405, 0.050),$$
$$(\overrightarrow{\Delta Q}\,)^{\rm Be-Cu} \simeq 10^{-3}(-1.982, -0.007, -2.464, -8.204, 0.039),$$
$$(\overrightarrow{\Delta Q}\,)^{\rm Cu-Pb(a)} \simeq 10^{-3}(-1.565, 0.033, 0.945, -1.764, -0.202),$$
$$(\overrightarrow{\Delta Q}\,)^{\rm Cu-Pb(b)} \simeq 10^{-3}(-1.413, 0.030, 0.951, -1.427, -0.184),$$

where $\rm Pb^{(a)}$ denotes the alloy of composition lead/antimony/tin (92%/7.75%/2.5%) [19] and $\rm Pb^{(b)}$ denotes the alloy of composition lead/aluminium (91.5%/8.5%) [21]. Note that we have denoted the $\rm Pb^{(a)}$ combination as Pb and $\rm Pb^{(b)}$ combination as Pb-alloy in the main text.

Finding directions in coupling space to which EP tests are weakly sensitive to.

In the five-dimensional vector space of couplings, we can construct a unit vector $\hat{Q}^\perp_{\rm Full}(m_\phi)$ orthogonal to four most stringent EP tests for each mass. For example, in the mass range of $2\times 10^{-12} \lesssim m_\phi/{\rm eV} \lesssim 5\times 10^{-9}$, the leading EP tests are Be-Ti, Be-Al, Be-Cu and Cu-$\rm Pb^{(a)}$ and in this mass range the orthogonal vector can be given as

$$\hat{Q}^\perp_{\rm Full}(m_\phi) \simeq \big(0.003\,,\; 0.987\,,\, 0.002\,,\; -0.001\,,\, 0.160\big)\,.$$

For masses below $m_\phi \lesssim 2\times 10^{-12}{\rm eV}$, the leading EP tests are Microscope, Be-Ti, Be-Al, and Cu-Pb and in this mass range the orthogonal vector can be given as

$$\hat{Q}^\perp_{\rm Full}(m_\phi) \simeq \big(0.004\,,\; 0.987\,,\, 0.003\,,\; -0.002\,,\, 0.161\big)\,.$$

For masses above $m_\phi \gtrsim 5\times 10^{-9}\,{\rm eV}$, the leading EP tests are Be-Ti, Be-Al, Cu-$\rm Pb^{(a)}$, and Cu-$\rm Pb^{(b)}$ in this mass range the orthogonal vector can be given as

$$\hat{Q}^\perp_{\rm Full}(m_\phi) \simeq \big(0.034\,,\; 0.982\,,\, 0.030\,,\; -0.016\,,\, 0.181\big)\,.$$

The existence of $\hat{Q}^\perp_{\rm Full}$ implies that models of light scalar DM with this combination of relative coupling amplitudes are not constrained by these four leading EP test experiments. Now, $\hat{Q}^\perp_{\rm Full}$ has a large overlap with the d_{m_e} direction (the $2^{\rm nd}$ entry of $\hat{Q}^\perp_{\rm Full}$). Thus, experiments that are sensitive to time-variation of the electron mass are sensitive to a sector of DM - SM coupling parameter space that the four best EP bounds

are insensitive to, barring a coincidence. For our experiments, $\hat{Q}^{\perp}_{\rm Full} \cdot \vec{Q}^{\rm A} \simeq -0.03$, and $\hat{Q}^{\perp}_{\rm Full} \cdot \vec{Q}^{\rm B} \simeq -0.87$; these values are approximately the sensitivity coefficients for $d_{m_{\rm e}}$. The sensitivity of our current experiments into the $\hat{Q}^{\perp}_{\rm Full}$ direction is indicated by the dotted lines in Fig. 5 in the main text (further projected onto the $d_{m_{\rm e}}$ direction for ease of display). The brown dotted line depicts the bound of the remaining $5^{\rm th}$-best EP experiment. In the $\hat{Q}^{\perp}_{\rm Full}$ direction EP tests constraints are stronger than our experiments by 2 - 3 orders of magnitude. This should be compared to models having only $d_{m_{\rm e}} \neq 0$, where the EP tests are stronger by 8 - 10 orders of magnitude.

A light dilaton and EP non-violation

If a scalar-field coupling to matter is fully aligned with that of gravity, then the scalar field will couple to the total mass of a body, and thus will not generate an equivalence-principle-violating acceleration between two test bodies. We know that gravity couples to the Ricci scalar R, and using Einstein's equation, one can write

$$-R = \frac{T^{\mu}_{\mu}}{M^2_{\rm Pl}} \tag{17}$$

where, T^{μ}_{μ} is the trace of the energy momentum tensor (EMT). So, if the scalar-field coupling to the SM is proportional to T^{μ}_{μ}, it will not generate any EP violation. However, this is an idealistic limit, and is realized only in pure dilaton models (see for instance [15] and refs. therein), where the dilaton (ϕ) couplings are precisely given by

$$\mathcal{L} \supset \frac{\phi}{f_{\rm dil}} T^{\mu}_{\mu}\,, \tag{18}$$

where $f_{\rm dil}$ is the conformal invariance breaking scale [22]. If we assume the SM is valid up to the scale $f_{\rm dil}$, then T^{μ}_{μ} can be written as

$$T^{\mu}_{\mu} = \frac{\beta(g_s)}{2g_s} G^2 + \frac{\beta(g_2)}{2g_2} W^2 + \frac{\beta(Y)}{2Y} B^2 + (1-\gamma) \sum_f m_f \bar{f} f \tag{19}$$

where g_s, g_2 are the coupling strength of $SU(3)$ and $SU(2)$ gauge groups, respectively, Y represents the hypercharge corresponding to $U(1)_Y$, and B is the corresponding gauge field. Also, f denotes the SM fermions with mass m_f. For simplicity, in the above formula we assume that the conformal invariance breaking scale $f_{\rm dil}$ is far below the Landau pole of $U(1)_Y$ and above the electro-weak scale. As the trace of the energy momentum tensor, T^{μ}_{μ} is invariant under the evolution of the renormalization group equation (RGE) (manifested in the above equation), through anomaly matching the dilaton will always couple to the the same quantity at any scale. For simplicity and for our purpose, we can consider our theory at the 1-GeV energy scale and we get a simpler expression for T^{μ}_{μ},

$$T^{\mu}_{\mu} = \frac{\beta(g_s)}{2g_s} G^2 + \frac{\beta(e)}{2e} F^2 + \sum_f m_f \bar{f} f\,, \tag{20}$$

where we have redefined the fermion masses in terms of their pole masses. Comparing with our Lagrangian written in Eq. (1) in the main text, we can write the dilaton coupling vector, $\vec{Q}_{\rm dil}$ as

$$\vec{Q}_{\rm dil} = (-\frac{2\beta(e)}{e}, 1, 1, 1, 0)\,, \tag{21}$$

where e is the electric charge and the fucntion $\beta(e) = e^3/(12\pi^2)$ describes the evolution of e with energy, via the RGE. As the RGE of the electric charge, e does not get any contribution below the scale of electron mass ($m_e \sim$ MeV), and with $\log({\rm GeV/MeV}) \sim 10$, we find $2\beta(e)/e \sim e^2/(6\pi^2) \times 10 \sim 0.015$. So, we get

$$\vec{Q}_{\rm dil} = (-0.015, 1, 1, 1, 0)\,. \tag{22}$$

Note that the dilaton would induce a Yukawa interaction between two bodies as given in Eq. (8), and that its strength can be written as (using Eq. (9)),

$$\alpha = \frac{1}{\sqrt{4\pi G_{\rm N}}} \frac{\partial \ln m(\phi)}{\partial \phi} \propto \frac{1}{f_{\rm dil}}\,, \tag{23}$$

as it couples to the total mass of a body. This shows that the dilaton couples to any test body universally with coupling strength determined by the conformal invariance breaking scale. Inserting this expression into Eq. (11), we obtain

$$\eta^{\rm Exp}_{\rm EP} \propto (\alpha^{\rm A} - \alpha^{\rm B}) = 0\,. \tag{24}$$

Thus, we have argued that a scalar DM model (dilaton), where the coupling is defined according to $\vec{Q}_{\rm dil} \cdot \vec{d}$, will not generate an EP-violating acceleration, as the direction is indistinguishable to that of gravity. We are also assuming that in order to be a viable DM candidate, the dilaton would acquire a small mass [23, 24].

However, using Eq. (23) and Eq. (10) in the presence of a dilaton, the acceleration of a test body can be written as

$$\vec{a}_{\rm A} = -\hat{r} \frac{G_{\rm N}\, m^{\rm S}}{r^2} \left[1 + \frac{2M^2_{\rm Pl}}{f^2_{\rm dil}} \left(1 + \frac{r}{\Lambda}\right) e^{-r/\Lambda}\right]\,, \tag{25}$$

where we write $M^2_{\rm Pl} = 1/(8\pi G_N)$. The above equation shows that a dilaton causes a deviation from the inverse-square-law force, and thus can be constrained by various experiments that test for deviations from Newtonian gravity (fifth-force searches) [25]. The crimson dot-dashed line in Fig. 5 of the main text shows the bounds from various fifth-force searches on a dilaton model.

We, finally, note that if the dilaton couplings are not perfectly aligned with that obtained from the trace of the energy momentum tensor, it will generate an EP-violating acceleration as discussed in [26, 27].

[1] D. Antypas, O. Tretiak, K. Zhang, A. Garcon, G. Perez, M. G. Kozlov, S. Schiller, and D. Budker, Quantum Science and Technology **6**, 034001 (2021).

[2] J. P. Turneaure, C. M. Will, B. F. Farrell, E. M. Mattison, and R. F. C. Vessot, Phys. Rev. D **27**, 1705 (1983).

[3] E. Savalle, A. Hees, F. Frank, E. Cantin, P.-E. Pottie, B. M. Roberts, L. Cros, B. T. McAllister, and P. Wolf, Phys. Rev. Lett. **126**, 051301 (2021).

[4] J. W. Foster, N. L. Rodd, and B. R. Safdi, Phys. Rev. D **97**, 123006 (2018).

[5] A. Derevianko, Phys. Rev. A **97**, 042506 (2018).

[6] G. P. Centers, J. W. Blanchard, J. Conrad, N. L. Figueroa, A. Garcon, A. V. Gramolin, D. F. J. Kimball, M. Lawson, B. Pelssers, J. A. Smiga, A. O. Sushkov, A. Wickenbrock, D. Budker, and A. Derevianko, Nat. Comm. (2021), 10.1038/s41467-021-27632-7.

[7] A. Derevianko, (private communication) (2021).

[8] J. D. Scargle, The Astrophys. J. **263**, 835 (1982).

[9] M. S. Turner, Phys. Rev. D **42**, 3572 (1990).

[10] A. V. Gramolin, A. Wickenbrock, D. Aybas, H. Bekker, D. Budker, G. P. Centers, N. L. Figueroa, D. F. Jackson Kimball, and A. O. Sushkov, Phys. Rev. D **105**, 035029 (2022).

[11] N. B. Anderson, A. Partenheimer, and T. D. Wiser, (2020), arXiv:2007.11016 [hep-ph].

[12] A. Banerjee, D. Budker, J. Eby, H. Kim, and G. Perez, Commun. Phys. **3**, 1 (2020).

[13] T. A. Wagner, S. Schlamminger, J. H. Gundlach, and E. G. Adelberger, Class. Quant. Grav. **29**, 184002 (2012).

[14] A. Hees, O. Minazzoli, E. Savalle, Y. V. Stadnik, and P. Wolf, Phys. Rev. D **98**, 064051 (2018).

[15] T. Damour and J. F. Donoghue, Phys. Rev. D **82**, 084033 (2010).

[16] P. Touboul *et al.*, Phys. Rev. Lett. **119**, 231101 (2017).

[17] J. Bergé, P. Brax, G. Métris, M. Pernot-Borràs, P. Touboul, and J.-P. Uzan, Phys. Rev. Lett. **120**, 141101 (2018).

[18] S. Schlamminger, K.-Y. Choi, T. A. Wagner, J. H. Gundlach, and E. G. Adelberger, Phys. Rev. Lett. **100**, 041101 (2008).

[19] G. L. Smith, C. D. Hoyle, J. H. Gundlach, E. G. Adelberger, B. R. Heckel, and H. E. Swanson, Phys. Rev. D **61**, 022001 (1999).

[20] Y. Su, B. R. Heckel, E. G. Adelberger, J. H. Gundlach, M. Harris, G. L. Smith, and H. E. Swanson, Phys. Rev. D **50**, 3614 (1994).

[21] P. G. Nelson, D. M. Graham, and R. D. Newman, Phys. Rev. D **42**, 963 (1990).

[22] A. Dymarsky, Z. Komargodski, A. Schwimmer, and S. Theisen, JHEP **10**, 171 (2015).

[23] F. Coradeschi, P. Lodone, D. Pappadopulo, R. Rattazzi, and L. Vitale, JHEP **11**, 057 (2013).

[24] A. Arvanitaki, J. Huang, and K. Van Tilburg, Phys. Rev. D **91**, 015015 (2015).

[25] E. Fischbach and C. Talmadge, in *31st Rencontres de Moriond: Dark Matter and Cosmology, Quantum Measurements and Experimental Gravitation* (1996) pp. 443–451, arXiv:hep-ph/9606249.

[26] T. R. Taylor and G. Veneziano, Phys. Lett. B **213**, 450 (1988).

[27] D. B. Kaplan and M. B. Wise, JHEP **08**, 037 (2000).

B.1.2 Search for Dark Matter Using Acetylene Spectroscopy

Title:
Search for oscillating fundamental constants using a paired detector and vibrational spectroscopy

Authors:
R. Oswald, **V. Vogt** and S. Schiller

Status / Year: ..... Published / 2025

Journal: ..... Physical Review D

DOI: 10.1103/PhysRevD.111.055003

Licence: ..... Creative Commons Attribution 4.0 International license.

Statement of Copyright:
"Copyright © 2011 by American Physical Society. All rights reserved.

Individual articles are copyrighted by the APS, as indicated on each article.

Individual articles may be downloaded for personal use; users are forbidden to reproduce, republish, redistribute, or resell any materials from this journal in either machine-readable form or any other form without permission of the APS or payment of the appropriate royalty for reuse."

Reuse policy for dissertation:
"[...] the author has the right to use the article or a portion of the article in a thesis or dissertation without requesting permission from APS, provided the bibliographic citation and the APS copyright credit line are given on the appropriate pages."

My Contribution:
I was responsible for setting up and operating the cavity system, which provided the ultra-stable reference light for detector 1. I created the schematic in Fig. 1, developed in collaboration with coauthors, and provided the measured data for the magenta line constituting the frequency noise density of the reference light. See Section 7.2.

Editors' Suggestion

Search for oscillating fundamental constants using a paired detector and vibrational spectroscopy

René Oswald, Victor Vogt, and Stephan Schiller*
Institut für Experimentalphysik, Heinrich-Heine-Universität Düsseldorf, 40225 Düsseldorf, Germany

(Received 9 September 2024; accepted 5 December 2024; published 5 March 2025)

Ultralight dark matter (UDM) may manifest itself through oscillating fundamental constants of normal matter. These can be experimentally searched for by implementing two dissimilar oscillators producing a beat between their frequencies and analyzing the beat-frequency time series for the presence of any temporal oscillations. Typically, the time series of such a detector contains contributions from nonstationary noise. In order to reduce the influence of such noise we propose and demonstrate paired detectors: two nominally identical detectors whose signals are synchronously recorded. The cross-spectrum of the two individual beat time series is then analyzed for UDM signatures. This approach permits us to suppress spurious signals appearing in uncorrelated fashion in either detector. We furthermore demonstrate detectors that are based on a vibrational molecular transition, which are advantageous due to their larger sensitivity to oscillations of the nuclear masses. The analysis of 274 hours of data yielded improved bounds for the coupling constants of UDM to nuclear mass and to electron mass in the frequency ranges 10–500 Hz and 10–122 kHz, with improvement factors between 6 and 10. These bounds are currently the strongest. Similar bounds are obtained for the fine-structure constant. The present approach may be generalized to large ensembles of detectors.

DOI: 10.1103/PhysRevD.111.055003

I. INTRODUCTION

It is today still unknown whether dark matter couples to normal matter and the mass (or masses) of dark matter (DM) particles are also unknown. In fact, the allowed mass range is poorly constrained, so far. Shedding light on these fundamental questions is one of the most important challenges in fundamental physics today. It is possible that DM particle masses are well below 1 eV. This so-called ultralight DM (UDM) can be described by a classical field $\phi(t)$ that, according to a common model [1], oscillates in a nearly monofrequent fashion at any given location on Earth. The characteristic frequency is the Compton frequency f_ϕ of the DM particle. The amplitude of the field is predicted to vary extremely slowly on the timescale of the oscillation period [2].

Furthermore, if UDM couples to normal matter, the coupling may be in the form of a Lagrangian function for the DM-normal matter interaction in which ϕ couples linearly to the energy densities of normal matter. Such densities arise from the fields associated with fermionic matter (electrons, quarks, gluons) and with the electromagnetic field. The interaction strengths are quantified by a set of coupling constants d_g. As a consequence, the fundamental constants (FCs) become functions of the dark matter field [2–7]

$$m_X(\phi) = m_X(1 + d_X\phi), \tag{1}$$

$$\alpha(\phi) \simeq \alpha(1 - d_\alpha\phi), \tag{2}$$

$$\alpha_s(\phi) \simeq \alpha_s\left(1 - \frac{2d_{g_s}\beta'(g_s)}{g_s}\phi\right). \tag{3}$$

Here m_X are the masses of the fermions, where $X = e, u, d, s$ stand for electron, up-quark, down-quark and strange-quark, respectively. α is the fine-structure constant, $g_s = \sqrt{4\pi\alpha_s}$ is the strong-interaction coupling constant, and the function $\beta'(g_s)$ describes the evolution of the coupling constant with energy.

A consequence of the above is that also the mass of any nucleus m_N depends on ϕ. This dependence involves essentially four coupling constants,

$$m_N(\phi) \simeq m_N(1 + (Q_N \cdot d_N)\phi), \tag{4}$$

with the shorthands $d_N = (d_{g_s}, d_{\hat{m}}, d_{\delta m}, d_s)$ and $Q_N \simeq 0.878 \times (0.994, 0.096, 3 \times 10^{-4}, 0.049)$. In this expression, the electromagnetic binding energy of the nucleus has been neglected, and $\hat{m} = (m_u + m_d)/2$, $\delta m = m_u - m_d$.

*Contact author: step.schiller@hhu.de

Published by the American Physical Society under the terms of the Creative Commons Attribution 4.0 International license. Further distribution of this work must maintain attribution to the author(s) and the published article's title, journal citation, and DOI. Funded by SCOAP³.

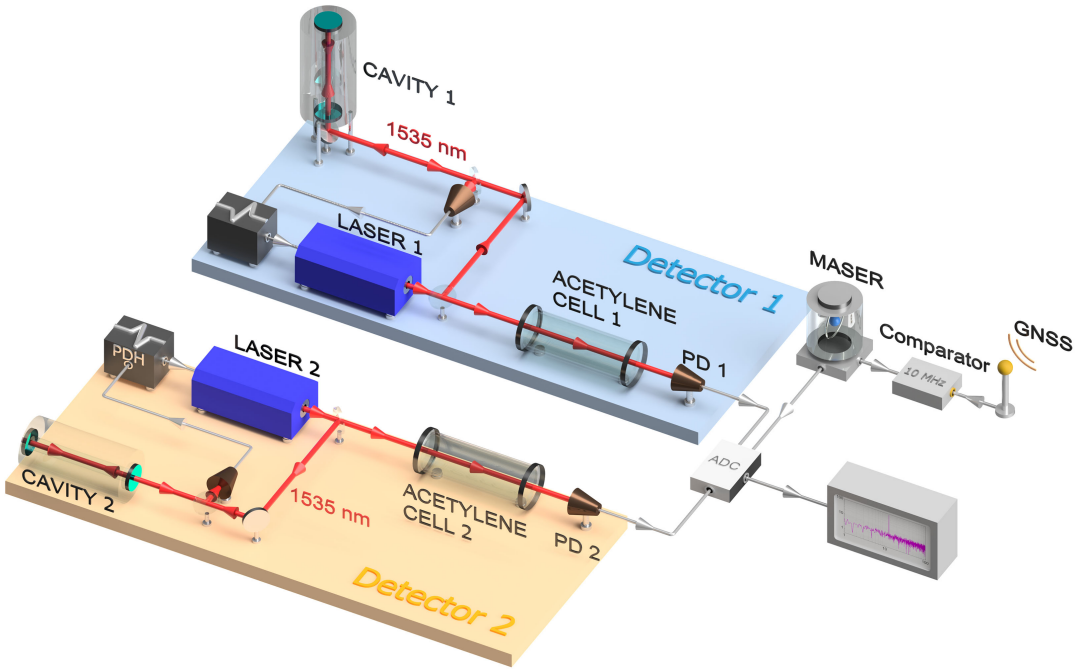


FIG. 1. Concept of the experimental apparatus. Two nominally identical detectors 1 and 2 generate output signals on respective photodetectors PD1, PD2 that are synchronously recorded by an analog-to-digital converter (ADC) and then processed.

Thus, the FCs inherit the oscillatory character of ϕ and may be (extremely weakly) oscillating "constants." It is the task of experiments to set bounds to the magnitude of the six coupling constants d_α, d_{m_e}, d_N. Already, a number of experiments have been performed to search for such oscillations [5,8–12]. They have addressed very different ranges of the Compton frequency f_ϕ, between 10^{-7} Hz to 100 MHz. Because most experiments have been based on cavities and atomic spectroscopy, their sensitivity to oscillating nuclear masses has been intrinsically small—only occurring through the reduced-mass effect of atomic transitions (for a different approach, see [8]). The sensitivity has also been particularly small because typically heavy atoms have been used. Therefore, recently two experiments have focused on molecular spectroscopy, where the vibrational energies provide direct access to the nuclear mass [6]. However, because electronic molecular transitions were interrogated, the contribution from vibrational energies was partially suppressed.

In this work, we present a new-generation UDM molecular spectroscopy experiment sketched in Fig. 1. Its aim is to allow setting stronger bounds for fast oscillations ($f_\phi > 10$ Hz) of the mentioned coupling constants. Its innovations are first, the use of a molecular gas in which a vibrational rather than an electronic transition is probed, leading to a substantial gain in sensitivity to the nuclear mass and to the electron mass. Second, two independent (but neighboring) detectors are operated simultaneously, and their signals are recorded with attention to using a common time base. Therefore, it is possible to perform a cross-correlation analysis of the two signals. This allows us to reject spurious signals that occur in one detector only as well as reducing the impact of uncorrelated noise present in both detectors. With this demonstration, we take the first step toward future (concentrated or distributed) arrays of tens, possibly hundreds or thousands of simultaneously operated detectors.

In more detail, each detector of a pair is exposed to various disturbances, e.g. mechanical vibration, acoustic noise, electrical noise. Their influence on the spectrum of the recorded time series is significant. In the case of having access only to a single detector, the only approach for reducing the impact of noise is to repeat data acquisition runs and then average the spectra over different experiments. This will reduce the importance of noise uncorrelated between runs, but it will not remove systematic disturbances, e.g. signals at constant frequency with slowly varying amplitude. Spurious signals are also difficult to remove, necessitating the detailed investigation of their spectrum.

A more efficient, but also more costly, approach is to have two detectors that take data simultaneously. Cross-correlating the data allows us to discriminate not only against uncorrelated stationary noise disturbances in each system, but also against systematic/spurious disturbances that are not common to the two systems. The cross-correlation spectrum [13] is a well-known construct that allows one to enhance a common signal—here the hypothetical UDM signal—in two independent noisy detectors. Of course, one can attempt to minimize correlated systematic disturbances by operating the two detectors independently (e.g. without any common power supply) and sufficiently distant from each other, so

that they are subject to qualitatively different environmental disturbances, but this is in practice not always feasible. If independent operation is implemented, it will be beneficial also when the cross-correlation analysis is applied.

II. CONCEPT OF THE APPARATUS

In each detector, we measure the difference $\nu(t)$ between the frequency ν_L of a laser and of a molecular transition, $\nu^{(2)}$, as a function of time. Since the molecular transition is interrogated by the laser, necessarily the laser frequency ν_L needs to be chosen to be within the spectral width of the molecular transition line. In practice, the laser frequency is stabilized to an evacuated, rigid optical cavity (a "reference" cavity), with resonance frequency $\nu^{(1)}$, in order to achieve a high sensitivity also for small oscillation frequencies f_ϕ of the UDM field. Thus, $\nu_L = \nu^{(1)}$ is ensured by a feedback system.

The dependence (sensitivity) of the frequency $\nu^{(i)}$ of any physical system i on a particular FC g is given by the fractional derivative $R_g^{(i)} = \partial \ln \nu^{(i)}/\partial g$. If any FC g oscillates with amplitude δg, this results in a modulation of the detuning $\nu = \nu^{(1)} - \nu^{(2)}$ with an amplitude $\delta\nu/\nu = \Delta R_g \times \delta g/g$, the net sensitivity being $\Delta R_g = R_g^{(1)} - R_g^{(2)}$.

It is desirable to employ a molecular species and a transition whose sensitivity $R_N^{(2)}$ to the mass of the nuclei is as large as possible. This sensitivity stems almost completely from the difference in vibrational energy of the lower and upper state involved in the transition. Each energy contribution is, in the Born-Oppenheimer approximation, given by $E_{\mathrm{vib}} \simeq hcR_\infty(v + 1/2)\gamma\sqrt{m_e/M_N}$. Here, v is the vibrational quantum number of the state, γ is a molecule-specific, electronic-state-specific numerical constant, and M_N is an effective (reduced) nuclear mass. The rotational energies contribute much less to the mass sensitivity. Electronic transitions in molecules have vibrational contributions, but in "standard" molecules, such as iodine (I_2), the vibrational contribution is modest relative to the purely electronic contributions. In a previous experiment [6], two electronic transitions in I_2 at 532 and 725 nm were employed. They exhibited sensitivities $R_N \simeq -0.06$, 0.07, respectively. Here, we use one particular component of the $\nu_1 + \nu_3$ combination vibrational band of $^{12}C_2H_2$ [14], specifically line P(17) at 1535.4 nm. For the neighboring component P(16), Constantin [15] has computed $R_N^{(2)} = -0.468$, very close to the Born-Oppenheimer value of $-1/2$. This value is a good approximation for our line P(17) as well, implying an approximately sevenfold improvement compared to the previously used iodine line at 532 nm. The sensitivities to the electron mass and to the fine-structure constant are $R_\alpha^{(2)} \simeq 2$, $R_{m_e}^{(2)} \simeq 1 - R_N^{(2)}$, where the contributions "2" and "1" stem from the proportionality of any molecular transition frequency to the Rydberg constant.

For the evacuated optical cavity, the frequency has the well-known dependence $\nu^{(1)} \propto L^{-1} \propto a_0^{-1} = m_e\alpha c/\hbar$, where L is the mirror distance, and a_0 is the Bohr radius. Therefore, the sensitivities of the cavity are $R_\alpha^{(1)} = 1$, $R_{m_e}^{(1)} = 1$, $R_N^{(1)} = 0$.

In total, the measured frequency difference ν has the combined sensitivities

$$\frac{\delta\nu}{\nu} = \Delta R_\alpha \frac{\delta\alpha}{\alpha} + \Delta R_{m_e}\frac{\delta m_e}{m_e} + \Delta R_N \frac{\delta m_N}{m_N}, \\ = -\frac{\delta\alpha}{\alpha} - 0.468\frac{\delta m_e}{m_e} + 0.468\frac{\delta m_N}{m_N}. \quad (5)$$

Since any reduced nuclear mass M_N is proportional to a generic nuclear mass m_N, we have altogether from Eqs. (1)–(4)

$$\frac{\delta\nu}{\nu} = (\Delta R_\alpha d_\alpha + \Delta R_{m_e} d_{m_e} + \Delta R_N (Q_N \cdot d_N))\phi. \quad (6)$$

For comparison, our previous "experiment A" in Ref. [6] had sensitivities

$$\frac{\delta\nu}{\nu} = -\frac{\delta\alpha}{\alpha} - 0.06\frac{\delta m_e}{m_e} + 0.06\frac{\delta m_N}{m_N}. \quad (7)$$

III. EXPERIMENTAL SETUP

A scheme of the apparatus configuration is presented in Fig. 2. The experiment uses two independent and nearly identical UDM detectors, here called detector 1 and detector 2. They were installed in different laboratories located approximately 10 m apart. Detector 1 received the laser light from laser system 1 via a 5-m-long polarization-maintaining fiber. Detector 2 was connected to laser system 2 via a 50-m-long single-mode fiber. The two lasers were housed in the same laboratory as detector 2.

Each detector contains one oscillator, a laser stabilized to a high-finesse reference resonator ($\nu^{(1)}$), and a molecular-gas vibrational spectroscopy unit. The molecular resonance frequency defines $\nu^{(2)}$.

For technical details we refer to Supplemental Material [16]. Briefly, in each system, the stabilized laser frequency is tuned to approximately the half-width of the Doppler-broadened molecular transition. Any variation of the frequency difference $\nu = \nu^{(1)} - \nu^{(2)}$ between laser frequency and molecular resonance frequency translates into a variation of the laser power transmitted through the molecular-gas cell and therefore a variation of the differential photocurrent signal from a balanced photodetector (BPD). This signal is acquired with one channel of an analog-to-digital converter (ADC). The second detector outputs its signal to the second channel of the same ADC, thus ensuring that the two signals are acquired perfectly synchronously. In addition, the ADC clock is referenced to

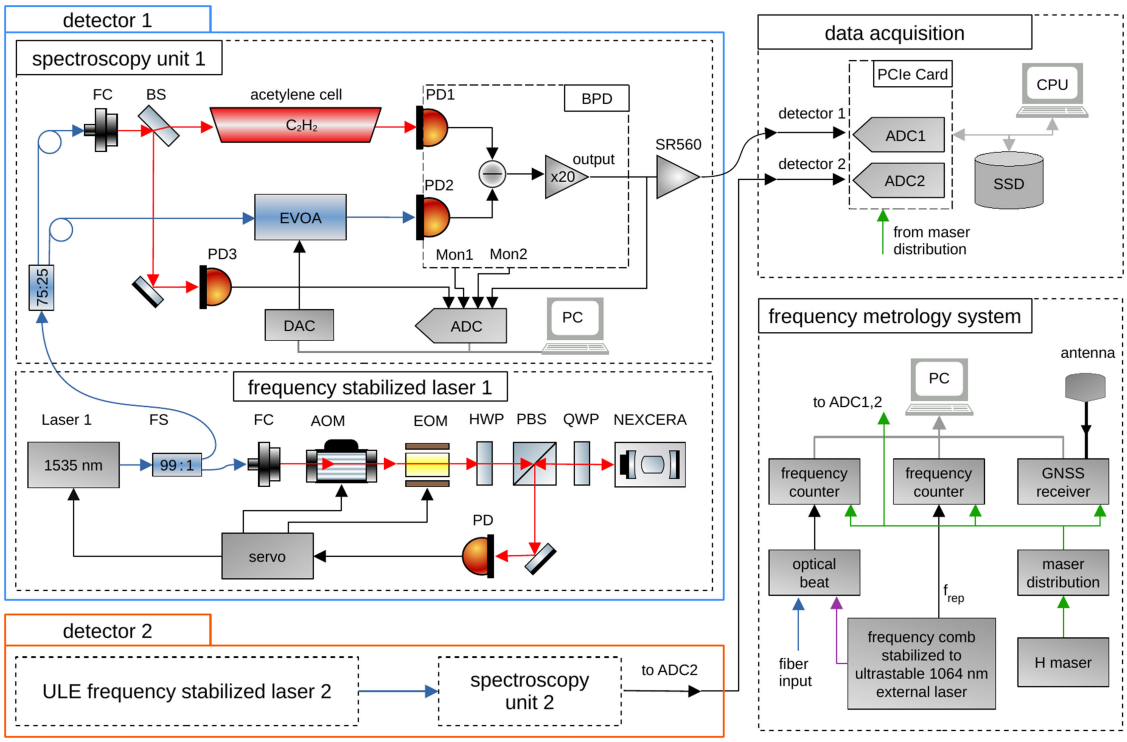


FIG. 2. Schematic of the paired UDM detector. Dashed boxes show subsystems. Blue lines, fiber-optical connections; red line, free-space laser beams; purple line, comb radiation at 1.5 μm; black lines, analog electrical connections; gray lines, digital connections; green lines, 10 MHz reference signal; FC, fiber out-coupler; FS, fiber splitter; BS, beam sampler; EVOA, electronic variable-optical attenuator; PD, photodetector; BPD, balanced photodetector; SR560, low-noise amplifier and filter; AOM, acousto-optical modulator; EOM, electro-optical modulator; HWP, half-wave plate; QWP, quarter-wave plate; PBS, polarizing beam splitter; NEXCERA, ultralow thermal expansion ceramic; ULE, ultralow-expansion glass. SSD, solid-state disk; GNSS, global navigation satellite system.

a hydrogen maser. We acquire data from both detectors during uninterrupted runs, each lasting 19 hours. The photocurrent signal is converted into frequency deviation units (Hz) using the measured amplifier gains and the slope of the molecular line shape. The time interval between the end of one run and the following varies.

IV. EXPERIMENTAL PROTOCOL AND DATA PROCESSING

A. Data acquisition

During each run, indexed by $m = 1, \ldots, 14$, the outputs of the two BPDs were amplified, separately bandpass filtered (SR560) and then synchronously sampled by two ADCs inside a two-channel PCIe card at 244 140 samples per second and the data streamed to memory. The time base of the card was connected to the 10 MHz reference output from a hydrogen maser to ensure long-term stability. The two data recordings were subsequently separately fast-Fourier-transformed and rescaled to provide the lists $\mathrm{FFT}_{j,m}$, the Fourier spectrum of the variations $\delta\nu$ of the cavity-molecular-vibration frequency difference $\nu^{(1)} - \nu^{(2)}$ of each detector $j = 1, 2$. The unit of the list elements is Hz.

All runs were vetted by inspection of the aggregated time series and frequency-domain data to ensure that there were no obvious excessive signal excursions. The term "aggregation" is explained below.

B. Calculation of the cross-spectrum

In order to achieve a suppression of non-common-mode noise, we apply the technique of cross-spectrum analysis [13]. It relies on the possibility of averaging a large number of cross-spectra taken independently over time. Stationary noise that is uncorrelated between two detectors is thereby averaged down. In addition, spurious signals appearing independently in the detectors are also suppressed.

First, we compute $S_{12,m}$, the cross-spectrum of each run m, from the fast-Fourier transforms (FFTs) of detectors 1 and 2, $\mathrm{FFT}_{1,m}$ and $\mathrm{FFT}_{2,m}$, as

$$S_{12,m} = \mathrm{Re}\{\mathrm{FFT}_{1,m} \times \mathrm{FFT}^*_{2,m}\}. \tag{8}$$

Then, the averaged cross-spectrum over M experiments is the mean value,

$$S_{12} = \frac{1}{M}\sum_{m=1}^{M} S_{12,m}. \tag{9}$$

S_{12} has unit Hz^2.

V. DETERMINATION OF THE DETECTION LIMITS

In order to determine the upper bounds for the UDM coupling constants d_g we found it useful to apply synthetic signals to the data. We now explain the procedure.

A. Definition of the synthetic signal

We numerically create a synthetic spectrum $\mathrm{FFT}(T)$ that emulates the effect of a UDM spectrum. $\mathrm{FFT}(T)$ can be added to the experimental spectra of the various runs. Here, T is a time domain representation related to a synthetic UDM field $\phi(t)$ impacting an observable or a fundamental constant g according to $\delta g(t) = d_g \phi(t) \times g$ and is defined further below. $\phi(t)$ is the dimensionless UDM field amplitude for a particle of Compton frequency f_ϕ [2,6,22],

$$\phi(t) = \frac{\phi_0}{2\pi f_\phi}\sum_i \alpha_i F'(f_i)\cos(2\pi f_i t + \varphi_i). \tag{10}$$

$\phi_0 = \sqrt{4\pi\rho_{\mathrm{DM}} G_N/c^2} \simeq 7\times 10^{-16}$ Hz is the normalized field amplitude of the UDM oscillation, $\rho_{\mathrm{DM}} \simeq 0.3\ \mathrm{GeV/cm^3}$ is the local DM density, G_N is the gravitational constant and c is the speed of light. The dimensionless amplitudes α_i are taken from a Rayleigh distribution with $\sigma_{\alpha_i} = 1$. The phases φ_i are taken from a uniform distribution over the range of $0 - 2\pi$, while $\{f_i\}$ is a set of frequencies sampling the distribution f_{DM}, spaced by Δf. The dimensionless $F'(f_i)$ is defined as $F'(f_i) = \sqrt{f_{\mathrm{DM}}(f_i)\Delta f}$, where $f_{\mathrm{DM}}(f)$ is a dimensional function that describes the UDM line shape around the Compton frequency f_ϕ.

The function is reproduced here from Eq. (3.35) of [23],

$$f_{\mathrm{DM}}(f_i) = \frac{2}{\sqrt{2\pi} f_\phi v_g v_{vir}} \exp\left(\frac{2\left(\frac{f_i}{f_\phi}-1\right)+v_g^2}{2v_{vir}^2}\right) \times \sinh\left(\frac{v_g}{v_{vir}^2}\sqrt{2\left(\frac{f_i}{f_\phi}-1\right)}\right). \tag{11}$$

Here $v_g \times c = 220$ km/s is the speed with which the Solar System moves through the Galactic halo. The velocity spread of the UDM particles is quantified by $v_{vir} \times c = 150$ km/s. The fractional full width of $f_{\mathrm{DM}}(f)$ at half maximum is approximately $\Delta f_\phi/f_\phi \simeq 2 \times v_{vir}^{-2} = 5\times 10^{-7}$. The sum of $F'(f_i)^2$ over all frequencies is equal to 1 [1].

We introduce the normalized and dimensionless function $T(t)$,

$$T(t) = \sum_i \alpha_i F'(2\pi f_i)\cos(2\pi f_i t + \varphi_i). \tag{12}$$

$T(t)$ oscillates nearly harmonically between almost equal positive and negative values, and the amplitude of this oscillation, of order 1, varies weakly on timescales much smaller than $(f_\phi v_{vir}^2)^{-1}$. On this and longer timescales, however, the amplitude varies substantially, even approaching zero at times [22]. The long-time mean of $T(t)^2$ is equal to 1 (effectively, Parseval's theorem).

The UDM field is then expressed as

$$\phi(t) = \frac{\phi_0}{2\pi f_\phi} T(t). \tag{13}$$

Since expression (12) is already a Fourier decomposition, we can trivially generate the Fourier transform of $T(t)$, $\mathrm{FFT}(T)$: We conveniently choose the frequencies $\{f_i\}$ to lie on the same grid as the experimental FFT. Thus, Δf introduced above is set equal to the bin width of the experimental FFT. For practical reasons, we limit the range of considered frequencies $\{f_i\}$ to $[f_\phi, f_\phi(1 + 3\Delta f_\phi/f_\phi)]$. We calculate $F'(f_i)$ according to Eq. (11).

We generate a set of m independent versions of a synthetic signal FFT, each denoted by $\mathrm{FFT}(T_m)$. These can be multiplied by a factor β (carrying the unit Hz) that describes the coupling strength of the UDM field to the observable recorded by the detector. These synthetic signals $\beta \times \mathrm{FFT}(T_m)$ are then added to the data of the corresponding experimental run m, and the cross-spectrum is computed

$$S_{12,m}(\beta) = \mathrm{Re}[(\mathrm{FFT}_{1,m} + \beta\ \mathrm{FFT}(T_m)) \times (\mathrm{FFT}_{2,m} + \beta\ \mathrm{FFT}(T_m))^*]. \tag{14}$$

The use of different realizations T_m is justified because during our campaign the delay between the end of run m and the start of run $m+1$ was long and varied.

Finally, we compute the average of the cross-spectrum including the synthetic UDM signal,

$$S_{12}(\beta) = M^{-1}\sum_{m=1}^{M} S_{12,m}(\beta).$$

Note that a UDM signal of the considered form generates, via the terms $\beta^2|\mathrm{FFT}(T_m)|^2$, a positive contribution to S_{12}, irrespective of the sign of β and therefore of the sign of the coupling constant d_g. Figure 3 top shows the effect of adding a synthetic signal with $f_\phi \simeq 12$ kHz to real data. We recognize that a synthetic signal of strength $\beta = 10$ Hz yields a clearly visible signature. We furthermore display in

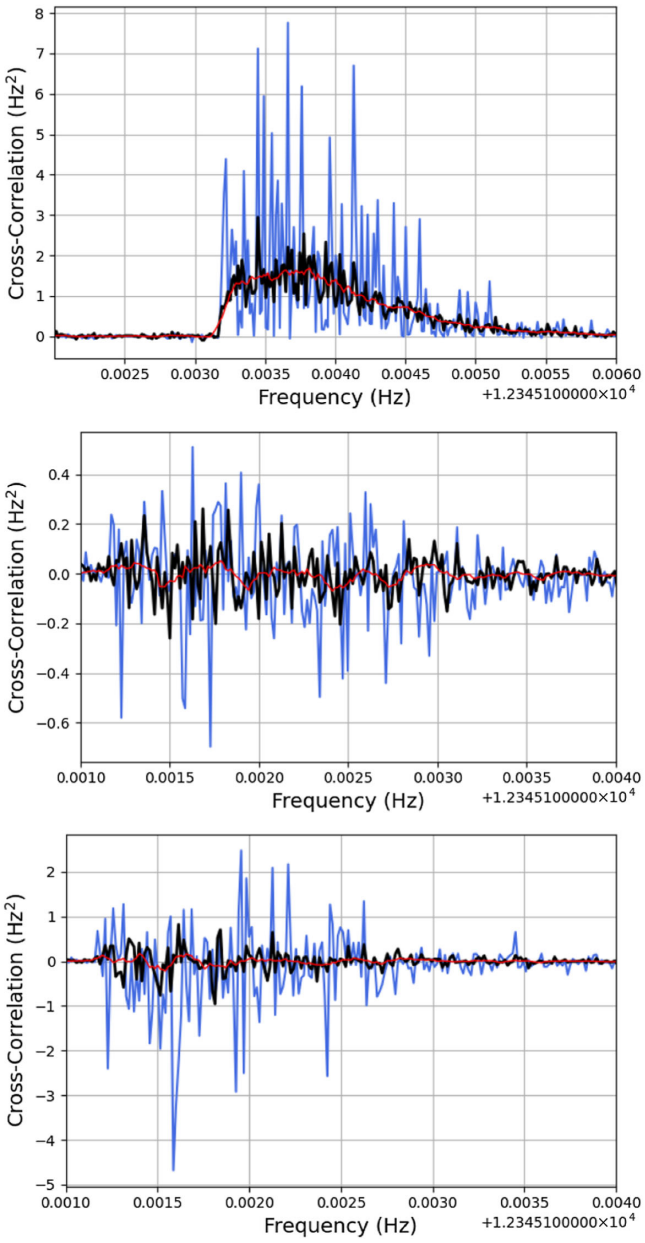


FIG. 3. Spectra of experimental data with added synthetic UDM signals. Top panel: in blue, cross-spectrum $S_{12,m}(\beta = 10\ \mathrm{Hz})$ of a particular experimental run m with added synthetic UDM signal ($f_\phi = 12.3451$ kHz) and in black the average over 14 runs, $S_{12}(\beta = 10\ \mathrm{Hz})$. Center and bottom panels: hypothetical cases in which different synthetic signals (but with the same frequency f_ϕ) are added to the experimental data $\mathrm{FFT}_{1,m}$, $\mathrm{FFT}_{2,m}$. Center panel: the synthetic signal is added only to $\mathrm{FFT}_{1,m}$ and the curves show $\mathrm{Re}[(\mathrm{FFT}_{1,m} + \beta\ \mathrm{FFT}(T_m)) \times (\mathrm{FFT}_{2,m})^*]$ and its averages. Bottom panel: different realizations of the synthetic signal are added to both $\mathrm{FFT}_{1,m}$ and $\mathrm{FFT}_{2,m}$. The curves show $\mathrm{Re}[(\mathrm{FFT}_{1,m} + \beta\ \mathrm{FFT}(T_m)) \times (\mathrm{FFT}_{2,m} + \beta\ \mathrm{FFT}(T_{m+1}))^*]$ and its averages. Blue lines refer to a particular individual experimental run m. Black lines: averages over $M = 14$ runs. Red lines: 0.124 mHz—running averages of S_{12}.

the same figure two examples meant to simulate spurious signals. As can be seen in the middle and lower panels, there is no UDM signature visible if the synthetic signal is added only to one detector's data or different synthetic signals are added to each detector. These examples are evidence that the cross-correlation is capable of suppressing such spurious signals.

B. Determination of the exclusion limits

The exclusion limits are determined in several steps, based on the experimental cross-spectrum $S_{12}(\beta = 0\ \mathrm{Hz})$, the aggregated cross-spectrum denoted by aCS, and cross-spectra with added synthetic UDM signals, $S_{12}(\beta \neq 0)$.

In step 1, we aggregate 128 GiB data per detector (1 GiB $= 2^{30}$ bytes) for each of the $M = 14$ runs into one 64 GiB file. The duration of a run, 19 hours, implies that the FFT has a frequency resolution (bin width) of 14 μHz. We compute the average $S_{12}(\beta = 0\ \mathrm{Hz})$ from a total of 3.6 TiB of data. We then aggregate each group of 4096 subsequent bins into one block having a width of 57 mHz, and generate the aggregated cross-spectrum aCS. This is simply a list of sets, where each set k is a summary of the cross-spectrum data $\{S_{12}\}_k$ in the kth block that starts at frequency f_k: minimum value (aCS-Min), maximum value (aCS-Max), mean value (aCS-Mean) and standard deviation (aCS-SD),

$$\mathrm{aCS}(f_k) = \{\mathrm{Min}(\{S_{12}\}_k), \mathrm{Max}(\{S_{12}\}_k), \mathrm{Mean}(\{S_{12}\}_k), \sigma(\{S_{12}\}_k)\}.$$

The aCS is presented in Fig. 4. The range between aCS-Max and aCS-Min appears in gray; the values of aCS-SD are plotted in green.

In step 2, a Daubechies sixth-order wavelet filter, denoted as F_{Db6}, is applied to the aCS-SD so as to remove "spikes" that occur on a scale of one block. This procedure could remove UDM candidates, but is nevertheless performed in order to generate a UDM strength bound. This filtered aCS-SD is shown in red in Fig. 4.

We define the detection limit $L(f_\phi)$ as the filtered aCS-SD multiplied by a factor 8,

$$L(f_k) = 8F_{Db6}(\sigma(\{S_{12}\}_k)). \tag{15}$$

It is plotted as a magenta line in Fig. 4.

In step 3, we compare L with the unfiltered aCS-SD of step 1 in order to identify outliers. Out of the 2^{20} blocks we identified approximately 618 whose minimum lies below $-L$ and approximately 583 whose maximum lies above $+L$. Only the latter blocks $\{k\}_c$ are inspected in step 5, because a UDM signal would lead to a positive signal lying above L, as demonstrated in Fig. 3.

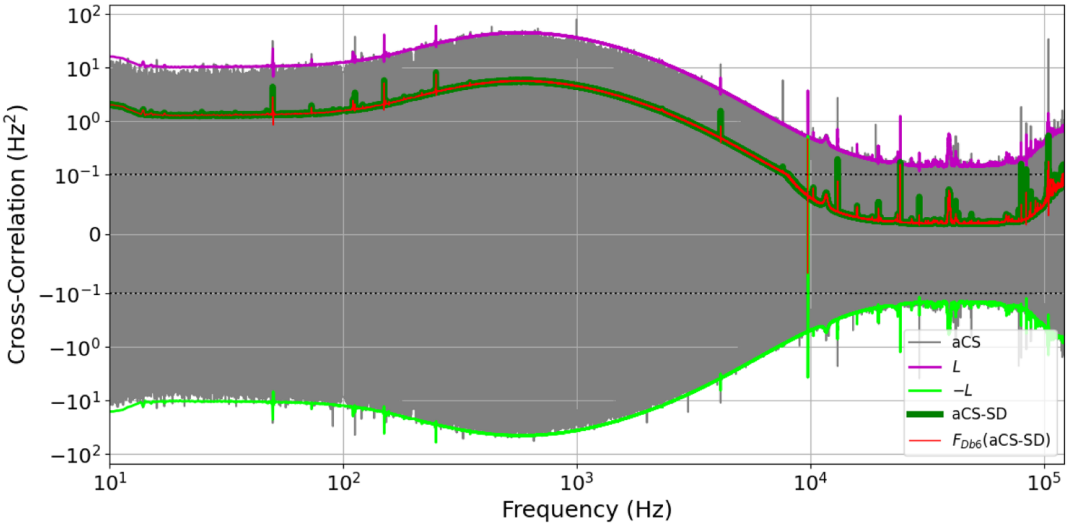


FIG. 4. Properties of the aggregated cross-spectrum aCS of $M = 14$ experiments of 19-h-duration each. Gray: minima and maxima of the aCS. Due to the finite resolution of the graph, the gray data points are dominated by the extreme values of the aCS-extrema. $2^{20} \simeq 1 \times 10^6$ blocks are shown. Green line: aCS-standard deviation (aCS-SD). Red line: Db6-filtered version of the green line. Purple: 8σ-bound L of the strength of a UDM signal. See text for details. Note that the plot is composite: Above the black dotted line the vertical scale is logarithmic, while it is linear below it. Technical noise peaks were identified and removed from the spectrum.

In step 4, we determine the set of signal strengths $\beta^*(f_k)$ required for the synthetic UDM signals $\beta^*(f_k)T(f_k)$ to cause a cross-spectrum value equal to $L(f_k)$,

$$S_{12}(\beta^*(f_k)) = L(f_k). \tag{16}$$

For a given frequency f_k we added a synthetic signal of strength β to the cross-spectrum and calculated the cross-correlation $S_{12}(\beta)$ as shown before in Fig. 3. We applied a running average filter of 124 μHz bandwidth and determined the maximum of the filtered UDM signal. By adjusting β we matched this maximum to have the same amplitude as $L(f_k)$ and store the final value as $\beta^*(f_k)$.

We repeated this procedure not for all blocks k, but only for a reduced number, 198, spanning the frequency range from 10 Hz to 122 kHz and picked to be equidistant on a logarithmic frequency scale. The frequency dependence of β^* is presented in Fig. 5. An example of a cross-spectrum containing a synthetic signal having an amplitude β close to the determined β^* is shown in Fig. 6. At the smallest analysis frequencies, $f \simeq 10$ Hz, the assumed physical UDM signal falls entirely into one bin only, and so does the synthetic signal. The strength of the latter is then influenced by statistical sampling, and varies strongly from one simulated realization to the next. However, because we average over $M = 14$ realizations, the variation averages out to some extent, and our derived limits are reliable.

In step 5, we inspect the blocks $\{k\}_c$ identified earlier, where $\mathrm{Max}(\{S_{12}\}_k)$ is above the limit $L(f_k)$. These blocks define candidate frequencies $\{f_c\}$. We then visually inspected the experimental cross-spectrum $S_{12}(\beta = 0)$ around each frequency f_c for any resemblance to a UDM line shape. An example is presented in Fig. 6. To support the inspection, we generated $S_{12}(\beta = \beta^*(f_k \approx f_c))$ and visually compared it with $S_{12}(\beta = 0)$. Additionally, continuous wavelet transformations (CWTs) of $S_{12}(\beta)$ and $S_{12}(\beta = 0)$ are calculated. As the center panel shows, the CWT of a synthetic signal creates a visually distinct pattern. Thus, CWTs help identify possible candidates. Such a pattern is absent in the data; see bottom panel. None of the 583 candidates could be confirmed as being consistent with the assumed UDM line shape.

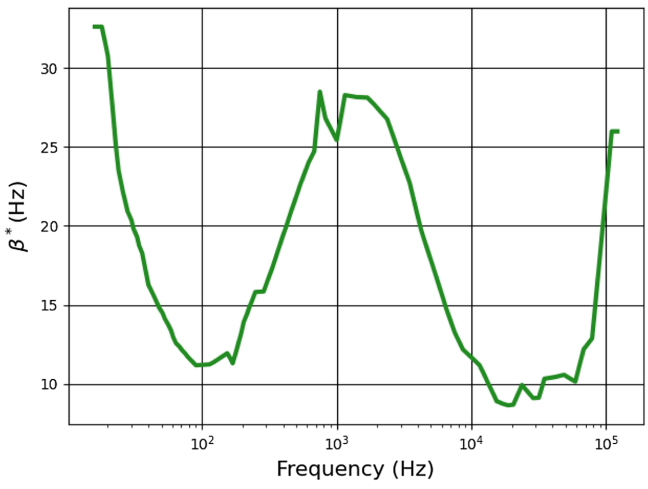


FIG. 5. Determination of the minimum signal strength β^* of a synthetic signal necessary to be considered a UDM candidate. The green line connects the set of 198 values $\beta^*(f_k)$.

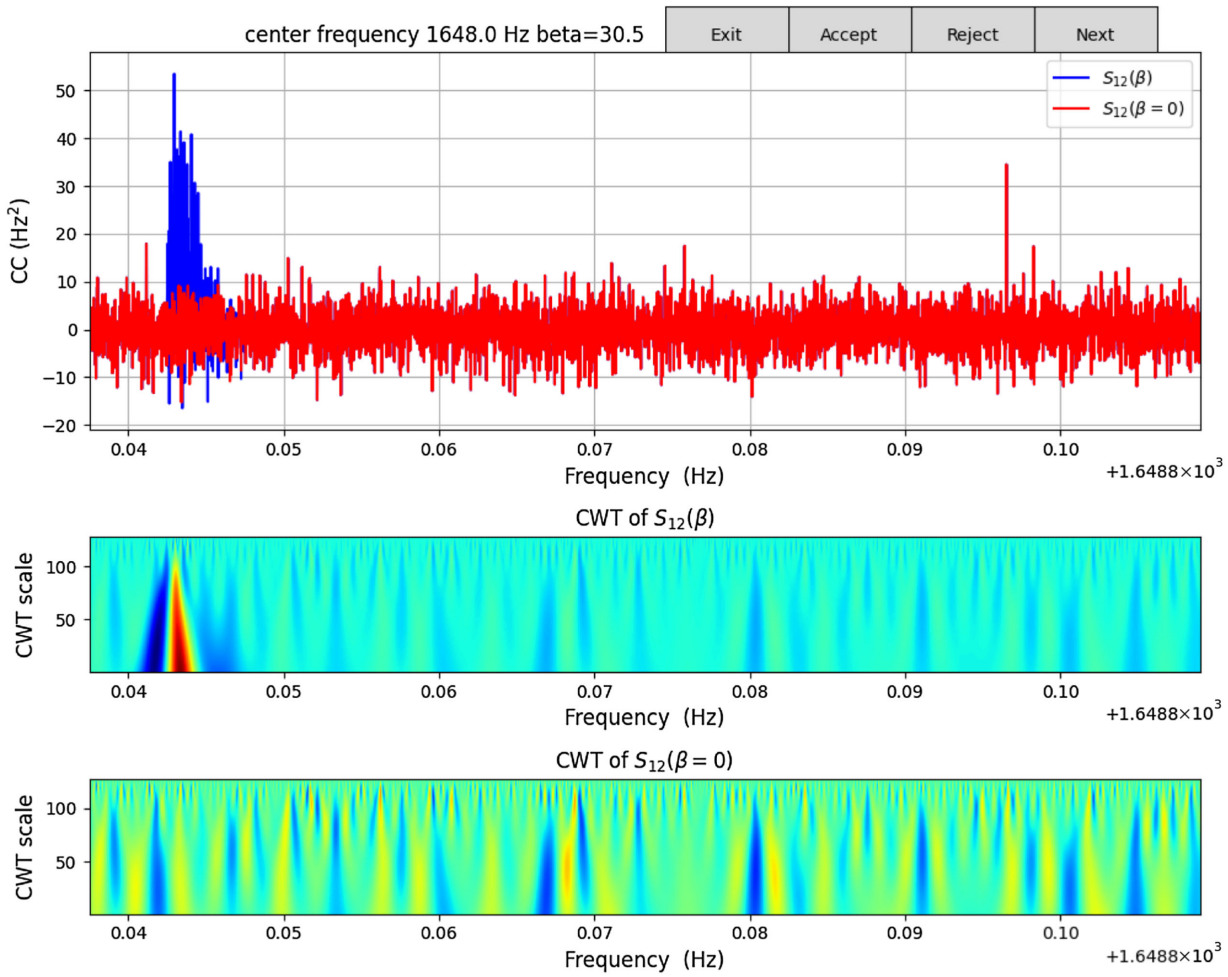


FIG. 6. Example for the visual inspection of a UDM candidate using a graphical user interface. Top panel: the red spectrum shows $S_{12}(\beta = 0)$. Note: The red peak at approximately 0.095 Hz offset frequency is the candidate that triggered the inspection. For comparison, the blue spectrum shows $S_{12}(\beta = 30.5$ Hz). Most of it is hidden by the red trace. Center panel: CWT of $S_{12}(\beta = 30.5$ Hz). Bottom panel: CWT of $S_{12}(\beta = 0)$ CC: cross-correlation.

In step 6, we finally calculate the exclusion limit for a coupling constant d_g as such. As it is customary, we assume in turn that only a single coupling constant is nonzero. We start from Eq. (6),

$$d_g\phi = \delta g/g = (\Delta R_g)^{-1}\delta\nu/\nu.$$

The parameter β was introduced to describe the effect of UDM on the experimental observable, for the predetermined normalized time dependence $T(t)$. Therefore we have the following equivalence,

$$\beta \leftrightarrow \frac{\phi_0}{2\pi f_\phi} d_g \times \Delta R_g \nu.$$

The determined bounds $\beta^*(f_k)$ therefore furnish the bounds of the coupling constant as

$$d_g(f_k) = \frac{2\pi f_k}{\phi_0}\frac{\beta^*(f_k)}{\nu \Delta R_g}. \tag{17}$$

VI. RESULTS AND DISCUSSION

Figure 7 shows the bound d'_N obtained for the nuclear mass. Here we define $d'_N = Q_N \cdot d_N$. The bound d_{m_e} for the electron mass is the same, while it is approximately a factor 2 lower for d_α; see Eq. (5).

In the range from 10 to 500 Hz we improve the bounds d'_N and d_{m_e} by a factor up to 10 compared to our previous iodine experiment A [6]. In the range of 10 to 122 kHz we improve by a factor up to 6. Our bounds for modulation of the nuclear mass are currently the strongest ones, to the best of our knowledge. Our bounds to d_α show only a small improvement by a factor of 1.5 in the range below 80 Hz. This is related to the fact that the shift from electronic

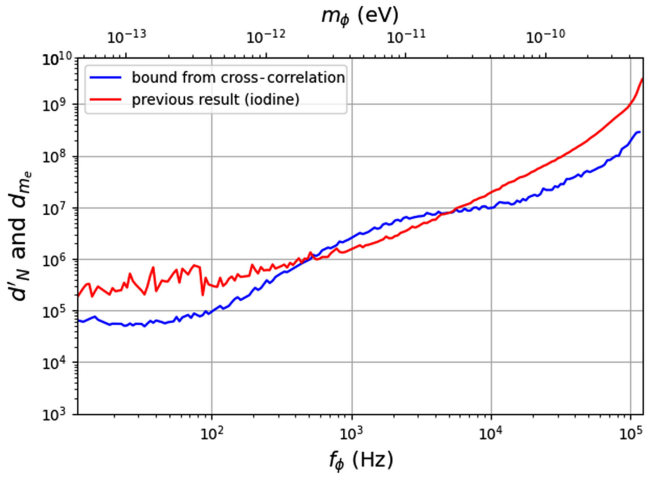


FIG. 7. Exclusion plot of the UDM coupling constant to nuclear mass d'_N and to electron mass d_{m_e}. Blue line: bound calculated from 272 hours of measurement. Red line: bound from our previous work on iodine spectroscopy, experiment A [6].

molecular spectroscopy to vibrational spectroscopy does not affect the sensitivity to α; see Eqs. (5) and (7).

In conclusion, an important achievement of this work is the first successful implementation of the cross-spectrum correlation technique to UDM searches. We succeeded in developing efficient data handling and analysis procedures. The number of spurious signals requiring manual investigation and rejection was found to be much smaller than in the iodine campaign. The impact in the low-frequency domain—below 100 Hz—has been quite beneficial. Note that the cross-spectrum analysis technique is completely independent of the particular spectroscopy approach used.

A second main result is proof that it is feasible to employ vibrational spectroscopy for a UDM search. With the combination of the two techniques introduced in this work, we achieve better bounds for two fundamental constants than a previous iodine spectroscopy campaign, even though in the latter the molecular transition linewidth was 160 times smaller, as Doppler-free saturation spectroscopy was employed. The larger linewidth in the present study implies lower sensitivity, but this effect is partially offset by the stronger signal available in simple absorption spectroscopy. In terms of technical simplicity and cost, the acetylene experiment is advantageous: An iodine experiment requires green laser light, for which the effort to provide a laser wave with ultralow-frequency noise is higher than at the present wavelength of 1.5 μm.

A. Outlook

This work may be extended in two ways. First toward higher Compton frequencies, an extension that entails concomitant higher data volume and processing effort if the frequency range is also extended. Second, toward Doppler-free spectroscopy of acetylene [24–26], promising lower noise and thus higher sensitivity for the spectral window from tens of Hz to approximately 1 MHz. Looking toward the future, the technique demonstrated here appears to be suitable to be extended to a large number ($2N$) of simultaneously recording detectors. Not every detector requires its own laser, since one laser can serve as many detectors as its frequency noise level permits. The lower the laser's frequency noise, the larger is the number. This approach could ensure that the cost incurred in and volume occupied by the large number of detectors $2N$ will not be prohibitive. The most efficient way to process $2N$ independent data streams needs future investigations [2]. One possibility is to construct an N-pair cross-correlation $\Pi_{j=1}^{N} S_{2j-1,2j}$. By construction, this quantity would suppress any oscillatory signal that is not present in every detector.

ACKNOWLEDGMENTS

We thank A. Nevsky for performing exploratory work on acetylene spectroscopy and E. Wiens for the operation of the ULE-cavity-stabilized laser system. U. Rosowski and D. Iwaschko helped with electronics. This work has received funding from the DFG via project SCHI 431/24-1 (S. S.) and from both DFG and the state of Nordrhein-Westfalen via Grant No. INST-208/774-1 FUGG (S. S.).

DATA AVAILABILITY

The data that support the findings of this article are not publicly available upon publication because it is not technically feasible and/or the cost of preparing, depositing, and hosting the data would be prohibitive within the terms of this research project. The data are available from the authors upon reasonable request.

[1] J. W. Foster, N. L. Rodd, and B. R. Safdi, Revealing the dark matter halo with axion direct detection, Phys. Rev. D **97**, 123006 (2018).

[2] A. Derevianko, Detecting dark-matter waves with a network of precision-measurement tools, Phys. Rev. A **97**, 042506 (2018).

[3] T. Damour and J. F. Donoghue, Equivalence principle violations and couplings of a light dilaton, Phys. Rev. D **82**, 084033 (2010).
[4] Y. V. Stadnik and V. V. Flambaum, Searching for dark matter and variation of fundamental constants with laser and maser interferometry, Phys. Rev. Lett. **114**, 161301 (2015).
[5] D. Antypas, D. Budker, V. V. Flambaum, M. G. Kozlov, G. Perez, and J. Ye, Fast apparent oscillations of fundamental constants, Ann. Phys. (Berlin) **532**, 1900566 (2020).
[6] R. Oswald, A. Nevsky, V. Vogt, S. Schiller, N. Figueroa, K. Zhang, O. Tretiak, D. Antypas, D. Budker, A. Banerjee, and G. Perez, Search for dark-matter-induced oscillations of fundamental constants using molecular spectroscopy, Phys. Rev. Lett. **129**, 031302 (2022).
[7] A. Arvanitaki, S. Dimopoulos, and K. Van Tilburg, Sound of dark matter: Searching for light scalars with resonant-mass detectors, Phys. Rev. Lett. **116**, 031102 (2016).
[8] E. Savalle, A. Hees, F. Frank, E. Cantin, P.-E. Pottie, B. M. Roberts, L. Cros, B. T. McAllister, and P. Wolf, Searching for dark matter with an optical cavity and an unequal-delay interferometer, Phys. Rev. Lett. **126**, 051301 (2021).
[9] M. Filzinger, S. Dörscher, R. Lange, J. Klose, M. Steinel, E. Benkler, E. Peik, C. Lisdat, and N. Huntemann, Improved limits on the coupling of ultralight bosonic dark matter to photons from optical atomic clock comparisons, Phys. Rev. Lett. **130**, 253001 (2023).
[10] X. Zhang, A. Banerjee, M. Leyser, G. Perez, S. Schiller, D. Budker, and D. Antypas, Search for ultralight dark matter with spectroscopy of radio-frequency atomic transitions, Phys. Rev. Lett. **130**, 251002 (2023).
[11] W. M. Campbell, B. T. McAllister, M. Goryachev, E. N. Ivanov, and M. E. Tobar, Searching for scalar dark matter via coupling to fundamental constants with photonic, atomic, and mechanical oscillators, Phys. Rev. Lett. **126**, 071301 (2021).
[12] C. J. Kennedy, E. Oelker, J. M. Robinson, T. Bothwell, D. Kedar, W. R. Milner, G. E. Marti, A. Derevianko, and J. Ye, Precision metrology meets cosmology: Improved constraints on ultralight dark matter from atom-cavity frequency comparisons, Phys. Rev. Lett. **125**, 201302 (2020).
[13] E. Rubiola and F. Vernotte, The cross-spectrum experimental method, arXiv:1003.0113.
[14] S. Gilbert and W. Swann, Acetylene C_2H_2 Absorption Reference for 1510 nm to 1540 nm Wavelength Calibration—SRM 2517a, NIST Special Publication **260–133** (2001), https://www.nist.gov/system/files/documents/srm/SP260-133.PDF.
[15] F. L. Constantin, Sensitivity to electron-to-proton mass ratio variation from $^{12}C_2H_2$ rovibrational transitions to $v_1 + v_3$ and $v_1 + v_2 + v_4 + v_5$ interacting levels, Vib. Spectrosc. **85**, 228 (2016).
[16] See Supplemental Material at http://link.aps.org/supplemental/10.1103/PhysRevD.111.055003 for technical details of setup and data processing which includes Refs. [17–21].
[17] J. I. Thorpe, K. Numata, and J. Livas, Laser frequency stabilization and control through offset sideband locking to optical cavities, Opt. Express **16**, 15980 (2008).
[18] A. Y. Nevsky, S. Alighanbari, Q. Chen, I. Ernsting, S. Vasilyev, S. Schiller, G. Barwood, P. Gill, N. Poli, and G. M. Tino, Robust frequency stabilization of multiple spectroscopy lasers with large and tunable offset frequencies, Opt. Lett. **38**, 4903 (2013).
[19] J. Vanderkooy and S. P. Lipshitz, Resolution below the least significant bit in digital systems with dither, J. Audio Eng. Soc. **32**, 106 (1984).
[20] W. Kester, *ADC Input Noise: The Good, The Bad, and The Ugly. Is No Noise Good Noise?* (Analog Devices Inc., 2005).
[21] J.-P. Marchal, J. Brondeau, and D. Canet, Measurement of small signals in the presence of intense peaks by fourier transform NMR, J. Magn. Reson. **33**, 469 (1979).
[22] G. P. Centers, J. W. Blanchard, J. Conrad, N. L. Figueroa, A. Garcon, A. V. Gramolin, D. F. J. Kimball, M. Lawson, B. Pelssers, J. A. Smiga, A. O. Sushkov, A. Wickenbrock, D. Budker, and A. Derevianko, Stochastic fluctuations of bosonic dark matter, Nat. Commun. **12**, 7321 (2021).
[23] E. Savalle, Tester la Relativité Générale avec des horloges dans l'espace, et explorer les possibilités de détection de matière noire avec des atomes froids dans l'espace et au sol, Theses, Université Paris Sciences et Lettres, 2020.
[24] M. Triches, M. Michieletto, J. Hald, J. K. Lyngsø, J. Lægsgaard, and O. Bang, Optical frequency standard using acetylene-filled hollow-core photonic crystal fibers, Opt. Express **23**, 11227 (2015).
[25] C. Cherfan, I. Manai, S. Zemmouri, J.-C. Garreau, J.-F. Clément, P. Szriftgiser, and R. Chicireanu, Acetylene-based frequency stabilization of a laser system for potassium laser cooling, Opt. Express **28**, 494 (2020).
[26] T. Billotte, M. Chafer, M. Maurel, F. Amrani, F. Gerome, B. Debord, and F. Benabid, Contaminant-free end-capped and single-mode acetylene photonic microcell for sub-Doppler spectroscopy, Opt. Lett. **46**, 456 (2021).

Supplemental Material: Search for oscillating fundamental constants using a paired detector and vibrational spectroscopy

René Oswald, Victor Vogt and Stephan Schiller
Institut für Experimentalphysik, Heinrich-Heine-Universität Düsseldorf, 40225 Düsseldorf, Germany

A. Details of the apparatus

Laser system for detector 1 A fiber laser (NKT E15) was frequency stabilized using a high-finesse optical resonator made of a NEXCERA ceramic, by means of the Pound-Drever-Hall (PDH) technique. The laser wave is coupled into an acousto-optic modulator (AOM) and split using a 99:1 fiber splitter. The smaller fraction of the light is further sent through a fiber-coupled EOM that impresses the PDH sidebands. We used sideband locking of the laser to the cavity [1, 2]. For this purpose, the phase modulator is driven by a signal of tunable frequency $\Omega/2\pi$ in the range of 100 - 400 MHz, that is itself phase modulated at a constant frequency 12.8 MHz. The upper laser sideband is locked to the TEM_{00} mode of the cavity. The laser's carrier frequency could be slowly but continuously shifted relative to the cavity frequency by adjusting $\Omega/2\pi$, over a range of few hundred MHz. The light power within the resonator was stabilized by maintaining the light power transmitted through the resonator stable. This was accomplished by regulating appropriately the amplitude of the AOM drive signal.

Laser system for detector 2 This laser system is similar to the system 1; however the ultrastable resonator was made out of standard ULE material.

The bandwidths of the frequency locks to the cavities are on the order of $f_{lock} \simeq 50$ kHz. Therefore, for detection frequencies $f > f_{lock}$ the laser frequency is determined by the laser resonator itself, as long as f is below f_2, the inverse time for sound propagation over the length of the resonator. The resonator is a section of doped silica optical fiber; from its length and speed of sound we estimate $f_2 \simeq (6\ \mathrm{km/s})/10\,\mathrm{cm} \simeq 60$ kHz. In the range $f_{lock} < f < f_2$, the sensitivity of the laser frequency to m_e and α is approximately the same as for $f < f_{lock}$, neglecting the fact that that the index of refraction of the fiber weakly depends on α and m_e. Within this approximation, we may state that for $f > f_2$ the laser frequency is almost not affected by the fundamental constants. With $R_\alpha^{(1)} \simeq 0$, $R_{m_e}^{(1)} \simeq 0$, $R_N^{(1)} = 0$ in the regime $f > f_2$, we obtain $\Delta R_\alpha \simeq -2$, $\Delta R_{m_e} \simeq 1.468$, $\Delta R_N \simeq 0.468$. The sensitivity to α is doubled, the sensitivity to m_e is tripled, compared to the regime $f < f_2$. The bounds presented in sec. V of the main document ignore this effect; they are therefore conservative.

Spectroscopy subsystems of detectors 1 and 2 In each subsystem, the laser wave was first split by a fiber splitter into a probe wave that interrogates the gas and a weaker reference wave. The probe wave was coupled out into free space and was formed into a beam of 3 mm diameter. The majority of this wave traversed a beam sampler and the 16.5 cm long gas cell. The cell contained acetylene gas under standard conditions [3]. The gas pressure was 6 Torr. The fractional absorption of the molecular resonance at our chosen wavelength of 1535.4 nm was approximately 30 %. The light transmitted through the cell was focused on detector PD1 of the balanced photodetector BPD (Femto HBPR-60K). The part of the probe wave reflected by the beam sampler was detected using photodetector PD3 in order to monitor the input power. The reference wave propagates in a fiber through an electronic variable optical attenuator (EVOA) to the second detector of the balanced photodetector, PD2. The balanced photodetector signal gain was set to 20 and a 20 MHz low-pass filter was applied directly in the BPD.

Data acquisition The output of each BPD was further amplified and bandpass filtered (SR560, Stanford Research Systems) with corner frequencies of usually 300 Hz and 300 kHz. The corner frequency of the lowpass was higher than the frequency range of interest, but subsequently compensated numerically. The signals of BPD 1 and 2 are recorded simultaneously by a PCIe-based 16-bit ADC card (Spectrum Instrumentation) referenced to the H-Maser. The resulting binary data was processed and analyzed after the recording by a PC with 96 GB RAM and a total of 12 TB SSD storage in RAID0 configuration. Furthermore, for monitoring purposes, in each detector the BPD output signal, both monitor signals Mon1, Mon2, and signal PD3 were recorded using a low-sampling-rate ADC card (ADC3). The digitized BPD signal was used to control the optical power level on the reference detector PD2, in order to equalize the powers on PD1 and PD2, therefore improving the suppression of technical noise. The servo was implemented using a digital 3-zone controller that adjusted the voltage applied to the EVOA approximately every 2 seconds via a DAC.

B. Characterization of the sensitivity of the spectroscopy subsystem

The sensitivity was investigated by frequency-scanning a free-running laser around the P17 line. The laser light was split into two parts; one part was sent to a wavemeter, the other part was split in two and and sent to the detectors 1 and 2. The frequency reading of the wavemeter and the monitor signals Mon1 and Mon2 of both detectors were recorded. For UDM detector 1 we show the transmission signal in Fig. 1. In the lower graph, the normalized first derivative of the transmission is shown. At the operating frequencies (**blue** and **orange** line) roughly 50 % of the incoming light is absorbed. The fractional variation of transmission T to frequency deviations $dT/d\nu = 0.18$ %/MHz was measured at PD2. During a typical experimental run, 1 mW power was detected on PD2 resulting in a sensitivity of $D_s = 27.8$ MHz/V at the output of the BPD of both detectors. The gain of the amplifier (see Fig. 2 of the main document) was set to $G_{j,m}$ in run m of detector $j = 1, 2$. Thus, the discriminator coefficient of a run was $D_{j,m} = D_s \times G_{j,m}$. A typical sensitivity was $D \approx 0.6$ MHz/V for a typical gain $G \approx 50$. The smallest frequency deviation resolvable is then presumably limited by the ADC resolution of 16 bit and its input voltage range. For a typical experiment the ADC voltage range was set to ± 0.2 V resulting in an presumable resolution limit of about 6 μVpp for a modulation signal (i.e. least significant bit, LSB), or equivalently 4 Hz pp. However, in the presence of broadband noise at the input of an ADC the resolution limit can be lower than the naive limit [4–6]. Under those conditions the inherent noise of the measurement sets the ultimate limit. In our experiment such broadband noise is indeed present. We verified that our system is able to resolve a signal of amplitude smaller than 1 LSB. In a trial experiment, we acquired 2^{32} samples in the presence of noise level of 0.3 mV (standard deviation; equivalent to far more than 1 LSB) and retrieved an applied coherent signal of 80 nV amplitude. This is equivalent to ≈ 90 mHz optical frequency difference modulation amplitude. This value is sufficiently small so that it does not affect our bound, the magenta line in Fig. 4 of the main document.

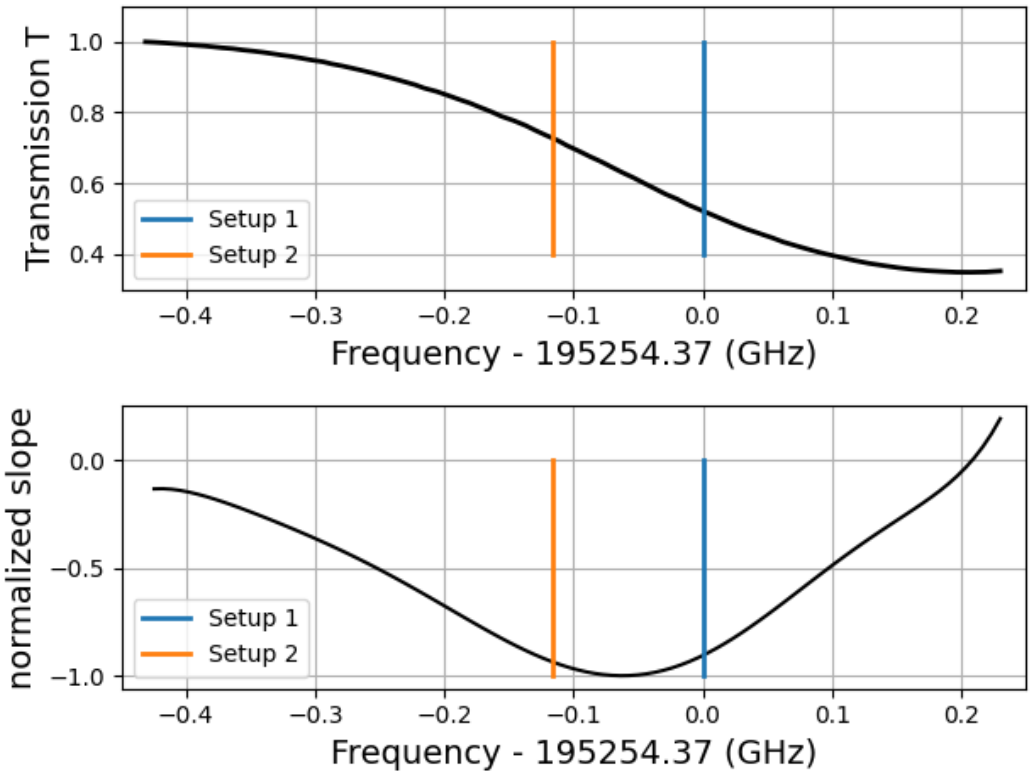


Figure 1. **Molecular discriminators and sensitivity.** Upper graph: the cell transmission on the wing of the acetylene line P17; **orange** and **blue** markers indicate the frequencies set during the actual data-taking runs. Lower graph: the normalized frequency derivative of the transmission. As can be seen, at the frequency settings employed during data taking the sensitivity of both detectors is similar.

C. Characterization of the laser systems

The frequency noise of the lasers is a fundamental limit to the sensitivity of the detectors. We therefore determined the frequency noise directly, by analyzing the beat note between the two independent lasers 1, 2. In Figure 2 the beat note's noise power spectral density S_b is depicted in **magenta**. This noise is the sum of the power spectral densities of the individual laser frequencies, and therefore represents an upper bound to the frequency noise of each laser.

The full detector signal, as measured at ADC1 or ADC2, can also be spectrally analyzed. Let $S_\mathrm{BPD}(f)$ be the power spectral density of voltage fluctuations of a detector including the ADC during a typical experimental run. The product of its root power spectral density $\sqrt{S_\mathrm{b}}$ and the detector discriminator coefficient, $D_s\sqrt{S_\mathrm{BPD}}$ (**black** in the figure), can be compared with the laser frequency noise. It can be seen that over most of the studied frequency range, the laser frequency noise is more than one order smaller than the detector noise. Thus, the laser frequency noise is negligible.

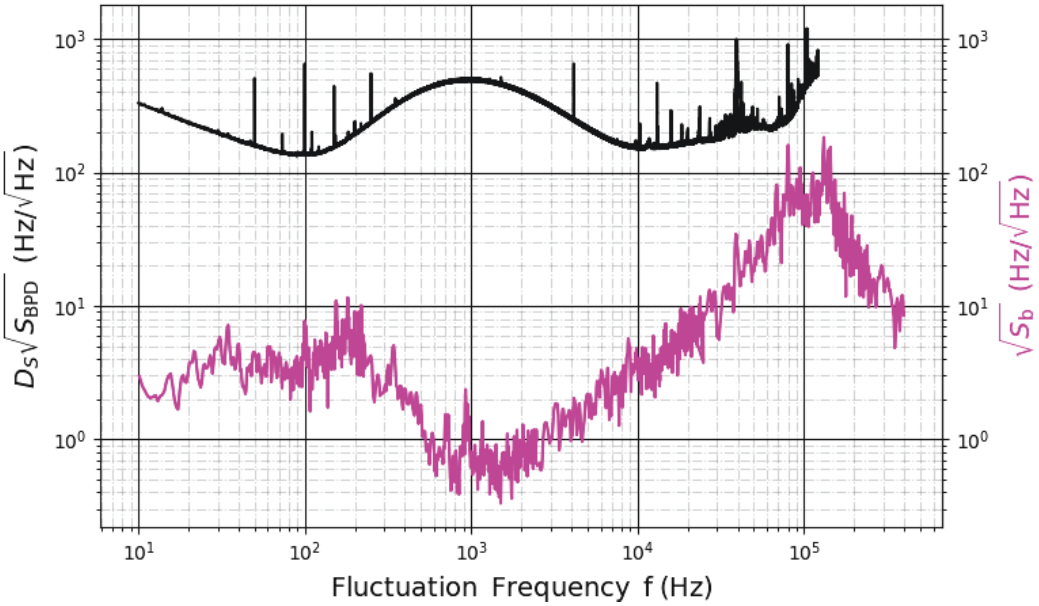


Figure 2. **Noise spectra. Black** : Typical total root power spectral density $D_s\sqrt{S_\mathrm{BPD}}$ of the rescaled ADC1 signal of an experimental run. This spectrum includes all noise sources. The narrow peaks are electromagnetic interference from power lines and from noise in the frequency-lock of laser 1 to its cavity. **Magenta:** Root power spectral density $\sqrt{S_\mathrm{b}}$ of the beat note between the two independent lasers 1 and 2. This is representative of the frequency noise of each laser.

D. Data acquisition

Referring to Fig. 3, an experimental run (indexed by m) consists of two simultaneously started measurements with detector 1 and 2. The BPD output voltages, amplified and bandpass filtered by amplifiers SR560, are denoted by $x^{(m)}(t)$. These are recorded at a sampling rate of 244 kSa/s and written onto a single file. These are the two time series of the two detectors; the identical sampling times are denoted by t_n. We chose a duration of 19 hours so that the number of samples per run, N, is a multiple of two, 2×2^{34} for the present choice. The recorded file is then split into two time series files, one for each detector. We also generate aggregated time series data and store them. We define aggregation as subdividing time-domain (frequency-domain) data into time (spectral) intervals of equal duration (span) and extracting from each interval the maximum, minimum, and mean value, as well as the standard deviation.

Afterwards, a FFT of the complete time series data of each detector is performed,

$$X_k^{(m)} = A \sum_{n=0}^{N-1} x^{(m)}(t_n) e^{-i2\pi \frac{n}{N}} \ .$$

Here X_k is the kth component of the FFT, A is a normalization constant, and N is the number of time samples. For ease of storage of the FFT, A is set to 1. As the input time series $x^{(m)}(t_n)$ is real valued the resulting components X_k are related by $X_k{=}(X_{N-k})^*$. In order to reduce memory usage, for further processing, only the frequency components with the index k running from 0 to $N/2$ are stored.

Thus, without loss of information we define $\mathrm{HFFT}_{j,m} := \{X_k^{(m)}\}_{0\ldots N/2}$ of detector j. The $\mathrm{HFFT}_{j,m}$ were subsequently normalized by setting A to $2/N$, further corrected for the amplitude reduction introduced by the bandpass filters (SR560), and multiplied by the above mentioned discriminator coefficients $D_{j,m}$. The result is denoted by $\mathrm{FFT}_{j,m} = D_{j,m} \times \mathrm{HFFT}_{j,m}$ and has units Hz. This is the Fourier spectrum of the variations $\delta\nu$ of the cavity-molecular-vibration frequency difference $\nu^{(1)} - \nu^{(2)}$.

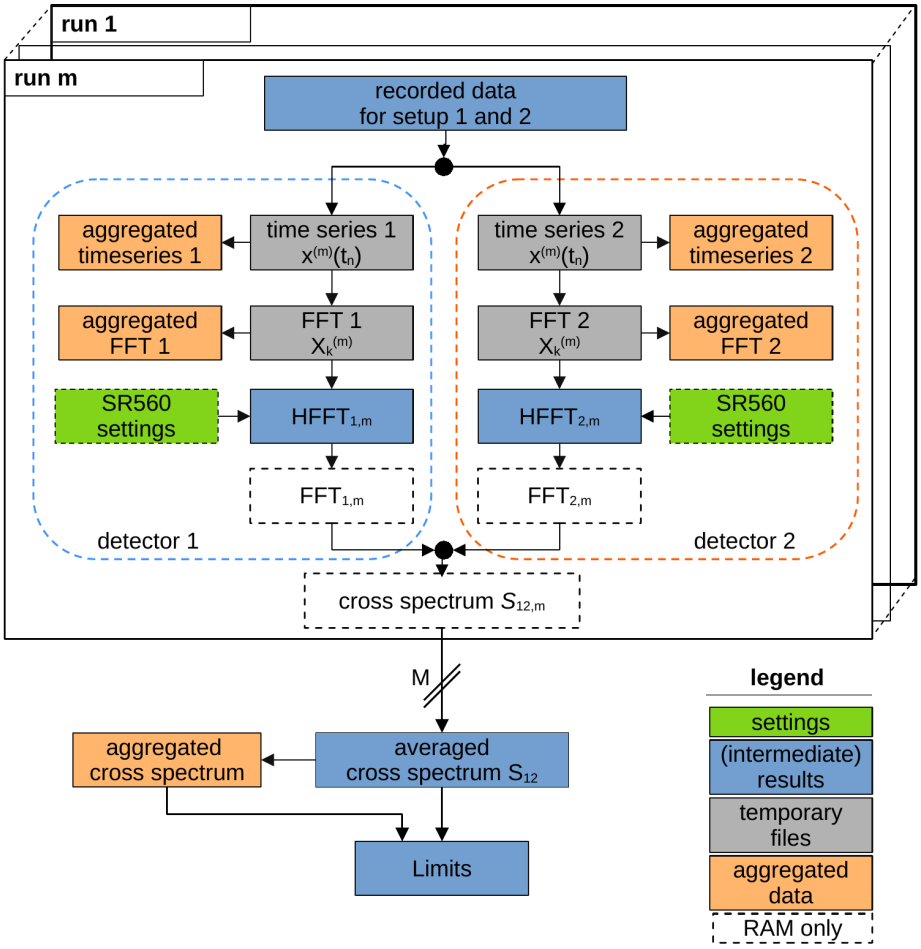


Figure 3. **Data processing flow**. **Blue** boxes: permanently saved data; **Grey** boxes: temporary data; **orange** boxes: aggregated data consisting of minimum, maximum, standard deviation and the mean value of all intervals; **green** boxes: settings relevant for data conversion; long-dashed boxes: data in RAM only.

[1] J. I. Thorpe, K. Numata, and J. Livas, Laser frequency stabilization and control through offset sideband locking to optical cavities, Opt. Express **16**, 15980 (2008).
[2] A. Y. Nevsky, S. Alighanbari, Q. Chen, I. Ernsting, S. Vasilyev, S. Schiller, G. Barwood, P. Gill, N. Poli, and G. M. Tino, Robust frequency stabilization of multiple spectroscopy lasers with large and tunable offset frequencies, Opt. Lett. **38**, 4903 (2013).
[3] S. Gilbert and W. Swann, Acetylene C_2H_2 Absorption Reference for 1510 nm to 1540 nm Wavelength Calibration - SRM 2517a, NIST Special Publication **260-133** (2001).
[4] J. Vanderkooy and S. P. Lipshitz, Resolution below the least significant bit in digital systems with dither, Journal of The Audio Engineering Society **32**, 106 (1984).
[5] W. Kester, ADC Input Noise: The Good, The Bad, and The Ugly. Is No Noise Good Noise? (Analog Devices Inc., 2005).
[6] J.-P. Marchal, J. Brondeau, and D. Canet, Measurement of small signals in the presence of intense peaks by fourier transform nmr, J. Magn. Reson. **33**, 469 (1979).

B.2 Spectroscopy of Molecular Hydrogen Ions

B.2.1 Rovibrational Spectroscopy of HD^+

Title:
Test of charged baryon interaction with high-resolution vibrational spectroscopy of molecular hydrogen ions

Authors:
S. Alighanbari, I. Kortunov, G. Giri and S.Schiller

Status / Year: ..... Published / 2023

Journal: ..... Nature Physics

DOI: 10.1038/s41567-023-02088-2

Statement of Copyright:
Springer Nature or its licensor (e.g. a society or other partner) holds exclusive rights to this article under a publishing agreement with the author(s) or other rightsholder(s); author self-archiving of the accepted manuscript version of this article is solely governed by the terms of such publishing agreement and applicable law.

Licence and Statement on reuse for dissertation:

License Number: 5902010896473

Type of Use: ..... Thesis/Dissertation

Grant and Scope of License:
"The Licensor [Springer Nature] grants [Victor A. Vogt] a personal, non-exclusive, non-transferable, non-sublicensable, revocable, world-wide License to reproduce, distribute, communicate to the public, make available, broadcast, electronically transmit or create derivative works using the Licensed Material for the purpose(s) specified in [the] RightsLink Licence Details only [...]".

Full License statement available upon reasonable request

My Contribution:
I performed the necessary measurements to evaluate the performance of the spectroscopy light. As shown in Extended Data Fig. 1, the red lines represent the results of a TCH analysis conducted by me. This analysis includes the linewidth and Allan deviation measurements. See Section 8.2.

nature physics

Article

https://doi.org/10.1038/s41567-023-02088-2

Test of charged baryon interaction with high-resolution vibrational spectroscopy of molecular hydrogen ions

Received: 27 May 2022

Accepted: 9 May 2023

Published online: 22 June 2023

Check for updates

S. Alighanbari, I. V. Kortunov, G. S. Giri & S. Schiller

Molecular hydrogen ions are of high interest in fundamental physics and metrology. In particular, the long-range baryon–baryon interaction and the degrees of freedom of baryon rotational and vibrational motion are key features of molecular hydrogen ions. Here we present the measurement of a one-photon transition of HD^+, a fourth overtone vibrational transition. Through a comparison of experimental and ab initio frequencies of this and previously measured transitions, we implement a test of the low-energy quantum physics of baryon interaction and motion. The results may also be interpreted as a test of Weinberg's quantum mechanics extension. Furthermore, we compare the value of the fundamental constant combination $\mu/m_e = m_p m_d/(m_p + m_d)m_e$ determined from our measurement with the value obtained from mass spectrometry experiments. This may also be regarded as a test of the quantum behaviour of baryons, revealing a moderate tension of 1.7 times the combined uncertainty. Combining our measurement result with some previous ones on HD^+, we obtain a least-squares-adjusted value for μ/m_e as well as a bound for the force between the proton and deuteron in a scenario that is beyond the Standard Model of particle physics. No evidence of a deviation from conventional quantum physics is found.

Because of their relative simplicity, molecular hydrogen ions (MHI) are calculable molecules. Applying the theory of non-relativistic quantum electrodynamics (NRQED)[1], Korobov and Karr[2] calculated vibrational transition frequencies with fractional uncertainty estimated to be 8×10^{-12}, limited by uncalculated NRQED contributions of high order in the fine structure constant α. This uncertainty is within a factor of 10 of the theory uncertainty achieved for the hydrogen atom. NRQED theory assumes, in particular, the conventional Coulomb interaction between the two baryons in the MHI. Actual predictions of MHI frequencies require the values of certain fundamental constants as the input, specifically the Rydberg constant R_∞, the ratio of the masses of the specific baryons (proton, deuteron, triton) relative to the electron mass and the charge radii of those baryons. Given that the predictions of the ab initio theory are so accurate, if the spectroscopy of MHI matches or surpasses this accuracy, it becomes possible to either accurately determine the mentioned fundamental constants or test for the presence of unconventional, hypothetical interactions, assuming values of constants measured on other systems. Recently, this has been implemented on a rotational transition and two vibrational transitions[3–5] that were measured with sub-Doppler resolution. We extend that work concerning three main aspects. First, we extend a spectroscopic technique—trapped ion cluster transverse excitation spectroscopy—to a shorter wavelength and substantially higher resolution. Second, we consequently achieve a metrological study of a previously unexplored transition—the fourth overtone vibrational transition of HD^+—with experimental accuracy higher than the theory prediction. Third, our data, by themselves or combined with previous data, enable two tests of quantum physics—one that relates to the Weinberg's

Institut für Experimentalphysik, Heinrich-Heine-Universität Düsseldorf, Düsseldorf, Germany. e-mail: step.schiller@hhu.de

Methods

Apparatus

The experimental apparatus used in the present work has been employed in previous spectroscopy experiments[3,4,40], but the spectroscopy laser source is replaced with a continuous-wave, high-power diode laser emitting at 1.15 μm. The laser is stabilized to a reference cavity and steered to a hydrogen maser on long timescales. In more detail, the laser is phase locked to a femtosecond fibre frequency comb, which is itself phase locked to an ultrastable 1.06 μm laser (reference laser 1). The phase-locked beats are constantly monitored and display sub-hertz linewidths. Extended Data Fig. 1 (left, blue trace in the inset) shows one of the two beats. The linewidth of the spectroscopy laser is, to a large extent, determined by the linewidth of reference laser 1. To characterize the latter, we obtained a direct beat between reference laser 1 and an independent reference laser 2 (also at 1.06 μm), frequency locked to its own ultrastable cavity. This reference laser 2 has sub-hertz linewidth and low frequency drift. The beat note (Extended Data Fig. 1, left, red trace) exhibits a full-width at half-maximum smaller than 3 Hz. Furthermore, the spectral transfer noise of the comb was determined in a separate experiment to be less than 2 Hz. The frequency noise occurring in the fibre connecting the comb and spectroscopy laser was measured to contribute approximately 4 Hz. We, therefore, infer that altogether, the linewidth of the spectroscopy laser wave is approximately 10 Hz.

The absolute optical frequency f of the spectroscopy laser is calculated in real time by measuring the repetition rate of the frequency comb and the carrier-envelope offset frequency with two frequency counters and the phase-locked-loop beats with spectrum analysers. The counters and spectrum analysers are referenced to a hydrogen maser (maser 1). A second hydrogen maser (maser 2), nominally identical to maser 1, verifies the stability of maser 1 (Extended Data Fig. 1, right, green trace). The slow frequency drift of the spectroscopy laser frequency of the order of 0.1 Hz min^{-1} (Extended Data Fig. 1, right, red trace for long averaging times) is actively compensated with a digital servo. The frequency instability of the spectroscopy laser frequency (Allan deviation) is less than 2×10^{-14} on all timescales. More precisely, for integration times smaller than 10 s, the instability is similar to the values given by the red curve, namely, $\lesssim 5 \times 10^{-15}$. Because of the drift of the reference cavity of reference laser 1 (to which the comb is locked), on long timescales (>200 s), the spectroscopy laser frequency is steered to the maser 1 frequency via the frequency comb. Extended Data Fig. 1 (right, blue trace) shows that this steering is effective: the blue trace drops below the red trace and does not exceed the green trace. For these long integration times, the Allan deviation of the spectroscopy laser is similar to the values of the green trace that indicate the instability of maser 1. Thus, the laser reaches an instability of 2×10^{-15} for integration times of the order of 1 h. The blue data (laser versus maser) are limited on short timescales (≤10 s) by the instability of maser 1 and the resolution of the frequency counter. The slight increase in the values for integration times of 80 to 200 s is probably due to a sub-optimal performance of the digital servo on this timescale.

The state preparation and destructive spectroscopy sequence underlying the reported measurements are the variation of a previously described procedure[3,4]. Each measurement cycle starts with 35 s of rotational laser cooling[41] to increase the population in the ground state ($v = 0$, $N = 0$). This consequently improves the signal-to-noise ratio. The first secular excitation (application of an RF voltage having a frequency close to the secular frequency $\omega \simeq 2\pi \times 800$ kHz to an electrode close to the trap, for 6 s) produces a signal proportional to the number of HD^+ ions in the trap. Then, the 1.15 μm spectroscopy laser and 266 nm photodissociation laser are applied for a total of 4 s, allowing vibrational excitation with REMPD of HD^+ ions to take place. To avoid a systematic shift induced by the 266 nm photodissociation laser, we employed a sequence of interleaved 1.15 μm and 266 nm irradiations during the REMPD. Since the excited state ($v' = 5$, $N' = 1$) has a lifetime of ~16 ms (ref. 10), we used fast optical shutters. The 1.15 μm and 266 nm laser pulse durations are 10 ms each and there was a delay of 100 μs between the two pulses. This sequence is repeated 190 times.

The sequence is followed by a second secular excitation of the same duration as the first. Then, a 4 s interval follows, during which only the photodissociation laser is applied as the spectroscopy laser is blocked. A third secular excitation is then applied. From the change in fluorescence levels caused by the first two secular excitations, the fractional decrease in the number of HD^+ ions due to laser vibrational excitation is computed, representing the spectroscopy plus background signal, whereas the last two secular excitations yield the background loss of ions. This determination of the background loss immediately after REMPD is different from how the background ion loss was determined in our previous works[3,4]. For each frequency detuning of the spectroscopy laser, the measurement cycle is repeated until adequate statistics is accumulated.

Systematic shifts

We measured several systematic effects (Table 1).

(1) A systematic frequency shift caused by the trap RF electric field is present. It may be due to the a.c. Stark shift and/or the a.c. Zeeman shift[3]. The measurement of the transition frequency for three different RF amplitudes (Fig. 2a(i),(ii)) allowed for an extrapolation to zero amplitude. The extrapolated value is compared with the value at our nominal operational RF amplitude (Table 1).

(2) We measured the transition frequency for three values of magnetic field $B < 1 \times 10^{-4}$ T (Fig. 2b(i),(ii)). Assuming the predicted quadratic-in-B scaling, an extrapolation to $B = 0$ was performed. The zero-field transition frequency offset from the frequency at the nominal magnetic field (3×10^{-5} T) is indicated as the d.c. Zeeman shift.

(3) The laser wave for beryllium-ion laser cooling (30–40 μW at 313 nm) and the spectroscopy wave potentially cause light shifts (a.c. Stark shifts) via the polarizability of the molecular ion. We measured the combined light shifts induced by these two waves by simultaneously increasing the respective laser powers by a factor of two (Fig. 2c(i),(ii)). This measurement determines a combined a.c. Stark effect correction. We find it to be consistent with zero within our resolution. The photodissociation laser (~30 mW at 266 nm) is not applied during the spectroscopy.

(4) An upper bound for the d.c. Stark shift was determined by measuring the transition frequency, once with the nominal trap operating conditions (when the spectroscopy HD^+-ion string is located along the symmetry axis of the Be^+ ion cluster) and again with an additional d.c. voltage of 5 V applied on two trap electrodes[3]. In the latter case, the Be^+ ion cluster is visibly displaced by approximately 100 μm, and leaves the HD^+-ion string undisplaced. The current experimental resolution does not allow to resolve the frequency shift (Fig. 2d(i),(ii)). As the applied displacement is large, we assign a zero correction to the transition frequency and an uncertainty equal to the statistical uncertainty of the line centre determination.

(5) The sensitivity of all the transition frequencies to external fields can be computed ab initio. This includes Zeeman shift[42], electric quadrupole shift[19], black-body radiation shift, spin-state-dependent d.c. Stark shift and light shift[43].
The quadratic Zeeman shift coefficients for the components $m_F = 0 \rightarrow m'_F = 0$ of line 12 and line 21 amount to −0.38 and −0.43 MHz mT^{-2}, respectively. The experimental shifts are consistent with this prediction.
The light shift of the lower and upper vibrational levels due to radiation of any wavelength can be computed from the

hyperfine component i and its frequency $f_{\mathrm{line}\,i}$ is the sum of $f_{\mathrm{spin-avg}}$ and a hyperfine (spin) frequency $f_{\mathrm{spin},i}$, of the order of 10 MHz (see 'Ab initio theory of transition frequency' section). Experimental values of $f_{\mathrm{line}\,i}$ can be corrected by subtracting the ab initio $f_{\mathrm{spin},i}^{(\mathrm{theor})}$ value, at the cost of introducing theory uncertainty. With the most recent improvements in hyperfine structure theory[13] (see 'Ab initio theory of transition frequency' section), the corresponding uncertainties $u\left(f_{\mathrm{spin},i}^{(\mathrm{theor})}\right)$ have been reduced to a level substantially smaller than the QED uncertainty.

BSM force

The effect of a weak BSM force between the proton and deuteron with arbitrary R_{pd} dependence on a spin-averaged transition frequency can be computed by the first-order perturbation theory as $h\Delta f_{\upsilon,N\to\upsilon',N'}(\{\lambda\}) = \langle V_5(\{\lambda\},R_{\mathrm{pd}})\rangle_{\upsilon',N'} - \langle V_5(\{\lambda\},R_{\mathrm{pd}})\rangle_{\upsilon,N}$, where $V_5 \propto \beta_{\mathrm{pd}}$ is the BSM potential and $\{\lambda\}$ are additional parameters of the potential. The individual expectation values of the potential, $\langle V_5\rangle_{\upsilon,N}$, are computed with respect to the nuclear vibrational wavefunction of the rovibrational level (υ, N). Korobov computed the shifts for the commonly considered case of a Yukawa potential as $V_5 = V_{\mathrm{Y}}$, characterized by a range $\{\lambda\} = \Lambda_{\mathrm{pd}}$. The effect of a BSM force on ratios $\mathcal{R}$ is obtained by computing the effect on each individual frequency $f_{\upsilon,N\to\upsilon',N'}$ appearing in the ratio. The sensitivity of various frequency ratios $\mathcal{R}$ and various frequencies f to the strength β_{pd} of the proton–deuteron potential V_{Y} is presented in Extended Data Fig. 2a. The four transition frequencies $f_{\upsilon'}$ are affected in different ways.

Similarly, we can consider weak BSM forces between the electron and proton (ep) or electron and deuteron (ed). Again, we require expectation values such as $V_5(\{\lambda\},R_{\mathrm{ep}})\rangle_{\upsilon,N}$ in case that the BSM force depends only on the electron–proton distance R_{ep}. Their calculation has been done with respect to the full Schrödinger wavefunction of the three-body problem in a given rovibrational level. These wavefunctions have three arguments, namely, distances R_{ep}, R_{ed} and R_{pd}. Extended Data Fig. 2b shows the sensitivities of a Yukawa-type potential $V_{\mathrm{Y}}(\Lambda_{\mathrm{ep}}, R_{\mathrm{ep}}) \propto \beta_{\mathrm{ep}}$ to strength β_{ep}, as a function of the assumed range Λ_{ep}. Because of the equal charge of the proton and deuteron and the small mass of the electron compared with the nuclear masses, the wavefunction is nearly symmetric with respect to R_{ep} and R_{ed} (Born–Oppenheimer approximation), and therefore, the sensitivities to β_{ep} and β_{ed} are nearly equal.

A comparison of Extended Data Fig. 2a,b shows that the sensitivities to electron–nucleus BSM forces are not negligible compared with the case of a proton–deuteron BSM force, for any (same) range Λ_{s}. In fact, they are larger in magnitude for the range $\Lambda_{\mathrm{s}} < 0.3$ Å, whereas in the limit of ranges exceeding the proton–deuteron equilibrium distance $R_{\mathrm{pd,eq}} = 1.06$ Å, the sensitivities of all the transitions to the three types of force (pd, ep and ed) are similar. Here $\mathcal{R}_{5,0}$ is only moderately less sensitive to the electron–nucleus BSM forces than to the proton–deuteron force (Extended Data Fig. 2a,b, black lines).

This implies that an encompassing test for BSM forces should include electron–nucleus BSM forces in the analysis[5,39]. However, HD^+ spectroscopy data alone are, at present, insufficient to allow an analysis that tests for β_{pd}, β_{ep} and β_{ed}, as well as adjusts R_∞, μ/m_{e}, r_{p} and r_{d}. If atomic hydrogen results are included in the analysis to provide inputs for R_∞, r_{p} and r_{d}, then for consistency, the effect of electron–nucleus BSM forces (β_{ep}, β_{ed}) on hydrogen frequencies must be treated[50,51]. Such an endeavour is beyond the scope of this work. Therefore, for simplicity, we shall assume $\beta_{\mathrm{ep}} = \beta_{\mathrm{ed}} = 0$. Bounds to β_{pd} can then be set from the ratios $\mathcal{R}$ or via LSA.

Bounds for β_{pd} can be translated to those for the often considered coupling parameter α_{G} that establishes the BSM potential strength relative to gravity via $\alpha_{\mathrm{G}} = 2(\beta_{\mathrm{pd}} \times 10^{-10}\ \mathrm{m})/(G_{\mathrm{N}} m_{\mathrm{p}} m_{\mathrm{d}})$, where G_{N} is the gravitational constant. For $\Lambda_{\mathrm{pd}} = 1$ Å, the bound from LSA-2 is $|\alpha_{\mathrm{G}}|_{2\sigma} < 8.2 \times 10^{25}$.

Mass ratios from f_5

From our μ/m_{e} in equation (3), we can determine the proton–electron mass ratio by using the value of $m_{\mathrm{d}}/m_{\mathrm{p}}$ determined by the most accurate Penning trap experiment[24] as

$$m_{\mathrm{p}}/m_{\mathrm{e}} = 1,836.152673463(10)_{\mathrm{exp}}(35)_{\mathrm{theor,QED}}(1)_{\mathrm{theor,spin}}(6)_{\mathrm{CODATA2018,Fink-Myers}}, \quad (10)$$

with the total fractional uncertainty $u_{\mathrm{r}} = 2.0 \times 10^{-11}$. This value is consistent with the ratio obtained from the atomic masses of electron[14] and proton[22], that is, 1,836.152673390(81), but is two times more accurate.

Furthermore, using the value m_{d}/u (ref. 23), we obtain the electron mass $m_{\mathrm{e}}/u = 5.48579909030(12) \times 10^{-4}$; it exhibits moderate tension compared with the CODATA 2018 value, the difference being $-3.5(2.0)_{\mathrm{tot}} \times 10^{-14}$.

Data availability

Source data are available for this paper. All other data that support the plots within this paper and other findings of this study are available from the corresponding author upon reasonable request.

Code availability

No custom code or software was used for analysis and presentation of the data associated with this paper.

References

40. Alighanbari, S., Hansen, M. G., Korobov, V. I. & Schiller, S. Rotational spectroscopy of cold and trapped molecular ions in the Lamb–Dicke regime. *Nat. Phys.* **14**, 555 (2018).
41. Schneider, T., Roth, B., Duncker, H., Ernsting, I. & Schiller, S. All-optical preparation of molecular ions in the rovibrational ground state. *Nat. Phys.* **6**, 275–278 (2010).
42. Bakalov, D., Korobov, V. & Schiller, S. Magnetic field effects in the transitions of the HD^+ molecular ion and precision spectroscopy. *J. Phys. B: At. Mol. Opt. Phys.* **44**, 025003 (2011).
43. Schiller, S., Bakalov, D., Bekbaev, A. K. & Korobov, V. I. Static and dynamic polarizability and the Stark and blackbody-radiation frequency shifts of the molecular hydrogen ions H_2^+, HD^+, and D_2^+. *Phys. Rev. A* **89**, 052521 (2014).
44. Karr, J.-P., Hilico, L., Koelemeij, J. C. J. & Korobov, V. I. Hydrogen molecular ions for improved determination of fundamental constants. *Phys. Rev. A* **94**, 050501 (2016).
45. Bakalov, D., Korobov, V. I. & Schiller, S. High-precision calculation of the hyperfine structure of the HD^+ ion. *Phys. Rev. Lett.* **97**, 243001 (2006).
46. Haidar, M. *Hyperfine Structure in the Hydrogen Molecular Ions*. PhD thesis, Univ. Sorbonne (2021).
47. Schiller, S. & Korobov, V. Test of time-dependence of the electron and nuclear masses with ultracold molecules. *Phys. Rev. A* **71**, 032505 (2005).
48. Tiesinga, E., Mohr, P. J., Newell, D. B. & Taylor, B. N. *Values of Fundamental Physical Constants* https://physics.nist.gov/cuu/Constants/index.html (2019).
49. Korobov, V. I. & Zhong, Z.-X.Bethe logarithm for the H_2^+ and HD^+ molecular ions. *Phys. Rev. A* **86**, 044501 (2012).
50. Kloor, H., Fischbach, E., Talmadge, C. & Greene, G. L. Limits on new forces coexisting with electromagnetism. *Phys. Rev. D* **49**, 2098–2113 (1994).
51. Karshenboim, S. G. Precision physics of simple atoms and constraints on a light boson with ultraweak coupling. *Phys. Rev. Lett.* **104**, 220406 (2010).

Acknowledgements

We are indebted to C.-J. Kwong and V. A. Vogt for contributing to the reference laser characterization, to E. Wiens for assistance with the

frequency comb measurements and to M. G. Hansen for the maser characterization. The studies of additional rovibrational transitions were performed with crucial contributions by M. R. Schenkel. We thank V. I. Korobov for providing the BSM force sensitivities and the spin-averaged frequency value, as well as for helpful comments on the paper. We thank him and J.-Ph. Karr for the communication of results on the hyperfine structure before publication. O. Kullie provided some theoretical data. We are indebted to J. Leute and P. Uhrich for their gracious help with the maser stability characterization. We thank G. Morigi for a helpful discussion. We appreciate the important suggestions of the reviewers. This work has received funding from the European Research Council (ERC) under the European Union's Horizon 2020 research and innovation programme (grant agreement no. 786306, 'PREMOL' (S.S.)) and from both Deutsche Forschungsgemeinschaft (DFG) and the state of Nordrhein-Westfalen via grants INST-208/737-1 FUGG (S.S.), INST-208/774-1 FUGG (S.S.) and INST-208/796-1 FUGG (S.S.).

Author contributions

S.A. and I.V.K. contributed equally to this work. S.A., I.V.K. and G.S.G. performed the experiments and analysed the data. I.V.K. developed and characterized the laser system. S.A. maintained the apparatus. S.S. performed the analyses and wrote the paper. All authors contributed to review of the data and paper contents.

Competing interests

The authors declare no competing interests.

Additional information

Extended data is available for this paper at https://doi.org/10.1038/s41567-023-02088-2.

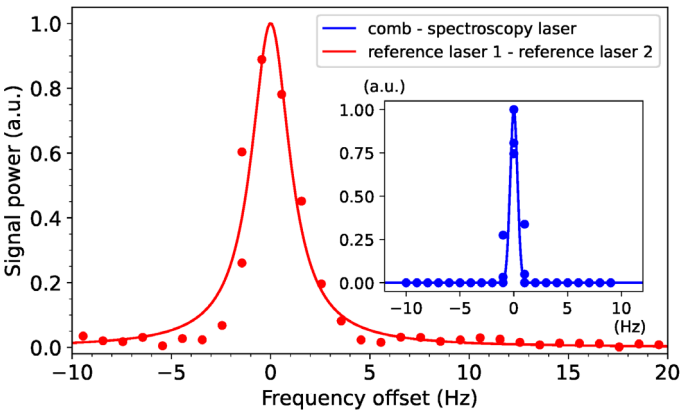
Supplementary information The online version contains supplementary material available at https://doi.org/10.1038/s41567-023-02088-2.

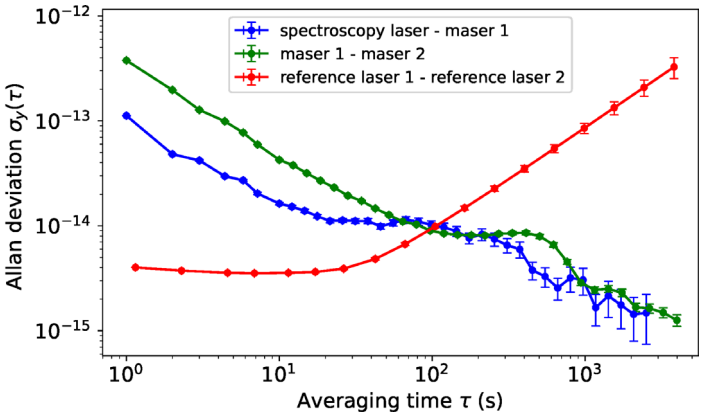
Correspondence and requests for materials should be addressed to S. Schiller.

Peer review information *Nature Physics* thanks Piotr Wcislo and the other, anonymous, reviewer(s) for their contribution to the peer review of this work.

Reprints and permissions information is available at www.nature.com/reprints.

https://doi.org/10.1038/s41567-023-02088-2





Extended Data Fig. 1 | Spectral characteristics of the 1.15 μm spectroscopy laser. Left: (red) spectrum analyzer trace of the heterodyne beat of the reference laser 1 (1.06 μm) and an independent sub-Hz-linewidth, low-drift frequency-stable laser of nearly same optical frequency (reference laser 2, 1.06 μm); (inset, blue) the heterodyne beat between the spectroscopy laser and the spectrally closest mode of the frequency comb, while the spectroscopy laser is phase-locked to the comb and the comb is phase-locked to the reference laser 1. The solid lines are the lorentzian fits to the data points. The frequency offsets are arbitrary. The linewidths of the two beats and additional characterizations indicate that the spectroscopy laser has a linewidth of less than 10 Hz. Resolution bandwidth of the spectrum analyzer: 1 Hz, red trace - single sweep, sweep time 6 s, blue trace - average of 10 sweeps, time span of 1 min. The error bars are smaller than data markers. **Right**: (blue) Allan deviation of the frequency of the spectroscopy laser, measured relative to a hydrogen maser (maser 1) via the frequency comb; (green) Allan deviation of maser 1 relative to a second independent maser (maser 2). The shown values are the Allan deviation of the beat frequency divided by $\sqrt{2}$; (red) Allan deviation of the beat of the reference laser 1 with reference laser 2. The error bars are estimated as 68% confidence intervals.

B.2.2 Rovibrational Spectroscopy of H_2^+

Title:
Laser spectroscopy of a rovibrational transition in the molecular hydrogen ion H_2^+

Authors:
M. Schenkel, S. Alighanbari and S.Schiller

Status / Year: ..... Published / 2024

Journal: ..... Nature Physics

DOI: 10.1038/s41567-023-02320-z

Statement of Copyright:
Springer Nature or its licensor (e.g. a society or other partner) holds exclusive rights to this article under a publishing agreement with the author(s) or other rightsholder(s); author self-archiving of the accepted manuscript version of this article is solely governed by the terms of such publishing agreement and applicable law.

Licence and Statement on reuse for dissertation:

License Number: 5902010926021

Type of Use: ..... Thesis/Dissertation

Grant and Scope of License:
"The Licensor [Springer Nature] grants [Victor A. Vogt] a personal, non-exclusive, non-transferable, non-sublicensable, revocable, world-wide License to reproduce, distribute, communicate to the public, make available, broadcast, electronically transmit or create derivative works using the Licensed Material for the purpose(s) specified in [the] RightsLink Licence Details only [...]".

Full License statement available upon reasonable request

My Contribution:
I provided the light that was used to stabilize the OFC and, which was then used by M. Schenkel to stabilize the spectroscopy laser during the measurements of nine out of twelve lines on HD^+ shown in Fig. 3. This includes the red lines in panels b, c, and d, as well as the green lines in panel a and the purple line in the center of panel a. During the measurement period, I ensured the robust lock and verified its stability by measuring it against a second reference. See Section 8.3.

nature physics

Article

https://doi.org/10.1038/s41567-023-02320-z

Laser spectroscopy of a rovibrational transition in the molecular hydrogen ion H_2^+

Received: 14 June 2023

Accepted: 6 November 2023

Published online: 12 January 2024

Check for updates

M. R. Schenkel, S. Alighanbari & S. Schiller ✉

Comparison of precise predictions of the energy levels of the molecular hydrogen ion H_2^+—the simplest molecule—with measured vibrational transition frequencies would allow a direct determination of the proton-to-electron mass ratio and of the proton's charge radius. Here we report vibrational laser spectroscopy of trapped and sympathetically laser-cooled H_2^+, which represents a step towards this goal. We studied a first-overtone electric-quadrupole transition and measured its two hyperfine components. The determined spin-averaged vibrational transition frequency has a fractional uncertainty of 1.2×10^{-8} and is in agreement with the theoretically predicted value. We measured an analogous electric-quadrupole transition in HD^+ to estimate systematic uncertainties. Here, we observed a vastly improved line quality factor compared to previous electric-quadrupole spectroscopy of molecular ions. Our work demonstrates that first-overtone electric-quadrupole transitions are suitable for precision spectroscopy of molecular ions, including H_2^+, and that determining the proton-to-electron mass ratio with laser spectroscopy could become competitive with mass spectrometry using Penning traps. Furthermore, achieving precision spectroscopy of H_2^+ is an essential prerequisite for a future test of combined charge, parity and time reversal symmetry based on a comparison with its antimatter counterpart.

In recent years, it has been shown that the accurate determination of transition frequencies between rovibrational levels of molecular ions can contribute to current endeavours in fundamental physics. In particular, precision rotational and vibrational spectroscopy of the molecular hydrogen ion (MHI) HD^+ has allowed testing some predictions of quantum electrodynamics theory[1], determining a fundamental constant and searching for physics beyond the standard model[2–5]. For a discussion, see refs. 5–7. The heteronuclear HD^+ system is advantageous from an experimental point of view because it allows for electric-dipole (E1) transitions. Such transitions can be driven by moderate laser power. Also, any vibrational excitation decays on a timescale of tens of milliseconds to the ground vibrational level $v = 0$ by spontaneous emission (v is the vibrational quantum number). After thermalization with black-body radiation, an ensemble of HD^+ contains a sufficiently large fraction of molecules in any of a small set of rovibrational levels ($v = 0$, $N = 0, 1, 2, 3, 4$, where N is the rotational quantum number), a favourable situation. However, HD^+ also has shortcomings. First, it has a complex hyperfine structure (HFS), complicating experimentation and extraction of the spin-averaged (HFS-free) frequency, and second, the key properties of its two dissimilar nuclei, namely the mass and charge radius, cannot be independently deduced from spectroscopic data.

To overcome the latter, intrinsic limitation, there is a need to investigate at least one of the homonuclear MHIs, H_2^+ and D_2^+. Due to the smaller spin of the proton (1/2) compared to the deuteron (1), the HFS of H_2^+ is simpler and this molecule may be preferred. In homonuclear diatomics, E1 transitions between rovibrational levels in the same electronic state are forbidden. As a consequence, the natural lifetimes of excited vibrational levels are extremely long, of the order of 1 week for H_2^+ (ref. 8). Thus, homonuclear MHIs lack a natural vibrational state preparation: they do not readily decay to the vibrational ground state. Conversely, the natural linewidths of transitions between these levels are extremely small. This leads to the exciting perspective of

Institut für Experimentalphysik, Heinrich-Heine-Universität Düsseldorf, Düsseldorf, Germany. ✉e-mail: step.schiller@hhu.de

https://doi.org/10.1038/s41567-023-02320-z

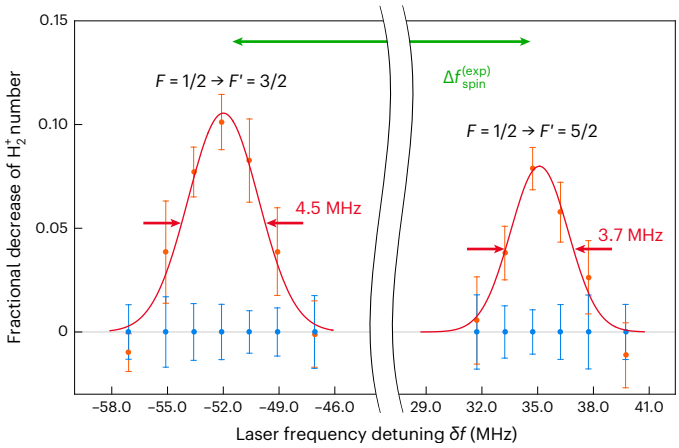


Fig. 2 | The two electron-spin-rotation components of the E2 rovibrational transition ($v = 1, N = 0$) → ($v' = 3, N' = 2$) in H_2^+. The laser frequency detuning δf is relative to the spin-averaged frequency $f_{spin\text{-}avg}^{(theor)} \approx 124$ THz. The red curves are guides for the eye. The horizontal axis is broken. The error bars are estimated standard errors of the means. The frequency errors are not shown because they are at a level of 10 Hz. F and F' are the total angular momentum quantum numbers of the initial and final states, respectively. The green arrow indicates the splitting of the two hyperfine components $\Delta f_{spin}^{(exp)}$. The measured linewidths (full-width at half-maximum) are shown as red arrows and labelled by their respective values.

non-degenerate states in absence of a magnetic field. One, therefore, expects two separate transitions: $\tilde{f}_-$: $(F = 1/2 \rightarrow F' = 3/2)$ and $\tilde{f}_+$: $(F = 1/2 \rightarrow F' = 5/2)$, since both satisfy the selection rules for E2 transitions.

Vibrational transition in H_2^+

To accomplish vibrational spectroscopy of H_2^+ and also obtain competitive accuracy, we trapped ensembles of molecules in a linear ion trap and sympathetically cooled them to millikelvin temperature using co-trapped laser-cooled beryllium ions[33]. An ensemble of H_2^+ was prepared from neutral para-H_2 gas leaked into the vacuum chamber and ionized by electron impact. This resulted in H_2^+ molecules being in a wide distribution of rovibrational levels[34]. Therefore, laser irradiation was applied to deplete the population in the upper spectroscopic level ($v' = 3, N' = 2$) and in rovibrational levels with equal or larger v. A spectroscopy beam with a wavelength of 2.4 μm was aligned to the trap's symmetry axis. Repeated cycles of H_2^+ loading, preparation and spectroscopic excitation followed by dissociation were required to accumulate sufficient data to give spectroscopic lines (Methods and Extended Data Fig. 1). Our spectroscopy protocol gave Doppler-limited resolution. The spectroscopy wave was produced by a continuous-wave optical parametric oscillator (OPO) that provides sufficient power to drive the E2 transition. To permit accurate frequency measurements at 2.4 μm, we developed an optical frequency metrology system (Methods).

Figure 2 shows the measured hyperfine components of the vibrational transition. The full linewidths of ~4 MHz are due to Doppler broadening (see below). The transition frequencies are

$$\tilde{f}_-^{(exp)} = 124,486,979.9(2.3)\,\text{MHz},$$

$$\tilde{f}_+^{(exp)} = 124,487,066.7(1.9)\,\text{MHz}.$$

The lines exhibit low signal-to-noise ratios. We, therefore, assigned the line half-width at half-maxima as the statistical uncertainties of the frequencies.

Study of systematic effects

The systematic shifts of the H_2^+ transition could not be determined because the corresponding studies would have taken a prohibitively long time. The reason is the small fraction of molecules in the lower spectroscopy state obtained in each loading and purification cycle, leading to a low data acquisition rate. This also precluded attempting to search for Doppler-free transitions. To circumvent this difficulty, we instead studied in detail an E2 transition of the related heteronuclear HD^+, for which a sufficient data acquisition rate can be realized. We took advantage of the above-mentioned spontaneous decay of the molecular ion to $v = 0$ levels after ionization of the HD precursor and additionally applied laser rotational cooling[35] to transfer approximately 75% of the ions into the single rovibrational level ($v = 0, N = 0$). We, therefore, chose to study the $(v = 0, N = 0) \rightarrow (v' = 2, N' = 2)$ first-overtone E2 transition at $\lambda_2 = 2.6$ μm using the same OPO system. The quadrupole transition matrix element is a factor 2 smaller than for the studied transition in H_2^+ (Methods). The spectroscopy beam was aligned perpendicular to the trap axis.

As Fig. 3 shows, we observed ultra-narrow, Doppler-free resonances, as we observed for the fundamental transition $v = 0 \rightarrow v' = 1$ (ref. 4) and for the fourth-overtone transition $v = 0 \rightarrow v' = 5$ (ref. 5). Linewidths as low as ~40 Hz, that is line resolutions of 2.7×10^{12}, were achieved. This is a fourfold improvement compared to the best MHI E1 transition result (6×10^{11}; ref. 5) and is comparable to a recent molecular E2 transition measurement of the neutral diatomic Sr_2, which had a line resolution of 2.9×10^{12} (ref. 36). Moreover, it is an improvement by a factor of ~10^6 compared to the only previous study of a molecular-ion E2 transition[22]. The observed linewidths are due to a combination of the natural linewidth (5 Hz; ref. 37), power-broadening, short exposure, as well as the linewidth and frequency instability of the spectroscopy laser.

Table 1 summarizes the characterized shifts. The transition frequencies measured under nominal conditions must be corrected by approximately −1.2 kHz or -1×10^{-11} fractionally. The uncertainty of the corrections is 1×10^{-12} fractionally for one component and twice as large for the other because of its larger linewidth. Light shifts might occur due to off-resonant E1 coupling of the two spectroscopy levels by the intense spectroscopy wave, but we did not observe such an effect and a theoretical estimate gives a shift consistent with the non-observation. The two studied stretched-state Zeeman components have equal and opposite, purely linear Zeeman shifts. Therefore, the $B = 0$ extrapolated frequency of the HFS component is the mean of the two corrected frequencies. It has an uncertainty of 0.12 kHz or 1×10^{-12} fractionally.

Turning to H_2^+, notice that the Zeeman shifts of individual Zeeman components of a rovibrational transition are different from those in HD^+ (ref. 38). In the absence of a direct measurement, we rely on a theoretical prediction[39]. The H_2^+ Zeeman shifts of the various components $|\Delta m_F| \leq 2$ of $\tilde{f}_+$ and $\tilde{f}_-$ are less than $|g_e \mu_B| \approx 28$ kHz μT^{-1} in magnitude (Methods and Extended Data Tables 1–3). During the H_2^+ spectroscopy intervals, we lowered the magnetic field to $|B| \leq 0.2$ μT, so that the shifts were negligible compared to the linewidths. Any light shift due to off-resonant coupling by the spectroscopy wave should be negligible in H_2^+ due to the vanishing E1 transition moments between rovibrational states (Methods).

In view of these considerations, we deduced that in the H_2^+ experiment, systematic shifts were not relevant compared to the measurement resolution of 2 MHz. We estimated that power-broadening is not relevant (Methods), so that we associated the observed linewidths with an H_2^+ ensemble temperature $T \approx 3.4$ mK. In separate experiments on strings of HD^+ ions, we found temperatures of ≈1.5 mK. The higher value observed here could be due to the larger number of trapped H_2^+, resulting in a three-dimensional rather than string-like arrangement and less efficient sympathetic cooling.

Comparison of experimental and theoretical results and the proton-to-electron mass ratio

The spin-rotation coefficient was deduced to be $c_e(v' = 3, N' = 2) = 2(\tilde{f}_+ - \tilde{f}_-)/5 = 34.8(1.2)$ MHz, which is consistent with the most accurate theoretical prediction $c_e^{(theor)}(v' = 3, N' = 2) = 34.73025(12)$ MHz (ref. 32).

https://doi.org/10.1038/s41567-023-02320-z

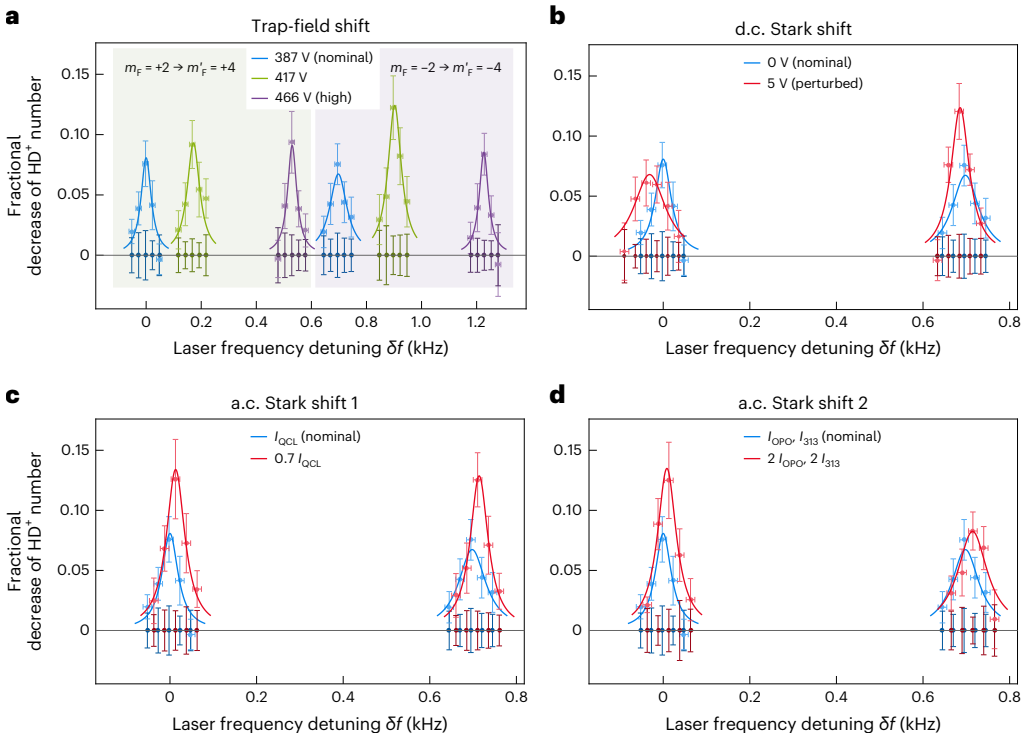


Fig. 3 | Two Zeeman components measured under different operating conditions. The two Zeeman components ($m_F = +2 \rightarrow m'_F = +4$) and ($m_F = -2 \rightarrow m'_F = -4$) of the hyperfine transition ($v = 0, N = 0, G_1 = 1, G_2 = 2, F = 2$) $\rightarrow$ ($v' = 2, N' = 2, G'_1 = 1, G'_2 = 2, F' = 4$) in HD^+, measured for a magnetic field strength of $B = 30$ μT. These are transitions between stretched spin states, that is states of maximum F and $|m_F|$. G_1 is the total spin of the proton–electron pair, and G_2 is the total particle spin, including also the deuteron. **a**, Each Zeeman component measured at trap-field amplitudes of 387, 417 and 466 V. The shaded regions group the same Zeeman component. **b**, Each Zeeman component measured at 0 and 5 V d.c. electric field. **c**, The a.c. Stark shift due to the quantum cascade laser (QCL) used for rotational cooling (Methods, 'HD^+ spectroscopy procedures') is studied by measuring the transitions at full (I_{QCL}) and 70% intensity. **d**, The a.c. Stark shift induced by the spectroscopy source and the cooling laser together, measured at nominal intensities (I_{OPO} and I_{313}, respectively) and doubled intensities. The lines measured under nominal conditions (blue points and blue curves) were measured once and are reproduced in each panel for illustration. The other points and corresponding curves in different colours are the lines measured under various conditions. The laser frequency detuning δf is relative to the optical frequency of the $m_F = +2 \rightarrow m'_F = +4$ component measured under nominal conditions. The coloured curves are guides for the eye. For display purposes, the data are divided into 25-Hz-wide bins and the average value of each bin is shown. The vertical error bars are standard error of the mean in the bin. The horizontal error bars are the frequency uncertainty of the spectroscopy laser stemming from its linewidth (Methods).

Our spin-averaged frequency is $f^{(\mathrm{exp})}_{\mathrm{spin\text{-}avg}} = (3\tilde{f}_+ + 2\tilde{f}_-)/5 = 124,487,032.7(1.5)$ MHz. This is a directly measured vibrational frequency in H_2^+. Remarkably, our value improves on the previous measurements of such a frequency by several orders of magnitude. The most accurate (indirect) measurement was performed by G. Herzberg and his team over half a century ago[40], using Rydberg series spectroscopy of neutral H_2 to obtain the first-overtone vibrational frequency with 7×10^{-5} uncertainty. With a fractional uncertainty of 1.2×10^{-8}, our value $f^{(\mathrm{exp})}_{\mathrm{spin\text{-}avg}}$ is now the most accurately measured property of H_2^+, including the HFS[26,41]. Note that the experimental uncertainty was too large to allow us to identify the presence or absence of a recoil shift (17.1 kHz).

The ab initio value for the frequency is $f^{(\mathrm{theor})}_{\mathrm{spin\text{-}avg}} = 124,487,032.45(6)$ MHz (Methods). The experimental and theoretical values agree.

The ab initio value requires as input the proton-to-electron mass ratio. This was taken from CODATA 2018. Instead, we can treat the mass ratio as an adjustable parameter in order to match the experiment with ab initio prediction, and obtain (Methods)

$$m_p/m_e = 1,836.152665(53).$$

The fractional uncertainty of this spectroscopically determined value (2.9×10^{-8}) is comparable to that which might be obtained from a comparison of experimental and theoretical results for the analogous transition in neutral H_2 (refs. 23,24). Note that the theoretical uncertainty of that transition[25] is twice as large as that quoted in refs. 23,24.

Outlook

A near-term goal of H_2^+ spectroscopy is to achieve a transition frequency uncertainty $u_{\mathrm{goal}} = u_r(f^{(\mathrm{exp})}_{\mathrm{spin\text{-}avg}}) \approx 2 \times 10^{-12}$, four times smaller than today's uncertainty for the quantum electrodynamics calculations (8×10^{-12}; ref. 1). This would lead to a theory-limited mass ratio uncertainty $u_r(m_p/m_e) \approx 1.8 \times 10^{-11}$. The present result obtained for an E2 transition of HD^+ indicates that the goal is realistic, provided that the Zeeman shifts can be controlled sufficiently well. For the present (or analogous) rovibrational transition, we have identified a suitable scheme (Extended Data Table 3). Four Zeeman components whose frequencies have pairwise opposite linear Zeeman shifts and tiny quadratic shifts can be combined to yield the spin-averaged frequency. The goal uncertainty u_{goal} is reached if each Zeeman component is measured with $u_r(f) \leq 4 \times 10^{-12}$ (0.5 kHz) total uncertainty. This requires a magnetic field stability $\delta B \approx 5 \times 10^{-2}$ μT (Methods), which is fulfilled with our apparatus. In the future, to achieve ultrahigh accuracy (10^{-16}-level uncertainty) in an RF trap, it appears more favourable to use a $(v, N = 2) \rightarrow (v', N' = 2)$ transition[42–45].

We briefly turn to the implications of this work for future vibrational spectroscopy of anti-H_2^+, which consists of two antiprotons bound by a positron and has never been observed. The spectroscopy would probe the charge and mass of the antiproton and of the positron as well as the antiproton–antiproton interaction and

Methods

Details of the experiment

H_2^+ spectroscopy procedures. The experimental apparatus is the same we have used in our previous experiments[4,5]. We employ a modified spectroscopy scheme that allows us to perform spectroscopy of H_2^+ without requiring rotational state preparation.

First, the spectroscopy laser frequency is set to a desired value. One cycle (Extended Data Fig. 1) then starts by loading an ensemble of H_2^+ ions by electron impact ionization from a reservoir of para-H_2 admitted into the vacuum chamber by a leak valve. This is followed by depleting the population in levels with $v \geq 2$, including the upper spectroscopy level $(v' = 3, N' = 2)$, by performing photodissociation with two continuous-wave lasers at wavelengths of 313 and 405 nm. Since for both wavelengths the photodissociation cross section decreases strongly with decreasing v (ref. 58), the dissociation of molecules in $v = 1$ is negligible. After a subsequent determination of the number of trapped H_2^+ (see below), the vibrational transition $(v = 1, N = 0) \rightarrow (v' = 3, N' = 2)$ is excited and detected using resonance-enhanced multi-photon dissociation (REMPD), which has two steps: (1) excitation of the spectroscopy transition with the OPO radiation and (2) dissociation of the molecule from the upper spectroscopy level with the 405 nm laser (50 mW and intensity 25 W cm^{-2}). To avoid a light shift induced by the dissociation laser, an interleaved shuttering scheme was employed to prevent the simultaneous exposure of the ions to both lasers. Completing the cycle, the number of still trapped H_2^+ is determined.

In the following cycle, the background is measured (blue data points in Fig. 2). All settings are unchanged except that the OPO beam remains blocked. These alternating spectroscopy and background cycles are repeated many times until satisfactory statistics is accumulated. After completing each cycle, the ion cluster is purged from any ions other than Be^+ and a new H_2^+ ensemble is loaded so that there is a sufficient population in the lower spectroscopy level. During the REMPD intervals of both signal cycles and background cycles, we applied a magnetic field of $B = 0.0(2)$ μT, whereas at all other times the magnetic field was set to $B_{\mathrm{cooling}} \approx 45$ μT. To acquire a spectroscopic line, we set the OPO frequency to a range of values.

The spectroscopy signal was obtained by comparing the number of trapped H_2^+ ions before and after the REMPD. The signal was computed as the normalized decrease of the number of trapped ions $(N_\mathrm{i} - N_\mathrm{f})/(N_\mathrm{i} - N_\mathrm{b})$, where N_i and N_f are the initial and final fluorescence peak strengths of the secular excitation signal of H_2^+, respectively, and N_b is the background level of fluorescence without any secular excitation. To determine the number of trapped H_2^+ ions, the transverse secular motion excitation spectrum was recorded over the range 450–1,250 kHz. The resonance frequency of H_2^+ under nominal conditions was approximately 1,000 kHz. The spectrum was fitted by two Gaussian functions. The peak strength of the H_2^+ signal, which is proportional to the number of trapped H_2^+ ions, was then determined. This approach differs from our previous ones for which we usually resonantly excited the secular motion at fixed frequency and did not record a spectrum. Here, the different approach is necessary because chemical reactions generate H_3^+ ions in the trap, and their presence modifies the Coulomb interactions within the cluster and, thus, also modifies the secular frequency of the H_2^+ ensemble.

HD^+ spectroscopy procedures. HD^+ ions are prepared in a string arrangement. The spectroscopy wave was aligned perpendicular to the string, allowing us to obtain Doppler-free resonances. The $v = 0$ rotational state preparation was implemented by a quantum cascade laser tuned to the $(v = 0, N = 2) \rightarrow (v' = 1, N' = 1)$ transition (5.5 μm). The REMPD scheme comprises three excitations: the spectroscopy transition $(v = 0, N = 0) \rightarrow (v' = 2, N' = 2)$, a subsequent vibrational excitation $(v' = 2, N' = 2) \rightarrow (v'' = 6, N'' = 3)$ (1.56 μm) and finally photodissociation by a 266 nm wave. The second excitation enhances the dissociation rate because the photodissociation cross section of the level $(v' = 2, N' = 2)$ is small at 266 nm.

The spectroscopy cycle sequence is the same as in refs. 4,5, except that the REMPD duration was increased to 30 s. We mention only the main aspects here. The spectroscopy wave was interleaved with the other two waves to avoid systematic shifts. Before and after REMPD the secular motion of HD^+ was resonantly excited to determine their number. Signal and background data were taken during alternating cycles. The cycles differ only in that the spectroscopy wave was kept blocked during the background cycle. On average, five signal and background cycle pairs can be executed before the HD^+ population has declined substantially. Once this has occurred, the Be^+ ion cluster is cleaned. That is, any ions other than beryllium are removed, and a fresh string of HD^+ ions is prepared. The quantum cascade laser was kept on during REMPD.

Spectroscopy laser system. The spectroscopy laser system is a continuous-wave OPO with an output power of >2 W at the H_2^+ and HD^+ transition wavelengths of 2.4 and 2.6 μm, respectively. The OPO wave was frequency-doubled to a second-harmonic wave that is suitable for generating a heterodyne beat with an erbium-fibre frequency comb. The second-harmonic wave was phase-locked to a comb line using this beat and feedback control to the OPO pump laser frequency. This effectively also locked the frequency of the spectroscopy wave to the comb.

To ensure the ultra-narrow linewidth of the spectroscopy radiation, the comb was optically stabilized by phase-locking to a near-infrared laser that is frequency-locked to a high-finesse resonator. Through a second beat with an independently optically stabilized frequency comb, we determined that the fractional frequency instability (Allan deviation) of the OPO spectroscopy wave frequency is below 1×10^{-13} for integration times longer than 1 s. An upper bound for the linewidth of the OPO radiation was obtained from an analysis of the beat. On the 5 s timescale, it was 10 Hz (full-width at half-maximum of a Lorentzian fit). This is also the main contribution to the OPO frequency uncertainty and as such determines the horizontal error bars shown in Fig. 3. Both combs were referenced to an active hydrogen maser, whose properties were characterized (Methods, 'Maser shift').

E2 transitions of H_2^+ and HD^+

E2 in H_2^+. The E2 reduced transition matrix element of the studied first-overtone transition is $Q_0 = Q_{H_2^+}(v = 1, N = 0 \rightarrow v' = 3, N' = 2) = -0.053268$ atomic units[11]. Note that Q_0 is larger by almost a factor of 2 compared to the first overtone starting from $v = 0$: $Q_{H_2^+}(v = 0, N = 0 \rightarrow v' = 2, N' = 2) = -0.028919$ atomic units[11]. However, Q_0 is smaller by a factor of 9 compared to the fundamental vibrational transition starting from the same lower level $(v = 1, N = 0 \rightarrow v' = 2, N' = 2)$. Our spectroscopy source has adequate power to compensate for this difference.

For the upper rovibrational level, the Einstein coefficient for spontaneous emission was computed as $A_{H_2^+}(v' = 3, N' = 2 \rightarrow v = 1, N = 0) \approx 7.8 \times 10^{-8}$ s^{-1} (refs. 11,59).

E2 in HD^+. E2 transitions in this heteronuclear molecule have been discussed in refs. 45,60. The E2 reduced transition matrix element is $Q_{HD^+}(v = 0, N = 0 \rightarrow v' = 2, N' = 2) = 0.025976$ atomic units. The reduced electric-dipole (E1) transition matrix elements for near-by transitions are 0.00436 for the $(v = 0, N = 0) \rightarrow (2, 1)$ transition and −0.00609 for the $(v = 0, N = 1) \rightarrow (2, 2)$ transition, in atomic units[61]. Thus, the Rabi frequencies for these E1 transitions are approximately one order larger than for the studied E2 transition of HD^+.

Power-broadening. The Rabi frequency for an E2 transition in H_2^+ can be estimated using equation (15) of ref. 11. Using the E2 transition matrix element Q_0 and considering the peak intensity of the spectroscopy wave (3.6 MW m^{-2}), we estimated an upper limit for the Rabi frequency to be $\Omega/(2\pi) \approx 0.5$ kHz. Therefore, power-broadening is negligible compared to the observed linewidth.

fine-structure constant α. Considering the present experimental accuracy, only the major contributions need to be included:

$$\begin{aligned} f_{\text{spin-avg}} &= 124,485,554.55\,\text{MHz} \quad (\text{nonrelativistic}) \\ &+ 2,002.70\,\text{MHz} \quad (\alpha^2\ \text{order}) \\ &- 521.35\,\text{MHz} \quad (\alpha^3\ \text{order}) \\ &- 3.69\,\text{MHz} \quad (\alpha^4\ \text{order}) \\ &+ 0.24(6)\,\text{MHz} \quad (\alpha^5\ \text{order}) \\ &= 124,487,032.45(6)\,\text{MHz}. \quad (\text{total}) \end{aligned}$$

The orders are relative to the non-relativistic contribution. The α^5 contribution is a simple estimate based on ref. 67. Once the need arises, this contribution can be computed accurately and so can contributions of higher order. The sensitivity of the spin-averaged frequency to m_p/m_e is computed by solving the non-relativistic Schrödinger equation for two different values of m_p/m_e. We find $\partial f_{\text{spin-avg}}/\partial(m_p/m_e) = -0.43976 \times f_{\text{spin-avg}}/(m_p/m_e)$.

Data availability

Source data are provided with this paper. All other data that support the plots within this paper and other findings of this study are available from the corresponding author upon reasonable request.

Code availability

No custom code or software was used for analysing or presenting the data associated with this paper.

References

58. Dunn, G. H. Photodissociation of H_2^+ and D_2^+: Theory. *Phys. Rev.* **172**, 1-7 (1968).
59. Olivares Pilón, H. & Baye, D. Quadrupole transitions in the bound rotational-vibrational spectrum of the hydrogen molecular ion. *J. Phys. B: At. Mol. Opt. Phys.* **45**, 065101 (2012).
60. Bekbaev, A. K., Aznabayev, D. T. & Korobov, I. V. Quadrupole transitions of the hydrogen molecular ion HD^+. In *Proc. International Conference on Precision Physics and Fundamental Physical Constants* Vol. 9 (eds Horváth, D., Karshenboim, S. & Siklér, F.) 058 (2019).
61. Bakalov, D. & Schiller, S. Static Stark effect in the molecular ion HD^+. *Hyperfine Interact.* **210**, 25–31 (2012).
62. Shen, J., Borodin, A. & Schiller, S. A simple method for characterization of the magnetic field in an ion trap using Be^+ ions. *Eur. Phys. J. D* **68**, 359 (2014).
63. Collopy, A. L., Schmidt, J., Leibfried, D., Leibrandt, D. R. & Chou, C.-W. Effects of an oscillating electric field on and dipole moment measurement of a single molecular ion. *Phys. Rev. Lett.* **130**, 223201 (2023).
64. Hegstrom, R. A. *g* factors and related magnetic properties of molecules. Formulation of theory and calculations for H_2^+, HD^+, and D_2^+. *Phys. Rev. A* **19**, 17–30 (1979).
65. Karr, J.-P. Leading-order relativistic corrections to the *g* factor of H_2^+. *Phys. Rev. A* **104**, 032822 (2021).
66. Schiller, S., Bakalov, D., Bekbaev, A. K. & Korobov, V. I. Static and dynamic polarizability and the Stark and blackbody-radiation frequency shifts of the molecular hydrogen ions H_2^+, HD^+, and H_2^+. *Phys. Rev. A* **89**, 052521 (2014).
67. Korobov, V. I., Hilico, L. & Karr, J.-P. Fundamental transitions and ionization energies of the hydrogen molecular ions with few ppt uncertainty. *Phys. Rev. Lett.* **118**, 233001 (2017).

Acknowledgements

We are indebted to V. I. Korobov for putting at our disposal his codes for the computation of the H_2^+ properties and for many important communications on the properties of MHI. We are grateful to S. Schlemmer (Universität zu Köln) for generously providing para-H_2 gas. G. S. Giri contributed to early tests of the spectroscopy. The assistance of U. Rosowski in the maintenance of the H maser and data analysis has been important. C. Wellers and V. Vogt contributed in obtaining and characterizing the OPO. M. G. Hansen and I. V. Kortunov are acknowledged for their help on setting up the locking and metrology scheme of the OPO. We also thank E. Wiens for support in the optical frequency measurements. We thank S. Sturm, F. Heiße, C. König and S. Ulmer for discussions about the CPT tests. This work has received funding from the European Research Council under the European Union's Horizon 2020 research and innovation programme (Grant Agreement No. 786306, PREMOL (S.S.)) and from both the German Research Foundation and the state of North-Rhine-Westphalia (Grant Nos. INST-208/774-1 FUGG (S.S.) and INST-208/796-1 FUGG (S.S.)).

Author contributions

M.R.S. and S.A. performed the experiments and analysed the data. M.R.S. developed and characterized the spectroscopy laser system. S.A. maintained the apparatus. S.S. conceived the experiment, supervised the project and performed analyses. All authors contributed to writing the manuscript and reviewing the data.

Competing interests

The authors declare no competing interests.

Additional information

Extended data is available for this paper at https://doi.org/10.1038/s41567-023-02320-z.

Supplementary information The online version contains supplementary material available at https://doi.org/10.1038/s41567-023-02320-z.

Correspondence and requests for materials should be addressed to S. Schiller.

Peer review information *Nature Physics* thanks Shui-Ming Hu, Krzysztof Pachucki and Xin Tong for their contribution to the peer review of this work.

Reprints and permissions information is available at www.nature.com/reprints.

B.3 Optical References and Frequency Metrology

B.3.1 Ultra-Stable Optical Parametric Oscillator

Title:
Metrology-grade spectroscopy source based on an optical parametric oscillator

Authors:
M. Schenkel, **V. Vogt** and S.Schiller

Status / Year: ..... Published / 2024

Journal: ..... Optics Express

DOI: 10.1364/OE.538442

Licence: ..... Creative Commons Attribution 4.0 International license.

Statement of Copyright:
"Published by Optica Publishing Group under the terms of the Creative Commons Attribution 4.0 License. Further distribution of this work must maintain attribution to the author(s) and the published article's title, journal citation, and DOI."

Reuse policy for dissertation:
CC BY License: "Our policies afford authors, their employers, and third parties the right to reuse the [...] final publisher Version of Record (VoR) of the article [...]." "Reuse purpose: Reproduction by authors in a compilation, in their thesis/dissertation or for teaching purposes short term (attribution must be included)."

My Contribution:
I was responsible for setting up and operating one of the two OFC systems, including its ultra-stable reference laser (L2). Additionally, I provided the ultra-stable reference laser (L1) of the second OFC, which stabilized the OPO. I made a significant contribution to the data collection and analysis of the OPO's performance in terms of linewidth, Allan deviation, and frequency noise density. See Section 4.3.

Research Article | Vol. 32, No. 24 / 18 Nov 2024 / Optics Express 43350
Optics EXPRESS

Metrology-grade spectroscopy source based on an optical parametric oscillator

M. R. SCHENKEL,[1,2] V. A. VOGT,[1] AND S. SCHILLER[1,3]

[1] Heinrich-Heine-Universität Düsseldorf, Mathematisch-Naturwissenschaftliche Fakultät, Institut für Experimentalphysik, 40225 Düsseldorf, Germany
[2] magnus.schenkel@hhu.de
[3] step.schiller@hhu.de

Abstract: Continuous-wave optical parametric oscillators (OPOs) are widely tunable and powerful sources of narrow-linewidth radiation. These properties make them suitable for a wide range of spectroscopic studies - but so far not at the metrological level. Indeed, although important technical OPO developments occurred more than two decades ago, and commercial devices have been available for nearly as long, the long-hoped-for the potential of these devices, providing simultaneously ultralow linewidth, ultrahigh frequency stability, ultrahigh frequency accuracy, and wide wavelength coverage has not yet become a reality. Here, we present an OPO metrology system suitable for optical spectroscopy with ultra-high resolution and accuracy in the 2.2 - 3.9 μm range. The system relies on the second-harmonic generation of the idler wave to bridge the gap to the near-infrared regime where frequency combs are readily available. By actively controlling the pump laser frequency, the idler radiation is phase-locked to an optically stabilized frequency comb, enabling a full transfer of the frequency comb's spectral properties to the idler radiation and measuring the idler frequency with ultra-high precision. We reach fractional line widths and Allan deviations of the idler radiation at the level of 4×10^{-14} and 1×10^{-14}, respectively. We also perform a thorough characterization of the stabilized OPO via a comparison with a second, independent optically stabilized frequency comb and thereby determine an overall idler frequency systematic uncertainty of less than 1.2×10^{-14}. Sources of residual frequency noise are identified. The system delivered excellent results in high-accuracy spectroscopy.

Published by Optica Publishing Group under the terms of the Creative Commons Attribution 4.0 License. Further distribution of this work must maintain attribution to the author(s) and the published article's title, journal citation, and DOI.

1. Introduction

High-resolution laser spectroscopy of atoms and molecules is a key branch of physics and physical chemistry. The spectroscopic study of many species can be performed with semiconductor lasers emitting in the near-infrared (NIR) spectral range and even in the visible range. But these sources do not satisfy all needs. An important area of laser spectroscopy is rovibrational spectroscopy, where one often wishes to measure a large set of transitions of a given molecular species, or of several different species, hence requiring a wide tuning range. The mid-infrared (MIR) range provides the most important window on rovibrational spectra. In this range, continuous-wave (cw) optical parametric oscillators (OPOs) are a unique type of spectroscopy source; their output can cover more than an octave in frequency, and the output power can be 1 W or higher. The combination of these properties sets them apart from other important MIR sources, such as DFB and quantum cascade lasers or difference-frequency generation.

Key developments in the design and performance of cw OPO devices and spectroscopy demonstrations, occurred more than two decades ago, with the first demonstrations of mode-hop-free oscillation [1–8]. Soon, the first commercial OPO devices became available. Since then, many groups have successfully used cw OPOs for diverse applications in molecular spectroscopy

#538442 https://doi.org/10.1364/OE.538442
Journal © 2024 Received 2 Aug 2024; revised 13 Sep 2024; accepted 15 Sep 2024; published 13 Nov 2024

Optics EXPRESS

[9–21], and in some instances atomic spectroscopy [22]. Only in the past decade has there been a greater need to achieve ultra-high resolution and corresponding frequency accuracy with OPOs. Metrology-grade OPOs would be useful, for example, in fundamental physics to probe the hyperfine transition of highly charged ions [23], the rovibrational transitions of simple (few-electron) molecules (such as the molecular hydrogen ions [24,25], the neutral hydrogen molecules [26–31], and the helium hydride ions ([32,33] and references therein)), or to search for a time-drift of molecular vibrational frequencies [34–37].

The wide tuning range of cw OPOs immediately raises the question of how to precisely determine the actual emission frequency. With the invention of the optical frequency comb (OFC) [38,39], a new tool emerged for measuring optical frequencies with an accuracy improved by many orders of magnitude compared to previous means. Already early studies explored how to combine an OPO with an OFC in order to enable OPO output frequency determination. Importantly, an OFC also offers the possibility to serve as a reference for stabilizing the OPO frequency by feedback control [40]. The latter option is superior to locking the frequency to molecular absorption lines because they do not offer a continuous wavelength coverage. An additional benefit would be a link of the visible and NIR regimes with the MIR regime [41]. These early demonstrations have been followed by further studies, and Table 1 presents a selection of those performed over the past decade and aimed at metrology. It is evident that it has not yet been possible to imbue an OPO with the four key properties of a metrology-grade spectroscopy source: ultralow linewidth, ultrahigh frequency stability, ultrahigh frequency accuracy, and wide wavelength coverage. The contrast with what has been achieved with diode lasers is striking: the first three properties are achieved in many metrological studies (mostly for atomic spectroscopy, e.g. for optical atomic clocks [42,43]). Clearly, there appears to be an unrealized potential for OPOs, i.e. the opportunity for developing methods capable of pushing both the linewidth and the long-term frequency instability down to the Hertz level.

Table 1. Comparison of some features of the present source in comparison to selected published works of other groups. The acronyms are defined in the text. τ is the integration time.

Ref.	Technique	Idler range (μm)	Frequency stability of idler radiation		Idler output power
			Short-term (linewidth)	Long-term (Allan deviation or other)	
Ricciardi et al. [14]	Frequency lock of pump and signal to NIR OFC	[2.7, 4.2]	$\leq$ 200 kHz at 100 ms	$\sigma_y \leq 3 \times 10^{-12}/\sqrt{\tau}$ for $\tau \in [1, 200]$ s	>1 W
Peltola et al. [44]	Frequency lock of idler's SH to NIR OFC	[2.7, 3.4]	$\simeq$ 1 MHz	$\sigma_y \in [10, 200]$ kHz for τ<10 s	>0.5 W
Ricciardi et al. [45]	Direct cavity stabilization	[2.7, 4.2]	920 Hz at 100 ms	not stated	$\simeq$ 0.5 W
Karhu et al. [46]	OPO locked to a MIR OFC	[2.5, 4.4]	0.5 MHz at 0.15 s, 1.5 MHz at 1 s	Standard deviation of 90 kHz over 20 min	up to 0.8 W
Zhang et al. [20]	Pump locked to NIR OFC, OPO cavity locked to ULE resonator	[2.6, 4.3]	<20 kHz at 1 – 5 s	σ_y<1 kHz for τ>1 s	$\simeq$ 0.4 W
This work	PLL of idler's SH to NIR OFC	[2.2, 3.9]	$\leq$ 5 Hz at 1 – 10^3 s	$\sigma_y \leq$ 3 Hz for τ>1 s	>1 W

Optics EXPRESS

Here we present a general and effective method of OPO frequency stabilization that is fairly independent of the desired output wavelength. By locking the OPO's idler frequency to an OFC, we simultaneously achieve all four of the key properties above, improving these parameters by a combined factor of more than 10^4. We thereby demonstrate a MIR spectroscopy source with a fractional frequency instability $\leq 1 \times 10^{-14}$ on timescales between 1 and 10^5 s, an idler linewidth on the order of a few Hertz, and an SI-traceable frequency. Our frequency stabilization scheme can be operated at different idler wavelengths. This demonstrates that the method is wavelength-independent.

1.1. Frequency stabilization approaches

Since the frequency conversion process in an OPO must satisfy energy conservation at the photon level, the frequencies ω_p, ω_s and ω_i of pump, signal and idler waves, respectively, are related by

$$\omega_p = \omega_s + \omega_i \,. \tag{1}$$

If the idler wave is the main interest for a spectroscopic application, two different approaches to stabilize its frequency ω_i may be distinguished.

Consider first the approach where both ω_p and ω_s are actively stabilized, so that according to Eq. (1) the idler frequency is also stabilized. To do so, both the pump and the signal wave frequencies must be stabilized separately. Both these frequencies usually fall into the NIR range (e.g. $\lambda_p = 1.06\,\mu$m and $\lambda_s \in [1.45\,\mu\text{m}, 2.07\,\mu\text{m}]$ in this work), where narrow-linewidth and ultra-stable optical frequency combs (OFCs) can be realized with relative routine. These two properties can be achieved by phase-locking the OFC to a reference laser, which is itself frequency-locked to an ultra-stable reference cavity.

The frequency of the pump wave can be stabilized to such a comb. It is more difficult to do so for the signal wave because its frequency is determined by the resonance of the OPO cavity. One needs the ability to control the optical path length of the cavity with high bandwidth. This is challenging in view of the typical design of the OPO cavity and the cavity length actuator. The task could be eased by employing either an OPO cavity that exhibits good passive stability or an intra-cavity electro-optic modulator for fast path-length control [20]. However, both options come with technical challenges.

For the most advanced applications, not only the provision of a narrow-linewidth spectroscopy wave (idler), but also the determination of its absolute frequency ω_i is required. Therefore, a second approach to idler frequency stabilization appears better suited: *measure* the idler frequency and act *only* on the pump frequency to control the idler frequency (see Fig. 1(a)). This control works by exploiting the 1:1 transfer coefficient from pump frequency change to idler frequency change when the signal frequency is not acted upon, Eq. (1). The frequency of the signal wave is at all times determined by the optical length of the OPO cavity, following its variations due to perturbations. This is a source of frequency noise that needs to be compensated. The pump frequency will be regulated so as to keep the idler frequency precisely fixed at a desired value, compensating for both the OPO cavity length fluctuations as well as the pump laser's own fluctuations. Note that with this approach, neither the pump frequency nor the signal frequency will exhibit a particularly low frequency instability.

An example of this approach is the work of Peltola *et al*. [44]. They used second-harmonic generation (SHG) to bridge the gap between the idler frequency and the NIR, where the frequency of the second-harmonic (SH) wave $2\,\omega_i$ can be compared to mode of an OFC. In that work, the OFC was stabilized by locking the repetition rate to a hydrogen maser (H-maser) and the frequency $2\,\omega_i$ was determined using a frequency measurement of its beat with the OFC. A servo system acting on the pump frequency allowed obtaining a long-term stable idler wave frequency with Allan deviations at the sub-MHz level, but no reduction of its linewidth. The achieved frequency stability is summarized in Table 1.

Optics EXPRESS

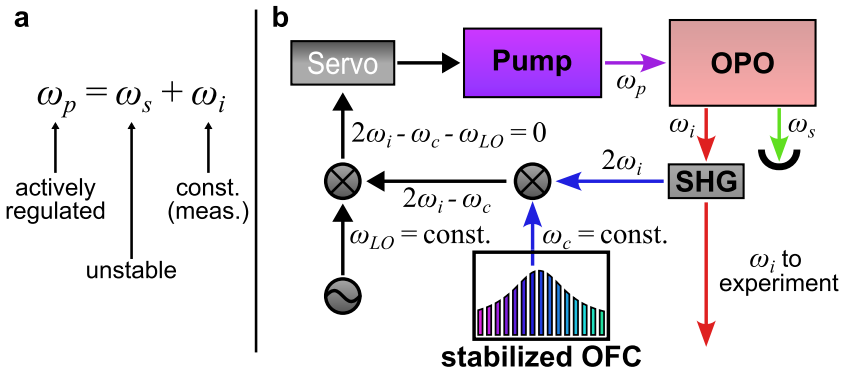


Fig. 1. Concept of the setup. a: The equation summarizes the concept. ω_p is regulated in order to keep the measured ω_i constant in time, while ω_s is left unstabilized and is affected by perturbations. **b:** An optically phase-locked OPO is implemented. The OPO is pumped at a frequency ω_p to generate the signal (ω_s) and idler (ω_i) frequencies. ω_i is then frequency-doubled in an SHG stage and mixed with an optically stabilized OFC, possessing a mode at frequency $\omega_c \approx 2\omega_i$. The generated beat is mixed with a local oscillator (LO) having a radio-frequency ω_{LO} in order to generate an error signal. It is the input to the servo that controls the pump frequency. Colored and black arrows are used for optical and analog signals, respectively. More details follow in Fig. 2.

In this work, we expand on this method, by implementing an ultrastable OFC and a phase-locked loop (PLL) of the idler frequency to this OFC, allowing to achieve not only long-term frequency stability but also excellent linewidth narrowing. The principle is shown in Fig. 1(b).

2. Experimental setup

Our apparatus consists of three main units, shown in Fig. 2. Unit 1 (top) comprises the OPO as well as the optical and electronic components of the locking subsystem. Unit 2 (center left) contains a first OFC (OFC1) and its reference laser (L1). These are used for the stabilization of the OPO's frequency. Unit 3 (bottom) serves to characterize the OPO in the locked state, and therefore includes a second OFC (OFC2) with its own reference laser (L2). Unit 4 (center right) provides the H-maser as a reference clock in the radio-frequency (RF) domain. It delivers ultrastable RF signals to the other three units and is also required for the optical frequency measurement. The H-maser is continuously compared to the national time standard PTB (Physikalisch-Technische Bundesanstalt, Braunschweig) via a common-view Global Navigation Satellite System (GNSS) technique. This ensures SI-traceability of the absolute frequencies. All units are computer-controlled and connected via a network. We now describe the units in more detail.

Unit 1 contains the actual OPO with its pump laser, a SHG stage to convert the idler radiation, a wavelength meter (High Finesse WS-7 IR Super Precision), locking and monitoring electronics. The OPO is a commercial system (TOPTICA DLC TOPO, [47]), that generates >1 W of output power over the idler wavelength range of 2.2 – 3.9 μm. The corresponding signal range is 1.45 – 2.07 μm. The system consists of the OPO laser head and a ytterbium-doped fiber amplifier (Yb-FA) with up to 10 W output power. To seed the amplifier, we employ a separate commercial semiconductor laser (1.06 μm, TOPTICA CTL 1050) to benefit from its narrower free-running linewidth (<10 kHz at 5 μs according to the manufacturer). When unstabilized, the linewidth of the OPO's idler was previously determined to be 1 – 2 MHz on a 25 ms timescale [47]. On similar timescales, but with the above seed laser, we observe a linewidth of ≃ 100 kHz, which

Optics EXPRESS

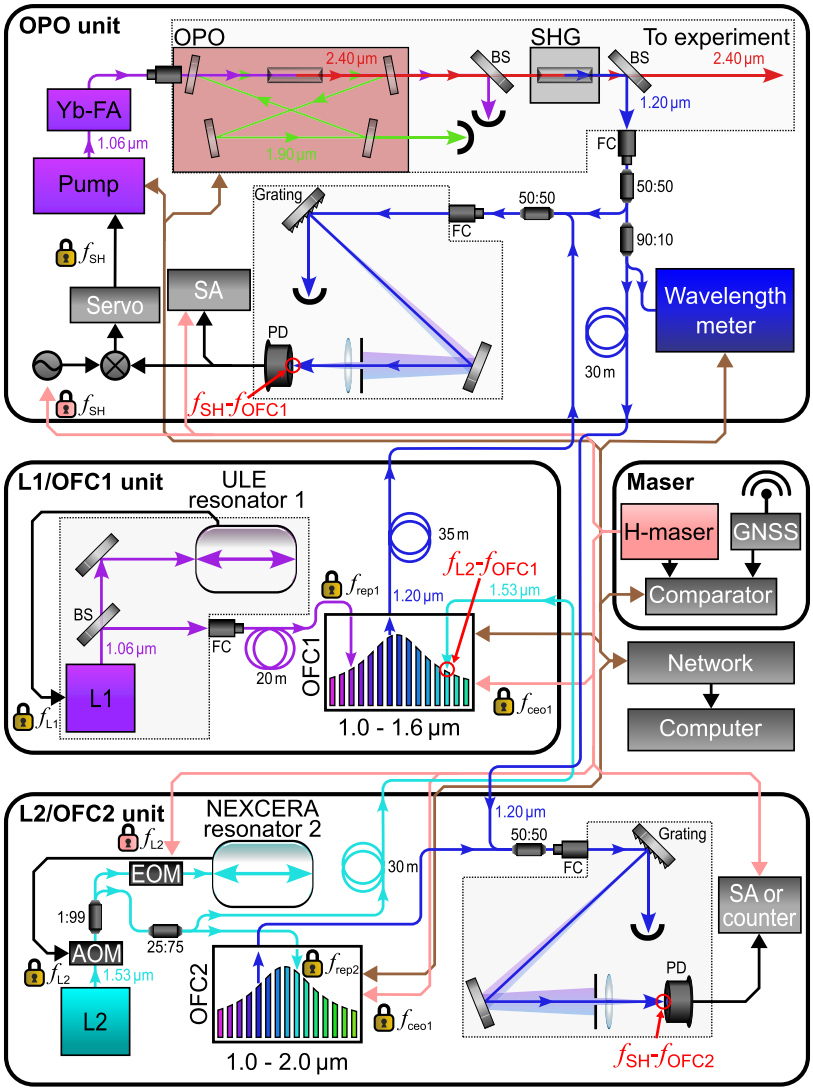


Fig. 2. Schematic of the setup. The individual black-framed boxes designate different units. **Top**: The OPO unit contains the OPO including pump and amplifier, the idler SHG unit and the wavelength meter, as well as the locking and monitoring electronics. **Center left**: The L1/OFC1 unit with the main reference laser L1, used to stabilize f_{rep1} of OFC1. A pick-off from OFC1 (shown here as an example centered at 1.2 μm) is sent to the OPO unit for idler frequency stabilization. **Bottom**: The L2/OFC2 unit, with L2 as the reference laser for f_{rep2} of OFC2. **Center right**: A hydrogen maser (H-maser) serves as the reference for all relevant RF sources. Individual wavelengths are shown in the figure by mapping the visible color spectrum to the wavelength range of the setup ([1.0 μm, 2.4 μm] $\rightarrow$ [purple, red]). Performance and measurements are monitored by computer control, connected to the individual components via network. Optical fibers are labeled for lengths >5 m. The H-maser analog signal, network connections, and other analog signals are shown in pink, brown, and black, respectively. Free-space parts of the setup are indicated as dashed-frame boxes. The padlocks symbolize active stabilization of the indicated frequency by a servo system (not shown). The padlock color gold denotes either a PLL lock or a PDH lock, while pink refers to a servo that implements a low-bandwidth frequency stabilization to the H-maser frequency. More details in the text. BS: beam splitter. FC: fiber coupler. AOM: acousto-optic modulator. EOM: electro-optic modulator. SA: spectrum analyzer.

Optics EXPRESS

increases to 3 – 5 MHz on timescales of a few seconds, due to jitter. Typical frequency variations are 200 MHz over several hours, with drift rates on the order of 0.6 MHz/min.

The seed laser can be frequency-modulated with a high bandwidth (several ten MHz) via its current, which is crucial for realizing our locking scheme where the pump laser current is the actuator. Before being sent to the experiment, the full power of the OPO's idler wave is sent through a single-pass SHG setup containing a periodically poled lithium niobate crystal. In order to be able to generate the harmonic wave of the whole idler spectral range, we employ a crystal containing multiple grating periods, with periods between 33.3 μm and 36.0 μm, and operating temperature in the range 20 – 200 °C. This combination of parameters allows us to find a suitable phase-matching condition for any wavelength in the idler's wavelength range. Owing to the high power of the idler radiation, a few milliwatts of the second-harmonic wave are generated in the single-pass configuration. This power is sufficiently high that the wave can be split into one part for generating a high-signal-to-noise-ratio beat with OFC1 and a second part for the wavelength meter, whose measurements are necessary for absolute frequency determination. To produce the beat, a fraction of the OFC1 output, spectrally centered around the idler's second-harmonic wavelength, is sent to the OPO unit via a 35 m long optical fiber, and there overlapped with the second-harmonic wave within the fiber, using a fiber combiner. The combined radiation is coupled out of the fiber, reflected off a grating, and directed onto the photodetector (PD). The signal-to-noise ratio of the beat generated in the PD is optimized by proper alignment of the grating. This beat signal is phase-locked to a RF signal of stable frequency (local oscillator, LO). To this end, the beat signal is mixed with the local oscillator (LO), and the low-frequency output of the mixer is the input to an appropriate servo that controls the pump laser's current, closing the loop. Overall, the idler frequency is phase-locked to a mode of the OFC.

Unit 2 contains the reference laser L1 (1.06 μm, Mephisto Innolight Nd:YAG) and OFC1 (Menlo Systems FC1500-250-ULN). Its repetition rate $f_{\mathrm{rep},1}$ is stabilized by phase-locking one comb mode to L1, while the carrier envelope offset frequency $f_{\mathrm{ceo},1}$ is stabilized to the H-maser. L1 itself is stabilized to a ULE resonator with a finesse of $\simeq$ 500 000 (resonator 1) using the Pound-Drever-Hall (PDH) technique, with the modulation applied to the laser's frequency actuator, a piezo-electric transducer.

Finally, in the lower part of Fig. 2, unit 3 contains the second OFC (OFC2) and a separate reference laser L2 at a wavelength of 1.53 μm (NKT Koheras Basik E15). Similar to above, the comb's repetition rate $f_{\mathrm{rep},2}$ is phase-locked to L2, while $f_{\mathrm{ceo},2}$ is stabilized to the H-maser. Except for the shared H-maser that provides f_{ceo} stabilization, the two combs are completely independent systems. L2 is also locked via the PDH technique to the resonator 2, a NEXCERA resonator [48] with a finesse of 700 000. NEXCERA is a novel spacer material for resonators [49], designed to be operated at room temperature. In contrast to L1, an acousto-optic modulator (AOM) is required for providing fast control of the frequency of the L2 output wave, since the laser itself does not have a high bandwidth modulation input. A sideband lock is implemented [50,51], where the laser wave is phase-modulated using an electro-optic modulator (EOM), and one of the modulation sidebands is locked to the resonator instead of the carrier. The sideband lock is used in order to be able to compensate the drift of the resonator. A detailed explanation is given in section 3.3. To characterize the performance of the two reference lasers, a portion of the radiation of L2 is sent to OFC1 and then measured against it.

3. Performance

In order to characterize the spectral properties of the OPO's idler radiation, beats between several sources were produced. In Fig. 2 these beats are indicated by red circles together with their corresponding optical frequency differences. First, a beat between OFC1 and L2, $f_{\mathrm{L2}} - f_{\mathrm{OFC1}}$, gives the combined instability level of the employed reference lasers L1, L2. Additionally, it

Optics EXPRESS

includes the locking performance of the PLL of OFC1 to L1 and any fiber noise originating from the 30 m long fiber used to send L2 radiation to OFC1.

In a second step, the PLL of the OPO is examined by monitoring the beat $f_{SH} - f_{OFC1}$ in the locked state. Finally, the absolute stability of the OPO's idler frequency is investigated, by measuring a beat between its SH wave and OFC2, $f_{SH} - f_{OFC2}$. This simultaneously gives the most accurate upper limit of the frequency instability for the system as a whole, including all fiber noise and other noises. The analysis for short timescales is presented in Section 3.1, and the analysis for long timescales follows in section 3.3. These analyses were performed with the OPO set to an idler wavelength of 2.81 μm, corresponding to a signal wavelength of 1.71 μm and an idler second-harmonic wavelength of 1.40 μm. In Sec. 3.5 we argue that the described performance can be achieved at all wavelengths within the output range of the OPO.

3.1. Short-term performance of the idler radiation

The beat $f_{L2} - f_{OFC1}$ shown in Fig. 3, panel 1a, is an average of many consecutive sweeps of the spectrum analyzer, each of duration 5 s and measured at a resolution bandwidth (RBW) of 1 Hz. Note that the individual traces could be averaged without any consideration of either resonator's drift, since the center frequency drifted by less than 1 Hz over the course of the entire data acquisition. This has two different reasons: in the case of resonator 1 the drift is negligible on the timescale of the measurement, and in the case of resonator 2 it is actively compensated, see sec. 3.3. From the beat we deduce a full-width half-maximum (FWHM) linewidth of 9 Hz. In the phase-noise spectrum of $f_{L2} - f_{OFC1}$, Fig. 3, panel 1b, small sidebands at frequencies of 50 Hz and 510 Hz can be observed. We believe that the origin is fiber noise occurring in both fibers that deliver the radiation from L1 and L2 to OFC1. Due to the modest strength of the sidebands, they are not significant for the current analysis and also have not impacted a recent spectroscopic study [25].

Data on the OPO's phase-locked loop performance, i.e. the frequency and phase noise of the beat $f_{SH} - f_{OFC1}$, is displayed in Fig. 3, center column. This data on the beat does not yet yield any information on the absolute stability of the idler frequency, but rather on how well it follows OFC1. The measured linewidth, 3 Hz FWHM, is caused by the RBW of the employed spectrum analyzer - as is expected for a properly working phase lock. From the phase-noise spectrum, panel 2b, we determine a signal-to-noise ratio of 70 dB in a RBW of 1 Hz. Additionally, a single significant sideband is observed, at a frequency of 810 Hz. The source for this is intrinsic to the setup: it is caused by acoustic noise originating from the Yb-FA, as was confirmed by a comparing the acoustic noise spectrum in the proximity of the OPO with the Yb-FA turned on and off.

Next, we consider the beat $f_{SH} - f_{OFC2}$. Its analysis is shown in Fig. 3, right column. Similar to panel 1a, panel 3a shows consecutive beat spectra measured over a total time of more than 30 min, averaged without any re-centering of individual traces. A Lorentzian fit finds a linewidth of 10 Hz (FWHM). This is only 1 Hz larger than the linewidth of the beat of the reference lasers (panel 1a). The spectrum (panel 1b) also exhibits several sidebands with frequencies in the range 10 - 50 Hz. These sidebands are not observed in the beats in panels 1a and 2a. The reason for this is that they are caused by fiber noise occurring in the 35 m long fiber guiding OFC1 radiation to the OPO (see Fig. 2), which only contributes to the measurements underlying panel 3, see section 3.2. In the phase-noise spectrum 3b, the sideband observed in the PLL signal at 810 Hz is again visible.

3.2. Fiber noise

To investigate the noise observed in the beat of the idler's second-harmonic and OFC2 (Fig. 3, panels 3a and 3b), the optical path between OFC1 and the OPO was investigated. To this end, a round-trip propagation path for the idler's second-harmonic was set up, by using two fibers similar

Optics EXPRESS

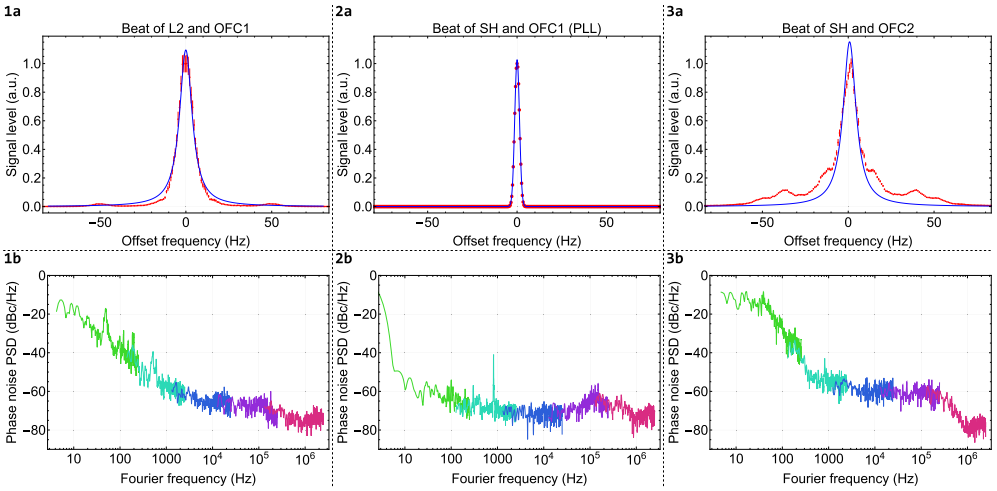


Fig. 3. Analysis of the beats between different units, marked by red circles in Fig. 2. **Left column:** beat $f_{L2} - f_{OFC1}$ between L2 and OFC1 locked to L1, showing the combined instability of the two reference lasers. **Center column** is the PLL of the OPO, specifically the beat between the second-harmonic of the idler and OFC1 in the phase-locked state, here at a second-harmonic wavelength of 1.4 μm. **Right column** shows the beat $f_{SH} - f_{OFC2}$ between the second-harmonic and OFC2, at the same wavelength 1.4 μm. This is a direct determination of an upper bound for the instability of the OPO's idler wave frequency and includes all noise sources of the system (e.g. noise of the lasers themselves and fiber noise). Each column is split into a determination of the linewidth of the beat (top) and the phase-noise power spectral density (bottom, PSD). For the linewidth plots of the first and last columns, the data are an average of many consecutive sweeps (order 10^2) of 5 s duration each, at 1 Hz RBW. The error bars are the standard error of the mean. The data are fit by a Lorentz function, giving a FWHM linewidth of 9 Hz and 10 Hz, respectively. For the middle column, the data is from a single spectrum analyzer sweep. It is fit by a Gauss function (FWHM 3 Hz), the appropriate form considering the digital band-pass of the spectrum analyzer.

to the one shown in Fig. 2 connecting OFC1 and OPO. The pick-off of the second-harmonic, previously sent to OFC2, is now sent to OFC1 and then back to the OPO. There, a self-beat is generated with a reference wave (the part that is usually sent to the wavelength meter). Additionally, sidebands are modulated onto the OPO's pump laser at 10 MHz, allowing a beat signal to be obtained at an RF frequency rather than at DC.

The result is shown in Fig. 4. As can be seen, multiple side-peaks are observed at different frequencies ranging from a few Hz to 80 Hz. This is not surprising, since the fiber is exposed to the environment and thus transfers acoustic and mechanical perturbations onto the light passing through it. Since the offset frequencies corresponding to the spectral peaks match well with the sideband frequencies observed in the beat between the idler's second-harmonic and OFC2, we infer that the sidebands are caused by this fiber noise. Additionally, a minor broadening of the carrier's linewidth is observed, 2 Hz. This can also explain the small broadening observed in the comparison of Fig. 3, panels 1a and 3a. We thus conclude that the fiber noise due to this fiber is the main source of frequency instability of the entire OPO metrology system, apart from the instability of the reference lasers themselves.

Optics EXPRESS

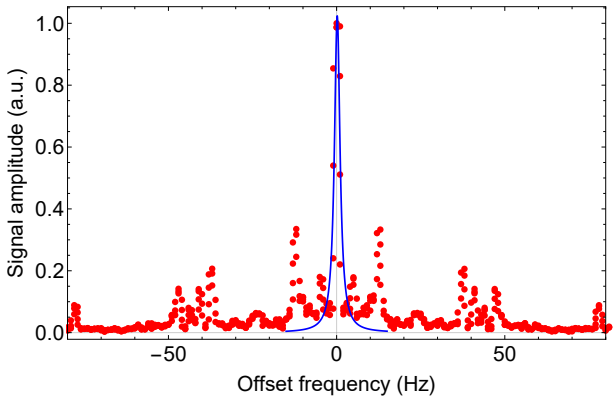


Fig. 4. Fiber noise of the longest fiber path in the system (35 m), connecting unit 1 and unit 2. The self-beat of the SH, sent on a round-trip to OFC1 and back, is shown in red. The blue curve is a Lorentzian fit to the central peak, yielding a FWHM linewidth of 2 Hz. The data was recorded using a spectrum analyzer with a sweep time of 200 s at a RBW of 1 Hz.

3.3. Compensation of the resonator drifts and frequency stability of the idler wave on long time intervals

As mentioned above, we actively compensate for both resonators' slow drifts. In the case of resonator 1, this is done in order to keep the idler frequency at a fixed absolute value, which is necessary for ultra-high precision spectroscopy. In the case of resonator 2, the OFC2 comb lines are kept at fixed values.

The drifts of resonator 1 and 2 are compensated independently and at a different stage of the optical setup. For laser L1, and consequently for OFC1, the resonator drift is not compensated. Instead, the LO frequency of the PLL of the idler to OFC1 is corrected; therefore, only the OPO's idler frequency will maintain a fixed absolute value. For resonator 2, the compensation is instead implemented via the EOM shown in the bottom unit in Fig. 2. Therefore, both the L2 output frequency (after the AOM) and the entire OFC2 are drift-compensated.

For both units, the compensation is implemented in a similar manner: the drift of each resonator is calculated from the absolute frequency value measured by each comb every 1 s relative to the H-maser. A moving average of the frequency data is computed and compared to a target frequency. The deviation of this average from the target is the error signal delivered to a digital PID loop that acts on the LO frequency or on the EOM frequency, respectively, for OPO and L2. Averaging times of 30 s for resonator 1 and 20 s for resonator 2 were found to lead to the best performance.

As a consequence of the two drift compensations, the idler frequency instability on long timescales shown in Fig. 5 (red) has to be interpreted in the following way. Since both of our combs measure the absolute frequency of the lasers relative to the H-maser frequency, the drift compensations described above effectively reference the idler's second-harmonic and the reference laser L2 (and thus also OFC2) to the H-maser. Since all RF devices used to record the shown data are also referenced to this H-maser, we are effectively measuring one maser-referenced frequency against another. Therefore, the instability averages down as the integration time increases.

Determining the absolute value of the optical frequency relative to the atomic unit of frequency (SI-traceability) requires that we continuously compare our H-maser frequency to a H-maser of PTB that is steered to the international atomic time. Our comparison occurs via common-view

Optics EXPRESS

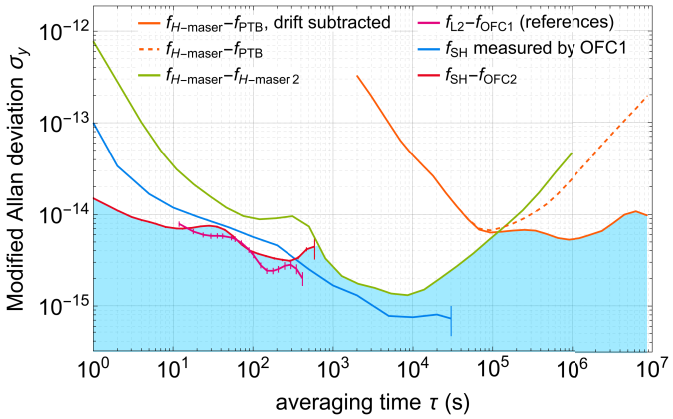


Fig. 5. Fractional Allan deviations of different signals. The magenta, blue and red traces show Allan deviations of an optical frequency. For magenta and red, the underlying data is the beat frequency between two waves, while for the blue trace it is the data calculated from Eq. (2), with f_{ceo1}, f_{rep1} and f_{beat1} measured simultaneously. All RF frequencies are either measured by a frequency counter or a spectrum analyzer, both of which are referenced to the H-maser. The green and orange traces show Allan deviations of the H-maser, evaluated by different methods. The upper limit of the blue shaded area depicts a conservative estimate of the fractional instability of the OPO's idler wave, inferred from the individual measurements. See text for explanations.

GNSS. The comparison determines the frequency offset of our H-maser's nominal 10 MHz signal and also the time drift of the offset. With this information, we can finally compute the lasers' absolute frequencies and their instabilities relative to the atomic frequency standard.

To demonstrate that our system is stabilized over long time intervals and to summarize the performance, we show in Fig. 5 six different fractional modified Allan deviations σ_y.

The dashed orange trace is the instability of the comparison of the frequency of our H-maser and the international atomic frequency standard at PTB. The upturn after approximately 1 day is due to the drift of the maser. The time-varying offset of our maser is recorded and taken into account in the OPO frequency data analysis in post-processing or in a feed-forward correction. The fractional drift rate is approximately 3×10^{-15} per day for this H-maser. The full orange line is obtained by removing the linear drift from the measured data and re-evaluating the Allan deviation. Since the GNSS receiver provides one reading every 15 min, no Allan deviation can be determined for short integration times.

The green trace is the Allan deviation of a comparison of the H-maser with a similar device, recorded at a different time. The Allan deviation reflects the combined instability of the two masers. Since both are nominally equal, the instability of the maser used in the OPO stabilization is expected to be slightly less than the values of the trace. This trace extends to integration times shorter than 15 min. The low instability verified on such shorter timescales is an important feature, since the drift compensation described above relies on locking the lasers' frequencies to the maser with time constants on the order of $10^1 - 10^2$ s.

The magenta trace shows the Allan deviation of the drift-removed beat $f_{L2} - f_{OFC1}$. This is the relative instability of the two independent reference lasers. Note that OFC1 is not drift-compensated, so that similar to the maser data, a linear function was fitted to the raw beat data and subtracted from it, before computing the Allan deviation.

Finally, the red and blue traces refer to the Allan deviation of f_{SH}, and are obtained by two different methods. The first trace (blue) is the absolute frequency value f_{SH} determined by OFC1. This is achieved through the classic frequency comb equation for a to-be-determined optical

Optics EXPRESS

frequency f_o

$$f_o = f_{ceo1} + nf_{rep1} + f_{beat1}, \tag{2}$$

where $f_{ceo1} = 35.600\,000\,00(1)$ MHz for OFC1, n is the index of the comb mode used for locking and determined using the wavelength meter, and $f_{beat1} = f_{SH} - f_{OFC1}$ is the beat frequency between the SH of the idler and the closest mode of OFC1. Under phase-lock, f_{beat1} is equal to the local oscillator's frequency, typically in the range of 40 – 100 MHz. The repetition rate $f_{rep1} \backsimeq 250$ MHz is here measured once per second by a high-resolution frequency counter (Microsemi 3120A) referenced to the H-maser. The blue trace for f_{SH} averages down with increasing integration time. These Allan deviation values do not reflect the actual (absolute) instability of the idler frequency, but indicate that it is locked well to the OFC1 on the short time scale and to the H-maser on the long time scale.

The second trace for f_{SH} (red) is the normalized Allan deviation $\sigma_y(f_{SH} - f_{OFC2})$. Here, the data was recorded with another frequency counter, also with 1 s integration time. In this measurement, and for short averaging times, the Allan deviation results from the independent frequency fluctuations of the idler SH wave and the OFC2 comb mode. Thus, the plotted red values represent an upper bound for the instability of the idler SH wave. This bound is $\sigma_y(f_{SH}) \leq 1 \times 10^{-14}$ and applies also to the idler frequency itself. The red trace is not extended to longer integration times because it then no longer reflects the actual instability of the idler frequency. As explained, f_{SH} and f_{OFC2} are not independent on long timescales.

3.4. Absolute frequency comparison

The two employed combs OFC1, OFC2 may be used not only to characterize the instability of the system, but also to compare and verify that the same absolute frequency is measured by both combs and associated equipment. The task is accomplished by measurements similar to those presented in sections 3.1 and 3.3. Equation (2) is now applied to the two independent combs, and (f_{ceo}, f_{rep}) are measured by independent frequency counters, n is calibrated using a common wavelength meter, and the two beat frequencies f_{beat1}, f_{beat2} are measured with a spectrum analyzer and a frequency counter for OFC1 and OFC2, respectively. All counters and the spectrum analyzer are referenced to the common H-maser. Thus, in this characterization we focus on the optical metrology, and not on the performance of the RF reference. In a variation to the previous sections, the data in this context was taken for an idler SH wavelength of 1.20 μm. Additionally, a different reference laser L3 and ULE resonator, at 1.53 μm, were used to stabilize OFC1. We confirmed that the stabilized laser L3 had a similar level of frequency instability as the laser L1 used in the above sections, by characterizing it in a similar manner as is described for the comparison of L1 and L2 in sections 3.1 and 3.3.

The result is shown in Fig. 6. The data underlying the figure was taken simultaneously with the two combs and spans a duration of 2330 s. The raw f_{SH} data were averaged with different averaging times, and the mean of the averaged values is displayed in the figure. The statistical error associated with the points is the standard error of the means. The frequency counter used to count f_{rep} with OFC2 has a lower precision than the counter for OFC1, causing the larger statistical uncertainty, particularly apparent for small averaging times. The systematic uncertainty is given by the combined inaccuracy of the RF devices used in both measurements. The dominant contribution is from the spectrum analyzer used in the OFC1 measurement, which contributes 1.2 Hz uncertainty. All other contributions are on the order of a few millihertz or smaller. We found that for all averaging times, the two frequency values obtained with the two measurement systems based on OFC1 and OFC2 agree within the combined uncertainty. For the longest averaging time $\tau = 500$ s, the difference between the two measured values is $\langle (f_{SH,OFC1})_\tau \rangle - \langle (f_{SH,OFC2})_\tau \rangle = (0.2 \pm 1.4)$ Hz, or $(0 \pm 6) \times 10^{-15}$ fractionally. Thus, 6×10^{-15} is a conservative estimate for the total fractional uncertainty of the idler frequency measurement

Optics EXPRESS

procedure by a single comb, excluding the uncertainty of the RF reference. (The latter is estimated to be at a similar level.)

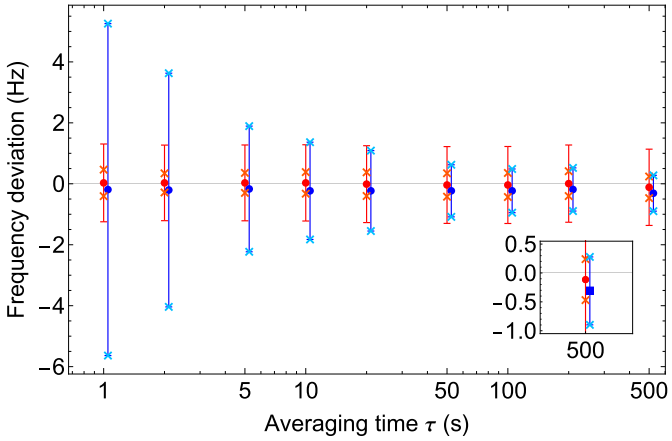


Fig. 6. The optical frequencies f_{SH} measured with OFC1 (red) and with OFC2 (blue), for different averaging times. The data are shown relative to an (arbitrary) offset frequency (approximately 249 THz). Two error bars are shown for each data set. The crosses represent the statistical standard error of the measurement, while the error bars denote the combination of statistical errors and systematic uncertainties. For clarity, the blue data points and errors are shown with a horizontal offset.

3.5. Stabilization of different idler wavelengths

As mentioned, the idler SHG sub-unit has been implemented in a way that it is capable of generating the second-harmonic wave over the entire tuning range of the idler. When changing the idler wavelength, it is necessary to change either the SHG crystal temperature, the grating period through which the laser wave propagates, or a combination of both. The crystal temperature is controlled by a commercial oven and an oven controller unit, obtained together with the crystal. We mounted the oven on a translation stage to allow for a fine adjustment of the crystal position perpendicular to the laser propagation direction. With this setup, a temperature change is possible within a few minutes, while a change of the grating period takes approximately thirty minutes due to the need for minor alignment optimization.

Therefore, the actual limiting factor of our method is the output range of the comb. For our OFC1, it is 1.0 – 1.6 μm, thus limiting the overall system's operation to the range 2.2 – 3.2 μm. Note that this could be extended by using OFC2 instead as the reference for the OPO, since it has a larger wavelength range than OFC1, reaching up to 2.0 μm. This potential exchange should not have a significant effect on the stability of the OPO, since both combs possess similar performance. For this reason, we believe that the full idler range of our OPO is lockable using our method.

We have phase-locked the OPO when tuned to the wavelengths 2.40, 2.60, 2.70, 2.81 μm, corresponding to 1.20, 1.30, 1.35, 1.40 μm for the SH. In all cases, we observed phase noise spectra and linewidths of the PLL similar to those shown in Fig. 3. These are provided as a supplemental document (see Supplement 1). We thus infer a similar level of idler frequency instability for these cases. For the specific cases of 2.40 μm and 2.60 μm, we have verified the performance by a beat with OFC2/L2, in the same way as was done for 2.80 μm, see sections 3.1 and 3.3. Therefore, we believe that our scheme will work well at any idler wavelength (even untested ones) and will provide similar frequency stability as the one presented above.

Optics EXPRESS

3.6. Long-term operation of the system

For providing long-term stability of the idler, we rely on the following procedure. After a thermalization of the setup, the range of the OPO's fast lock is sufficient to maintain the lock for a few hours. During operation, the SH frequency is measured by the wavelength meter, denoted f_{WM}. Due to an imperfect calibration of the wavelength meter, the value f_{WM} is offset from the correct value measured by the comb, by an amount $\Delta f_{\mathrm{WM}} = f_{\mathrm{WM}} - f_{\mathrm{SH,OFC1}}$, typically $10 - 30$ MHz. Therefore, while the OPO is in the locked state, Δf_{WM} is calibrated. When the OPO falls out of lock, f_{WM} will change. A digital control loop then pushes the frequency back to the calibrated offset, with feedback applied to the pump laser's piezo actuator. When the frequency is close to the lock point, the fast lock automatically re-engages, restoring the locked state. This procedure effectively re-centers the fast lock output and typically takes a few seconds.

We show in Fig. 7 f_{WM} over the course of a day. In the locked state, the idler accurately maintained the same target frequency, as confirmed by the continuous measurement with OFC1. Occasionally, wavelength jumps were detected by the wavelength meter. These are situations, where the OPO fell out of phase-lock and was quickly re-locked by the digital loop described above. The jumps are a result of the thermal drift of the OPO, which in our current setup is not compensated for by a slow lock, e.g. by controlling the piezo actuator of the pump laser.

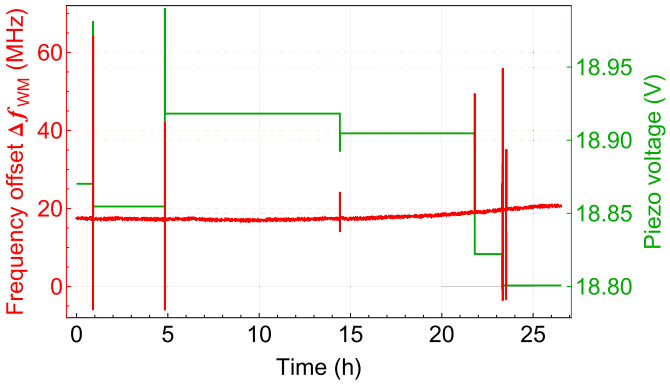


Fig. 7. Long-term stability of the system during of a typical measurement day. The red trace shows the wavelength of the idler's second harmonic measured by the wavelength meter (converted to frequency) relative to the value measured by OFC1. The nearly constant trace shows that the OPO was operating in the locked state nearly all the time. The offset ($\Delta f_{\mathrm{WM}} \simeq 18$ MHz) and its drift (3 MHz over 1 day) are systematic errors of the wavelength meter, consistent with its specifications. The green trace shows the voltage applied to the piezo actuator of the pump laser, which is used to re-lock the OPO. Jumps in the recorded wavelength meter reading correspond to instants when the OPO fell out of phase-lock and was subsequently automatically re-locked by changing the piezo actuator voltage. Typically, the out-of-lock periods lasted a few seconds.

The total unlocked time in Fig. 7 (67 s) relative to the measurement interval of 26 h corresponds to a duty cycle of 99.93 %. Importantly, we have operated the system in this configuration at multiple wavelengths daily over the course of more than two years, proving the stability and robustness of the setup. No major flaws or issues arose during this time.

4. Conclusion, application, and perspectives

We have developed an optical frequency metrology system based on an optical-parametric-oscillator. It exhibits a fractional frequency instability at the 1×10^{-14} level or smaller for integration times between 1 and 10^5 s and a linewidth of similar magnitude. Both of these

Optics EXPRESS

properties represent more than a hundredfold improvement over the previous state-of-the-art [20,45]. Our scheme was employed at several wavelengths within the idler range, proving the flexibility of the method. Additionally, the system has been operated long-term with a duty cycle above 99.9 %. The idler frequency is SI-traceable through a hydrogen-maser-referenced optical frequency comb that is continuously calibrated to the national standard via common-view GNSS. The total uncertainty of the idler frequency measurement relative to the RF reference is less than 6×10^{-15} and the RF frequency accuracy is approximately 1×10^{-14}, resulting in a total uncertainty of less than 1.2×10^{-14}. The system has been thoroughly analyzed and sources of noise have been identified. We find that the performance of the system is limited by the instability of the reference lasers and of the H-maser, as well as by fiber noise. In principle, these limits could be overcome by implementing a more stable reference laser [52,53], an optical fiber link to a national metrology laboratory [54–56], and active fiber noise cancellation [57], all of which have been demonstrated elsewhere.

In separate work, this system enabled the first Doppler-free spectroscopy of electric quadrupole vibrational transitions in a molecular ion, and furthermore permitted a SI-referenced measurement of their frequencies. Owing to the exceptional stability of the idler frequency, frequency scan step sizes as small as 5 Hz could be taken. This enabled measurements of spectroscopic lines with linewidths as small as $\simeq 6$ Hz, corresponding to line quality factors of up to 2.2×10^{13} [25,58]. This application example provides a separate confirmation of the results presented here. We have thus realized a powerful tool for mid-infrared precision spectroscopy, in particular when high power is required.

Based on the present work, we expect that the system can be expanded to alternatively stabilize the OPO's signal wave frequency (1.45 - 2.07 μm) to a similar stability level as shown here for the idler wave. Most of the wavelength range of the signal can be beaten directly with OFC2. A SHG unit is thus not required to bridge to the NIR regime, which simplifies the setup. However, the locking scheme employed here does not work for the signal wave, due to the OPO's cavity being resonant for the latter. Instead, we propose to implement a feedback control scheme using an AOM in the output path of the signal wave, which will act as a fast frequency shifter. A down-stream beat with the OFC would enable both the generation of an error signal for a PLL with feedback applied to the AOM as well as an absolute frequency measurement. Note that long-term stability requires the absence of mode-hops. The mode-hop free tuning range of the signal radiation is on the order of 10^2 MHz, which is similar in magnitude to its drift over a few hours (inferred from the observation of the idler drift, see Sec. 2). Therefore, we expect that long-term stability can be achieved by incorporating a slow servo that controls the OPO cavity length. Note that in this case, the idler locking scheme does not need to be operated and that the pump and idler radiations remain unaffected since the AOM frequency shift is applied once the signal radiation has left the OPO. With such a scheme, it should be possible to extend the output spectral range of the metrology system to include 1.45 - 2.07 μm.

Longer wavelengths than those presented in this work should also be realizable as an extension of our setup, as follows. With the use of an additional laser source in the NIR range, e.g. an amplified fiber laser at 1.5 μm, phase-locked to the same OFC, and a suitable crystal that allows for difference-frequency generation (DFG), the generation of cw radiation up to $\simeq 8$ μm is straightforward [59,60]. The 1.5 μm radiation can be mixed with either the frequency-stable idler wave or the frequency-stable signal wave, resulting in far-IR radiation with frequency stability expected to be similar to that presented here for the idler.

Funding. Heinrich-Heine-Universität Düsseldorf; Deutsche Forschungsgemeinschaft (INST-208/774-1 FUGG, INST-208/796-1 FUGG); H2020 European Research Council (786306, "PREMOL"); European Partnership on Metrology (23FUN04 COMOMET).

Acknowledgments. The assistance of U. Rosowski in the maintenance of the H-maser and with concomitant data analysis has been important and is much appreciated. C. Wellers contributed in conceptual analyses and in procuring the OPO. M. G. Hansen and I. V. Kortunov are also acknowledged for their contributions to procurement of the OPO and for

Optics EXPRESS

their help during set up of the OPO's and comb's infrastructure. We thank E. Wiens for the provision of L3. C. J. Kwong assisted in the maintenance of OFC2. The performance of the system was validated in high-resolution spectroscopy in joint work with S. Alighanbari.

Disclosures. The authors declare no conflicts of interest.

Data availability. Data underlying the results presented in this paper are not publicly available at this time but may be obtained from the authors upon reasonable request.

Supplemental document. See Supplement 1 for supporting content.

References

1. S. T. Yang, R. C. Eckardt, and R. L. Byer, "Continuous-wave singly resonant optical parametric oscillator pumped by a single-frequency resonantly doubled Nd:YAG laser," Opt. Lett. **18**(12), 971–973 (1993).
2. W. R. Bosenberg, A. Drobshoff, J. I. Alexander, *et al.*, "93% pump depletion, 3.5-W continuous-wave, singly resonant optical parametric oscillator," Opt. Lett. **21**(17), 1336–1338 (1996).
3. K. Schneider, P. Kramper, S. Schiller, *et al.*, "Toward an optical synthesizer: a single-frequency parametric oscillator using periodically poled $LiNbO_3$," Opt. Lett. **22**(17), 1293–1295 (1997).
4. S. Schiller and J. Mlynek, "Continuous-wave optical parametric oscillators," Appl. Phys. B **66**(6), 661–764 (1998). Special Issue, Editors: S. Schiller, J. Mlynek.
5. D. J. M. Stothard, M. Ebrahimzadeh, and M. H. Dunn, "Low-pump-threshold continuous-wave singly resonant optical parametric oscillator," Opt. Lett. **23**(24), 1895–1897 (1998).
6. M. H. Dunn and M. Ebrahimzadeh, "Parametric Generation of Tunable Light from Continuous-Wave to Femtosecond Pulses," Science **286**(5444), 1513–1517 (1999).
7. D. Weise, U. Strößner, A. Peters, *et al.*, "Continuous-wave 532-nm-pumped singly resonant optical parametric oscillator with periodically poled $KTiOPO_4$," Opt. Commun. **184**(1-4), 329–333 (2000).
8. T. Petelski, R. S. Conroy, K. Bencheikh, *et al.*, "All-solid-state, tunable, single-frequency source of yellow light for high-resolution spectroscopy," Opt. Lett. **26**(13), 1013–1015 (2001).
9. E. V. Kovalchuk, D. Dekorsy, A. I. Lvovsky, *et al.*, "High-resolution Doppler-free molecular spectroscopy with a continuous-wave optical parametric oscillator," Opt. Lett. **26**(18), 1430–1432 (2001).
10. A. Hecker, M. Havenith, C. Braxmaier, *et al.*, "High resolution Doppler-free spectroscopy of molecular iodine using a continuous wave optical parametric oscillator," Opt. Commun. **218**(1-3), 131–134 (2003).
11. D. D. Arslanov, S. M. Cristescu, and F. J. M. Harren, "Optical parametric oscillator based off-axis integrated cavity output spectroscopy for rapid chemical sensing," Opt. Lett. **35**(19), 3300–3302 (2010).
12. M. Vainio, M. Merimaa, and L. Halonen, "Frequency-comb-referenced molecular spectroscopy in the mid-infrared region," Opt. Lett. **36**(21), 4122–4124 (2011).
13. S. Thorwirth, J. Krieg, V. Lutter, *et al.*, "High-resolution OPO spectroscopy of Si_2C_3 at 5μm: Observation of hot band transitions associated with ν_3," J. Mol. Spectrosc. **270**(1), 75–78 (2011).
14. I. Ricciardi, E. D. Tommasi, P. Maddaloni, *et al.*, "Frequency-comb-referenced singly-resonant OPO for sub-Doppler spectroscopy," Opt. Express **20**(8), 9178–9186 (2012).
15. D. Zhao, K. D. Doney, and H. Linnartz, "High-resolution infrared spectra of vibrationally excited HC_4H in a supersonic hydrocarbon plasma jet," J. Mol. Spectrosc. **296**, 1–8 (2014).
16. H. Chadwick, P. M. Hundt, M. van Reijzen, *et al.*, "Quantum state specific reactant preparation in a molecular beam by rapid adiabatic passage," J. Chem. Phys. **140**(3), 034321 (2014).
17. M. Vainio and L. Halonen, "Mid-infrared optical parametric oscillators and frequency combs for molecular spectroscopy," Phys. Chem. Chem. Phys. **18**(6), 4266–4294 (2016).
18. C. R. Markus, S. Thorwirth, O. Asvany, *et al.*, "High-resolution double resonance action spectroscopy in ion traps: vibrational and rotational fingerprints of $CH_2NH_2^+$," Phys. Chem. Chem. Phys. **21**(48), 26406–26412 (2019).
19. C. R. Markus and B. J. McCall, "Highly accurate experimentally determined energy levels of H_3^+," J. Chemical Phys. **150**(21), 214303 (2019).
20. Z.-T. Zhang, C.-F. Cheng, Y. R. Sun, *et al.*, "Cavity ring-down spectroscopy based on a comb-locked optical parametric oscillator source," Opt. Express **28**(19), 27600–27607 (2020).
21. D. Gupta, W. G. D. P. Silva, J. L. Doménech, *et al.*, "High-resolution rovibrational and rotational spectroscopy of the singly deuterated cyclopropenyl cation, c-$C_3H_2D^+$," Faraday Discuss. **245**, 298–308 (2023).
22. C. Wunderlich and C. Balzer, "Quantum measurements and new concepts for experiments with trapped ions," in *Advances in Atomic, Molecular, and Optical Physics* Vol. 49, (Academic Press, 2003), pp. 295–376.
23. S. Schiller, "Hydrogenlike Highly Charged Ions for Tests of the Time Independence of Fundamental Constants," Phys. Rev. Lett. **98**(18), 180801 (2007).
24. E. G. Myers, "CPT tests with the antihydrogen molecular ion," Phys. Rev. A **98**(1), 010101 (2018).
25. M. R. Schenkel, S. Alighanbari, and S. Schiller, "Laser spectroscopy of a rovibrational transition in the molecular hydrogen ion H_2^+," Nat. Phys. **20**(3), 383–388 (2024).
26. M. Niu, E. Salumbides, G. Dickenson, *et al.*, "Precision spectroscopy of the $X^1\Sigma_g^+, \nu = 0 \rightarrow 1(J = 0 - 2)$ rovibrational splittings in H_2, HD and D_2," J. Mol. Spectrosc. **300**, 44–54 (2014).
27. A. Fast and S. A. Meek, "Sub-ppb Measurement of a Fundamental Band Rovibrational Transition in HD," Phys. Rev. Lett. **125**(2), 023001 (2020).

Optics EXPRESS

28. A. Fast and S. A. Meek, "Precise measurement of the D_2 $S_1(0)$ vibrational transition frequency," Mol. Phys. **120**(19-20), e1999520 (2022).
29. H. Fleurbaey, A. O. Koroleva, S. Kassi, *et al.*, "The high-accuracy spectroscopy of H_2 rovibrational transitions in the (2-0) band near 1.2 μm," Phys. Chem. Chem. Phys. **25**(21), 14749–14756 (2023).
30. J. Komasa, "Energy levels of the hydrogen molecule from relativistic nonadiabatic calculations," in *International Conference on Precision Physics and Fundamental Physical Constants (FFK)*, (Vienna, Austria, 2023).
31. Q.-H. Liu, Y. Tan, C.-F. Cheng, *et al.*, "Precision spectroscopy of molecular hydrogen," Phys. Chem. Chem. Phys. **25**(41), 27914–27925 (2023).
32. K. Pachucki and J. Komasa, "Rovibrational levels of helium hydride ion," J. Chemical Phys. **137**(20), 204314 (2012).
33. M. Kajita and N. Kimura, "Prospect for Vibrational Transition Frequency Measurement of Rare-gas Hydride Ions," J. Phys. Soc. Jpn. **89**(11), 114301 (2020).
34. S. Schiller, D. Bakalov, and V. I. Korobov, "Simplest molecules as candidates for precise optical clocks," Phys. Rev. Lett. **113**(2), 023004 (2014).
35. J.-P. Karr, "H_2^+ and HD^+: candidates for a molecular clock," J. Mol. Spectrosc. **300**, 37–43 (2014).
36. M. Kajita, G. Gopakumar, M. Abe, *et al.*, "Test of m_p/m_e changes using vibrational transitions in N_2^+," Phys. Rev. A **89**(3), 032509 (2014).
37. F. Wolf, J. C. Heip, M. J. Zawierucha, *et al.*, "Prospect for precision quantum logic spectroscopy of vibrational overtone transitions in molecular oxygen ions," New J. Phys. **26**(1), 013028 (2024).
38. S. A. Diddams, D. J. Jones, L.-S. Ma, *et al.*, "Optical frequency measurement across a 104-THz gap with a femtosecond laser frequency comb," Opt. Lett. **25**(3), 186–188 (2000).
39. R. Holzwarth, T. Udem, T. W. Hänsch, *et al.*, "Optical Frequency Synthesizer for Precision Spectroscopy," Phys. Rev. Lett. **85**(11), 2264–2267 (2000).
40. H. Inaba, T. Ikegami, F.-L. Hong, *et al.*, "Phase locking of a continuous-wave optical parametric oscillator to an optical frequency comb for optical frequency synthesis," IEEE J. Quantum Electron. **40**(7), 929–936 (2004).
41. E. V. Kovalchuk, T. Schuldt, and A. Peters, "Combination of a continuous-wave optical parametric oscillator and a femtosecond frequency comb for optical frequency metrology," Opt. Lett. **30**(23), 3141–3143 (2005).
42. N. Poli, C. W. Oates, P. Gill, *et al.*, "Optical atomic clocks," Rivista del Nuovo Cimento **36**, 555 (2013).
43. A. D. Ludlow, M. M. Boyd, J. Ye, *et al.*, "Optical atomic clocks," Rev. Mod. Phys. **87**(2), 637–701 (2015).
44. J. Peltola, M. Vainio, T. Fordell, *et al.*, "Frequency-comb-referenced mid-infrared source for high-precision spectroscopy," Opt. Express **22**(26), 32429–32439 (2014).
45. I. Ricciardi, S. Mosca, M. Parisi, *et al.*, "Sub-kilohertz linewidth narrowing of a mid-infrared optical parametric oscillator idler frequency by direct cavity stabilization," Opt. Lett. **40**(20), 4743–4746 (2015).
46. J. Karhu, M. Vainio, M. Metsälä, *et al.*, "Frequency comb assisted two-photon vibrational spectroscopy," Opt. Express **25**(5), 4688–4699 (2017).
47. D. B. Foote, M. J. Cich, W. C. Hurlbut, *et al.*, "High-resolution, broadly-tunable mid-IR spectroscopy using a continuous wave optical parametric oscillator," Opt. Express **29**(4), 5295–5303 (2021).
48. C. J. Kwong, M. G. Hansen, J. Sugawara, *et al.*, "Characterization of the long-term dimensional stability of a NEXCERA block using the optical resonator technique," Meas. Sci. Technol. **29**(7), 075011 (2018).
49. I. Ito, A. Silva, T. Nakamura, *et al.*, "Stable CW laser based on low thermal expansion ceramic cavity with 4.9 mHz/s frequency drift," Opt. Express **25**(21), 26020–26028 (2017).
50. J. I. Thorpe, K. Numata, and J. Livas, "Laser frequency stabilization and control through offset sideband locking to optical cavities," Opt. Express **16**(20), 15980–15990 (2008).
51. A. Y. Nevsky, S. Alighanbari, Q. Chen, *et al.*, "Robust frequency stabilization of multiple spectroscopy lasers with large and tunable offset frequencies," Opt. Lett. **38**(22), 4903 (2013).
52. S. Häfner, S. Falke, C. Grebing, *et al.*, "8×10^{-17} fractional laser frequency instability with a long room-temperature cavity," Opt. Lett. **40**(9), 2112–2115 (2015).
53. A. Didier, S. Ignatovich, E. Benkler, *et al.*, "946-nm Nd:YAG digital-locked laser at 1.1×10^{-16} in 1 s and transfer-locked to a cryogenic silicon cavity," Opt. Lett. **44**(7), 1781–1784 (2019).
54. K. Predehl, G. Grosche, S. M. F. Raupach, *et al.*, "A 920-kilometer optical fiber link for frequency metrology at the 19th decimal place," Science **336**(6080), 441–444 (2012).
55. D. Husmann, L.-G. Bernier, M. Bertrand, *et al.*, "SI-traceable frequency dissemination at 1572.06 nm in a stabilized fiber network with ring topology," Opt. Express **29**(16), 24592–24605 (2021).
56. C. Clivati, M. Pizzocaro, E. Bertacco, *et al.*, "Coherent Optical-Fiber Link Across Italy and France," Phys. Rev. Appl. **18**(5), 054009 (2022).
57. L.-S. Ma, P. Jungner, J. Ye, *et al.*, "Delivering the same optical frequency at two places: accurate cancellation of phase noise introduced by an optical fiber or other time-varying path," Opt. Lett. **19**(21), 1777–1779 (1994).
58. S. Alighanbari, M. R. Schenkel, S. Schiller, *et al.*, subm.
59. S. Vasilyev, S. Schiller, A. Nevsky, *et al.*, "Broadly tunable single-frequency cw mid-infrared source with milliwatt-level output based on difference-frequency generation in orientation-patterned GaAs," Opt. Lett. **33**(13), 1413–1415 (2008).
60. K. Devi, P. G. Schunemann, and M. Ebrahim-Zadeh, "Continuous-wave, multimilliwatt, mid-infrared source tunable across 6.4-7.5μm based on orientation-patterned GaAs," Opt. Lett. **39**(23), 6751–6754 (2014).

Supplemental Document

Optics EXPRESS

Metrology-grade spectroscopy source based on an optical parametric oscillator: supplement

M. R. SCHENKEL,[1,2,] V. A. VOGT,[1] AND S. SCHILLER[1,3]

[1] *Heinrich-Heine-Universität Düsseldorf, Mathematisch-Naturwissenschaftliche Fakultät, Institut für Experimentalphysik, 40225 Düsseldorf, Germany*
[2] *magnus.schenkel@hhu.de*
[3] *step.schiller@hhu.de*

This supplement published with Optica Publishing Group on 13 November 2024 by The Authors under the terms of the Creative Commons Attribution 4.0 License in the format provided by the authors and unedited. Further distribution of this work must maintain attribution to the author(s) and the published article's title, journal citation, and DOI.

Supplement DOI: https://doi.org/10.6084/m9.figshare.27044743

Parent Article DOI: https://doi.org/10.1364/OE.538442

A metrology-grade spectroscopy source based on an optical parametric oscillator: Supplement 1

1. FIGURE OF PLL BEATS AT VARIOUS WAVELENGTHS

Figure S1 shows the linewidths and phase noise spectra of the PLL for three different idler wavelengths in the same style as Fig. 3 of the main text.

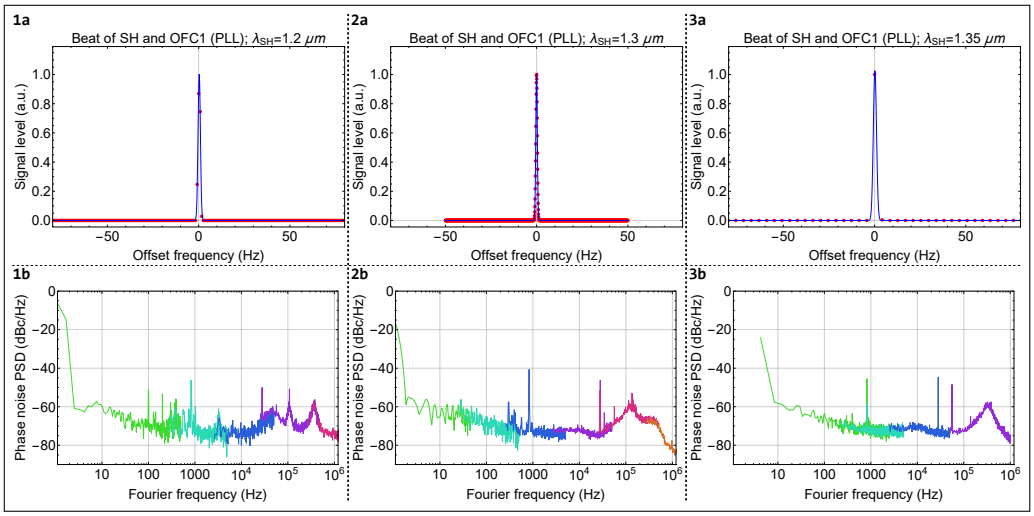


Fig. S1. Beat spectrum shown as a zoom-in of the beat (top row) and the phase-noise power spectral density (PSD, bottom row) of the beat between the idler SH and OFC1 in the locked state for three different idler wavelengths. Columns 1, 2, 3 correspond to idler wavelengths of 2.4, 2.6, 2.7 μm, respectively. For the top row, all data are taken with a RBW of 1 Hz and are normalized to the peak level of the fitted function. Due to a different frequency resolution used for the individual data sets, the center peak in panel 3a is not well resolved. In this case, the Gaussian fit function is shown for illustrative purposes only. For the bottom row, individual colors correspond to individual measurements, which are normalized to their RBW. The signal-to-noise ratio is in all cases similar to the 70 dB stated in the main text. Compared to the PSD measurement in Fig. 3, panel 2b of the main text, the PSDs exhibit additional noise peaks. This is due to an incomplete optimization of the lock settings. Such an optimization is required after tuning the wavelength of the idler, which results in a change of the beat signal level.

B.3.2 Design Guidelines for Ultra-Stable Lasers

Title:
Guidelines for designs for ultrastable laser with 10^{-17} fractional frequency instability

Authors:
J. Barbarat, E. Benkler, M. Bober, C. Clivati, J. Dickmann, B. Fang, C. Fluhr, T. Fordell, J. Gillot, V. Giordano, D. Gustavsson, K. Hanhijärvi, M. Hartman, S. Herbers, A. Jaros, J. Kawohl, Y. Kersalé, S. Kroker, C. Kwong, C. Lacroûte, R. Targat, T. Legero, M. Lindén, T. Lindvall, J. Lodewyck, C. Ma, R. Meyer, P. Morzyński, J. Millo, M. Narożnik, D. Nicolodi, A. Penza, B. Pointard, L. Rippe, M. Risaro, P. Roset, S. Sauer, P. Savio, S. Schiller, L. Neto, U. Sterr, O. Vartehparvar, **V. Vogt**, N. Wagner, A. Wallin, E. Wiens, J. Yu, M. Zawada and M. Zelan

Status / Year: ..... Published / 2025

Journal: ..... arXiv

DOI: 10.48550/arXiv.2504.06213

Licence: ..... Creative Commons Attribution 4.0 International license.

Statement of Copyright:
This license allows reusers to distribute, remix, adapt, and build upon the material in any medium or format, so long as attribution is given to the creator. The license allows for commercial use.

Statement on reuse for dissertation:
“If [the author is] the copyright holder of the work, [the author does] not need arXiv’s permission to reuse the full text.”

My Contribution:
I contributed to the first chapter, "Low thermal noise cavity designs," which is the only chapter fully reproduced here. I was responsible for writing the section on the N118C NEXCERA cavity and providing its data on linewidth, and Allan deviation. See Section 4.4.

NEXTLASERS

EMPIR

EURAMET

The EMPIR initiative is co-funded by the European Union's Horizon 2020 research and innovation programme and the EMPIR Participating States

arXiv:2004.10269v1 [physics.optics] 8 Apr 2020

Guidelines for designs for ultrastable laser with 10^{-17} fractional frequency instability

Joanne Barbarat[1], Erik Benkler[2], Marcin Bober[3], Cecilia Clivati[4], Johannes Dickmann[8], Bess Fang[5], Christophe Fluhr[1], Thomas Fordell[6], Jonathan Gillot[1], Vincent Giordano[1], David Gustavsson[7], Kalle Hanhijärvi[6], Michael Hartman[5], Sofia Herbers[2], Angelina Jaros[2], Jan Kawohl[2], Yann Kersalé[1], Stefanie Kroker[8], Chang Jian Kwong[9], Clément Lacroûte[1], Rodolphe Le Targat[5], Thomas Legero[2], Marcus Lindén[10], Thomas Lindvall[6], Jérôme Lodewyck[5], Chun Yu Ma[2], Rémi Meyer[1], Piotr Morzyński[3], Jacques Millo[1], Mateusz Narożnik[3], Daniele Nicolodi[2], Alessia Penza[4], Benjamin Pointard[5], Lars Rippe[7], Matias Risaro[4], Pierre Roset[1], Steffen Sauer[8], Paolo Savio[11], Stephan Schiller[9], Liam Shelling Neto[8], Uwe Sterr[2], Omid Vartehparvar[3], Victor Vogt[9], Nico Wagner[9], Anders E. Wallin[6], Eugen Wiens[9], Jialiang Yu[2], Michał Zawada[3], and Martin Zelan[10]

Edited by Uwe Sterr[2]

[1] *Université de Franche-Comté, SUPMICROTECH, CNRS, Institut FEMTO-ST, F-25000 Besançon, France*
[2] *Physikalisch-Technische Bundesanstalt, Bundesallee 100, 38116 Braunschweig, Germany*
[3] *Institute of Physics, Faculty of Physics, Astronomy and Informatics, Nicolaus Copernicus University, Grudziądzka 5, PL-87-100 Toruń, Poland*
[4] *Istituto Nazionale di Ricerca Metrologica, Strada delle Cacce 91, 10135 Torino, Italy*
[5] *LNE-SYRTE, Observatoire de Paris, Université PSL, CNRS, Sorbonne Université, 61 Avenue de l'Observatoire, 75014 Paris, France*
[6] *VTT Technical Research Centre of Finland Ltd, National Metrology Institute VTT MIKES, P.O. Box 1000, FI-02044 VTT, Finland*
[7] *Department of Physics, Lund University, PO Box 118, SE-22100 Lund, Sweden*
[8] *Technical University of Braunschweig, Institute for Semiconductor Technology, Hans-Sommer-Str. 66, Braunschweig, Germany*
[9] *Institut für Experimentalphysik, Heinrich-Heine-Universität Düsseldorf, 40225 Düsseldorf, Germany*
[10] *Measurement Science and Technology, RISE Research Institutes of Sweden, SE-501 15 Borås, Sweden*
[11] *Fondazione LINKS, 10135 Torino, Italy*

Guidelines for designs for ultrastable laser with 10^{-17} fractional frequency instability
https://www.ptb.de/empir2021/nextlasers
2024

Edited by Uwe Sterr
e-mail: uwe.sterr@ptb.de

This work was carried out within the EMPIR project 20FUN08 NEXTLASERS. This project has received funding from the EMPIR programme co-financed by the European Union's Horizon 2020 research and innovation programme and the EMPIR Participating States.

Contents

Contents 3

Preface 5

Acronyms 6

1 Low thermal noise cavity designs 8
- 1.1 Introduction . . . 8
- 1.2 Crystalline AlGaAs/GaAs coatings . . . 9
  - 1.2.1 Experimental setup . . . 9
  - 1.2.2 Noise characterization of the Si cavity at 124 K . . . 10
  - 1.2.3 Photo-induced effects at room temperature . . . 11
- 1.3 Meta-surface coated mirrors . . . 13
- 1.4 NEXCERA spacer . . . 15
  - 1.4.1 Mechanical loss measurements of NEXCERA . . . 15
  - 1.4.2 First-generation NEXCERA cavities . . . 16
- 1.5 Compact cavities with large spot size on mirror . . . 19
  - 1.5.1 Coatings and substrates thermal noise reduction . . . 20
  - 1.5.2 Stability conditions . . . 20
  - 1.5.3 Convex mirror substrate . . . 24
- 1.6 Conclusion and Prospects . . . 24

2 Rare-earth ion-based frequency references 26
- 2.1 Introduction . . . 26
- 2.2 Thermal noise in SHB . . . 26
- 2.3 Environmental influences . . . 28
- 2.4 Detection schemes . . . 29
- 2.5 A highly dispersive Eu:YSO slow light crystal cavity . . . 30
  - 2.5.1 Evaluation of the lifetime of the spectral transmission . . . 31
  - 2.5.2 Identification of the critical slow light cavity parameters . . . 32
- 2.6 Summary and conclusion . . . 33

3 Low frequency vibration isolation 34
- 3.1 Introduction . . . 34
- 3.2 Characterization of Sensors and Cavities . . . 35
  - 3.2.1 Acceleration sensors and tiltmeters . . . 35
  - 3.2.2 Vibration sensors for cryogenic environments . . . 37
  - 3.2.3 Optical sensing of cavity position and velocity . . . 37
  - 3.2.4 Transfer functions of active vibration isolation systems . . . 39
  - 3.2.5 Transfer functions of cavity systems to accelerations . . . 40
- 3.3 Low-frequency active vibration control . . . 50
- 3.4 Feedforward techniques . . . 51

3.4.1 Hardware for optimised feedforward correction . . . 52
3.4.2 Feedforward corrections in combination with passive vibration isolation . 54
3.4.3 Feedforward corrections in combination with active vibration isolation . 54
3.5 Mitigation of vibrations in closed-cycle cryostats . . . 58
3.5.1 Reducing the sensitivity of SHB crystal to residual vibrations . . . 58

4 Optical references in closed cycle cryostats 61
4.1 Introduction . . . 61
4.2 Description of the resonators . . . 62
4.2.1 124 K Fabry-Perot cavity . . . 62
4.2.2 Fabry-Perot cavity below 1 K . . . 62
4.2.3 Spectral hole burning in doped crystal at 2 K . . . 62
4.2.4 Spectral hole burning in doped crystal below 1 K . . . 63
4.3 Passive vibration rejection . . . 63
4.3.1 Pulse-tube cryocoolers . . . 64
4.3.2 Dilution cryostats . . . 66
4.4 Temperature stability . . . 68
4.4.1 Single-crystal silicon cavities operated at 124 K . . . 68
4.4.2 Single-crystal silicon cavities operated below 1 K . . . 68
4.4.3 Spectral-hole-burning crystals operated below 1 K . . . 70
4.5 Linewidths of the optical references . . . 72
4.5.1 Finesse of the 124 K Fabry-Perot cavity . . . 72
4.5.2 Finesse of the sub-kelvin Fabry-Perot cavity . . . 72
4.5.3 SHB reference below 1 K . . . 73
4.6 Temperature sensitivity of the resonators . . . 75
4.6.1 124 K Fabry-Perot cavity . . . 75
4.6.2 Fabry-Perot cavity below 1 K coefficient of thermal expansion . . . 75
4.6.3 Temperature sensitivity of spectral holes . . . 76
4.7 Expected performances and preliminary stability measurements of the cryogenic optical frequency references . . . 76
4.7.1 Fabry-Perot cavity at 124 K . . . 76
4.7.2 Fabry-Perot cavity below 1 K . . . 79
4.7.3 SHB below 1 K . . . 80

5 Stability transfer 83
5.1 Introduction . . . 83
5.2 Delivery of laser beams to the comb . . . 84
5.3 Single-branch optical combs . . . 87
5.4 Improving the SNR of comb beatnotes . . . 89
5.5 Digital phase-locks for highly performing, flexible and multi-wavelength spectral transfer . . . 90
5.6 Distributing the feedback information . . . 96

Bibliography 98

Preface

Lasers with long coherence time and narrow linewidth are an essential tool for quantum sensors and clocks. Ultrastable cavities and laser systems are now commercially available with fractional frequency instabilities in the mid 10^{-16} range. Ultrastable frequencies can now be distributed both locally and over long distances [1]. With femtosecond combs, lasers at different wavelengths can be compared, allowing frequency stability transfer from one wavelength to another [2–4] with added fluctuations well below 10^{-17} and microwaves generation with exceptionally low phase noise [5]. This enables interrogation times of optical clocks longer than a second [6]. Cavity-stabilized lasers have become very reliable and can even replace masers as flywheels to bridge downtimes of optical clocks to create a fully optical and continuous timescale [7].

For both in-field or in-space use of transportable clocks, many transportable cavity designs and setups have been developed, the best reaching 1.6×10^{-16} instability [8]. Laser instabilities as low as 7×10^{-17} and 4×10^{-17} have been reported for room temperature and cryogenic cavities respectively [1, 9].

This document aims to provide technical guidance for researchers starting in the field of ultrastable lasers. The target audience includes national metrology institutes (NMIs) wanting to set up optical clocks (or subsystems thereof) and PhD students and postdocs entering the field. Another potential audience is academic groups with experience in atomic physics and atom or ion trapping, but with less experience of time and frequency metrology and optical clock requirements.

These guidelines have arisen from the scope of the EMPIR project “Next generation ultrastable lasers” (NEXTLASERS). Examples are given from European partners, even though similar work is carried out all over the world.

NEXTLASER aimed to push the development of ultrastable lasers, based both on ultrastable optcal resonators and on spectral holes that are burnt in special crystals. It also covers the transfer of frequency stability from the ultrastable laser to other wavelength, required for interrogation of optical clocks. As one of the project’s deliverables, this document fulfills objective 6 of the NEXTLASERS project to facilitate the takeup of the technology by sharing the knowledge acquired by the project consortium, and by providing practical guidance on each of these aspects in the following chapters.

July 2024

Uwe Sterr
NEXTLASERS coordinator

Thomas Legero
NEXTLASERS work package ’Creating Impact’

Acronyms

AC	Alternate Current
ADC	Analog to Digital Converter
ADEV	Allan Deviation
AM	Amplitude Modulation
AOM	Acousto-Optic Modulator
AR	Anti Reflection
ARTIQ	Advanced Real-Time Infrastructure for Quantum physics
AVI	Anti-Vibration Isolation
BS	Beam Splitter
CCD	Charge Coupled Device
CNRS	Centre National de la Recherche Scientifique
CTE	Coefficient of Thermal Expansion
DAC	Digital to Analog Converter
DC	Direct Current
DDS	Direct Digital Synthesis
EMPIR	European Metrology Programme for Innovation and Research
EOM	Electro-Optic Modulator
FEM	Finite Element Method
FF	Feed Forward
FPGA	Field-Programmable Gate Array
FS	Fused Silica
FSR	Free Spectral Range
FWHM	Full Width at Half Maximum
HDL	Hardware Description Language
HHUD	Heinrich Heine University Düsseldorf
HNLF	Highly Nonlinear Fiber
HOM	Higher Order Modes
I/Q	In-Phase/Quadrature
IIR	Infinite Impulse Response (filter)
LED	Light Emitting Diode
LN2	Liquid Nitrogen
LNE	Laboratoire National de Métrologie et d'Essais
MADEV	Modified Allan Deviation

MIMO	Multiple Input / Multiple Output
MX	Mixing Plate
NEXCERA®	low thermal expansion ceramic material (trademark of Krosaki Harima Corporation)
NHNM	New High (seismic) Noise Model
NLNM	New Low (seismic) Noise Model
NMI	National Metrology Institute
OBSPARIS	Observatoire de Paris
PBS	Polarizing Beam Splitter
PD	Photodiode
PDH	Pound-Drever-Hall (laser stabilization)
PID	Proportional Integral Differential
PM	Phase Modulation
PPLN	Periodically Poled Lithium Niobate
PSD	Power Spectral Density
PTB	Physikalisch-Technische Bundesanstalt
RAM	Residual Amplitude Modulation
RCWA	Rigorous Coupled Wave Analysis
RF	Radio Frequency
RIN	Relative Intensity Noise
RMS	Root Mean Squared
ROC	Radius of Curvature
SCS	Silicon Cryogenic Cavity
SHB	Spectral Hole Burning
SHG	Second Harmonic Generation
SNR	Signal to Noise Ratio
SYRTE	Système de Références Temps-Espace
SoC	System on Chip
TEM	Transverse Electro-Magnetic (mode)
THA	Tracking and Hold Amplifier
TUBS	Technical University Braunschweig
ULE®	Ultra-Low Expansion (glass) (trademark of Corning)
UMK	Uniwersytet Mikołaja Kopernika w Toruniu
USRP	Universal Software-defined Radio Peripheral
VTT	Technical Research Centre of Finland Ltd
YSO	Yttrium Orthosilicate (Y_2SiO_5)
ZCTE	Zero of Coefficient of Thermal Expansion

1 Low thermal noise cavity designs

Marcin Bober[4], Johannes Dickmann[2], Thomas Fordell[5], Stefanie Kroker[2], Chang Jian Kwong[1], Thomas Legero[3], Chun Yu Ma[3], Mateusz Narożnik[4], Liam Shelling Neto[2], Steffen Sauer[2], Stephan Schiller[1], Uwe Sterr[3], Omid Vartehparvar[4], Victor Vogt[1], Nico Wagner[2], Eugen Wiens[1,†], Jialiang Yu[3], Michał Zawada[4]

[1] *Institut für Experimentalphysik, Heinrich-Heine-Universität Düsseldorf, 40225 Düsseldorf, Germany*
[2] *Technical University of Braunschweig, Institute for Semiconductor Technology, Hans-Sommer-Str. 66, Braunschweig, Germany*
[3] *Physikalisch-Technische Bundesanstalt, Bundesallee 100, 38116 Braunschweig, Germany*
[4] *Institute of Physics, Faculty of Physics, Astronomy and Informatics, Nicolaus Copernicus University, Grudziądzka 5, PL-87-100 Toruń, Poland*
[5] *VTT Technical Research Centre of Finland Ltd, National Metrology Institute VTT MIKES, P.O. Box 1000, FI-02044 VTT, Finland*
[†] e-mail: eugen.wiens@hhu.de

This chapter presents the results of investigations aimed toward the reduction of the thermal noise limit in state-of-the-art reference systems based on lasers stabilized to optical Fabry-Perot resonators.

The reduction of thermal noise contribution of mirror coatings was studied on crystalline AlGaAs/GaAs coatings with low thermal noise and on newly developed meta-surface coated mirrors. NEXCERA ceramic as a material for cavity spacers was investigated by setting up and characterizing two first-generation NEXCERA cavities for their vibration sensitivities, long-term drift, and thermal noise. Additionally, a measurement of NEXCERA loss angle was determined. An optical and optomechanical study was carried out to determine a viable configuration for short room temperature cavities with large spot sizes on the cavity mirrors to reduce thermal noise.

1.1 Introduction

State-of-the-art laser instabilities as low as 7×10^{-17} and 4×10^{-17} have been reported for room-temperature and cryogenic cavities, respectively [1, 9]. Similar to large gravitational-wave detectors [10, 11], the performance of these best sub-meter sized ultrastable optical resonators is currently limited by the Brownian fluctuations of the usually employed dielectric mirror coatings [12, 13]. Brownian thermal noise is related to the mechanical loss by internal friction [14] through the fluctuation-dissipation theorem [15, 16]. It can be in principle reduced by employing optical coatings with lower mechanical loss, using spacers and mirror substrates made of suitable materials with low loss, or by increasing the spot size of the laser beam using curved mirrors with a large radius of curvature.

The general design of ultrastable lasers and the techniques to narrow the linewidth has been described elsewhere in great detail [17, 18]. This chapter describes ideas and work in progress toward the reduction of the thermal noise limit in state-of-the-art reference systems based on lasers stabilized to optical Fabry-Perot resonators. The reduction of thermal noise contribution of mirror coatings was studied by implementing novel crystalline AlGaAs/GaAs coatings with low thermal noise and investigating meta-surface coated mirrors.

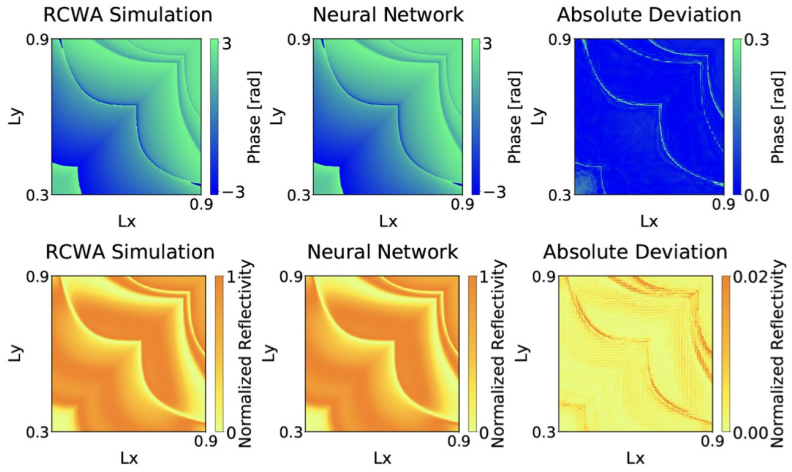


Figure 1.8. Left: Ground truth training data from the RCWA simulation. Middle: Forward predictions of the trained neural networks (for reflectivity and phase) on the ground truth data. Right: Absolute deviation of both, phase and reflectivity predictions, showing excellent performance of the neural networks.

the cross-shaped meta-atoms. Fig. 1.9 displays the phase profile with an overall design reflectivity of $R = 99.993\%$. First structures have been fabricated and are currently being characterized.

1.4 NEXCERA ceramic as spacer material for optical resonators

NEXCERA ceramic, developed by Krosaki Harima in Japan, is an ultra-low expansion cordierite ($2MgO - 2Al_2O_3 - 5SiO_2$) based ceramic material. The NEXCERA ceramic has a nominal zero coefficient of thermal expansion at room temperature, i.e. $|\alpha| < 0.03 \times 10^{-6} K^{-1}$ at 23 °C. Apart from ultra-low expansion properties, the mechanical properties of NEXCERA ceramic, with its larger ratio of Young's modulus to density, offers the possibility of lower acceleration sensitivity compared to ultra-low expansion (ULE) glass. Furthermore, a preliminary characterisation of an optical cavity made of N117B NEXCERA material has found a long-term linear drift of 4.9 mHz/s [19], which is another potential advantage compared to ULE cavity.

Some of the relevant properties of NEXCERA ceramic are shown in Tab. 1.2.

	N113B	N117B	N118C	N119C	ULE
Bulk density (g/cm^3)	2.5	2.55	2.58	2.5	2.21
Young's modulus (GPa)	130	140	140	130	68
Poisson ratio ($GPa/(g/cm^3)$)	0.30	0.31	0.31	0.31	0.17
Thermal expansion coefficient at 23°C ($\times 10^{-6}/°C$)	< 0.03	< 0.03	< 0.05	< 0.05	(0 ± 0.03)

Table 1.2. Properties of NEXCERA ceramic [39] and ULE glass.

1.4.1 Mechanical loss measurements of NEXCERA

The mechanical loss is a critical parameter for the thermomechanical noise of spacer and mirror materials in ultra-stable laser cavities. To minimize excess suspension (or clamping) losses we employed the Gentle Nodal Suspension (GeNS) technique developed by Cesarini *et al.* [40]. In this

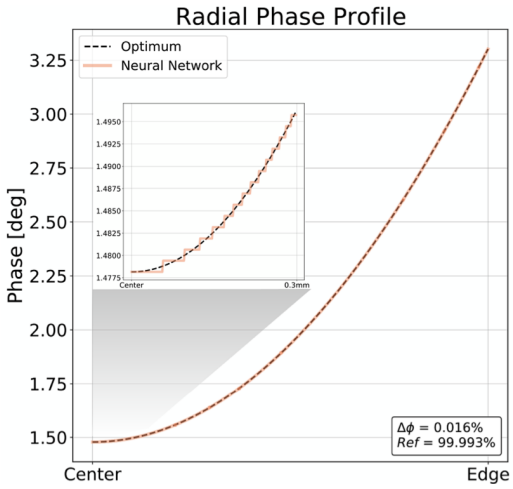


Figure 1.9. Radial phase profile of the metasurface with excellent phase agreement and high reflectivity.

technique, the sample is suspended on a sphere minimizing the contact area of the sample and the suspension. In our configuration, using a 4.5 mm steel sphere with a quality class of G3 according to DIN 5401 standards, the contact area radius of the disks (diameter 50 mm, thickness 0.5 mm) is approximately 10 μm.

The mechanical vibration excited by an AC electric field through a comb structure is detected as a spatial oscillation of the beam of a laser diode on a quadrant detector. The electric field is controlled by a custom-built high-voltage amplifier. Positioned approximately 2 mm above the sample, the structure applies an oscillating voltage up to 800 V to excite the eigenmodes of the disc. The mechanical loss of 3 disks of raw material has been measured at room temperature. All mechanical losses are at or below 3×10^{-5}. The losses of the different samples do not show systematic deviations. It is known from literature that the mechanical loss increases with the increasing surface-to-volume ratio. This means that "geometrically small" samples (such as thin disks) will have larger mechanical losses than bigger samples, for example, in geometries as used for typical spacers in laser cavities. That is why the determined minimum loss of $1.894(41)\times10^{-5}$ of the NEXCERA N117B disks is very promising as novel low-noise material [41]. The determined values can be considered as a worst-case scenario for the thermo-mechanical noise performance of typical spacer geometries.

1.4.2 First-generation NEXCERA cavities

At HHUD a 30 cm long cavity made of the N117B NEXCERA ceramic has been developed for the frequency stabilization of a 698 nm laser. Another cavity with a length of 12 cm made of N118C NEXCERA material was developed for 1.5 μm laser stabilization.

We characterized the frequency instabilities and other properties of these cavities integrated with respective laser systems to investigate the potential of NEXCERA ceramic as a spacer material for ultrastable cavities.

N117B NEXCERA cavity

The N117B NEXCERA cavity consists of the NEXCERA spacer and a pair of ULE mirrors with a finesse of 2×10^5. The cavity is operated inside its dedicated vacuum chamber that is installed within a home-built trolley to allow for transportation of the cavity system. The cavity system is shown in Fig. 1.10.

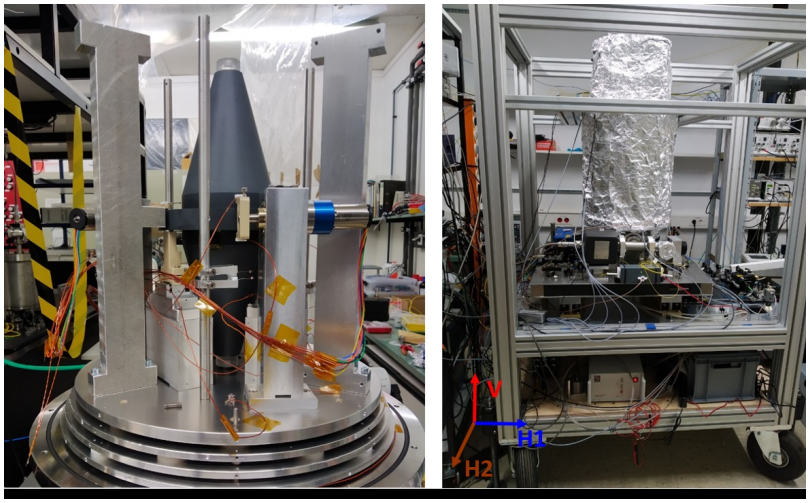


Figure 1.10. The transportable 30 cm N117B NEXCERA vertical optical resonator system. (Left) Optical resonator with support after removal of the outer vacuum shield and the two thermal insulation shields. (Right) The closed vacuum chamber containing the optical resonator sitting on the active vibration isolation (AVI) system inside the transportable trolley.

To characterize the acceleration sensitivity of the NEXCERA cavity, we swept a phase-locked 698 nm laser across the resonance of the cavity while recording the cavity-transmitted laser power. Simultaneously, we used the active vibration isolation as a shaker by driving it with a sinusoidal signal at frequencies of 5 Hz, 7 Hz, 10 Hz, and 15 Hz, and measured the excited vibrations on the cavity breadboard with a 731A accelerometer amplified by a P31 amplifier from Wilcoxon Sensing Technologies.

The acceleration sensitivities for all three directions as well as the total acceleration sensitivity calculated as the root-mean-squared (RMS) value of the three sensitivities are plotted in Fig. 1.11. The directions of horizontal vibrations, H1 and H2, are defined with respect to the AVI mounts (see Fig. 1.10). The acceleration sensitivities of the cavity in all three directions are in the range of low to mid $10^{-10}g^{-1}$ for all frequencies, which are comparable to state-of-the-art room temperature optical cavity [26]. These acceleration sensitivities are obtained by placing the Viton ball mounts at its nominal vibration-insensitive support points. The acceleration sensitivities of the cavity can potentially be reduced to the level of $10^{-11}g^{-1}$ by optimizing the positions of the Viton balls that hold the optical cavity.

A Toptica DLPro 698 nm laser is locked to the NEXCERA cavity via the Pound-Drever-Hall (PDH) scheme. An initial characterization of the laser frequency stability was done using a frequency comb phase-locked to a 1064 nm reference laser with a frequency instability of 3×10^{-15}. The fractional laser frequency instability was found to be 5.1×10^{-15} at 1 s averaging time that averages down to a minimum of 2.5×10^{-15} at 100 s averaging time. Fig. 1.12 shows the results of the characterization of the laser frequency instability. The observed beat note instability is limited by the instability of the reference laser. Assuming a mechanical loss of 3×10^{-5} measured in Sec. 1.4.1 and using the evaluation method from Numata *et al.*[42], the thermal noise of the N117B 30 cm NEXCERA cavity is evaluated to be 2×10^{-16}. This suggests that an improvement of a factor of 10 may be possible for the N117B cavity.

The temperature of zero coefficient thermal expansion (ZCTE) is found to lie within the range of 17.6 to 17.7 °C.

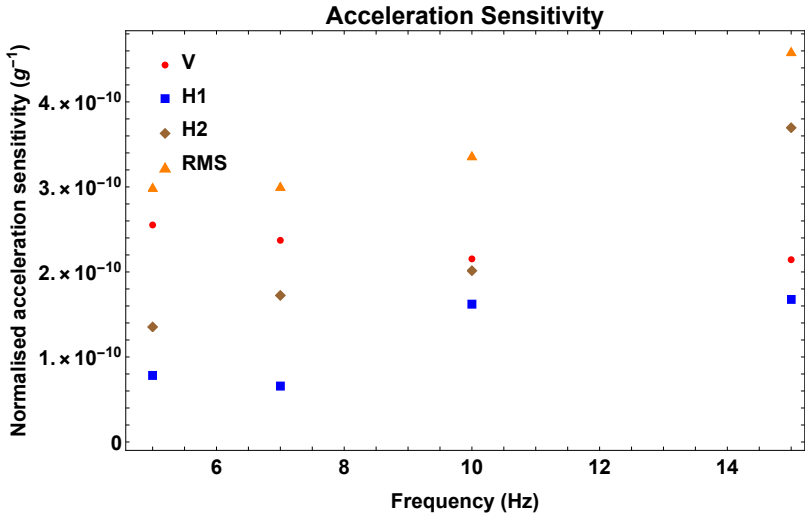


Figure 1.11. Acceleration sensitivities of the N117B NEXCERA cavity along the three spatial axes and the RMS acceleration sensitivity.

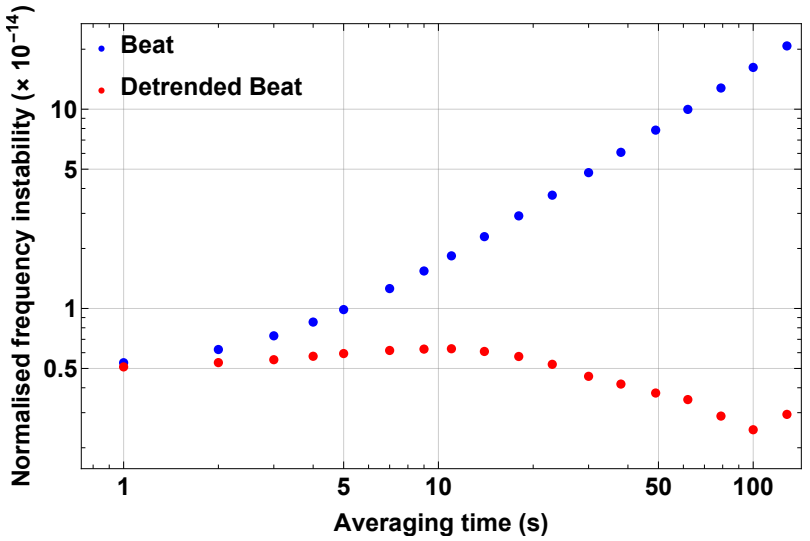


Figure 1.12. Fractional 698 nm laser frequency instability locked to the 30 cm N117B NEXCERA cavity.

N118C NEXCERA cavity

This cavity comprises two ultra-high finesse $\left(7 \times 10^5\right)$ fused silica mirrors, optimized for a wavelength of 1.5 μm, which have been optically contacted to a 12 cm long NEXCERA spacer that includes ULE compensation rings [43]. With a mechanical loss of 3×10^{-5} for the spacer material, this configuration has a predicted thermal noise floor of approximately 3×10^{-16}. The resonator assembly is oriented vertically within a vacuum chamber, that is actively stabilized to maintain a constant temperature. Previous work on this cavity spacer with a different mirror configuration has been shown in [44], including ZCTE and drift rate characterization.

To lock the laser frequency to the resonator, the PDH technique is utilized. Additionally, several noise reduction strategies are employed, including active vibration isolation and power stabilization, to minimize disturbances. Measurements determined the ZCTE temperature to be 17.8°C.

Linewidth characterization was performed using beat note analysis with a 1064 nm ULE-

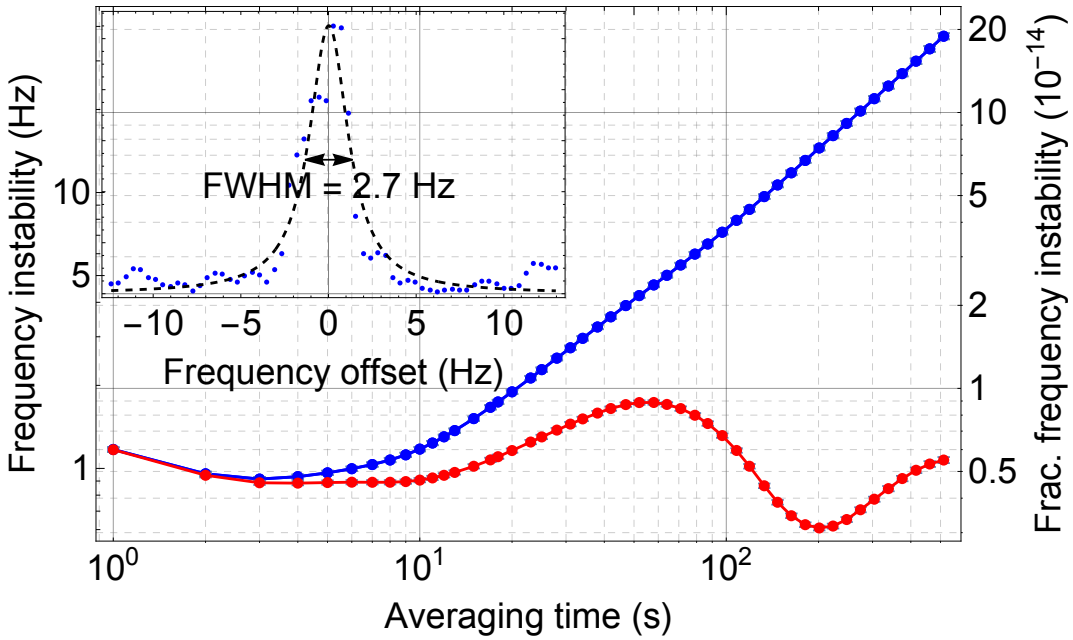


Figure 1.13. Performance of the short NEXCERA (N118C) resonator: The blue data represents the measurement of the beat-note with another ultra stable laser. The red curve shows the Allan deviation after subtracting a linear drift of the raw data.

stabilized reference laser and a frequency comb, while the Allan deviation was evaluated through a direct beat measurement with another 1.5 µm ULE-stabilized laser. Representative data is shown in Fig. 1.13. The Allan deviation remains below 1×10^{-14} for averaging times ranging from 1 second to 500 seconds, reaching a minimum of 3×10^{-15} at an averaging time of 200 seconds. Detrending of resonator drifts was performed for this analysis. This level provides another upper limit for the thermal noise; the actual level is limited by the reference laser instability. The linewidth of the beat-note is approximately 3 Hz. Long-term stability assessment revealed that the resonator drift is less than 3 mHz per second over 110 days. This is an outstanding value.

1.5 Compact cavities with large spot size on mirror

Based on the fluctuation-dissipation theorem, Brownian thermal noise depends on temperature T, mechanical loss ϕ, and the laser beam spot radius w on the coating's surface $S^{Br}_{x,ct} \sim \phi T/w^2$. To reduce Brownian noise, one can look for substrates and coatings with a lower ϕ or lower the operational temperature (as demonstrated with SCS and sapphire cavities [45, 46]). We propose an alternative method for reducing thermal noise by increasing the beam spot on mirrors using a convex-concave mirror configuration. We demonstrate the feasibility and advantages of using a cavity with a radius of curvature (ROC) ranging from 20 m to -25 m for 10 cm and 30 cm long cavity spacers. This approach significantly reduces both the coatings' and substrate's thermal noises as well as thermoelastic and thermo-optic noises, compared to the usual ROCs and plano-concave design. Fig. 1.14 shows the conceptual scheme of placing the convex-concave configuration in comparison to the typical plano-concave with respect to the Gaussian beam and its wavefront curvature. In Fig. 1.14, the increase in the beam spot size on the mirror is visible. Unlike plano-concave or concave-concave configuration waist is placed outside the cavity.

Bibliography

[1] M. Schioppo, J. Kronjäger, A. Silva, R. Ilieva, J. W. Paterson, C. F. A. Baynham, W. Bowden, I. R. Hill, R. Hobson, A. Vianello, M. Dovale-Álvarez, R. A. Williams, G. Marra, H. S. Margolis, A. Amy-Klein, O. Lopez, E. Cantin, H. Álvarez-Martínez, R. Le Targat, P. E. Pottie, N. Quintin, T. Legero, S. Häfner, U. Sterr, R. Schwarz, S. Dörscher, C. Lisdat, S. Koke, A. Kuhl, T. Waterholter, E. Benkler, and G. Grosche, *Comparing ultrastable lasers at* 7×10^{-17} *fractional frequency instability through a 2220 km optical fibre network*, Nature Commun. **13**, 212 (2022).

[2] D. Nicolodi, B. Argence, W. Zhang, R. Le Targat, G. Santarelli, and Y. Le Coq, *Spectral purity transfer between optical wavelengths at the* 10^{-18} *level*, Nature Photonics **8**, 219–223 (2014).

[3] E. Benkler, B. Lipphardt, T. Puppe, R. Wilk, F. Rohde, and U. Sterr, *End-to-end topology for fiber comb based optical frequency transfer at the* 10^{-21} *level*, Opt. Express **27**, 36886–36902 (2019), also see erratum [125].

[4] P. Li, A. Rolland, J. Jiang, and M. E. Fermann, *Coherent frequency transfer with* $< 5 \times 10^{-21}$ *stability via a multi-branch comb with noise cancellation*, Opt. Express **30**, 22957–22962 (2022).

[5] X. Xie, R. Bouchand, D. Nicolodi, M. Giunta, W. Hänsel, M. Lezius, A. Joshi, S. Datta, C. Alexandre, M. Lours, P.-A. Tremblin, G. Santarelli, R. Holzwarth, and Y. Le Coq, *Photonic microwave signals with zeptosecond level absolute timing noise*, Nature Photonics **11**, 44–47 (2017).

[6] S. Origlia, M. S. Pramod, S. Schiller, Y. Singh, K. Bongs, R. Schwarz, A. Al-Masoudi, S. Dörscher, S. Herbers, S. Häfner, U. Sterr, and C. Lisdat, *Towards an optical clock for space: Compact, high-performance optical lattice clock based on bosonic atoms*, Phys. Rev. A **98**, 053443 (2018).

[7] W. R. Milner, J. M. Robinson, C. J. Kennedy, T. Bothwell, D. Kedar, D. G. Matei, T. Legero, U. Sterr, F. Riehle, H. Leopardi, T. M. Fortier, J. A. Sherman, J. Levine, J. Yao, J. Ye, and E. Oelker, *Demonstration of a timescale based on a stable optical carrier*, Phys. Rev. Lett. **123**, 173201 (2019).

[8] S. Herbers, S. Häfner, S. Dörscher, T. Lücke, U. Sterr, and C. Lisdat, *Transportable clock laser system with an instability of* 1.6×10^{-16}, Opt. Lett. **47**, 5441–5444 (2022).

[9] D. G. Matei, T. Legero, S. Häfner, C. Grebing, R. Weyrich, W. Zhang, L. Sonderhouse, J. M. Robinson, J. Ye, F. Riehle, and U. Sterr, 1.5 μm *lasers with sub-10 mHz linewidth*, Phys. Rev. Lett. **118**, 263202 (2017).

[10] G. M. Harry, H. Armandula, E. Black, D. R. M. Crooks, G. Cagnoli, J. Hough, P. Murray, S. Reid, S. Rowan, P. Sneddon, M. M. Fejer, R. Route, and S. D. Penn, *Thermal noise from optical coatings in gravitational wave detectors*, Appl. Opt. **45**, 1569–1574 (2006).

[11] M. Granata, A. Amato, G. Cagnoli, M. Coulon, J. Degallaix, D. Forest, L. Mereni, C. Michel, L. Pinard, B. Sassolas, and J. Teillon, *Progress in the measurement and reduction of thermal noise in optical coatings for gravitational-wave detectors*, Appl. Opt. **59**, A229–A235 (2020).

[12] D. Kedar, J. Yu, E. Oelker, A. Staron, W. R. Milner, J. M. Robinson, T. Legero, F. Riehle, U. Sterr, and J. Ye, *Frequency stability of cryogenic silicon cavities with semiconductor crystalline coatings*, Optica **10**, 464–470 (2023).

[13] J. Yu, S. Häfner, T. Legero, S. Herbers, D. Nicolodi, C. Y. Ma, F. Riehle, U. Sterr, D. Kedar, J. M. Robinson, E. Oelker, and J. Ye, *Excess noise and photoinduced effects in highly reflective crystalline mirror coatings*, Phys. Rev. X **13**, 041002 (2023).

[14] Y. Levin, *Internal thermal noise in the LIGO test masses: A direct approach*, Phys. Rev. D **57**, 659–663 (1998).

[15] H. B. Callen and T. A. Welton, *Irreversibility and generalized noise*, Phys. Rev. **83**, 34–40 (1951).

[16] R. Kubo, *The fluctuation-dissipation theorem*, Rep. Prog. Phys. **29**, 255–284 (1966).

[17] M. Abdel-Hafiz, P. Ablewski, A. Al-Masoudi, H. Álvarez Martínez, P. Balling, G. Barwood, E. Benkler, M. Bober, M. Borkowski, W. Bowden, R. Ciuryło, H. Cybulski, A. Didier, M. Doležal, S. Dörscher, S. Falke, R. M. Godun, R. Hamid, I. R. Hill, R. Hobson, N. Huntemann, Y. Le Coq, R. Le Targat, T. Legero, T. Lindvall, C. Lisdat, J. Lodewyck, H. S. Margolis, T. E. Mehlstäubler, E. Peik, L. Pelzer, M. Pizzocaro, B. Rauf, A. Rolland, N. Scharnhorst, M. Schioppo, P. O. Schmidt, R. Schwarz, Ç. Şenel, N. Spethmann, U. Sterr, C. Tamm, J. W. Thomsen, A. Vianello, and M. Zawada, Guidelines for developing optical clocks with 10^{-18} fractional frequency uncertainty, arXiv:1906.11495 [physics.atom-ph] (2019).

[18] J. A. Boyd and T. Lahaye, *A basic introduction to ultrastable optical cavities for laser stabilization*, Am. J. Phys. **92**, 50–58 (2024).

[19] I. Ito, A. Silva, T. Nakamura, and Y. Kobayashi, *Stable CW laser based on low thermal expansion ceramic cavity with 4.9 mHz/s frequency drift*, Opt. Express **25**, 26020–26028 (2017).

[20] G. D. Cole, W. Zhang, M. J. Martin, J. Ye, and M. Aspelmeyer, *Tenfold reduction of Brownian noise in optical interferometry*, Nature Photonics **7**, 644–650 (2013).

[21] G. D. Cole, S. Ballmer, G. Billingsley, S. B. Cataño Lopez, M. Fejer, P. Fritschel, A. M. Gretarsson, G. M. Harry, D. Kedar, T. Legero, C. Makarem, S. D. Penn, D. Reitze, J. Steinlechner, U. Sterr, S. Tanioka, G. W. Truong, J. Ye, and J. Yu, *Substrate-transferred GaAs/AlGaAs crystalline coatings for gravitational-wave detectors*, Appl. Phys. Lett. **122**, 110502 (2023).

[22] G. D. Cole, *Cavity optomechanics with low-noise crystalline mirrors*, in *Optical Trapping and Optical Micromanipulation IX*, Proc. SPIE, Vol. 8458 (SPIE, 2012) p. 845807.

[23] S. D. Penn, M. M. Kinley-Hanlon, I. A. O. MacMillan, P. Heu, D. Follman, C. Deutsch, G. D. Cole, and G. M. Harry, *Mechanical ringdown studies of large-area substrate-transferred GaAs/AlGaAs crystalline coatings*, J. Opt. Soc. Am. B **36**, C15–C21 (2019).

[24] K. Yamamoto, S. Miyoki, T. Uchiyama, H. Ishitsuka, M. Ohashi, K. Kuroda, T. Tomaru, N. Sato, T. Suzuki, T. Haruyama, A. Yamamoto, T. Shintomi, K. Numata, K. Waseda, K. Ito, and K. Watanabe, *Measurement of the mechanical loss of a cooled reflective coating for gravitational wave detection*, Phys. Rev. D **74**, 022002 (2006).

[25] J. M. Robinson, E. Oelker, W. R. Milner, D. Kedar, W. Zhang, T. Legero, D. G. Matei, S. Häfner, F. Riehle, U. Sterr, and J. Ye, *Thermal noise and mechanical loss of SiO_2/Ta_2O_5 optical coatings at cryogenic temperatures*, Opt. Lett. **46**, 592–595 (2021).

[26] S. Häfner, S. Falke, C. Grebing, S. Vogt, T. Legero, M. Merimaa, C. Lisdat, and U. Sterr, 8×10^{-17} *fractional laser frequency instability with a long room-temperature cavity*, Opt. Lett. **40**, 2112–2115 (2015).

[27] T. Legero, T. Kessler, and U. Sterr, *Tuning the thermal expansion properties of optical reference cavities with fused silica mirrors*, J. Opt. Soc. Am. B **27**, 914–919 (2010).

[28] A. Farsi, M. Siciliani de Cumis, F. Marino, and F. Marin, *Photothermal and thermo-refractive effects in high reflectivity mirrors at room and cryogenic temperature*, J. Appl. Phys. **111**, 043101 (2012).

[29] C. Y. Ma, J. Yu, T. Legero, S. Herbers, D. Nicolodi, M. Kempkes, F. Riehle, D. Kedar, J. M. Robinson, J. Ye, and U. Sterr, *Ultrastable lasers: investigations of crystalline mirrors and closed cycle cooling at 124 K*, J. Phys.: Conf. Ser. **2889**, 012055 (2024).

[30] X.-Q. Zhu, X.-Y. Cui, D.-Q. Kong, H.-W. Yu, X. Jiang, P. Xu, H.-N. Dai, Y.-A. Chen, and J.-W. Pan, *Photo-birefringent effects of crystalline coatings in ultra-stable cavities*, in *Fourteenth International Conference on Information Optics and Photonics (CIOP 2023)*, Vol. 12935, edited by Y. Yang, International Society for Optics and Photonics (SPIE, 2023) p. 1293541.

[31] B. Kraus, *A highly stable UV clock laser*, Ph.D. thesis, QUEST-Leibniz-Forschungsschule der Gottfried Wilhelm Leibniz Universität Hannover (2023).

[32] G. D. Cole, W. Zhang, B. J. Bjork, D. Follman, P. Heu, C. Deutsch, L. Sonderhouse, J. Robinson, C. Franz, A. Alexandrovski, M. Notcutt, O. H. Heckl, J. Ye, and M. Aspelmeyer, *High-performance near- and mid-infrared crystalline coatings*, Optica **3**, 647–656 (2016).

[33] L. W. Perner, G. Winkler, G.-W. Truong, G. Zhao, D. Bachmann, A. S. Mayer, J. Fellinger, D. Follman, P. Heu, C. Deutsch, D. M. Bailey, H. Peelaers, S. Puchegger, A. J. Fleisher, G. D. Cole, and O. H. Heckl, *Mid-infrared interference coatings with excess optical loss below 10 ppm: erratum*, Optica **11**, 619–620 (2024).

[34] B. Monemar, K. K. Shih, and G. D. Pettit, *Some optical properties of the $Al_xGa_{1-x}As$ alloys system*, J. Appl. Phys. **47**, 2604–2613 (1976).

[35] M. D. Sturge, *Optical absorption of gallium arsenide between 0.6 and 2.75 eV*, Phys. Rev. **127**, 768–773 (1962).

[36] J. A. Hutchby and R. L. Fudurich, *Theoretical analysis of $Al_xGa_{1-x}As$-GaAs graded band-gap solar cell*, J. Appl. Phys. **47**, 3140–3151 (2008).

[37] J. Dickmann, C. Rojas Hurtado, R. Nawrodt, and S. Kroker, *Influence of polarization and material on Brownian thermal noise of binary grating reflectors*, Phys. Lett. A **382**, 2275–2281 (2018).

[38] F. Brückner, D. Friedrich, T. Clausnitzer, M. Britzger, O. Burmeister, K. Danzmann, E.-B. Kley, A. Tünnermann, and R. Schnabel, *Realization of a monolithic high-reflectivity cavity mirror from a single silicon crystal*, Phys. Rev. Lett. **104**, 163903 (2010).

[39] Krosaki Harima Corporation, Ceramics Division, NEXCERA ultra low thermal expansion ceramics (2023).

[40] E. Cesarini, M. Lorenzini, E. Campagna, F. Martelli, F. Piergiovanni, F. Vetrano, G. Losurdo, and G. Cagnoli, *A "gentle" nodal suspension for measurements of the acoustic attenuation in materials*, Rev. Sci. Instrum. **80**, 053904 (2009).

[41] N. Wagner, M. Narożnik, M. Bober, S. Sauer, M. Zawada, and S. Kroker, Mechanical losses and stability performance of NEXCERA in ultra-stable laser cavities, arXiv:2409.14120 [physics.optics] (2024).

[42] K. Numata, A. Kemery, and J. Camp, *Thermal-noise limit in the frequency stabilization of lasers with rigid cavities*, Phys. Rev. Lett. **93**, 250602 (2004).

[43] M. R. Schenkel, V. A. Vogt, and S. Schiller, *Metrology-grade spectroscopy source based on an optical parametric oscillator*, Opt. Express **32**, 43350–43365 (2024).

[44] C. J. Kwong, M. G. Hansen, J. Sugawara, and S. Schiller, *Characterization of the long-term dimensional stability of a NEXCERA block using the optical resonator technique*, Meas. Sci. Technol. **29**, 075011 (2018).

[45] W. Zhang, J. M. Robinson, L. Sonderhouse, E. Oelker, C. Benko, J. L. Hall, T. Legero, D. G. Matei, F. Riehle, U. Sterr, and J. Ye, *Ultrastable silicon cavity in a continuously operating closed-cycle cryostat at 4 K*, Phys. Rev. Lett. **119**, 243601 (2017).

[46] S. Schiller, C. Lämmerzahl, H. Müller, C. Braxmaier, S. Herrmann, and A. Peters, *Experimental limits for low-frequency space-time fluctuations from ultrastable optical resonators*, Phys. Rev. D **69**, 027504 (2004).

[47] H. Wang, M. Dovale-Álvarez, C. Collins, D. D. Brown, M. Wang, C. M. Mow-Lowry, S. Han, and A. Freise, *Feasibility of near-unstable cavities for future gravitational wave detectors*, Phys. Rev. D **97**, 022001 (2018).

[48] R. Hauck, H. Kortz, and H. Weber, *Misalignment sensitivity of optical resonators*, Appl. Opt. **19**, 598–601 (1980).

[49] A. E. Siegman, *Lasers* (University science books, 1986).

[50] M. D. Álvarez, *Optical cavities for optical atomic clocks, atom interferometry and gravitational-wave detection* (Springer, 2019).

[51] S. Amairi, T. Legero, T. Kessler, U. Sterr, J. B. Wübbena, O. Mandel, and P. O. Schmidt, *Reducing the effect of thermal noise in optical cavities*, Applied Physics B **113**, 233–242 (2013).

[52] M. J. Thorpe, L. Rippe, T. M. Fortier, M. S. Kirchner, and T. Rosenband, *Frequency stabilization to* 6×10^{-16} *via spectral-hole burning*, Nature Photonics **5**, 688–693 (2011).

[53] N. Wagner, J. Dickmann, B. Fang, M. T. Hartman, and S. Kroker, Temperature-dependent mechanical losses of Eu^{3+}:Y_2SiO_5 for spectral hole burning laser stabilization, arXiv:2409.14126 [physics.optics] (2024).

Bibliography

[1] A. L. Schawlow, C. H. Townes, Infrared and Optical Masers, Phys. Rev. 112 (1958) 1940–1949. doi:10.1103/PhysRev.112.1940.

[2] T. Maiman, Stimulated Optical Radiation in Ruby, Nature 187 (1960) 493. doi:10.1038/187493a0.

[3] T. S. Jaseja, A. Javan, J. Murray, C. H. Townes, Test of Special Relativity or of the Isotropy of Space by Use of Infrared Masers, Phys. Rev. 133 (1964) A1221–A1225. doi:10.1103/PhysRev.133.A1221.

[4] Fox, A. G. and Li, Tingye, Resonant modes in a maser interferometer, The Bell System Technical Journal 40 (2) (1961) 453–488. doi:10.1002/j.1538-7305.1961.tb01625.x.

[5] R. W. P. Drever, J. L. Hall, F. V. Kowalski, J. Hough, G. M. Ford, A. J. Munley, H. Ward, Laser phase and frequency stabilization using an optical resonator, Appl. Phys. B 31 (1983) 97. doi:doi.org/10.1007/BF00702605.

[6] C. Eisele, A. Nevsky, S. Schiller, A laboratory test of the isotropy of light propagation at the 10^{-17} level, Phys. Rev. Lett. 103 (2009) 090401. doi:10.1103/PhysRevLett.103.090401.

[7] A. Abramovici, W. E. Althouse, R. W. P. Drever, Y. Gürsel, S. Kawamura, F. J. Raab, D. Shoemaker, L. Sievers, R. E. Spero, K. S. Thorne, R. E. Vogt, R. Weiss, S. E. Whitcomb, M. E. Zucker, LIGO: The Laser Interferometer Gravitational-Wave Observatory, Science 256 (5055) (1992) 325–333. doi:10.1126/science.256.5055.325.

[8] B. P. Abbott et al., LIGO: the Laser Interferometer Gravitational-Wave Observatory, Reports on Progress in Physics 72 (7) (2009) 076901. doi:10.1088/0034-4885/72/7/076901.

[9] P. Kwee, C. Bogan, K. Danzmann, M. Frede, H. Kim, P. King, J. Pöld, O. Puncken, R. L. Savage, F. Seifert, P. Wessels, L. Winkelmann, B. Willke, Stabilized high-power laser system for the gravitational wave detector advanced LIGO, Opt. Express 20 (10) (2012) 10617–10634. doi:10.1364/OE.20.010617.

[10] B. P. Abbott et al., Observation of Gravitational Waves from a Binary Black Hole Merger, Phys. Rev. Lett. 116 (2016) 061102. doi:10.1103/PhysRevLett.116.061102.

[11] B. P. Abbott et al., GW170817: Observation of Gravitational Waves from a Binary Neutron Star Inspiral, Phys. Rev. Lett. 119 (2017) 161101. doi:10.1103/PhysRevLett.119.161101.

[12] T. Accadia et al., Virgo: a laser interferometer to detect gravitational waves, Journal of Instrumentation 7 (03) (2012) P03012. doi:10.1088/1748-0221/7/03/P03012.

[13] F. Acernese et al, Advanced virgo: a second-generation interferometric gravitational wave detector, Classical and Quantum Gravity 32 (2) (2014) 024001. doi:10.1088/0264-9381/32/2/024001.

[14] T. Akutsu et al., KAGRA: 2.5 generation interferometric gravitational wave detector, Nature Astronomy 3 (1) (2019) 35–40. doi:10.1038/s41550-018-0658-y.

[15] P. Amaro-Seoane et al., Laser Interferometer Space Antenna (2017). doi:10.48550/arXiv.1702.00786.

[16] M. Takamoto, I. Ushijima, N. Ohmae, T. Yahagi, K. Kokado, H. Shinkai, H. Katori, Test of general relativity by a pair of transportable optical lattice clocks, Nature Photonics 14 (7) (2020) 411–415. doi:10.1038/s41566-020-0619-8.

[17] S. Schiller et al., Optical Clocks in Space, Nuclear Physics B - Proceedings Supplements 166 (2007) 300–302, proceedings of the Third International Conference on Particle and Fundamental Physics in Space. doi:10.1016/j.nuclphysbps.2006.12.032.

[18] C. W. Chou, D. B. Hume, J. C. J. Koelemeij, D. J. Wineland, T. Rosenband, Frequency Comparison of Two High-Accuracy Al^+ Optical Clocks, Phys. Rev. Lett. 104 (2010) 070802. doi:10.1103/PhysRevLett.104.070802.

[19] J. Müller, D. Dirkx, S. M. Kopeikin, G. Lion, I. Panet, G. Petit, P. N. A. M. Visser, High Performance Clocks and Gravity Field Determination, Space Science Reviews 214 (1) (2017) 5. doi:10.1007/s11214-017-0431-z.

[20] T. E. Mehlstäubler, G. Grosche, C. Lisdat, P. O. Schmidt, H. Denker, Atomic clocks for geodesy, Reports on Progress in Physics 81 (6) (2018) 064401. doi:10.1088/1361-6633/aab409.

[21] J. Millo, M. Abgrall, M. Lours, E. M. L. English, H. Jiang, J. Guena, A. Clairon, M. E. Tobar, S. Bize, Y. Le Coq, G. Santarelli, Ultralow noise microwave generation with fiber-based optical frequency comb and application to atomic fountain clock, Applied Physics Letters 94 (14) (2009) 141105. doi:10.1063/1.3112574.

[22] B. J. Bloom, T. L. Nicholson, J. R. Williams, S. L. Campbell, M. Bishof, X. Zhang, W. Zhang, S. L. Bromley, J. Ye, An optical lattice clock with accuracy and stability at the 10^{-18} level, Nature 506 (7486) (2014) 71. doi:10.1038/nature12941.

[23] C. Grebing, A. Al-Masoudi, S. Dörscher, S. Häfner, V. Gerginov, S. Weyers, B. Lipphardt, F. Riehle, U. Sterr, C. Lisdat, Realization of a timescale with an accurate optical lattice clock, Optica 3 (6) (2016) 563–569. doi:10.1364/OPTICA.3.000563.

[24] W. F. McGrew, X. Zhang, R. J. Fasano, S. A. Schäffer, K. Beloy, D. Nicolodi, R. C. Brown, N. Hinkley, G. Milani, M. Schioppo, T. H. Yoon, A. D. Ludlow, Atomic clock performance enabling geodesy below the centimetre level, Nature 564 (7734) (2018) 87–90. doi:10.1038/s41586-018-0738-2.

[25] A. Aeppli, K. Kim, W. Warfield, M. S. Safronova, J. Ye, Clock with 8×10^{-19} Systematic Uncertainty, Phys. Rev. Lett. 133 (2024) 023401. doi:10.1103/PhysRevLett.133.023401.

[26] G. W. Hoth, J. A. Sherman, A. G. Radnaev, P. Mitchell, V. Gerginov, NIST-F3, a cesium fountain frequency reference, Tech. rep., National Institute of Standards and Technology (2023).

[27] Physikalisch-Technische Bundesanstalt, The primary clocks CS1 and CS2 of PTB, accessed: 2025-06-16 (2025).

[28] Observatoire de Paris, The atomic fountains, accessed: 2025-06-16 (2025).

[29] C. Eisele, M. Okhapkin, A. Y. Nevsky, S. Schiller, A crossed optical cavities apparatus for a precision test of the isotropy of light propagation, Opt. Commun. 281 (2008) 1189. doi:10.1016/j.optcom.2007.10.071.

[30] C. Eisele, A precision test of Lorentz Invariance using room-temperature high-finesse optical resonators, Ph.D. thesis, Heinrich-Heine-Universität Düsseldorf (2009).

[31] S. Alighanbari, M. G. Hansen, V. I. Korobov, S. Schiller, Rotational spectroscopy of cold and trapped molecular ions in the Lamb-Dicke regime, Nat. Phys. 14 (2018) 555. doi:10.1038/s41567-018-0074-3.

[32] S. Alighanbari, G. S. Giri, F. L. Constantin, V. I. Korobov, S. Schiller, Precise test of quantum electrodynamics and determination of fundamental constants with HD^+ ions, Nature 581 (2020) 152 – 158. doi:10.1038/s41586-020-2261-5.

[33] I. V. Kortunov, S. Alighanbari, M. G. Hansen, G. S. Giri, V. I. Korobov, S. Schiller, Proton-electron mass ratio by high-resolution optical spectroscopy of ion ensembles in the resolved-carrier regime, Nat. Phys. 17 (2021) 569–573. doi:10.1038/s41567-020-01150-7.

[34] S. Alighanbari, I. V. Kortunov, G. S. Giri, S. Schiller, Test of charged baryon interaction with high-resolution vibrational spectroscopy of molecular hydrogen ions, Nature Physics 19 (2023) 1263–1269. doi:10.1038/s41567-023-02088-2.

[35] M. R. Schenkel, S. Alighanbari, S. Schiller, Laser spectroscopy of a rovibrational transition in the molecular hydrogen ion H_2^+, Nature Physics 20 (2024) 383–388. doi:10.1038/s41567-023-02320-z.

[36] R. Oswald, A. Nevsky, V. Vogt, S. Schiller, N. Figueroa, K. Zhang, O. Tretiak, D. Antypas, D. Budker, A. Banerjee, G. Perez, Search for Dark-Matter-Induced Oscillations of Fundamental Constants Using Molecular Spectroscopy, Physical Review Letters 129 (2022) 031302. doi:10.1103/PhysRevLett.129.031302.

[37] R. Oswald, V. Vogt, S. Schiller, Search for oscillating fundamental constants using a paired detector and vibrational spectroscopy, Phys. Rev. D 111 (2025) 055003. doi:10.1103/PhysRevD.111.055003.

[38] S. Schiller et al., The space optical clocks project: Development of high-performance transportable and breadboard optical clocks and advanced subsystems, in: European Frequency and Time Forum (EFTF), 2012, 2012, pp. 412–418. doi:10.1109/EFTF.2012.6502414.

[39] S. Origlia et al., Development of a strontium optical lattice clock for the soc mission on the iss, Proc. SPIE 9900, Quantum Optics, 990003 (2016). doi:10.1117/12.2229473.

[40] S. Origlia, M. S. Pramod, S. Schiller, Y. Singh, K. Bongs, R. Schwarz, A. Al-Masoudi, S. Dörscher, S. Herbers, S. Häfner, U. Sterr, C. Lisdat, Towards an optical clock for space: Compact, high-performance optical lattice clock based on bosonic atoms, Phys. Rev. A 98 (2018) 053443. doi:10.1103/PhysRevA.98.053443.

[41] S. Alighanbari, M. R. Schenkel, V. I. Korobov, S. Schiller, to appear.

[42] H. Dehmelt, Economic synthesis and precision spectroscopy of anti-molecular hydrogen ions in Paul trap, Physica Scripta T59 (1995) 423–423. doi:10.1088/0031-8949/1995/t59/060.

[43] E. G. Myers, CPT tests with the antihydrogen molecular ion, Phys. Rev. A 98 (2018) 010101. doi:10.1103/PhysRevA.98.010101.

[44] S. Schiller, Precision spectroscopy of molecular hydrogen ions: an introduction, Contemporary Physics 63 (2022) 247–279. doi:10.1080/00107514.2023.2180180.

[45] H. Schnitzler, Development of an experiment for trapping, cooling, and spectroscopy of molecular hydrogen ions, Ph.D. thesis, Universität Konstanz (2001).

[46] S. Alighanbari, Frequency metrology of HD^+ by ultra-high resolution rotational spectroscopy, Ph.D. thesis, Heinrich-Heine-Universität Düsseldorf (2021).

[47] M. Haidar, Hyperfine structure in the hydrogen molecular ions, Ph.D. thesis, Université Sorbonne.

[48] M. R. Schenkel, to appear, Ph.D. thesis, Heinrich-Heine-Universität Düsseldorf (2025).

[49] S. Patra, M. Germann, J.-P. Karr, M. Haidar, L. Hilico, V. I. Korobov, F. M. J. Cozijn, K. S. E. Eikema, W. Ubachs, J. C. J. Koelemeij, Proton-electron mass ratio from laser spectroscopy of HD^+ at the part-per-trillion level, Science 369 (2020) 1238–1241. doi:10.1126/science.aba0453.

[50] C. W. Chou, A. L. Collopy, C. Kurz, Y. Lin, M. E. Harding, P. N. Plessow, T. Fortier, S. Diddams, D. Leibfried, D. R. Leibrandt, Frequency-comb spectroscopy on pure quantum states of a single molecular ion, Science 367 (2020) 1458–1461. doi:10.1126/science.aba3628.

[51] F. Zwicky, Die Rotverschiebung von extragalaktischen Nebeln, Helvetica Physica Acta 6 (1933) 110–127.

[52] V. C. Rubin, W. K. Ford, Jr., Rotation of the Andromeda Nebula from a Spectroscopic Survey of Emission Regions, Astrophysical Journal 159 (1970) 379. doi:10.1086/150317.

[53] W. Sutherland, Gravitational microlensing—A report on the MACHO project, Rev. Mod. Phys. 71 (1999) 421–434. doi:10.1103/RevModPhys.71.421.

[54] L. Roszkowski, E. M. Sessolo, S. Trojanowski, WIMP dark matter candidates and searches–current status and future prospects, Reports on Progress in Physics 81 (6) (2018) 066201. doi:10.1088/1361-6633/aab913.

[55] E. G. M. Ferreira, Ultra-light dark matter, The Astronomy and Astrophysics Review 29 (1) (2021) 7. doi:10.1007/s00159-021-00135-6.

[56] Y. K. Semertzidis, S. Youn, Axion dark matter: How to see it?, Science Advances 8 (8) (2022) eabm9928. doi:10.1126/sciadv.abm9928.

[57] J. W. Foster, N. L. Rodd, B. R. Safdi, Revealing the dark matter halo with axion direct detection, Phys. Rev. D 97 (2018) 123006. doi:10.1103/PhysRevD.97.123006.

[58] C. Hagemann, C. Grebing, T. Kessler, S. Falke, N. Lemke, C. Lisdat, H. Schnatz, F. Riehle, U. Sterr, Providing 10^{-16} short-term stability of a 1.5 μm laser to optical clocks, IEEETIM 62 (2013) 1556–1562. doi:10.1109/TIM.2013.2242597.

[59] T. Kessler, C. Hagemann, C. Grebing, T. Legero, U. Sterr, F. Riehle, M. J. Martin, L. Chen, J. Ye, A sub-40-mHz-linewidth laser based on a silicon single-crystal optical cavity, Nat. Photon. 6 (2012) 687. doi:10.1038/nphoton.2012.217.

[60] S. Häfner, S. Falke, C. Grebing, S. Vogt, T. Legero, M. Merimaa, C. Lisdat, U. Sterr, 8×10^{-17} fractional laser frequency instability with a long room-temperature cavity, Opt. Lett. 40 (9) (2015) 2112–2115. doi:10.1364/OL.40.002112.

[61] D. G. Matei, T. Legero, S. Häfner, C. Grebing, R. Weyrich, W. Zhang, L. Sonderhouse, J. M. Robinson, J. Ye, F. Riehle, U. Sterr, 1.5 μm Lasers with Sub-10 mHz Linewidth, Phys. Rev. Lett. 118 (2017) 263202. doi:10.1103/PhysRevLett.118.263202.

[62] E. Wiens, Q. Chen, I. Ernsting, H. Luckmann, A. Y. Nevsky, U. Rosowski, S. Schiller, A silicon single-crystal cryogenic optical resonator, Opt. Lett. 39 (2014) 3242–3245. doi:10.1103/PhysRevLett.117.271102.

[63] E. Wiens, A. Y. Nevsky, S. Schiller, Resonator with Ultrahigh Length Stability as a Probe for Equivalence-Principle-Violating Physics, Phys. Rev. Lett. 117 (2016) 271102. doi:10.1103/PhysRevLett.117.271102.

[64] E. Wiens, C. J. Kwong, T. Müller, S. Schiller, A simplified cryogenic optical resonator apparatus providing ultra-low frequency drift, Rev. Sci. Instrum. 91 (4) (2020) 045112. doi:10.1063/1.5140321.

[65] E. Wiens, S. Schiller, A simple and efficient passive vibration isolation system for large loads in closed-cycle cryostats, Rev. Sci. Instrum. 92 (9) (2021) 095101. doi:10.1063/5.0053381.

[66] E. Wiens, C. J. Kwong, T. Müller, K. Bongs, Y. Singh, S. Schiller, Optical frequency reference based on a cryogenic silicon resonator, Opt. Express 31 (25) (2023) 42059–42076. doi:10.1364/OE.497365.

[67] J. Barbarat et al., Guidelines for designs for ultrastable laser with 10^{-17} fractional frequency instability (2025). doi:10.48550/arXiv.2504.06213.

[68] M. R. Schenkel, V. Vogt, S. Schiller, Metrology-grade spectroscopy source based on an optical parametric oscillator, Opt. Express 32 (2024) 43350–43365. doi:10.1364/OE.538442.

[69] Q. Yang, Finesse of ring resonators, AIP Advances 13 (8) (2023) 085225. doi:10.1063/5.0157450.

[70] S. Häfner, S. Herbers, S. Vogt, C. Lisdat, U. Sterr, Transportable interrogation laser system with an instability of mod $\sigma_y = 3\times10^{-16}$, Opt. Express 28 (11) (2020) 16407–16416. doi:10.1364/OE.390105.

[71] C. Hagemann, C. Grebing, C. Lisdat, S. Falke, T. Legero, U. Sterr, F. Riehle, M. J. Martin, J. Ye, Ultrastable laser with average fractional frequency drift rate below 5×10^{-19}/s, Opt. Lett. 39 (17) (2014) 5102–5105. doi:10.1364/OL.39.005102.

[72] Q.-F. Chen, A. Nevsky, M. Cardace, S. Schiller, T. Legero, S. Häfner, A. Uhde, U. Sterr, A compact, robust, and transportable ultra-stable laser with a fractional frequency instability of 1×10^{-15}, Rev. Sci. Instrum. 85 (2014) 113107. doi:10.1063/1.4898334.

[73] T. Kessler, T. Legero, U. Sterr, Thermal noise in optical cavities revisited, J. Opt. Soc. Am. B 29 (1) (2012) 178–184. doi:10.1364/JOSAB.29.000178.

[74] J. Zhang, Y. Luo, B. Ouyang, K. Deng, Z. Lu, J. Luo, Design of an optical reference cavity with low thermal noise limit and flexible thermal expansion properties, The European Physical Journal D 67 (2) (2013) 46. doi:10.1140/epjd/e2013-30458-2.

[75] G. Xu, D. Jiao, L. Chen, L. Zhang, R. Dong, T. Liu, J. Wang, Thermal Noise in Cubic Optical Cavities, Photonics 8 (7) (2021). doi:10.3390/photonics8070261.

[76] V. Greco, F. Marchesini, G. Molesini, Optical contact and van der Waals interactions: the role of the surface topography in determining the bonding strength of thick glass plates, Journal of Optics A: Pure and Applied Optics 3 (1) (2001) 85. doi:10.1088/1464-4258/3/1/314.

[77] K. Numata, A. Kemery, J. Camp, Thermal-Noise Limit in the Frequency Stabilization of Lasers with Rigid Cavities, Phys. Rev. Lett. 93 (25) (2004) 250602. doi:10.1103/PhysRevLett.93.250602.

[78] F. Bondu, P. Hello, J.-Y. Vinet, Thermal noise in mirrors of interferometric gravitational wave antennas, Physics Letters A 246 (3) (1998) 227–236. doi:10.1016/S0375-9601(98)00450-2.

[79] K. H. Wanser, Fundamental phase noise limit in optical fibres due to temperature fluctuations, Electronics Letters 28 (1992) 53. doi:10.1049/el:19920033.

[80] L. Duan, Thermal Noise-Limited Fiber-Optic Sensing at Infrasonic Frequencies, IEEE Journal of Quantum Electronics 51 (2) (2015) 1–6. doi:10.1109/JQE.2014.2384914.

[81] J. Dong, J. Huang, T. Li, L. Liu, Observation of fundamental thermal noise in optical fibers down to infrasonic frequencies, Applied Physics Letters 108 (2) (2016) 021108. doi:10.1063/1.4939918.

[82] Thorlabs GmbH, SMF-28-100 Single Mode Fiber, accessed: 2025-05-20 (2025).

[83] E. D. Black, An introduction to Pound-Drever-Hall laser frequency stabilization, Am. J. Phys. 69 (1) (2001) 79–87. doi:10.1119/1.1286663.

[84] J. I. Thorpe, K. Numata, J. Livas, Laser frequency stabilization and control through offset sideband locking to optical cavities, Opt. Express 16 (2008) 15980–15990. doi:10.1364/OE.16.015980.

[85] A. Y. Nevsky, S. Alighanbari, Q. Chen, I. Ernsting, S. Vasilyev, S. Schiller, G. Barwood, P. Gill, N. Poli, G. M. Tino, Robust frequency stabilization of multiple spectroscopy lasers with large and tunable offset frequencies, Opt. Lett. 38 (2013) 4903–6. doi:10.1364/OL.38.004903.

[86] J. Gillot, S. F. Tetsing-Talla, S. Denis, G. Goavec-Merou, J. Millo, C. Lacroûte, Y. Kersalé, Digital control of residual amplitude modulation at the 10^{-7} level for ultra-stable lasers, Opt. Express 30 (20) (2022) 35179–35188. doi:10.1364/OE.465597.

[87] N. C. Wong, J. L. Hall, Servo control of amplitude modulation in frequency-modulation spectroscopy: demonstration of shot-noise-limited detection, J. Opt. Soc. Am. B 2 (9) (1985) 1527–1533. doi:10.1364/JOSAB.2.001527.

[88] W. Zhang, M. J. Martin, C. Benko, J. L. Hall, J. Ye, C. Hagemann, T. Legero, U. Sterr, F. Riehle, G. D. Cole, M. Aspelmeyer, Reduction of residual amplitude modulation to 1×10^{-6} for frequency modulation and laser stabilization, Opt. Lett. 39 (7) (2014) 1980–1983. doi:10.1364/OL.39.001980.

[89] J. Bi, Y. Zhi, L. Li, L. Chen, Suppressing residual amplitude modulation to the 10^{-7} level in optical phase modulation, Appl. Opt. 58 (3) (2019) 690–694. doi:10.1364/AO.58.000690.

[90] E. A. Whittaker, M. Gehrtz, G. C. Bjorklund, Residual amplitude modulation in laser electro-optic phase modulation, J. Opt. Soc. Am. B 2 (8) (1985) 1320–1326. doi:10.1364/JOSAB.2.001320.

[91] A. E. Domínguez, W. E. O. Larcher, C. N. Kozameh, Fundamental residual amplitude modulation in electro-optic modulators (2021). doi:10.48550/arXiv.1710.10719.

[92] X. Shi, J. Zhang, X. Zeng, X. Lü, K. Liu, J. Xi, Y. Ye, Z. Lu, Suppression of residual amplitude modulation effects in Pound-Drever-Hall locking, Applied Physics B 124 (8) (2018) 153. doi:10.1007/s00340-018-7021-y.

[93] M. Descampeaux, G. Feugnet, F. Bretenaker, New method for residual amplitude modulation control in fibered optical experiments, Opt. Express 29 (22) (2021) 36211–36225. doi:10.1364/OE.438879.

[94] J. Ye, S. T. Cundiff, Femtosecond Optical Frequency Comb: Principle, Operation and Applications, Springer New York, NY, 2005. doi:10.1007/b102450.

[95] W. Demtröder, Laser Spectroscopy, Basic Concepts and Instrumentation, Springer Berlin, Heidelberg, 1996. doi:10.1007/978-3-662-08260-7.

[96] A. M. Weiner, Ultrafast Optics, John Wiley & Sons, Ltd, 2009. doi:10.1002/9780470473467.

[97] L.-S. Ma, P. Jungner, J. Ye, J. L. Hall, Delivering the same optical frequency at two places: accurate cancellation of phase noise introduced by an optical fiber or other time-varying path, Optics Letters 19 (1994) 1777–1779. doi:10.1364/OL.19.001777.

[98] S. Noe, D. Husmann, N. Müller, J. Morel, A. Fichtner, Long-range fiber-optic earthquake sensing by active phase noise cancellation, Scientific Reports 13 (1) (2023) 13983. doi:10.1038/s41598-023-41161-x.

[99] A. Tofful, C. F. A. Baynham, E. A. Curtis, A. O. Parsons, B. I. Robertson, M. Schioppo, J. Tunesi, H. S. Margolis, R. J. Hendricks, J. Whale, R. C. Thompson, R. M. Godun, 171 Yb^+ optical clock with 2.2×10^{-18} systematic uncertainty and absolute frequency measurements, Metrologia 61 (4) (2024) 045001. doi:10.1088/1681-7575/ad53cd.

[100] Q. F. Chen, A. Nevsky, S. Schiller, Locking the frequency of lasers to an optical cavity at the 1.6×10^{-17} relative instability level, Applied Physics B: Lasers and Optics 107 (2012) 679–683. doi:10.1007/s00340-012-5014-9.

[101] Q. Chen, E. Magoulakis, S. Schiller, High-sensitivity crossed-resonator laser apparatus for improved tests of Lorentz invariance and of space-time fluctuations, Phys. Rev. D 93 (2016) 022003. doi:10.1103/PhysRevD.93.022003.

[102] V. A. Vogt, Construction and characterization of a resonator set-up for a next-generation Michelson-Morley experiment, Master's thesis, HHU Düsseldorf (2019).

[103] V. A. Vogt, Development of a resonator set-up for a next-generation Michelson-Morley experiment, Bachelor's thesis, HHU Düsseldorf (2017).

[104] Z. Hou, Stabilization of Laser Light to high Finesse optical Resonators, Bachelor's thesis, Heinrich-Heine-Universität Düsseldorf (2023).

[105] Corning Inc., ULE® Corning Code 7972 Ultra Low Expansion Glass, accessed: 2025-05-18 (2016).

[106] W. H. Souder, P. Hidnert, Measurements on the Thermal Expansion of Fused Silica, United States. Government Printing Office. Washington D.C., 1926.

[107] T. Legero, T. Kessler, U. Sterr, Tuning the thermal expansion properties of optical reference cavities with fused silica mirrors, J. Opt. Soc. Am. B 27 (5) (2010). doi:10.1364/JOSAB.27.000914.

[108] Corning Inc., Corning® HPFS® 7979, 7980, 8655 Fused Silica, accessed: 2025-05-18 (2016).

[109] P. F. Egan, J. A. Stone, J. H. Hendricks, J. E. Ricker, G. E. Scace, G. F. Strouse, Performance of a dual Fabry-Perot cavity refractometer, Opt. Lett. 40 (17) (2015) 3945–3948. doi:10.1364/OL.40.003945.

[110] S. Herbers, S. Häfner, S. Dörscher, T. Lücke, U. Sterr, C. Lisdat, Transportable clock laser system with an instability of 1.6×10^{-16}, Opt. Lett. 47 (20) (2022) 5441–5444. doi:10.1364/OL.470984.

[111] X.-Q. Zhu, X. Cui, D.-Q. Kong, H.-W. Yu, X.-M. Zhai, M.-Y. Zheng, X.-P. Xie, Q. Zhang, X. Jiang, X.-B. Zhang, P. Xu, H.-N. Dai, Y.-A. Chen, J.-W. Pan, An ultrastable 1397-nm laser stabilized by a crystalline-coated room-temperature cavity, Review of Scientific Instruments 95 (2024). doi:10.1063/5.0200553.

[112] Z. Wang, Z. Ma, W. Wei, J. Chang, J. Zhang, Q. Wu, W. Yuan, K. Deng, Z. Lu, J. Zhang, Noise characterization of an ultra-stable laser for optical clocks, Review of Scientific Instruments 95 (5) (2024) 053002. doi:10.1063/5.0204016.

[113] Y. Y. Jiang, A. D. Ludlow, N. D. Lemke, R. W. Fox, J. A. Sherman, L.-S. Ma, C. W. Oates, Making optical atomic clocks more stable with 10^{-16}-level laser stabilization, Nature Photonics 5 (2011) 158–161. doi:10.1038/nphoton.2010.313.

[114] T. L. Nicholson, M. J. Martin, J. R. Williams, B. J. Bloom, M. Bishof, M. D. Swallows, S. L. Campbell, J. Ye, Comparison of two independent sr optical clocks with 1×10^{-17} stability at 10^3s, Phys. Rev. Lett. 109 (2012) 230801. doi:10.1103/PhysRevLett.109.230801.

[115] G. D. Cole, W. Zhang, M. J. Martin, J. Ye, M. Aspelmeyer, Tenfold reduction of Brownian noise in high-reflectivity optical coatings, Nature Photonics 7 (644) (2013). doi:10.1038/nphoton.2013.174.

[116] G. D. Cole, W. Zhang, B. J. Bjork, D. Follman, P. Heu, C. Deutsch, L. Sonderhouse, J. Robinson, C. Franz, A. Alexandrovski, M. Notcutt, O. H. Heckl, J. Ye, M. Aspelmeyer, High-performance near- and mid-infrared crystalline coatings, Optica 3 (6) (2016) 647–656. doi:10.1364/OPTICA.3.000647.

[117] J. M. Robinson, E. Oelker, W. R. Milner, W. Zhang, T. Legero, D. G. Matei, F. Riehle, U. Sterr, J. Ye, Crystalline optical cavity at 4 k with thermal-noise-limited instability and ultralow drift, Optica 6 (2) (2019) 240–243. doi:10.1364/OPTICA.6.000240.

[118] J. Valencia, G. Iskander, N. V. Nardelli, D. R. Leibrandt, D. B. Hume, Cryogenic sapphire optical reference cavity with crystalline coatings at 1×10^{-16} fractional frequency instability, Review of Scientific Instruments 95 (10) (2024) 103002. doi:10.1063/5.0214790.

[119] I. Ito, A. Silva, T. Nakamura, Y. Kobayashi, Stable CW laser based on low thermal expansion ceramic cavity with 4.9 mHz/s frequency drift, Opt. Express 25 (21) (2017) 26020–26028. doi:10.1364/OE.25.026020.

[120] C. J. Kwong, M. G. Hansen, J. Sugawara, S. Schiller, Characterization of the long-term dimensional stability of a NEXCERA block using the optical resonator technique, Measurement Science and Technology 29 (2018) 075011. doi:10.1088/1361-6501/aac3b0.

[121] Krosaki Harima Corporation, NEXCERA^{TM} ultra low thermal expansion ceramics, accessed: 2025-05-18 (2025).

[122] P. Schulte, Implementierung eines ultrastabilen 1.5 µm-Lasersystems, Bachelor's thesis, Heinrich-Heine-Universität Düsseldorf (2022).

[123] N. Wagner, M. Narożnik, M. Bober, S. Sauer, M. Zawada, S. Kroker, Mechanical losses and stability performance of NEXCERA in ultra-stable laser cavities (2024). doi:10.48550/arXiv.2409.14120.

[124] S. Sturm, I. Arapoglou, A. Egl, M. Höcker, S. Kraemer, T. Sailer, B. Tu, A. Weigel, R. Wolf, J. C. Lopez-Urrutia, K. Blaum, The ALPHATRAP experiment, Eur. Phys. J. Spec. Top. 227 (2019) 1425–1491. doi:10.1140/epjst/e2018-800225-2.

[125] F. Heiße, M. Door, T. Sailer, P. Filianin, J. Herkenhoff, C. M. König, K. Kromer, D. Lange, J. Morgner, A. Rischka, C. Schweiger, B. Tu, Y. N. Novikov, S. Eliseev, S. Sturm, K. Blaum, High-Precision Determination of g Factors and Masses of $^{20}Ne^{9+}$ and $^{22}Ne^{9+}$, Phys. Rev. Lett. 131 (2023) 253002. doi:10.1103/PhysRevLett.131.253002.

[126] J. Morgner, B. Tu, C. M. König, T. Sailer, F. Heiße, H. Bekker, B. Sikora, C. Lyu, V. A. Yerokhin, Z. Harman, J. R. Crespo López-Urrutia, C. H. Keitel, S. Sturm, K. Blaum, Stringent test of QED with hydrogen-like tin, Nature 622 (7981) (2023) 53–57. doi:10.1038/s41586-023-06453-2.

[127] C. M. König, F. Heiße, J. Morgner, T. Sailer, B. Tu, D. Bakalov, K. Blaum, S. Schiller, S. Sturm, Nondestructive control of the rovibrational ground state of a single molecular hydrogen ion in a penning trap, Phys. Rev. Lett. 134 (2025) 163001. doi:10.1103/PhysRevLett.134.163001.

[128] J. Morgner, B. Tu, M. Moretti, C. M. König, F. Heiße, T. Sailer, V. A. Yerokhin, B. Sikora, N. S. Oreshkina, Z. Harman, C. H. Keitel, S. Sturm, K. Blaum, g Factor of Boronlike Tin, Phys. Rev. Lett. 134 (2025) 123201. doi:10.1103/PhysRevLett.134.123201.

[129] V. I. Korobov, Ro-vibrational states of H_2^+. Variational calculations, Molecular Physics 116 (2018) 93–98. doi:10.1080/00268976.2017.1367427.

[130] S. Cheon, M. Cho, Difference Frequency Generation Spectroscopy as a Vibrational Optical Activity Measurement Tool, The Journal of Physical Chemistry A 113 (11) (2009) 2438–2445, pMID: 19228046. doi:10.1021/jp809652x.

[131] E. Jaatinen, D. J. Hopper, J. Back, Residual amplitude modulation mechanisms in modulation transfer spectroscopy that use electro-optic modulators, Measurement Science and Technology 20 (2) (2008) 025302. doi:10.1088/0957-0233/20/2/025302.

[132] L. Li, F. Liu, C. Wang, L. Chen, Measurement and control of residual amplitude modulation in optical phase modulation, Review of Scientific Instruments 83 (4) (2012) 043111. doi:10.1063/1.4704084.

[133] L. Li, H. Shen, J. Bi, C. Wang, S. Lv, L. Chen, Analysis of frequency noise in ultra-stable optical oscillators with active control of residual amplitude modulation, Applied Physics B 117 (2014) 1025–1033. doi:10.1007/s00340-014-5923-x.

[134] J. Sathian, E. Jaatinen, Reducing residual amplitude modulation in electro-optic phase modulators by erasing photorefractive scatter, Opt. Express 21 (10) (2013) 12309–12317. doi:10.1364/OE.21.012309.

[135] H. Shen, L. Li, J. Bi, J. Wang, L. Chen, Systematic and quantitative analysis of residual amplitude modulation in Pound-Drever-Hall frequency stabilization, Phys. Rev. A 92 (2015) 063809. doi:10.1103/PhysRevA.92.063809.

[136] X. Dangpeng, W. Jianjun, L. Mingzhong, L. Honghuan, Z. Rui, D. Ying, D. Qinghua, H. Xiaodong, W. Mingzhe, D. Lei, T. Jun, Weak etalon effect in wave plates can introduce significant FM-to-AM modulations in complex laser systems, Opt. Express 18 (7) (2010) 6621–6627. doi:10.1364/OE.18.006621.

[137] M. Bregant, G. Cantatore, F. D. Valle, G. Ruoso, G. Zavattini, Frequency locking to a high-finesse Fabry–Perot cavity of a frequency doubled Nd:YAG laser used as the optical phase modulator, Review of Scientific Instruments 73 (12) (2002) 4142–4144. doi:10.1063/1.1519933.

[138] B. Willke, N. Uehara, E. K. Gustafson, R. L. Byer, P. J. King, S. U. Seel, R. L. Savage, Spatial and temporal filtering of a 10-W Nd:YAG laser with a Fabry–Perot ring-cavity premode cleaner, Opt. Lett. 23 (21) (1998) 1704–1706. doi:10.1364/OL.23.001704.

[139] Y. Zhang, K. Hayasaka, K. Kasai, Efficient noise suppression of an amplified diode-laser by optical filtering and resonant optical feedback, Applied Physics B 86 (4) (2007) 643–646. doi:10.1007/s00340-006-2436-2.

[140] J. Labaziewicz, P. Richerme, K. R. Brown, I. L. Chuang, K. Hayasaka, Compact, filtered diode laser system for precision spectroscopy, Opt. Lett. 32 (5) (2007) 572–574. doi:10.1364/OL.32.000572.

[141] T. Nazarova, C. Lisdat, F. Riehle, U. Sterr, Low-frequency-noise diode laser for atom interferometry, J. Opt. Soc. Am. B 25 (10) (2008) 1632–1638. doi:10.1364/JOSAB.25.001632.

[142] Y. Zhang, S. Miyakawa, K. Kasai, Y. Okada-Shudo, M. Watanabe, Efficient phase noise suppression of an external-cavity diode-laser by optical filtering and resonant optical feedback, Applied Physics B 108 (1) (2012) 39–42. doi:10.1007/s00340-012-4918-8.

[143] F. Schmid, J. Weitenberg, T. W. Hänsch, T. Udem, A. Ozawa, Simple phase noise measurement scheme for cavity-stabilized laser systems, Opt. Lett. 44 (11) (2019) 2709–2712. doi:10.1364/OL.44.002709.

[144] N. Jiao, R. Li, Y. Wang, W. Zhang, C. Zhang, L. Tian, Y. Zheng, Laser phase noise suppression and quadratures noise intercoupling in a mode cleaner, Optics & Laser Technology 154 (2022) 108303. doi:10.1016/j.optlastec.2022.108303.

[145] L. Krinner, K. Dietze, L. Pelzer, N. Spethmann, P. O. Schmidt, A low phase noise cavity transmission self-injection locked laser system for atomic physics experiments (2023). doi:10.48550/arXiv.2311.03461.

[146] Y.-X. Chao, Z.-X. Hua, X.-H. Liang, Z.-P. Yue, L. You, M. K. Tey, Pound-Drever-Hall feedforward: laser phase noise suppression beyond feedback, Optica 11 (7) (2024) 945–950. doi:10.1364/OPTICA.516838.

[147] L. F. Stokes, M. Chodorow, H. J. Shaw, All-single-mode fiber resonator, Opt. Lett. 7 (6) (1982) 288–290. doi:10.1364/OL.7.000288.

[148] D. G. Rabus, Realization of optical filters using ring resonators with integrated semiconductor optical amplifiers in GaInAsP/InP, Ph.D. thesis, Technische Universität Berlin (2002). doi:10.14279/depositonce-565.

[149] P. Grüning, A. Chaouche-Ramdane, K. Manamanni, T. Aoudjit, V. Roncin, F. Du-Burck, All-fiber ring-cavity for frequency stability transfer at 1.55 µm, Appl. Opt. 58 (6) (2019) 1502–1507. doi:10.1364/AO.58.001502.

[150] B. Little, S. Chu, H. Haus, J. Foresi, J.-P. Laine, Microring resonator channel dropping filters, Journal of Lightwave Technology 15 (6) (1997) 998–1005. doi:10.1109/50.588673.

[151] W. Bogaerts, P. De Heyn, T. Van Vaerenbergh, K. De Vos, S. Kumar Selvaraja, T. Claes, P. Dumon, P. Bienstman, D. Van Thourhout, R. Baets, Silicon microring resonators, Laser & Photonics Reviews 6 (1) (2012) 47–73. doi:10.1002/lpor.201100017.

[152] B. Mou, Y. Boxia, Q. Yan, W. Yanwei, H. Zhe, Y. Fan, W. Yu, Ultrahigh Q SOI ring resonator with a strip waveguide, Optics Communications 505 (2022) 127437. doi:https://doi.org/10.1016/j.optcom.2021.127437.

[153] K. Saleh, A. Bouchier, P. H. Merrer, O. Llopis, G. Cibiel, Fiber ring resonator based optoelectronic oscillator: phase noise optimisation and thermal stability study, in: R. L. Nelson, D. W. Prather, C. A. Schuetz (Eds.), RF and Millimeter-Wave Photonics, Vol. 7936, International Society for Optics and Photonics, SPIE, 2011, p. 79360A. doi:10.1117/12.873755.

[154] K. Saleh, P.-H. Merrer, O. Llopis, G. Cibiel, Optical scattering noise in high Q fiber ring resonators and its effect on optoelectronic oscillator phase noise, Opt. Lett. 37 (4) (2012) 518–520. doi:10.1364/OL.37.000518.

[155] H. Lee, M.-G. Suh, T. Chen, J. Li, S. A. Diddams, K. J. Vahala, Spiral resonators for on-chip laser frequency stabilization, Nature Communications 4 (1) (2013) 2468. doi:10.1038/ncomms3468.

[156] L. Winkler, A. van Rees, P. van der Slot, C. Nölleke, K.-J. Boller, Frequency stabilization of a hybrid-integrated InP-Si3N4 diode laser by locking to a fiber ring resonator, Conference: 25th Annual Symposium of the IEEE Photonics Benelux Chapter 2021, University of Mons, Mons, Belgium, 2021.

[157] A. van Rees, L. V. Winkler, P. Brochard, D. Geskus, P. J. M. van der Slot, C. Nölleke, K.-J. Boller, Long-Term Absolute Frequency Stabilization of a Hybrid-Integrated InP-Si3N4 Diode Laser, IEEE Photonics Journal 15 (5) (2023) 1–8. doi:10.1109/JPHOT.2023.3320393.

[158] V. V. Spirin, J. L. B. Escobedo, D. A. Korobko, P. Mégret, A. A. Fotiadi, Stabilizing DFB laser injection-locked to an external fiber-optic ring resonator, Opt. Express 28 (1) (2020) 478–484. doi:10.1364/OE.28.000478.

[159] G. Perin, D. Mammez, A. Congar, P. Besnard, K. Manamanni, V. Roncin, F. D. Burck, S. Trebaol, Compact fiber-ring resonator for blue external cavity diode laser stabilization, Opt. Express 29 (23) (2021) 37200–37210. doi:10.1364/OE.435513.

[160] B. Merkel, D. Repp, A. Reiserer, Laser stabilization to a cryogenic fiber ring resonator, Opt. Lett. 46 (2) (2021) 444–447. doi:10.1364/OL.413847.

[161] Corning Inc., Corning® ClearCurve® LBL Optical Fiber, accessed: 2025-05-18 (2025).

[162] Corning Inc., Corning® ClearCurve® ZBL Optical Fiber, accessed: 2025-05-18 (2025).

[163] M. J. A. Castelein, Aufbau und Charakterisierung eines Faserresonators, Bachelor's thesis, Heinrich-Heine-Universität Düsseldorf (2024).

[164] Corning Inc., Corning® SMF-28® Ultra Optical Fiber, accessed: 2025-05-18 (2025).

[165] Thorlabs GmbH, Narrowband Fiber Optic Coupler 1550 nm, 50:50 Ratio, accessed: 2025-05-20 (2025).

[166] Thorlabs GmbH, Narrowband Fiber Optic Coupler 1550 nm, 75:25 Ratio, accessed: 2025-05-20 (2025).

[167] Thorlabs GmbH, Narrowband Fiber Optic Coupler 1550 nm, 90:10 Ratio, accessed: 2025-05-20 (2025).

[168] Thorlabs GmbH, Narrowband Fiber Optic Coupler 1550 nm, 99:1 Ratio, accessed: 2025-05-20 (2025).

[169] W. Zhu, E. R. Numkam Fokoua, A. A. Taranta, Y. Chen, T. Bradley, M. N. Petrovich, F. Poletti, M. Zhao, D. J. Richardson, R. SlavÃk, The Thermal Phase Sensitivity of Both Coated and Uncoated Standard and Hollow Core Fibers Down to Cryogenic Temperatures, Journal of Lightwave Technology 38 (8) (2020) 2477–2484. doi:10.1109/JLT.2019.2960437.

[170] Linden Photonics, Inc., Phase Stabilised STOFC Cost Effective, accessed: 2025-05-20 (2025).

[171] M. Bousonville, M. Czwalinna, M. Felber, T. Ladwig, H. Schlarb, S. Schulz, C. Sydlo, P. Kownacki, S. Jablonski, New phase stable optical fiber, Conference: Beam Instrumentation Workshop, Newport News, Virginia, USA, 2012.

[172] S. Hirata, T. Akatsuka, Y. Ohtake, A. Morinaga, Sub-hertz-linewidth diode laser stabilized to an ultralow-drift high-finesse optical cavity, Applied Physics Express 7 (2) (2014) 022705. doi:10.7567/APEX.7.022705.

[173] L. Berthier, G. Biroli, Glasses and Aging, A Statistical Mechanics Perspective on, Springer New York, New York, NY, 2009, pp. 4209–4240. doi:10.1007/978-0-387-30440-3_248.

[174] J. Keupp, A. Douillet, T. E. Mehlstäubler, N. Rehbein, E. M. Rasel, W. Ertmer, A high-resolution Ramsey-Bordé spectrometer for optical clocks based on cold Mg atoms, The European Physical Journal D - Atomic, Molecular, Optical and Plasma Physics 36 (3) (2005) 289–294. doi:10.1140/epjd/e2005-00302-7.

[175] N. O. Zhadnov, K. S. Kudeyarov, D. S. Kryuchkov, G. A. Vishnyakova, K. Y. Khabarova, N. N. Kolachevsky, Long ULE Cavities with Relative Fractional Frequency Drift Rate below 5×10^{-16}/s for Laser Frequency Stabilization, Bulletin of the Lebedev Physics Institute 47 (9) (2020) 257–261. doi:10.3103/S1068335620090079.

[176] I. R. Hill, R. J. Hendricks, S. Donnellan, P. Gaynor, B. Allen, G. P. Barwood, P. Gill, Dual-axis cubic cavity for drift-compensated multi-wavelength laser stabilisation, Opt. Express 29 (22) (2021) 36758–36768. doi:10.1364/OE.436019.

[177] A. Takahashi, Long-term dimensional stability of a line scale made of low thermal expansion ceramic NEXCERA, Measurement Science and Technology 23 (3) (2012) 035001. doi:10.1088/0957-0233/23/3/035001.

[178] S. M. F. Raupach, T. Legero, C. Grebing, C. Hagemann, T. Kessler, A. Koczwara, B. Lipphardt, M. Misera, H. Schnatz, G. Grosche, U. Sterr, Subhertz-linewidth infrared frequency source with a long-term instability below 5×10^{-15}, Applied Physics B 110 (4) (2013) 465–470. doi:10.1007/s00340-012-5280-6.

[179] K. Hosaka, H. Inaba, D. Akamatsu, M. Yasuda, J. Sugawara, A. Onae, F.-L. Hong, A Fabry-Pérot Etalon with an Ultralow Expansion Ceramic Spacer, Japanese Journal of Applied Physics 52 (3R) (2013) 032402. doi:10.7567/JJAP.52.032402.

[180] D. Antypas, O. Tretiak, K. Zhang, A. Garcon, G. Perez, M. G. Kozlov, S. Schiller, D. Budker, Probing fast oscillating scalar dark matter with atoms and molecules, Quantum Science and Technology 6 (2021) 034001. doi:10.1088/2058-9565/abe472.

[181] V. I. Korobov, L. Hilico, J.-P. Karr, Fundamental Transitions and Ionization Energies of the Hydrogen Molecular Ions with Few ppt Uncertainty, Phys. Rev. Lett. 118 (2017) 233001. doi:10.1103/PhysRevLett.118.233001.

[182] W. Paul, H. Steinwedel, Ein neues Massenspektrometer ohne Magnetfeld, Z. Naturforschg. 8a (1953) 448–450.

[183] W. Paul, Electromagnetic traps for charged and neutral particles, Rev. Mod. Phys. 62 (1990) 531–540. doi:10.1103/RevModPhys.62.531.

[184] P. H. Dawson (Ed.), Quadrupole Mass Spectrometry and Its Applications, American Institute of Physics, 1997.

[185] M. Drewsen, A. Brøner, Harmonic linear Paul trap: Stability diagram and effective potentials, Phys. Rev. A 62 (2000). doi:10.1103/PhysRevA.62.045401.

[186] S. Chu, L. Hollberg, J. E. Bjorkholm, A. Cable, A. Ashkin, Three-dimensional viscous confinement and cooling of atoms by resonance radiation pressure, Phys. Rev. Lett. 55 (1985) 48–51. doi:10.1103/PhysRevLett.55.48.

[187] W. D. Phillips, H. Metcalf, Laser Deceleration of an Atomic Beam, Phys. Rev. Lett. 48 (1982) 596–599. doi:10.1103/PhysRevLett.48.596.

[188] C. N. Cohen-Tannoudji, W. D. Phillips, New Mechanisms for Laser Cooling, Physics Today 43 (10) (1990) 33–40. doi:10.1063/1.881239.

[189] H. J. Metcalf, P. Van der Straten, Laser Cooling And Trapping, Springer, New York, 1999. doi:10.1007/978-1-4612-1470-0.

[190] F. G. Major, V. N. Gheorghe, G. Werth, Charged Particle Traps, Springer-Verlag, 2005. doi:10.1007/b137836.

[191] R. H. Dicke, The effect of collisions upon the Doppler width of spectral lines, Phys. Rev. 89 (1953) 472–473. doi:10.1103/PhysRev.89.472.

[192] P. Bowe, L. Hornekæer, C. Brodersen, M. Drewsen, S. Hangst, J. Schiffer, Sympathetic Crystallization of Trapped Ions, Phys. Rev. Lett. 82 (1999) 2071–2074. doi:10.1103/PhysRevLett.82.2071.

[193] B. Roth, S. Schiller, Cold Molecules, Taylor and Francis, 2009, Ch. Sympathetically cooled molecular ions: from principles to first applications, pp. 651–704. doi:10.48550/arXiv.0812.1154.

[194] K. Chen, S. T. Sullivan, E. R. Hudson, Neutral Gas Sympathetic Cooling of an Ion in a Paul Trap, Phys. Rev. Lett. 112 (2014) 143009. doi:10.1103/PhysRevLett.112.143009.

[195] G. Zitzer, J. Tiedau, M. V. Okhapkin, K. Zhang, C. Mokry, J. Runke, C. E. Düllmann, E. Peik, Sympathetic cooling of trapped Th^{3+} alpha-recoil ions for laser spectroscopy, Phys. Rev. A 109 (2024) 033116. doi:10.1103/PhysRevA.109.033116.

[196] B. Roth, J. C. J. Koelemeij, H. Daerr, S. Schiller, Rovibrational spectroscopy of trapped molecular hydrogen ions at millikelvin temperatures, Phys. Rev. A 74 (2006) 040501. doi:10.1103/PhysRevA.74.040501.

[197] C. Wellers, M. R. Schenkel, G. S. Giri, K. R. Brown, S. Schiller, Controlled preparation and vibrational excitation of single ultracold molecular hydrogen ions, Molecular Physics 120 (19-20) (2022) e2001599. doi:10.1080/00268976.2021.2001599.

[198] F. Penning, Ein neues Manometer für niedrige Gasdrucke, insbesondere zwischen 10^{-3} und 10^{-5} mm, Physica 4 (2) (1937) 71–75. doi:10.1016/S0031-8914(37)80123-8.

[199] H. Dehmelt, A single atomic particle forever floating at rest in free space: New value for electron radius, Physica Scripta 1988 (T22) (1988) 102. doi:10.1088/0031-8949/1988/T22/016.

[200] M. Bonaldi, P. Falferi, R. Dolesi, M. Cerdonio, S. Vitale, High Q tunable LC resonator operating at cryogenic temperature, Review of Scientific Instruments 69 (10) (1998) 3690–3694. doi:10.1063/1.1149166.

[201] S. Ulmer, H. Kracke, K. Blaum, S. Kreim, A. Mooser, W. Quint, C. C. Rodegheri, J. Walz, The quality factor of a superconducting rf resonator in a magnetic field, Review of Scientific Instruments 80 (12) (2009) 123302. doi:10.1063/1.3271537.

[202] M. S. Ebrahimi, N. Stallkamp, W. Quint, M. Wiesel, M. Vogel, A. Martin, G. Birkl, Superconducting radio-frequency resonator in magnetic fields up to 6 T, Review of Scientific Instruments 87 (7) (2016) 075110. doi:10.1063/1.4958647.

[203] E. A. Cornell, R. M. Weisskoff, K. R. Boyce, D. E. Pritchard, Mode coupling in a Penning trap: π pulses and a classical avoided crossing, Phys. Rev. A 41 (1990) 312–315. doi:10.1103/PhysRevA.41.312.

[204] S. Goudsmit, R. F. Bacher, The Paschen-Back Effect of Hyperfine Structure, Phys. Rev. 34 (1929) 1499–1500. doi:10.1103/PhysRev.34.1499.

[205] C. M. König, F. Heiße, J. Morgner, T. Sailer, B. Tu, D. Bakalov, K. Blaum, S. Schiller, S. Sturm, Nondestructive Control of the Rovibrational Ground State of a Single Molecular Hydrogen Ion in a Penning Trap, Phys. Rev. Lett. 134 (2025) 163001. doi:10.1103/PhysRevLett.134.163001.

[206] L. S. Brown, G. Gabrielse, Precision spectroscopy of a charged particle in an imperfect Penning trap, Phys. Rev. A 25 (1982) 2423–2425. doi:10.1103/PhysRevA.25.2423.

[207] H. Dehmelt, New continuous Stern-Gerlach effect and a hint of "the" elementary particle, Zeitschrift für Physik D Atoms, Molecules and Clusters 10 (2) (1988) 127–134. doi:10.1007/BF01384846.

[208] C. Smorra, K. Blaum, L. Bojtar, M. Borchert, K. Franke, T. Higuchi, N. Leefer, H. Nagahama, Y. Matsuda, A. Mooser, M. Niemann, C. Ospelkaus, W. Quint, G. Schneider, S. Sellner, T. Tanaka, S. Van Gorp, J. Walz, Y. Yamazaki, S. Ulmer, BASE - The Baryon Antibaryon Symmetry Experiment, Eur. Phys. J. Spec. Top. 224 (2015) 3055–3108. doi:10.1140/epjst/e2015-02607-4.

[209] S. Ulmer, C. Smorra, A. Mooser, K. Franke, H. Nagahama, G. Schneider, T. Higuchi, S. V. Gorp, K. Blaum, Y. Matsuda, W. Quint, J. Walz, Y. Yamazaki, High-precision comparison of the antiproton-to-proton charge-to-mass ratio, Nature 524 (2015) 196–199. doi:10.1038/nature14861.

[210] C. Smorra, S. Sellner, M. J. Borchert, J. A. Harrington, T. Higuchi, H. Nagahama, T. Tanaka, A. Mooser, G. Schneider, M. Bohman, K. Blaum, Y. Matsuda, C. Ospelkaus, W. Quint, J. Walz, Y. Yamazaki, S. Ulmer, A parts-per-billion measurement of the antiproton magnetic moment, Nature 550 (2017) 371–374. doi:10.1038/nature24048.

[211] F. Heiße, S. Rau, F. Köhler-Langes, W. Quint, G. Werth, S. Sturm, K. Blaum, High-precision mass spectrometer for light ions, Phys. Rev. A 100 (2019) 022518. doi:10.1103/PhysRevA.100.022518.

[212] M. Leonhardt et al., Proton transport from the antimatter factory of CERN, Nature 641 (8064) (2025) 871–875. doi:10.1038/s41586-025-08926-y.

[213] H. Häffner, S. Gulde, M. Riebe, G. Lancaster, C. Becher, J. Eschner, F. Schmidt-Kaler, R. Blatt, Precision Measurement and Compensation of Optical Stark Shifts for an Ion-Trap Quantum Processor, Phys. Rev. Lett. 90 (2003) 143602. doi:10.1103/PhysRevLett.90.143602.

[214] S. Schiller, D. Bakalov, A. K. Bekbaev, V. I. Korobov, Static and dynamic polarizability and the Stark and blackbody-radiation frequency shifts of the molecular hydrogen ions H_2^+, HD^+, and D_2^+, Phys. Rev. A 89 (2014) 052521. doi:10.1103/PhysRevA.89.052521.

[215] S. Schiller, V. I. Korobov, D. Bakalov, I. A. Aucar, Energy shifts of the molecular hydrogen ions in strong magnetic field, in preparation (2025).

[216] C. Cohen-Tannoudji, B. Diu, F. Laloe, Quantum Mechanics, Volume 2, Vol. 2, 1986.

[217] D. Bakalov, V. Korobov, S. Schiller, Magnetic field effects in the transitions of the HD^+ molecular ion and precision spectroscopy, J. Phys. B: At. Mol. Opt. Phys. 44 (2011) 025003. doi:10.1088/0953-4075/44/2/025003.

[218] J.-P. Karr, S. Schiller, V. I. Korobov, S. Alighanbari, Determination of a set of fundamental constants from molecular hydrogen ion spectroscopy: A modeling study, Phys. Rev. A 112 (2025) 022809. doi:10.1103/jz54-7f7b.

[219] R. A. Hegstrom, g factors and related magnetic properties of molecules. Formulation of theory and calculations for H_2^+, HD^+, and D_2^+, Phys. Rev. A 19 (1979) 17–30. doi:10.1103/PhysRevA.19.17.

[220] E. Hecht, Optik, 7th Edition, De Gruyter, 2018. doi:10.1515/9783110526653.

[221] D. J. Griffiths, Introduction to Electrodynamics, 4th Edition, Cambridge University Press, 2017. doi:10.1017/9781108333511.

[222] M. Born, E. Wolf, Principles of Optics, 7th Edition, Cambridge University Press, 1999. doi:10.1017/CBO9781139644181.

[223] P. W. Milonni, J. H. Eberly, Laser Physics, John Wiley & Sons, Ltd, 2010. doi:10.1002/9780470409718.

[224] I. H. Malitson, Interspecimen Comparison of the Refractive Index of Fused Silica, J. Opt. Soc. Am. 55 (10) (1965) 1205–1209. doi:10.1364/JOSA.55.001205.

[225] C. Tan, Determination of refractive index of silica glass for infrared wavelengths by IR spectroscopy, Journal of Non-Crystalline Solids 223 (1) (1998) 158–163. doi:10.1016/S0022-3093(97)00438-9.

[226] S. Sarkar, V. Gupta, M. Kumar, J. Schubert, P. T. Probst, J. Joseph, T. A. F. König, Hybridized Guided-Mode Resonances via Colloidal Plasmonic Self-Assembled Grating, ACS Applied Materials & Interfaces 11 (14) (2019) 13752–13760. doi:10.1021/acsami.8b20535.

[227] M. Polyanskiy, Refractive Index Database, https://refractiveindex.info, accessed: 2025-05-05.

[228] J. D. L. Allan W. Snyder, Optical Waveguide Theory, 1st Edition, Springer New York, NY, 1983. doi:10.1007/978-1-4613-2813-1.

[229] W. Nagourney, Quantum Electronics for Atomic Physics and Telecommunication, Oxford University Press, 2014.

[230] C. Yeh, Handbook of Fiber Optics: Theory and Applications, Academic Press, 2013.

[231] A. E. Siegman, Lasers, University Science Books, 1986.

[232] M. C. T. Bahaa E. A. Saleh, Fundamentals of Photonics, John Wiley & Sons, Ltd, 1991. doi:10.1002/0471213748.

[233] A. Yariv, P. Yeh, Photonics: Optical Electronics in Modern Communications, Oxford University Press, 2007.

[234] W. Riley, D. Howe, Handbook of Frequency Stability Analysis, Special Publication (NIST SP), National Institute of Standards and Technology, Gaithersburg, MD, 2008.

[235] W. T. Silfvast, Laser Fundamentals, 2nd Edition, Cambridge University Press, 2004.

[236] G. F. Franklin, J. D. Powell, A. Emami-Naeini, Feedback Control of Dynamic Systems, 3rd Edition, Addison-Wesley ed., 1995.

[237] S. Zacher, M. Reuteri, Regelungstechnik für Ingenieure, Springer Vieweg Wiesbaden, 2014. doi:10.1007/978-3-8348-2216-1.

[238] P. Woolf, et al., Chemical Process Dynamics and Controls, University of Michigan, 2009.

[239] E. Rubiola, Phase Noise and Frequency Stability in Oscillators, The Cambridge RF and Microwave Engineering Series, Cambridge University Press, 2008.

[240] F. Riehle, Frequency standards: basics and applications, Wiley, 2005.

[241] G. Harry, T. Bodiya, R. DeSalvo, Optical Coatings and Thermal Noise in Precision Measurement, Cambridge University Press, 2012. doi:10.1017/CBO9780511762314.

[242] E. Rubiola, F. Vernotte, The Companion of Enrico's Chart for Phase Noise and Two-Sample Variances, IEEE Transactions on Microwave Theory and Techniques 71 (7) (2023) 2996–3025. doi:10.1109/TMTT.2023.3238267.